UNIVERSITÉ DE LORRAINE | BIBLIOTHÈQUES UNIVERSITAIRES

AVERTISSEMENT
DROIT D'AUTEUR

Ce document est le fruit d'un long travail approuvé par le jury de soutenance et mis à disposition de l'ensemble de la communauté universitaire élargie.

Il est soumis à la propriété intellectuelle de l'auteur. Ceci implique une obligation de citation et de référencement lors de l'utilisation de ce document. Toute contrefaçon, plagiat ou reproduction illicite encourt une poursuite pénale.

Contact bibliothèque : ddoc-theses-contact@univ-lorraine.fr
(Cette adresse ne permet pas de contacter les auteurs)

Code de la Propriété Intellectuelle. articles L 122. 4
Code de la Propriété Intellectuelle. articles L 335.2- L 335.10

UNIVERSITÉ DE LORRAINE
34 COURS LÉOPOLD — CS 25233
54052 NANCY CEDEX
TÉL : 03 54 50 54 00
CONTACT@UNIV-LORRAINE.FR
WWW.UNIV-LORRAINE.FR

UNIVERSITÉ DE LORRAINE
École doctorale C2MP
Institut Jean Lamour

Université franco-allemande
Deutsch-Französische Hochschule

RPTU Rheinland-Pfälzische Technische Universität Kaiserslautern Landau

Heusler compounds for magnonic and spintronic applications

PhD thesis
Thèse / Dissertation

Anna Maria Friedel

Thèse présentée et soutenue publiquement pour l'obtention du titre de

Docteur de l'université de Lorraine
mention: **Physique**

par **Anna Maria Friedel**

sous la direction de **Dr. Stéphane Andrieu,**
Dr. Sébastien Petit-Watelot,
Dr. Philipp Pirro

dans le cadre d'une cotutelle avec le RPTU Kaiserslautern-Landau à Kaiserslautern, Allemagne.

Date de la soutenance de thèse: 03.09.2025.

Vom Fachbereich Physik der Rheinland-Pfälzischen Technischen Universität Kaiserslautern-Landau zur Verleihung des akademischen Grades

Doktor der Naturwissenschaften

genehmigte Dissertation, durchgeführt im Rahmen einer gemeinsamen Promotion mit der Université de Lorraine in Nancy, Frankreich,

unter Anleitung von **Dr. Stéphane Andrieu,**
Dr. Sébastien Petit-Watelot,
Dr. Philipp Pirro.

Datum der wissenschaftlichen Aussprache: 03.09.2025.

Examination committee / Membres du jury / Prüfungskommission:

President, Reviewer	**Dr. Grégoire de Loubens**	**Research director (CEA)** *SPEC CEA Saclay, Gif-sur-Yvette, France*
Reviewer	**Dr. Matthieu Bailleul**	**Research director (CNRS)** *IPCMS, Strasbourg, France*
Examinators	**Dr. Pauline Rovillain**	**Lecturer (Maître de conférences)** *Sorbonne Université, Paris, France*
	Dr. Angela Wittmann	**Junior Professor** *JGU, Mainz, Germany*
	Dr. Mathias Weiler	**Professor** *RPTU Kaiserslautern-Landau, Kaiserslautern, Germany*
Supervisors	**Dr. Philipp Pirro**	**Junior Professor** *RPTU Kaiserslautern-Landau, Kaiserslautern, Germany*
	Dr. Sébastien Petit-Watelot	**Lecturer (Maître de conférences)** *Université de Lorraine, Nancy, France*
	Dr. Stéphane Andrieu	**Professor** *Université de Lorraine, Nancy, France*

DE-386

Context of this PhD thesis

A joint French-German doctorate within an international *cotutelle* agreement

The work presented in this thesis with the title *Heusler compounds for magnonic and spintronic applications* was conducted between July 2021 and June 2025 within a binational PhD programme (*cotutelle internationale*) at the Institut Jean Lamour, Université de Lorraine (Nancy, France) and the Rheinland-Pfälzische Technische Universität (RPTU) Kaiserslautern-Landau (Kaiserslautern, Germany).

The author of this thesis was officially registered as a doctoral student in both universities and the doctorate was carried out according to an individual cotutelle agreement concluded between the two universities, the three supervisors and the PhD student, recoginising the applicable doctoral degree regulations of both, the doctoral school C2MP (*école doctorale chimie, mécanique, matériaux, physique*) of the Université de Lorraine as well as the department of physics (*Fachbereich Physik*) of the RPTU Kaiserslautern-Landau.

The dissertation was submitted to the department of physics in Kaiserslautern as well as the doctoral school C2MP in Nancy on Tuesday, 24. June 2025. The dissertation was evaluated on the basis of written review reports submitted by Dr. Grégoire de Loubens, Dr. Matthieu Bailleul and Dr. Philipp Pirro. The joint PhD defence took place in Nancy, France on Wednesday, 03. September 2025, before the examination committee comprised of:

President:	Dr. Grégoire de Loubens	Research director (CEA), SPEC CEA Saclay, France
Reviewers:	Dr. Grégoire de Loubens	Research director (CEA), SPEC CEA Saclay, France
	Dr. Matthieu Bailleul	Research director (CNRS), IPCMS Strasbourg, France
Examinators:	Dr. Pauline Rovillain	Lecturer, Sorbonne Université Paris, France
	Dr. Angela Wittmann	Junior Professor, JGU Mainz, Germany
	Dr. Mathias Weiler	Professor, RPTU Kaiserslautern-Landau, Germany
Supervisors:	Dr. Philipp Pirro	Junior Professor, RPTU Kaiserslautern-Landau, Germany
	Dr. Sébastien Petit-Watelot	Lecturer, Université de Lorraine, France
	Dr. Stéphane Andrieu	Professor, Université de Lorraine, France

This PhD thesis was supported by a cotutelle de thèse stipend funded by the Deutsch-Französische Hochschule (DFH) / Université franco-allemande (UFA).

Colophon

Template, typesetting and compatibility

This document was typeset using LaTeX and the KOMA-Script bundle, employing the kaobook class template by Frederico Marotta, itself based on the doctoral thesis of Ken Arroyo Ohori and on the Tufte-LaTeX class. The template choice and style of this thesis was inspired by the doctoral thesis of Lukas Körber equally typeset in the kaobook class. To suit the layout requirements for this thesis, some minor adaptations were made to the kaobook template by Frederico Marotta. To ensure a compatibility across common systems, the main text is typeset in Palatino (serif) and the text in figures is embedded as curves. The figures were created using `matplotlib` and Affinity Designer 2 unless stated otherwise. The figures in this document, in particular the high resolution images in the transmission electron microscopy chapter 3, are optimised for a display on screen.

Versioning

Submitted version: 24. June 2025.
Published version: 28. January 2026.

Université de Lorraine
Institut Jean Lamour
Campus Artem
54000 Nancy
France

RPTU Kaiserslautern-Landau
Fachbereich Physik
Erwin-Schrödinger-Str. 56
67663 Kaiserslautern
Germany

Abstract

This thesis explores the potential of Co_2Mn-based Heusler compounds for bridging the gap between nonlinear magnonic and spintronic applications, with a particular focus on the half-metallic Co_2MnSi. The overarching goal positions this work right at the heart of state-of-the-art research efforts towards overcoming timely societal challenges linked to the increasing importance of Artificial Intelligence and the resulting exploding demand in computation power and unconventional computing approaches.

A key potential for unconventional computing lies in the field of magnetism, notably in the sub-fields of magnonics and spintronics, where the intrinsic nonlinearity of the magnetisation dynamics promises vast possibilities for a natural device functionality beyond the conventional CMOS technology. Hereby, research in magnonics is centred around spin waves, the collective excitations of an ordered magnetic system, and their application for information transport and processing. Spintronic applications make use of spin-dependent electron transport in the form of spin (polarised) currents and its interaction with the magnetisation of a material.

Recently, sub-communities in both fields have increasingly developed towards an exploitation of the intrinsic nonlinearity, notably in the direction of nonlinear spin wave dynamics in magnonics, and nonlinear magnetisation dynamics driven by spin (polarised) currents in spintronic oscillators. Advances in both fields promise great potential for neuromorphic computing approaches. Naturally, the two fields increasingly intertwine and many promising advances and preliminary device prototypes aim at combining the "best of both worlds". This request for a combination naturally comes with a few challenges and open issues to address. Notably, the concept of spin polarisation and its implications in combination with magnonic spin transport becomes increasingly important for research at the intersection between both fields, an open issue which is particularly timely also in view of the recently increasing interest in the spin polarisation of altermagnets and its fundamental implications.

An ideal model system intrinsically positioned at the intersection of magnonics and spintronics is given by half-metals, magnetic materials which present a full spin polarisation linked to their peculiar band structure. In particular the Heusler compound Co_2MnSi promises great potential for nonlinear applications combining desirable key parameters with the experimentally proven full spin polarisation, and additionally the high saturation magnetisation and a record-low magnetic damping for metallic films. Yet, while exploration has been done on the spintronics side, research on the magnonics side is still scarce.

In view of this context, this thesis is dedicated to an evaluation of the suitability of the half-metallic Heusler compound Co_2MnSi for an exploitation towards nonlinear magnonic and spintronic applications. To this aim, several key aspects are addressed, resulting in a few major conclusions:

- Record-low nonlinear threshold powers are obtained in a microsized Co_2MnSi device with experimentally verified half-metallicity.
- A significant signature of the self-induced nonlinear shift is observed and can enable a frequency selective self-enhancement/self-capping behaviour as commonly sought-after in neuromorphic circuits.
- A defect-less device fabrication preserving an impeccable $L2_1$-order is achieved, showcasing the successful patterning of structures down to the smallest intended structure sizes of $w \approx 50\,\mathrm{nm}$ waveguide width.
- A significant cubic anisotropy is determined, not only defining the nonlinear instability ranges, but also pointing towards a significant second order term with a peculiar fingerprint on the expectable spin wave characteristics.

With these major findings, the thesis consolidates the potential of the half-metallic Heusler compound Co_2MnSi as a model system even at the nanoscale. Moreover, the results pave the way for a future exploitation in hybrid magnonic and spintronic applications, and outline several promising perspectives for future work in this freshly opened field of half-metal magnonics.

Résumé français

Cette thèse explore le potentiel des composés de Heusler à base de Co_2Mn pour combler le fossé entre les applications magnoniques non linéaires et spintroniques, en mettant particulièrement l'accent sur le Co_2MnSi demi-métallique. L'objectif global place ce travail au cœur des efforts de recherche de pointe visant à relever les défis sociétaux actuels liés à l'importance croissante de l'intelligence artificielle et à l'explosion de la demande en puissance de calcul et en approches informatiques non conventionnelles qui en résulte.

Le magnétisme, et plus particulièrement les sous-domaines de la magnonique et de la spintronique, offre un potentiel clé pour l'informatique non conventionnelle. En effet, la non-linéarité intrinsèque de la dynamique de l'aimantation ouvre de vastes possibilités pour la mise au point de dispositifs dépassant naturellement les capacités de la technologie CMOS conventionnelle. La recherche en magnonique est centrée sur les ondes de spin, qui sont des excitations collectives d'un système magnétique ordonné, et sur leur application au transport et au traitement de l'information. Les applications spintroniques utilisent le transport d'électrons dépendant du spin sous forme de courants de spin (polarisés) et son interaction avec l'aimantation d'un matériau.

Récemment, des sous-communautés dans ces deux domaines se sont de plus en plus orientées vers l'exploitation de la non-linéarité intrinsèque, notamment dans le sens de la dynamique non linéaire des ondes de spin en magnonique et de la dynamique non linéaire de l'aimantation induite par des courants de spin (polarisés) dans les oscillateurs spintroniques. Les progrès réalisés dans ces deux domaines sont très prometteurs pour les approches de calcul neuromorphique. Naturellement, ces deux domaines s'entremêlent de plus en plus et de nombreuses avancées prometteuses et dispositifs préliminaires visent à combiner « le meilleur des deux mondes ». Cette demande de combinaison s'accompagne naturellement de quelques défis et questions ouvertes à résoudre. Notamment, le concept de polarisation de spin et ses implications en combinaison avec le transport de spin magnonique devient de plus en plus important pour la recherche à l'intersection des deux domaines, une question ouverte qui est particulièrement d'actualité compte tenu de l'intérêt croissant récent pour la polarisation de spin dans l'altermagnétisme et ses implications fondamentales.

Les demi-métaux, matériaux magnétiques qui présentent une polarisation de spin totale liée à leur structure de bande particulière, constituent un système modèle idéal, intrinsèquement situé à l'intersection de la magnonique et de la spintronique. En particulier, le composé de Heusler Co_2MnSi offre un grand potentiel pour des applications non linéaires combinant des paramètres clés souhaitables avec une polarisation de spin de 100% prouvée expérimentalement, ainsi qu'une aimantation à saturation élevée et un amortissement magnétique record-bas pour les films métalliques. Cependant, si des recherches ont été menées dans le domaine de la spintronique, celles portant sur la magnonique sont encore rares.

Dans ce contexte, cette thèse est consacrée à l'évaluation de l'adéquation du composé de Heusler demi-métallique Co_2MnSi pour une exploitation dans des applications magnoniques et spintroniques non linéaires. À cette fin, plusieurs aspects clés sont abordés, qui aboutissent à quelques conclusions majeures :

- Des puissances de seuil non-linéaires les plus basses jamais reportées sont obtenues dans un dispositif Co_2MnSi de taille microscopique avec une demi-métallicité vérifiée expérimentalement.
- Une signature significative du décalage de fréquence non-linéaire auto-induit est observée et peut permettre un comportement d'auto-amélioration/auto-limitation sélectif en fréquence, très recherché dans les circuits neuromorphiques.
- La fabrication des dispositifs sans défaut préservant un ordre $L2_1$ parfait a été réalisée, démontrant la réussite de la structuration jusqu'aux plus petites tailles prévues de $w \approx 50\,\text{nm}$ de largeur de guide d'onde.
- Une anisotropie cubique significative a été déterminée, définissant non seulement les plages d'instabilité non-linéaire, mais indiquant également un terme d'ordre deux significatif avec une empreinte particulière sur les caractéristiques attendues des ondes de spin.

Grâce à ces découvertes majeures, la thèse consolide le potentiel du composé demi-métallique Heusler Co_2MnSi en tant que système modèle, même à l'échelle nanoscopique. De plus, les résultats ouvrent la voie à une exploitation future dans des applications hybrides magnoniques et spintroniques, et esquissent plusieurs perspectives prometteuses pour les travaux futurs dans ce nouveau domaine de la magnonique demi-métallique.

Deutsche Kurzzusammenfassung

Diese Arbeit untersucht das vielversprechende Potenzial von Co_2Mn-basierten Heusler-Legierungen für die Überbrückung der Lücke zwischen nichtlinearen magnonischen und spintronischen Anwendungen, wobei ein besonderer Schwerpunkt auf der 100% spin-polarisierten Heusler-Legierung Co_2MnSi liegt. Das übergeordnete Ziel positioniert diese Arbeit im Herzen der aktuellen Forschungsbemühungen zur Bewältigung heutiger gesellschaftlicher Herausforderungen besonders im Zusammenhang mit der zunehmenden Bedeutung der künstlichen Intelligenz und dem daraus resultierenden explosionsartigen Bedarf an Rechenleistung und unkonventionellen Rechenansätzen.

Ein wesentliches Potenzial für unkonventionelles Computing liegt im Bereich des Magnetismus, insbesondere in den Teilgebieten Magnonik und Spintronik, wo die intrinsische Nichtlinearität der Magnetisierungsdynamik enorme Möglichkeiten für eine natürliche Funktionalität jenseits der herkömmlichen CMOS-Technologie verspricht. Dabei konzentriert sich die Forschung in der Magnonik auf Spinwellen, die kollektiven Anregungen eines geordneten magnetischen Systems, und deren Anwendung für den Transport und die Verarbeitung von Informationen. Spintronische Anwendungen hingegen nutzen den spinabhängigen Elektronentransport in Form von Spinströmen und spinpolarisierten Strömen und deren Wechselwirkung mit der Magnetisierung eines Materials.

In den letzten Jahren haben sich Subfelder in beiden Bereichen zunehmend auf die Nutzung der intrinsischen Nichtlinearität konzentriert, insbesondere in Richtung nichtlinearer Spinwellen-Dynamik in der Magnonik und Spinstrom-getriebener nichtlinearer Magnetisierungsdynamik in spintronischen Oszillatoren. Fortschritte in beiden Bereichen versprechen ein großes Potenzial für neuromorphe Computing-Ansätze. Dementsprechend verflechten sich die beiden Bereiche zunehmend, und einige vielversprechende Fortschritte zielen darauf ab, das „Beste aus beiden Welten" zu vereinen. Dieser Wunsch nach einer Kombination bringt einige Herausforderungen und offene Forschungsfragen mit sich. Insbesondere das Konzept der Spinpolarisation und seine Auswirkungen in Kombination mit dem magnonischen Spintransport gewinnen für die Forschung an der Schnittstelle beider Bereiche zunehmend an Bedeutung – eine offene Frage, die auch angesichts des zuletzt gestiegenen Interesses an der Spinpolarisation von Altermagneten und ihren grundlegenden Auswirkungen besonders aktuell ist.

Ein ideales Modellsystem, das sich intrinsisch an der Schnittstelle zwischen Magnonik und Spintronik befindet, sind halb-metall-magnetische Materialien, die aufgrund ihrer besonderen Bandstruktur eine vollständige Spinpolarisation aufweisen. Insbesondere die Heusler-Verbindung Co_2MnSi verspricht großes Potenzial für nichtlineare Anwendungen, da sie wünschenswerte Schlüsselparameter mit der experimentell nachgewiesenen vollständigen Spinpolarisation sowie einer hohen Sättigungsmagnetisierung und einer rekordverdächtig niedrigen magnetischen Dämpfung für metallische Schichten kombiniert. Während auf der Seite der Spintronik bereits einige Untersuchungen an diesem Material durchgeführt wurden, sind auf der Seite der Magnonik noch kaum Forschungsarbeiten zu verzeichnen.

Vor diesem Hintergrund widmet sich diese Arbeit der Bewertung der Eignung der halbmetallischen Heusler-Verbindung Co_2MnSi für nichtlineare magnonische und spintronische Anwendungen. Zu diesem Zweck werden mehrere Schlüsselaspekte untersucht, die zu einigen wichtigen Schlussfolgerungen führen:

- In einem mikrodimensionierten Co_2MnSi-Wellenleiter mit experimentell nachgewiesener 100% Spinpolarisation werden rekordverdächtig niedrige nichtlineare Schwellenleistungen erzielt.
- Es wird ein deutliches Anzeichen für eine selbstinduzierte nichtlineare Verschiebung beobachtet, die ein frequenzselektives Selbstverstärkungs-/Selbstbegrenzungsverhalten ermöglichen könnte, wie es in neuromorphen Anwendungen häufig angestrebt wird.
- Es wird eine erfolgreiche Mikrostrukturierung unter Beibehaltung einer einwandfreien $L2_1$-Ordnung erreicht, die die Strukturierung bis hin zu den kleinsten vorgesehenen Strukturgrößen mit einer Wellenleiterbreite von $w \approx 50\,\mathrm{nm}$ demonstriert.
- Es wird ein signifikanter kubischer Anisotropiebeitrag bestimmt, der nicht nur die Bereiche der nichtlinearen Instabilität definiert, sondern auch auf einen nicht vernachlässigbaren Term zweiter Ordnung mit besonderen Auswirkungen auf die zu erwartenden Spinwellencharakteristika hinweist.

Mit diesen wichtigen Erkenntnissen festigt die Arbeit das Potenzial der 100% spinpolarisierten Heusler-Verbindung Co_2MnSi als Modellsystem sogar im Nanobereich. Darüber hinaus ebnen die Ergebnisse den Weg für eine zukünftige Nutzung in hybriden magnonischen und spintronischen Anwendungen und die Schlussfolgerungen skizzieren werden mehrere vielversprechende Perspektiven für zukünftige Forschungsarbeiten in dem neu begründeten Forschungsfeld der Halb-Metall-Magnonik.

16. Der Inhalt der Physik geht die Physiker an, die Auswirkung alle Menschen.

17. Was alle angeht, können nur alle lösen.

18. Jeder Versuch eines Einzelnen, für sich zu lösen, was alle angeht, muß scheitern.

– Friedrich Dürrenmatt (1962), *'21 Punkte zu den >Physikern<'*

Acknowledgements, Remerciments, Danksagung

Doing a PhD in experimental physics is an educational process with quite many analogies to training for a glider pilot license. To me, this analogy is particularly beautiful and well-fitting, as it a personal one, which holds true on various levels from the general setting to funny details, but also because both experiences have been very formative and because both would've been impossible without incountable contributions by numerous people.

Both start with the need to find a suitable group offering the desired training, that is at least one instructor and a host institution joined by the shared interest or passion, be it a supervisor in a research institute or a flying club with flight instructors. I would like to thank my supervisors Stéphane Andrieu, Sébastien Petit-Watelot and Philipp Pirro, for giving me the opportunity to pursue this project and the freedom in doing so, for supporting me and believing in me from the start to the end, for trusting me with the supervision of Bachelor/Master students and for continuously challenging me to outgrow myself. In terms of clubs, I got the chance to formally join two research groups, the SPIN Team at IJL lead at the time by Stéphane Mangin, now Thomas Hauet, as well as the magnetism group at RPTU lead by Burkard Hillebrands, and I would like to express my thanks to both for their support.

Before starting, there is often an administrative process to be mastered, and in the case of an all-time-first cotutelle this can become surprisingly complex. Here, huge thanks go to the staff at école doctorale C2MP, the RH team at the IJL and the Dekanat of the department of physics at the RPTU, for all the help with the paperwork and admin steps we naively (luckily) hadn't seen coming.

Finally admitted to the training phase, neither gliding nor a PhD can be easily pursued without a crew, and I would like to thank all members of the various *centres de compétences* at the Institut Jean Lamour, notably the entire CC D.a.u.m. team, the CC 3M team, particularly Sylvie Migot and Jaafar Ghanbaja, the CC MagCryo team, especially Stéphane Suire, as well as the CC X-Gamma, CC Ermione and CC Minalor teams. On the RPTU-side, I would like to equally thank the entire team of the Nanostructuring centre. Also, I am very grateful to all the peers who helped with various steps in this work, particular thanks go to Claudia de Melo Sanchez, Victor Palin, Alberto Anadón, Héloïse Damas, Nicolas Fermon, Moritz Bechberger and Björn Heinz, and all other great colleagues in the SPIN Team at IJL as well as all the members of the RPTU research groups on magnetism, nanoscaled magnonic hybrids and applied spin phenomena. Special mention to Julius Hohlfeld for giving me an unexpected pre-defence confidence boost by placing the first "order" of my PhD thesis manuscript. Thank you all for the supportive team spirit, the fun and friendly work atmosphere and the inspiring discussions around physics and beyond.

Ultimately, the intense training leads to increasing autonomy and brings memorable milestones along the way. There are big intermediate steps, such as the first solo flight every glider pilot remembers, probably just like every PhD student under Stéphane Andrieu remembers the first time they were allowed to start a process on the holy MBE without Stéphane or any other senior user present*. Quite some contributions stem from fruitful collaborations with people from neither of the two institutes, here I would like to thank Matthieu Bailleul, Yves Henry and José Solano from IPCMS in Strasbourg for the fruitful collaboration and the spin wave Doppler shift devices aka *the baby*, John Gregg, Sally Lord, Finlay Ryburn and William Henderson from University of Oxford for the inspiring discussions and the collaboration on the coupled Heusler multilayers, Nicolas Fermon from Ecole Normale Superieure Paris-Saclay for his great work during his M1 research work in Kaiserslautern, and Iciar Arnay at imdea nanociencia in Madrid as well as Cecilia Granados-Miralles at CSIC Instituto de Cerámica y Vidrio in Madrid for the collaboration around our joint IEEE magnetics society seed funding project. Finally, there are two big and very memorable milestones in the end: the thesis itself and the final exam or defence. For the former, I would like to thank Lukas Körber for the stylistic and graphical inspiration drawn from his beautifully crafted PhD thesis. For the latter, I would like to thank the reviewers Grégoire de Loubens and Matthieu Bailleul, as well as the examinators Pauline Rovillain, Angela Wittmann and Mathias Weiler for kindly taking over the roles in the examination committee.

There are many more memories than could be recounted here, and none of this would have been possible without the funding I received supporting my collaborations, mobility and four-year PhD position, notably from the IEEE Magnetics Society, the Deutsch-Französische Hochschule, and my supervisors' ANR and ERC grants.

* Funnily enough, one is often asked after the first solo flight whether one sang a song alone up there in the air, and although I still haven't come to a conclusion to which point this might be relevant in either case, I have indeed sung/hummed in both moments (unsurprisingly, I know).

Most of these memories are tied to the people who have accompanied me along this journey.

Many thanks to my numerous office mates at IJL and RPTU, Kaushalya, Philippe Scheid, Boris Seng, Jérémy Létang, Alberto Anadón, Mariam Martirosyan, Corentin Pfaff, Jingya Huang, Harvey Weinberger, Misbah Yaqoob, Moritz Geilen, Abbas Koujok for the fantastic atmosphere, discussions and shared joy and tears.

Many thanks to the break crews in various constellations at IJL, from croissant breaks to lunch breaks to coffee breaks or tea breaks, cheers to the 101s Quentin Remy, Jean-Loïs Bello, Maxime Vergès, Valentin Desbuis, Héloïse Damas, Alberto Anadón, Jon Gorchon, Sébastien Petit-Watelot, Junta Igarashi, Eva Diaz, Sandrine Lopes, Jun-Xiao Lin, Po-Wei Lee, Yi Peng, Yann Le Guen, Jude Compton-Stewart, Akilan K, Harjinder Singh, Tobias Sparmann, Corentin Aulagnet, Hyacinthe Cabrel Tadaha, Leo Petitdemange, Pierre Chailloleau, Victor Huet, to the "Pause IJL" group on the 2nd floor Mariam Martirosyan, Maxence Antoine, Guillaume Lo-Cascio, Nathan Boulangeot, Clovis Lapointe, Loris Raspado, Lucie Gutman, Sebastien Geyskopf, and to the Cuban bubble Claudia de Melo Sanchez, Alejandro Borroto Ramírez, Alexis Carlos García Wong, Agathe Virfeu, Adrian Alberto Benedit Cardenas.

Many thanks to all the people who've provided me with a home, formed a home or helped me move from one home to another. Claudia y Alejandro, gracias por acogerme durante semanas en vuestro salón, por compartir trabajo y descansos, comidas y actividades. Me habéis hecho sentir como en casa desde el primer momento, muchas gracias por todo. Seb, Amélie et Romane, je vous remercie pour l'acceuil chaloureux en famille, pour l'hébergement, pour toutes les repas partagés, et lectures de *Die kleine Raupe Nimmersatt*, pour me faire découvrir vos endroits préférés à Nancy et toutes les mots comme *licorne* que je n'aurais probablement jamais appris autrement, et surtout pour tout l'aide à m'installer à Nancy après. Eva and Junta, thank you for being my Nancy-home, for the many moments, meals, cocktails and late night chats we shared, all the things we've mastered together and for being a reliable space to safely return home to. Many thanks also to Stéphane Mangin and Karine Dumesnil for setting us up and entrusting us with the miraculous "professor's house" and our beloved Gustave, who's been an astonishingly precise alarm every morning at 06h30, but still has won my heart with ease. Jude, thank you for joining our Nancy-home for a while, for hours of garden work, NJP concerts, and numerous other memories, many of which can be summarised as: Thank you for not being mad about my chaotic organisation. Friends and family who've helped me with moving houses a million times, Ben, Martin, Ralf, Andrea, Eva, Jude, Yann, Valentin, Héloïse, Junta, Eva, Philipp, Moritz, Nessa and most importantly Mama, Laura, Georg, Eddie, danke, danke, danke.

And then there are all the friends I've been able to count on in these four years. I am unable to list everybody for German privacy regulations, but you all have contributed to incountable shared memories, from simply hanging out or talking for hours on the phone, to political and philosophical discussions around coffee, activities like board game nights, improving my film education with movie nights or cinema visits, dressing up for a funky Kappensitzung, thermal bath sessions, picknicks, attempting to eat through all restaurants in Nancy (we failed), climbing trees in Romania, dancing everywhere, concert and festival visits, spontanous day trips, weekend escapes or even full holidays around Spain, France, Belgium, the UK ... Thank you all! Most importantly, I've been able to count on your friendship and support not only for simple things like moving houses, but also in the most challenging times. Sometimes things go crazy, and here special thanks go to Quentin, Jean-Loïs, Valentin, for the encouragement, to Jon, for being there, and to María José and Sarah, for being impressive. Massive thanks also to Alberto, Héloïse, Nicolas, Quentin, Elias, Philipp, Lukas, Lukas and Ben, for the support when maxxed-out stress levels were too much to bear alone. Thanks also to Yahya, Elias and Nico for cheering me up with surprise postcards, particularly throughout the final year. Plus, Hélo, Jude and Nico, thank you so much for carrying all the defence party organisation together with my mum.

Finally, I would like to thank my family, who have always supported me in whatever I have undertaken, from pilot licences to a PhD in physics and anything in between. Mama und Papa, danke, dass ihr mich ermuntert habt, jede Ausbildung, Auslandserfahrung und sonstige Gelegenheit zum stetigen Lernen anzunehmen, all diese Chancen als solche gesehen und gefördert habt. Danke, dass ihr immer an mich glaubt, "sowieso alles mit links" zu schaffen. Laura, Georg und Eddie, und der Julian ist auch dabei, ihr seid der Hit und ich bin super stolz auf euch. Riesengroßensuperdank für alles, we are shipping, woher kommen die Gläser, this is forbidden, was heißt eigentlich Sackkarre auf Englisch, Anna du arbeitest viel zu viel, uzuzuz, oh das war der 2h-cut von meinem Telefon, nächster Umzug mal ohne Klavier, undundund. Vor allem für eure Unterstützung, den besten Abgabetag, den ich mir wünschen konnte, die beste Aussprachefeier der Welt, und, dass ihr inzwischen manchmal besser wisst als ich, was ich brauch. Ihr seid mir wichtig, ich hab' euch lieb. Zu guter Letzt, danke auch an Leo pupsidupsi.

Confirming what Dürrenmatt noted long ago: none of this could have been achieved alone. Thank you all.

Contents

Abstract iii

Résumé français v

Kurzzusammenfassung vii

Acknowledgements xi

Contents xiii

Introduction and context of this thesis 1

Part I
Structural properties of Co_2Mn-based Heusler thin films and nanostructures 5

1 *Background:* Co_2Mn-based Heusler compounds 7
1.1 Crystal structure of Heusler compounds . . . 7
1.2 Half-metal magnetism . . . 8
1.2.1 Composition dependence in half-metallic Heusler compounds . . . 9
1.2.2 Implications of half-metal magnetism for spintronics and magnonics . . . 10
1.3 Factors affecting the half-metallicity . . . 11
1.3.1 Chemical disorder phenomena . . . 12
1.4 Selection of compounds in this thesis . . . 13
1.4.1 Focus on Co_2MnSi . . . 13
1.4.2 Reference values for Heusler compounds in this thesis . . . 15
1.5 Concluding remarks . . . 16

2 *Samples:* Epitaxial thin film growth and sample series in this work 17
2.1 Epitaxy setup and experimental methods . . . 17
2.1.1 Molecular beam epitaxy (MBE) setup . . . 17
2.1.2 Reflection high-energy electron diffraction (RHEED) . . . 19
2.1.3 Auger spectroscopy . . . 22
2.2 Epitaxial growth process . . . 23
2.2.1 Substrate preparation . . . 23
2.2.2 Heusler layer deposition . . . 24
2.2.3 Capping layer deposition . . . 26
2.3 List of sample series and purpose . . . 28
2.3.1 Co_2MnSi series for magnonic micro/nanostructures . . . 29
2.3.2 Co_2MnX series for magneto-optical signal study . . . 30
2.3.3 $Co_2MnSi/X/Co_2MnAl$ series for coupling investigations . . . 31
2.3.4 Cr/V seed layer series for interface dislocation tests . . . 32

3 Structural characterisation and effects of micro/nanofabrication 33
3.1 Sample preparation and experimental methods . . . 33
3.1.1 Cross section preparation by Ga^+ FIB . . . 33
3.1.2 TEM sample geometry and chemical contrast . . . 35

3.1.3 Energy dispersive X-ray spectroscopy . . . 36
3.2 Co_2Mn-based Heusler thin film stacks: interfaces, chemical ordering and capping . . . 37
3.2.1 Chemical ordering . . . 37
3.2.2 Lattice mismatch with MgO and interface dislocations . . . 39
3.2.3 Protection by the capping layer . . . 43
3.3 Co_2MnSi micro/nanostructures . . . 46
3.3.1 Micro-/Nanostructuring process . . . 47
3.3.2 Sample layout and FIB cut . . . 49
3.3.3 Lithography results and defect analysis . . . 50
3.4 Conclusions . . . 60

Part II
Magnetic and magneto-optical properties of Co_2Mn-based Heusler thin films 63

4 *Background:* Fundamental concepts of magnetism, spin dynamics and magneto-optical interactions 65
4.1 Ferromagnetism, anisotropies and hysteresis . . . 65
4.1.1 Magnetic ordering . . . 65
4.1.2 Magnetic anisotropy . . . 68
4.1.3 Magnetic hysteresis . . . 73
4.2 Magnetisation oscillations and magnetic damping . . . 75
4.2.1 Equation of motion . . . 75
4.2.2 Linearisation and magnetic susceptibility . . . 76
4.2.3 Ferromagnetic resonance . . . 78
4.2.4 Resonance linewidths in the LLG formalism and beyond . . . 79
4.2.5 Magnetic damping mechanisms . . . 81
4.3 Magneto-optical interactions . . . 85
4.3.1 Magneto-optical Kerr effect . . . 85
4.3.2 Brillouin light scattering . . . 90
4.4 Concluding remarks . . . 92

5 *Methods:* Magnetic and magneto-optical thin film characterisation 93
5.1 Vibrating sample magnetometry (VSM) . . . 93
5.1.1 Measurement principle and experimental setup . . . 93
5.1.2 Data post-processing . . . 95
5.2 Ferromagnetic resonance (FMR) spectroscopy . . . 97
5.2.1 Broadband-FMR (BB-FMR): experimental setup and technique . . . 97
5.2.2 Non-calibrated BB-FMR: effect of the data analysis procedure on the resonance linewidth 100
5.3 Magneto-optical Kerr effect (MOKE) magnetometry . . . 106
5.3.1 Measurement principle and experimental setup . . . 106
5.3.2 Separation of linMOKE and QMOKE contributions . . . 108
5.4 Conventional Brillouin light scattering (BLS) . . . 109
5.4.1 Measurement principle and experimental setup . . . 109
5.4.2 Data evaluation for the BLS intensity analysis . . . 110

6 Magnetic properties of epitaxial Co_2MnSi and Co_2MnAl Heusler thin films 111
6.1 Static properties: Magnetic moment and hysteresis . . . 111
6.1.1 Co_2MnSi film . . . 112
6.1.2 Co_2MnAl film . . . 114
6.1.3 Comparison of Co_2MnSi and Co_2MnAl . . . 116

6.2 Magnetisation dynamics . . . 118
6.2.1 Anisotropic FMR analysis . . . 121
6.2.2 Anisotropy interpretation . . . 129
6.2.3 Linewidth analysis . . . 133
6.3 Conclusions . . . 136

7 Magneto-optical signal from Co_2Mn-based Heusler thin films **137**
7.1 MOKE measurements and QMOKE signature . . . 137
7.1.1 Magnetic anisotropy in the linMOKE . . . 139
7.1.2 Magneto-optical anisotropy in the QMOKE . . . 140
7.2 Wavelength dependence in linMOKE and QMOKE . . . 142
7.3 Signal intensity from thermal spin waves in conventional BLS . . . 145
7.4 Conclusions . . . 147

Part III
Nonlinear magnonic spin transport in Co_2MnSi-based microstructures **149**

8 *Background:* Concepts of spin dynamics in anisotropic microstructures **151**
8.1 Linear spin waves . . . 151
8.1.1 Dispersion relation for anisotropic thin films . . . 152
8.1.2 Limitations of the Kalinikos-Slavin approximation . . . 153
8.1.3 Properties of spin waves in thin films . . . 153
8.1.4 Effective anisotropy tensors and their influence on the ellipticity of the precession . . . 155
8.1.5 Demagnetisation and width modes in waveguides . . . 161
8.2 Nonlinear spin waves . . . 162
8.2.1 Multi-magnon scattering and Suhl instabilities . . . 162
8.2.2 Nonlinear frequency shift . . . 164
8.2.3 Hamilton formalism for spin wave dynamics . . . 165
8.2.4 Nonlinear dynamics in the Hamiltonian . . . 166
8.3 Concluding remarks . . . 169

9 *Methods:* Probing spin wave dynamics in half-metallic Co_2MnSi microstructures **171**
9.1 Sample specifications and device geometry . . . 171
9.1.1 Thin film stack and structural properties . . . 171
9.1.2 Spin wave Doppler shift device . . . 173
9.2 Microfocused Brillouin light scattering (μBLS) . . . 175
9.2.1 Time-resolved μBLS measurements . . . 176

10 Nonlinear spin waves in a microsized half-metallic Co_2MnSi waveguide **177**
10.1 Spin wave excitation spectra . . . 178
10.1.1 Overview of detected spectral characteristics . . . 178
10.1.2 Antenna excitation and dispersion relation . . . 181
10.2 2nd order Suhl instability onset . . . 183
10.2.1 Frequency dependency . . . 186
10.2.2 Power dependency . . . 188
10.2.3 Time-resolved instability onset . . . 199
10.3 Conclusion . . . 202

Conclusion and perspectives **205**

Appendix **211**

A RHEED image sequences of the entire growth process **213**

B Further EDXS mapping of the structured samples **215**

C Anisotropy - energy, fields and tensors **221**

D Kalinikos-Slavin dispersion formula and FMR **249**

E FMR data evaluation comparison **253**

F Synthèse en français **269**

Bibliography **283**

List of figures **310**

List of tables **311**

List of symbols and abbreviations **312**

Alphabetical Index **313**

Publications **315**

Curriculum vitae **317**

Introduction and context of this work

Throughout physics history, expanding the experimentally accessible range of parameters has generally opened new playgrounds for scientists, often enabling a verification of established theories and sometimes even allowing for breakthrough discoveries.

Prominent examples can be found along the list of Nobel Prizes, including, for instance, the 2007 Nobel Prize awarded to Albert Fert and Peter Grünberg [1, 2] for the discovery of the giant magneto resistance (GMR) in 1988 [3, 4], in part enabled by advances in ultrathin epitaxial film growth [1]. These groundbreaking reports on the GMR rapidly led to commercialised applications [5] and boosted the research interest in the field of spin-dependent electron transport, nowadays commonly referred to as *spintronics* [6–12].

[1]: Fert (2008)
[2]: Grünberg (2008)
[3]: Baibich et al. (1988)
[4]: Binasch et al. (1989)
[5]: Daughton (1999)
[6]: Ohno (2001)
[7]: Wolf et al. (2001)
[8]: Grundler (2002)
[9]: Žutić et al. (2004)
[10]: Chappert et al. (2007)
[11]: Bader et al. (2010)
[12]: Tsymbal et al. (2019)

Spintronics, magnonics and the spin polarisation

A central point of interest in spintronics is the concept of spin transport in the form of spin currents. Various milestone works span for instance the generation of spin currents and spin-charge interconversion [13–16] and the magnetisation manipulation and switching [17–22] among other aspects. Hereby, it is commonly differentiated between *spin polarised currents*, i.e. charge currents with an imbalance of spin-up and spin-down electrons, and *pure spin currents* with zero net charge flow.

[13]: Dyakonov et al. (1971)
[14]: Hirsch (1999)
[15]: Kato et al. (2004)
[16]: Saitoh et al. (2006)
[17]: Slonczewski (1996)
[18]: Berger (1996)
[19]: Katine et al. (2000)
[20]: Zhang et al. (2004)
[21]: Yang et al. (2008)
[22]: Brataas et al. (2012)

In magnetic materials, the spin polarisation is an intrinsic material property linked to the time-reversal symmetry breaking spin-splitting in the electronic band structure. The first prediction of a full spin polarisation in the half-Heusler compound NiMnSb [23] introduced the concept of *half-metal magnetism* and attracted great attention to the fascinatingly versatile class of Heusler compounds in search of further half-metal candidates [24–29]. Apart from the potential in view of device applications, half-metals theoretically offer a unique model system of an extreme case in spintronics.

[23]: De Groot et al. (1983)
[24]: Hillebrands et al. (2006)
[25]: Graf et al. (2011)
[26]: Mizukami et al. (2015)
[27]: Hirohata et al. (2015)
[28]: Felser et al. (2016)
[29]: Xie et al. (2025)

Indeed, the 100% spin polarisation yields a great tool especially for investigations on the experimentally observable implications of the spin polarisation, a general interest in which is currently fuelled by the spin polarisation forming a key characteristic for the distinction between different magnetic phases, such as altermagnetic and antiferromagnetic materials [30–32]. Curiously, in half-metals, the common concept of pure spin currents becomes impossible to combine with the complete absence of states for one spin type at the Fermi energy. This principally imposes a restriction of pure spin transport to the form of *spin waves* [33] as is common in magnetic insulators and central to the research field of *magnonics* [34–42]. Half-metals are therefore particularly interesting to address principal questions on the spin polarisation related magnonic spin transport characteristics.

[30]: Šmejkal et al. (2022)
[31]: Šmejkal et al. (2022)
[32]: Fedchenko et al. (2024)
[33]: Kajiwara et al. (2010)
[34]: Kruglyak et al. (2006)
[35]: Serga et al. (2010)
[36]: Khitun et al. (2010)
[37]: Lenk et al. (2011)
[38]: Chumak et al. (2015)
[39]: Pirro et al. (2021)
[40]: Barman et al. (2021)
[41]: Chumak et al. (2022)
[42]: Flebus et al. (2024)

Moreover, contrary to magnetic insulators commonly employed in magnonics, the half-metallic materials allow for an exploitation of fully polarised charge currents. This is not only a desirable property for hybrid magnonic-spintronic applications [43–49], but also intrinsically positions the half-metallic materials at the intersection of magnonics and spintronics, essentially defining the contextual frame of this thesis.

[43]: Vlaminck et al. (2008)
[44]: Madami et al. (2011)
[45]: Evelt et al. (2016)
[46]: Gladii et al. (2016)
[47]: Meyer et al. (2018)
[48]: Demidov et al. (2020)
[49]: Salikhov et al. (2023)

Co_2MnSi for nonlinear magnetisation dynamics

In recent years, the research within both fields has increasingly developed towards the exploitation of nonlinear magnetisation dynamics, especially motivated by the potential for neuromorphic computing approaches. On the spintronics side, remarkable advances are centred around spin torque oscillators [50–52] and simultaneous advances in nonlinear magnonics [53–58] have led to an increased intertwining of the two fields for combined devices towards an unconventional computing in the GHz regime [59–62]. The motivated intrinsic intersectional positioning of half-metallic materials naturally points to a consideration as candidates for such hybrid approaches, where particularly the full spin polarisation could offer great efficiency for the spin torque induced nonlinear threshold control [60], amplification [61], and redirection [62] of spin waves.

Indeed, especially the Co_2Mn-based Heusler compounds combine various desirable properties: Notably for Co_2MnSi, the combination of a large saturation magnetisation $M_S \approx 1000\,\mathrm{kA/m}$ [63] and the record-low Gilbert damping parameter for metallic thin films of 4.6×10^{-4} [64] promise low nonlinear thresholds, high spin wave group velocities and large propagation distances. And in particular for its promised full spin polarisation, the material has been studied extensively in spintronic applications already in the early 2000s [65–67].

However, although the half-metallicity of Co_2MnSi was predicted in 1995 [68], a direct experimental verification has only been reported recently [69, 70], mainly linked to the particularly crucial requirement of a precise stoichiometry and chemical ordering [24, 28, 71]. Hence, only since the experimental confirmation, notably enabled by the advances on the epitaxial growth of impeccable $L2_1$-ordered Co_2MnSi films [71], the half-metallic Heusler compound has become a realistic choice for a reliably fully spin polarised material.

Nevertheless, the strong dependence on the crystallographic and chemical ordering [72, 73] makes the materials particularly sensitive to structural damage [74–76] and hence still implies great challenges for maintaining the desirable properties throughout a device fabrication process [77].

Moreover, while various studies have investigated the spintronic properties and application of the half-metallic Co_2Mn-based compounds [78–81], experimental research on the magnonics side is rather scarce. This is in parts linked to the peculiar magneto-optical properties and resulting relatively poor magneto-optical signal from Co_2MnSi in the accessible wavelength range by Brillouin light scattering (BLS) [82, 83], and has resulted in earlier studies mainly focusing on the compound $Co_2Mn_{0.6}Fe_{0.4}Si$ instead [84–88].

Only recently, the half-metallic Co_2MnSi has been employed in a study on the spin wave propagation distance in macroscopic (90 µm wide) waveguides [89], in another on the spin wave modes in a magnonic crystal [90], and, in relation to the work in the present thesis, in a third study on the spin-polarized transport in a microscopic (10 µm wide) spin wave Doppler shift device [91]. The results promise spin wave propagation lengths of up to 100 µm [89], a potential for an exploitation of the cubic anisotropy [90] and an experimentally proven 100% spin polarisation even in the microstructured spin wave Doppler shift device [91].

In view of this context, an experimental study of the half-metallic Co_2MnSi compound towards nonlinear magnonic-spintronic applications is of great interest and particularly timely.

[50]: Torrejon et al. (2017)
[51]: Grollier et al. (2020)
[52]: Marrows et al. (2024)
[53]: Brächer et al. (2018)
[54]: Wang et al. (2020)
[55]: Papp et al. (2021)
[56]: Fripp et al. (2023)
[57]: Wang et al. (2024)
[58]: Breitbach et al. (2024)
[59]: Hamadeh et al. (2022)
[60]: Hache et al. (2023)
[61]: Merbouche et al. (2024)
[62]: Menezes et al. (2024)
[63]: Webster (1971)
[64]: Guillemard et al. (2019)
[65]: Schmalhorst et al. (2004)
[66]: Sakuraba et al. (2005)
[67]: Sakuraba et al. (2006)
[68]: Ishida et al. (1995)
[69]: Jourdan et al. (2014)
[70]: Andrieu et al. (2016)
[71]: Guillemard et al. (2020)
[72]: Gaier et al. (2008)
[73]: Shaw et al. (2018)
[74]: Hamrle et al. (2007)
[75]: Abdallah et al. (2016)
[76]: Abdallah et al. (2017)
[77]: Mantion et al. (2022)
[78]: Chudo et al. (2011)
[79]: Sasaki et al. (2020)
[80]: Létang et al. (2021)
[81]: De Melo et al. (2021)
[82]: Silber et al. (2020)
[83]: Friedel (2021)
[84]: Sebastian et al. (2012)
[85]: Sebastian et al. (2013)
[86]: Pirro et al. (2014)
[87]: Sebastian et al. (2015)
[88]: Sebastian et al. (2016)
[89]: Stückler et al. (2018)
[90]: Mantion et al. (2024)
[91]: Solano Córdova (2024)

Scope, open questions and outline of this work

Consequently, the overarching goal of this work is to explore the suitability of the half-metallic Heusler compound Co_2MnSi for an exploitation in nonlinear applications at the intersection of magnonics and spintronics.

In view of the above context, various key questions are to be addressed prior to a successful exploitation in devices:

- How are the crucial structural properties affected by a typical nanofabrication process?
- What is the signature of the cubic anisotropy and its impact on the expectable spin wave properties?
- Can the magneto-optical signal be optimised by an adequate choice of parameters for a detection by BLS and μBLS?
- Can the expectable low nonlinear threshold be confirmed? What are the characteristics of the nonlinear spin wave dynamics?

These questions will be addressed in this thesis, which is, to this aim, structured in three parts:

1. The first part is dedicated to the thin film fabrication and the structural properties of the Co_2Mn-based Heusler compounds. In three chapters[1] it will introduce the peculiar material properties of this group, the sample fabrication by epitaxial thin film growth, and a structural characterisation by transmission electron microscopy.
    - A particular point of interest in this first part is the structural analysis of the effects of a typical top-down nanofabrication process involving electron lithography and ion beam etching, in context with recent reports on the impact of structural damage to the resulting magnetisation dynamics [77]. Here, it can already be anticipated that waveguides with widths of $w \approx 50\,\mathrm{nm}$ were successfully fabricated with an impeccable structure even at the etched borders.
2. The second part is dedicated to the study of the general magnetic and magneto-optical properties of epitaxial Co_2Mn-based Heusler thin films and is organised in four chapters[2], presenting a brief introduction to the fundamental concepts, an overview over the experimental techniques, and the results on the magnetic and magneto-optical characterisation of Co_2Mn-based Heusler thin films.
    - This part can be considered as a fundamental pre-step, in particular the evaluation of the key parameters for the magnetisation dynamics by ferromagnetic resonance spectroscopy, where a main focus is set on the investigation of the relevant anisotropy terms and particular attention is employed in the study of the narrow resonance linewidths. A notable result here is the non-negligible second order cubic anisotropy term and its direction-dependent silimarity with an out-of-plane anisotropy for (001) oriented films.
    - Additionally, a magneto-optical study explores the attainable signal intensities in the compounds, in context with the peculiar magneto-optical behaviour reported for Co_2MnSi in [82].
3. The third part is dedicated to the study of the spin wave characteristics in a half-metallic Co_2MnSi-based magnonic micro-device. This part is again organised in three chapters[3], first introducing the relevant conceptual

1: See:
chapter 1 from page 7,
chapter 2 from page 17,
chapter 3 from page 33.

[77]: Mantion et al. (2022)

2: See:
chapter 4 from page 65,
chapter 5 from page 93,
chapter 6 from page 111,
chapter 7 from page 137.

[82]: Silber et al. (2020)

3: See:
chapter 8 from page 151,
chapter 9 from page 171,
chapter 10 from page 177.

frame of linear and nonlinear spin waves, followed by a brief methodological chapter, before presenting an analysis of the predominantly nonlinear spin wave dynamics observed in a first exploratory study.

- Here, an interesting point is the principal directional dependence introduced by the cubic anisotropy terms and one direct implication of the non-negligible anisotropy is an increased frequency threshold for first order Suhl instability processes.
- In the experiments, record-low nonlinear thresholds are obtained which is linked to the device design and in parts attributed to the experimentally proven half-metallicity in the studied spin wave Doppler shift device [91] in comparison with an analogous study [86] on a non-epitaxial $Co_2Mn_{0.6}Fe_{0.4}Si$ waveguide of comparable parameters[4].
- Additionally, the peculiar antenna characteristics allow to explore the impact of the self-induced nonlinear frequency shift, and here it can be anticipated that based on the results in this thesis great potential is expected particularly when for the use in nonlinear ring resonators [54] in view of an application towards neuromorphic magnonic-spintronic circuits.

Given the broad range of topics covered and the substantial length of certain discussions, each non-technical chapter will conclude with a summary highlighting the key findings and their implications for further research within and beyond the scope of this thesis.

A final concluding chapter will synthesise the main results and explore future perspectives for half-metallic Co_2Mn-based Heusler compounds in magnonic and spintronic device applications.

[91]: Solano Córdova (2024)

[86]: Pirro et al. (2014)

4: $Co_2Mn_{0.6}Fe_{0.4}Si$ waveguide in [86]:
$M_S = 1003\,\mathrm{kA/m}$,
$A_{exch} = 13\,\mathrm{pJ/m}$,
$\alpha = 3 \times 10^{-3}$,
$w = 5\,\mu\mathrm{m}$,
$d = 30\,\mathrm{nm}$.
Co_2MnSi waveguide here [91]:
$M_S = 1058\,\mathrm{kA/m}$,
$A_{exch} = 19.5\,\mathrm{pJ/m}$,
$\alpha = 1 \times 10^{-3}$,
$w = 10\,\mu\mathrm{m}$,
$d = 20\,\mathrm{nm}$.

[54]: Wang et al. (2020)

Part I
Structural properties of Co_2Mn-based Heusler thin films and nanostructures

Background: Co_2Mn-based Heusler compounds

1

This PhD work is centred around Co_2Mn-based Heusler compounds, with a focus set on the half-metallic compound Co_2MnSi, investigating their applicability to research areas in the fields of magnonics and spintronics. Co_2Mn-based Heusler compounds form a particular subgroup in the vast class of Heusler materials, which has been known for over a century [92].

Indeed, the class of Heusler materials has gained increasing research interest since the first reports, part of which is summarised in detail in a recent book on the matter [28]. The class includes compounds with various magnetic phenomena, and additionally comes with the possibility of engineering certain compounds to exhibit desired parameters, resulting in a colloquial labelling as a material group "with *à la carte* magnetic properties" [93].

Consequently, Heusler compounds are of particular interest to the magnetism community and, more specifically, the subgroup of Co_2Mn-based Heusler compounds has gained increasing importance for applications in the fields of spintronics and magnonics, an exemplary representation of which can be obtained when looking at the recently completed PhD works covering the topic, see selected examples in [91, 94–107]. Studies performed in the last two decades solely in this niche field range from the characterisation of various magnetic and magneto-optical properties [94, 95, 98, 99, 101, 102] to application-oriented investigations such as the engineering of the compounds' spin polarisation or magnetic anisotropies [103, 105] or the effects of microstructuring processes [99, 106] and the spin wave properties in microstructures [91, 96, 97, 100], and even a few specific device applications such as the implementation in vortex oscillators [104] or magnonic crystals [106].

This chapter aims at giving a brief overview of the relevant concepts of Heusler compounds in order to provide a base for the further discussions in this thesis. A specific focus is set on the peculiar characteristics of Co_2Mn-based Heusler compounds, in particular of Co_2MnSi, and on the resulting implications for spintronic/magnonic applications, for which the properties are set in context with other common materials in the field.

1.1 Crystal structure 7
1.2 Half-metal magnetism . . . 8
Composition dependence . 9
Implications 10
1.3 Factors affecting the half-metallicity 11
Chemical disorder 12
1.4 Compounds in this thesis . 13
Focus on Co_2MnSi 13
Reference values 15
1.5 Concluding remarks 16

[92]: Knowlton et al. (1912), 'The Heusler alloys'
[28]: Felser et al. (2016), *Heusler Alloys*
[93]: Galanakis (2016), '1: Theory of Heusler and Full-Heusler Compounds'

[91]: Solano Córdova (2024)
[94]: Gaier (2009)
[95]: Ortiz Hernandez (2013)
[96]: Sebastian (2013)
[97]: Pirro (2014)
[98]: Neggache (2014)
[99]: Abdallah (2016)
[100]: Meyer (2017)
[101]: Pradines (2017)
[102]: Silber (2019)
[103]: Guillemard (2019)
[104]: Létang (2020)
[105]: Palin (2023)
[106]: Mantion (2023)
[107]: Islam (2025)

1.1 Crystal structure of Heusler compounds

Heusler compounds are characterised by a 2:1:1 stoichiometric composition of X_2YZ, where X and Y are usually transition metals and Z is a main group element. They generally crystallise in the $L2_1$ structure in the Strukturbericht notation (cubic space group no. 225, $Fm\bar{3}m$ in the Hermann-Mauguin notation), essentially consisting of four face-centred-cubic (fcc) sublattices as is shown in the schematic in figure 1.1 (a).

The class of Heusler materials also contains compounds with a 1:1:1 stoichiometry, corresponding to a chemical formula XYZ and resulting in the resulting in the $C1_b$ structure (cubic space group no. 216, $F\bar{4}3m$), which are typically specified as *half-Heusler* or *semi-Heusler* materials [93]. The difference lies essentially in one of the sublattices in figure 1.1 (a) being left unoccupied, and the Heusler compounds with chemical formula X_2YZ are therefore occasionally denoted as *full Heusler* compounds for a clear distinction.

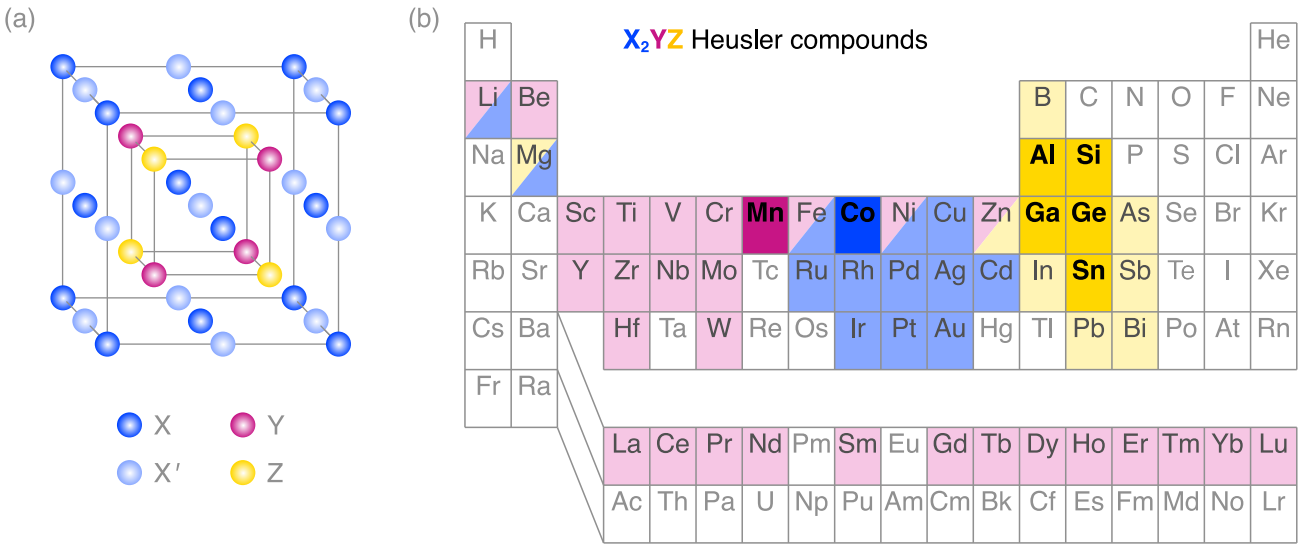

Figure 1.1: Illustration of (a) the general Heusler lattice structure with the four sublattices and (b) a periodic table, with a colour code for possible combinations of elements on the different lattice sites. In full Heuslers, the X and X' sublattices are occupied by the same element, resulting in the X_2YZ formula and the $L2_1$ structure[1]. In half-Heuslers, the X' sublattice is unoccupied, yielding XYZ and the $C1_b$ structure. Only full Heusler compounds were studied in this thesis work and the related elements are highlighted in bold fonts and colours. Mn and Co can occupy the X and Y sublattice, but for clarity have been highlighted here only in the colour corresponding to the Co_2Mn-based compounds used in this work. Figure based on [25].

All Co_2Mn-based Heusler compounds studied in this work are *full Heusler* compounds, and the selection of chemical compositions relevant for this thesis is indicated in figure 1.1 (b).

1.2 Half-metal magnetism

The concept of half-metal magnetism was introduced in 1983 by de Groot *et al.* [23] with their prediction concerning the half-Heusler compound NiMnSb. For full Heusler compounds, first predictions of potential half-metallicity were published in 1995 by Ishida *et al.* [68] in their studies on Co_2Mn-based Heusler compounds.

In general, half-metallicity defined as the property of materials presenting a particular band structure: The electronic bands of only one spin direction exhibit a band gap at the Fermi energy throughout the whole Brillouin zone, while for the other spin direction a non-zero density of states is observed at the Fermi energy. In consequence, only the electrons of the latter can contribute to the conduction. The term *half-metal* describes thus the coexistence of two different conduction behaviours (metallic for one spin type, semiconducting/insulating for the other) in one single material.

The spin-dependent band gap is therefore essential for the occurrence of half-metallicity, and the underlying origin of the phenomenon generally depends on the type of band gap[2] present [109]. While initially discovered in Heusler compounds, the phenomenon is not unique to this material class but has indeed been found or predicted for materials in other classes as well: One example[3] of significance in spintronics is the manganite $La_{0.7}Sr_{0.3}MnO_3$ (LSMO) [93, 110]. Yet, some candidates and notably LSMO only exhibit half-metallicity at very low temperatures [110]. Heusler compounds on the other hand, especially in the subgroup of Co_2Mn-based compounds, present comparably large Curie temperatures and a significant temperature robustness, making them a popular choice for the exploitation of half-metals in spintronic applications.

1: Note that in this schematic the atomic positions are shifted by $(\frac{1}{4}, \frac{1}{4}, \frac{1}{4})$ with respect to the standard cell of the $Fm\bar{3}m$ structure [108].

[108]: Kandpal et al. (2007), 'Calculated electronic and magnetic properties of the half-metallic, transition metal based Heusler compounds'

[25]: Graf et al. (2011), 'Simple rules for the understanding of Heusler compounds'

[23]: De Groot et al. (1983), 'New Class of Materials'

[68]: Ishida et al. (1995), 'Search for Half-Metallic Compounds in Co_2MnZ (Z=IIIb, IVb, Vb Element)'

2: Fang *et al.* [109] report different microscopic origins for covalent band gaps, charge-transfer band gaps, and d-d band gaps and emphasise the importance of that differentiation notably concerning the robustness to disorder, defects, interfaces or external perturbations.

[109]: Fang et al. (2002), 'Spin-polarization in half-metals (invited)'

3: Apart from (full and half-) Heusler compounds, 9 other material groups are known to contain half-metals: "some oxides (e.g. CrO_2 and Fe_3O_4), the magnanites (e.g. $La_{0.7}Sr_{0.3}MnO_3$), the double perovskites (e.g. Sr_2FeReO_6), the pyrites (e.g. CoS_2), the transition metal chalcogenides (e.g. CrSe) and pnictides (e.g. CrAs) in the zinc-blende or wurtzite structures, the europium chalcogenides (e.g. EuN), the diluted magnetic semiconductors (e.g. Mn impurities in Si or GaAs) and the so-called d^0 ferromagnets like CaAs" [93].

[93]: Galanakis (2016), '1: Theory of Heusler and Full-Heusler Compounds'

[110]: Park et al. (1998), 'Direct evidence for a half-metallic ferromagnet'

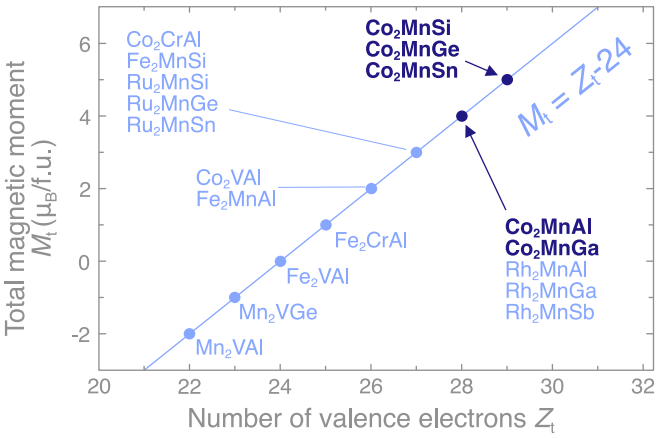

Figure 1.2: Slater-Pauling behaviour of a selection of half-metallic X_2YZ Heusler compounds: The calculated magnetic moment scales linearly with the number of valence electrons. Compounds studied in this work are highlighted in bold. Figure adapted from [114].

1.2.1 Composition dependence in half-metallic Heusler compounds

Slater-Pauling behaviour of the magnetic moment

Slater-Pauling curves were initially introduced for the classification of the types of magnetic behaviour in metallic alloys [111], evaluating the linear relationship of the transition metal magnetisation as a function of the electron-to-atom ratio [112]. Shortly after the discovery of half-metal magnetism in Heusler compounds [23], the Slater-Pauling construction was expanded to include non-transition metals [112] and Heusler compounds were tested on the behaviour in multiple subsequent studies, e.g. [113, 114].

Indeed, the magnetisation of many half-metallic Heusler compounds has been confirmed in theoretical works [108, 113, 114] as well as in experimental studies [71, 115] to follow the Slater-Pauling rule, i.e. a linear relation between the total magnetic moment and the number of valence electrons in a unit cell [114]. For full Heusler compounds, this rule is given by the formula

$$M_t = Z_t - 24 \tag{1.1}$$

where $M_{f.u.}$ is given in μ_B/f.u., i.e. Bohr magneton per formula unit[4], and Z_t is the total number of valence electrons [114]. In particular, the Co_2Mn-based Heusler compounds studied in this work are known to follow the Slater-Pauling rule in equation 1.1, yielding a total magnetic moment of 4 μ_B/f.u. for Co_2MnAl and Co_2MnGa, as well as 5 μ_B/f.u. for Co_2MnSi, Co_2MnGe and Co_2MnSn, as shown in figure 1.2.

Tunability

As suggested by the Slater-Pauling curve in figure 1.2, quarternary compounds like $Co_2MnAl_xSi_{1-x}$ allow for a tuning of the magnetisation between the values of the respective two full Heusler compounds [116]. In addition, the composition of quarternary Heusler compounds has been reported to yield a tunability of various properties like the lattice constant, the spin polarisation and the related magnetic damping parameter as well as the ultrafast demagnetisation time [116], and is therefore an important feature towards the aforementioned "*à la carte*" application of Heusler compounds.

[114]: Galanakis et al. (2002), 'Slater-Pauling behavior and origin of the half-metallicity of the full-Heusler alloys'

[111]: Friedel (1958), 'Metallic alloys'

[112]: Williams et al. (1983), 'Generalized Slater-Pauling curve for transition-metal magnets'

[23]: De Groot et al. (1983), 'New Class of Materials'

[108]: Kandpal et al. (2007), 'Calculated electronic and magnetic properties of the half-metallic, transition metal based Heusler compounds'

[113]: Kübler (1984), 'First principle theory of metallic magnetism'

[114]: Galanakis et al. (2002), 'Slater-Pauling behavior and origin of the half-metallicity of the full-Heusler alloys'

[71]: Guillemard et al. (2020), 'Issues in growing Heusler compounds in thin films for spintronic applications'

[115]: Brown et al. (2000), 'The magnetization distributions in some Heusler alloys proposed as half-metallic ferromagnets'

4: The related magnetisation in kA/m can be obtained by

$$M\left[\frac{\mathrm{kA}}{\mathrm{m}}\right] = M\left[\frac{\mu_B}{\mathrm{f.u.}}\right] \cdot \frac{\mu_B \cdot N_{\mathrm{f.u.}}}{V_{\mathrm{u.c.}}} \tag{1.2}$$

where $V_{\mathrm{u.c.}} = a^3$ is the volume of a unit cell with lattice parameter a and $N_{\mathrm{f.u.}}$ the number of formula units per unit cell. $N_{\mathrm{f.u.}} = 4$ for the Heusler compounds.

[116]: Guillemard et al. (2020), 'Engineering $Co_2MnAl_xSi_{1-x}$ Heusler Compounds as a Model System to Correlate Spin Polarization, Intrinsic Gilbert Damping, and Ultrafast Demagnetization'

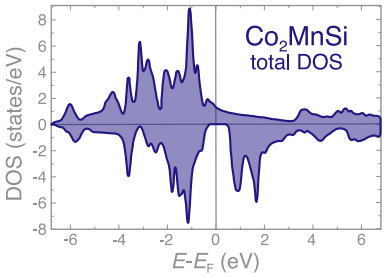

Figure 1.3: Illustration of a half-metallic density of states (DOS): The full band gap at the Fermi energy E_F results in a zero DOS for one spin type only, and consequently a 100% spin polarisation is obtained. Figure adapted from [117].

[117]: Kumar et al. (2024)

1.2.2 Implications of half-metal magnetism for spintronics and magnonics

The interest of half-metals in particular for spintronic and magnonic applications is mainly due to two properties which are direct consequences of the half-metallic band structure: the full spin polarisation and the associated low damping due to the suppression of spin flip scattering.

Spin polarisation

The spin polarisation is generally given by the difference in the densities of states for the majority and minority spin bands, $D_\uparrow$ and $D_\downarrow$, an example of which is illustrated in figure 1.3. Precisely, the spin polarisation is

$$P(E_F) = \frac{D_\uparrow(E_F) - D_\downarrow(E_F)}{D_\uparrow(E_F) + D_\downarrow(E_F)} \tag{1.3}$$

at the Fermi energy E_F, and in half-metallic materials yields $P(E_F) = 100\%$.

The concept of spin polarisation is substantial in spintronics, where many effects and device efficiencies scale with the degree of spin polarisation. One famous[5] example are magnetoresistive effects in *spin valves* [3, 4] or *magnetic tunnel junctions* (MTJ) [118]. In such heterostructures, not only the magnetoresistive effects increase with increasing degree of spin polarisation, but it also enables the switching of the magnetic configuration: Upon injection of a *spin polarised current*, the magnetisation can be manipulated by *spin transfer torque* (STT) [17, 18]. Notably, the combination of both, MTJs and STT switching, has led to the development of STT-MRAM storage, one of the few commercially established spintronic applications [119, 120]. Current developments in the field involve the use of *spin orbit torque* (SOT) switching for improved device efficiencies, relying on *pure spin currents*, i.e. currents with a 100% spin polarisation, typically injected from a heterostructure involving a non-magnetic heavy-metal [121]. Due to their full spin polarisation, half-metal magnets are generally of high interest for such spintronic applications.

Certainly, the importance of spin polarisation is not limited to the field spintronic storage engineering. The operation of MTJs with spin polarised currents below critical current densities[6] [122], i.e. avoiding STT switching, allows for the excitation of magnetisation oscillations in the devices [123]. These device applications are typically referred to as *spin torque oscillators* (STO) or *spin torque nano-oscillators* (STNO), and have notably paved the way for the rapidly expanding field of neuromorphic spintronic computing [50–52, 124–126].

Given the possibility of magnetisation manipulation using spin polarised or pure spin currents, the spin polarisation is equally important in magnonics, the field of spin wave physics. Here, ST(N)Os are used as building blocks in magnonic circuits, e.g. for the emission, manipulation or detection of spin waves [127–129]. Another example for the application of spin polarisation in magnonics is the recently reported experimental realisation of a SOT induced spin wave amplification using synchronised pure spin current pulses [61]. Moreover, the report of a current-induced spin wave Doppler shift [43], i.e. a current-induced shift of propagating spin wave frequencies mediated by the STT, has showcased the potential of not only manipulating spin waves by spin polarised currents, but equally of using spin waves as a probe for the spin polarisation in ferromagnetic microstructures.

5: Nobel-prize worthy, see introduction.

[3]: Baibich et al. (1988)
[4]: Binasch et al. (1989)
[118]: Julliere (1975)

[17]: Slonczewski (1996)
[18]: Berger (1996)

[119]: Ikegawa et al. (2021)
[120]: Worledge et al. (2024)

[121]: Liu et al. (2012)

6: The critical current density for STT switching is notably defined by the spin polarisation among other material parameters: For the example of thin-film devices in the current-perpendicular-to-plane (CPP) geometry, the critical switching current density at an applied external field H_{ext} is given by [122]

$$J_{crit}^{STT-switching} = \frac{2e}{\hbar} \cdot (H_{ext} + H_{ani}) \cdot \frac{\alpha M_S d}{P} \tag{1.4}$$

with the saturation magnetisation M_S, the spin polarisation P, the magnetisation oscillation damping parameter α, the anisotropy field H_{ani} and the switching layer thickness d.

[122]: Sun (2000)

[123]: Kiselev et al. (2003)

[50]: Torrejon et al. (2017)
[51]: Grollier et al. (2020)
[52]: Marrows et al. (2024)
[124]: Yang et al. (2021)
[125]: Böhnert et al. (2023)
[126]: Roy et al. (2024)

[127]: Demokritov et al. (2013)
[128]: Locatelli et al. (2014)
[129]: Urazhdin et al. (2014)

[61]: Merbouche et al. (2024)

[43]: Vlaminck et al. (2008)

Suppressed spin flip scattering and associated magnetic damping

The band gap and the resulting lack of available states at the Fermi energy for only one spin type results in the suppression of spin flip scattering in half-metallic materials. This mechanism corresponds to one of the main magnetic damping channels, the concepts of which will be introduced in section 4.2 in the second part of this thesis. Thus, half-metals are expected to present reduced magnetic damping parameters compared to normal metals.

Low magnetic damping parameters yield an important consequence for some spintronic applications where current-induced spin torques are used to counteract the damping torque, e.g. for driving spin-torque auto-oscillators [130]. Moreover, in magnonics, low magnetic damping parameters directly relate to long spin wave lifetimes and large spin wave decay lengths, hence implying desirable features for spin wave applications as well.

Experimental confirmation of the low damping associated with half-metals has recently been reported by Guillemard *et al.* [64], who have measured ultralow Gilbert damping parameters of $\alpha_{Co_2MnSi} = 4.6\times10^{-4}$ and $\alpha_{Co_2MnGe} = 5.3\times10^{-4}$ in epitaxial Co_2MnSi and Co_2MnGe thin films. To date, these remain the lowest reported damping values in conductive thin films[7] and are close to typical damping parameters in thin films of the widely used ferromagnetic insulator $Y_3Fe_5O_{12}$ (YIG) with $\alpha_{YIG} \approx 10^{-4}$ [131, 132]. In result, spin wave propagation lengths of 100 μm have been observed in Co_2MnSi [89], which is an order of magnitude larger than in common conductive thin films, e.g. around 10 μm in CoFeB [133] or 15 μm in Permalloy [134].

[130]: Slavin et al. (2009), 'Nonlinear Auto-Oscillator Theory of Microwave Generation by Spin-Polarized Current'

[64]: Guillemard et al. (2019), 'Ultralow Magnetic Damping in Co_2Mn-Based Heusler Compounds'

7: To the best of my knowledge.

[131]: Gurjar et al. (2019), 'Structural and magnetic properties of high quality single crystalline YIG thin film'

[132]: Dubs et al. (2020), 'Low damping and microstructural perfection of sub-40nm-thin yttrium iron garnet films grown by liquid phase epitaxy'

[89]: Stückler et al. (2018), 'Spin wave propagation detected over 100um in half-metallic Heusler alloy Co_2MnSi'

[133]: Rana et al. (2017), '*Supplementary Material:* Excitation of coherent propagating spin waves in ultrathin CoFeB film by voltage-controlled magnetic anisotropy'

[134]: Manago et al. (2015), 'Damping factor estimation using spin wave attenuation in permalloy film'

1.3 Factors affecting the half-metallicity

Since the half-metallic character is essentially defined by the electronic band structure of the material, it generally relies on an intact crystal structure and, consequently, any deviations from the ideal lattice can in principle yield strong reductions of the spin polarisation.

Additionally, the spin polarisation of half-metals can in principle be strongly temperature dependent, as mentioned above for the example of LSMO [110]. Yet, temperature effects are fairly unimportant in the case of half-metallic Heusler compounds [93], which have been shown to exhibit comparably high temperature robustness with large Curie temperatures and a 100% spin polarisation in thin films even at ambient temperatures [69].

Typical issues yielding a loss of half-metallicity in Heusler compounds are known to arise on a global scale from certain types of chemical disorder. On a more localised scale, a loss of half-metallicity often arises from interfaces [135, 136] but can also originate from local appearances of chemical disorder, as well as lattice defects, impurities or vacancies [137].

Among these defects, the chemical disorder phenomena are the type of defect that had most influence in the course of this work[8]. Being unique to the class of Heusler compounds, the disorder phenomena will be briefly introduced in the following subsection.

[110]: Park et al. (1998), 'Direct evidence for a half-metallic ferromagnet'

[93]: Galanakis (2016), '1: Theory of Heusler and Full-Heusler Compounds'

[69]: Jourdan et al. (2014), 'Direct observation of half-metallicity in the Heusler compound Co_2MnSi'

[135]: Picozzi et al. (2003), 'First principles study of electronic and magnetic properties of Co_2MnGe/GaAs interfaces'

[136]: Picozzi et al. (2003), 'Spin injection at Heusler/semiconductor interfaces'

[137]: Kumar et al. (2024), 'Effect of point defects and lattice distortions on the structural, electronic, and magnetic properties of Co_2MnAl Heusler alloy'

8: Many other defects can be sufficiently suppressed by a high control of the growth process combined with a specific sample design: High stoichiometric control like in state-of-the-art epitaxy systems will reduce stoichiometric defects, impurities and vacancies [71]. The right choice of the substrate or a seed layer can reduce the lattice mismatch and consequently the related occurrence of lattice deformations and dislocations [81]. The precautions taken in this work will be detailed in chapter 2.

[71]: Guillemard et al. (2020), 'Issues in growing Heusler compounds in thin films for spintronic applications'

[81]: De Melo et al. (2021), 'Unveiling transport properties of Co_2MnSi Heusler epitaxial thin films with ultra-low magnetic damping'

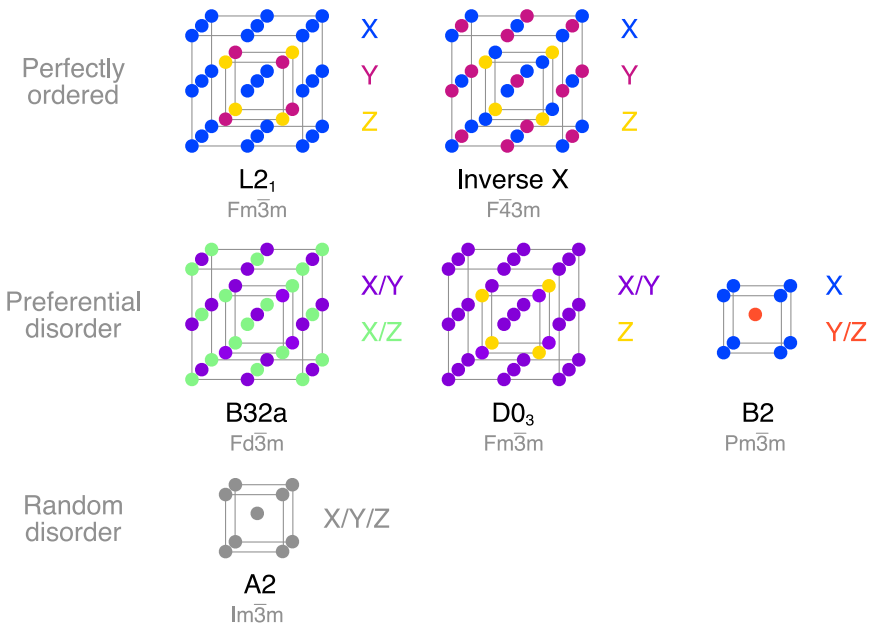

Figure 1.4: Schematic of the six possible (dis)ordering types in X_2YZ Heusler compounds, with the denomination and the corresponding space group[9] in the Hermann-Mauguin notation indicated below each illustration. Figure adapted from [71].

9: Like in above figure 1.1 the atomic positions are shifted by $(\frac{1}{4}, \frac{1}{4}, \frac{1}{4})$ with respect to the standard cell of the Fm3̄m structure.

[71]: Guillemard et al. (2020), 'Issues in growing Heusler compounds in thin films for spintronic applications'

1.3.1 Chemical disorder phenomena

Chemical disorder can occur in Heusler compounds even without a deviation of the (global) stoichiometry or a presence of physical lattice defects. The various chemical disorder types are illustrated in figure 1.4, classified by the degree of randomisation present: The lowest ordering is observed in the A2 disorder, which essentially represents a full randomisation of the atoms in all sublattices. The B32a, $D0_3$ and B2 disorder consist only of a partial randomisation, i.e. an intermixing of selected sublattices. The $L2_1$ and *inverse Heusler* (X) structure both describe a maximal degree of ordering, i.e. zero randomisation, where the difference only lies in a swap of the elements occupying the X' and Y sublattices in figure 1.1.

As the occurrence of chemical disorder changes the atomic distribution and therefore the interatomic bonds, it is directly linked to the electronic band structure of the crystal and can therefore significantly affect the related parameters including the half-metallicity and the related damping parameter. Moreover, an influence on the crystal lattice parameter and the saturation magnetisation cannot be excluded.

A generalisation of disorder effects is hardly possible and especially difficult concerning the half-metallicity, due to the strong dependence on the individual case and type of band gap present [109]. Experimentally, a systematic investigation of disorder effects is limited to a technically accessible range for each individual case, i.e. the type and amount of intrinsically occurring disordering as well as the possibility of tuning the ordering degree e.g. through annealing steps [72, 73, 138] or ion irradiation [76]. Theoretical studies, on the other hand, allow for a broader investigation of any possible combination of disorder types and any degree of disordering by means of first principle or ab initio calculations. Therefore, systematic conclusions on the effects of disorder are mostly drawn from theoretical band structure studies, see for instance [139–141].

This is important for the interpretation of the reported conclusions: For example, first principles studies on the $L2_1$, B2 and A2 (dis)order in Co_2MnSi come to the conclusion of a robustness of the half-metallicity and the related low Gilbert damping parameter for the case of the B2 disorder [139, 140]. However,

[109]: Fang et al. (2002), 'Spin-polarization in half-metals (invited)'
[72]: Gaier et al. (2008), 'Influence of the $L2_1$ ordering degree on the magnetic properties of Co_2MnSi Heusler films'
[73]: Shaw et al. (2018), 'Magnetic damping in sputter-deposited Co_2MnGe Heusler compounds with A2, B2, and $L2_1$ orders'
[138]: Saito et al. (2021), 'Magnetic and thermoelectric properties of Co_2MnT (T = Ga, Si) Heusler compounds'
[76]: Abdallah et al. (2017), 'Evolution of magnetic properties and damping coefficient of Co_2MnSi Heusler alloy with Mn/Si and Co/Mn atomic disorder'
[139]: Sakuma (2015), 'First-principles study of the Gilbert damping constants of Heusler alloys based on the torque correlation model'
[140]: Pradines et al. (2017), 'First-principles calculation of the effects of partial alloy disorder on the static and dynamic magnetic properties of Co_2MnSi'
[141]: Kumar et al. (2022), 'B2-disorder effects on the structural, electronic and magnetic properties of Co_2MnAl Heusler alloy'

in experimental studies ultralow Gilbert damping parameters have only been observed in epitaxial $L2_1$-ordered thin films [64, 71] and in general larger values are reported in samples with B2 disorder [71]. Yet, the damping parameter is also strongly affected by the occurrence of lattice defects [81], which limits the study of the purely disorder-induced effects especially when applying ion irradiation for the tuning of the ordering degree [76]. The analogous behaviour was confirmed in an experimental study on the Co_2MnGe compounds: Here, the decrease of damping could be correlated with the increasing annealing temperature and ordering degree [73]. Similarly, an annealing study on Co_2MnSi thin films has correlated an increase of the exchange stiffness with increasing $L2_1$ ordering degree [72].

[64]: Guillemard et al. (2019), 'Ultralow Magnetic Damping in Co_2Mn-Based Heusler Compounds'
[71]: Guillemard et al. (2020), 'Issues in growing Heusler compounds in thin films for spintronic applications'
[81]: De Melo et al. (2021), 'Unveiling transport properties of Co_2MnSi Heusler epitaxial thin films with ultra-low magnetic damping'
[76]: Abdallah et al. (2017), 'Evolution of magnetic properties and damping coefficient of Co_2MnSi Heusler alloy with Mn/Si and Co/Mn atomic disorder'
[73]: Shaw et al. (2018), 'Magnetic damping in sputter-deposited Co_2MnGe Heusler compounds with A2, B2, and $L2_1$ orders'
[72]: Gaier et al. (2008), 'Influence of the $L2_1$ ordering degree on the magnetic properties of Co_2MnSi Heusler films'

Overall, it is important to conclude that chemical disorder effects certainly have a large potential of disturbing the desired properties in Heusler compounds. Therefore, the investigated samples in this work were grown on an epitaxial system as will be described in chapter 2, following the thorough approach described in the tutorial by Guillemard *et al.* [71] in order to achieve a maximal growth control. Moreover, the occurrence of chemical disorder was then verified in chemical analyses by high angle annual dark field (HAADF) imaging in scanning transmission electron microscopy (STEM) experiments, as will be detailed in chapter 3. This allowed for a differentiation between avoidable disorder-induced effects and inevitable intrinsic effects in the further analysis throughout the work.

1.4 Selection of compounds in this thesis

In this work, a selection of Co_2MnX Heusler compounds was studied, where $X \in \{Al, Si, Ga, Ge, Sn, Al_xSi_{1-x}, Ge_xGa_{1-x}\}$. Experimentally measured band gaps in the minority spin bands have been reported for all members of this selection [142], but not in all cases the band gaps are at the Fermi energy. Hence, the full spin polarisation is not obtained in all compounds of the selection, precisely only in Co_2MnSi and Co_2MnGe [64, 71].

[142]: Guillemard et al. (2019)

[64]: Guillemard et al. (2019)
[71]: Guillemard et al. (2020)

1.4.1 Focus on Co_2MnSi

The largest spin gap in the selection is presented by Co_2MnSi, consequently also yielding the lowest Gilbert damping value [71]. Therefore, a particular focus is set on Co_2MnSi in this work, studying the compound's potential especially towards hybrid magnonic-spintronic applications.

Half-metallicity

Co_2MnSi is a confirmed half-metal according to multiple computational studies [68, 108, 114, 117, 140, 143–146] as well as experimental works [64, 69, 70].

[68]: Ishida et al. (1995)
[108]: Kandpal et al. (2007)
[114]: Galanakis et al. (2002)
[117]: Kumar et al. (2024)
[140]: Pradines et al. (2017)
[143]: Fujii et al. (1990)
[144]: Picozzi et al. (2002)
[145]: Kübler et al. (2007)
[146]: Liu et al. (2009)

The electronic structure of the Heusler compound is defined principally by ionic bonds between the constituent Co, Mn and Si atoms, potentially mixed with co-valent bonding [117]. The spin polarised band structure yields a full band gap in the minority spin bands at the Fermi energy, where the main contribution to the minority spin density originates from the Co atoms [140]. The spin band gap is reported to extend over 0.7 eV for epitaxial single crystalline as well as polycrystalline Co_2MnSi thin films [71].

[64]: Guillemard et al. (2019)
[69]: Jourdan et al. (2014)
[70]: Andrieu et al. (2016)
[71]: Guillemard et al. (2020)

Ultralow Gilbert damping (for a metallic compound)

The associated low Gilbert damping parameter for Co_2MnSi is related to the half-metallic band structure, and can be approximated in a simple picture assuming zero spin orbit coupling (SOC) as a full suppression of the contributions involving the minority spin channel [146]. Indeed, even if the spin orbit coupling is non-zero in Co_2MnSi, a theoretical study by Liu *et al.* [146] using a SOC parameter of 0.043 eV for Co_2MnSi yields a negligible increase of the damping parameter due to the SOC-induced mixing of the Bloch states.

[146]: Liu et al. (2009)

Still, experimentally reported Gilbert damping parameters in epitaxial Co_2MnSi thin films are typically in the range of $4.6-21\times10^{-4}$ [64, 81, 90], which is larger than the theoretical predictions down to 0.6×10^{-4} [146]. The difference, and in particular the increase of the measured damping parameter in some samples compared to the lowest experimentally measured value of 4.6×10^{-4} [64], is typically linked to the high sensitivity to the appearance of disorder [71] as well as to inhomogeneities or even small deviations from the 2:1:1 stoichiometry [71, 81].

[64]: Guillemard et al. (2019)
[81]: De Melo et al. (2021)
[90]: Mantion et al. (2024)
[146]: Liu et al. (2009)
[71]: Guillemard et al. (2020)

Compared to other commonly used metallic materials, such as the alloys Permalloy ($Ni_{81}Fe_{19}$) with 63×10^{-4} [134], or $Co_{40}Fe_{40}B_{20}$ (CoFeB) with 45×10^{-4} [147], the magnetisation damping in half-metallic Co_2MnSi thin films is thus an order of magnitude smaller and closer to thin films of the ferrimagnetic insulator YIG [132].

[134]: Manago et al. (2015)
[147]: Conca et al. (2014)
[132]: Dubs et al. (2020)

Large saturation magnetisation

The magnetisation of Co_2MnSi follows the aforementioned Slater-Pauling behaviour with 5 μ_B/f.u., where the largest magnetic moment is contributed by the Mn atoms with $\approx 3\ \mu_B$/f.u. [117]. This yields a saturation magnetisation of $M_S \approx 1000$ kA/m at room temperature in Co_2MnSi thin films [71, 148]. A direct consequence of this large saturation magnetisation is a strong shape anisotropy[10], which results in an increased ellipticity of the magnetisation oscillations for in-plane magnetised samples and thus promises an exploitability of the compound for applications utilising a parametric pumping of spin waves. Other consequences of the large saturation magnetisation are for instance a reduced threshold for nonlinear magnonic phenomena[11], especially in combination with low Gilbert damping parameters, as well as an increase of the critical current threshold for STT switching[12], which allows for an operation of the aforementioned ST(N)Os.

[117]: Kumar et al. (2024)
[71]: Guillemard et al. (2020)
[148]: Mantion et al. (2022)

10: Due to the large demagnetisation fields, see sections 4.1.2 and 8.1.4 in this work.

11: Some nonlinear spin wave dynamics stem from processes which do not conserve the number of magnons. These spin wave interactions are mediated by the dipolar coupling and therefore scale with the saturation magnetisation, see section 8.2 in this work.

12: The critical current threshold depends on multiple parameters: As detailed on page 10, the critical switching current is proportional to $\alpha \cdot M_S/P$, i.e. the Gilbert damping parameter, the saturation magnetisation and the spin polarisation. Thus, the increase/reduction of the switching current is the result of a competition between large saturation magnetisation on the one hand (increase), and large spin polarisation as well as low damping on the other (reduction).

In comparison, the saturation magnetisation of Co_2MnSi thin films is nearly an order of magnitude larger than that of YIG thin films, i.e. $M_S \approx 115-140$ kA/m [131, 132], and lies in the range of other metallic ferromagnets, which typically exhibit much larger damping parameters: Examples are Permalloy ($Ni_{81}Fe_{19}$) thin films with $M_S \approx 836$ kA/m [134], CoFeB thin films with $M_S \approx 1200$ kA/m [133, 147] or pure Co thin films with $M_S \approx 1420$ kA/m [149].

[131]: Gurjar et al. (2019)
[132]: Dubs et al. (2020)
[134]: Manago et al. (2015)
[133]: Rana et al. (2017)
[147]: Conca et al. (2014)
[149]: Kharmouche (2024)

High Curie temperature

High Curie temperatures are typically reported for Co_2MnSi: $T_C \approx 1000$ K was confirmed experimentally [63] as well as theoretically [145]. Guaranteeing thermal stability and device functionality even well above ambient temperatures, this is an important advantage over other low-damping materials such as the aforementioned half-metallic LSMO with $T_C \approx 350$ K [110] or YIG with $T_C \approx 560$ K [150].

[63]: Webster (1971)
[145]: Kübler et al. (2007)
[110]: Park et al. (1998)
[150]: Cherepanov et al. (1993)

Cubic anisotropy

The cubic Heusler lattice structure introduced in figure 1.1 imposes a cubic magnetocrystalline anisotropy in Co_2MnSi thin films, which typically present magnetic hard axes along the principal axes of the cubic lattice [72, 151]. First order cubic anisotropy constants for sputtered thin films lie reportedly around $-9\,kJ/m^3$ [72] to $-18\,kJ/m^3$ [151] corresponding to an anisotropy field of 18 mT to 36 mT respectively. Reports on second order cubic anisotropy constants are hardly found across literature[13], but investigations in chapter 6 of this work show a significant second order contribution for the case of Co_2MnSi.

[72]: Gaier et al. (2008)
[151]: Abdallah et al. (2017)
[152]: Qiao et al. (2015)
13: See for instance [72, 151, 152], which all only report a first order cubic anisotropy in Co_2MnSi.

The cubic anisotropy has been reported to enable a reconfigurability of magnetic devices such as magnonic crystals, linked to the significant difference in the achievable remanent magnetic configurations for different initial saturation field directions [148]. Additionally, the cubic anisotropy leads to an angular dependence of the magnetisation switching direction which is observed in a sign change of the quadratic MOKE signal in chapter 7 of this work. Moreover, it results in a peculiar anisotropic distortion of the magnetisation's precession trajectory, as well as an anisotropic threshold for the nonlinear spin wave instabilities as will be explored in chapter 8 and chapter 10 of this work.

[148]: Mantion et al. (2022)

Tunability

The Al_xSi_{1-x} substitution in quarternary $Co_2MnAl_xSi_{1-x}$ compounds allows to tune the parameters in the full range between the two pure compounds Co_2MnAl and Co_2MnSi, as reported in two systematic studies [116, 153] for the following parameters

[116]: Guillemard et al. (2020)
[153]: Kubota et al. (2009)

- $60\,\% \leq P(E_F) \leq 100\,\%$ for the spin polarisation $P(E_F)$ [116]
- $11 \times 10^{-4} \geq \alpha \geq 4.6 \times 10^{-4}$ for the damping parameter α [116]
- $270\,fs \leq \tau_M \leq 380\,fs$ for the ultrafast demagnetisation time τ_M [116]
- $4.3\,\mu_B/f.u. \leq \mathcal{M} \leq 5\,\mu_B/f.u.$ for the total magnetic moment $\mathcal{M}$ [116]
- corresponding to $851\,kA/m \leq M_{eff} \leq 1042\,kA/m$ for the effective magnetisation M_{eff} [71]
- $4.8 \leq A \leq 23.5\,pJ/m$ for the exchange constant A [153]

[116]: Guillemard et al. (2020)

[71]: Guillemard et al. (2020)
[153]: Kubota et al. (2009)

with the value for Co_2MnAl always stated first. Moreover, a theoretical study on quarternary $Co_2MnGe_xSi_{1-x}$ compounds [154] predicts a tunability of the band gap in the DOS, while keeping the total magnetic moment and full spin polarisation at the Fermi energy unaffected.

[154]: Özduran et al. (2020)

This principally allows for an engineering of the key parameters according to individual requirements for applications. Yet, the tunability is limited: Some parameters, like the cubic anisotropy constant, were found to be independent of the Al_xSi_{1-x} substitution [153], and thus untunable.

[71]: Guillemard et al. (2020)
[116]: Guillemard et al. (2020)
[142]: Guillemard et al. (2019)
[155]: Chernov et al. (2021)
14: The listed spin polarisation and Gilbert damping parameter from [71, 116] were studied on the same epitaxial sample series of monocrystalline Co_2MnX films (and this sample series was also used for the magneto-optical study in this work and details are therefore listed in table 2.2). Note the exception for Co_2MnGa in table 1.1: While the study on the monocrystalline films in [71] yielded $P(E_F) = 100\,\%$, the study on polycrystalline films in [142] reported $P(E_F) = 55\,\%$ for the Co_2MnGa film and no indication for a full band gap, and the latter is backed by the conclusions from band structure calculations [155]. The discrepancy between the experimental values is attributed to an inaccessibility of the entire Brillouin zone in the SR-PES measurements on the monocrystalline film [71].

1.4.2 Reference values for Heusler compounds in this thesis

All Heusler compounds in the Co_2MnX selection studied in this work, where $X \in \{Al, Si, Ga, Ge, Sn, Al_xSi_{1-x}, Ge_xGa_{1-x}\}$, exhibit quite similar properties to the Co_2MnSi compound. A comparison of the key parameters for the ternary compounds, i.e. Co_2MnX with $X \in \{Al, Si, Ga, Ge, Sn\}$, is given in table 1.1.

The systematic correlation between spin polarisation and Gilbert damping parameter is observed throughout the Co_2MnX series as listed in table 1.1[14]

Table 1.1: Summarised reference values of the aforementioned parameters: the spin polarisation at the Fermi energy P (E_F), the Gilbert damping parameter α, the saturation magnetisation M_S, the Curie temperature T_C and the first-order cubic anisotropy constant K_{c1}, additionally listing the exchange constant A_{exch}, the bulk lattice parameter a_{bulk} and the expected (dis)order. References from [63, 71, 72, 116, 142, 151, 153, 156–161].

	P (E_F) (%)	α (10^{-4})	M_S (kA/m)	T_C (K)	K_{c1} (kJ/m^3)	A_{exch} (pJ/m)	a_{bulk} (nm)	expected (dis)order
Co_2MnAl	63 [116]	11 [116]	851 [71]	693 [63]	-2.5 [160]	4.8 [153]	0.576 [63]	B2 [71]
Co_2MnSi	100 [71] 100 [142]	4.6 [116]	981 [158] 1040 [63] 1042 [71]	985 [63]	-9 [72] -18 [151]	19 [151] 23.5 [153]	0.565 [63] 0.566 [71]	$L2_1$ [71]
Co_2MnGa	(100) [71] 55 [142]	21 [71]	908 [161] 1058 [71]	694 [63]	-2-7 [161]	16.8 [161]	0.577 [63]	$L2_1$ [71]
Co_2MnGe	100 [71] (90) [142]	5.3 [71]	971 [71]	905 [63]	-3.2 [157] -13.2 [156]	10.7-13.8 [159]	0.574 [63]	$L2_1$ [71]
Co_2MnSn	81 [71]	9.1 [71]	955 [71]	829 [63]	(?)	(?)	0.600 [63]	X [103]

[63]: Webster (1971)
[71]: Guillemard et al. (2020)
[72]: Gaier et al. (2008)
[116]: Guillemard et al. (2020)
[142]: Guillemard et al. (2019)
[151]: Abdallah et al. (2017)
[153]: Kubota et al. (2009)
[156]: Ambrose et al. (2000)
[157]: Yang et al. (2002)
[158]: Ritchie et al. (2003)
[159]: Belmeguenai et al. (2009)
[160]: Meng et al. (2017)
[161]: Swekis et al. (2021)
[103]: Guillemard (2019)
[117]: Kumar et al. (2024)

15: See section 4.1.2. The negative constants in table 1.1 indicate an identification of hard axes along the principal cubic lattice directions in the respective references. Yet, especially on the compounds with small anisotropy constants, i.e. Co_2MnAl and Co_2MnGa, the identification is not consistent throughout literature (see e.g. the hysteresis loops in figure 2.31 in [103] showing a different behaviour), and the discrepancy is likely a result of different growth-induced strain and lattice distortions.

16: The critical current threshold depends on multiple parameters: As detailed on page 10, the critical switching current is proportional to $\alpha \cdot M_S/P$, i.e. the Gilbert damping parameter, the saturation magnetisation and the spin polarisation. Thus, the increase/reduction of the switching current is the result of a competition between large saturation magnetisation on the one hand (increase), and large spin polarisation as well as low damping on the other (reduction).

[148]: Mantion et al. (2022)

Moreover, all compounds present a high saturation magnetisation with the main contribution originating from the Mn atoms [103, 117]. The compounds all exhibit a cubic magnetocrystalline anisotropy with an identification of the principal lattice axes as magnetic hard axes[15].

1.5 Concluding remarks

This chapter has introduced the class of Heusler compounds, focusing on the peculiar features of the half-metallic Co_2Mn-based subgroup and the implications for spintronic and magnonic devices, which are in short:

- **High Curie temperature** → Ensures thermal stability and thus allows for a functional device operation at ambient temperatures and above.
- **High spin polarisation** → Enables the exploitation of spin (polarised) currents and related transport phenomena, and leads to reduced critical switching currents[16] for STT and SOT switching.
- **Low Gilbert damping parameter** → Promises increased spin wave lifetimes and propagation lengths compared to common metals and also reduces critical switching currents[16] for STT and SOT switching.
- **Large saturation magnetisation** → Leads to a strong shape anisotropy, a reduced threshold for nonlinear spin wave phenomena, and an increased critical current threshold[16] which can facilitate the operation of ST(N)Os.
- **Cubic anisotropy** → Results in anisotropic precession trajectories as well as anisotropic thresholds for nonlinear dynamics, and promises the potential for reconfigurable magnonic devices [148].
- **Tunability** → Yields the potential to engineer compounds with custom properties to match specific application requirements [116, 153].

All of the studied Co_2MnX Heusler compounds exhibit an individual combination of these key properties, as summarised in table 1.1.

In this thesis, the focus is set on Co_2MnSi, as this compound presents an outstandingly low Gilbert damping parameter, associated with the largest minority spin band gap in the series. In addition, Co_2MnAl was chosen to serve as a reference, not only due to the experimentally proven tunability in quarternary $Co_2MnAl_xSi_{1-x}$ compounds, but also because the two compounds define the extrema of nearly all parameter ranges listed in table 1.1.

Samples: Epitaxial thin film growth and sample series in this work

2

This first experimental chapter is dedicated to the thin film growth process and the resulting sample series fabricated in the course of this research project. All samples were fabricated using molecular beam epitaxy (MBE), where the growth was monitored in-situ using reflection high energy electron diffraction (RHEED) and in-situ Auger spectroscopy was performed in addition when testing the coverage of a new stack. The first section of the chapter will give an overview of the experimental techniques and the second section of the chapter will present the details of the growth process on the exemplary case of the samples studied in chapter 6 and 10 later on. The third section will present an overview of all samples grown in the course of this research project, including an indication of their individual purpose as well as a listing of the respective appearance in this manuscript.

2.1 Experimental methods . . 17
MBE setup 17
In-situ RHEED 19
In-situ Auger spectroscopy 22
2.2 Epitaxial growth process . 23
Substrate preparation 23
Heusler layer deposition . . 24
Capping layer deposition . 26
2.3 Sample series 28
Magnonics series 29
Magneto-optical series . . . 30
Bilayer series 31
Cr/V buffer series 32

2.1 Epitaxy setup and in-situ characterisation techniques

The term *epitaxy* was proposed in 1928 [162] to refer to the oriented crystalline growth of a material when deposited on an adequate substrate or seed layer. If a suitable match between the substrate (or seed layer) and the crystal lattice of the deposited material is possible for a crystallographic orientation, the material can principally grow as a monocrystalline film.

[162]: Royer (1928), 'Recherches expérimentales sur l'épitaxie ou orientation mutuelle de cristaux d'espèces différentes'

To achieve monocrystalline epitaxial growth for compounds like the Co_2Mn-based Heusler films in this work, three key conditions need to be met:

1. The substrate or seed layer must be monocrystalline and the lattice structure of the surface must match to at least one crystal plane of the material to be deposited [163]. In this study, monocrystalline MgO (001) substrates are chosen for all samples due to the suitable match with the Co_2MnSi lattice, see e.g. [71].
2. A contamination during the deposition must be avoided as it can lead to local defects or in severe cases to a disruption of the crystalline order. This is typically prevented by ensuring an ultrahigh vacuum environment during the growth process.
3. A sufficient control over the growth process is necessary, especially for the fabrication of alloys or compounds involving a deposition of multiple primary materials, where a precise stoichiometry control is only achieved by a decent regulation and monitoring of the growth parameters [163]. Especially for the deposition of monocrystalline Co_2Mn-based Heusler films, the precise stoichiometry control is of high importance [71, 142].

[71]: Guillemard et al. (2020), 'Issues in growing Heusler compounds in thin films for spintronic applications'
[142]: Guillemard et al. (2019), 'Polycrystalline Co_2Mn-based Heusler thin films with high spin polarization and low magnetic damping'

[163]: Andrieu et al. (2005), *Les surfaces solides*

2.1.1 Molecular beam epitaxy (MBE) setup

Molecular beam epitaxy (MBE) is an experimental method enabling epitaxial growth by the simultaneous co-evaporation of multiple materials while independently controlling various growth parameters. Key parameters are in particular the individual deposition flux rates of the different primary materials as well as the deposition time, the combination of which ultimately

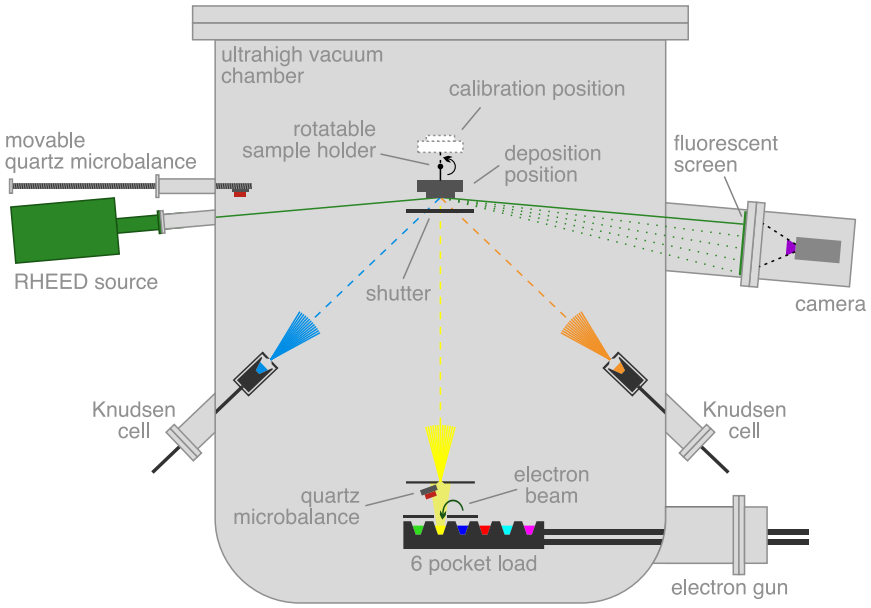

Figure 2.1: Illustration of the MBE system used for the epitaxial thin film growth in this work. The schematic is simplified and shows only two of the six Knudsen cells and one of the three electron guns. The system is equipped with four quartz microbalances, one per electron gun and an insertable one for the sample position, of which two are shown. The sample holder is repositionable (as indicated by the dashed calibration position), but also rotatable in the plane to ensure a homogeneous deposition, as well as heatable to allow for a control of the deposition temperature. Figure adapted from [83].

determines the film thickness[1]. Another important factor is the control over the substrate temperature, allowing not only for a preliminary outgassing procedure of the substrate but also for a control over the substrate temperature during the deposition as well as in subsequent annealing steps, which is of high importance for the chemical ordering in the crystal lattice of the Co_2Mn-based Heusler compounds [71, 72].

The MBE setup used for the fabrication of all samples in this study is a COMPACT 21 EB 200 MBE system from RIBER situated at the Institute Jean Lamour and schematically illustrated in figure 2.1. The system is operated with a base pressure of 4×10^{-11} hPa and allows to load 24 materials at a time, spread over 3 electron beam evaporators with 6 material pockets each, as well as 6 Knudsen cells. The MBE setup is equipped with four quartz microbalances and an INFICON IC6 controller with a maximal rate resolution of 4.33×10^{-4} nm every 0.1 second [164] enabling a precise calibration and real time control of the deposition fluxes. The sample holder is repositionable as indicated by the dashed calibration position in figure 2.1, but also rotatable in the sample plane to ensure a homogeneous deposition, and is additionally heatable to allow for a control of the substrate temperature during the outgassing, deposition or annealing steps. Moreover, the system is equipped with a pyrometer[2] to measure the sample surface temperature, as well as an in-situ reflection high energy electron diffraction (RHEED) setup for the real-time monitoring of the growth process.

Regulation of the Knudsen cells

Knudsen cells are effusion units named after Knudsen for his work on the effusion and the molecular flow of gases through pinholes [165, 166]. Knudsen cells typically consist of a crucible shielded in a pocket chamber with a pinhole, as illustrated schematically in figure 2.1, and are equipped with a heating filament as well as a cooling system allowing for a temperature regulation of the material loaded in the crucible.

In this work, Mn, Al and Ti were deposited using Knudsen cells. Contrary to the electron beam evaporators, the Knudsen cells in the MBE setup were not equipped with individual quartz microbalances for a real time control of the deposition fluxes. Instead, the Knudsen cells were regulated to a constant flux

[83]: Friedel (2021), *Thin film materials with ultralow damping for novel magnonic phenomena*

1: Assuming no adhesion problems and an equal sticking factor of 1 on the quartz microbalances as well as on the sample.

[71]: Guillemard et al. (2020), 'Issues in growing Heusler compounds in thin films for spintronic applications'
[72]: Gaier et al. (2008), 'Influence of the $L2_1$ ordering degree on the magnetic properties of Co_2MnSi Heusler films'

[164]: INFICON (2015), *Brochure: IC6 Thin Film Deposition Controller for Optical Applications*

2: The pyrometer was operated with an arbitrary emissivity set to 85% since the emissivity of the Co_2MnX compounds is unknown. Consequently, the actual temperatures may differ depending on the emissivity coefficient of each material. The pyrometer was used for all samples fabricated in the course of this work, but not for the additional sample series listed in table 2.2, since it had been added to the MBE system just before the start of this work in the course of the thesis of Victor Palin [105]. Temperature measurements prior to the addition of the pyrometer relied on the temperature sensor of the sample holder, yet the actual temperature of the sample/-substrate could deviate from the sample holder depending on the thermal coupling between the two (varying e.g. with the fixing pressure).

[105]: Palin (2023), 'Heusler compounds for spin-orbitronics: exploration of topological effects and magnetic anisotropy engineering'

[165]: Knudsen (1909), 'Die Gesetze der Molekularströmung und der inneren Reibungsströmung der Gase durch Röhren'
[166]: Knudsen (1909), 'Die Molekularströmung der Gase durch Öffnungen und die Effusion'

prior to each deposition process: The sample was moved to the calibration position indicated in figure 2.1 and the movable quartz microbalance was inserted to the sample position. The temperature of the Knudsen cells was then stabilised to achieve a desired flux[3] measured on the movable quartz microbalance, which was calibrated jointly with the quartz microbalances on the electron guns. Subsequently, during the growth process the Knudsen cells were kept fixed at the temperature corresponding to the calibrated flux rates.

3: Since pressure variations can have a significant impact on the sublimation point in the Knudsen cell, the shutter/lid was opened and closed multiple times during the calibration process in order to verify a stable regulation.

Regulation of the electron beam evaporators

The electron beam evaporation units consist of an electron gun for the creation of a focused electron beam which is directed onto a crucible with the loaded material, as illustrated schematically in figure 2.1. The electron beam locally heats the target material and causes a local sublimation or melting resulting in a vapor of the target material. The flux is regulated by the acceleration voltage of the electron beam as well as the sweep pattern on the target material.

In this work, MgO, Co and Si were evaporated from electron guns. All three electron beam evaporators were equipped with quartz microbalances, hence allowing for a real time control of the flux during the entire growth process by a feedback loop to the high voltage control of the electron beam.

2.1.2 Reflection high-energy electron diffraction (RHEED)

Reflection high-energy electron diffraction (RHEED) is a surface sensitive characterisation technique and was used in this work for the real time monitoring of the growth process during all steps from the outgassing of the substrate to the completion of the capping layer.

A complete description of the principle and intricacies of the RHEED technique is given in [167] and [163]. The unique RHEED patterns arise from variations in the amplitude of the reflected electron beam caused by the scattering from the crystal lattice of the sample, to which only the surface atomic planes contribute due to the grazing angle of incidence [163]. Consequently, the technique allows for the investigation of various surface properties, such as the verification of the epitaxial relationship between the different layers by an analysis of the characteristic diffraction pattern along different orientations [163, 168], an estimation of the surface roughness and conclusions on the dimensionality of the growth mode from the width of the streaks and the appearance of a modulation of the intensity along a single streak in the diffraction pattern [163, 168], and even a real time measurement of the growth rate from the intensity oscillations on the intensity maxima in the diffraction pattern [167, 169–174].

A typical RHEED setup involves a high voltage electron source emitting a collimated electron beam which is directed onto the sample under a low angle of incidence, as schematically illustrated in figure 2.1. In this work, the electrons were accelerated by a 15 kV voltage and striking the sample surface at a shallow angle of incidence ($\approx 1°$). The scattered electron beam is directed onto a fluorescent screen from which the displayed diffraction pattern is captured by a camera.

Analogous to X-ray or Neutron diffraction experiments [175, 176], the diffraction pattern is defined by the electron wave vector (and hence the electron energy), the reciprocal lattice of the sample and its orientation to the incidence plane of the electron beam, as well as the atomic form factors of the different elements.

[163]: Andrieu et al. (2005), *Les surfaces solides*
[168]: Chevrier et al. (1991), 'A RHEED Study of Epitaxial Growth of Iron on a Silicon Surface'
[167]: Braun (1999), *Applied RHEED*
[169]: Harris et al. (1981), 'Oscillations in the surface structure of Sn-doped GaAs during growth by MBE'
[170]: Van Hove et al. (1985), 'The dependence of RHEED oscillations on MBE growth parameters'
[171]: Dobson et al. (1987), 'Current understanding and applications of the RHEED intensity oscillation technique'
[172]: Petrich et al. (1989), 'On the origin of RHEED intensity oscillations'
[173]: Braun et al. (1998), 'New model for reflection high-energy electron diffraction intensity oscillations'
[174]: Haeni et al. (2000), 'RHEED Intensity Oscillations for the Stoichiometric Growth of SrTiO3 Thin Films by Reactive Molecular Beam Epitaxy'
[175]: Fejgin (1987), *Structure Analysis by Small-Angle X-Ray and Neutron Scattering*
[176]: Ibach et al. (2009), *Solid-State Physics*

Underlying principles of diffraction from periodic lattice structures

The observable intensity I of radiation[4] scattered by matter is given by [176]

$$I(\mathbf{K}) \sim |A(\mathbf{K})|^2 \sim \left| e^{-i\omega t} \int \varrho(\mathbf{r})\, e^{i\mathbf{K}\cdot\mathbf{r}} \mathrm{d}\mathbf{r} \right|^2 \tag{2.1}$$

where $\mathbf{K} = \mathbf{k}_{\mathrm{scat}} - \mathbf{k}_{\mathrm{inc}}$ is the scattering vector accounting for the wavevector difference between scattered and incident radiation respectively, and $\varrho(\mathbf{r})$ is the complex scattering density accounting for the amplitude and phase difference between the scattered and the incident radiation. For structures that are constant in time[5], the observed intensity is thus simply proportional to the square of the Fourier transform of $\varrho(\mathbf{r})$ with respect to $\mathbf{K}$, making the complex scattering density the defining property of the scattering process[6].

In periodic lattice structures, the scattering density can be expanded in a Fourier series [176]

$$\varrho(\mathbf{r}) = \sum_{\mathbf{G}} \varrho_{hkl} e^{i\mathbf{G}\cdot\mathbf{r}} \tag{2.2}$$

with the reciprocal lattice vector $\mathbf{G} = h\mathbf{g}_1 + k\mathbf{g}_2 + l\mathbf{g}_3$ defining the reciprocal base $\{\mathbf{g}_1, \mathbf{g}_2, \mathbf{g}_3\}$ via the condition

$$\mathbf{G}\cdot\mathbf{r}_n = 2\pi m \quad \text{with} \quad m \in \mathbb{Z} \tag{2.3}$$

which ensures a translation invariance of $\varrho(\mathbf{r})$ for all lattice vectors $\mathbf{r}_n = n_1\mathbf{e}_1 + n_2\mathbf{e}_2 + n_3\mathbf{e}_3$ with $n_i \in \mathbb{Z}$ and the crystal base $\{\mathbf{e}_1, \mathbf{e}_2, \mathbf{e}_3\}$ in the real space. A direct consequence of the series expansion is the Laue condition [177]

$$\mathbf{G} = \mathbf{K} \tag{2.4}$$

for the occurrence of non-zero intensities in the diffraction pattern[7]. This condition is fundamental to the diffraction of radiation from periodic structures and typically represented by an Ewald sphere construction [163, 176].

The scattering condition (Laue or equivalently Bragg) determines the position of the non-zero intensity reflexes in the diffraction pattern. The intensity of the respective reflex is determined by the Fourier coefficients of the series expansion in equation 2.2 given by

$$\varrho_{hkl} = \frac{1}{V_{\mathrm{cell}}} \int_{\mathrm{cell}} \varrho(\mathbf{r})\, e^{-i\mathbf{G}\cdot\mathbf{r}} \mathrm{d}\mathbf{r} \tag{2.5}$$

with the integral spanning over a unit cell with the volume V_{cell}. Since typically the scattering from valence band electrons is negligible over the scattering from the core electrons, the integral can be separated into individual integrals for the atoms by separating the position vector as $\mathbf{r} = \mathbf{r}_n + \mathbf{r}_\alpha + \mathbf{r}'$ as illustrated in figure 2.2, i.e. defining the position $\mathbf{r}_n$ of the nth unit cell, the relative position $\mathbf{r}_\alpha$ of each atomic core within the unit cell, and the inner atomic position vector $\mathbf{r}'$ pointing from the core of the atom to an electron position. This transforms the Fourier coefficients to the expression

$$\varrho_{hkl} = \frac{1}{V_{\mathrm{cell}}} \sum_\alpha e^{-i\mathbf{G}\cdot\mathbf{r}_\alpha} \int \varrho_\alpha(\mathbf{r}') e^{-i\mathbf{G}\cdot\mathbf{r}'} \mathrm{d}\mathbf{r}' =: \frac{1}{V_{\mathrm{cell}}} \sum_\alpha e^{-i\mathbf{G}\cdot\mathbf{r}_\alpha} \cdot f_\alpha =: \frac{1}{V_{\mathrm{cell}}} \cdot S_{hkl} \tag{2.6}$$

defining the *atomic form factor* as $f_\alpha := \int \varrho_\alpha(\mathbf{r}') e^{-i\mathbf{G}\cdot\mathbf{r}'} \mathrm{d}\mathbf{r}'$ which repesents the electronic distribution within the atom[8], as well as the *structure factor* as $S_{hkl} = \sum_\alpha e^{-i\mathbf{G}\cdot\mathbf{r}_\alpha} \cdot f_\alpha$ which accounts for the lattice structure[9].

4: For the description of diffraction processes, a quasiclassical approach is typically chosen using a wave-based description of the incident and emitted radiation combined with a classical formulation of the scattering events between the waves and the matter. The problem is typically simplified by the assumption of a stimulation of spherical waves by the incident radiation at all points $\mathbf{r}$ as well as the consideration of a fixed phase between the incident radiation and the scattered wave. Additionally, secondary scattering events are neglected, which corresponds to the Born approximation.

5: For the duration of the scattering experiment.

6: This implies, for instance, that the smaller the investigated crystal structure (i.e. the higher the desired resolution), the higher the scattering vace vector $\mathbf{K}$ must be, and hence the larger is the required incident wave vector $\mathbf{k}_{\mathrm{inc}}$ (and consequently the electron energy to be set).

7: Interpreting $\mathbf{G} = \mathbf{K}$ as the reciprocal lattice vector being perpendicular to the lattice planes in the real space defined by the Miller indices hkl, the Laue scattering condition transforms to the Bragg condition $\lambda = 2d_{hkl}\sin(\theta)$ with the lattice plane distance $d_{hkl} = 2\pi/|\mathbf{G}_{hkl}|$ and the scattering angle θ.

[163]: Andrieu et al. (2005), *Les surfaces solides*
[176]: Ibach et al. (2009), *Solid-State Physics*

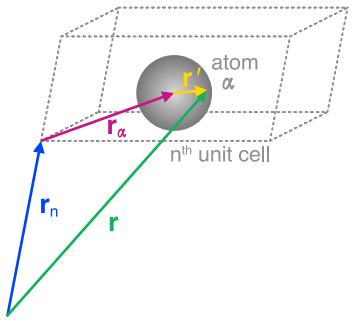

Figure 2.2: Definition of the vectors for the atomic form factor and the structure factor. Figure adapted from [176].

[176]: Ibach et al. (2009), *Solid-State Physics*

8: This might as well be interpreted as the form of the electronic shells around the atomic core, giving rise to the name *atomic form factor*. Sometimes it is also named *atomic scattering factor* [176].

9: Clearly, for primitive lattices (a single atom per unit cell), there is no difference between the two factors, i.e. $S = f$.

Typical streak diffraction pattern from RHEED experiments

In the case of RHEED, the scattering matter can be assumed as purely two-dimensional as for a negligible penetration into the sample volume only the top atomic layer contributes to the interaction with the electron beam. The condition $\mathbf{G} \cdot \mathbf{r}_n = 2\pi m$ from equation 2.3 then yields no constraint in the direction perpendicular to the atomic plane, and consequently the reciprocal lattice is a formation of streaks infinitely elongated in this direction, as illustrated in figure 2.3.

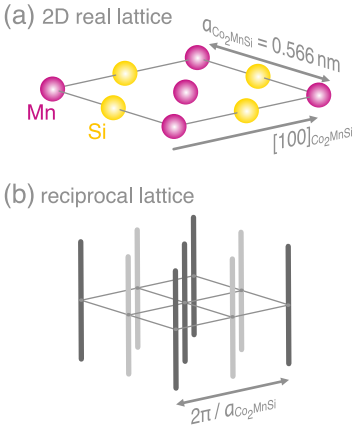

Figure 2.3: Schematic illustration of (a) an atomic plane of Mn-Si in the Heusler lattice and (b) the resulting reciprocal lattice with the difference in the respective atomic form factors marked as different intensities on the streaks. Figure after [103, 163].

[103]: Guillemard (2019), 'Half-metal magnets Heusler compounds for spintronics'
[163]: Andrieu et al. (2005), *Les surfaces solides*

However, this does not directly translate to the typically captured streak intensity pattern on the fluorescent screen: From the simple Ewald sphere construction of the scattering condition in equation 2.4, a streak-like reciprocal lattice as illustrated in 2.3 (b) would still lead to a point pattern on the screen[10] [163]. Yet, streak patterns are typically obtained in RHEED experiments, which is attributed to uncertainties in the scattering experiment from Heisenberg's uncertainty principle as well as extrinsic contributions such as a divergence of the electron beam or a dispersion of the electron energy. These can be introduced in the construction as a width Δk_{inc} of the Ewald sphere with the radius $|\mathbf{k}_{\text{inc}}|$, consequently resulting in the streak pattern on the screen.

10: Clearly, the intersections of the Ewald sphere with the reciprocal lattice streaks does not result in streaks but in points.

Surface roughness → Finite streak width

The finite streak width observed in the RHEED experiments is attributed to the thermal excitation of the atoms, the coherence of the electron beam as well as the surface roughness of the sample [163], where in particular the latter is of importance in the epitaxial growth process: Real sample surfaces typically present a non-zero surface roughness in the form of large islands or terraces of a certain size L. This leads to an increase of diffuse scattering from the surface modulations (terrace/island edges) and hence in a beam divergence captured as a finite streak width $2\pi/L$ in the intensity pattern on the fluorescent screen [163]. This is often accompanied by an intensity modulation towards spotty streaks as detailed in the next subsection.

Consequently, a reduction of the streak width, as is typically observed during the process of annealing of a layer an example of which is shown in figure 2.4, corresponds to a decrease of terrace/island edges on the surface and hence a reduction of the crystal surface roughness.

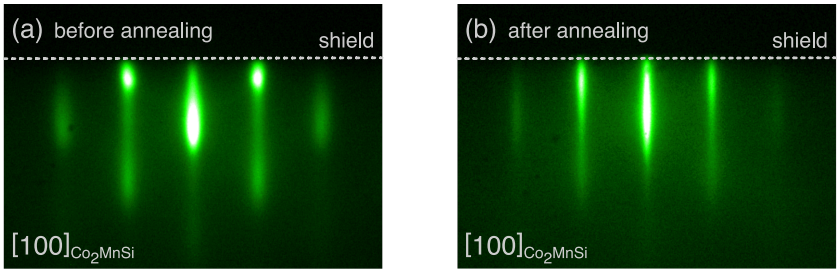

Figure 2.4: Exemplary RHEED patterns obtained from a Co_2MnSi film along the [100] direction (a) right after the growth process presenting a superposition of a point reflex and a stripe pattern and (b) after the annealing step presenting more even streaks of a reduced width compared to (a). The shield is introduced to protect the fluorescent screen from the directly reflected electron beam.

Island growth → Spotty intensity modulation along the streaks

Occasionally, the RHEED intensity patterns present a spot-like modulation along the streaks or even transform to a point reflex pattern as is typical for volume diffraction experiments. This is a sign of a superposition with the respective 3D diffraction image and points towards a penetration of the electron beam into the crystal structure of the sample.

Such a penetration can occur for instance in the case of island formations on the sample surface as is the case of 3D growth modes[11]: As opposed to the case of large flat terraces resulting from a 2D layer-by-layer growth[12] leading

11: The 3D growth modes are commonly referred to as the *Volmer-Weber* (pure island growth) or the *Stranski-Krastanow* (mixed island growth and layer formation) growth mode [163], named after the pioneering works by the researchers e.g. in [178, 179].
[178]: Volmer et al. (1926)
[179]: Stranski et al. (1937)

12: Analogously referred to as the *Frank-van der Merwe* growth mode for [180–182].
[180]: Frank et al. (1949)
[181]: Frank et al. (1949)
[182]: Frank et al. (1949)

to the aforementioned streak pattern with a finite width, the electron beam can be transmitted through the smaller islands and hence penetrates into the crystal structure resulting in the superposition of the 2D streak-like and 3D point-like diffraction image.

This was for instance observed during the growth of the Heusler layers prior to annealing, as can be seen in the example given in figure 2.4 (a), and is attributed to the 3D growth of the Co_2MnX Heusler crystal on MgO [103].

[103]: Guillemard (2019), 'Half-metal magnets Heusler compounds for spintronics'

Chemical order → Intensity modulation between different streaks

Additionally, when the atomic plane contains multiple elements, the scattering intensities for the respective streaks differ from each other, modulating the resulting intensity pattern.

In some cases, this allows already for conclusions on the chemical ordering within an alloy or a compound, as is for instance partly[13] the case for the Co_2Mn-based Heusler compounds: With the symmetry of the Heusler structure in the $L2_1$ order and the different atomic factors for Mn and Si, the Mn-Si-planes of the crystal will result in the appearance of streaks with different intensities upon scattering along the [110] direction, as shown in the example in figure 2.5. However, if the Mn and Si atoms appear randomised (i.e. the crystal presenting a B2 or A2 disorder as introduced in figure 1.4), the respective streaks marked as "L" (lower intensity) in figure 2.5 do not appear since the corresponding atomic structure factors cancel out for the Mn/Si randomisation [183].

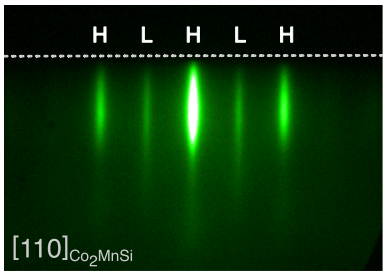

Figure 2.5: Typical RHEED pattern from Co_2MnSi along the [110] direction resulting in an intensity modulation of the streaks, which is labelled with "H" for high and "L" for low intensity respectively.

13: Only partly, because not all disorder types introduced in section 1.3.1 can be distinguished in the RHEED intensity patterns.

[183]: Neggache et al. (2014), 'Testing epitaxial $Co_{1.5}Fe_{1.5}Ge$(001) electrodes in MgO-based magnetic tunnel junctions'

[184]: Auger (1925), 'Sur l'effet photoélectrique composé'

[185]: Meitner (1922), 'Über die Entstehung der ß-Spektren radioaktiver Substanzen'

2.1.3 Auger spectroscopy

Auger spectroscopy is a chemical surface analysis method based on the Auger effect, discovered in the 1920s [184, 185] and named after the significant contributions of Auger. The technique was used only briefly in this work, but for an important reason: It allowed to check the coverage of the MgO/Ti and MgO/Al bilayer cappings, a necessary step since the samples in this work were the first Heusler films with such bilayer capping stacks to be produced on this MBE setup.

In Auger spectroscopy experiments, the atoms in the sample are excited by a bombardment with high energy electron beams[14] resulting in an ejection of electrons from the core shells. Subsequently, the Auger effect forms a radiationless de-excitation mechanism [187] which consists of a secondary electron transition from a higher level to the vacancy in the core shell combined with a transfer of the released transition energy to an electron on the outer shell, finally resulting in an emission of the latter. The emitted electrons are commonly named Auger electrons.

The effect depends purely on the atomic energy levels and does not depend on the energy of the excitation radiation [163], therefore a measurement of the kinetic energy of the ejected Auger electrons results in spectral peaks that are unique to the transition energies of the different elements and therefore allows for conclusions on the chemical composition of the sample surface[15], where depending on the atomic number different transitions are the most likely: For Co, Mn and Si the Auger spectroscopy is most sensitive to the LMM transition, while for lighter atoms like O the KLL transition is typically measured.

Naturally, the experiments need to be done in a high vacuum environment [186], and in this work were performed on an Auger spectroscopy setup that is connected to the MBE growth chamber by an ultrahigh vacuum transport chamber[16] allowing for an in-situ analysis without breaking the vacuum.

14: Principally, also high energy X-rays can be used for the excitation, as the incident radiation simply needs to be sufficient to ionise the core electrons. Electron guns are often chosen for their technical advantages (easy construction and maintenance) as well as their high beam intensity and the possibility of focusing plus x-y-deflection (allowing for a scanning of different areas of the sample surface) [186].

[186]: Hofmann (2013), *Auger- and X-ray photoelectron spectroscopy in materials science*

[187]: Burhop (1935), 'The Auger effect'

[163]: Andrieu et al. (2005), *Les surfaces solides*

15: For a detection of the characteristic energies, the Auger electrons need to leave the crystal without being subject to inelastic scattering, and hence the technique is sensitive only to the first few atomic layers of the sample surface [186].

16: The setups are part of the *Tube D.A.U.M. facility* at the Institut Jean Lamour, consisting of a 70 m long vacuum chamber (tube) which connects various growth and analysis setups.

2.2 Epitaxial growth process

The experimental techniques introduced in the previous section were used in this work for the growth of the epitaxial thin film samples. All samples were grown following the same procedure, which will be described in the following mainly on the example of the samples produced for the studies presented in chapters 6 and 10.

The growth protocol for epitaxial Co_2Mn-based Heusler films followed in this work was established on the same setup in [103] and has since been followed in various studies [64, 71, 80, 81, 83, 103, 105, 116, 188]. An extensive description is given in the tutorial in [71], to which it is referred for more details on the different process steps.

Note that the temperatures reported in the following may differ from the tutorial in [71], since in the meantime the pyrometer was added to the MBE system, see the aforementioned sidenote[2].

[103]: Guillemard (2019), 'Half-metal magnets Heusler compounds for spintronics'
[64]: Guillemard et al. (2019)
[71]: Guillemard et al. (2020)
[80]: Létang et al. (2021)
[81]: De Melo et al. (2021)
[83]: Friedel (2021)
[103]: Guillemard (2019)
[105]: Palin (2023)
[116]: Guillemard et al. (2020)
[188]: Palin et al. (2023)
[71]: Guillemard et al. (2020), 'Issues in growing Heusler compounds in thin films for spintronic applications'

2.2.1 Substrate preparation

The Heusler thin films were grown on 500 µm thick monocrystalline MgO (001) substrates, in order to achieve the aforementioned match of the substrate and the crystallographic direction of the desired material to be grown.

The (001) plane of the Co_2MnX compounds grows on MgO(001) substrates with an epitaxial relationship between the lattice directions

$$[110]_{Co_2MnX} \parallel [100]_{MgO} \tag{2.7}$$

in the film plane, as illustrated in figure 2.6 for the example of Co_2MnSi. The lattice parameters of the two crystals result in a slight lattice mismatch η of

$$\eta = 1 - \frac{a_{Co_2MnSi}}{\sqrt{2} \cdot a_{MgO}} \approx 4.9\,\% \tag{2.8}$$

which has been observed to result in the formation of lattice dislocations at the interface as a compensation [81, 83], but is small enough to allow for an epitaxial monocrystalline growth of the Co_2MnX layer.

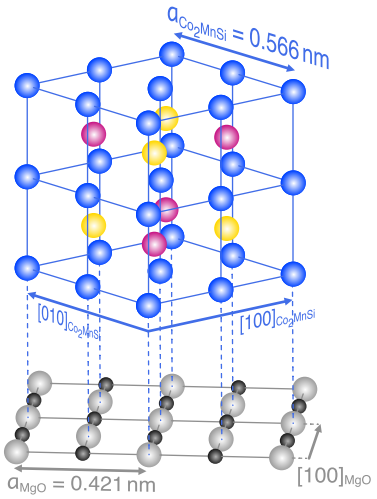

Figure 2.6: Illustration of the epitaxial relation ship of Co_2MnSi on MgO (001): The cubic unit cell of Co_2MnSi is rotated by 45° with respect to the MgO lattice. Figure adapted from [71].

The substrates were first outgassed at substrate temperatures of around $T_{pyro} \approx 730°C - 800°C$. Once the pressure of the system stabilised, the sample holder was kept at a constant power setting corresponding to $T_{pyro} \approx 620 - 730°C$ and an MgO buffer layer was deposited to smooth the surface and cover potential contaminations of the substrate [71, 189].

Exemplary RHEED images of an MgO buffer layer are presented in figure 2.7 jointly with a subsequently deposited Co_2MnSi layer. A comparison of the diffraction patterns along the corresponding sample orientations (presented below each other) clearly confirms the epitaxial relationship $[110]_{Co_2MnSi} \parallel [100]_{MgO}$ illustrated in figure 2.6. Moreover, the thin diffraction streaks with little modulation in figure 2.7 (1.a) and (1.b) are an indication for the smoothness of the sample surface after the deposit of the MgO buffer layer, allowing for the epitaxial growth of the subsequent Heusler film.

[81]: De Melo et al. (2021), 'Unveiling transport properties of Co_2MnSi Heusler epitaxial thin films with ultra-low magnetic damping'
[83]: Friedel (2021), *Thin film materials with ultralow damping for novel magnonic phenomena*
[71]: Guillemard et al. (2020), 'Issues in growing Heusler compounds in thin films for spintronic applications'
[189]: Sicot et al. (2006), 'On the quality of molecular-beam epitaxy grown Fe/MgO and Co/MgO(001) interfaces'

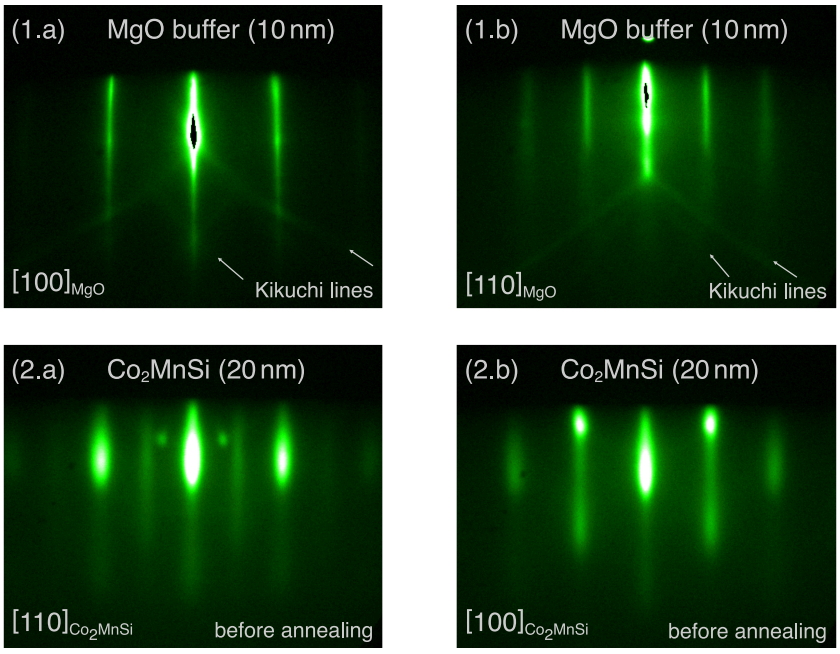

Figure 2.7: Exemplary RHEED images of the first two growth steps from the sample studied in chapter 10: (1.a) and (1.b) presenting the diffraction patterns obtained after the growth of the MgO buffer layer along the $[100]_{MgO}$ and $[110]_{MgO}$ directions, and (2.a) and (2.b) presenting the diffraction patterns captured after the growth of the Co_2MnSi layer accordingly. The epitaxial relationship $[110]_{Co_2MnSi} \parallel [100]_{MgO}$ illustrated in figure 2.6 is confirmed by the respective RHEED diffraction patterns with the RHEED images presented below each other captured along corresponding sample orientations: Images in (x.a) were taken along an edge of the sample which corresponds to a $[100]_{MgO}$ direction of the MgO(001) substrate, and images in (x.b) were taken along a sample diagonal, corresponding to a $[110]_{MgO}$ direction accordingly. The RHEED captures of the MgO layer additionally presented Kikuchi lines[17].

17: Kikuchi lines are often observed in RHEED patterns from isolating materials [163] and generally attributed to incoherent scattering effects [190, 191]. The systematic analysis of the Kikuchi lines can for instance be used for an estimation of the surface morphology [192], yet the concepts cannot be described by the simple plane wave diffraction approach and hence a quantitative analysis of the Kikuchi lines can become tedious [191] and was outside the scope of this work.

[163]: Andrieu et al. (2005), *Les surfaces solides*

[190]: Omoto et al. (2002), 'Simulations of Kikuchi patterns due to thermal diffuse scattering on MgO crystals'

[191]: Pawlak et al. (2021), 'An Analysis of Kikuchi Lines Observed with a RHEED Apparatus for a TiO2-Terminated SrTiO3 (001) Crystal'

[192]: Gotoh et al. (1981), 'Surface Rumpling of MgO(001) Deduced from Changes in RHEED Kikuchi Pattern. I. Experimental'

[71]: Guillemard et al. (2020), 'Issues in growing Heusler compounds in thin films for spintronic applications'

2.2.2 Heusler layer deposition

As stated above, apart from the proper substrate choice and a contamination free environment, the third essential requisite for the epitaxial growth of the Co_2Mn-based Heusler thin films is a proper calibration and regulation of the deposition rates with a precise stoichiometry control.

To this aim, a calibration of the atomic fluxes φ of the different materials was performed prior to each deposition as working with the atomic fluxes allows to assign the desired stoichiometry in a straightforward manner to $\varphi_{Co} = 2\varphi_{Mn} = 2\varphi_X$, which was in this work fixed to

$$\varphi_{Co} = 10^{14}\,\frac{\text{atoms}}{\text{cm}^2 \cdot \text{s}} \quad \Rightarrow \quad \varphi_{Mn} = \varphi_X = 5 \cdot 10^{13}\,\frac{\text{atoms}}{\text{cm}^2 \cdot \text{s}} \tag{2.9}$$

for the Co_2MnX films. The deposition rates v_i (in cm/s) are then [71]

$$v_i = \frac{\varphi_i}{n_i} = \frac{\varphi_i \cdot \mathcal{M}_i}{\rho_i \cdot \mathcal{N}_A} \tag{2.10}$$

and thus are defined by the respective atomic flux φ_i either combined with the atomic density n_i (in atoms/cm^3), or combined with the mass density ρ_i (in g/cm^3), the molar mass $\mathcal{M}_i$ (in g/mol) and the Avogadro number $\mathcal{N}_A = 6.02214076 \cdot 10^{23}$ atoms/mol.

The deposited film thickness d_{Co_2MnX} is a function of the deposition time t_{dep} and given by [71]

$$d_{Co_2MnX} = t_{dep} \cdot \frac{v_{Co}\rho_{Co} + v_{Mn}\rho_{Mn} + v_X\rho_X}{\rho_{Co_2MnX}} \tag{2.11}$$

and depends on the individual mass densities as well as the final density ρ_{Co_2MnX}. Instead, it is more convenient to work with the virtual deposition rates v'_i, as established in [71, 103], using

$$d_{Co_2MnX} = t_{dep} \cdot \left(v'_{Co} + v'_{Mn} + v'_X\right) \quad \text{with} \quad v_i = \frac{\varphi_i \cdot \mathcal{M}_i}{\rho_{Co_2MnX} \cdot \mathcal{N}_A} \tag{2.12}$$

[71]: Guillemard et al. (2020), 'Issues in growing Heusler compounds in thin films for spintronic applications'

[103]: Guillemard (2019), 'Half-metal magnets Heusler compounds for spintronics'

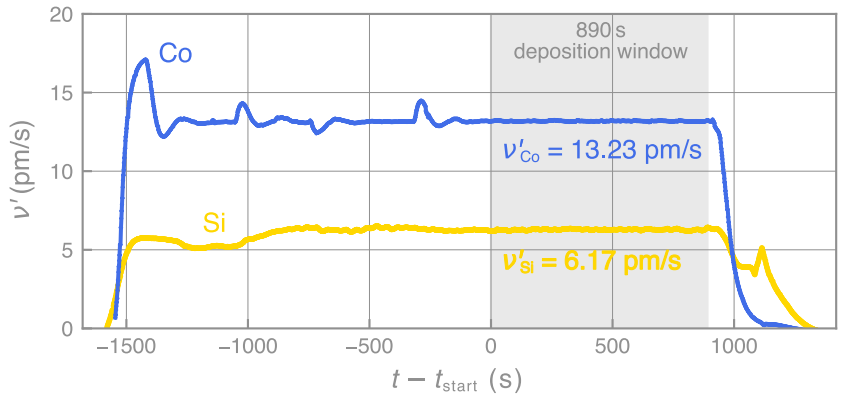

Figure 2.8: Example of the recorded growth rates during the deposition of the Co_2MnSi layer for the sample studied in chapter 6. The growth rates were measured with the quartz microbalances on the electron beam evaporation units from which Co and Si were evaporated. Once the growth rates had stabilised, the deposition process was started by opening the shutter protecting the sample (see figure 2.1) at $t - t_{start} = 0$ s, and stopped after 890 s corresponding to the growth of a 20 nm thick film.

i.e. by fixing the density for each element equal to the density of the expected compound, instead of using the individual densities as in equations 2.10 and 2.11.

With the fluxes set as in equation 2.9 and using the density of the respective Heusler compound, the achieved growth rates are in the order of picometers per second and result in an achievable accuracy of the stoichiometry control of around ±1% for each element of the alloy [71]. Precisely, for the case of Co_2MnSi with the mass density $\rho_{Co_2MnSi} = 7.4\,\mathrm{g/cm^3}$, one obtains

$$v'_{Co} = 13.23\,\frac{\mathrm{pm}}{\mathrm{s}} \quad , \quad v'_{Mn} = 3.16\,\frac{\mathrm{pm}}{\mathrm{s}} \quad \text{and} \quad v'_{Si} = 6.17\,\frac{\mathrm{pm}}{\mathrm{s}} \tag{2.13}$$

for the virtual growth rates and consequently it takes $t_{dep} = 890\,\mathrm{s} = 14\,\mathrm{min}\,50\,\mathrm{s}$ for the growth of a 20 nm thick Co_2MnSi film.

An exemplary recording of the Co and Si growth rates is shown in figure 2.8, corresponding to the measured regulations from the growth process of the sample studied in chapter 6: The deposition process was started by opening the shutter close to the sample position once the deposition rates measured by the quartz microbalances had stabilised. The sample was rotated and the substrate was heated during the deposition process: In the typical sample stacks with a single[18] Heusler layer the Co_2MnX films were grown at surface temperatures of approximately $T_{pyro} \approx 400°C$.

Exemplary RHEED diffraction images of a Co_2MnSi film right after the deposition process are presented in figure 2.7 (2.a) and (2.b) (and recalled in figure 2.9): The typical diffraction pattern is obtained showing the expected intensity modulation between the different streaks along the $[110]_{Co_2MnSi}$ direction in figure 2.7 (2.a), which is attributed to the chemical ordering as introduced in section 2.1.2 on page 22. At this stage prior to the annealing step, the Co_2MnSi film clearly presents a surface roughness leading to the aforementioned intensity modulation along the individual streaks in the RHEED pattern, which is attributed to a 3D growth mode resulting in the formation of islands, as equally introduced above in section 2.1.2. Additionally, the RHEED image along the $[110]_{Co_2MnSi}$ direction in figure 2.7 (2.a) shows two diffraction reflexes outside of the general streak pattern, which could be a result of defects like stacking faults for instance which are easily formed along (111) in fcc structures, but disappears after the subsequent annealing step and therefore was not further analysed.

Afterwards, the samples were annealed at temperatures up to[19] $T_{pyro} \approx 630°C$ which is known to result in an improvement of the crystal structure and chemical ordering in the Heusler compounds [72, 193–196], and has even been

[71]: Guillemard et al. (2020), 'Issues in growing Heusler compounds in thin films for spintronic applications'

18: When growing multilayer samples, the subsequent layers could not be grown at equally high temperatures anymore (and naturally also not be annealed) as a thermally assisted intermixing of the stack needs to be prevented.

19: Precisely, for the two most important samples in this work, the annealing temperatures were $T_{pyro} \approx 632°C$ recorded for the sample Q220102 (S1.1) in table 2.1, while $T_{pyro} \approx 541°C$ was recorded for the sample Q240212 (S1.4) in table 2.1. (Sample S1.1 is studied in the third part of this work, sample S1.4 is studied in the anisotropy analysis in the second part of this work.) The variation in temperatures is mainly attributed to a different coupling between the substrate and the sample holder, as the annealing process was controlled with fixed heating powers. The annealing time was on the order of $t_{annealing} \approx 15 - 20$ min, during which the RHEED pattern was monitored and the process was stopped when no change could be observed anymore (over a couple of minutes).

[72]: Gaier et al. (2008), 'Influence of the $L2_1$ ordering degree on the magnetic properties of Co_2MnSi Heusler films'

[193]: Kämmerer et al. (2004), 'Co_2MnSi Heusler alloy as magnetic electrodes in magnetic tunnel junctions'

[194]: Kudryavtsev et al. (2007), 'Evolution of the magnetic properties of Co_2MnGa Heusler alloy films'

[195]: Trudel et al. (2011), 'Effect of annealing on $Co_2FeAl_{0.5}Si_{0.5}$thin films: A magneto-optical and x-ray absorption study'

[196]: Takamura et al. (2009), 'Analysis of $L2_1$-ordering in full-Heusler Co_2FeSi alloy thin films formed by rapid thermal annealing'

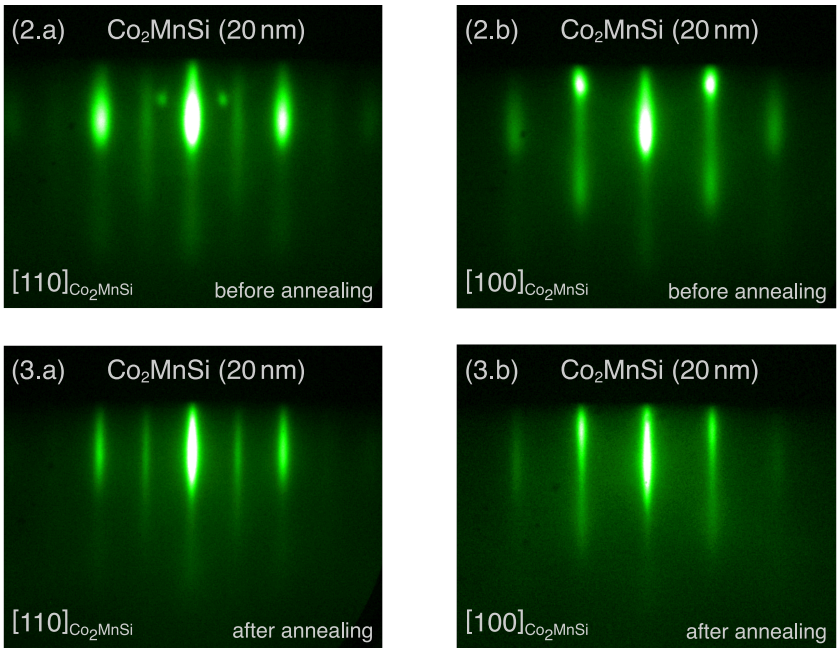

Figure 2.9: Examplary RHEED images captured before and after annealing of the Co_2MnSi layer from the sample studied in chapter 10 (the same as shown in figure 2.7): (2.a) and (2.b) are recalled from figure 2.7 and represent the RHEED diffraction images captured right after the termination of the growth process of the Co_2MnSi layer. (3.a) and (3.b) present the RHEED images obtained after the annealing step at $T_{pyro} \approx 630°C$ (measured at the sample surface with the pyrometer, or $T_{manip} \approx 860°C$ measured by the thermal contact to the sample holder).

used in other studies for a tuning of the chemical ordering degree, see e.g. the study in [72].

Indeed, the annealing step yields a significant improvement as is presented in the example in figure 2.9: Not only do the additional diffraction spots from figure 2.9 (2.a) (recalled from figure 2.7 (2.a)) disappear after the annealing process, as can be seen in the comparison to figure 2.9 (3.a). Additionally, the annealing leads to the aforementioned refinement of the RHEED streaks and furthermore significantly reduces the intensity modulation along the individual streaks corresponding to the point-like 3D diffraction pattern, both of which are attributed to a significant reduction of the surface roughness.

2.2.3 Capping layer deposition

Various capping layers were used in this work: Initially, the samples were capped with a Au capping layer according to the established protocol from [71, 103]. Other metals were used occasionally, for instance for test studies towards the microfabrication of devices containing heavy metals: One Co_2MnSi film was capped with Pd and served as a test sample for the HRTEM/STEM study on the effects of micro-/nanostructuration on Heusler thin films, which will be presented in chapter 3.

Most importantly, in the course of this work, the growth of bilayer cappings with MgO/Ti or MgO/Al was introduced on the system initiated by the need for comparable top and bottom interfaces of the Co_2MnSi layer for a collaborative work on the devices presented in chapter 9. While a simple MgO layer is theoretically sufficient to satisfy this comparability of top and bottom interfaces, the oxide needs to be protected against water adsorption[20]. The second capping layer was chosen based on the known coverage of the MgO surface by Ti and Al from successful reports in literature, see e.g. [199, 200], and due to the simplicity of the stack (only one material to be deposited at a time) the growth process of the capping was straightforward. The capping layers were grown in this work after a cooldown of the sample and without additional heating in order to avoid any effect on the Heusler layer. The MgO layer was grown from an electron beam deposition unit (just like the buffer

[71]: Guillemard et al. (2020), 'Issues in growing Heusler compounds in thin films for spintronic applications'
[103]: Guillemard (2019), 'Half-metal magnets Heusler compounds for spintronics'

20: Not always an undesired feature: In other research fields, MgO nanoparticles are even investigated as adsorbents for wastewater treatment, particularly for the removal of metal contaminations e.g. in drinking water [197] or heavy metals in industrial wastewater [198].

[197]: Szymoniak et al. (2022), 'Application of Magnesium Oxide Media for Remineralization and Removal of Divalent Metals in Drinking Water Treatment'
[198]: Perera et al. (2024), 'Magnesium oxide (MgO) nanoadsorbents in wastewater treatment'

[199]: Kado (2000), 'Structure of Ti films deposited on MgO(001) substrates'
[200]: Sun et al. (2018), 'Heterogeneous nucleation of pure Al on MgO single crystal substrate accompanied by a $MgAl_2O_4$ buffer layer'

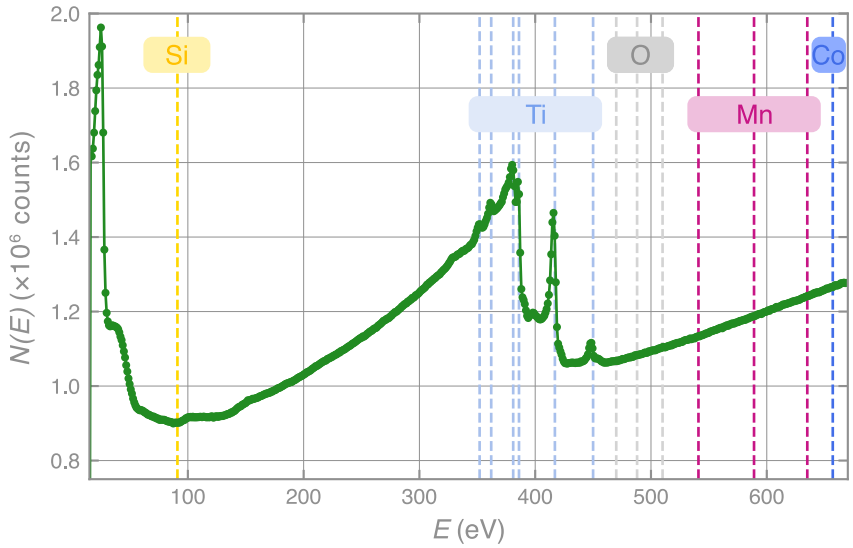

Figure 2.10: Auger spectrum after the deposition of the MgO/Ti capping bilayer. The dashed lines indicate the reference transition energies at which a peak is expected for the respective elements. No signal from Co, Mn, Si or O could be resolved, indicating a decent coverage of the capping layer. Reference values for the transition lines were taken from [201].

layer beneath the Heusler film), whereas the Ti and Al were grown from a Knudsen cell.

The coverage of the bilayer capping stack was tested on the initial samples by performing in-situ Auger spectroscopy after the growth of the capping layers, an example of which is presented in figure 2.10. A qualitative comparison with the literature Auger transition lines in [201] revealed no sign of Auger transitions that could correspond to Co, Mn, Si or O, hence allowing for the conclusion of a complete coverage. Nevertheless, the capping was further investigated in HRTEM and STEM measurements, examples of which will be presented in the next chapter 3.

In fact, these bilayer capping systems proved more reliable than the previously used Au capping particularly on compounds like Mn_3Ge in the framework of the PhD studies in [105], and additionally bear the advantage of an electrical isolation[21] of the Heusler layer. Moreover, while the deposited Al capping was found to have formed an inhomogeneous capping layer in the subsequent HRTEM study, the Ti film was found to have grown homogeneously, simply forming an oxide layer when exposed to air as will be presented in chapter 3. Consequently, the MgO/Ti capping bilayer replaced the previously used Au films as the new standard capping in the growth protocol.

[201]: McGuire (1979), *Auger Electron Spectroscopy Reference Manual*

[201]: McGuire (1979), *Auger Electron Spectroscopy Reference Manual*

[105]: Palin (2023), 'Heusler compounds for spin-orbitronics: exploration of topological effects and magnetic anisotropy engineering'

21: At least in the stacks in this work, where the Heusler film then only has the isolating MgO as adjacent layers (top and bottom).

2.3 List of sample series and purpose

Inevitably, the research towards the implementation of the half-metallic Heusler compound Co_2MnSi into magnonic applications involved multiple preliminary test studies and hence required various sample series for different purposes:

- Firstly, the thorough characterisation of the structural properties was an essential prerequisite in this work, involving studies on the sample stack like the stability of certain capping layers, or the effect of the nanostructuring process on the Heusler compounds' structural properties, some of which will be reported on in this first part of the thesis.
- In addition, the magneto-optical properties of different Heusler compounds were investigated requiring yet another set of samples. For this study, a composition dependence was necessary and the samples originating from [103] were used, as this allowed for a comparison with results in [83].
- And finally various magnetic properties were characterised on multiple sets of samples, aiming for instance for an investigation of the anisotropy effects of the compounds, as well as the magnetisation dynamics in thin films and microstructures, as will be presented in the second and final part of this thesis.

[103]: Guillemard (2019), 'Half-metal magnets Heusler compounds for spintronics'

[83]: Friedel (2021), *Thin film materials with ultralow damping for novel magnonic phenomena*

In addition to the results presented in this thesis[22], the research for this work involved multiple other sample series for different characterisation purposes, such as the effects of the lattice dislocations on the switching behaviour, or the magnetic coupling in Co_2Mn-based bilayer/trilayer systems.

22: Inevitably, many samples were grown for the various test studies and were essential for the further development, but not all of those test measurements can be detailed in the thesis.

2.3.1 Co_2MnSi series for magnonic micro/nanostructures

The main goal of this thesis was to work towards a fabrication of Co_2MnSi-based magnonic devices. The fabrication of such devices involves a fabrication of Co_2MnSi thin films and subsequently a nanofabrication of the device structures (top-down approach). Therefore, different test samples were grown for different steps towards this goal, and the series is listed in table 2.1.

Table 2.1: Sample list for micro-/nanofabrication towards Co_2MnSi-based magnonic devices. ssp = single side polished, dsp = double side polished.

Sample	Growth ID	Full stack	Purpose	Appearance in this thesis
S1.1	Q220102	0: MgO(001) ssp (500 µm) 1: MgO (10 nm) 2: Co_2MnSi (20 nm) 3: MgO (8 nm) 4: Ti (4 nm)	collaboration sample: - grown for spin wave Doppler shift experiments in Strasbourg - device used for study of nonlinearities in this work	- chap. 2: exemplary RHEED images - chap. 3: structural characterisation - chap. 9: device specifications - chap. 10: magonic results
S1.2	Q230403	0: MgO(001) dsp (500 µm) 1: MgO (5 nm) 2: Co_2MnSi (20 nm) 3: Pd (3 nm)	test sample: - structuring test with heavy metal capping: check the influence of structuring processes (etching) on the crystal structure and the chemical ordering in TEM and EDXS	- chap. 3: structuring effects
S1.3	Q240208	0: MgO(001) ssp (500 µm) 1: MgO (5 nm) 2: Co_2MnSi (10 nm) 3: MgO (0.6 nm) 4: Al (3 nm)	test sample: - check the coverage of the MgO/Al capping in TEM and EDXS	- chap. 3: structural characterisation
S1.4	Q240212	0: MgO(001) dsp (500 µm) 1: MgO (10 nm) 2: Co_2MnSi (20 nm) 3: MgO (1 nm) 4: Al (5 nm)	sample for future devices: - structuring test with bilayer capping: check the influence of structuring processes (etching) on the crystal structure and the chemical ordering in TEM and EDXS - goal: Co_2MnSi-based magnonic micro-/nanosized devices	- chap. 2: exemplary growth rate regulations - chap. 3: structuring effects - chap. 5: effects of FMR data analysis - chap. 6: thin film characterisation - chap. 8: implications on the spin wave dispersion

2.3.2 Co_2MnX series for magneto-optical signal study

The magneto-optical properties of the Heusler compounds were investigated on a composition dependent sample series, listed in table 2.2. This sample series was not fabricated within this work, but was taken from a previous work by C. Guillemard [103]. More details on this sample series can be found in [103], and a preliminary optical signal study was done in [83], where in particular a list of the relevant parameters is given in the tables in appendix A.1.2 in [83].

Table 2.2: Co_2MnX sample series for the magneto-optical study in chapter 7.

Sample	Growth ID	Full stack	Purpose	Appearance in this thesis
S2.1	Q181101	0: MgO(001) ssp (500 µm) 1: MgO 2: Co_2MnAl (17.2 nm) 3: Au	magneto-optical signal study: - MOKE anisotropies - BLS signal intensity VSM/FMR study for bilayers: - annealed Co_2MnAl reference	mentioned in 6 results in chap. 7
S2.2	Q190303	0: MgO(001) ssp (500 µm) 1: MgO 2: $Co_2MnAl_{0.75}Si_{0.25}$ (20.4 nm) 3: Au	magneto-optical signal study: - BLS signal intensity	results in chap. 7
S2.3	Q181003	0: MgO(001) ssp (500 µm) 1: MgO 2: Co_2MnSi (17.0 nm) 3: Au	magneto-optical signal study: - MOKE anisotropies - BLS signal intensity	results in chap. 7
S2.4	Q181102	0: MgO(001) ssp (500 µm) 1: MgO 2: Co_2MnGa (20.6 nm) 3: Au	magneto-optical signal study: - MOKE anisotropies - BLS signal intensity	results in chap. 7
S2.5	Q191020	0: MgO(001) ssp (500 µm) 1: MgO 2: $Co_2MnGa_{0.75}Ge_{0.25}$ (20.6 nm) 3: Au	magneto-optical signal study: BLS signal intensity	results in chap. 7
S2.6	Q191017	0: MgO(001) ssp (500 µm) 1: MgO 2: $Co_2MnGa_{0.5}Ge_{0.5}$ (20.7 nm) 3: Au	magneto-optical signal study: - reference from preliminary study [83]	referred to in chap. 7
S2.7	Q191015	0: MgO(001) ssp (500 µm) 1: MgO 2: Co_2MnGe (21.0 nm) 3: Au	magneto-optical signal study: - reference from preliminary study [83]	referred to in chap. 7
S2.8	Q181103	0: MgO(001) ssp (500 µm) 1: MgO 2: Co_2MnSn (21.0 nm) 3: Au	magneto-optical signal study: - MOKE anisotropies - BLS signal intensity	results in chap. 7

2.3.3 $Co_2MnSi/X/Co_2MnAl$ series for coupling investigations

A side study during this work involved the investigation of Co_2MnSi/Co_2MnAl bilayer and $Co_2MnSi/X/Co_2MnAl$ trilayer samples. For this, a test sample of non-annealed Co_2MnAl was grown to serve as a reference for the non-annealed Co_2MnAl in the multilayer stacks (as mentioned above, when growing multilayers only the first Heusler film could be annealed at very high temperatures, as an intermixing needs to be avoided). While the rest of the series does not appear in the main part of this thesis, the Co_2MnAl single layer sample appears in this thesis in the comparative VSM and FMR study in chapter 6.

Table 2.3: Bilayer sample series for test purposes and a coupling study. *1 atp* is short for "1 atomic plane". *ssp* is short for "single side polished". Only the samples appearing in this thesis are listed.

Sample	Growth ID	Full stack	Purpose	Appearance in this thesis
S3.1	Q230604	0: MgO(001) ssp (500 µm) 1: MgO (5 nm) 2: Co_2MnAl (20 nm) 3: MgO (2 nm) 4: Ti (1.5 nm)	non-annealed Co_2MnAl reference	thin film characterisation in chap. 6
S3.2	Q210302	0: MgO(001) ssp (250 µm) 1: MgO (10 nm) 2: Co_2MnSi (20 nm) 3: MgO (1 nm) 4: Co_2MnAl (20 nm) 5: Au (3 nm)	coupled Heusler multilayers	structural characterisation in chap. 3
S3.3	Q210303	0: MgO(001) ssp (250 µm) 1: MgO (10 nm) 2: Co_2MnSi (20 nm) 3: Mn (1 atp) 4: Co_2MnAl (20 nm) 5: Au (3 nm)	coupled Heusler multilayers	structural characterisation in chap. 3
S3.4	Q210304	0: MgO(001) ssp (250 µm) 1: MgO (10 nm) 2: Co_2MnSi (20 nm) 3: Co_2MnAl (5 nm) 4: Au (3 nm)	bilayer optical signal tests	structural characterisation in chap. 3

2.3.4 Cr/V seed layer series for interface dislocation tests

Another side study in this work involved the investigation of Co_2MnGe films on Cr and V seed layers, mostly for the verification of the link between the lattice mismatch and the formation of edge dislocation defects along the interface.*

Note that for both, V and Cr, the unit cell is turned by 45° when grown on MgO. Also, Co_2MnGe was chosen as a Heusler layer in this test series because of the best match with the Cr lattice, i.e.

$$\eta = 1 - \frac{a_{Co_2MnGe}}{2 \cdot a_{Cr}} = 0\,\% \tag{2.14}$$

with $a_{Co_2MnGe} = 0.576\,\text{nm}$ [71] and $a_{Cr} = 0.288\,\text{nm}$ [71], whereas the lattice mismatch with the V lattice

$$\eta = 1 - \frac{a_{Co_2MnGe}}{2 \cdot a_{Cr}} \approx 5\,\% \tag{2.15}$$

with $a_V = 0.303\,\text{nm}$ [71] is non-negligible.

Table 2.4: Seed layer sample series for a side study on the formation of edge dislocations along the interface. *dsp* is short for "double side polished".

Sample	Growth ID	Full stack	Purpose	Appearance in this thesis
S4.1	Q210401	0: MgO(001) dsp (500 µm) 1: MgO (20 nm) 2: Cr (20 nm) 3: Co_2MnGe (20 nm) 4: Au (3 nm)	minimal lattice mismatch	dislocation study in chap. 3
S4.2	Q210403	0: MgO(001) dsp (500 µm) 1: MgO (20 nm) 2: V (10 nm) 3: Co_2MnGe (20 nm) 4: Au (3 nm)	maximal lattice mismatch	dislocation study in chap. 3

* Additionally, an attempt to study the expected pinning of domains during the magnetisation reversal in Kerr microscopy experiments on these samples was carried out in the framework of a research project by bachelor student Benjamin Brachmann, which was supervised by the author of this thesis. However, only very poor magneto-optical signal was obtained from the samples (which is in consistency with the results from the BLS study, see figure 7.7 (b) in chapter 7), and unfortunately made a conclusive interpretation impossible.

Structural characterisation and effects of micro/nanofabrication

3

Following the growth process with a limited in-situ characterisation, a subsequent transmission electron microscopy (TEM) study was carried out for most samples in this thesis allowing particularly to verify the chemical ordering in the Heusler compounds as detailed in [71, 103].

This chapter will give details on this structural characterisation step, focusing particularly on the major results that are different to the previously developed standard case[1] such as the introduced capping bilayer stacks. To this aim, the first section of this chapter will briefly introduce the experimental details which are necessary for the interpretation of the results presented in the second section.

Additionally, the high resolution and the chemical contrast in scanning transmission electron microscopy (STEM) using a high angle annular dark field (HAADF) detector allowed for a study of the micro-/nanofabrication effects on the Heusler crystal structure as will be presented in the third subsection, which forms an important preliminary step towards the fabrication of nanoscaled half-metallic spintronic/magnonic devices for integrated circuits. For this study, two Co_2MnSi films with different capping layers were patterned and cross sections of the thin films as well as the structured samples were subsequently investigated on signs of structural faults or chemical disorder.

3.1 Experimental methods . . 33
FIB cutting 33
TEM and HAADF-STEM . 35
EDXS 36
3.2 Co_2Mn-based film stacks . 37
Chemical ordering 37
Lattice mismatch with MgO and interface dislocations . 39
Capping layer 43
3.3 Structured Co_2MnSi 46
Structuring process 47
Sample layout 49
Lithography results and defect analysis 50
3.4 Conclusions 60

[71]: Guillemard et al. (2020), 'Issues in growing Heusler compounds in thin films for spintronic applications'
[103]: Guillemard (2019), 'Half-metal magnets Heusler compounds for spintronics'

3.1 Sample preparation and experimental methods

As implied by the name, TEM experiments rely primarily on a transmission of an electron beam through the sample, where subsequently various modes can involve for instance the conventional imaging in a high resolution TEM (HRTEM) or in a scanning TEM (STEM) mode, in both of which sub-Ångström resolutions can be achieved in modern setups [202].

Apart from the appropriate electron microscopy setup with adequate achievable acceleration voltages[2], a key ingredient for the successful experiments is a thorough sample preparation, which here consisted of sufficiently thin cross sections cut from the thin films or patterned samples by focused ion beam (FIB) etching[3].

3.1.1 Cross section preparation by Ga^+ FIB

Cross sections of the samples were prepared by Sylvie Migot[4] by focused ion beam (FIB) etching with a Ga^+ ion beam. Prior to etching, a thin carbon layer ($d \approx 10 - 20\,\text{nm}$) was deposited on the patterned samples to avoid charging effects leading to beam drifts during the FIB cutting process [203].

The extraction site for the FIB cross sections was chosen such that all cross sections were cut along the crystal direction $[110]_{Co_2MnX} \parallel [100]_{MgO}$ in which only monoelemental columns are observed in an ideal ordering case, allowing for a distinction between various chemical (dis)orders in the subsequent HAADF-STEM experiments [71]. Additionally, in the case of the patterned

1: Taking the growth procedure and results detailed in [71] as a standard, as introduced in the previous chapter.
[71]: Guillemard et al. (2020), 'Issues in growing Heusler compounds in thin films for spintronic applications'

[202]: Oxley et al. (2017), 'Ultra-high resolution electron microscopy'

2: Not forgetting a skilled operator to perform the high precision experiments.

3: Equally requiring a highly skilled operator, especially for obtaining very thin cross sections with little surface roughness to allow for high resolution TEM imaging.

4: The FIB preparation as well as the TEM experiments were carried out at the *microscopies, microprobes and metallography competence center* (CC3M competence center) of the Institut Jean Lamour in Nancy, France. - The FIB preparation of the sample cross sections was carried out by Sylvie Migot, in consultation with the author of this work to determine the orientation and selected location of the cross section (especially for the patterned samples).
[203]: Orloff et al. (2003), *High Resolution Focused Ion Beams*
[71]: Guillemard et al. (2020), 'Issues in growing Heusler compounds in thin films for spintronic applications'

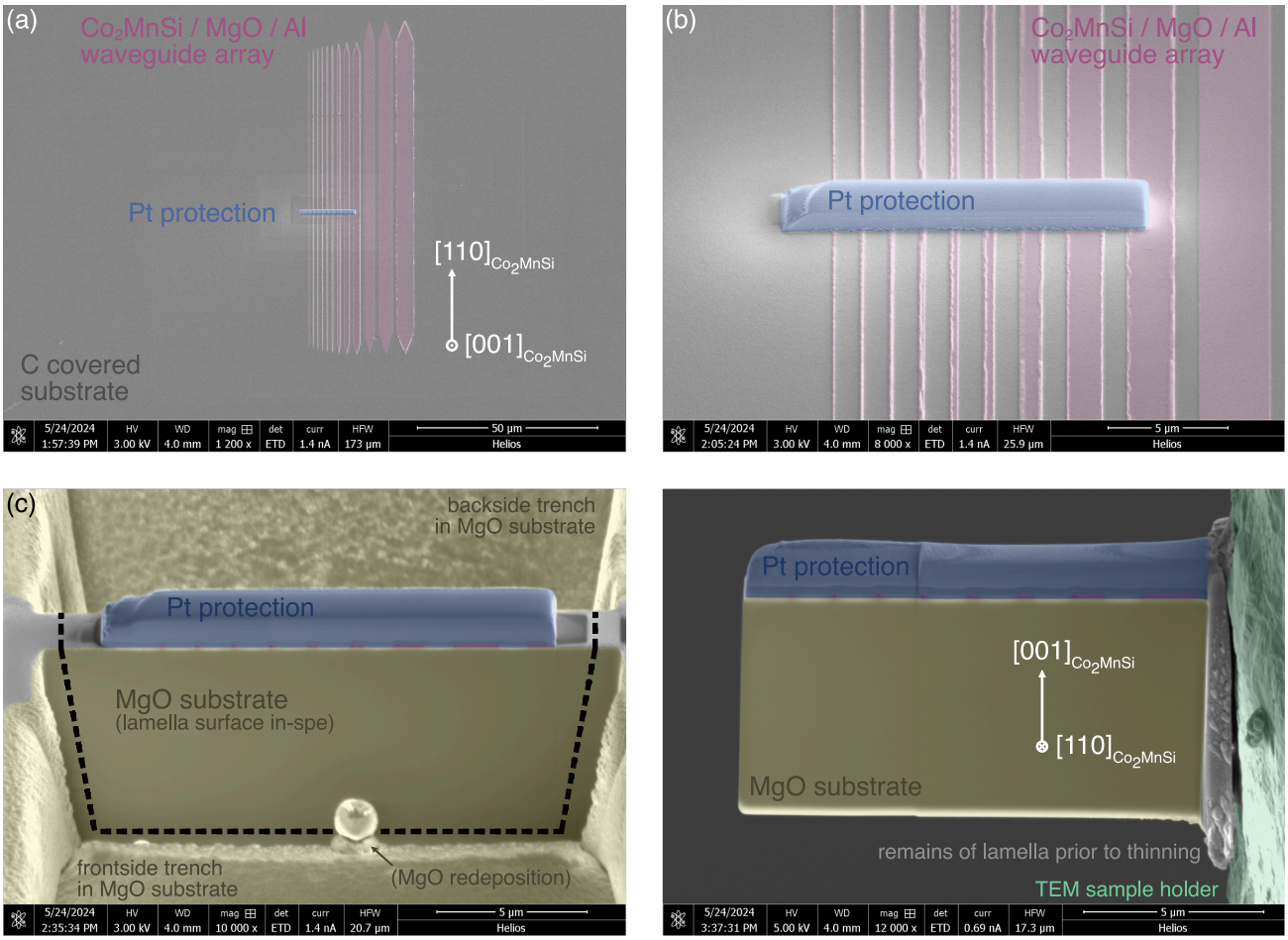

Figure 3.1: Example of a FIB cross section captured by scanning electron microscopy at various stages in the preparation process (images were tinted to improve clarity): (a) waveguide array with a locally deposited Pt protection layer marking the extraction site, (b) close-up after the completion of the Pt protection layer, (c) exposed lamella after the milling of the trenches in the substrate, with the dashed black lines marking the path along which the lamella is to be cut-out after being fixed to a micromanipulator (soldered onto the top left part of the Pt protection, not shown), (d) lamella attached to the TEM sample holder and after several thinning steps (although not the final one - the waveguides could not be made out anymore after the final step). All images correspond to the lamella from a structured piece of the sample S1.4 (Q240212) in table 2.1.

samples, the cross sections were cut perpendicular to the structure to investigate, and the probing location was chosen such that multiple structures could be included at a time.

[204]: Giannuzzi et al. (1999)

The TEM cross section samples were prepared following steps analogous to the *FIB lift-out technique* described in [204], some of which are shown in figure 3.1 on an example of a patterned sample. In short, the protocol was: At the extraction site, a layer of Pt was deposited in two steps[5] locally in order to protect the sample surface during the cutting process, see figure 3.1 (a) and (b). Next, approximately 10 – 15 µm long lamellas were exposed perpendicular to the sample surface by cutting trenches on both sides of the desired extraction site, see figure 3.1 (c). A micromanipulator was soldered onto the lamella before the latter was cut loose by locally etching the sides and the bottom along the dashed lines indicated in figure 3.1 (c). The obtained lamellas were then soldered onto a TEM sample holder and the micromanipulator was removed by a FIB cut, the result of which is shown in figure 3.1 (d). Subsequently, the lamellas were thinned by FIB milling sweeping along the lamella with a gradual decrease of the milling power (reducing the acceleration voltage and the beam current in steps from 30 kV, 790 pA down to 1 kV, 15 pA). The final TEM cross section samples have a thickness of approximately 50 nm at the top, whilst a slightly larger thickness is maintained at the bottom of the bar[6].

[205]: Giannuzzi et al. (2005)
[206]: Kwong et al. (2005)

5: First by focused electron beam induced deposition and second by focused ion beam induced deposition: The first Pt layer serves to prevent damage from the ion beam [205, 206] and the second step allows for higher deposition rates.

6: A trapezoidal cross section is a common side-effect of FIB prepared TEM samples, and referred to as *the classic V-shape* in [204] for instance, where it is attributed to the "competition between sputtering and redeposition" [204] during the FIB milling process. Conveniently, it can help to prevent bending of the FIB lamella, for which additionally a small strip located at approximately 5 µm from the free lamella end was kept thicker than the rest.

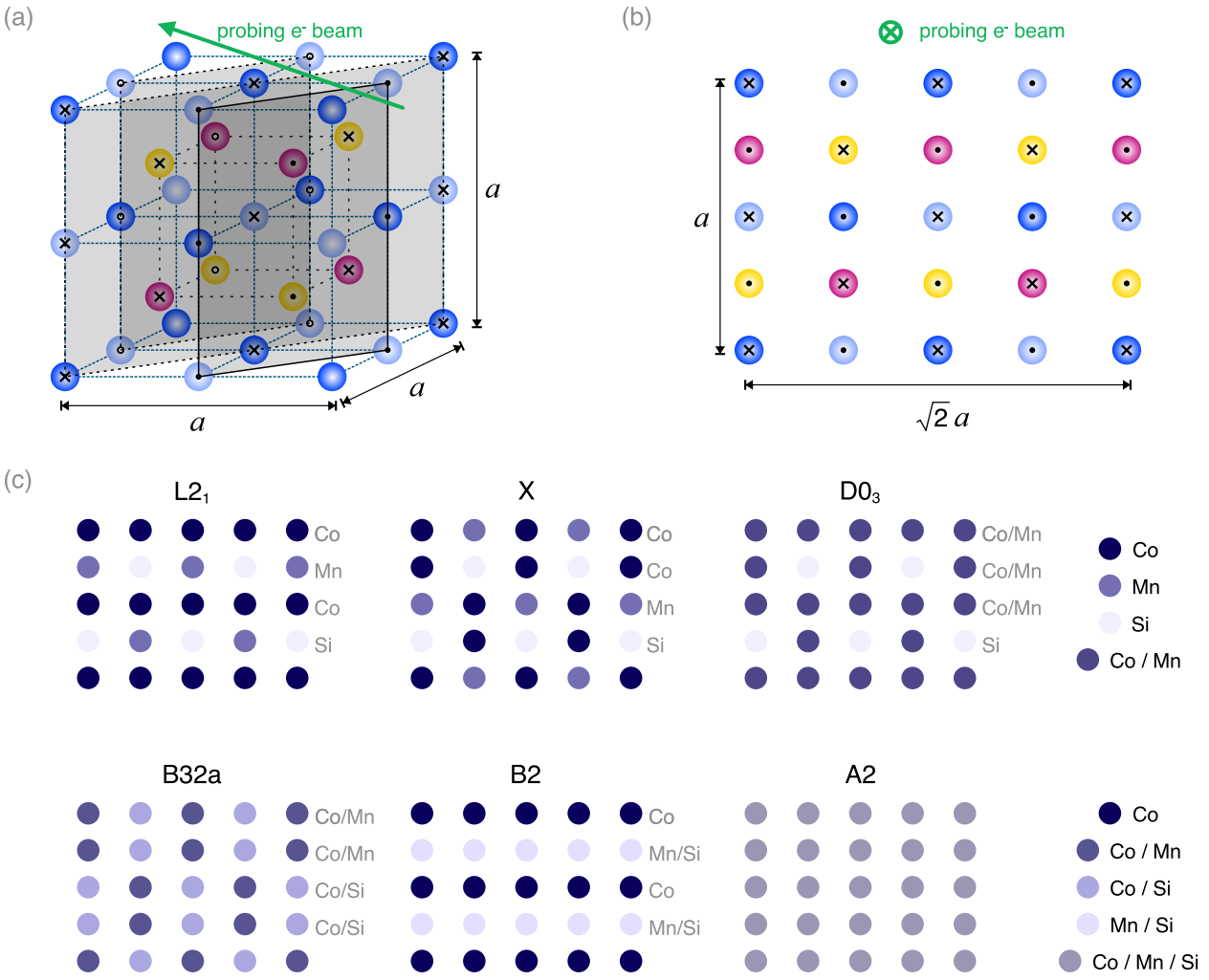

Figure 3.2: Illustration of the (110) atomic planes drawn into the Heusler lattice in (a) where the filled dots, crosses and empty dots mark the element sites lying in the same atomic plane. In a TEM measurement, the electron beam probes all (110) planes behind each other and the obtained image corresponds to the illustration in (b), where monoelemental columns lign up in the transmission direction (perpendicular to the figure/paper plane) for the ordered crystal. Consequently, the (dis)order types introduced in figure 1.4 result in different patterns as illustrated in (c), which can be distinguished when imaged with a chemical contrast as in the by HAADF-STEM imaging mode. Figure adapted from [83].

3.1.2 TEM sample geometry and chemical contrast

Transmission electron microscopy measurements were performed by Dr. Jaafar Ghanbaja[7] on a Jeol JEM-ARM 200F Cold FEG electron microscope with an acceleration voltage of 200 kV. The imaging was performed in two operation modes: (high resolution) transmission electron microscopy (TEM/HRTEM) where the sample is static and illuminated with a parallel beam, as well as scanning transmission electron microscopy (STEM) where the electron beam was focused on the sample. In the STEM mode, the bright field and dark field images were recorded simultaneously where for the latter a high angle annular dark field (HAADF) detector was used, allowing for an imaging with a site-specific chemical contrast[8] [207].

The samples were cut along the $[110]_{Co_2MnX} \parallel [100]_{MgO}$ direction in order to exploit the symmetry of the Heusler lattice for the chemical contrast analysis in HAADF-STEM: In this geometry, monoelemental atomic columns align in the transmission direction for the ordered case, as shown in figure 3.2 (a) and (b). The different (dis)order types result in unique changes to the atomic columns along this direction as illustrated in figure 3.2 (c), which can be distinguished by the resulting intensity pattern in the HAADF-STEM mode [71, 208].

[83]: Friedel (2021)

7: At the *CC3M competence center* of the Institut Jean Lamour in Nancy, France. - All electron microscopy measurements presented in this work were carried out by Dr. Jaafar Ghanbaja in the presence of the author of this work. - The recorded data was afterwards analysed by the author of this work.

8: Sometimes also explicitly indicated as *Z contrast*, the chemical contrast manifests as an intensity difference for atoms of different atomic number Z in the HAADF-STEM micrographs. Precisely, a higher intensity is obtained for the atomic columns with the larger (average) atomic number linked to the increased scattering from heavier atoms. Consequently, the highest contrast in the Co_2MnX compounds studied in TEM/STEM in this work is obtained between sites containing the element X ($Z_{Al} = 13$, $Z_{Si} = 14$) and sites containing Mn and/or Co ($Z_{Mn} = 25$, $Z_{Co} = 27$).

[207]: Treacy et al. (1978)

[71]: Guillemard et al. (2020)
[208]: Nakatani et al. (2010)

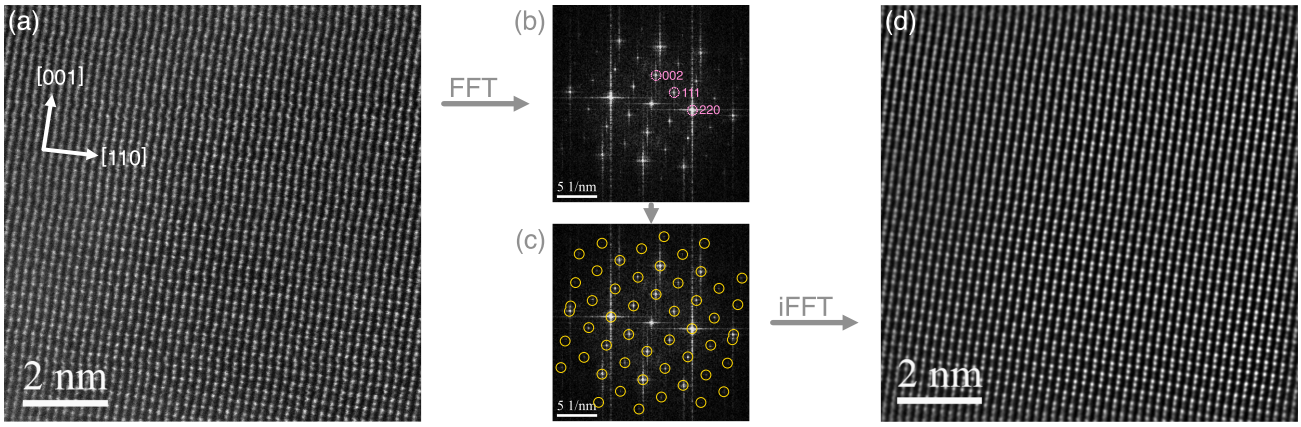

Figure 3.3: Fourier filtering for a contrast enhancement on the example of a HAADF-STEM micrograph captured from the thin film (non-patterned) sample S1.4 (Q240212) in table 2.1. The unfiltered HAADF-STEM micrograph in (a) shows a zoom-in on the Co_2MnSi layer in the $Co_2MnSi/MgO/Al$ thin film stack. Processing the image via the reciprocal lattice pattern obtained by a Fast Fourier Transform (FFT) shown in (b) allows for a filtering: For example, for a noise reduction and contrast enhancement, all reflexes can be selected as marked by the yellow circles in (c), and the selected data can be processed through a back-transformation resulting in the filtered micrograph in (d). The filtered micrograph in (d) undoubtedly presents the intensity pattern corresponding to the $L2_1$ order, while the noise in the raw data especially in the top left of (a) did not allow for a definite conclusion. *Improved image resolution in the digital document.*

In the analysis routine, an image filtering can be employed by processing the Fast Fourier Transformation (FFT) of the micrographs and using only a selection of the data for the back-transformation by the inverse FFT. Depending on the selection of diffraction spots in the reciprocal lattice pattern, the filtering can be performed for multiple purposes: Involving all diffraction spots for instance simply corresponds to a noise filtering as shown in the example in figure 3.3. Another useful filter is the elimination of the information perpendicular to the film plane by allowing only diffraction spots with $(hkl) = (hk0)$ to be back-transformed, which was employed in this work for the analysis of lattice dislocations at the interfaces.

3.1.3 Energy dispersive X-ray spectroscopy

Energy dispersive X-ray spectroscopy (EDX, EDS or EDXS) was employed in this work for a qualitative measurement of the sample composition. The measurements were carried out[9] on the same electron microscope as the TEM/STEM measurements, using a focused electron beam scanning the sample (lamella cross section) surface like in the STEM operation mode, and additionally using an X-ray detection unit for the elemental analysis.

Similar to the Auger spectroscopy used for the in-situ surface analysis before[10], the focused high energy electron beam serves to eject eletrons from inner atomic shells. Yet, contrary to the Auger effect forming a radiationless de-excitation mechanism, the EDXS measurements rely on the occurrence of a de-excitation by an outer shell electron under the emission of radiation with a frequency corresponding to the difference of the associated energy levels. This radiation is typically in the X-ray range and as for the Auger spectroscopy the unique transition energies can be linked to the elements in the sample.

In this work, EDXS measurements were performed mostly in the form of areal scans, i.e. recording spectra at various positions in a scanning mode, which allowed for a mapping of the present elements in the scanned window. Occasionally also linescans were performed, where multiple spectra were recorded at selected points typically along the normal direction of the film plane, allowing for a longer counting time per point and an approximate conclusion on the composition[11].

9: On the same Jeol JEM-ARM 200F Cold FEG electron microscope as the TEM/STEM measurements (the EDXS measurements were performed in the same session on the same lamella) - as mentioned above, the microscope was operated by Jaafar Ghanbaja, including the EDXS measurements.

10: See the brief introduction of the Auger spectroscopy in section 2.1.3.

11: Note that this is still limited: The EDXS measurements and analysis were employed in this work only qualitatively since for a quantitative analysis the system would need to be thoroughly calibrated with calibration standard samples for the specific material(s) to be examined.

3.2 Co_2Mn-based Heusler thin film stacks: interfaces, chemical ordering and capping

Concerning the thin film samples, transmission electron microscopy measurements were performed on most[12] samples in this work for a structural characterisation of the Heusler films after the growth process.

A main focus was set on the verification of the chemical ordering in the Heusler compound, and additionally the analysis allowed for a random[13] control for structural faults like interface defects, chemical impurity penetrations or an intermixing of the layers. Moreover, the measurements enabled a characterisation of all changes to the established process in [71] such as the introduction of the aforementioned capping bilayers.

12: Precisely, a TEM study was always performed after growth when significant changes were made to the established standard process in [71], e.g. by the introduction of a new capping layer. Apart from that, a TEM study was also sometimes performed as a verification at a later point, e.g. when anomalies were observed in other measurements.

13: Only one FIB lamella was analysed per sample, except for the patterned samples. Hence, the analysis was carried out under the assumption that the randomly located FIB cut cross section represents the structure of the entire sample.

[71]: Guillemard et al. (2020), 'Issues in growing Heusler compounds in thin films for spintronic applications'

3.2.1 Chemical ordering

The chemical ordering was verified by an evaluation of the obtained intensity patterns in the HAADF-STEM micrographs. The different intensity patterns illustrated in figure 3.2 can be distinguished by a comparison of three planes per (dis)order type: The combination of one vertical line profile and two horizontal line profiles taken either from consecutive rows or separated by an even number of rows, is unique to each pattern and hence allows for an identification of the (dis)ordering present in the sample.

An example of an intensity analysis is shown in figure 3.4 on a HAADF-STEM micrograph captured from the Co_2MnSi/MgO/Ti thin film sample S1.1 (Q220102) in table 2.1, a microstructure of which is investigated in the third part of this work. Horizontal and vertical line profiles were extracted along the coloured lines in the filtered micrograph in figure 3.4 (a) and are plotted as a function of the distance[14] in figure 3.4 (b) and figure 3.4 (c). The line profiles corresponding to the vertical lines V1, V2 and the horizontal lines H1, H2 shown in figure 3.4 (b) indicate an undisturbed $L2_1$ intensity pattern in the top left part of the sample. However, the profiles V3, V4 and H3, H4 spanning the bottom right corner of the micrograph reveal a transition from the $L2_1$ order to the B2 disorder as is marked by the dashed orange bars in figure 3.4 (c). The corresponding position is transferred to the HAADF-STEM micrograph in figure 3.4 (a), where it is equally marked by orange bars and indicates a limitation of the B2 disorder zone. A qualitative evaluation by a comparison of the intensity patterns in the filtered micrograph in figure 3.4 (a) with the expected patterns illustrated in figure 3.4 (d) corresponding to the two ordering types in play allows to trace an approximate boundary of the B2 disorder zone as indicated by the dashed white line in figure 3.4 (a).

14: The distance is measured from the individual starting point of each line in the direction indicated by the respective arrow on the line.

A predominant $L2_1$ ordering was confirmed in all Co_2MnSi films in this work, consistent with the results reported in [71, 103]. Occasionally small areas indicating a B2 disorder were detected as in the example shown in figure 3.4, yet most HAADF-STEM analyses indicated mainly an $L2_1$ order such as the clear pattern in figure 3.3 before. No intensity pattern indicating any of the other (dis)ordering types illustrated in figures 1.4 and 3.2 were detected in any of the samples.

[71]: Guillemard et al. (2020), 'Issues in growing Heusler compounds in thin films for spintronic applications'
[103]: Guillemard (2019), 'Half-metal magnets Heusler compounds for spintronics'

Considering this, two points are important to make: First, the impression of a B2 disorder can also arise from an appearance of two $L2_1$ ordered zones, which are shifted by half a Heusler lattice cell[15]. When appearing behind each other, this would result in a swap of the Mn and Si columns along the transmission direction, which hence could result in the falsified conclusion

15: In fact, the alignment of multiple shifted $L2_1$ ordered domains behind each other is in the limiting case (a shift appearing at every half of a Heusler lattice cell) exactly equal to the lattice presenting the B2 disorder.

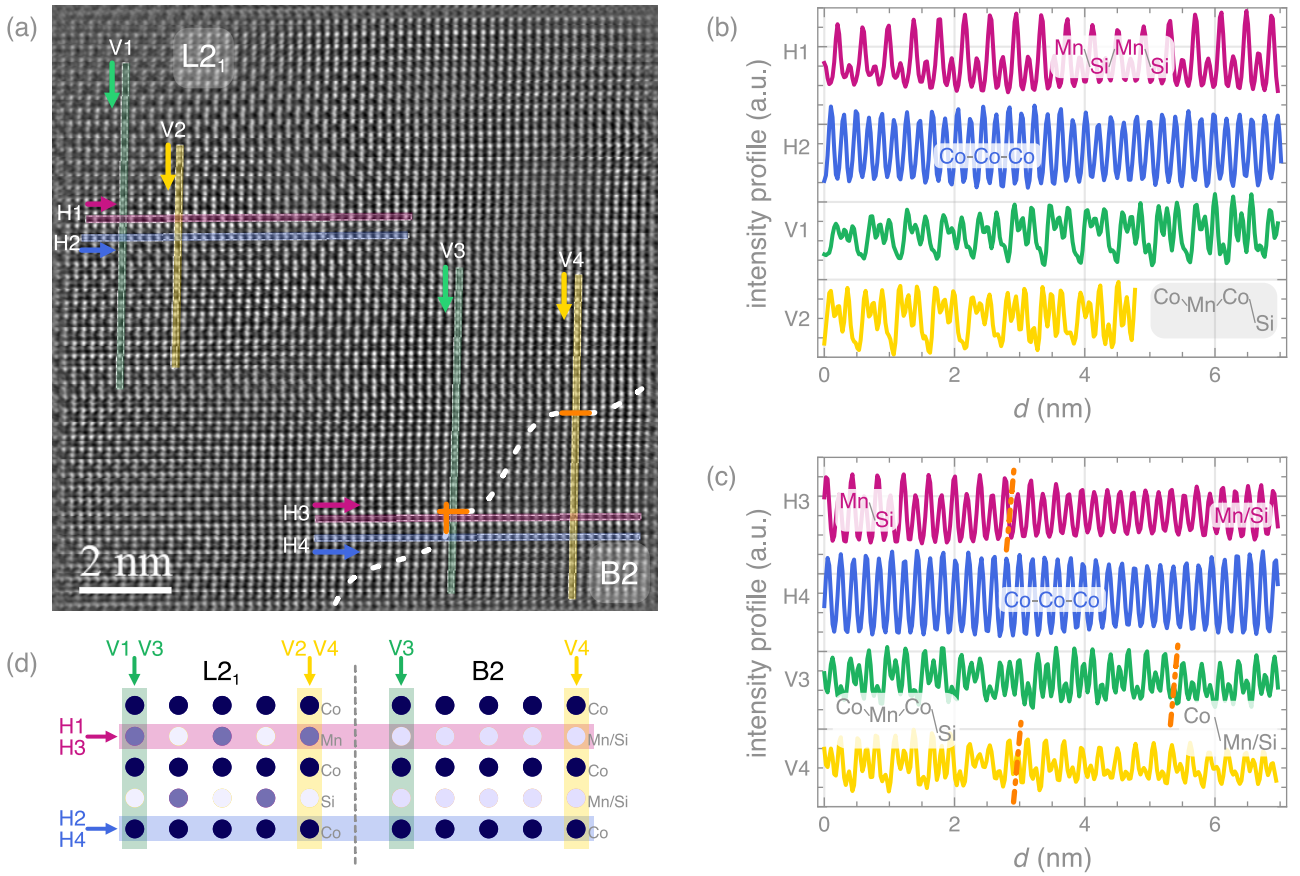

Figure 3.4: Example of the chemical ordering analysis on the Co_2MnSi/MgO/Ti thin film sample S1.1 (Q220102) in table 2.1: Vertical and horizontal intensity profiles were extracted along the lines marked in the filtered HAADF-STEM micrograph in (a) and are plotted in (b) and (c). The intensity pattern in (b) corresponds to the (110) plane of the $L2_1$ ordering, while the intensity pattern in (c) reveals a transition from the $L2_1$ order to the B2 disorder marked by the orange dashed lines "cutting" the intensity profiles. The respective lines are marked in the corresponding distributions of the atomic columns shown in (d). The transition lines were transferred accordingly into the HAADF-STEM micrograph in (a) and equally marked in orange, additionally the white dashed line indicates an approximate limitation of the B2 disorder zone based on a comparison of the intensity pattern in the micrograph to the expected pattern shown in (d). *Improved image resolution in the digital document.*

on a B2 disorder. Such a shift of the chemical ordering could potentially be induced by the appearance of additional atomic planes linked to the lattice mismatch (see next subsection).

Second, it shall be noted that the different zones of chemical ordering are purposefully not denoted as *grains* in order to distinguish from crystallographic grains and grain boundaries as commonly studied in polycrystalline samples: Monocrystalline Heusler films were obtained in all samples in this work, with an intact (physical) crystal lattice detected throughout all micrographs spread across the FIB cut lamella. The variation of the intensity patterns in HAADF-STEM corresponds to a change in the elemental occupation on the corresponding lattice sites and does not imply a physical disruption of the crystal lattice.

Contrary to the $L2_1$-ordered Co_2MnSi, the Co_2MnAl compound is known to grow in the B2 disorder as detailed in [71]. This was confirmed in Co_2MnAl films in various multilayer samples and the single film sample S3.1 (Q230604) in table 2.3 results of which are presented in chapter 6 is expected to present the same B2 disorder, but was not explicitly imaged (yet).

[71]: Guillemard et al. (2020), 'Issues in growing Heusler compounds in thin films for spintronic applications'

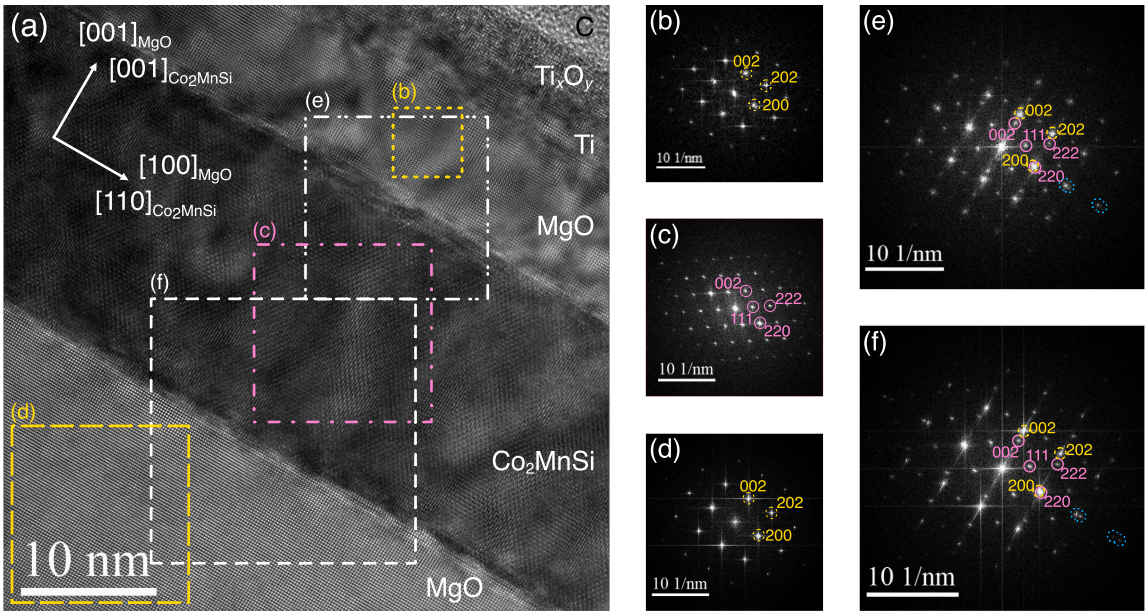

Figure 3.5: Epitaxy of the MgO/Co_2MnSi/MgO stack on the example of the Co_2MnSi/MgO/Ti thin film sample S1.1 (Q220102) in table 2.1. The HRTEM micrograph (unfiltered / raw data) in (a) shows the entire sample stack where the areas corresponding to the FFTs in (b-f) are marked: (b) FFT of the marked area in the top MgO layer, (c) FFT of the marked area in the Co_2MnSi film, (d) FFT of the marked area in the bottom MgO layer, (e) FFT of the top Co_2MnSi interface, (f) FFT of the bottom Co_2MnSi interface. The Miller indices of the lowest order reflexes are indicated and can be continued accordingly. *Improved image resolution in the digital document.*

3.2.2 Lattice mismatch with MgO and interface dislocations

The only physical defects of the Heusler lattice were found to appear along the interfaces which is in consistency with the reports in previous studies [81, 83] where the atomic plane dislocations were detected along the MgO/Co_2MnSi interface (bottom interface of the Heusler layer) and were attributed to the finite lattice mismatch

$$\eta = 1 - \frac{a_{Co_2MnSi}}{\sqrt{2} \cdot a_{MgO}} \approx 4.9\,\% \tag{3.1}$$

as introduced in chapter 2 on page 23, where the $\sqrt{2}$ factor accounts for the 45° rotation corresponding to the epitaxial relationship $[110]_{Co_2MnX} \parallel [100]_{MgO}$.

The lattice mismatch can be visualised by processing the FFT of selected areas in a micrograph of the sample stack, an example of which is shown in figure 3.5. Multiple areas of the HRTEM micrograph in figure 3.5 (a) were processed, where (b-d) correspond to sites of the individual materials (top MgO film, Co_2MnSi film and bottom MgO buffer/substrate respectively) and (e, f) correspond to the top and bottom interface respectively. Note that only the Miller indices for the lowest order reflexes are indicated (and only for one quadrant of the pattern), but the indexing can be continued accordingly.

The obtained reciprocal lattice patterns not only confirm the $[110]_{Co_2MnSi} \parallel [100]_{MgO}$ relationship recalled in the illustration in figure 3.6, but also highlight the slight mismatch along the $[110]_{Co_2MnSi} \parallel [100]_{MgO}$ direction as the corresponding reflexes in the FFTs of the interface areas in figures 3.5 (e) and 3.5 (f) do not fully coincide: While the $(220)_{Co_2MnSi}$ and the $(002)_{MgO}$ spots can hardly be distinguished, an increased separation is obtained for the $(440)_{Co_2MnSi}$ and $(004)_{MgO}$ as well as the $(660)_{Co_2MnSi}$ and $(006)_{MgO}$ spots as marked by the dashed blue outlines in figure 3.5 (e) and 3.5 (f).

Comparing the effect in figure 3.5 (e) and 3.5 (f) corresponding to the top and

[81]: De Melo et al. (2021), 'Unveiling transport properties of Co_2MnSi Heusler epitaxial thin films with ultra-low magnetic damping'
[83]: Friedel (2021), *Thin film materials with ultralow damping for novel magnonic phenomena*

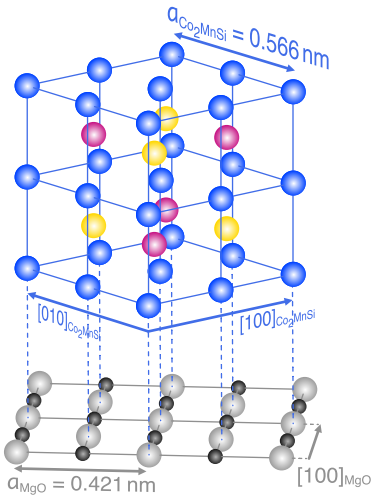

Figure 3.6: Illustration of the epitaxial relation ship of Co_2MnSi on MgO (001): The cubic unit cell of Co_2MnSi is rotated by 45° with respect to the MgO lattice. Illustration recalled from figure 3.6, original figure adapted from [71].

[71]: Guillemard et al. (2020), 'Issues in growing Heusler compounds in thin films for spintronic applications'

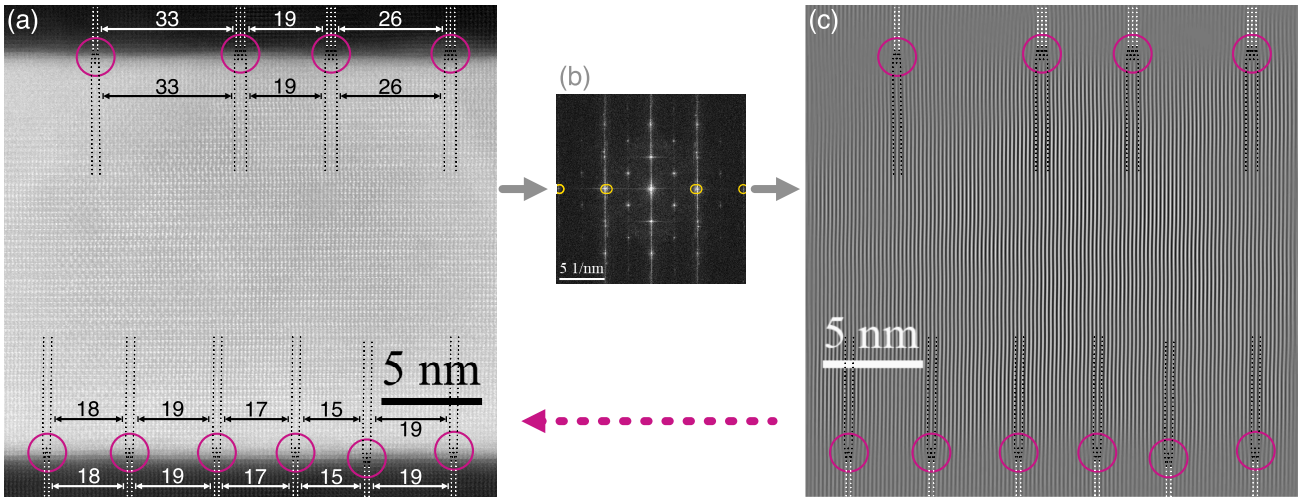

Figure 3.7: Dislocations at the Co_2MnSi interfaces with the adjacent MgO layers on the example of the Co_2MnSi/MgO/Ti thin film sample S1.1 (Q220102) in table 2.1: (a) unfiltered HAADF-STEM micrograph (raw data) showing a close-up of the Co_2MnSi film between the adjacent MgO layers, (b) FFT of the entire micrograph with marks of the applied filtering mask and (c) inverse FFT obtained from the signal within the filtering mask. The applied filter removes all information on intensity modulations perpendicular to the film plane and consequently the atomic plane dislocations are easily identified as marked by the pink circles in the fourier filtered micrograph (c). The corresponding atomic planes were traced as indicated by the dashed lines and subsequently the location marks (traces and circles) were transferred to the original HAADF-STEM micrograph indicating the corresponding sites. Additionally, the count of (undisturbed) atomic planes between the traces planes is evaluated on both sides of the interface as is indicated by the numbers on the arrows (not counting the traced columns - this needs to be considered for the evaluation of the periodicity). *Improved image resolution in the digital document.*

16: Attention needs to be employed when the interfaces are too close to the border of the image, as the Fourier image filtering can yield distortions along the borders of the processed image / area selection, which can falsify the analysis when overlapping with the interface information.

17: Since compared to the oriented volume part of the film, the local distortion of the crystal lattice results in a misalignment of the atomic columns with respect to the probing electron beam.

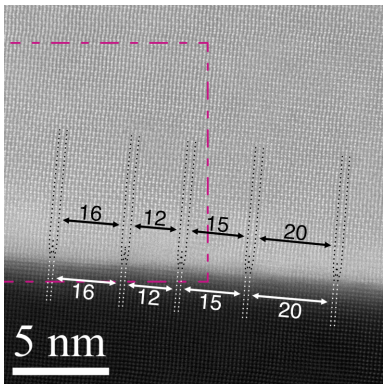

Figure 3.8: Unfiltered HAADF-STEM micrograph from the (non-patterned) thin film sample S1.4 (Q240212) in table 2.1, where the high signal to noise ratio allowed for a direct tracing of the atomic columns in the high resolution HAADF-STEM micrograph as indicated by the dashed lines following the respective atomic planes. The numbers on the arrows indicate the count of lattice planes between the dashed lines and the pink dashed square indicates the area of the close-up shown in figure 3.11. *Improved image resolution in the digital document.*

bottom interface respectively, it seems more pronounced in the latter. This could suggest an adaptation of the top MgO layer to the Co_2MnSi film, but can also be an artifact of the lower resolution in figure 3.5 (e) arising from the smaller data selection area in the micrograph in figure 3.5 (a).

Nevertheless, the observation is in agreement with the reduced number of dislocations observed at the top interface compared to the bottom interface.

The identification of the dislocations is difficult in the raw data, as it typically requires a lower magnification in order to conclude on the periodicity of the feature, but at the same time requires a high enough resolution for a decent precision. Moreover, a sufficient part of the area on both sides of the interface needs to be captured[16] and additionally the local distortion of the lattice typically results in an increased noise in the surrounding area in the micrograph[17] as can be seen in figure 3.7 (a). Therefore, the analysis was performed after a selective filtering process, in which only the diffraction spots containing no information perpendicular to the film plane were selected for a back-transformation as is indicated by the yellow marks in figure 3.7 (b). The result is an intensity pattern showing the atomic planes as lines, since the information on the intensity modulation along the film normal is lost in the filtering process. As indicated in the example in figure 3.7 (c), this facilitates the localisation of the atomic plane dislocations marked by the pink circles, which can then be transferred to the original micrograph. Subsequently, the trace of the surrounding atomic columns was checked for a confirmation of the additional atomic plane.

In HAADF-STEM micrographs with little noise, the dislocations can be identified directly as is shown in the example in figure 3.8. All detected dislocations match the pattern of edge dislocations, a schematic of which is illustrated in figure 3.9.

As the lamella cut was taken along an arbitrary $[110]_{Co_2MnSi} \parallel [100]_{MgO}$ direction and is imaged under the assumption of a representative random cross section sample of the thin film, the same dislocation features must be

expected to occur perpendicular to the imaged plane, i.e. in the depth of the lamella or along the beam transmission direction. Hence, a lattice of dislocation lines is obtained, where the Bruges vector is likely to point either along the $\langle 110\rangle_{Co_2MnSi}$ or the $\langle 100\rangle_{Co_2MnSi}$ directions of the Heusler film.

Drawing a conclusion on the orientation of the lattice dislocation network from the imaging along a single direction is non-trivial, and indeed if only a single atomic plane was imaged it would be impossible. Yet, the combination of the finite thickness of the lamella and the successful imaging in all cut cross sections indicates an orientation of the Bruges vectors along the $\langle 110\rangle_{Co_2MnSi}$ directions: Assuming the FIB cut to be along a random $[110]_{Co_2MnSi} \parallel [100]_{MgO}$ direction and hence the crystal to present equal features perpendicular to the imaged plane, the distances between which are in the range of 2.5 – 4.5 nm, implies that approximately 10-20 of such dislocation features should equally occur in the depth of the ~ 50 nm thick lamella (in the transmission direction of the electron beam). If the dislocation planes were oriented along the $[100]_{Co_2MnSi} \parallel [110]_{MgO}$, the 10-20 deformations in the depth of the lamella would be present at any site[18], and consequently each imaged atomic column in the micrographs would be distorted approximately 10-20 times. This is expected to result in a significant increase of the overall noise due to the distortion along the entire interface, which is contradicted by the rather neat imaging of the interface in the unfiltered micrographs e.g. in figures 3.7 (a) or 3.8. It is therefore assumed to be more likely that the network of dislocations aligns with the principal axes of the MgO lattice, i.e. that the Bruges vectors are oriented along the $\langle 110\rangle_{Co_2MnSi}$ directions.

In all samples, the dislocations along the bottom MgO/Co_2MnSi interface were found to present a rather regular pattern with a periodicity[19] of approximately 19±3 planes in sample S1.1 (Q220102) and 17±4 planes in sample S1.4 (Q240212), which corresponds roughly to the $\eta \approx 5\,\%$ lattice mismatch between MgO and Co_2MnSi: Given the epitaxial relationship $[110]_{Co_2MnSi} \parallel [100]_{MgO}$ and the imaging along the $[110]_{Co_2MnSi}$ direction, the distance between the atomic planes (100) of the MgO lattice are expected to be[20]

$$d_{1atp,MgO} = \frac{a_{MgO}}{2} \approx 0.21\,\text{nm} \tag{3.2}$$

for a lattice parameter $a_{MgO} = 0.421$ nm as indicated in figure 3.6, since two planes are imaged per unit cell. The distance between the atomic planes (110) of the Co_2MnSi lattice are analogously obtained by

$$d_{1atp,Co_2MnSi} = \frac{a_{Co_2MnSi}}{2 \cdot \sqrt{2}} \approx 0.2\,\text{nm} \tag{3.3}$$

with $a_{Co_2MnSi} = 0.566$ nm as indicated in figure 3.6 respectively. Hence, after 20 atomic planes (10 MgO unit cells), the accumulated mismatch in this direction is in principle equal to the distance between the (110) planes of the Co_2MnSi lattice and the formation of an additional atomic plane in the Co_2MnSi crystal can thus counteract the accumulated displacement. Along the top Co_2MnSi/MgO interface, a decreased regularity and increased maximal distance between the dislocations was detected, as seen in figure 3.7, which is likely linked to a partial adaptation of the MgO capping layer to the Co_2MnSi lattice.

The link between the dislocation defects and the lattice mismatch was verified in a side study on Co_2MnGe films grown on Cr or V seed layers (see table 2.4). As shown in the exemplary micrograph cut-outs in figure 3.10, no[21] edge dislocation defects were observed along the Cr/Co_2MnGe interface with

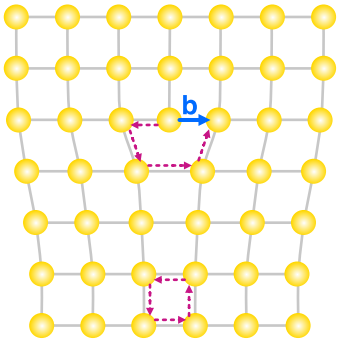

Figure 3.9: Schematic illustration of an edge dislocation with the defining Burgers vector **b**, which indicates the displacement that is obtained at the dislocation site when performing a sequence of steps which in the undisturbed lattice would result in a return to the initial position (compare the dashed pink arrows at the dislocation site to the dashed pink arrows at the bottom). For edge dislocations, the Burgers vector is perpendicular to the dislocation line. Figure adapted from [176, 177].

[176]: Ibach et al. (2009), *Solid-State Physics*
[177]: Ibach et al. (2009), *Festkörperphysik*

18: With their location changing in the depth for each site, but as the captured micrographs correspond to an accumulated picture with no depth information on each site, this difference is lost.

19: Note that the counts in figures 3.7, 3.8 and 3.11 indicate the amount of atomic planes **between** the marked planes (dashed lines) and hence the counts need to be increased by 1 for the evaluation of the periodicity.

20: The abbreviation "1atp" is used here for *1 atomic plane*.

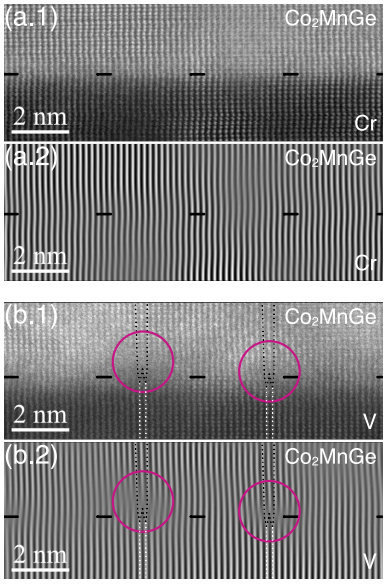

Figure 3.10: Exemplary HAADF-STEM micrographs of (a) the Cr/Co_2MnGe sample with minimal lattice mismatch and (b) the V/Co_2MnGe sample with maximal lattice mismatch, where (a.1, b.1) are the unfiltered and (a.2, b.2) the filtered micrographs.

21: No dislocation was detected in any of the more than 20 HAADF-STEM micrographs showing the Cr/Co_2MnGe interface in a sufficient resolution.

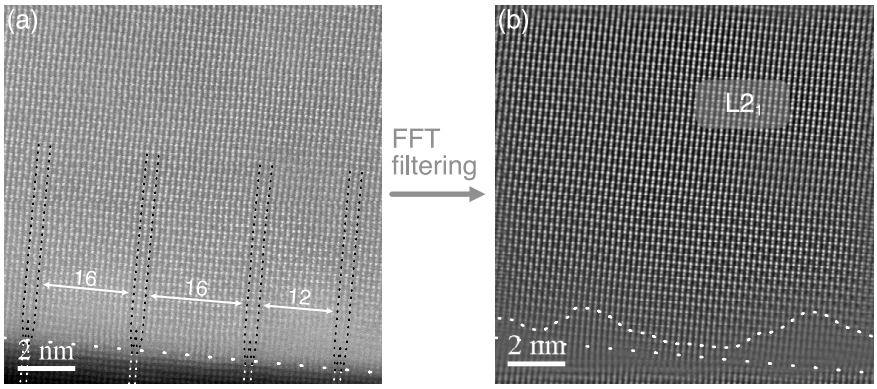

Figure 3.11: Zoom-in on the marked area in figure 3.8: (a) unfiltered HAADF-STEM micrograph from the (non-patterned) thin film sample S1.4 (Q240212) in table 2.1, (b) filtered micrograph presenting the $L2_1$ intensity pattern in the entire captured area (except of uncertainty in the distorted region around some dislocations). *Improved image resolution in the digital document.*

the minimal lattice mismatch ($\eta \approx 0\,\%$), whereas dislocations were indeed observed along the entire V/Co_2MnGe interface with the non-negligible lattice mismatch ($\eta \approx 5\,\%$). Moreover, the noise in the HAADF-STEM micrographs on the sample with the V seed layer was significantly increased at the V/Co_2MnGe interface[22], making the tracing of the atomic columns impossible without the selective FFT filtering described in figure 3.7. This is contrary to the observations along all MgO/Co_2MnSi interfaces, where often an identification of all atomic columns even around the dislocation sites was possible in the unfiltered images as is shown in the example in figure 3.12. The less neat interface in the V/Co_2MnGe sample might be due to an increased lamella roughness/deformation which could be linked to the increased strain at the interface, but can also signify a mis-alignment of the atomic columns in the probing direction (depth of the lamella), e.g. due to the dislocated planes being aligned along the $[100]_V \parallel [100]_{Co_2MnSi} \parallel [110]_{MgO}$ directions (at 45° to the lamella cut) as discussed above.

22: I.e. a significantly increased noise in the micrographs was detected only at the V/Co_2MnGe interface, but not in the remaining parts of the data.

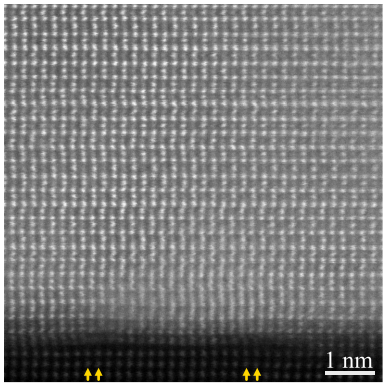

Figure 3.12: Unfiltered (raw data) HAADF-STEM micrograph of an MgO/Co_2MnSi interface, where the edge dislocations are directly imaged. This is sample S3.3 in table 2.4. *Improved image resolution in the digital document.*

Furthermore, the lattice deformations at the interface around the dislocation sites were found to affect only 1-2 Heusler unit cells along the film normal, i.e. approximately $0.5 - 1.2\,\text{nm}$ measured from the interface into the Co_2MnSi layer. Beyond this, a relaxation was observed as all lattice planes were found to be parallel[23] throughout the captures in all samples in this work. The physical lattice deformation induced by the dislocation network is therefore expected to affect mainly the interface properties and not to yield a significant change of the volume properties within the film. This conclusion is backed by the report in [81, 83], where a Co_2MnSi sample series with film thicknesses between $4 - 44\,\text{nm}$ was investigated: A deviation from the bulk behaviour is reported for the smallest thicknesses in the magnetisation dynamics properties from FMR measurements on the thin films (manifesting as an increasing damping, increasing inhomogeneity, decreasing effective magnetisation) as well as in the electrical resistivity measurements on Hall bar structures (increasing resistivity, decreasing electron mobility, increasing inelastic scattering).

Moreover, it is noted that the occurrence of the dislocations does not seem to have a significant direct impact on the chemical ordering, since the $L2_1$ intensity pattern was detected in direct proximity of most of the dislocations, as shown in the example in figure 3.11 (corresponding to the marked area in figure 3.8) and figure 3.12. This observation is of particular importance for the parameters defining the magnetisation dynamics, since the magnetic moment is expected to decrease [140] with an increasing B2 disorder ratio (Mn/Si swap), and also the Gilbert damping of Co_2MnSi was reported to increase in experimental as well as theoretical studies [72, 140]. Yet, occasionally small zones of presenting the B2 disorder pattern were observed as was discussed above on the example of the chemical ordering analysis. Concerning this, it is noted that the formation of a dislocation lattice aligns with the hypothesis of

23: In the limit of the detection precision: Drifts during the measurement, as well as a potential surface roughness of the lamella can for instance also result in the impression of a "deformed" lattice, but have a different signature than the localised deformations around the dislocations.

[81]: De Melo et al. (2021), 'Unveiling transport properties of Co_2MnSi Heusler epitaxial thin films with ultra-low magnetic damping'

[83]: Friedel (2021), *Thin film materials with ultralow damping for novel magnonic phenomena*

[72]: Gaier et al. (2008), 'Influence of the $L2_1$ ordering degree on the magnetic properties of Co_2MnSi Heusler films'

[140]: Pradines et al. (2017), 'First-principles calculation of the effects of partial alloy disorder on the static and dynamic magnetic properties of Co_2MnSi'

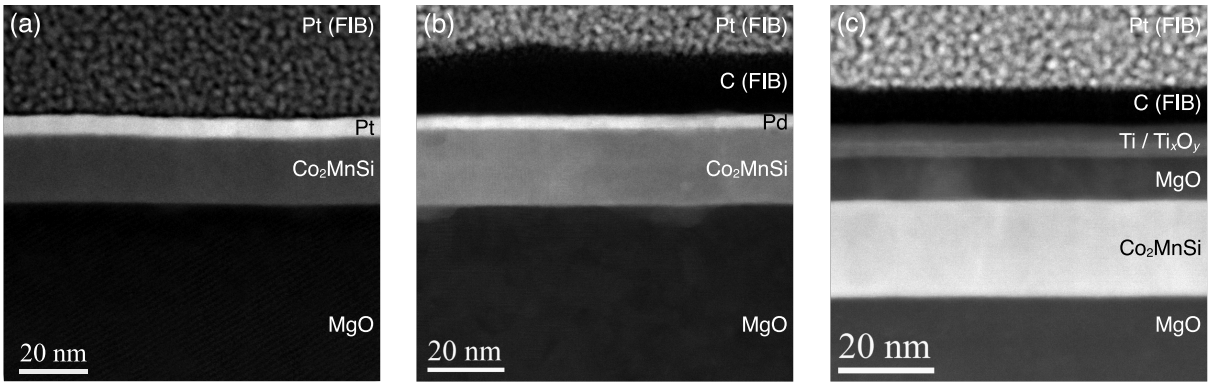

Figure 3.13: HAADF-STEM micrograph examples of the continous thin film cappings obtained with (a) Pt, (b) Pd and (c) MgO/Ti throughout all respective samples across each lamella.

some "falsified" detection of B2 disorder potentially arising from an alignment of shifted zones of $L2_1$ order in the transmission direction: As approximately 10-20 additional planes appear "inserted" in the probing direction (in the depth of the lamella), such an alignment of e.g. two $L2_1$ ordered zones "behind each other" (in transmission direction) is not unlikely and could indeed result in the micrographs presenting a B2 disorder pattern.

The presence of a network of atomic plane dislocations is not only important for its structural aspects and effects on the chemical ordering, but is of relevance in various other contexts as well: Just like any other crystal defect, the atomic plane dislocations can act as pinning centres for magnetic domains e.g. affecting the magnetisation reversal in the thin films, which could give rise to the persistent loop opening (*tails*) of the subsequently measured hysteresis loops as detailed in the second part in section 6.1. Moreover, a network of dislocations mimicking the lattice symmetry can yield an anisotropic damping contribution due to the directional increase of inhomogeneities [209, 210], which is consequently considered in the discussion of the rotational FMR linewidth study in section 6.2. Lastly, the different amount of dislocations at the top and bottom interfaces can principally have an impact on the reciprocity of the surface spin waves, yet the results from propagating spin wave spectroscopy (PSWS) measurements on a piece of the sample S1.1 (Q220102) studied in [91] suggest a negligible difference between the magnetic properties of the two interfaces.

[209]: Heinrich et al. (2004), 'Magnetic properties of NiMnSb(001) films grown on InGaAs/InP(001)'
[210]: Woltersdorf et al. (2004), 'Spin dynamics in ultrathin film structures with a network of misfit dislocations'
[91]: Solano Córdova (2024), 'Temperature dependent spin wave study of magnetic properties and spin-polarized electron transport in $Fe_{1-X}V_X$ and Co_2MnSi epitaxial films'

3.2.3 Protection by the capping layer

Various capping layers were used for the different samples in this work as was detailed in chapter 2: Initially, the standard procedure consisted of a Au capping following the process in [71, 103]. In order to produce Heusler films with comparable top and bottom interfaces particularly for the spin wave studies in [91] as well as in the third part of this work, the MgO/Ti and MgO/Al capping layers were introduced. Finally, Pt can be used as heavy metal capping layer and was grown for a magnetotransport series in a different study, for which the sample with a Pd capping served as a structuring test.

[71]: Guillemard et al. (2020), 'Issues in growing Heusler compounds in thin films for spintronic applications'
[103]: Guillemard (2019), 'Half-metal magnets Heusler compounds for spintronics'

The cappings of MgO/Ti, Pd and Pt were observed to have formed continuous thin films in all samples, examples of which are shown in figure 3.13. The heavy metal cappings formed inert layers which do not react when exposed to air. On the other hand, the Ti layer in the MgO/Ti bilayer capping of sample[24] S1.1 was found to have oxidised leading to the formation of a trilayer capping[25], as can be seen in figure 3.13 (c), which was found to be homogeneous across the

24: This is the sample of which a device was produced by collaborators (see section 9.1.1) which is studied in chapter 10.

25: The capping thicknesses were measured from HRTEM micrographs on the sample: $d_{MgO} = 8.7 \pm 0.1$ nm and $d_{Ti/TiO} = 6.7 \pm 0.1$ nm, with the separation into $d_{Ti} = 3.2 \pm 0.1$ nm and $d_{TiO} = 3.5 \pm 0.1$ nm.

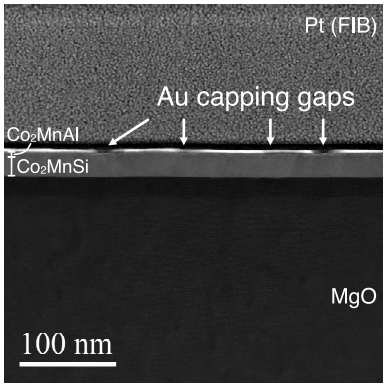

Figure 3.14: Example of an Au capping film presenting gaps in a HAADF-STEM micrograph, corresponding to sample S3.4 in table 2.3. The Au layer corresponds to the brightest contrast in this micrograph. Note that while the exterior two gaps (at the most left / most right) are "full gaps" across the lamella thickness, the inner two are "partial gaps" where still some Au is detected, but the change in contrast and the damage in the Heusler layer underneath imply a gap in a part of the probed volume at that site.

[103]: Guillemard (2019), 'Half-metal magnets Heusler compounds for spintronics'

26: In order to verify the protection, two EDXS mappings were recorded: One at a random site with a large amount of MgO/Al detected in HAADF-STEM (darkest contrasts, similar to the island on the left in the frame of figure 3.15 (b)) and one at a random site with little capping detected in HAADF-STEM (between two thinner islands).

entire lamella. With all three capping layers shown in figure 3.13, consistently well-protected and intact Heusler films were obtained at any probed site.

This is different for the (initial default) capping consisting of an Au layer: Especially with Au thicknesses below 5 nm, an example of which is shown in figure 3.14, occasional gaps were found in the capping layer, resulting in an exposure of the Heusler film to air and hence a local oxidation. The damage due to oxidation was found to be dependent on the exposed area, and apart from a few exceptions was limited to penetration depths below ~ 5 nm. It is important to note that these gaps were not observed consistently in all samples, yet the irregularity leads to the conclusion of an unreliable protection by the Au capping layer imposing a need to verify the complete coverage, especially for Au thicknesses below 5 nm. However, concerning the sample series listed in itable 2.2 for the magneto-optical study in chapter 7, homogeneous, complete Au capping layers were assumed and were not verified since the sample series had been produced and thoroughly studied in [103], where no coverage issues were reported on the capping.

Lastly, the MgO/Al bilayer capping was the only one not forming a homogeneous film at all: The Al was found to grow in islands, examples of which are shown in figure 3.15. The island growth (and subsequent oxidation) lead to an amorphous capping layer in the test sample (S1.3 in table 2.1) presenting a poor crystal definition in the HRTEM micrographs as seen in figure 3.15 (a) due to the oxidation as observed in the EDXS mapping[26], see figures B.1 and B.2 in the appendix B. As detailed in the related evaluation discussion on page 215, the chemical mapping of this test sample lead to the conclusion that albeit the island growth a decent protection can be principally achieved with the MgO/Al bilayer capping (as a sufficient protection of the Heusler film was detected beneath the islands), but the individual layer thicknesses need to be slightly increased for a complete coverage.

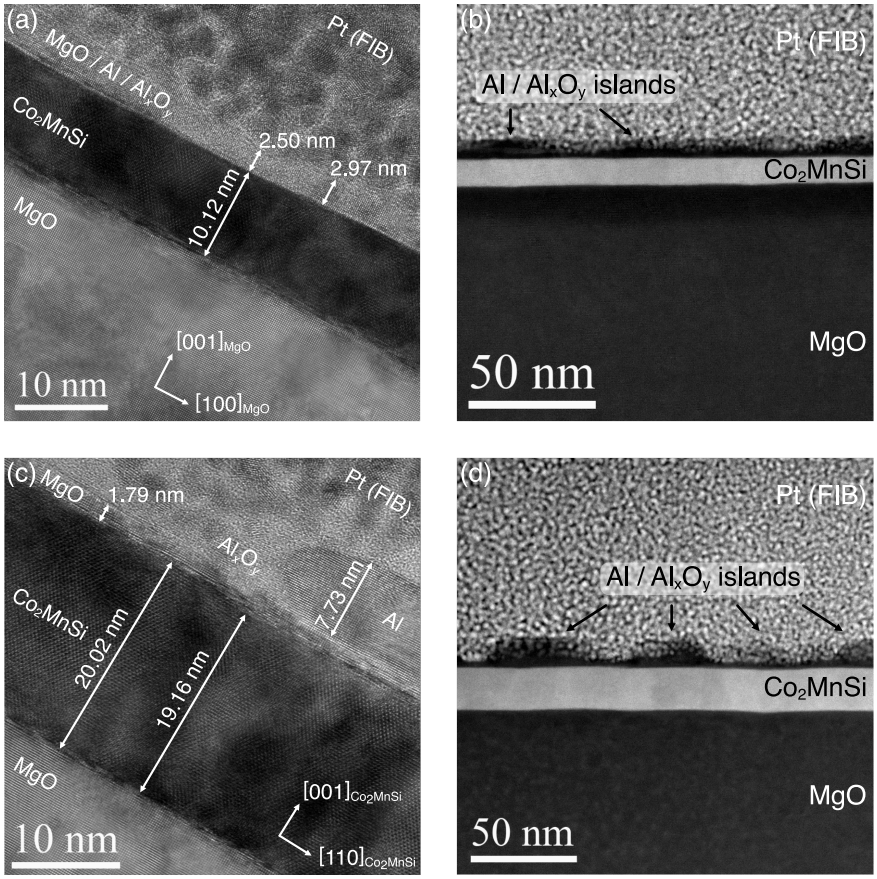

Figure 3.15: Islands in the MgO/Al bilayer capping. (a) a HRTEM micrograph and (b) a HAADF-STEM micrograph of the test sample S1.3 with deposited thicknesses of $d_{MgO} = 0.6$ nm and $d_{Al} = 3$ nm as listed in table 2.1. (c) a HRTEM micrograph and (d) a HAADF-STEM micrograph of the sample S1.4 with deposited thicknesses of $d_{MgO} = 1$ nm and $d_{Al} = 5$ nm. An inhomogeneous, mostly amorphous capping layer was obtained in the test sample (a,b) in which it was impossible to resolve the individual layers of the deposited MgO/Al bilayer stack. The related EDXS measurements in the appendix B and showed that no complete coverage and protection of the Heusler film was achieved in this sample. Based on these results, the capping layer thicknesses were increased for the sample S1.4 (c,d). Here, the MgO layer was distinguishable across the entire lamella and islands of Al surrounded by an amorphous oxide could be resolved (c). Due to the formation of islands with larger thicknesses, the surface roughness was found to be larger compared to the test sample (d vs. b). *Improved image resolution in the digital document.*

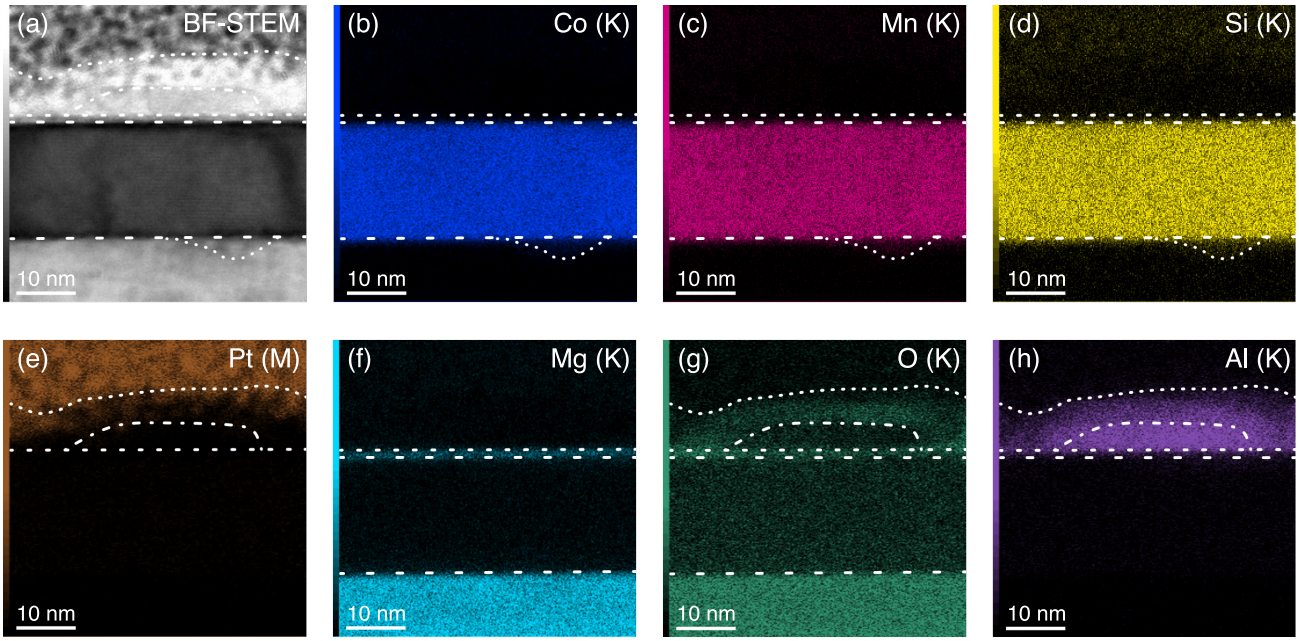

Figure 3.16: EDXS elemental mapping of the Co_2MnSi/MgO/Al thin film stack corresponding to sample S1.4 (Q240212) in table 2.1: (a) BF-STEM (bright field STEM) micrograph captured before the spectral mapping, (b-d) mapping of the Heusler compound elements Co, Mn and Si, using the K-lines, (e) mapping of the deposited Pt from the FIB process, using the M-lines, (f-h) mapping of the substrate and capping elements Mg, O, Al, using the K-lines. The dashed lines were added as guides for the comparison of the different elemental maps.

Consequently, the deposited capping layer thicknesses were increased from $d_{MgO} = 0.6\,nm$ and $d_{Al} = 3\,nm$ in this test sample to $d_{MgO} = 1\,nm$ and $d_{Al} = 5\,nm$ in the final sample S1.4. This resulted in clearly distinguishable parts of the capping bilayer where the MgO film and some non-oxidised Al island cores could now be resolved in all HRTEM micrographs as opposed to the test sample S1.3, see the examples in figure 3.15 (a) and (c). Yet, the increased Al deposit leads to the formation of larger islands and hence increased (and normally undesirable) surface roughness, as can be seen when comparing the HAADF-STEM micrographs in figure 3.15 (b) and (d).

The protection of the Co_2MnSi Heusler film was again verified by two EDXS mappings, an example[27] of which is shown in figure 3.16. The comparison of the elemental mappings lead to the following conclusions on the capping:

- A complete protection of the Heusler film was successfully achieved for the deposited layer thicknesses $d_{MgO} = 1\,nm$ and $d_{Al} = 5\,nm$ in sample S1.4 (but not for $d_{MgO} = 0.6\,nm$ and $d_{Al} = 3\,nm$ in sample S1.3).
- At sites of insufficient protection (in the test sample S1.3), no impurity penetration was found inside the Heusler layer, but Si was detected at the surface seeming to have formed an oxide.
- The Al (islands) equally oxidised at the exposed surfaces, but in larger islands non-oxidised cores could be detected.
- The MgO layer in sample S1.4 is homogeneous and intact (see for instance figure 3.16 (f) ang (g)), even between the Al islands.

Additionally, the elemental mapping in figure 3.16 reveals a roughness of the deposited MgO buffer layer as Co, Mn and Si were detected below the interface[28] of sample S1.4. Three such sites could also be identified in HAADF-STEM by a slight contrast difference, see for instance figure 3.17. No indication for an effect on the Heusler film was found at any of the sites, nor a propagation of the interface roughness through the Heusler layer. Still, the observation is important notably allowing to exclude a structuring process step as the cause[29] for the discussion in the following section, where similar features were observed in the patterned sample.

27: A second EDXS mapping recorded at a site between two islands is shown in figure B.4 in the appendix B on page 218.

28: Compare figures 3.16 (a-d) and (f-g).

29: Instead, an irregularity during the deposition process is more likely to be the cause.

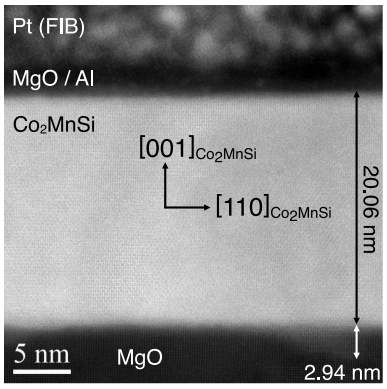

Figure 3.17: A HAADF-STEM micrograph of sample S1.4 showing one (of only three) observed uneven MgO buffer layer sites. No effect on the Heusler film, epitaxy, crystal structure or film roughness was observed at any of the sites. *Improved image resolution in the digital document.*

3.3 Co_2MnSi micro/nanostructures

Micro- and nanostructured devices and circuits form a substantial part of the current research field on magnonics, with applications including spin wave logic gates, magnonic crystals, neuromorphic spin wave circuits and many more [40, 211, 212]. A persisting challenge in the field is the fabrication of well-defined magnonic devices with a sufficient structural quality and unaffected properties after the fabrication process [40].

Indeed, although Co_2Mn-based Heusler compounds offer a vast range of desirable properties for various application needs as was introduced in chapter 1, keeping these properties through a successful device fabrication process is not trivial: The requirement of an epitaxial film growth imposes a device fabrication in the top-down approach[30], i.e. the micro-/nanostructures are fabricated from the thin films in a subsequent patterning process, typically involving lithography and milling steps. Such downscaling/patterning processes are known to affect the magnetic properties of various materials, a common issue for instance in YIG [214–216]. Also in the case of Co_2Mn-based Heusler compounds, especially for the half-metallic Co_2MnSi, the potential structural damage during the patterning process is expected to be particularly important due to their properties' strong dependence on the intact crystal structure, the precise stoichiometry and the chemical ordering [71, 72].

A recent example of this criticality for the spin wave dynamics in Co_2MnSi nanostructures is given in a study by Mantion *et al.* [77] reporting on the significant influence of the Ga^+ implantation and the irradiation damage on the spin wave modes of a Co_2MnSi-based magnonic crystal consisting of a focused ion beam (FIB) etched antidot lattice produced from an *uncapped* 50 nm thick Co_2MnSi film on an MgO(001) substrate. The study in [77] is based on a thorough micromagnetic evaluation of a simplified model system requiring several assumptions to estimate the structural damage and the induced defects in the Co_2MnSi crystal lattice: Firstly, the impacted volume was not experimentally quantified[31], but is estimated to correspond to the entire edge of the etched antidot. Secondly, a generalised lateral damage due to ion collisions with the Co_2MnSi structure is considered to account for point defects, such as vacancies or Frenkel defects[32], based on the results of previous studies on He^+ and Ga^+ irradiated Co_2-based Heusler compounds [75, 76]. Thirdly, the implantation of Ga^+ ions into the Co_2MnSi structure is simulated and assumed to drastically reduce the magnetic properties based on another study of Ga^+ irradiated Co_2FeSi [74].

To date, the study by Mantion *et al.* [77] is the only known[33] report on the impact of structural defects from a top-down fabrication process on the spin wave properties of a microstructured Co_2MnSi-based magnonic device[34]. Their results emphasise the importance of fabrication-induced defects on the magnetisation dynamics, which is underlined by similar generalised conclusions from studies on ion-irradiated thin films [74–76] as well as glass-coated microwires [217, 218]. Yet, the involved simulations and assumptions in [77] for an approximate estimation of the induced damage, and additionally the negligence of oxidation effects on the exposed Co_2MnSi albeit an expected amorphisation of 2−5 nm from previous studies [106] highlight the necessity for a thorough structural quantification of potential fabrication defects especially in the prospect of a successful magnonic device development.

Therefore, the impact of a typical micro/nano-structuring process in a top-down approach involving electron beam lithography and ion beam milling was investigated in this work and will be presented in this subsection.

[40]: Barman et al. (2021)
[211]: Chumak et al. (2014)
[212]: Heinz et al. (2020)

[213]: Abid et al. (2022)

30: The fabrication processes of micro/-nanostructures are generally classified into *top-down* and *bottom-up* approaches, mainly specifying whether the process starts with a larger volume of the (bulk) material and involves a down-scaling by a partial destruction/removal (= top-down) as in this work, or whether the process involves an assembly of the micro/nanostructure from the individual atoms/molecules (= bottom-up). [213]

[214]: Jungfleisch et al. (2015)
[215]: Kiechle et al. (2023)
[216]: Greil et al. (2025)

[71]: Guillemard et al. (2020)
[72]: Gaier et al. (2008)

[77]: Mantion et al. (2022)

31: I.e. no measurement of the atomic damage and the volume of the impacted crystal structure presenting damage or implantations was made. Instead, SEM imaging was carried out for a measurement of the edge geometry, measuring the top and bottom extent of the antidots. The damaged volume was then estimated to correspond to the entire edge, i.e. the difference between top area and bottom area from the SEM analysis.

32: Definition by Ibach-Lüth (p.45 in [176]): "The so-called *Frenkel defect* consists of an atom displaced from its regular site to an interstitial site. The atom in the interstitial site and the vacancy in the regular site together are named *Frenkel pair*."

[75]: Abdallah et al. (2016)
[76]: Abdallah et al. (2017)

[74]: Hamrle et al. (2007)

33: To the best of my knowledge.

34: Several studies on Co_2MnSi microwires and the impact of the aspect ratio on the chemical ordering and related magnetic properties can be found as well, but these wires are produced by the Taylor–Ulitovsky method - a multi-step process involving the formation of a glass capillary filled with molten Co_2MnSi, yielding a glass-coated metallic microwire after a cooling process [217]. These studies conclude on an important relation between the aspect ratio of the microwires and the resulting chemical ordering and related magnetic properties, yet the phenomenon is mainly linked to microwire-specific fabrication and device specifications [218] and hence does not allow for specific conclusions on the magneto-structural properties of Co_2MnSi microstructures fabricated from thin films.

[217]: Salaheldeen et al. (2022)
[218]: Wederni et al. (2023)

[106]: Mantion (2023)

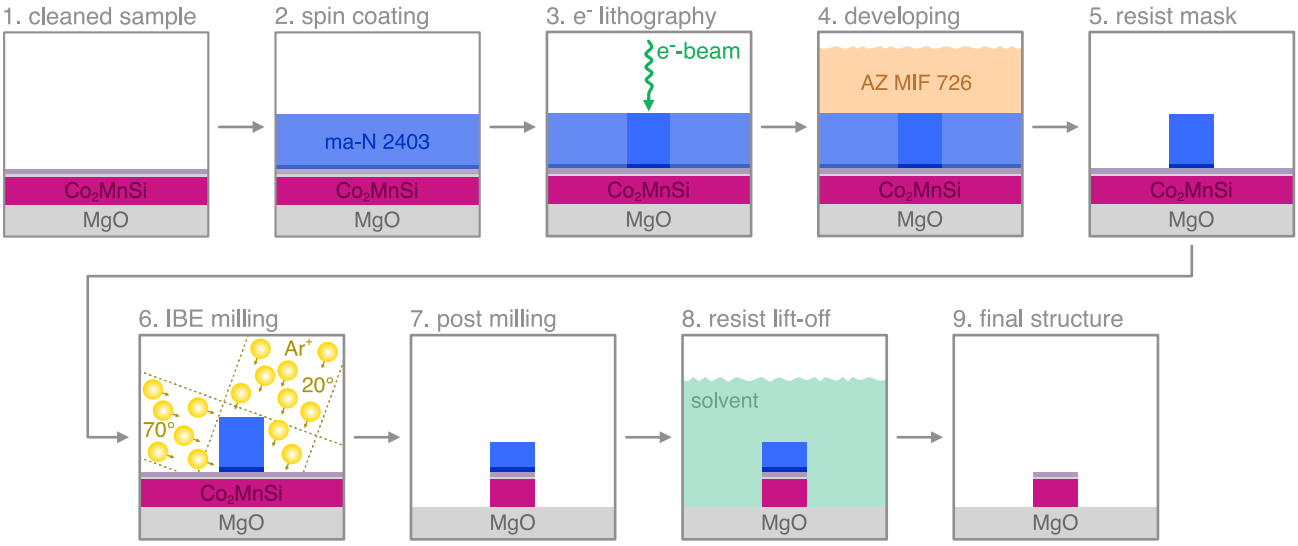

Figure 3.18: Schematic illustration of the lithography process steps enumerated as listed in the text. The thicknesses are not to scale and the thin unlabelled layers correspond to the MgO/Al capping (grey and violet in frames 1-9) and the HMDS adhesion agent (dark blue, frames 2-8). The charge dissipating coating ESPACER 300Z is not shown and also the profilometer measurements are not specifically illustrated, but were performed in the process steps corresponding to frame 5, 7 and 9. Note that the IBE milling illustrated in frame 6 is simplified for an improved clarity: The real beam size is significantly larger than the sample size, and also the sample was rotated during the IBE milling in step 6 in order to reduce shadowing effects. Figure inspired by a similar schematic in [219].

3.3.1 Micro-/Nanostructuring process

For this study, two epitaxial Co_2MnSi thin film samples with different cappings were grown by MBE: The sample S1.2 in table 2.1 with the Pd capping serves to replicate lithography conditions for studies, where a heavy metal capping layer is desired for instance for the exploitation of spin Hall effects. And the sample S1.4 in table 2.1 with the MgO/Al bilayer is a test case for studies, where an insulating capping is beneficial e.g. to avoid a direct electrical contact with antenna structures.

Each sample was cut into multiple pieces of approximately $10 \times 10\,mm^2$ in order to allow for the separation of at least one non-processed sample piece serving as a thin film reference. The entire lithography process was carried out at the Nanostructuring Center (NSC) of the RPTU Kaiserslautern-Landau in Kaiserslautern by Dr. Björn Heinz and Moritz Bechberger. The electron beam lithography setup was operated by Dr. Bert Lägel.[35]

A full[36] nanostructuring process was carried out on at least one of the $10 \times 10\,mm^2$ pieces from each sample, following a typical resist mask ion beam milling procedure as illustrated in figure 3.18:

1. Step: Sample preparation.
   - In a first step, the samples (sample pieces) were sonicated[37] sequentially in acetone and isopropanol, each for 5 min, and subsequently blow-dried with N_2.
   - *Sample with MgO/Al capping only:* Following an incomplete first structuring attempt (development of the resist mask, but no milling), this sample underwent various additional cleaning steps[38] in order to remove the first resist mask.
2. Step: Spin coating for photoresist application.
   - Prior to the spin coating process step, the samples were heated for 5 min on a hot plate at 100°C.

[219]: Heinz et al. (2020), '*Supplementary Material:* Propagation of Spin-Wave Packets in Individual Nanosized Yttrium Iron Garnet Magnonic Conduits'

35: The author of this work was involved in the execution of very few cleanroom process steps only, but contributed to the development of the final structuring process plan based on the test structuration results. Moreover, the author took over the preparation of electron lithography designs in consultation with Dr. Björn Heinz.

36: Prior to the final structuring for the further TEM investigations, several process tests were carried out in order to verify the resist adhesion, and determine technical process parameters such as the IBE etching rates, the resulting required resist mask thickness and the electron lithography parameters.

37: The standard parameters for the ultrasonic bath were set to operate at a frequency of 35 kHz in the sweep mode (few kHz frequency modulation around the set frequency to avoid a formation of standing waves leading to an inhomogeneous cleaning).

38: As this proved difficult, different solvents (acetone, isopropanol, dimethyl sulfoxide (DMSO), N-Methyl-2-pyrrolidone (NMP)) and process parameters (ultrasonic/non-ultrasonic baths, room temperature, heating, incubation time) were used. Additionally, the sample was twice exposed to an Oxygen cleaning plasma. The removal of the initial resist mask was verified with an optical microscope, where finally only faint traces of the initial structures were visible and the profilometer measurements yielded heights below 6 nm.

- For an improved resist adhesion, a hexamethyldisilazane (HMDS) layer was applied on the samples by spin coating, and after a resting time of 30 s was baked on a hot plate at 100°C for 60 s.
- Then, the negative tone[39] resist ma-N 2403 was applied by spin coating, and immediately pre-baked on a hot plate at 90°C for 60 s.
- *Sample with MgO/Al capping only:* To avoid charging effects disturbing the e⁻-beam lithography process, this sample was additionally coated with the charge dissipating agent ESPACER 300Z, which was applied to the sample and left to rest for 30 s prior to spin coating, then baked on a hot plate at 90°C for 60 s.

3. Step: Electron beam lithography.
   - The electron beam writing step was carried out on a Raith Voyager electron beam lithography system with 50 kV acceleration voltage.
   - On some samples, the prepared lithography design involved a repetition of the same structures to be written with different electron beam dose factors[40].
4. Step: Development to remove unexposed resist.
   - *Sample with MgO/Al capping only:* To remove the ESPACER 300Z, the sample was swirled in ultrapure water and blow-dried with N_2.
   - A dip development was carried out by submerging the samples in a bath of the TMAH[41]-based developer AZ MIF 726 for 30 s. The samples were swirled during the development process.
   - The development was stopped by dipping the samples in a bath of ultrapure water, in which they were swirled for 120 s.
5. Step: Pre-milling profilometer control[42] - thickness of resist mask.
   - *Sample with Pd capping:* 264 nm thickness
   - *Sample with MgO/Al capping:* 245 nm thickness
6. Step: Ar^+ ion beam etching[43] (IBE).
   - The milling was carried out in four process steps with 60 s, 20 s, 35 s, 25 s exposure times, separated by a 60 s break after each step[44]. The milling steps involved an Ar^+ ion bombardment at an angle of incidence (to the film normal) of 70°, 70°, 20° and 70° respectively, all under a constant sample rotation set to 20 rpm.
7. Step: Post-milling profilometer control - resist mask & etched sample.
   - *Sample with Pd capping:* 152 nm thickness
   - *Sample with MgO/Al capping:* 157 nm thickness
8. Step: Lift-off to remove remaining resist mask.
   - *Sample with Pd capping:* The remaining resist was removed by sequentially sonicating the samples in acetone and isopropanol[45].
   - *Sample with MgO/Al capping:* The lift-off process on this sample was done in three steps using NMP[46] and ultrapure water: (1) 15 min non-ultrasonic bath in NMP at 75°C. (2) 15 min ultrasonic bath in NMP at 70°C. (3) 15 min ultrasonic bath in ultrapure water at 70°C.
9. Step: Post-Lift-off profilometer control - etched sample.
   - *Sample with Pd capping:* 31 nm thickness
   - *Sample with MgO/Al capping:* 30 nm thickness

The comparison of the profilometer measurements allowed for two conclusions: Firstly, the Co_2MnSi is expected to be fully removed between the masked structures, since the remaining ~ 30 nm profiles of the etched structures are

39: In the negative tone resists, the (sufficient) exposure induces an increased molecular crosslinking, which results in a reduced dissolvability in the developer solution. Hence, the exposed resist remains on the sample surface, while the non-exposed resist is removed in the developing step.

40: The dose modulation by a (close to unity) factor is typically employed for a correction of the proximity effect, i.e. for a correction of the disturbing over-exposure of the photoresist outside of the primary incident electron beam spot (scanning the defined design pattern) due to a scattering of the incident high-energy electrons with electrons or nuclei in the resist or underlying sample. Here, the repetition of the same structure with different doses allowed to counteract the slight uncertainty on the best parameter arising from a technical shut down of the setup between the preliminary tests and the final fabrication.

41: TMAH: tetramethylammonium hydroxide.

42: Using a Bruker Dektak XT profilometer.

43: On a Roth & Rau IonSys 500 system.

44: Note that the breaks are introduced for two reasons: (1) to reduce a heating of the sample due to the ion irradiation, and (2) to allow for a changing of the angle of incidence. - The angle of incidence is varied to improve the edge properties of the etched structures, and notably to reduce redeposition. In the case of the Pd capping, this was only partly successful - see analysis hereafter.

45: Each for 5 min, analogous to the clearning process (step 1) above.

46: NMP: N-Methyl-2-pyrrolidone, an organic solvent.

47: The total (nominal) stack thicknesses are d_{tot} = 23 nm for the Pd capping sample S1.2, and d_{tot} = 26 nm for the MgO/Al capping sample S1.4, see table 2.1 on page 29.

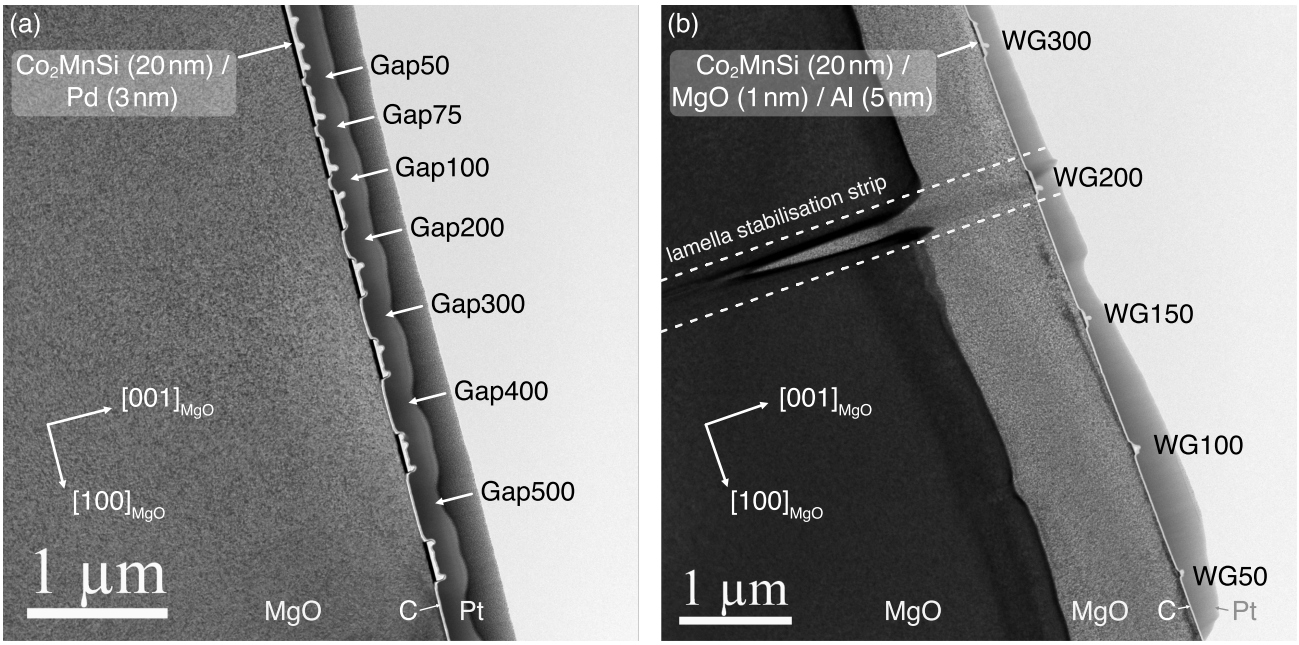

Figure 3.19: HRTEM micrographs with the lowest magnification showing approximately half of (a) the lamella with the Co_2MnSi/Pd waveguide array with varying gap sizes, and (b) the lamella with the Co_2MnSi/MgO/Al waveguide array with varying waveguide widths. The numbers indicate the nominal (target) feature sizes in nm (e.g. *Gap50* → 50 nm gap width, *WG50* → 50 nm waveguide width). *Improved image resolution in the digital document.*

larger than the total stack thicknesses[47]. Secondly, the resist mask thickness was sufficient to provide a protection throughout the entire milling process and thus the surface (capping) of the structures is expected to be intact[48].

Additionally, the fabrication results were verified by SEM imaging carried out by Moritz Bechberger on the structured sample with the Pd capping. Based on the imaged observations, the best defined structures[49] were selected for the FIB cuts and TEM measurements on this sample. To allow for the SEM measurements on the isolating MgO substrates, the sample was again coated with ESPACER 300Z. Yet, the removal of the charge dissipation coating by an ultrasonic bath in solvents[50] after the SEM imaging was partly unsuccessful[51]. Therefore, no SEM imaging was carried out on the second sample with the MgO/Al capping[52], apart from the images during the FIB process, some of which are shown in figure 3.1.

3.3.2 Sample layout and FIB cut

Arrays of waveguides were produced for the TEM study of the structuring effects, since a uniform cross section along the probing direction needs to be ensured in the transmission measurements. Moreover, the waveguides were structured with their symmetry axis along a $[110]_{Co_2MnSi}$ direction, in order to exploit the Heusler symmetry for the chemical ordering analysis in the HAADF-STEM mode as introduced with figure 3.2 on page 35. Ensuring both conditions, the TEM lamellas were cut[53] perpendicular to the waveguide axes by the above-described FIB lift-out technique, as was seen in in figure 3.1.

Three lamellas with different arrays of waveguides were investigated in TEM, a partial overview of two of which is shown in figure 3.19:

1. A first lamella[54] was cut from an array of waveguides with a constant width of ~ 280 nm, between which the spacing/gap was varied as shown in figure 3.19 (a) in order to determine the minimal feature distance.

48: Since more than 100 nm resist were removed in the lift-off process. Yet, as the milling was carried out under an angle of up to 70° to the film normal, the surface could still be affected by the lateral ion bombardment.

49: It is recalled, that the same design was written with multiple dose factors on this sample.

50: As before: first acetone, then isopropanol, each with the parameters as above (5 min, 35 kHz, sweep mode).

51: The TEM measurements on this sample revealed residuals of the charge dissipator ESPACER 300Z. It is assumed that the coating must have hardened / polimerised from the e^--beam exposure during the SEM measurements, and therefore was (unintentionally) not fully removed in the subsequent cleaning step.

52: This sample was structured 2 months after the TEM measurements on the first, Pd-capped sample.

53: It is recalled that a thin Carbon layer (~ 10 nm) was deposited on the structured samples prior to the FIB process to avoid charging effects during the lamella preparation.

54: This lamella was cut from a structured piece of sample S1.2 (Pd capping).

55: This lamella was cut from a structured piece of sample S1.4 (MgO/Al capping).

56: This lamella was cut from a structured piece of sample S1.2 (Pd capping).

57: Due to the large separation of each waveguide-ring pair in the second lamella, only 3 pairs of waveguide-ring structures were incorporated on this third lamella. Additionally, the bended edges of the ring cross sections lead to blurry features in the TEM/STEM micrographs, and hence the analysis on this lamella was mostly limited to the 3 straight waveguides. The majority of the investigations was thus focused on the other two lamellas. Still, the investigations on this third lamella were not unnecessary, but notably allowed to conclude on the one-sided proximity effects.

58: Simultaneously recording the HAADF-STEM and bright field STEM (BF-STEM) signal as micrographs.

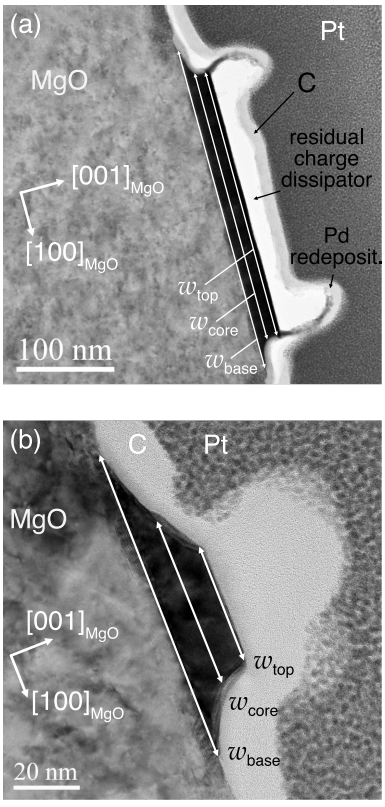

Figure 3.20: Exemplary HRTEM micrographs of two waveguide cross sections corresponding to (a) a well-separated Co_2MnSi/Pd waveguide on the first lamella with more than 500 nm gap distance to the adjacent structures and (b) the smallest fabricated Co_2MnSi/MgO/Al waveguide on the second lamella marked as WG50 in figure 3.19 (b). *Improved image resolution in the digital document.*

59: The charge dissipation coating yields very bright contrast in HRTEM as in figure 3.20 (a) as well as BF-STEM, and very dark contrast in HAADF-STEM, even brighter/-darker than the C layer (deposited as a charge dissipation coating prior to the FIB etching process).

2. A second lamella[55] was cut from an array of waveguides of different widths as shown in figure 3.19 (b), ranging from 1 µm to 50 nm in order to study scaling effects.
3. A third lamella[56] was cut from an array of well-separated[57] waveguides with a constant width of ~ 280 nm, each with an adjacent local ring structure on one side only, where the gap size between the two was varied in order to study proximity effects on the waveguide structure.

Additionally, a thin film reference lamella was cut from the separated reference pieces, in order to distinguish defects originating from the structuring process from other faults or inhomogeneities in the samples. The general results from the thin film lamellas are presented within the discussion in section 3.2.

3.3.3 Lithography results and defect analysis

The three structured lamellas and two reference thin film lamellas were thoroughly studied in transmission electron microscopy in the HRTEM and STEM[58] modes. Additionally, several EDXS cartographies were recorded for a chemical analysis of the etched structures. A total of 79 HRTEM micrographs, 76 STEM micrograph pairs and 8 EDXS cartographies were recorded from the etched samples covering all structures on the three lamellas. However, naturally a focus was set on the investigation of the smallest features, i.e. the smallest waveguide widths or gap distances.

Macroscopic geometry, shape and dimensions

General shape observations: Fully etched, intact structures were successfully fabricated on both samples as was already expected from the profilometer control measurements. Two exemplary waveguide cross-sections from the first and second lamella are shown in figure 3.20.

All cross sections of the structures on the two lamellas from the Co_2MnSi/Pd sample present shapes similar to the example shown in figure 3.20 (a) with U-shaped edge cross sections and a redeposition at the borders of the structures in the form of inwards-bent "horns" with maximal lengths of approximately 80 nm. Later EDXS analyses on this sample reveal the horns to be a Pd redeposition from the milled capping layer. The structures as well as the etched area in between are partially or fully covered with residuals of the charge dissipating ESPACER 300Z coating for SEM measurements, which can be identified as such based on the contrast[59] and the localisation as it is also detected in the fully etched areas between the structures which thus excludes an identification as a left-over coating from the lithography process.

The waveguide cross sections from the Co_2MnSi/MgO/Al sample present an asymmetric shape as in the example in figure 3.20 (b) with a slight, non-negligible edge-roughness in the range of ~ 5 nm on both sides which leads to contrast variations in the HRTEM/STEM micrographs as seen in figure 3.20 (b) and is also observable in the SEM images recorded during the FIB process, see figure 3.1 (b). In general, U-shaped edges are observed on all structures on the side which is oriented towards the next smaller structure, i.e. the "bottom" edge in figures 3.19 (b) and 3.20 (b). The edges on the other sides of the structures, i.e. oriented towards the next larger structure or the top in figures 3.19 (b) and 3.20 (b), are generally flatter and present a triangular shape for the smallest two waveguides which slightly transforms to a strongly flattened U-shape for the wider structures. The significant spacing between the individual

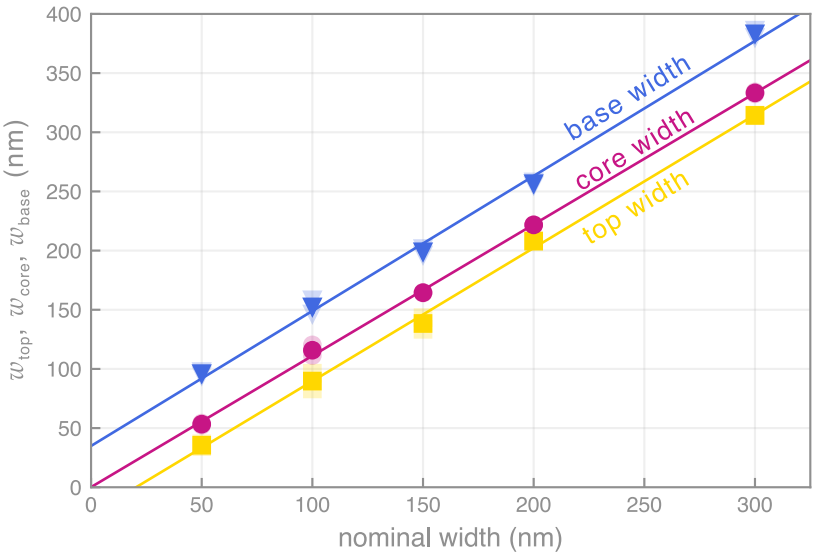

Figure 3.21: Waveguide width study on the $Co_2MnSi/MgO/Al$ waveguide array: The top, core and base widths w_{top}, w_{core}, w_{base} of the smallest five waveguides were evaluated from two HRTEM micrographs per nominal thickness. The average value is plotted in bold colours and the lines are linear regressions on the average value. The width measurements at all three positions (heights) clearly scale linearly and with approximately the same slope, indicating roughly constant edge dimensions on the waveguides. Note that the *core width* is measured at half the height, but consistently closer to the top width than the bottom, which is a signature of the predominant U-shape edge geometry.

structures (distances > 1 µm see figure 3.19 (b)) excludes a shadowing effect during the IBE milling to be the underlying cause. Moreover, the consistency in the shape and the orientation of the cross section asymmetry suggests a directional problem / asymmetry in the fabrication process on this sample. An obvious potential cause can be for instance a faulty / inhomogeneous rotation during the IBE process, yet this process is monitored and no rotation issues or other technical problems were remarked during the execution. Another potential cause is an asymmetry in the resist mask itself, produced during the e^--beam writing process, e.g. by an overexposure or increased backscattering on one side of the structures only. Such issues have been observed before in nanofabrication processes on the same system, where the asymmetry of the features was linked to the writing mode[60]. The asymmetry of the resulting resist mask propagates through the milling process and hence translates to the asymmetry in the final structures.

60: The lithography design is usually "written" into the resist by scanning the designed feature area with the electron beam, where various writing modes can be set for the rasterised exposure. Depending on the scanning mode and the orientation (e.g. the scanning pattern along or perpendicular to the long axis of the structures), this can result in an overexposure on one boundary of the area, compared to the other boundary. As stated in the main text, such problems were already observed in similar fabrication processes for other studies in the research group in Kaiserslautern.

Downscaling and minimal features: Two different dimensional variations were fabricated for this study: the reduction of the gap size as well as the downscaling of the waveguide widths. To this aim, the widths are evaluated at three positions as indicated in figure 3.20: The waveguide base width w_{base} is measured at the bottom interface, the waveguide core width w_{core} is measured at half the height between the top and bottom interface, and the waveguide top width w_{top} is measured at the top interface. Analogously, the gap distances are labelled as g_{base}, g_{core} and g_{top}, and additionally the gap of the Pd capping is measured as $g_{capping}$.

The downscaling of the waveguide widths was investigated on the lamella from the $Co_2MnSi/MgO/Al$ sample. All intended structures were successfully etched and intact, including the smallest waveguide *WG50* of the array as shown in figure 3.20 (b), which yields

$$w_{WG50} = \begin{pmatrix} w_{top} \\ w_{core} \\ w_{base} \end{pmatrix} = \begin{pmatrix} 35.5\,nm \\ 53.3\,nm \\ 96.0\,nm \end{pmatrix} \tag{3.4}$$

for the width measurements, all with an error of $\Delta w = 2\,nm$. Analogously, the top, core and base widths of the five smallest waveguides were determined from two HRTEM micrographs per waveguide and the results are presented in figure 3.21 against the nominal (target) thickness. Additionally, a linear regression on the average values is plotted which not only underlines the linear

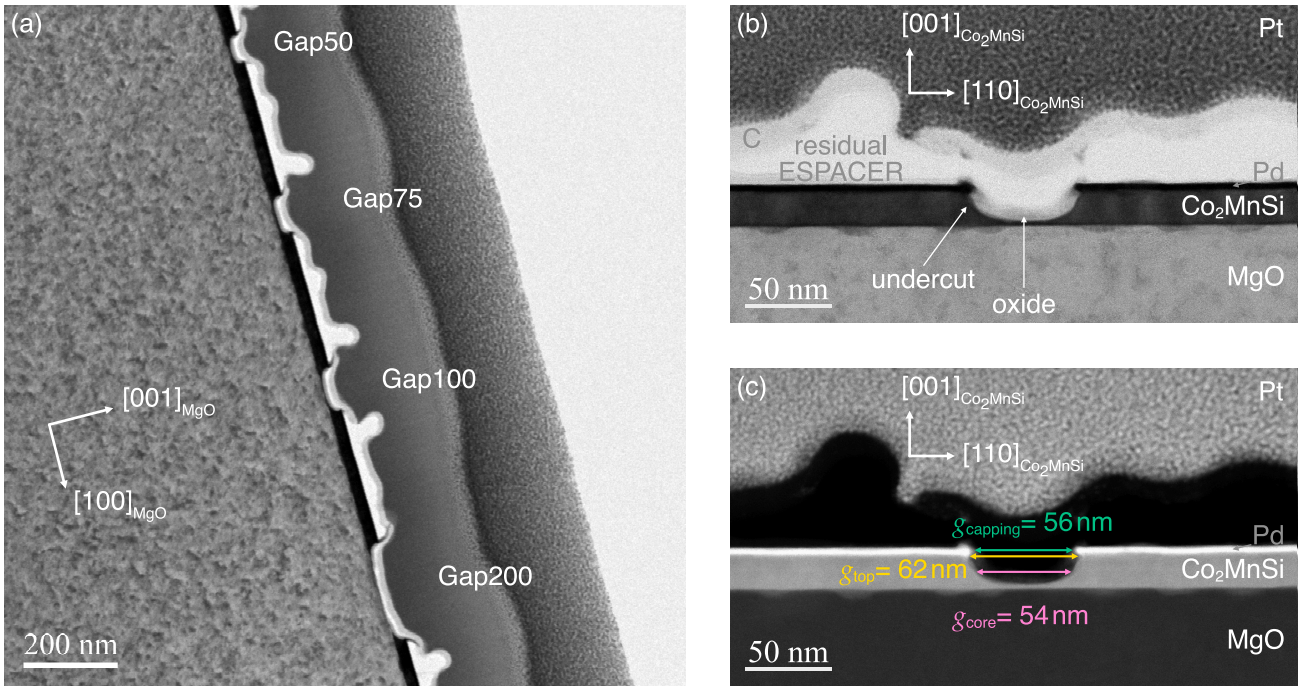

Figure 3.22: Gap distance study on the Co_2MnSi/Pd waveguide array: (a) HRTEM micrograph showing the smallest four gaps, of which only Gap200 presents a clear exposure of the substrate, (b) BF-STEM micrograph and (c) simultaneously recorded HAADF-STEM micrograph of Gap50, the smallest partially etched gap on the lamella. The error on the measurements g_{capping}, g_{top}, g_{core} indicated in (c) is $\Delta g = 1\,\text{nm}$.

scaling of the individual features, but also the approximately equal slopes of the three regression lines indicate nearly constant edge dimensions for all waveguide widths in the range[61].

The reduction of the gap size between the structures was investigated on the lamellas from the Co_2MnSi/Pd sample. The smallest gap with a clear exposure of the substrate[62] is observed on the lamella[63] with the waveguide-ring pairs and yields $g_{\text{capping}} \approx 168\,\text{nm} \pm 5\,\text{nm}$, yet due to the bended edge of the ring waveguide a precise analysis of the gap is hardly possible. The smallest gaps on the lamella[64] with the straight waveguide array with different spacings are shown in figure 3.22 (a). Here, the minimal fully etched gap with a clear exposure of the substrate is labelled as *Gap200* and has a gap size of

$$g_{\text{Gap200}} = \begin{pmatrix} g_{\text{capping}} \\ g_{\text{top}} \\ g_{\text{core}} \\ g_{\text{base}} \end{pmatrix} = \begin{pmatrix} 210\,\text{nm} \\ 214\,\text{nm} \\ 203\,\text{nm} \\ 166\,\text{nm} \end{pmatrix} \tag{3.5}$$

with an error of $\Delta g = 2\,\text{nm}$ on each measurement.

Partially etched gaps: Three smaller gaps are partially etched as shown in figure 3.22 and only connected by an ultrathin[65] layer of Co_2MnSi, the smallest of which is shown in the STEM micrographs in figure 3.22 (b) and (c), and a zoom-in on the area is shown in the HRTEM micrographs in figure 3.23. The Co_2MnSi at the bottom of these incomplete gaps is found to be amorphous, which is determined by the evaluation of the FFT pattern from small selection areas in the micrographs. An example is shown in figure 3.23, where the inset (c) shows the FFT of the yellow marked area in the micrograph in (b). Along the entire gap, no sign for a diffraction-like spot pattern is present in the FFTs where the Co_2MnSi thickness was below 5 nm, hence implying an amorphous layer in the region. However, for $d_{Co_2MnSi} > 5\,\text{nm}$ towards the outside of the gaps a crystal ordering can be detected in the Co_2MnSi.

61: Note that only one constant waveguide width was fabricated on the Pd sample (but instead the distance is varied). Therefore, a verification of the linear downscaling of the structures is not possible on that sample, but in principle is expected to work analogously.

62: *clear exposure of the substrate* meaning that within the gap, the MgO substrate is exposed and not covered by remains of Co_2MnSi or another material (either from redeposition or incomplete etching or shadowing effects). - An example can be seen when comparing *Gap200* with *Gap75* in figure 3.22 (a).

63: Lamella no.3 in the list on page 49.

64: Lamella no.1 in the list on page 49.

65: The minimal thicknesses measured approximately in the middle of the gap yields $d_{Co_2MnSi} = 3.2\,\text{nm}$ and increases towards the edges of the adjacent Co_2MnSi structures. For the central $\sim 35\,\text{nm}$ of the gap, the Co_2MnSi thickness is $d_{Co_2MnSi} < 5\,\text{nm}$. Along this central region, all FFTs of the Co_2MnSi show no diffraction-like pattern, i.e. the central $\sim 35\,\text{nm}$ are amorphous.

Although the incomplete etching of the gaps was unintended, such partially etched gaps with little residual magnetic material connecting the adjacent structures can be of interest for the design of coupling regions in magnonic devices: While in the case of fully etched, separated structures the coupling can only rely on the dipolar interaction, the residual magnetic material for instance in incompletely etched gaps principally forms an *exchange bridge* allowing for an additional coupling of the magnetisation dynamics in the two adjacent structures via the exchange interaction. In that case, a tuning of the coupling strength can be imaginable based on two effects: Firstly, the inter-structural coupling via the *exchange bridge* can be expected to be reduced compared to the intra-structural coupling[66], simply for the reduced material thickness. Secondly, the exchange coupling strength is affected (reduced) by an irradiation-induced degeneration of the material within the *exchange bridge* such as the amorphisation observed in this study, a known effect particularly on the Co_2-based Heusler compounds [74, 76].

66: Here, "inter-structural" is used to signify a coupling between two structures, e.g. a coupling of the magnetisation (dynamics) between two waveguides. "Intra-structural" analogously indicates a coupling within a single structure, i.e. an exchange coupling of the atomic magnetic moments.

[74]: Hamrle et al. (2007), 'Ion beam induced modification of exchange interaction and spin–orbit coupling in the Co_2FeSi Heusler compound'

[76]: Abdallah et al. (2017), 'Evolution of magnetic properties and damping coefficient of Co_2MnSi Heusler alloy with Mn/Si and Co/Mn atomic disorder'

Redeposition, oxidation and fabrication-induced defect observations

General observations: In particular the HRTEM micrographs on the sample with the Pd capping revealed unexpected features such as the aforementioned redeposition leading to the formation of "horns" as seen in figure 3.20 (a) as well as figure 3.22 (a).

Additionally, the exposed edges and gaps are covered by an amorphous layer, which is best resolved in the HRTEM micrographs in figure 3.23. (Note that the conclusions on an oxide as labelled in the HRTEM micrographs is based on the further EDXS mappings on the next pages.) This amorphous layer has a thickness of $d_{\text{oxide}} = 4.5 - 8\,\text{nm}$ (measured at various sites along the entire gap, always perpendicular to interface with Co_2MnSi).

The significant contrast change in the HRTEM micrographs in figure 3.23 (a,b) and the BF-STEM micrographs in figure 3.22 (b) implies a strongly reduced mass-density in comparison with the adjacent, amorphous Co_2MnSi. A quite similar contrast is observed in all imaging modes in the Carbon layer from the FIB process located on top of the residual charge dissipation coating. Yet given the clear separation by the residual ESPACER 300Z, it can be concluded that the amorphous layer located between the charge dissipation coating and the adjacent etched Heusler structure must be an effect of the fabrication process or the post-fabrication exposure to air. Consequently, the presence of a similar amorphous layer around the etched $Co_2MnSi/MgO/Al$ structures on the other sample is expected based on the equal fabrication process, but is impossible to resolve in the respective micrographs due to the similarity with the contrast obtained from the adjacent Carbon layer, and the lacking clear separation by the (intentionally avoided) charge dissipation coating.

Moreover, the vanishing signal in the respective area in the HAADF-STEM micrographs, see e.g. in figure 3.22 (c), implies a low average atomic number Z in the amorphous region[67] similar to the adjacent residuals of the charge dissipation coating (ESPACER 300Z), as well as the subsequent Carbon layer, and therefore indicates little to no presence of any heavier elements in this area, i.e. hardly any Pd, Co or Mn from the milled materials, except of the gradual transition to the Pd capping, as seen in figure 3.23 (a).

Therefore, multiple EDXS cartographies were recorded on different sites on the three lamellas, to allow for further conclusions based on the elemental mappings.

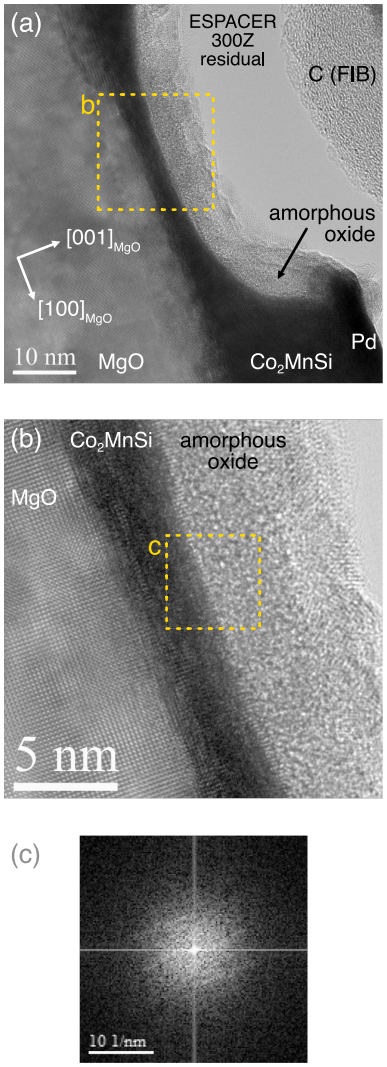

Figure 3.23: HRTEM study of the smallest partially etched gap *Gap50*: (a) raw HRTEM micrograph of the region, (b) zoom-in (digital magnification) of the area marked in (a) by the dashed square, (c) reduced FFT of the marked area in (b). Based on similar FFT analyses along the whole gap, as well as no perceivable order in the residual Co_2MnSi, it is concluded that the thin Co_2MnSi layer is amorphous in the central $\sim 35\,\text{nm}$ of the gap, where $d_{Co_2MnSi} < 5\,\text{nm}$. *Improved image resolution in the digital document.*

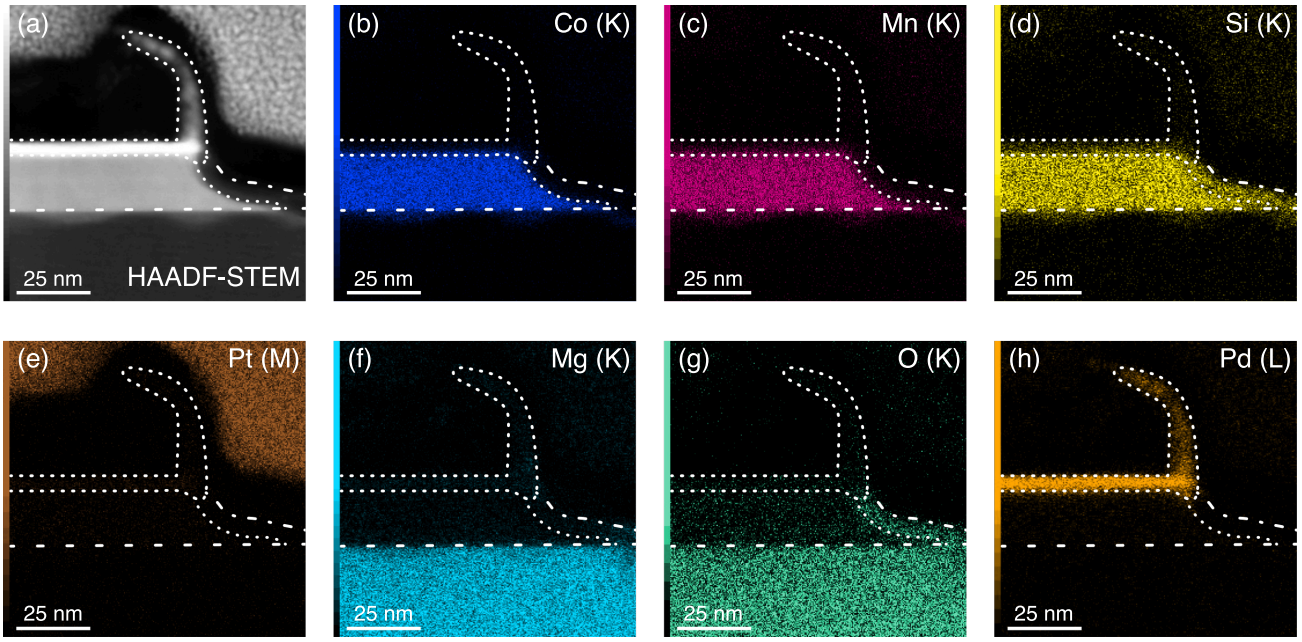

Figure 3.24: EDXS elemental cartography of a waveguide edge from the structured Co_2MnSi/Pd film from sample S1.2 (Q230403) in table 2.1: (a) HAADF-STEM micrograph captured before the spectral mapping, (b-d) mapping of the Heusler compound elements Co, Mn and Si (e) mapping of Pt deposited as a protection prior to the FIB cutting, (f-h) mapping of the substrate and capping elements Mg, O, Pd. The K, L and M in the brackets indicate the respective shell corresponding to the mapped spectral EDXS signal. The dashed lines were added as guides for the comparison of the different elemental maps. Note that the lamella surface is exposed to air, when transferring the sample from the FIB setup to the TEM setup, and hence can oxidise at the lamella surfaces and thus increase the background signal in the O mapping.

Redeposition of Pd: An exemplary EDXS cartography recorded on a waveguide edge on the Co_2MnSi/Pd distance array lamella[68] is shown in figure 3.24. For a facilitated discussion, the approximate outlines of the Co signal, the O signal and the Pd signal are traced as guides.

The aforementioned "horns" detected along the borders of the structure are identified as a redeposition of the Pd capping[69]: During the milling process the waveguide is protected by a resist mask on top of the Pd layer. The formation of these "horns" is likely a result of a redeposition of the Pd capping on the edges of the resist mask covering the waveguides[70]. After the lift-off, the resist mask is removed and the Pd "horns" remain, and indeed a tracing of the curved Pd redeposition horns yielded total lengths of roughly ~ 80 nm, which corresponds to ~ 2/3 of the remaining resist mask thickness[71] after the milling process. The curving towards the centre of the waveguides is likely to happen during the lift-off process, as the stabilising resist mask is gradually dissolved and less redeposit is expected with increasing distance from the sample surface, both making the structure increasingly unstable towards the top end. Potentially also some of the top part of the Pd redeposition structures is broken off or some redeposition even fully removed during the lift-off process, which cannot be verified but could be the origin of the few smaller "horns" for instance in figure 3.22 (a) around *Gap75* and *Gap100*, or the entirely vanished "horns" in figure 3.22 (b, c) around *Gap50*.

Apart from the redeposition formation, the Pd capping layer is found to be intact and yields a well-defined interface with the Co_2MnSi along which no signs of structural defects or chemical faults are identified, neither in the EDXS nor in the HRTEM/STEM measurements, indicating a persistent protection of the Co_2MnSi by the Pd capping.

It is noted that the formation of these horns might be reducible by a further improvement of the IBE milling process parameters, e.g. at other angles of incidence, particularly when patterning such samples in the prospect of a real

67: It is recalled that the HAADF-STEM detection yields a Z-contrast.

68: Lamella no.1 in the list on page 49.

69: For this entire section on the Pd redeposition, the Pd mapping in figure 3.24 (h) is compared to the cartography in the other frames.

70: This can obviously not be seen in the EDXS cartography, but one can easily imagine the mask as a box as wide as the waveguide core width and approximately 250 nm high (exceeding the EDXS frame by far).

71: Taking the difference of the profilometer controls in step 7 after the milling with 152 nm thickness and step 9 after the lift-off with 31 nm thickness, yields a remaining resist thickness of ~ 120 nm.

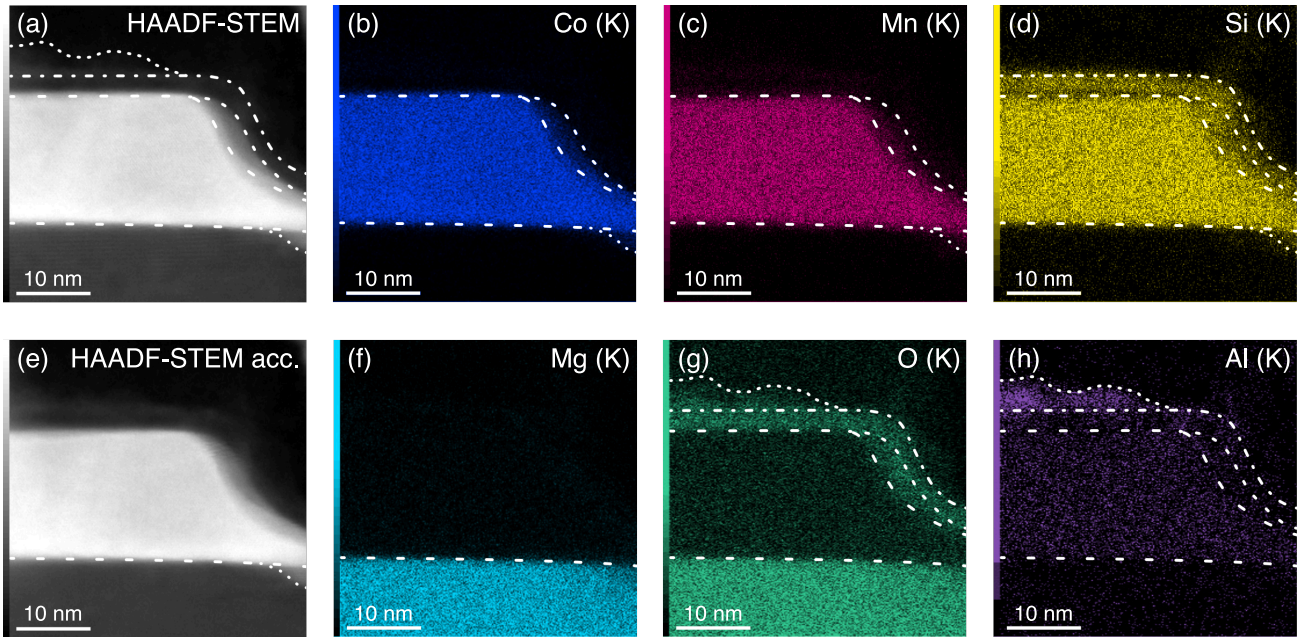

Figure 3.25: EDXS elemental cartography of a waveguide edge from the structured $Co_2MnSi/MgO/Al$ film from sample S1.4 (Q240212) in table 2.1: (a) HAADF-STEM micrograph captured before the spectral mapping, (b-d) mapping of the Heusler compound elements Co, Mn and Si (e) accumulated HAADF-STEM micrograph showing no signs of shift or drifting during the process (f-h) mapping of the substrate and capping elements Mg, O, Al. The investigated waveguide is the WG50 with the smallest width (core width $w_{core} \approx 53\,nm$) in the array on the lamella. This lamella is the same as presented in figure 3.1. The K and M in the brackets indicate the respective shell corresponding to the mapped spectral EDXS signal. The dashed lines were added as guides for the comparison of the different elemental maps. Note that the lamella surface is exposed to air, when transferring the sample from the FIB setup to the TEM setup, and hence can oxidise at its surfaces increasing the background signal in the O mapping.

device fabrication including typically a second process to fabricate antennas on top. Yet, for the present study focusing on the structural damage, the reduction of the redeposition is not further relevant. It is, however, indeed interesting to remark that the Pd redeposition is mostly observed towards the top and hardly any Pd is detected at the edges of the Co_2MnSi structures, except of the little fading dip at the top[72]. Furthermore, the observation of an oxide layer along the exposed edge of the waveguides, as will be discussed in the next paragraph, is detected exactly in "prolongation" of the Pd "horns" and particularly of the little fading dip at the top, as is indicated by the dashed lines highlighting the respective area in figure 3.24. This can be an indication for the two forming simultaneously, as will be relevant to the discussion hereafter.

Oxide layer covering exposed edges: The etched Co_2MnSi waveguide edges are covered by an oxide layer, as can be concluded from the Oxygen K-line mapping in figure 3.24 (g), which corresponds to the aforementioned amorphous layer observed in the HRTEM micrographs. As expected, this is observed on all waveguide edges studied in the EDXS mappings, not only on the Co_2MnSi/Pd structures as in figure 3.24, but also on the edges of the $Co_2MnSi/MgO/Al$ waveguides[73], an example is shown in figure 3.25.

Note that the exemplary edge in figure 3.25 corresponds to the smallest waveguide *WG50*, on which an edge roughness in the probing direction ($\sim 50\,nm$ lamella thickness) was observed and manifests here as a contrast change in the HAADF-STEM micrograph in frame 3.25 (a). Obviously, this roughness along the probing direction will automatically yield a detection of all adjacent materials in this region, which must not be confused with an impurity penetration. Therefore this "area of superposition" is carefully outlined by the dashed white tracing lines[74] in figure 3.25. Also, the stability of the frame is always verified by the accumulated STEM micrograph[75] and still yields sharp edges with no sign for a drifting, as shown in figure 3.25 (e).

72: This is also observed in the HRTEM micrographs, as was remarked in the discussion of figure 3.23 (a) just before.

73: Lamella no.2 in the list on page 49.

74: Precisely: The outer border beyond which no signal is detected in HAADF-STEM micrograph is traced based on the micrograph in (a), and the inner border is traced based on the Oxygen mapping in (g) and transferred to all other frames. As this inner border matches the contrast change in (b) and (c) from the region of a maximal saturation of Co and Mn signal to the "rough edge" region, where less Co and Mn signal is detected, it can be concluded that no Oxygen has penetrated into the core structure. Moreover, the crystal ordering is later investigated on this exact edge, showing perfect ordering even inside the area of faint signal due to the rough edge.

75: The recording of EDXS mappings was left to count for $\sim 20 - 40\,min$, depending on the clarity of the signal and the available time.

In all EDXS mappings of the etched structures[76], only Oxygen and Silicon are detected in the area/layer covering the waveguide edges, as can be seen in figure 3.24 (g), (d) as well as figure 3.25 (g), (d). However, this does not allow for an identification of the oxide layer as a Silicon oxide, since the full periodic table of elements cannot be mapped for two reasons: The elements with lowest atomic numbers present no X-ray emission lines, and also among the other elements many emission peaks overlap. Instead, only a selection of elements is usually evaluated in the mapping, based on the expected materials in the sample and the detected spectral peaks[77].

Principally two likely processes can lead to the formation of this oxide layer: an oxidation of the exposed Co_2MnSi, or a redeposition of milled material during the IBE process. Concerning this, it is relevant to note that the IBE process is principally carried out in vacuum, but O is introduced with the sample. Hence, neither of the two origins can be excluded at this point. Yet, not only the aforementioned likeliness of a simultaneous process with the Pd redeposition, but also the evaluation of the further observation on the capping layer as well as the analysis of the underlying crystal structure are indications pointing towards an auto-formation of a (re)deposited, passivised oxide barrier during the IBE process, as will be detailed hereafter.

Decomposition of MgO/Al capping: Astonishingly, no signal of Magnesium is detected in the $Co_2MnSi/MgO/Al$ structures, neither on top of the waveguide cartographied in figure 3.25, nor in the EDXS mappings of the other sites in appendix B.3. Oxygen, on the other hand, is detected along the entire interface. Before searching for an interpretation, it is important to note all related observations concerning the entire capping stack:

- Exclusion of a resolution limit: Since the MgO layer was successfully resolved in all EDXS cartographies of the non-processed thin film reference sample[78], this is unlikely to be due to a resolution problem[79] and hence must be linked to the fabrication process.
- Increase of the O thickness: It is remarked that the thickness of the oxide layer on top of the Co_2MnSi waveguide is significantly increased compared to the MgO layer observed in the unprocessed thin film: Instead of the $\sim 1-2\,\mathrm{nm}$ as measured on the thin film reference, the oxide layer on top of the waveguide now yields $\sim 4-5\,\mathrm{nm}$ based on the three EDXS mappings[80].
- Unexpected Si presence: Unexpectedly, Silicon is detected in the capping layer, nearly in the entire oxide area as is seen in figure 3.25 (d) and (g) by comparing the signal within the dashed lines outlining the lower Oxygen signal border, and the upper Silicon signal border.
- Si separation between capping and structure: It is remarked that exactly at the interface to the waveguide core / the outline of the Oxygen signal border (matching with the Co and Mn signal), slightly less Silicon signal is obtained yielding the impression of a faint black line between the core of the waveguide and the capping layer. This observation is consistently made on in all three EDXS cartographies[81] on different waveguide cross sections of the sample.
- Perceived reduction of Al: Moreover, in all three EDXS mappings on this sample, Al islands were still found to on top of the waveguide, see for instance figure 3.25 (h), but the signal is much reduced compared to the results obtained on the sites of the reference thin film[82]. Due to the general inhomogeneity of the Al capping layer (islands), and the EDXS mapping of only a few sites per sample, the reduced signal cannot certainly be linked to the fabrication process.

76: More EDXS mapping are shown in the appendix B.

77: A preselection is usually done taking only those elements into account which can possibly occur in the sample. Unexpected elements are only considered when unidentified peaks remain in the spectra (full spectra are recorded in the background, and for the mapping of each element, the accumulated signal within a limited spectral range around the respective expected energy is evaluated by the system). Additionally, the respective spectral evaluation ranges can be adapted in order to avoid an overlapping.

78: See the example in figure 3.16 on page 45 in this chapter, as well as the additional mappings in the appendix B.2.

79: In fact, even a faint trace of the thinner MgO layer in the capping layer test sample S1.3 was resolved in EDXS mappings, see appendix B.1. These are incomplete and quite faint, but still more than detected in the structured sample S1.4 (where the MgO thickness was nearly doubled compared the test sample S1.3).

80: The outline of the oxide layer is not clearly resolved in the HRTEM/STEM micrographs, see e.g. figure 3.20.

81: See the other two figures in appendix B.3.

82: Again: See the example in figure 3.16 on page 45 in this chapter, as well as the additional mappings in the appendix B.2.

- Exclusion of direct exposure during IBE: The observation of Al on top of the etched structures, especially combined with the profilometer control information on a ~ 120 nm thick residual of the resist mask present after the milling process (and subsequently removed in the lift-off), allow to exclude an insufficient capping, surface exposure or overetching during the milling process as an origin for the vanishing of the Magnesium from the capping stack.

The decomposition of the MgO/Al capping is certainly the most unexpected result of this study, and particularly in combination with the seeming replacement of Magnesium by Silicon might appear quite mysterious. Indeed, a clear determination of the underlying origin cannot be made in this study, as various chemical reactions, redeposition and even a penetration of elements into the materials can occur during the milling process. The most intuitive first interpretation attempt is to attribute the Si in the capping to a potentially damaged Co_2MnSi structure related to the decomposition of the capping, similar to the oxidation at the exposed waveguide edges. Yet, this is assumed to be rather unlikely given the consistent impeccable Heusler structure along the edges as well as along the altered interface, as will be detailed in the paragraph hereafter. Another potential process is linked to the utilised adhesion promoter HMDS, which might also contribute to the aforementioned redeposition of an oxide containing Si and O on the waveguide edges, and will therefore be discussed subsequently.

Intact crystallographic and chemical ordering: The investigation of fabrication-induced defects on the crystal structure of the waveguides was mainly based on HAADF-STEM measurements, particularly focusing on the exposed Co_2MnSi edges as well as the area below the altered capping layer.

An example of a set of measurements is shown in figure 3.26, corresponding to the same corner of the smallest waveguide *WG50* as is studied in the EDXS mapping in figure 3.25 and as shown in the HRTEM micrograph in figure 3.20 (b). As remarked before, the waveguide presents an edge roughness* resulting in the step-wise intensity reduction imaged in the HAADF-STEM micrograph in figure 3.26 (b).

Remarkably, the exposed edges and top corner of the waveguide present a fully intact crystal lattice with no signs of impurity implantations, vacancies or other structural faults even within the rough (modulated) area of the etched edge, as can be already perceived in the raw data in figure 3.26 (b), but is even clearer in the Fourier filtered micrograph in figure 3.26 (c). In general, no signs for an ion implantation, vacancies or other structural faults linked to the nanofabrication process are observed in the Co_2MnSi lattice structure on any of the three lamellas. Precisely, the only structural faults observed in the recorded micrographs are lattice dislocations at the MgO interface as well as inhomogeneities of the MgO buffer layer leading to *dips* of the Co_2MnSi. Both features are equally observed on the thin film reference lamellas, as was discussed in section 3.2, and are therefore not attributed to the nanofabrication process.

In addition to the undisturbed crystal lattice structure, the chemical $L2_1$ ordering is found to be maintained even right at the etched waveguide edges

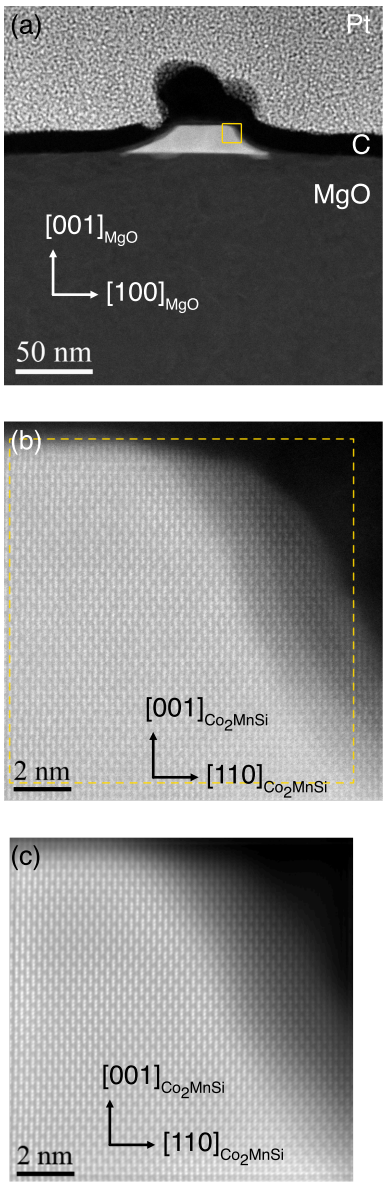

Figure 3.26: Exemplary set of HAADF-STEM micrographs taken on the smallest etched waveguide *WG50*, which was also studied in EDXS 3.25: (a) unfiltered HAADF-STEM micrograph of the entire waveguide cross section, (b) unfiltered HAADF-STEM micrograph of the top right corner as marked in (a) by the yellow square, (c) filtered HAADF-STEM micrograph corresponding to the area marked in (b) by the yellow dashed square. The gradual decrease of the intensity at the edge is attributed to a roughness along the probing direction. An intensity analysis yields the $L2_1$ pattern in the entire frame, even at the exposed edges where it was confirmed by various line profile extractions (not shown, but analogous to figure 3.4). *Improved image resolution in the digital document.*

* Inhomogeneities along the entire waveguide edges can already be seen in the SEM images recorded during the FIB lamella preparation, see figure 3.1 (b). As the lamella is cut perpendicular to the waveguide array and has a finite thickness of ~ 50 nm, part of this edge modulation is included in the lamella volume, and translates to a modification of the material density probed by the transmitted beam in this area. Consequently, the outline of the imaged waveguide cross sections is not sharp, but yields a gradient which is perceived in figure 3.26 (b) as a 3-step intensity reduction.

where clear intensity patterns are observed, an example of which is shown in figure 3.26. Further intensity analyses at various sites of waveguide edges as well as along the top interfaces of the Co_2MnSi confirm an unaffected ordering throughout the structures.

Moreover, as in particular the chemical ordering is quite sensitive to the precise stoichiometry in the crystal, the detection of the $L2_1$ order even right at the border/interfaces of the etched structures implies an unaffected 2:1:1 stoichiometry. Consequently, the Silicon detected in the amorphous oxide layer around the waveguide structure is unlikely to be extracted from the fabricated structure (exposed waveguide), but probably the result of a redeposition from the milled material similar to the Pd horns.

In fact, this redeposited Silicon-containing oxide layer covering the waveguide edges seems to yield a passivised barrier protecting the underlying Co_2MnSi structures from further oxidation and consequently an intact crystallographic and chemical ordering is maintained within the structured Co_2MnSi.

Potential auto-formation process of the passivised oxide barrier

The auto-formation of a protective oxidation barrier is a rather unexpected result from this nanostructuring study: Indeed, the etched Co_2MnSi structures were expected to form an oxide along the exposed edges, yet remarkably neither Co nor Mn is detected in the oxidised area, and also the intact crystal structure and chemical ordering even within the rough edges do not confirm this expectation.

Instead, the amorphous oxide layer is likely formed during the IBE milling process, where two origins probably contribute to the formation:

Firstly, the milling of the Co_2MnSi results in the release of Si atoms. Simultaneously free Oxygen atoms are released from the milling of the oxidised Al capping as well as the MgO in the capping and the substrate. Potentially, not all Silicon and Oxygen atoms leave the sample area, but instead react with the sample or other surrounding atoms and a redeposition leads to the formation of the amorphous Silicon-containing oxide covering the waveguide edges.

Secondly, the hexamethyldisilazane (HMDS) adhesion promoter contains Si (chemical formula: $NH[Si(CH_3)_3]_2$) and works by a reaction with the sample surface, where the HMDS splits and chemical bonds are formed between the Si atoms of the $Si(CH_3)_3$ groups and the Oxygen atoms in the sample[83]. Naturally, this chemical is applied directly onto the sample surface and hence in direct contact with the oxidised MgO/Al capping of the sample, which consequently could give rise to the detected Silicon in the capping of the structured sample. The reduced Al and vanished Mg could then be a potential secondary effect due to the Si bonding with the O atoms in the capping and thus releasing some of the Al and Mg atoms[84]. Moreover, this origin of Si in the capping would match the aforementioned observation of a faint line of reduced Si content separating the Si in the capping layer from the Si in the Heusler compound.

Curiously, the hexamethyldisilazane (HMDS) is not only used as an adhesion promoter, but in other contexts also used as a precursor for the chemical vapor deposition (CVD) for instance for the production of silicon carbonitride (SiCN), SiC or SiN films [221–223] for which typically Argon or Nitrogen gases are used. Especially the conditions in ion beam induced chemical vapor deposition (IBI-CVD) studies which reportedly yield amorphous SiCN, SiC, SiN films [223] principally resemble the process of the IBE milling employed in this work[85]. Moreover, the HMDS was applied by spin coating in this

[220]: MicroChemicals (2025), *Application Note Substrate Pretreatment: Cleaning and Adhesion Promotion*

83: See the respective information on the *MicroChemicals website* or in the application note [220].

84: In a very simple picture. Note that for a more precise conclusion, a chemical analysis accounting e.g. for the bonding energies would be necessary, but is outside the scope (and interest) of this study.

[221]: Demin et al. (2015), 'Laser plasmochemical synthesis of hard protective SiCN films'
[222]: Menshakov et al. (2018), 'Investigation of the conditions for the formation of SiCN-based coatings in arc discharge with self-heated hollow cathode'
[223]: Yoshimura et al. (2021), 'Low-energy Ar+ and N+ ion beam induced chemical vapor deposition using hexamethyldisilazane for the formation of nitrogen containing SiC and carbon containing SiN films'

85: In this work, HMDS is applied directly to the sample surface as an adhesion promoter (and covered with a photoresist mask), and subsequently the sample is bombarded with Ar^+ ions for a milling of the structures. In processes for the CVD growth of SiCN, SiN or SiC films, HMDS is used as a precursor (typically in vapor form, but sometimes also applied directly to the sample surface like in this study) and the CVD growth of the SiCN, SiN or SiC films is induced by an Ar^+ ion beam.

study, which is indicated to yield comparably thick HMDS layers and is therefore unrecommended for the adhesion promotion since the abundant HMDS is known to be quite reactive[86]. Given the likely abundance of HMDS, its seemingly high reactivity as well as the principle process similarities to the IBI-CVD growth of SiCN, SiN and SiC films, such compounds could potentially also be formed during the IBE milling of the sample and hence lead to a redeposition of SiC, SiN and SiCN on the edges of the nanostructures.

For more precise conclusions on the composition and formation of the auto-formed amorphous oxide barrier, as well as the similarly altered capping layer on the MgO/Al sample, further chemical characterisation measurements would be necessary, e.g. by electron energy loss spectroscopy (EELS), which particularly for light atoms can yield an improved precision. A further characterisation potentially also as a function of the IBE process parameters could be interesting to confirm the accidential HMDS-induced growth hypothesis, which could subsequently allow to exploit the process in the fabrication of other materials (or contrarily could help to ensure an avoiding of an accidential HMDS-induced material growth when exploiting the chemical for the adhesion promotion properties).

Yet for the purpose of this study, the conclusion on an auto-formation of an amorphous Silicon-containing oxide layer covering the structures and yielding a passivised, protective oxidation barrier is a sufficiently specific characterisation. And particularly the impeccable Heusler structure even in the edges in direct contact with this oxide layer are a welcome effect, which is additionally assumed to be reproducible given the consistent results on all structures investigated on the three lamellas from the two samples fabricated in separate processes. Hence no further investigations were carried out and the protective oxide layer is expected to form in all structuring processes (ensuring the same conditions).

86: According to the manufacturer, see the respective information on the *MicroChemicals website* or in the application note [220].

[220]: MicroChemicals (2025), *Application Note Substrate Pretreatment: Cleaning and Adhesion Promotion*

3.4 Conclusions

In summary, the structural characterisation study presented in this chapter yields several conclusions which are of relevance for the further study of the Heusler thin films and particularly for the fabrication of magnonic devices from Co_2MnSi microstructures.

First, a consistently predominant $L2_1$ ordering is detected throughout all studied samples. This is not only desired for its relation to various key properties, such as the correct stoichiometry, or the half-metallicity and the related Gilbert damping parameter, but also the consistency throughout the various samples studied by TEM in the course of this project is a sign for the reliability on the growth control and resulting sample quality.

Second, the analysis of the interfaces with MgO yields the conclusion on a network of lattice dislocations identified as edge dislocations. The formation is due to the lattice mismatch between the MgO lattice and the Co_2MnSi lattice, and can be principally tuned by an adequate buffer layer as was verified on two tests samples. The orientation of the dislocation network is assumed to be along the $[110]_{Co_2MnSi}$ directions, which is concluded from the successful neat imaging of the distortion at the lattice sites albeit an expectation of approximately $10-20$ dislocation features in the probing direction. An impact of the occurrence of the dislocations on the chemical ordering is excluded based on the observation of $L2_1$ ordered Co_2MnSi in direct proximity to multiple dislocations. Still, the lattice dislocation network implies a directional variation of the inhomogeneities in the sample, which can act as pinning centres for magnetic domains and have reportedly resulted in anisotropic inhomogeneous damping contributions [209, 210]. This result is therefore of particular relevance for the study of the anisotropic magnetisation dynamics in the thin films, which will be presented in chapter 6.

[209]: Heinrich et al. (2004), 'Magnetic properties of NiMnSb(001) films grown on InGaAs/InP(001)'
[210]: Woltersdorf et al. (2004), 'Spin dynamics in ultrathin film structures with a network of misfit dislocations'

Third, the coverage of different cappings was verified with a particular interest in the bilayer capping stacks MgO/Al and MgO/Ti, both of which were found to have formed oxides at the exposed surfaces. In the case of the MgO/Al capping, the island growth of the Al layer yields a significant surface roughness with varying island sizes and oxidation. In the case of the MgO/Ti capping, a homogeneous film stack is obtained and the oxidation of the deposited Ti film yields a separation into an oxidised top-layer and a non-oxidised bottom part with a clear interface between the two indicating a passivation of this capping.

Finally, a nanofabrication study was carried out in order to determine the fabrication effects and induced damage on the structural properties of the Heusler material. Nanostructures are fabricated by an electron beam lithography process with a resist mask IBE milling step on two representative samples, one with a metallic Pd capping and the second with the oxidised MgO/Al bilayer capping.

Except of capping-specific observations, the fabrication on both samples was found to yield similar results. The principal conclusion from this nanostructuring study is a successful downscaling to feature sizes of $\sim 50\,\mathrm{nm}$, for both the smallest waveguide widths as well as the smallest partially (majorly) etched gap sizes. Precisely, the smallest fabricated waveguide yielded

$$w_{\mathrm{WG50}} = \begin{pmatrix} w_{\mathrm{top}} \\ w_{\mathrm{core}} \\ w_{\mathrm{base}} \end{pmatrix} = \begin{pmatrix} 35.5\,\mathrm{nm} \\ 53.3\,\mathrm{nm} \\ 96.0\,\mathrm{nm} \end{pmatrix} \tag{3.6}$$

with an error of $\Delta w = 2\,\text{nm}$ on each measurement, where it is noted that no smaller waveguide was designed, hence this "smallest" waveguide might not be the absolute smallest producible limit. A general linear scalability was obtained on the downscaling of the waveguide widths. The smallest successfully etched gap widths are

$$g_{\text{Gap50}} = \begin{pmatrix} g_{\text{capping}} \\ g_{\text{top}} \\ g_{\text{core}} \\ g_{\text{base}} \end{pmatrix} = \begin{pmatrix} 56\,\text{nm} \\ 62\,\text{nm} \\ 54\,\text{nm} \\ - \end{pmatrix} \tag{3.7}$$

for the smallest partially etched gap, as shown in figure 3.22 (c), and

$$g_{\text{Gap200}} = \begin{pmatrix} g_{\text{capping}} \\ g_{\text{top}} \\ g_{\text{core}} \\ g_{\text{base}} \end{pmatrix} = \begin{pmatrix} 210\,\text{nm} \\ 214\,\text{nm} \\ 203\,\text{nm} \\ 166\,\text{nm} \end{pmatrix} \tag{3.8}$$

for the smallest fully etched gap, again with an error of $\Delta g = 2\,\text{nm}$ on each measurement. At the etched borders (waveguide edges), hardly any damage on the Heusler crystal structure was observed in the HRTEM, STEM and EDXS study on the structures, and notably the chemical $L2_1$ ordering was maintained. The residual Co_2MnSi at the bottom of the partially etched gaps was found to be amorphous, and could potentially serve for the exchange coupling of the adjacent structures with reduced strength compared to the exchange interaction in the bulk material. All etched interfaces were found to be covered by an amorphous oxide layer, which is assumed to form during the milling process by a redeposition onto the sample surface and yields a protective coating of the fabricated nanostructures.

A redeposition is also observed on the Pd capping leading to the formation of inwards bent Pd "horn" structures. While these Pd redeposition structures are irrelevant for the main goal of the study, i.e. the investigation of the induced damage on the Heusler structure, it is noted that the effect with observed feature sizes of up to 80 nm could be relevant particularly for the fabrication of typical device structures, e.g. with a secondary process step aiming at the patterning of antennas on top of the etched structures. In that case, a further IBE process optimisation might allow for a reduction of the redeposition. Apart from the redeposition onto the edges of the resist mask, the Pd capping was found to be unchanged.

Contrary to this, the MgO/Al capping did not seem to withstand the fabrication process as no sign of the Magnesium could be resolved in the capping of the etched structures. Instead, Silicon is found to have penetrated into the capping and the chemical alteration is likely linked to the chemical reaction of the sample surface with the HMDS adhesion promoting coating. Still, the structures are well protected by the altered capping, similar to the oxide cover at the etched borders.

The underlying process auto-formation of a protective coating preventing the oxidation of the etched Co_2MnSi nanostructures could not be precisely determined, but two likely origins are pointed out. The consistent results on the three lamellas from different samples leads to the expectation of comparable results from similar fabrication processes.

Part II
Magnetic and magneto-optical properties of Co_2Mn-based Heusler thin films

Background: Fundamental concepts of magnetism, spin dynamics and magneto-optical interactions

4

Before diving into the magnetic characterisation of Co_2Mn-based Heusler compounds, in particular their anisotropic behaviour, magnetisation oscillations and magneto-optical suitability, this chapter briefly introduces the underlying fundamental concepts. The first section of this chapter focuses on the necessary concepts of magnetism required for the discussion of magnetisation, hysteresis and anisotropy within a magnetometric study in chapter 6.1. The second section of this chapter briefly introduces the conceptual framework of magnetisation oscillations based on which the ferromagnetic resonance spectroscopy results will be discussed in the subsequent chapter 6.2. The third section gives an introduction to magneto-optical phenomena and basic concepts necessary for the discussion of the magneto-optical studies in chapter 7.

A detailed description of the presented concepts in this chapter can be found in most textbooks in the field of magnetism, e.g. [224–229] to name only a few.

4.1 Ferromagnetism, anisotropies and hysteresis 65
Magnetic ordering 65
Magnetic anisotropy 68
Magnetic hysteresis 73
4.2 Magnetisation oscillations and magnetic damping . . 75
Equation of motion 75
Linearisation 76
FMR 78
LLG linewidth and beyond 79
Magnetic damping 81
4.3 Magneto-optical interactions 85
MOKE 85
BLS 90
4.4 Concluding remarks 92

[224]: Morrish (2001), *The physical principles of magnetism*
[225]: Gurevich et al. (1996), *Magnetization oscillations and waves*
[226]: Hillebrands et al. (2005), '5. Magnetismus'
[227]: Stancil et al. (2009), *Spin waves*
[228]: Chikazumi et al. (2009), *Physics of ferromagnetism*
[229]: Rezende (2020), *Fundamentals of Magnonics*

4.1 Ferromagnetism, anisotropies and hysteresis

Ferromagnetic solids present a *spontanenous magnetisation*, i.e. a magnetic moment in absence of an external magnetic field, resulting from the parallel alignment of the strongly coupled atomic magnetic dipole moments in the material [224]. The magnetisation

$$\mathbf{M} = \frac{1}{\Delta V^2} \int_{\Delta V} \mu(\mathbf{r}) d^3 r \tag{4.1}$$

gives the spatial distribution of the atomic moments $\mu(\mathbf{r})$ per unit of volume ΔV and is often expressed in a *continuum approximation*[1] through the normalised vector field $\mathbf{m}$, i.e.

$$\mathbf{M}(\mathbf{r}) = M_S \, \mathbf{m}(\mathbf{r}) \tag{4.2}$$

where M_S is the magnitude of the magnetisation commonly referred to as the *saturation magnetisation* M_S. Thermal fluctuations promote the misalignment between the microscopic magnetic moments, and therefore the saturation magnetisation of ferromagnets is a monotonously decreasing function of the temperature. The magnetic ordering is broken above a critical temperature T_C, the *Curie temperature*, resulting in a vanishing magnetisation and thus the material becoming *paramagnetic*. Typical ferromagnets at room temperature are Fe, Ni, Co, and many of their alloys including the Co_2Mn-based Heusler compounds studied in this thesis[2].

1: The description by a continuous vector field is precisely only valid for materials with exchange length scales larger than the lattice constant, as will be detailed below.

2: Precisely, $T_C \gtrapprox 700\,\mathrm{K}$ for these compounds as listed in table 1.1 on page 16 in the material introduction chapter 1.

4.1.1 Magnetic ordering

The ordered alignment of magnetic moments of a solid at vanishing external field is mediated by quantum mechanical exchange interactions, the foundation of which lies in the Pauli principle for the quantum state of multiple fermions. The Pauli principle only allows many-particle wave functions that are antisymmetric with respect to the exchange of particles in the system and thus results in a coupling of the Coulomb interaction and the spin state of the

electrons, yielding a preferred magnetic ordering as a function of the spatial distance between the electrons [224].

Consequently, the description of the microscopic origins of ferromagnetism in metallic solids is a rather complex matter, tackled e.g. in the Stoner model for itinerant ferromagnetism. However, under the assumption of localised electrons[3], the Heisenberg exchange model yields a rather intuitive description of the implications of the quantum mechanical exchange interaction which has been found to adequately describe the phenomena in the majority of materials including metallic ferromagnets [230].

[224]: Morrish (2001), *The physical principles of magnetism*

3: Technically, the assumption of localised electrons is not adequate for the micromagnetic description of ferromagnetism in conductive solids. Yet, the qualitative agreement of the description with the experimentally observed phenomena is attributed to the Heisenberg exchange formalism yielding an expression of the exchange energy which corresponds to a formulation of the "lowest order phenomenological energy expression that penalises inhomogeneous magnetisation configurations" [230].

[230]: Abert (2019), 'Micromagnetics and spintronics'

[231]: Heisenberg (1928), 'Zur Theorie des Ferromagnetismus'

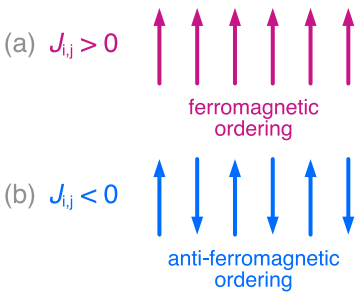

Figure 4.1: Common schematic depiction of the collinear ordering described by the Heisenberg exchange formalism, sketched for the simple example of a 1D spin chain: (a) a exchange integral imposes a parallel alignment of the spins, yielding ferromagnetic order and a non-zero net magnetisation, while (b) a negative exchange integral yields anti-ferromagnetic order which results in a vanishing net magnetisation.

Heisenberg exchange

Derived in the Heisenberg formalism nearly a century ago [231], the exchange Hamiltonian of a given atom i

$$\mathcal{H}_{\text{exch,i}} = -2\mathbf{S}_i \sum_j J_{i,j}^{\text{exch}} \mathbf{S}_j \tag{4.3}$$

describes the interaction of an atom i with its neighbours j and their total spins $\mathbf{S}_{i,j} = \sum \mathbf{s}_{i,j}$. The exchange integral $J_{i,j}^{\text{exch}}$ accounts for the overlap between the wavefunctions of the atoms and is inversely proportional to the interatomic distance. Its sign indicates the preferred order, i.e. a parallel or antiparallel alignment of the spins yielding ferromagnetic or antiferromagnetic ordering as illustrated in figure 4.1. In most cases it is negligible for all but the nearest neighbours, making the exchange interaction a significant interaction only over short-range distances [224].

The Hamiltonian of an entire crystal is then obtained in a first approximation[4] as the sum over all atoms i with neighbours j

$$\mathcal{H}_{\text{exch}} = -2J_{\text{exch}} \sum_{i \neq j} \mathbf{S}_i \cdot \mathbf{S}_j \tag{4.4}$$

and considering the spin operators as classical vectors with small angles ϕ_{ij} of misalignment between neighbouring spins, the associated free exchange energy[5] $F_{\text{exch}} = -2J_{\text{exch}}S^2 \sum_{i \neq j} \cos \phi_{ij}$ can be expressed as a function of the normalised, continuous magnetisation field $\mathbf{m}(\mathbf{r})$ [230]

$$F_{\text{exch}} = -2J_{\text{exch}}S^2 \sum_{i \neq j} \mathbf{m}(\mathbf{r}_i) \cdot \mathbf{m}\left(\mathbf{r}_i + \Delta\mathbf{r}_{ij}\right) \tag{4.5}$$

with the distance $\Delta\mathbf{r}_{ij} = \mathbf{r}_j - \mathbf{r}_i$ between sites j and i. The sum can be expanded as a Taylor series with $\mathbf{m}(\mathbf{r}_i) \cdot \mathbf{m}\left(\mathbf{r}_i + \Delta\mathbf{r}_{ij}\right) \approx 1 - \frac{1}{2}\left(\nabla\mathbf{m}(\mathbf{r}_i) \cdot \Delta\mathbf{r}_{ij}\right)^2 + \mathcal{O}\left(\Delta\mathbf{r}_{ij}^3\right)$ and assuming a periodic spin lattice where $\Delta\mathbf{r}_{ij}$ is identical for all i, j, integration yields a continuous expression of the exchange energy[6]

$$F_{\text{exch}} = \int_{\Delta V} \sum_{i \neq j} A_j \left(\frac{\partial \mathbf{m}_i}{\partial r_j}\right)^2 d\mathbf{r} \tag{4.6}$$

where the exchange matrix coefficients A_j account for the periodic exchange couplings induced by the crystal structure [230]. In cubic crystals, like the Heusler compounds studied in this work, the exchange energy simplifies to

$$F_{\text{exch}} = \int_{\Delta V} A_{\text{exch}} \left(\nabla\mathbf{m}(\mathbf{r})\right)^2 d\mathbf{r} \tag{4.7}$$

4: Assuming: (i) the same exchange integral for all electrons, (ii) constant (omittable) exchange between the electrons of the same atom, (iii) negligible exchange for all but nearest neighbours, (iv) isotropic exchange.

5: For clarity, F is chosen here as a symbol for the energy contributions, in order to avoid confusion with electrical fields $\mathbf{E}$ notably in the subsequent section focusing on magneto-optics. Equally, energy densities will be denoted as ℓ in order to avoid confusion with the permittivity ε. A list of the mathematical symbol conventions in this work is given in table 27 on page 312.

6: Neglecting constant terms and choosing a coordinate system which diagonalises the exchange matrix A_{ij} [230].

[230]: Abert (2019), 'Micromagnetics and spintronics'

where $(\nabla \mathbf{m}(\mathbf{r}))^2 = \sum_{i \neq j} \left(\frac{\partial \mathbf{m}_i}{\partial r_j} \right)^2$ and the associated energy density is given by $\ell_{\text{exch}} = A_{\text{exch}} (\nabla \mathbf{m}(\mathbf{r}))^2$. In the case of this work (i.e. for cubic crystals), the exchange matrix is simplified to a scalar constant

$$A_{\text{exch}} = C \cdot \frac{J_{\text{exch}} S^2}{a} \tag{4.8}$$

linked to the exchange integral J_{exch} and the cubic lattice parameter a where the factor C accounts for the number of atoms per unit cell in the specific lattice structure [232]. The resulting torque acting on an inhomogeneous (normalised) magnetisation $\mathbf{m}(\mathbf{r})$, is often expressed by the associated effective magnetic field term [233]

$$\mathbf{H}_{\text{exch}}(\mathbf{r}) = \frac{2A_{\text{exch}}}{\mu_0 M_S} \Delta \mathbf{m}(\mathbf{r}) \tag{4.9}$$

with the Laplacian operator Δ, as it facilitates the incorporation into micromagnetic problems[7].

In current literature in the field of magnetic materials and magnetisation dynamics, the exchange strength is not only expressed in form of the introduced Heisenberg exchange integral J_{exch} or the related exchange constant A_{exch} (in $\text{J}\cdot\text{m}^{-1}$), but also often represented by the *exchange stiffness* or *spin wave stiffness* D (in $\text{J}\cdot\text{m}^2$), or the effective field constant D_{B} (in $\text{T}\cdot\text{m}^2$) induced by the exchange energy of a spin wave. The relationship

$$D_{\text{B}} = \frac{D}{g\mu_{\text{B}}} = \frac{2A_{\text{exch}}}{M_S} \tag{4.10}$$

links all constants to each other [234].

Non-collinear exchange

The simple picture of Heisenberg exchange relies on the two essential assumptions of negligible orbital magnetic moments and localised spins. Still, it successfully describes magnetic interactions in many common material systems and has therefore become a widely accepted approximative model for the description of spontaneous magnetic ordering. However, the Heisenberg model can only account for bilinear exchange and is therefore of limited use for the description of non-collinear spin states [235]. To this aim, higher order correction terms are commonly added to the bilinear Heisenberg Hamiltonian and one of the most common corrections involves the addition of a *biquadratic exchange* term of the form [236]

$$\mathcal{H}_{\text{exch,biq}} = -2J_{\text{biq}} \sum_{ij} (\mathbf{S}_i \cdot \mathbf{S}_j)^2 \tag{4.11}$$

to the exchange Hamiltonian in equation 4.4. The addition of this biquadratic exchange term is not unique to a single microscopic model [237], but can be motivated by different origins including superexchange, magneto-elastic mechanisms [236] and interlayer exchange coupling [238].

The biquadratic term essentially favours a 90° coupling and is therefore necessary to describe canted spin structures [235], such as in two-dimensional magnets exhibiting complex spin textures [239] or in certain stacks of magnetic multilayers with non-collinear interlayer coupling [240–242]. In particular, notable biquadratic coupling contributions have been reported in Co_2MnSi-based Heusler trilayer systems [243–248].

[232]: Bergmann et al. (1975), *Aufbau der Materie*

[233]: Henry et al. (2016), *Propagating spin-wave normal modes*

7: This effective field term is of little necessity for the introduction of the concepts at this point, but will be motivated later in equation 4.32 as the consideration of an effective field facilitates the incorporation into the equation of motion, and thus the micromagnetic modelling of dynamic magnetisation problems [233].

[234]: Gaier et al. (2009), 'Exchange stiffness in the Co_2FeSi Heusler compound'

[235]: Iwashita et al. (1976), 'Effects of biquadratic exchange in ferromagnets'

[236]: Harris et al. (1963), 'Biquadratic Exchange Between Mn^{2+} Ions in MgO'

[237]: Hoffmann et al. (2020), 'Systematic derivation of realistic spin models for beyond-Heisenberg solids'

[238]: Bruno (1993), 'Interlayer exchange coupling'

[239]: Kartsev et al. (2020), 'Biquadratic exchange interactions in two-dimensional magnets'

[240]: Fuß et al. (1992), 'Short- and long period oscillations in the exchange coupling of Fe across epitaxially grown Al- and Au-interlayers'

[241]: Gutierrez et al. (1992), 'Strong temperature dependence of the 90° coupling in Fe/Al/Fe(001) magnetic trilayers'

[242]: Slonczewski (1993), 'Origin of biquadratic exchange in magnetic multilayers (invited)'

[243]: Bosu et al. (2007), 'Interlayer coupling in epitaxial Co_2MnSi/X/Co_2MnSi (X=Cr and V) trilayer structures'

[244]: Bosu et al. (2008), 'Biquadratic Exchange Coupling in Epitaxial Co_2MnSi/Cr/Fe Trilayers'

[245]: Bosu et al. (2010), 'Chemical ordering dependence of interlayer exchange coupling in Co-Mn-Si/Cr/Co-Mn-Si trilayer structures'

[246]: Kakeno et al. (2010), '*Ab initio* study of magnetic structure and exchange coupling in Co_2MnSi / Cr / Co_2MnSi trilayers'

[247]: Goripati et al. (2011), 'Bi-quadratic interlayer exchange coupling in Co_2MnSi/Ag/Co_2MnSi pseudo spin-valve'

[248]: Inoue et al. (2019), 'Origin of biquadratic interlayer exchange coupling in Co_2MnSi-based current-perpendicular-to-plane pseudo spin valves'

4.1.2 Magnetic anisotropy

The exchange interaction principally imposes a homogeneous alignment of the microscopic magnetic moments and is of isotropic nature. Yet, ferromagnetic specimen typically present a magnetic anisotropy, specifically an orientation dependence of the total energy density ℓ_{tot} of the magnetic system manifesting in a preferential alignment of the magnetisation along specific directions even in the absence of an external magnetic field. These directions are called *easy axes* of the specimen and correspond to the minima of ℓ_{tot}.

For this phenomenon to arise, the total energy density ℓ_{tot} of the system must involve anisotropic energy contributions in addition to the exchange energy (density). Such magnetic anisotropy contributions can have various origins, where the two principal ones in this work arise from the specimen's shape mediated by the dipolar interaction as well as the crystalline structure mediated by the spin-orbit coupling.

Dipolar interaction, demagnetisation energy and shape anisotropy

The energy contribution arising from the dipolar interaction accounts for the dipole-dipole coupling of magnetic dipolar moments mediated by the magnetic field

$$\mathbf{H}_{\text{dip},j}(\mathbf{r}) = \frac{1}{4\pi}\left[\frac{3\mathbf{r}(\mathbf{r}\cdot\boldsymbol{\mu}_j)}{r^5} - \frac{\boldsymbol{\mu}_j}{r^3}\right] \tag{4.12}$$

any magnetic dipolar moment $\boldsymbol{\mu}_j$ creates at a distance $\mathbf{r}$ to its position [249]. While the dipolar interaction is relatively weak compared to the strong exchange interaction, it is of longer range and therefore of significance for the magnetic properties of a solid [226]. For a magnetic moment $\boldsymbol{\mu}_i$, the sum of all surrounding magnetic dipolar fields results in the energy

$$F_i = -\mu_0 \boldsymbol{\mu}_i \sum_j \mathbf{H}_{\text{dip},j}(\mathbf{r_i}) \tag{4.13}$$

with $\mathbf{H}_{\text{dip},j}(\mathbf{r_i})$ indicating the dipolar field created by the magnetic moment at site j acting on the magnetic moment $\boldsymbol{\mu}_i$ at the point $\mathbf{r}_i$.

The dipolar interaction as such is not intrinsically anisotropic: In an infinite, homogeneously magnetised medium, the dipolar fields completely compensate for each other and thus can be disregarded. However, it gives rise to anisotropy in finite or inhomogeneously magnetised ferromagnetic media, where the dipolar fields no longer fully cancel out. This results in a finite effective field term, commonly named the *demagnetisation field* within the ferromagnetic medium, or the *stray field* outside the medium.

The sum over all magnetic moments $\boldsymbol{\mu}_i$ in the solid results in the demagnetisation energy term $F_{\text{demag}} = -\frac{\mu_0}{2}\sum_i \boldsymbol{\mu}_i \sum_j \mathbf{H}_{\text{dip},j}(\mathbf{r_i})$, where double counting is avoided by the factor 1/2. As above for the exchange energy, the discrete expression can be transformed into a continuous function by integration yielding the *demagnetisation energy*

$$F_{\text{demag}} = -\frac{\mu_0}{2}\int_{\text{V}} \mathbf{M}(\mathbf{r})\cdot\mathbf{H}_{\text{demag}}(\mathbf{r})\mathrm{d}V \tag{4.14}$$

with the demagnetisation field $\mathbf{H}_{\text{demag}}$ accounting for all field terms originating from the dipolar interaction[8] and the magnetisation $\mathbf{M}(\mathbf{r})$ of the solid.

[249]: Jackson (2013), *Klassische Elektrodynamik*

[226]: Hillebrands et al. (2005), '5. Magnetismus'

8: I.e. dipolar fields as well as higher order fields like quadrupolar fields for instance.

To minimise this contribution, the demagnetisation field must be minimised, which essentially implies a competition between the exchange energy favouring a homogeneous alignment of the microscopic magnetic moments and the demagnetisation energy favouring a reduction of the uncompensated magnetic moments at the boundaries of the ferromagnetic body. This is typically quantified by the *dipole-exchange length*[9]

$$\lambda_{\text{exch}} = \sqrt{\frac{2A_{\text{exch}}}{\mu_0 M_S^2}} =: \sqrt{\frac{A_{\text{exch}}}{K_{\text{demag}}}} \tag{4.15}$$

defining the width $d = \pi\lambda_{\text{exch}}$ of the associated Néel domain walls, where a demagnetisation anisotropy constant $K_{\text{demag}} = \mu_0 M_S^2/2$ can be introduced[10]. In the case of large demagnetisation contributions, this leads to small domain wall widths, i.e. favouring the formation of multiple magnetic domains. On the other hand, in the case of a governing exchange contribution, a single domain state with a favoured alignment of the magnetisation along the longest axis of the ferromagnetic body is preferential.

Consequently, the optimal orientation is influenced by the geometry of the sample, a phenomenon commonly referred to as *shape anisotropy*. In the case of homogeneously magnetised samples of ellipsoidal shapes such as spheres, ellipsoids, cylinders, and infinite thin films, the demagnetisation field can be simplified to

$$\mathbf{H}_{\text{demag}} = -\hat{N}_{\text{demag}}\mathbf{M} \tag{4.16}$$

and the associated demagnetisation energy density reads

$$\ell_{\text{demag}} = \frac{\mu_0}{2}\mathbf{M}(\hat{N}_{\text{demag}}\mathbf{M}) \tag{4.17}$$

with the *demagnetisation tensor* $\hat{N}_{\text{demag}}$ depending on the shape of the sample. In general, $\hat{N}_{\text{demag}}$ is a symmetric tensor that becomes diagonal when transformed onto the principal axes of the ellipsoid [225, 226]. Its trace $\text{Tr}(\hat{N}_{\text{demag}})$ is always equal to unity for uniform demagnetisation fields, and locally equal to unity for sample shapes with non-uniform demagnetisation fields [227].

9: Sometimes also simply denoted *exchange length*, its ratio over the lattice parameter defines the validity of the continuum approach mentioned on page 65.

10: Matching the analogous formulation of the anisotropy-exchange length in the next subsection.

[225]: Gurevich et al. (1996), *Magnetization oscillations and waves*
[226]: Hillebrands et al. (2005), '5. Magnetismus'
[227]: Stancil et al. (2009), *Spin waves*

Magnetocrystalline anisotropy

The magnetocrystalline anisotropy energy accounts for the influence of the spatial distribution of the atoms, i.e. the crystal lattice, on the electron orbitals mediated by the spin-orbit coupling. Due to the interaction of spin and orbital magnetic moments, any anisotropy of the electron orbitals translates to an anisotropic contribution F_{ani} or ℓ_{ani} to the total energy (density) F_{tot} or ℓ_{tot} which naturally depends on the relative orientation of magnetisation and the symmetry axes of the anisotropy energy.

Cubic anisotropy: The subject of interest in this work are cubic monocrystals with a high lattice symmetry imposing two conditions on the magnetocrystalline anisotropy expression: Firstly, magnetisation reversal along any crystal axis must not affect the anisotropy energy, thus imposing a function of even powers of the direction cosines m_i, where the symmetry axes $i = 1, 2, 3$ coincide with the principal axes of the cubic lattice[11]. Secondly, the indifference to an interchange of any two crystal axes must be given, which implies a function of at least fourth order[12] of the direction cosines m_i [224].

11: Note that the formulation of the cubic anisotropy energy is only intuitive (to me at least) in the coordinate system of the underlying cubic lattice structure. However, this coordinate system is not necessarily adequate for any case: The demagnetisation energy and external field are typically easiest to define in a global coordinate system given by the sample geometry. Additionally, a third coordinate system is often handy to introduce such that the equilibrium position of the magnetisation coincides with one axis, as this facilitates the linearisation of the equation of motion (see the next section 4.2). The correct calculation of the transformation matrices is therefore crucial at this point in order to incorporate the cubic anisotropy into the broader physical problem.

12: Since the second order term $o \cdot m_1^2 + p \cdot m_2^2 + q \cdot m_3^2$ with any factors o, p, q and the interchangeability requirement imposing $o = p = q$, reduces to reduces to the term $m_1^2 + m_2^2 + m_3^2 = 1$, from which no anisotropy can arise.

These conditions are satisfied by the expression

$$\ell_{\text{ani,cubic}} = K_{c1}(m_1^2 m_2^2 + m_2^2 m_3^2 + m_3^2 m_1^2) + K_{c2} m_1^2 m_2^2 m_3^2 + \ldots \tag{4.18}$$

for the cubic anisotropy energy density with the first order and second order cubic anisotropy constants K_{c1} and K_{c2} in $\mathrm{J/m^3}$ [224, 227]. Following a common convention, the cubic anisotropy constants K_{ci} are here defined such that $K_{ci} > 0$ for all i indicates the identification of the crystal axes as easy axes, while $K_{ci} < 0$ for all i corresponds to the case of the crystal axes representing hard axes.

In many cases it is sufficient to consider the first order cubic anisotropy term and neglect all higher orders, i.e. set $K_{ci} = 0$ for $i > 1$. The resulting energy surfaces are illustrated in figure 4.2: For positive K_{c1}, the anisotropy energy presents minima along the crystal axes ⟨100⟩ and the maxima are located along the ⟨111⟩ directions (body diagonals of the cubic lattice), hence the system exhibits 6 easy axes and 8 hard axes. For negative K_{c1}, the situation is flipped with the crystal axes ⟨100⟩ corresponding to maxima of the anisotropy energy and the ⟨111⟩ directions correspond to minima, thus such systems present 8 easy axes and 6 hard axes. In both cases, the ⟨110⟩ directions (face diagonals of the cubic lattice) present saddle points of the three-dimensional energy surface, counting 12 in total.

The second order cubic anisotropy term on its own is illustrated in figure 4.3: Given the contribution of all three direction cosines (projections of the magnetisation on the principal crystal axes), the contribution $K_{c2} m_1^2 m_2^2 m_3^2$ is maximal (minimal) for $K_{c2} > 0$ ($K_{c2} < 0$) for an orientation along the ⟨111⟩ directions, and vanishes for any orientation where one of the direction cosines becomes zero, i.e. for the principal lattice axes ⟨100⟩ as well as all arbitrary directions ⟨$hk0$⟩ within any principal lattice plane (001), including the face diagonals ⟨110⟩.

Consequently, in combination with the first order cubic anisotropy, the second order cubic anisotropy simply reinforces the maximum (minimum) of the energy for the diagonal orientation ⟨111⟩ if K_{c1} and K_{c2} are of the same sign. This is shown in figure 4.4 (a) for the example of both constants being negative (crystal axes corresponding to hard axes of the magnetic system) and a ratio of $K_{c2}/K_{c1} = 20$. However, if K_{c1} and K_{c2} are of opposite sign, three different cases need to be distinguished depending on the ratio between the two anisotropy constants [250], as is listed in table 4.1. Exemplary illustrations of the three cases are shown in figure 4.4 for $K_{c1} < 0$: In figure 4.4 (b), the addition of a second order anisotropy term with $|K_{c2}/K_{c1}| < 9/4$ keeps the same identification of anisotropy axes as are obtained for the two constants being of the same sign. The middle case in figure 4.4 (c) with $9/4 < |K_{c2}/K_{c1}| < 9$ describes a situation, where intermediate local maxima appear along the body diagonals of the cubic lattice ⟨111⟩. And for a large second order cubic anisotropy, i.e. $9 < |K_{c2}/K_{c1}|$ like illustrated in figure 4.4 (d), the maxima along the diagonal direction ⟨111⟩ correspond to global maxima, having surpassed the now local maxima along the principal axes ⟨100⟩. Hence, the addition of the cubic anisotropy yields a transition of the ⟨111⟩ directions from minima to maxima of the magnetocrystalline anisotropy energy for $K_{c1} < 0$ and K_{c2} from 0 to $+\infty$. Analogously, for the case of $K_{c1} > 0$ and K_{c2} from 0 to $-\infty$, a transition from maxima to minima is obtained along the ⟨111⟩ directions (not illustrated here, but see the identifications in table 4.1). As a result, incorporating the second order cubic anisotropy term allows for a representation of quite complex anisotropy landscapes, as will be a focus in chapter 6.

[224]: Morrish (2001), *The physical principles of magnetism*
[227]: Stancil et al. (2009), *Spin waves*

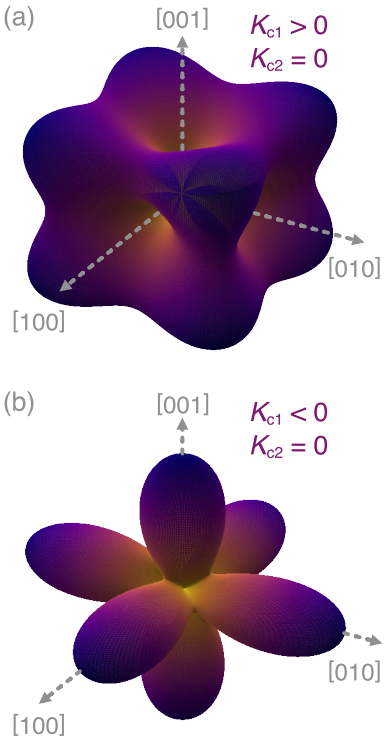

Figure 4.2: Illustration of the first order cubic magnetocrystalline energy as a surface plot for (a) $K_{c1} > 0$ and (b) $K_{c1} < 0$.

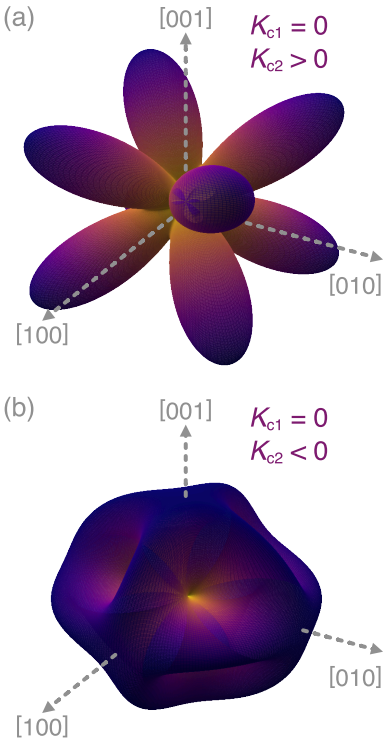

Figure 4.3: Illustration of the second order cubic magnetocrystalline energy as a surface plot for (a) $K_{c2} > 0$ and (b) $K_{c2} < 0$.

	$K_{c1} > 0$			$K_{c1} < 0$		
$\frac{K_{c2}}{\lvert K_{c1}\rvert}$	$+\infty$ to $-\frac{9}{4}$	$-\frac{9}{4}$ to -9	-9 to $-\infty$	$-\infty$ to $\frac{9}{4}$	$\frac{9}{4}$ to 9	9 to $+\infty$
easy	⟨100⟩	⟨100⟩	⟨111⟩	⟨111⟩	⟨110⟩	⟨110⟩
medium	⟨110⟩	⟨111⟩	⟨100⟩	⟨110⟩	⟨111⟩	⟨100⟩
hard	⟨111⟩	⟨110⟩	⟨110⟩	⟨100⟩	⟨100⟩	⟨111⟩

Table 4.1: Effect of the second order cubic anisotropy contribution for different ratios of the first and second order anisotropy constants. Table after [250].

[250]: Cullity et al. (2009), *Introduction to magnetic materials*

[227]: Stancil et al. (2009), *Spin waves*

The cubic anisotropy energy thus favours an alignment of the magnetisations along one of the 6, 8 or 12 easy directions, the number and orientation of which is defined by the ratio of the anisotropy constants K_{c1} and K_{c2} (neglecting higher orders). For deflections of the magnetisation away from the easy axes, the crystalline anisotropy thus exerts a reorienting torque on the magnetisation which, analogous to the shape anisotropy (demagnetisation energy), can be described by an associated internal *anisotropy field* representing the generalised force to the magnetic system. An expression for this field can be easily calculated as the functional derivative [227] of the magnetocrystalline anisotropy energy density in the crystal coordinate system, i.e.

$$\mathbf{H}_{\text{ani,cub}} = -\frac{1}{\mu_0}\frac{\delta \ell_{\text{ani,cubic}}}{\delta \mathbf{M}} \tag{4.19}$$

$$= -\frac{2K_{c1}}{\mu_0 M_S}\sum_i \left(m_i \sum_{j\neq i} m_j^2\right)\hat{\mathbf{e}}_i - \frac{2K_{c2}}{\mu_0 M_S}\sum_i \left(m_i \prod_{j\neq i} m_j^2\right)\hat{\mathbf{e}}_i \tag{4.20}$$

where the m_i, m_j are the projections of the normalised vector field $\mathbf{m}(\mathbf{r})$ defined in equation 4.2 on the crystal symmetry axes $i, j = 1, 2, 3$.

For the description of magnetisation oscillations and spin waves, as will be discussed in the course of this work, a tensor representation analogous to the demagnetisation tensor in equation 4.16 can be convenient to account for the distortion of the oscillation due to the anisotropy field. An approximative form can be derived by expressing the normalised magnetisation $\mathbf{m} = \frac{\mathbf{M}}{M_S}$ as a combination of a static equilibrium component and a small dynamic perturbation, i.e. $\mathbf{m}(\mathbf{r}, t) = \mathbf{m}_0(\mathbf{r}) + \delta\mathbf{m}(\mathbf{r}, t)$. Keeping only terms of the lowest order in the perturbation $\delta\mathbf{m}$, the magnetocrystalline anisotropy field reads then

$$\mathbf{H}_{\text{ani,cub}} = \mathbf{H}^{\text{static}}_{\text{ani,cub}} + \delta\mathbf{h}_{\text{ani,cub}} \tag{4.21}$$

with the static part[13]

$$\mathbf{H}^{\text{static}}_{\text{ani,cub}} = -\frac{2K_{c1}}{\mu_0 M_S}\begin{pmatrix} m_{01}\cdot(1-m_{01}^2) \\ m_{02}\cdot(1-m_{02}^2) \\ m_{03}\cdot(1-m_{03}^2)\end{pmatrix} - \frac{2K_{c2}}{\mu_0 M_S}\begin{pmatrix} m_{01}\cdot m_{02}^2\cdot m_{03}^2 \\ m_{02}\cdot m_{03}^2\cdot m_{01}^2 \\ m_{03}\cdot m_{01}^2\cdot m_{02}^2\end{pmatrix} \tag{4.22}$$

and the dynamic part

$$\delta\mathbf{h}_{\text{ani,cub}} = -\hat{N}^{\text{cub}}_{\text{ani}}\cdot M_S\delta\mathbf{m} = -\left(\hat{N}^{\text{c1}}_{\text{ani}} + \hat{N}^{\text{c2}}_{\text{ani}}\right)\cdot M_S\delta\mathbf{m} \tag{4.23}$$

where

$$\hat{N}^{\text{c1}}_{\text{ani}} = \frac{2K_{c1}}{\mu_0 M_S^2}\begin{bmatrix} 1-m_{01}^2 & 2m_{01}m_{02} & 2m_{01}m_{03} \\ 2m_{01}m_{02} & 1-m_{02}^2 & 2m_{02}m_{03} \\ 2m_{01}m_{03} & 2m_{02}m_{03} & 1-m_{03}^2\end{bmatrix} \tag{4.24}$$

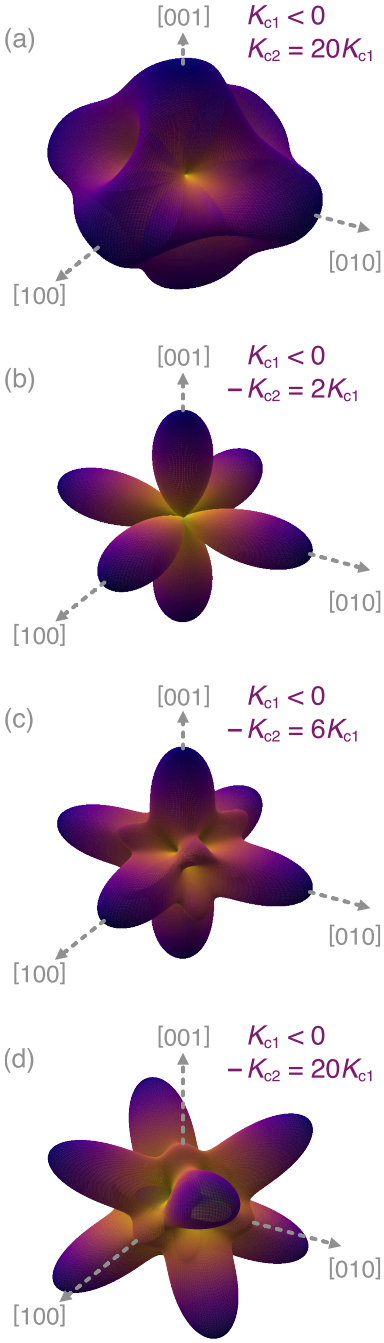

Figure 4.4: Illustration of the cubic magnetocrystalline energy as a surface plot for $K_{c1} < 0$ and various K_{c2} for the different cases distinguished in table 4.1:
(a) $\frac{K_{c2}}{\lvert K_{c1}\rvert} = -20 < \frac{9}{4}$, (b) $\frac{K_{c2}}{\lvert K_{c1}\rvert} = 2 < \frac{9}{4}$,
(c) $\frac{9}{4} < \frac{K_{c2}}{\lvert K_{c1}\rvert} = 6 < 9$, (d) $9 < \frac{K_{c2}}{\lvert K_{c1}\rvert} = 20$.

13: In analogy to the direction cosines m_1, m_2, m_3 introduced for equation 4.18 for the normalised magnetisation $\mathbf{m}(\mathbf{r}, t)$, the m_{01}, m_{02}, m_{03} are used for the direction cosines of the static part of the magnetisation $\mathbf{m}_0(\mathbf{r}) = \mathbf{M}_0(\mathbf{r})/M_S$.

and

$$\hat{N}_{\text{ani}}^{\text{c2}} = \frac{2K_{\text{c2}}}{\mu_0 M_{\text{S}}^2} \begin{bmatrix} m_{02}^2 \cdot m_{03}^2 & 2m_{01}m_{02}m_{03}^2 & 2m_{01}m_{02}^2m_{03} \\ 2m_{01}m_{02}m_{03}^2 & m_{03}^2 \cdot m_{01}^2 & 2m_{01}^2m_{02}m_{03} \\ 2m_{01}m_{02}^2m_{03} & 2m_{01}^2m_{02}m_{03} & m_{01}^2 \cdot m_{02}^2 \end{bmatrix} \tag{4.25}$$

are the first and second order cubic anisotropy tensors in the coordinate system defined by the crystal axes $i = 1, 2, 3$, where a transformation into any other coordinate system can be achieved by the adequate transformation matrices.

Uniaxial anisotropy: Analogous to the cubic anisotropy having three symmetry axes, the uniaxial anisotropy represents the case of a single symmetry axis corresponding to a minimum or maximum in the energy (density). Although this anisotropy is not natural to perfect monocrystalline cubic lattice structures, but rather observed in other lattice types such as hexagonal crystals [227] or in polycrystalline samples, such a uniaxial anisotropy contribution can still arise in cubic monocrystals when the symmetry is broken: In the case of epitaxial samples as studied in this work, origins of such an additional uniaxial anisotropy term include the broken symmetry at surfaces and interfaces, as well as growth induced strain due to a lattice mismatch between adjacent layers in the sample stack [227]. Furthermore, in the case of structured samples, the micro/nano-patterning process steps such as for instance ion milling can yield directional local destructions of the lattice symmetry, which can lead to an additional uniaxial anisotropy contribution, too. It is thus important to note that, depending on the origin of the uniaxial anisotropy term, the symmetry axis of the uniaxial anisotropy contribution does not necessarily coincide with a symmetry axis of the crystal lattice.

[227]: Stancil et al. (2009), *Spin waves*

[224]: Morrish (2001), *The physical principles of magnetism*

[229]: Rezende (2020), *Fundamentals of Magnonics*

The uniaxial anisotropy must also be independent of magnetisation reversal and, the associated energy (density) contribution a function of even powers of the direction cosines $m_{\text{u}} = \cos(\theta_{\text{u}})$ [224], i.e. the projection of the magnetisation onto the symmetry axis with the angle θ_{u} between the two. This yields the common expression of the uniaxial anisotropy energy density

$$\ell_{\text{ani,uni}} = -K_{\text{u1}}m_{\text{u}}^2 - K_{\text{u2}}m_{\text{u}}^4 - \dots \tag{4.26}$$

where again the uniaxial anisotropy constants K_{ui} are given in J/m^3 and defined such that positive K_{ui} correspond to an *easy axis*, i.e. $\theta_{\text{proj}} = 0$ being a minimum in energy density, and negative K_{ui} correspond to a maximum in energy density or *hard axis* respectively [229].

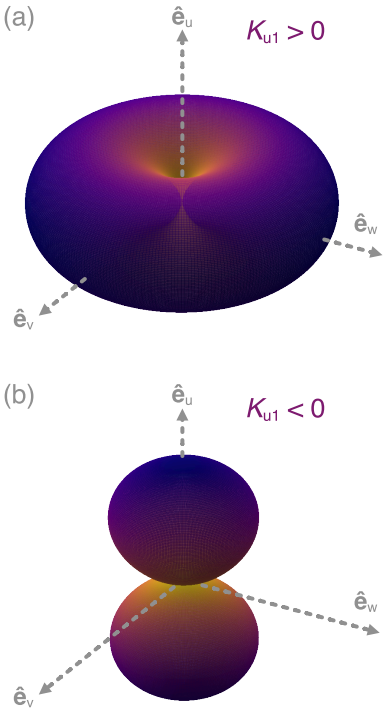

Figure 4.5: Illustration of the first order uniaxial energy as a surface plot for (a) $K_{\text{u1}} > 0$ and (b) $K_{\text{u1}} < 0$, both with the anisotropy axis along $\hat{\mathbf{e}}_{\text{u}}$.

An illustration of the first order uniaxial anisotropy energy density as a surface plot is shown in figure 4.5. If the anisotropy axis coincides with the normal direction on a thin film plane, the case of positive K_{u1} illustrated in figure 4.5 (a) corresponds to the perpendicular magnetic anisotropy case, i.e. where a magnetisation alignment along the film normal (easy axis) is favourable. The case of negative K_{u1} illustrated in figure 4.5 (b) is sometimes called *easy plane* anisotropy, as it favours the alignment of the magnetisation in the film plane.

Contrary to the cubic anisotropy energy density, the simple symmetry of the uniaxial anisotropy density enables an easy expression of a generalised form

$$\begin{aligned} \ell_{\text{ani,uni}} = &-K_{\text{u1}} \cdot \left[\sin(\theta_{\text{M}}) \cdot \sin(\theta_{\text{Ku}}) \cdot \cos(\varphi_{\text{M}} - \varphi_{\text{Ku}}) + \cos(\theta_{\text{M}}) \cdot \cos(\theta_{\text{Ku}}) \right]^2 \\ &- K_{\text{u2}} \cdot \left[\sin(\theta_{\text{M}}) \cdot \sin(\theta_{\text{Ku}}) \cdot \cos(\varphi_{\text{M}} - \varphi_{\text{Ku}}) + \cos(\theta_{\text{M}}) \cdot \cos(\theta_{\text{Ku}}) \right]^4 \\ &- \dots \end{aligned} \tag{4.27}$$

in spherical coordinates with the magnetisation direction (θ_M, φ_M), which allows to include any arbitrarily oriented uniaxial anisotropy contribution with axis $(\theta_{Ku}, \varphi_{Ku})$ into complex problems.

Analogous to above, the associated *uniaxial anisotropy field* can be obtained from the the functional derivative [227]

[227]: Stancil et al. (2009), *Spin waves*

$$\mathbf{H}_{\text{ani,uni}} = -\frac{1}{\mu_0}\frac{\delta f_{\text{ani,uni}}}{\delta \mathbf{M}} = \frac{2K_{u1}}{\mu_0 M_S^2} M_u \hat{\mathbf{e}}_u + \frac{4K_{u2}}{\mu_0 M_S^4} M_u^3 \hat{\mathbf{e}}_u + \dots \tag{4.28}$$

to express the respective force acting on the magnetisation $\mathbf{M}(\mathbf{r})$ upon deflection from the uniaxial anisotropy axis $\hat{\mathbf{e}}_u$.

In analogy to the dipole-exchange length defined for the competition between the dipole-dipole interaction and the exchange interaction, an anisotropy-exchange length is often defined as

$$\lambda_{\text{exch,K}} = \sqrt{\frac{A_{\text{exch}}}{K_{\text{ani}}}} \tag{4.29}$$

which determines the width of Bloch domain walls and serves to quantify the ratio between the governing anisotropy contribution defined by K_{ani} and the exchange interaction by A_{exch}. Although the definition of domain wall widths is irrelevant in this work[14], a consideration of the exchange lengths is of importance notably for the third part of this work: The dipole-exchange length indicates the wavelength range for the transition from exchange-dominated (short wavelengths, large wavevectors) to dipole-dominated (long wavelengths, small wavevectors) spin waves. Additionally, in micromagnetic simulations it is typically necessary to consider the smaller one of these exchange lengths for the discretisation scaling of the simulation (cell size / mesh size), within which the simulation parameters are assumed constant.

14: The main part of this work was performed in external magnetic fields, which are large enough to saturate the ferromagnetic samples into a single domain state.

4.1.3 Magnetic hysteresis

Exposing a ferromagnetic specimen to an external magnetic field $\mathbf{H}_{\text{ext}}(\mathbf{r})$, a torque is exerted on the magnetisation due to the Zeeman energy density

$$f_{\text{Zeeman}}(\mathbf{r}) = -\mu_0 \mathbf{M}(\mathbf{r}) \mathbf{H}_{\text{ext}}(\mathbf{r}) \tag{4.30}$$

giving a minimal contribution when magnetisation $\mathbf{M}(\mathbf{r})$ and external field are aligned.

The reorientation of the ferromagnet's magnetisation subject to the applied magnetic field is then determined by the combination of all energy density contributions in the total energy density

$$f_{\text{tot}}(\mathbf{M}) = f_{\text{Zeeman}}(\mathbf{M}) + f_{\text{ex}}(\mathbf{M}) + f_{\text{demag}}(\mathbf{M}) + f_{\text{ani}}(\mathbf{M}) + \dots \quad , \tag{4.31}$$

[227]: Stancil et al. (2009), *Spin waves*

the combination of which can be considered as an *effective magnetic field* [227]

$$\mathbf{H}_{\text{eff}}(\mathbf{r}, t) = -\frac{1}{\mu_0}\frac{\delta f_{\text{tot}}}{\delta \mathbf{M}} \tag{4.32}$$

exerting a torque $\mathbf{T}(\mathbf{r}, t) = \mathbf{M}(\mathbf{r}, t) \times \mathbf{H}_{\text{eff}}(\mathbf{r}, t)$ on the magnetisation. Assuming a simplified model of a single magnetic domain with its magnetisation representable by a single macrospin, also referred to as the *macrospin approximation*, the magnetisation's equilibrium position is then obtained for a vanishing

torque, i.e. an alignment of the magnetisation along the direction of the effective field, which corresponds to a minimum of the total energy density as first derived by Stoner and Wohlfarth in 1948 [251].

[251]: Stoner et al. (1948), 'A mechanism of magnetic hysteresis in heterogeneous alloys'

As a result, the magnetisation becomes a function of the applied magnetic field, basically dependent on a competition between the magnetic anisotropies in the specimen and the Zeeman term from the external magnetic field resulting in a *magnetic hysteresis* mainly described by four key properties, as schematically illustrated in figure 4.6.

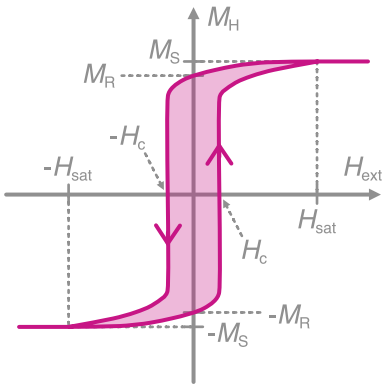

Figure 4.6: Common schematic depiction of a ferromagnetic hysteresis loop, i.e. the trace of the magnetisation projection M_H along the applied field direction as a function of the applied external field strength H_{ext}. The defining key properties are marked as M_S for the saturation magnetisation, M_R for the remanence magnetisation, H_c for the coercive field strength and H_{sat} for the saturation field.

Hysteresis interpretation in the macrospin approximation: When measuring the magnetisation along the applied field direction, the *saturation magnetisation* M_S is obtained at absolute field values above the *saturation field* H_S where the magnetisation is fully aligned with the magnetic field. Reducing the applied field, the anisotropy terms can lead to a rotation of the magnetisation and the projection onto the field axis decreases. The *remanence magnetisation* M_R is the value obtained at zero applied fields and in the macrospin approximation yields $M_R = M_S$. The *coercive field* H_c is the magnetic field that needs to be applied in the opposite direction to obtain a vanishing magnetisation $M(H_c) = 0$ switching to opposite values when increasing the field in that direction and finally resulting in a saturation along the opposite field direction for large enough field values $|H| > H_S$. Hereby, the coercive field depends on the temperature as in the macrospin approximation $H_c = H_S$ for $T = 0$, and $H_c < H_S$ for $T > 0$.

Hysteresis interpretation in the case of domain formation: As stated above, the Stoner-Wohlfarth model does not account for the formation of multiple magnetic domains and their impact on the magnetisation reversal. Yet, the formation of magnetic domains is often non-negligible and essentially originating from the competition of the exchange energy favouring a single domain state aligned with the external field and the anisotropy energies: The demagnetisation energy favours the formation of a multi-domain state or an alignment along the longest axis of the specimen to minimise stray fields, and the magnetocrystalline anisotropy energies favours an alignment along an easy axis defined by the magnetocrystalline anisotropy fields.

The appearance of magnetic domains changes the interpretation of the magnetisation reversal mechanism: In the macrospin (Stoner-Wohlfarth) case, a coherent rotation of the magnetisation is observed and the coercive field therefore solely depends on the anisotropy energies. With the formation of domains however, the interpretation of the coercivity becomes less straightforward [252]: While the nucleation of domains can lead to a faster drop of the net magnetisation, i.e. lower the coercivity, the pinning of domain walls can occur at defects such as grain boundaries, lattice dislocations or chemical impurities, which leads to an enhancement of the coercive field. As a result, the interpretation of the magnetic hysteresis becomes more complex when domains are involved in the reversal process.

[252]: Döring (1948), 'Über die Trägheit der Wände zwischen Weißschen Bezirken'

4.2 Magnetisation oscillations and magnetic damping

The magnetisation dynamics in a ferromagnet are commonly discussed following a phenomenological description initially proposed by Landau and Lifshitz in 1935 [253]. Subsequently, various modifications have been proposed to incorporate a phenomenological term for the dissipation of magnetic energy, i.e. 'losses' or magnetic damping effects. The most suitable approach for the present study is the description proposed by Gilbert in 1955 [254]. Building upon this foundational description, the present section will briefly outline the resulting characteristics of magnetisation dynamics, emphasizing the determination of key parameters of interest.

[253]: Landau et al. (1935), 'On the theory of the dispersion of magnetic permeability in ferromagnetic bodies'

[254]: Gilbert (2004), 'A Phenomenological Theory of Damping in Ferromagnetic Materials'

4.2.1 Equation of motion

The equation of motion of a spatially and temporally varying magnetisation $\mathbf{M}(\mathbf{r}, t)$ subject to a magnetic field $\mathbf{H}_{\text{eff}}(\mathbf{r}, t)$ has first been introduced by Landau and Lifshitz in 1935 [225, 253] in the form of the *Landau-Lifshitz equation*

$$\frac{\partial \mathbf{M}}{\partial t} = -\gamma_{\text{LL}}(\mathbf{M} \times \mu_0 \mathbf{H}_{\text{eff}}) + \frac{\lambda_{\text{LL}}}{M_{\text{S}}^2}(\mathbf{M} \times (\mathbf{M} \times \mu_0 \mathbf{H}_{\text{eff}})) \tag{4.33}$$

where μ_0 is the vacuum permeability and λ_{LL} is the Landau-Lifshitz damping constant. The Landau-Lifshitz gyromagnetic ratio γ_{LL} is defined as

$$\gamma_{\text{LL}} \equiv |\gamma| = \left| \frac{g \mu_{\text{B}}}{\hbar} \right| \tag{4.34}$$

with the Bohr magneton μ_{B}, the reduced Planck constant $\hbar$ and the Landé factor g. Note that the identification of γ_{LL} as equivalent to the electron gyromagnetic ratio γ is not intrinsically defined but only a common convention especially in historically motivated introductions of the magnetisation dynamics. This convention is debatable and will be revised for the convention in this thesis, as will be addressed on the next page.

[225]: Gurevich et al. (1996), *Magnetization oscillations and waves*
[253]: Landau et al. (1935), 'On the theory of the dispersion of magnetic permeability in ferromagnetic bodies'

[254]: Gilbert (2004), 'A Phenomenological Theory of Damping in Ferromagnetic Materials'
[255]: Gilbert (1956), 'Formulation, foundations and applications of the phenomenological theory of ferromagnetism'

[256]: Garanin (1997), 'Fokker-Planck and Landau-Lifshitz-Bloch equations for classical ferromagnets'
[257]: Atxitia et al. (2017), 'Fundamentals and applications of the Landau–Lifshitz–Bloch equation'

A different form of the equation of motion was proposed in 1955 by Gilbert [254, 255] and is nowadays known as the *Landau-Lifshitz-Gilbert equation*

$$\frac{\partial \mathbf{M}}{\partial t} = -\gamma_{\text{LLG}}(\mathbf{M} \times \mu_0 \mathbf{H}_{\text{eff}}) + \frac{\alpha}{M_{\text{S}}}\left(\mathbf{M} \times \frac{\partial \mathbf{M}}{\partial t}\right) \tag{4.35}$$

which can be obtained from eq. 4.33 introducing the Landau-Lifshitz-Gilbert gyromagnetic ratio $\gamma_{\text{LLG}} = \gamma_{\text{LL}} \cdot (1 + \alpha^2)$ and the Gilbert damping constant $\alpha = \frac{\lambda_{\text{LL}}}{\gamma_{\text{LL}} \cdot M_{\text{S}}}$ [225, 254]. Note that both formalisms yield the equilibrium position $\mathbf{M}_0 \parallel \mathbf{H}_{\text{eff}}$ by setting $\frac{\partial \mathbf{M}}{\partial t} = 0$ and ensure the condition

$$\frac{\partial \mathbf{M}^2}{\partial t} = 0 \tag{4.36}$$

i.e. the conservation of the magnitude of $\mathbf{M}$, and are consequently suitable for the consideration of damping processes which conserve the amplitude of the magnetisation.[15]

Neglecting damping ($\alpha = 0$), the two forms are equivalent and describe a precessional motion of the magnetisation around its equilibrium position

15: For the consideration of damping processes which do not conserve the amplitude of the magnetisation vector $\mathbf{M}$, a different damping term similar to the two-relaxation-time formalism of Nuclear magnetic resonance was proposed by Bloch and Bloembergen in the *Bloch-Bloembergen equation* [225]. This formalism is not introduced here, since such processes are irrelevant in this work. However, an incorporation of a Bloch-term can be necessary for instance for the description of magnetisation dynamics in ferromagnets close to the Curie temperature T_{C} [256, 257].

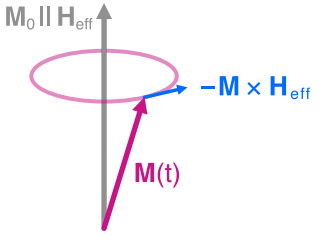

Figure 4.7: Common schematic depiction of the undamped precession of the magnetisation around its equilibrium axis.

$\mathbf{M}_0 \parallel \mathbf{H}_{\text{eff}}$ with the frequency

$$\omega_0 = |\gamma| \mu_0 \mathbf{H}_{\text{eff}} \tag{4.37}$$

induced by the torque $\mathbf{T} = \mathbf{M} \times \mu_0 \mathbf{H}_{\text{eff}}$ as schematically illustrated in figure 4.7. Note that in this case $\gamma_{\text{LLG}} = \gamma_{\text{LL}}$ and the equivalence question to the electron gyromagnetic ratio γ is irrelevant.

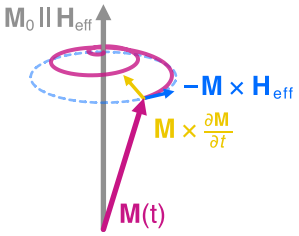

Figure 4.8: Schematic illustration of the damped magnetisation oscillation.

Considering damping ($\alpha \neq 0$), the two approaches differ mainly in the influence on the precession rate: While both forms describe a return to the equilibrium position, the Landau-Lifshitz damping term leaves the precession frequency unchanged, whereas the Gilbert damping term is proportional to the frequency of the precession and therefore also referred to as *viscous damping* [255]. A schematic illustration of the resulting spiralling motion is shown in figure 4.8. For small damping coefficients ($\alpha^2 \ll 1$), the difference between the two formulations is negligible. However, for larger damping coefficients, the resulting behaviours differ significantly: the Landau-Lifshitz model describes the physically implausible behaviour of a nearly instantaneous return to the equilibrium position with an unchanged precession rate, whereas the damping introduced by Gilbert results in a reduced precession rate and an increased relaxation time [258, 259]. **Therefore, the *Landau-Lifshitz-Gilbert equation* (eq. 4.35) will be considered henceforth as the suitable equation of motion for this work.** It is noted that following the same reasoning, i.e. the improved physical plausibility with the Gilbert damping formalism, the gyromagnetic ratio γ_{LLG} can be identified as equivalent to the electron gyromagnetic ratio, i.e.

$$\gamma_{\text{LLG}} \equiv |\gamma| = \left| \frac{g \mu_{\text{B}}}{\hbar} \right| \tag{4.38}$$

instead of equation 4.34, giving rise to the debatability pointed out above. Yet, while acknowledging the fundamental difference concerning the principal question of which parameter is a better representation of the real physical property, it is noted that the correction is only relevant for cases of rather large damping and for the Heusler compounds with $\alpha \approx 10^{-3}$ the resulting change on γ is 0.1 % and therefore rather negligible.

[255]: Gilbert (1956), 'Formulation, foundations and applications of the phenomenological theory of ferromagnetism'

[258]: Mallinson (1987), 'On damped gyromagnetic precession'

[259]: Kikuchi (1956), 'On the Minimum of Magnetization Reversal Time'

4.2.2 Linearisation and magnetic susceptibility

Expressions for the magnetic susceptibility and the ferromagnetic resonance can be derived from the equation of motion by a linearisation approach as described in detail in multiple textbooks, e.g. [224, 225, 227, 260]. To this aim, the torques acting on the magnetisation can be directly expressed using the effective field terms and their relation to the derivatives of the free energy (density) terms as given in equation 4.32 above. The formulation of the LLG with free energy terms as functions of angular coordinates was first proposed by Smit, Beljers and Suhl in 1955 [261, 262] and allows for an easy incorporation of anisotropy effects with the terms introduced in the previous section.

As the amplitude of the magnetisation is conserved by the LLG, the magnetisation oscillation can be pictured as a spiralling motion on a spherical surface, and the formulation in angular coordinates r, θ, φ allows to reduce the problem to two dimensions (as the radial component is conserved, its time derivative is zero)[16].

The magnetisation oscillation can thus equally be expressed as the motion of

[224]: Morrish (2001), *The physical principles of magnetism*

[225]: Gurevich et al. (1996), *Magnetization oscillations and waves*

[227]: Stancil et al. (2009), *Spin waves*

[260]: Kittel (1948), 'On the Theory of Ferromagnetic Resonance Absorption'

[261]: Smit et al. (1955), 'Ferromagnetic resonance absorption in $BaFe_{12}O_{19}$, a highly anisotropic crystal'

[262]: Suhl (1955), 'Ferromagnetic Resonance in Nickel Ferrite Between One and Two Kilomegacycles'

16: The description in angular coordinates is limited, however, as it cannot be used for the case of the sample being magnetised perpendicular to the film plane where it would yield diverging terms. Solutions for this geometry can either be obtained from an analogous derivation in a Cartesian coordinate system, or by continuity of the limit of the functions.

the normalised magnetisation field $\mathbf{m}(\mathbf{r}) = \frac{\mathbf{M}(\mathbf{r})}{M_S}$, with

$$\begin{cases} \dot{\theta} & = -\dfrac{\gamma}{M_S \sin\theta} f_\varphi + \gamma\, \mu_0\, \delta h_\varphi - \alpha\, \dot{\varphi} \sin\theta \\ \dot{\varphi} \sin\theta & = \dfrac{\gamma}{M_S} f_\theta - \gamma\, \mu_0\, \delta h_\theta + \alpha\, \dot{\theta} \end{cases} \tag{4.39}$$

with $\gamma = \gamma_{LLG} \approx \gamma_{LL}$ written for simplicity and $\delta\mathbf{h} = \delta h_r \cdot \hat{\mathbf{e}}_r + \delta h_\theta \cdot \hat{\mathbf{e}}_\theta + \delta h_\varphi \cdot \hat{\mathbf{e}}_\varphi$ introduced as a small magnetic pumping field in addition to the effective field. Such a small pumping field is typically induced by microwave antennas in experimental setups serving to excite the magnetisation dynamics. $f_\theta = \frac{\partial}{\partial\theta} f_{tot}$ and $f_\varphi = \frac{\partial}{\partial\varphi} f_{tot}$ are the partial derivatives of the total energy density f_{tot} and θ, φ determine the alignment of the (normalised) magnetisation $\mathbf{m}$.

The magnetisation (and hence the magnetisation-dependent effective field) can then be separated into a static and a dynamic contribution by introducing the perturbations $\theta(t) = \theta_0 + \delta\theta(t)$ and $\varphi(t) = \varphi_0 + \delta\varphi(t)$, a schematic of the angle definitions is shown in figure 4.9.

The separation in static and dynamic parts leads to the expressions[17]

$$f_\theta = f_\theta(\theta_0, \varphi_0) + f_{\theta\theta}(\theta_0, \varphi_0)\delta\theta(t) + f_{\theta\varphi}(\theta_0, \varphi_0)\delta\varphi(t) \tag{4.43}$$

$$\text{and} \quad f_\varphi = f_\varphi(\theta_0, \varphi_0) + f_{\varphi\theta}(\theta_0, \varphi_0)\delta\theta(t) + f_{\varphi\varphi}(\theta_0, \varphi_0)\delta\varphi(t) \tag{4.44}$$

for the partial derivatives of the total energy density.

Since the equilibrium position is a minimum of f_{tot}, which directly implies $f_\varphi(\theta_0, \varphi_0) = f_\theta(\theta_0, \varphi_0) = 0$, the coupled differential equations transform to

$$\begin{cases} \dot{\delta\theta} = -\dfrac{\gamma}{M_S \sin(\theta_0 + \delta\theta)}[f_{\varphi\theta}\delta\theta + f_{\varphi\varphi}\delta\varphi] + \gamma\mu_0\delta h_\varphi - \alpha\dot{\delta\varphi}\sin(\theta_0 + \delta\theta) \\ \dot{\delta\varphi}\sin(\theta_0 + \delta\theta) = \dfrac{\gamma}{M_S}[f_{\theta\theta}\delta\theta + f_{\theta\varphi}\delta\varphi] - \gamma\mu_0\delta h_\theta + \alpha\dot{\delta\theta} \end{cases} . \tag{4.45}$$

Now the approximation of small perturbations[18] allows to keep only first order terms in the Taylor expansion of equation 4.45 simplifying the coupled differential equations to

$$\begin{cases} \dfrac{1}{\gamma}\left[\dot{\delta\theta} + \alpha\,\dot{\delta\varphi}\right] + \dfrac{1}{\mu_0 M_S}\left[\dfrac{f_{\varphi\theta}}{\sin(\theta_0)}\,\delta\theta + \dfrac{f_{\varphi\varphi}}{\sin^2(\theta_0)}\,\sin(\theta_0)\,\delta\varphi\right] & = \mu_0\delta h_\varphi \\ \dfrac{1}{\gamma}\left[\alpha\,\dot{\delta\theta} - \sin(\theta_0)\,\dot{\delta\varphi}\right] + \dfrac{1}{\mu_0 M_S}\left[f_{\theta\theta}\,\delta\theta + f_{\theta\varphi}\,\delta\varphi\right] & = \mu_0\delta h_\theta \end{cases} \tag{4.46}$$

or in the matrix form

$$\frac{1}{\gamma}\begin{pmatrix} \alpha & -1 \\ 1 & \alpha \end{pmatrix}\begin{pmatrix} \dot{\delta\theta} \\ \sin(\theta_0)\,\dot{\delta\varphi} \end{pmatrix} + \frac{1}{M_S}\begin{pmatrix} f_{\theta\theta} & \frac{f_{\theta\varphi}}{\sin(\theta_0)} \\ \frac{f_{\varphi\theta}}{\sin(\theta_0)} & \frac{f_{\varphi\varphi}}{\sin^2(\theta_0)} \end{pmatrix}\begin{pmatrix} \delta\theta \\ \sin(\theta_0)\delta\varphi \end{pmatrix} = \mu_0\begin{pmatrix} \delta h_\theta \\ \delta h_\varphi \end{pmatrix} . \tag{4.47}$$

Finally, setting the previously introduced small perturbation field to follow the form $\delta\mathbf{h}(t) = \tilde{\mathbf{h}}(\omega)\, e^{i\omega t}$, i.e. representing a periodic oscillation as typically used for the excitation of spin waves, and analogously expressing the dynamic component of the normalised magnetisation $\delta\mathbf{m}(t) = \tilde{\mathbf{m}}(\omega)\, e^{i\omega t}$, allows to write equation 4.47 as $\hat{G}(\omega) \cdot M_S\tilde{\mathbf{m}}(\omega) = \tilde{\mathbf{h}}(\omega)$ with the gyromagnetic tensor $\hat{G}(\omega)$, or more commonly with the inverse relation $M_S\tilde{\mathbf{m}}(\omega) = \hat{\chi}(\omega) \cdot \tilde{\mathbf{h}}(\omega)$

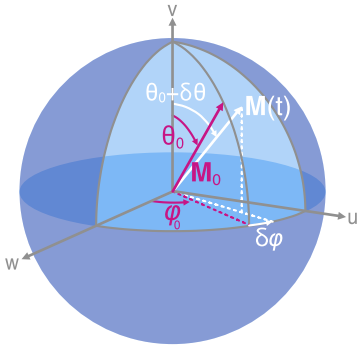

Figure 4.9: Definition of the spherical coordinates used for the linearisation of the LLG. The radius of the sphere is given by M_S. $\mathbf{M}_0$ is the equilibrium position of the magnetisation, which corresponds to a minimum in f_{tot} and therefore coincides with the direction of the static effective field $\mathbf{H}_0$. Here, the global coordinates uvw are chosen such that $\hat{\mathbf{e}}_v$ is normal to the film plane. This definition of coordinates will used again in section 8.1.1.

17: Analogous to the previous introduction of f_θ and f_φ as the partial derivatives of the total energy density, the abbreviations

$$f_{\theta\varphi} = \frac{\partial}{\partial\varphi}\frac{\partial}{\partial\theta} f_{tot} = \frac{\partial}{\partial\theta}\frac{\partial}{\partial\varphi} f_{tot} = f_{\varphi\theta} \tag{4.40}$$

$$f_{\theta\theta} = \frac{\partial^2}{\partial\theta^2} f_{tot} \tag{4.41}$$

$$f_{\varphi\varphi} = \frac{\partial^2}{\partial\varphi^2} f_{tot} \tag{4.42}$$

are introduced for the second derivatives.

18: $\sin(\delta\theta) \approx \delta\theta$ and $\cos(\delta\theta) \approx 1$

defining the dynamic susceptibility as

$$\hat{\chi}(\omega) = \frac{\gamma^2 M_S \mu_0}{(1+\alpha^2)[\omega_0^2 - \omega^2 + i\omega\Delta\omega]} \cdot \begin{bmatrix} \frac{\ell_{\varphi\varphi}}{M_S \sin^2(\theta_0)} + \frac{i\omega\alpha}{\gamma} & -\frac{\ell_{\theta\varphi}}{M_S \sin(\theta_0)} + \frac{i\omega}{\gamma} \\ -\frac{\ell_{\varphi\theta}}{M_S \sin(\theta_0)} - \frac{i\omega}{\gamma} & \frac{\ell_{\theta\theta}}{M_S} + \frac{i\omega\alpha}{\gamma} \end{bmatrix} \tag{4.48}$$

where ω_0 and $\Delta\omega$ are introduced as

$$\omega_0^2 = \frac{\gamma^2}{(1+\alpha^2)M_S^2 \sin^2(\theta_0)} \left(\ell_{\theta\theta}\ell_{\varphi\varphi} - \ell_{\varphi\theta}\ell_{\theta\varphi}\right) \tag{4.49}$$

and

$$\Delta\omega = \frac{\alpha\gamma}{M_S}\left(\ell_{\theta\theta} - \frac{\ell_{\varphi\varphi}}{\sin^2(\theta_0)}\right) \tag{4.50}$$

representing the resonance frequency and linewidth respectively. The high symmetry solutions, i.e. with the external field applied in the film plane or perpendicular to the film plane, are typically of special interest and will be discussed in the following subsection.

4.2.3 Ferromagnetic resonance

The resonance at the frequency given by equation 4.49 is commonly named *ferromagnetic resonance* and its frequency and linewidth are typically studied as a function of the external field (entering via the Zeeman energy term into ℓ_{tot}) to assess the defining parameters γ and α, as well as potential anisotropy contributions. To this aim, the field is usually applied along a symmetry direction, that is in the film plane or perpendicular to the film plane, since the resonance condition then simplifies.

For the field applied perpendicular to the film plane, the **out-of-plane FMR case**, the resonance condition reduces to a linear form[19]

$$\omega_{oop} = \omega_H + \omega_{exch} + \omega_{ani} - \omega_M \tag{4.51}$$

where the gyrotropic frequencies correspond to the respective field terms as commonly introduced in literature[20].

For the field applied in the film plane, the **in-plane FMR case**, the solution can be usually[21] factorised into field contributions perpendicular and parallel to the film plane, which yields

$$\omega_{ip} = \sqrt{\left(\omega_H + \omega_{exch} + \omega_{ani}^{\parallel}\right)\left(\omega_H + \omega_{exch} + \omega_{ani}^{\perp} + \omega_M\right)} \tag{4.56}$$

was first described by Kittel [260] and is therefore often referred to as *Kittel equation* or *Kittel formula*. The expression for the anisotropy fields $H_{ani}^{\parallel}$ and $H_{ani}^{\perp}$ depend on the anisotropies in the system, and including the first and second order cubic anisotropy terms for a (cubic) crystal with the [001] direction

19: Only if the anisotropy field does not induce an elliptical precession for this field orientation (which is not the case for the geometry chosen in this work).

20: Precisely,

$$\omega_H = \gamma\mu_0 H_{ext} \tag{4.52}$$
$$\omega_M = \gamma\mu_0 M_S \tag{4.53}$$
$$\omega_{ani} = \gamma\mu_0 H_{ani} \tag{4.54}$$
$$\omega_{exch} = \gamma\mu_0 H_{exch} \tag{4.55}$$

where the expression for H_{ani} depends on the anisotropy terms in play (excluding the shape anisotropy, which is separately accounted for by ω_M linked to the demagnetisation energy) and the exchange field $H_{exch} = \frac{2A_{ex}}{\mu_0 M_S} \cdot k_n^2$ with the quantised wave vector $k_n = \frac{n \cdot \pi}{d}$ describes the formation of standing thickness modes due to the finite film thickness.

21: For cubic anisotropies, this is only true for selected crystal orientations, see details in appendix chapters C and D.

[260]: Kittel (1948), 'On the Theory of Ferromagnetic Resonance Absorption'

coinciding with the film normal, the anisotropy fields yield

$$H_{\text{ani}}^{\parallel} = \frac{2K_{\text{c1}}}{\mu_0 M_{\text{S}}} \cdot \left(1 - 6 \cdot \sin^2\left(\varphi_{100}\right)\cos^2\left(\varphi_{100}\right)\right) \tag{4.57}$$

$$H_{\text{ani}}^{\perp} = \frac{2K_{\text{c1}}}{\mu_0 M_{\text{S}}} + \frac{2K_{\text{c2}}}{\mu_0 M_{\text{S}}} \cdot \sin^2\left(\varphi_{100}\right)\cos^2\left(\varphi_{100}\right) \tag{4.58}$$

as derived in the appendix D, where K_{c1} and K_{c2} are the first and second order cubic anisotropy constants and φ_{100} is the in-plane angle to the [100] axis.

Depth profiles arising from a confinement along the same axis are commonly referred to as **perpendicular standing spin waves** (PSSWs)[22] [263]. In thin films, this is due to the finite film thickness d and consequently a wave vector $k_n = \frac{n \cdot \pi}{d}$ can be attributed to the mode with number n, defining the corresponding exchange field $H_{\text{exch}} = \frac{2A_{\text{exch}}}{\mu_0 M_{\text{S}}} \cdot k_n^2$ with the exchange constant A_{exch}. Hence, the spatially uniform FMR corresponds to the PSSW with mode number $n = 0$ in either geometry, and consequently the analysis of this fundamental mode with $n = 0$ as well as a higher order PSSW mode $n > 0$ allows to quantify the exchange constant[23] A_{exch}.

22: Sometimes also named SSWMs for *standing spin wave modes*.

[263]: Maksymov et al. (2015), 'Broadband stripline ferromagnetic resonance spectroscopy of ferromagnetic films, multilayers and nanostructures'

23: See equation 4.10 for a relation to other expressions of the exchange strength.

4.2.4 Resonance linewidths in the LLG formalism and beyond

The resonance linewidths $\Delta\omega$ are typically investigated for a quantification of the damping terms in the system, where for the out-of-plane case a linear function of the resonance frequency is obtained[24] with

$$\Delta\omega_{\text{oop}} = 2\alpha\omega_{\text{oop}} \tag{4.59}$$

while for the in-plane case the elliptical precession yields[25]

$$\Delta\omega_{\text{ip}} = \alpha \cdot (2\omega_{\text{H}} + \omega_{\text{M}}) \tag{4.60}$$

both defined by the Gilbert damping parameter α accounting for the viscous energy dissipation in the system. Note that the term *Gilbert linewidth* will be used hereafter to refer to the definitions as in equations 4.59 and 4.60.

24: Here: expression for the FWHM.

25: Again: expression for the FWHM. Also, the expression is given for the simplified case of negligible anisotropies.

Gilbert linewidth and contributions beyond the LLG formalism

It is crucial to acknowledge that these expressions of the resonance linewidths are limited to two major assumptions: Firstly, by definition the LLG approach only considers pure Gilbert-like (viscous) damping processes, hence the above specified naming as the *Gilbert linewidth*. Secondly, while the LLG can principally account for a spatial variation in the magnetisation orientation, as is for instance fundamental to its use in micromagnetic modelling, it is not adequate for a change in the absolute magnetisation value. Hence, the derivation of the resonance linewidth expressions does a priori not account for magnetisation inhomogeneities, and neither accounts for inhomogeneities in the effective field terms[26]. No great theoretical derivation is needed to motivate that these factors lead to changes in the resonance linewidth.

Nevertheless, the Landau-Lifshitz-Gilbert formalism is a commonly employed approach even for systems where such contributions play a role: As long as the Gilbert damping is the major contribution, the formalism is often still preferential and "simply" altered by "minor" adaptations, the most common of which is certainly the *ad hoc* introduction of an inhomogeneous linewidth contribution.

26: Note that the two are strongly interlinked: For instance local defects can be considered as a local reduction of the magnetic moment, but can also be accounted for by a field inhomogeneity.

Importantly, **once such adjustments are introduced, the modelling exceeds the Landau-Lifshitz-Gilbert formalism** in the strict sense.

Particularly the addition of an *inhomogeneous linewidth* is often simply introduced due to the observation of an offset in the linewidths from FMR experiments and typically not further motivated. Yet, the ad hoc introduction of a linewidth offset is not trivial and specifically opens the choice of an adjustment in the form of $\Delta\omega_0$ or in the form of ΔH_0, i.e. a constant frequency or a constant field offset. While this naturally raises the question about the physical interpretation of this adjustment and the extracted values, the point is rather difficult to address[27] and preferably neglected for various reasons:

- First, the question on the correct formulation of the adaptation is non-trivial as it technically requires an identification of the underlying dissipation mechanism in order to allow for a suitable expression and physical interpretation. Yet, particularly for the non-Gilbert like dissipation mechanisms, the scaling of the respective damping with the field/frequency can be non-trivial and unique to the process at hand[28].
- Second, it needs to be noted again that the Gilbert linewidth itself is a solution of the linearisation of the LLG. Hence, even the most intuitive reason for an expression of ΔH_0, i.e. to account for inhomogeneities in the effective field, would technically require an incorporation as an uncertainty in the effective field right from the start in the above formalism, which translates to an uncertainty in the associated energy term and accordingly would result in a frequency linewidth contribution through equation 4.50 to $\Delta\omega$ in above equations 4.59 and 4.60.
- A third, certainly historically grown reason for the rarely specified motivation especially for the use of ΔH_0 is the established counter-intuitive[29] probing of the FMR resonance curves by sweeping the applied field rather than the applied frequency[30]. Naturally, the straightforward analysis of the resulting spectra results in the extraction of field linewidths ΔH instead of the frequency linewidths defined above, and the addition of a ΔH_0 seems a rather intuitive choice (intuitive with reference to the measurement procedure, not necessarily the underlying physical phenomena).

Given the complexity of the problem, a conclusion on the preference of one approach over the other is not attempted to be drawn here. Still, it is important to note that the general transformation between the two linewidth formulations is linked to the scaling of the resonance frequency with the applied field, i.e. [264]

$$\Delta H_{\mathrm{res}} = \Delta\omega_{\mathrm{res}} \cdot \left(\frac{\partial\omega_{\mathrm{res}}}{\partial H_{\mathrm{ext}}}\right)^{-1} \tag{4.61}$$

and hence the two formulations, i.e. $\Delta\omega_0$ or ΔH_0, can lead to different signatures in the field/frequency dependence. Note that especially for the case of Co_2MnSi with a large saturation magnetisation M_S and a rather small resonance linewidth, the impact of this nonlinear transformation factor $\frac{\partial\omega_{\mathrm{res}}}{\partial H_{\mathrm{ext}}}$ can persist over a rather large field/frequency range. Therefore, this issue will be addressed in the subsequent chapter 5 particularly concerning the implications within the data analysis approach chosen in this work, and subsequently referred to in chapter 6 where the FMR linewidths from a Co_2MnSi film will be analysed.

27: Statement by no means meant as a criticism on other studies, but simply highlighting the non-triviality of the underlying problematic.

28: One complex example is for instance the multi-magnon scattering introduced in the next subsection. The frequency/field dependence here principally depends on the available scattering partners, i.e. suitable modes / available states in the dispersion relation. Yet, finding the frequency/-field dependence of the damping term is a rather complex task as these processes are nonlinear and an analytical formulation of the dispersion is impossible, see chapter 8 in the third part of this work.

29: From the theoretical description point of view: Clearly, in the entire linearisation section above, the magnetic field is expected to be fixed as it defines the energy of the system, from which the resonance condition is derived.

30: More specifications will be given in the methods chapter. – Note that this is mainly related to the technical development: Most research and development on the measurement of the FMR and its resonance linewidth have taken place prior to the development e.g. of suitable vector network analysers (VNA) allowing for precise frequency sweep measurements. Instead, often microwave cavities were used to fix the frequency and (loaded with the sample) were placed in an external magnetic field to sweep over the resonance condition of the magnetic sample under investigation.

[264]: Kuanr et al. (2005), 'Narrowing of the frequency-linewidth in structured magnetic strips'

4.2.5 Magnetic damping mechanisms

Energy dissipation implies a damping of the magnetisation oscillation and therefore leads to the magnetisation reaching its equilibrium position in a finite amount of time. Various dissipation channels exist and are generally sample specific, depending not only on the magnetic material itself, but also arising from the surrounding stack or experimental setup specifications for instance.

In literature, damping processes are often categorised as *intrinsic* or *extrinsic* contributions although typically lacking precise definition about the exact distinction between the two [265]. Such a classification is generally avoided in this work. Precisely, no separation of different damping contributions is made in the experimental analysis of this work, and the various processes are only separated at this point in order to briefly introduce the different origins of magnetic damping.

[265]: Heinrich (2005), '5. Spin Relaxation in Magnetic Metallic Layers and Multilayers'

The above considered phenomenological damping term in the Landau-Lifshitz-Gilbert equation of motion following the Gilbert formalism [254] only accounts for *viscous damping* processes, which is a valid simplification for the typical significant damping contributions such as Eddy currents and direct scattering with electrons in metallic samples, as well as direct scattering with lattice modes to a first approximation. Especially in metals, *Gilbert-like*[31] dissipation processes typically govern the total magnetic losses, validating the use of this description. Yet, *non-Gilbert-like* damping processes can occur as well and are often expressed in experimental analyses in terms of a constant *inhomogeneous linewidth* as they usually only lead to important contributions at low frequencies, where the linewidth broadening arising from Gilbert-like losses is vanishing. Some non-Gilbert-like processes relevant to this work will be briefly introduced in the last subsection.

[254]: Gilbert (2004), 'A Phenomenological Theory of Damping in Ferromagnetic Materials'

31: *Gilbert-like* and *viscous* are used as synonyms in this work, signifying a 'friction-like' damping proportional to the microwave frequency ω and allowing for the description by a parameter α as introduced in the LLG equation 4.35.

Electron scattering

The incoherent scattering of electron-hole pair excitations by phonons and magnons is the main dissipation channel in conductive ferromagnets [265]. These can be classified into *intraband transitions*, i.e. scattering events within a single band where the spin remains unchanged, and *interband transitions*, where scattering events involve a transition between different electronic bands and a spin flip. The damping linked to intraband transitions (no spin flip) can be understood as a delay (phase lag) originating from the electrons repopulating the *breathing Fermi surface*[32]. The damping involving interband transitions (spin flip) originates from the s-d exchange interaction and can be understood as a phase lag between the precessing magnetic moments of localised and itinerant electrons mediated via an (instantaneous, local) effective field term accounting for the exchange coupling [265].

[265]: Heinrich (2005), '5. Spin Relaxation in Magnetic Metallic Layers and Multilayers'

32: The *breathing Fermi surface* model describes the change of the Fermi surface with the magnetisation direction: As the magnetisation oscillates, it induces a periodical distortion of the Fermi surface and thus requires the electrons to repopulate the changing states, which results in a phase lag with respect to the oscillating magnetisation.

[265]: Heinrich (2005), '5. Spin Relaxation in Magnetic Metallic Layers and Multilayers'

Both scattering mechanisms result in a phase lag proportional to the microwave frequency, i.e. a viscous damping which can be accounted for by an effective Gilbert damping parameter [146]

$$\alpha^{\text{elec}} \sim \left\langle \sum_{m,n} \left| \Gamma^{-}_{m\mathbf{k},n\mathbf{k}} \right|^2 W_{m\mathbf{k},n\mathbf{k}} \right\rangle_{\mathbf{k}} \tag{4.62}$$

where $\mathbf{k}$ is the electron wave vector, n and m are the indices of the electronic bands involved in the transition, $\Gamma^{-}_{m\mathbf{k},n\mathbf{k}}$ are the transition matrix elements and the function $W_{m\mathbf{k},n\mathbf{k}}$ describes the spectral overlap[33] of the electronic

[146]: Liu et al. (2009), 'Origin of low Gilbert damping in half metals'

33: Precisely,

$$W_{m\mathbf{k},n\mathbf{k}}(\mathbf{k}) = \frac{1}{\pi} \int \eta(E) \langle D(E_{m\mathbf{k}}) \rangle \times \langle D(E_{n\mathbf{k}}) \rangle dE \tag{4.63}$$

with $\eta(E)$ being the negative derivative of the Fermi function around the Fermi level and $\langle D(E_{m\mathbf{k}}) \rangle = \frac{1}{\pi} \frac{\delta}{(E-E_{m\mathbf{k}})^2+\delta^2}$ the averaged DOS where the width $\delta = \frac{\hbar}{2\tau}$ depends on the orbital lifetime τ accounting for electron-lattice scattering processes [146].

bands in the density of states. For intraband transitions ($n = m$), the damping coefficient becomes directly proportional to the electron scattering time, which is often described as a *conductivity-like damping*, whereas interband transitions ($n \neq m$) result in an inverse proportionality of damping coefficient and electron scattering, hence named *resistivity-like damping* [266–268].

[266]: Kamberský (1970), 'On the Landau–Lifshitz relaxation in ferromagnetic metals'
[267]: Cochran et al. (1980), 'Microwave transmission through ferromagnetic metals'
[268]: Khodadadi et al. (2020), 'Conductivitylike Gilbert Damping due to Intraband Scattering in Epitaxial Iron'

Half-metals, like Co_2MnSi, present reduced Gilbert damping parameters compared to normal metals [64] associated with the high spin polarisation resulting from the band gap for minority spins at the Fermi level. In a simplified picture in the limit of no spin-orbit interaction, this can be understood as a suppression of spin-flip scattering therefore resulting in a reduced damping parameter compared to typical transition metals. However, the presence of spin-orbit coupling leads to a mixing of majority and minority components of the itinerant electron states and hence a non-negligible contribution from processes involving the minority carriers (even if reduced compared to the typical transition metals with lower spin polarisation). A thorough modelling of the resulting damping parameter therefore requires the application of perturbation theory as done for instance in reference [146].

[64]: Guillemard et al. (2019), 'Ultralow Magnetic Damping in Co_2Mn-Based Heusler Compounds'

[146]: Liu et al. (2009), 'Origin of low Gilbert damping in half metals'

Eddy currents (Foucault's currents)

In metallic samples, the precessing magnetic moments induce electrical currents according to Faraday's induction law, which in return reinduce an alternating magnetic field again acting on the magnetisation. The resulting torque is out of phase with respect to the magnetisation oscillation and therefore resulting in a dephasing of the magnetisation dynamics and thus leading to a linewidth broadening (damping contribution) which can be calculated by solving Maxwell's equations in the sample [269]. In the case of thin films this yields[34] an effective Gilbert damping parameter

$$\alpha^{\text{Eddy}} \sim \sigma d^2 \tag{4.64}$$

which is proportional to the electrical conductivity σ and the squared sample thickness d and becomes negligible in the ultrathin film limit [270]. In the thick film limit[35], the dynamic magnetisation becomes inhomogeneous over the thickness and the FMR linewidth broadening originates from the resulting radiofrequency variation of the exchange fields, hence is proportional to

$$\alpha^{\text{Eddy}} \sim \sqrt{\sigma A_{\text{exch}}} \tag{4.65}$$

where A_{exch} is the previously introduced exchange constant of the material, see equation 4.10. This mechanism is also referred to as the *exchange-conductivity mechanism* [265] and can be of increased significance in (thick film) samples with an additional surface anisotropy leading to a surface pinning and hence enhancing the spatial variation of the magnetisation.

[269]: Heinrich et al. (2002), 'Magnetic relaxation in metallic films'

34: By integrating Maxwell's equations across the film thickness as long as a full penetration of the microwave field is ensured.

[270]: Lock (1966), 'Eddy current damping in thin metallic ferromagnetic films'

35: For film thicknesses larger than the skin depth.

[265]: Heinrich (2005), '5. Spin Relaxation in Magnetic Metallic Layers and Multilayers'

Radiative damping

In ferromagnetic resonance (FMR) experiments, the inductive coupling between the magnetisation precession in the sample and the conductive microwave antenna leads to an additional damping term referred to as *radiation damping* or *radiative damping* [271–273]. The underlying principle is analogous to the Eddy current mechanism[36]: the alternating magnetic flux due to the precessing magnetisation induces a microwave current in the adjacent conducting antenna which can then propagate away from the sample.

[271]: Sanders et al. (1974), 'Radiation damping in magnetic resonance. II. Continuous-wave antiferromagnetic-resonance experiments'
[272]: Wende (1976), 'Radiation damping in FMR measurements in a nonresonant rectangular waveguide'
[273]: Schoen et al. (2015), 'Radiative damping in waveguide-based ferromagnetic resonance measured via analysis of perpendicular standing spin waves in sputtered permalloy films'

36: Radiative damping and Eddy current damping effectively differ in the localisation of the induced currents: *radiative damping* refers to the generation of eddy currents in the microwave antenna, whereas *Eddy current damping* is used to refer to the induction of Eddy currents in the ferromagnet itself. While the latter requires the ferromagnet to be conductive and scales with the conductivity, radiative damping is independent of the magnetic material's conductivity and can occur equally in the case of ferromagnetic insulators such as YIG.

The radiative damping contribution is determined by the strength of the coupling between the magnetisation oscillation in the sample and the conductive waveguide. A resulting effective Gilbert damping contribution for radiative damping can be derived by calculating the induced power dissipation and yields

$$\alpha^{\mathrm{rad}} \sim \frac{\eta\gamma M_{\mathrm{S}} d l}{Z_0 w} \tag{4.66}$$

for the case of uniform driving fields and infinitesimal spacing between the sample and the waveguide [273], where α^{rad} depends on the microwave antenna (impedance Z_0 and antenna waveguide width w), the sample geometry (magnetic layer thickness d, sample length l along the antenna waveguide axis) and the magnetic precessional properties (gyromagnetic ratio γ, saturation magnetisation M_{S} and a mode profile parameter η). As the inductive coupling between sample and waveguide decreases with increasing spacing, the radiative damping contribution can be suppressed in experiments by adding insulating spacer layers in between.

[273]: Schoen et al. (2015), 'Radiative damping in waveguide-based ferromagnetic resonance measured via analysis of perpendicular standing spin waves in sputtered permalloy films'

Magnon-phonon coupling

The damping contribution arising from magnon-phonon coupling in metallic samples is usually negligible [209] compared to typical contributions from magnon-electron scattering and Eddy (Foucault) currents, and can only become of significance in the condition of *ferromagnetoelastic resonance* (FMER) [274] where the elastic wave forms a resonant mode along the structural constraint (film thickness in the case of thin films) matching the FMR frequencies. In the limit of small geometries with homogeneous magnetisation and lattice strain, the damping contribution arising from direct magnon-phonon coupling is in first order Gilbert-like with

$$\alpha^{\mathrm{mag-phon}} \sim \eta\gamma \cdot \left(\frac{B_2 \cdot (1+\nu)}{E}\right)^2 \tag{4.67}$$

as derived by Suhl [275], where η is the phonon viscosity, E is Young's modulus[37], ν is the Poisson ratio[38] and B_2 is the magneto-elastic shear constant [265]. Although usually negligible in metallic samples particularly when not matching the FMER, direct magnon-phonon coupling results in significant contributions to the damping in insulating materials such as Yttrium Iron Garnet (YIG) [276, 277], where it is recently increasingly exploited for applications [278].

[209]: Heinrich et al. (2004), 'Magnetic properties of NiMnSb(001) films grown on InGaAs/InP(001)'

[274]: Kobayashi et al. (1973), 'Ferromagnetoelastic Resonance in Thin Films. I. Formal Treatment'

[275]: Suhl (1998), 'Theory of the magnetic damping constant'

37: The Young's modulus is a measure for the longitudinal deformation of a solid subject to a mechanical force.

38: The Poisson ratio quantifies the (transversal) deformation of the material perpendicular to the stressing force.

[265]: Heinrich (2005), '5. Spin Relaxation in Magnetic Metallic Layers and Multilayers'

[276]: Man et al. (2017), 'Direct observation of magnon-phonon coupling in yttrium iron garnet'

[277]: Streib et al. (2019), 'Magnon-phonon interactions in magnetic insulators'

[278]: Bozhko et al. (2020), 'Magnon-phonon interactions in magnon spintronics (Review article)'

Spin pumping

Spin pumping can occur in multilayer stacks where the ferromagnetic layer is adjacent to a non-magnetic metallic layer. The coherent magnetisation oscillation at the interface of the ferromagnet creates a spin current which is injected into the adjacent non-magnetic metal, where it can lead to spin accumulation [279]. The injected spin current $\mathbf{J}_{\mathrm{S}}^{\mathrm{pump}}(\mathbf{m}) = \frac{\hbar}{4\pi}\left(A_{\mathrm{r}}\mathbf{m}\times\frac{d\mathbf{m}}{dt} - A_{\mathrm{i}}\frac{d\mathbf{m}}{dt}\right)$ [280] consists of a *damping-like* and a *field-like* term respectively[39] weighted by the complex factor[40] $A = A_{\mathrm{r}} + iA_{\mathrm{i}}$. For usual interfaces it is in first approximation real as $A_{\mathrm{i}} \ll A_{\mathrm{r}}$ [281] and thus the resulting losses are Gilbert-like and can be described by the parameter

$$\alpha^{\mathrm{spin-pump}} = \frac{\gamma\hbar}{4\pi M_{\mathrm{S}} V} A_{\mathrm{eff}} \tag{4.68}$$

[279]: Weiler et al. (2013), 'Spin Pumping and Spin Currents in Magnetic Insulators'

[280]: Tserkovnyak et al. (2002), 'Enhanced Gilbert Damping in Thin Ferromagnetic Films'

39: The terms *damping-like* and *field-like* are commonly used in referral to the analogy with the respective torques in the LLG.

40: The factor A mainly depends on the spin mixing conductance (sometimes also spin-pumping conductance), which is an interfacial parameter to quantify "the transparency of the interface to the flow of spin current" [229] from the ferromagnetic layer into the non-magnetic metal.

[281]: Tserkovnyak et al. (2002), 'Spin pumping and magnetization dynamics in metallic multilayers'

for a ferromagnetic body of volume V [282] where the effective parameter $A_{\text{eff}} = C \cdot A_{\text{r}}$ accounts for the reduction of the spin-mixing conductance by a factor C due to back-flowing spin currents arising from the spin accumulation in the non-magnetic metal. Although at this point only briefly introduced for the effective damping contribution, spin pumping is an essential mechanism in spintronics and commonly exploited for the generation of spin currents.

Non-Gilbert-like damping mechanisms

Although viscous Gilbert-like damping processes usually govern the magnetic losses in most (metallic) ferromagnets [265], additional non-Gilbert contributions can arise particularly in the presence of inhomogeneities or defects. These processes play a particular role at low precessional frequencies, where the viscous damping contribution to the linewidth broadening is not significant.

Two-magnon scattering is the scattering of the uniform magnetisation precession (FMR) into non-uniform short wavelength dipolar spin wave modes (with non-zero wave vector $\mathbf{k}$[41]) which are degenerate with the FMR [283]. This damping process is mediated by scattering at defects or inhomogeneities and can lead to the observation of anisotropic damping in the case of a non-uniform repartition of defects, e.g. a network of lattice misfit dislocations [209, 284]. Due to the related loss of translational invariance at the scattering centre, two magnon scattering does not obey momentum conservation [265]. The energy however is conserved and the processes therefore do not involve a direct irreversible loss of magnetic energy into the lattice[42], but basically only a mode conversion which primarily leads to a dephasing of the precessing magnetisation components resulting in a linewidth broadening. One characteristic of the two magnon scattering contribution to the linewidth in thin films is the inverse proportionality to the film thickness, arising from the interface contribution to the inhomogeneity in the system typically yielding the most significant number of scattering centres [265]. Secondly, the contribution cancels for a field applied perpendicular to the film plane [283, 285]. Moreover, the two magnon scattering contribution to the linewidth does not scale linearly with the microwave frequency ω, but presents a significant non-linear increase at low frequencies and saturates for high frequencies [286, 287].

Multi-magnon scattering happens notably at high excitation powers where the linearisation of the LLG is no valid approximation anymore. These nonlinear processes can lead to an energy transfer from the directly excited mode into secondary spin wave modes under conservation of energy and momentum (unlike the defect-bound two-magnon scattering), and thus a redistribution of the energy within the magnetic system which in result can be perceived as an effective damping channel of the directly excited mode [288–291]. These processes are not of relevance in the present part of the work, and will be introduced in chapter 8.

[282]: Tserkovnyak et al. (2005), 'Nonlocal magnetization dynamics in ferromagnetic heterostructures'

[265]: Heinrich (2005), '5. Spin Relaxation in Magnetic Metallic Layers and Multilayers'

41: Spin waves and their quanta, magnons, have not been formally introduced at this point. A detailed knowledge of non-zero wavenumber spin waves is not necessary for the introduction of two-magnon scattering. Here, it is only necessary to note that various spin waves modes exist which generally have non-linear disperion relations that naturally depend on the magnetic field (and other parameters). The ferromagnetic resonance can be understood as a spin wave with $\mathbf{k} = 0$. Given the complex dispersion relation, it can be possible to find modes that are degenerate with the FMR, therefore allowing for the two-magnon scattering process. For further details, see chapter 8 in the third part of this thesis, which focuses on the work towards magnonic applications.

[283]: Arias et al. (1999), 'Extrinsic contributions to the ferromagnetic resonance response of ultrathin films'

[209]: Heinrich et al. (2004), 'Magnetic properties of NiMnSb(001) films grown on InGaAs/InP(001)'

[284]: Woltersdorf et al. (2004), 'Two-magnon scattering in a self-assembled nanoscale network of misfit dislocations'

[265]: Heinrich (2005), '5. Spin Relaxation in Magnetic Metallic Layers and Multilayers'

42: Yet, as these modes equally scatter with itinerant electrons or lattice excitations, the energy can ultimately dissipate from the magnetic system into the lattice leading to a relaxation of the magnetic excitation.

[265]: Heinrich (2005), '5. Spin Relaxation in Magnetic Metallic Layers and Multilayers'

[283]: Arias et al. (1999), 'Extrinsic contributions to the ferromagnetic resonance response of ultrathin films'

[285]: McMichael et al. (1998), 'Ferromagnetic resonance linewidth in thin films coupled to NiO'

[286]: Lenz et al. (2006), 'Two-magnon scattering and viscous Gilbert damping in ultrathin ferromagnets'

[287]: Lindner et al. (2004), ''Non-Gilbert-type' damping of magnetic excitations in ultrathin ferromagnets'

[288]: Suhl (1957), 'The theory of ferromagnetic resonance at high signal powers'

[289]: Schlömann (1959), 'Fine Structure in the Decline of the Ferromagnetic Resonance Absorption with Increasing Power Level'

[290]: Schlömann et al. (1960), 'Recent Developments in Ferromagnetic Resonance at High Power Levels'

[291]: Dobin et al. (2004), 'Intrinsic nonlinear ferromagnetic relaxation (invited)'

4.3 Magneto-optical interactions

The discovery of magneto-optical interactions dates back to the 1840s, when Faraday discovered a rotation of the polarisation of light upon transmission through a magnetised specimen [292]. Subsequently, an analogous effect upon reflection from a magnetised sample was discovered in the 1870s by Kerr [293, 294] and is commonly named *magneto-optical Kerr effect* (MOKE). Since the latter does not rely on the optical transparency of the studied specimen, it can be easily applied to the study of magnetic metals and is therefore of key interest for the study of magneto-optical anisotropies in the present work.

[292]: Faraday (1846), 'I. Experimental researches in electricity.—Nineteenth series'

[293]: Kerr (1877), 'XLIII. *On rotation of the plane of polarization by reflection from the pole of a magnet*'

[294]: Kerr (1878), 'XXIV. *On reflection of polarized light from the equatorial surface of a magnet*'

While Faraday effect and MOKE describe the change of the polarisation of light upon interaction with a magnetised medium, other magneto-optical phenomena can be of interest for the study of magnetic materials. In the present study in particular, the inelastic scattering of light by spin waves is utilised, also named *Brillouin light scattering* (BLS) after the theoretical prediction by Brillouin [295]. In both, MOKE and BLS experiments, the reflected / back-scattered light is investigated and indeed the magneto-optical signals resulting from the two effects are linked [296]. This section will first introduce the concept of MOKE, the underlying microscopic origin and a phenomenological description, before introducing BLS and comparing the two phenomena.

[295]: Brillouin (1922), 'Diffusion de la lumière et des rayons X par un corps transparent homogène'

[296]: Hamrle et al. (2010), 'Analytical expression of the magneto-optical Kerr effect and Brillouin light scattering intensity arising from dynamic magnetization'

4.3.1 Magneto-optical Kerr effect

The magneto-optical Kerr effect (MOKE) describes the phenomenon of the change of the polarisation of light when reflected from a magnetic material. Its primary use lies in sensing the magnetic state of a medium, traditionally for the characterisation of static magnetic properties in thin films, i.e. the reorientation of the magnetisation, its hysteretic behaviour and the related anisotropies in the sample. However, experimental development in the last few decades has led to significant progress in pump-probe techniques using pulsed lasers resulting in an increasing use of time-resolved MOKE notably for the study of ultrafast magnetisation dynamics [297, 298]. Moreover, MOKE is increasingly employed for the study of magnetotransport phenomena, e.g. when quantifying spin-orbit torques in magnetic insulators [299] or detecting spin accumulation in heavy metals [300, 301].

[297]: Beaurepaire et al. (1996), 'Ultrafast Spin Dynamics in Ferromagnetic Nickel'

[298]: Hohlfeld et al. (1997), 'Nonequilibrium Magnetization Dynamics of Nickel'

[299]: Montazeri et al. (2015), 'Magneto-optical investigation of spin–orbit torques in metallic and insulating magnetic heterostructures'

[300]: Stamm et al. (2017), 'Magneto-Optical Detection of the Spin Hall Effect in Pt and W Thin Films'

[301]: Hirohata et al. (2018), 'Magneto-optical detection of spin accumulation under the influence of mechanical rotation'

Microscopic origin

The microscopic origin of the magneto-optical Kerr effect lies essentially in the exchange interaction and spin-orbit coupling of the material under investigation: The exchange interaction results in a splitting of the electronic states with a different population of the split electronic levels and therefore a spontaneous magnetisation as mentioned above. The spin-orbit coupling leads to an additional splitting of the electronic levels, resulting in different absorption frequencies for left- and right-circular polarised light.

A schematic for an exemplary $d \rightarrow p$ transition is shown in figure 4.10, where dipole transitions fulfilling the selection rules

$$\Delta s = 0, \quad \Delta l = \pm 1, \quad \Delta m = \pm 1 \tag{4.69}$$

are shown as vertical arrows in figure 4.10 (a). The combination of exchange splitting and splitting due to spin-orbit coupling results in an energy shift of the respective peaks in the absorption spectra for left- and right-circular

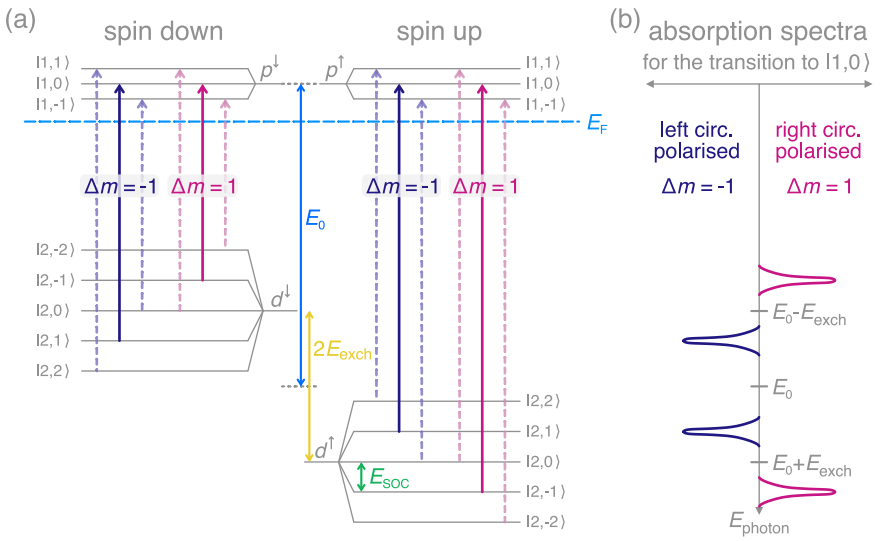

Figure 4.10: Simplified sketch of MOKE transitions and the resulting absorption spectra: (a) Schematic of the energy levels involved in the $d \rightarrow p$ transitions, where the exchange interaction is responsible for the shift removing the degeneracy in s, and the spin-orbit coupling yields an additional shift removing the degeneracy in l. Transitions for $\Delta s = 0$, $\Delta l = -1$ and $\Delta m = \pm 1$ are indicated by the coloured arrows. (b) The resulting absorption spectra simplified for the transitions to $|1,0\rangle$ only (the respective transitions are indicated in bold colours in (a) as well), which clearly present different spectral absorption signatures for left- and right-circular polarised light. Figure adapted from [302, 303].

[302]: Hamrle (2003), 'Magneto-optical determination of the in-depth magnetization profile in magnetic multilayers'
[303]: Bruno et al. (1996), 'Magneto-optical Kerr effect in a paramagnetic overlayer on a ferromagnetic substrate'

polarised light, as illustrated in figure 4.10 (b). In return, the absence of either exchange interaction or spin-orbit coupling clearly results in a vanishing magneto-optical effect as the shift for the different polarisation states in the absorption spectra becomes zero.

The resulting magneto-optical effects are described by the off-diagonal elements of the complex conductivity tensor, a quantitative derivation of which involves time-dependent perturbation theory [304]. The tensor elements essentially depend on the difference in the transition rates $\lambda^{\pm}_{\alpha\rightarrow\beta}$ for the transition of an electron from state α to β for left- and right-circular polarised light,

$$\lambda^{\pm}_{\alpha\rightarrow\beta} \sim \left|\langle\beta|\pi^{\pm}|\alpha\rangle\right|^2 \cdot \rho(E_\beta) \quad , \tag{4.70}$$

[304]: Bennett et al. (1965), 'Faraday Effect in Solids'

also known as Fermi's golden rule. The transition rates and hence also the conductivity tensor elements are thus proportional to two key ingredients [305]: Firstly, $\langle\beta|\pi^{\pm}|\alpha\rangle$ are the matrix elements of the electron's kinetic momentum operator $\hat{\pi} = \hat{p} + B \cdot \hat{A}_M + C \cdot \hat{S} \times \nabla V$ with the canonical momentum operator $\hat{p}$, the vector potential of the uniform magnetic field $\hat{A}_M$, the Pauli spin operator $\hat{S}$ and the periodic potential V accounting for the symmetry of the crystal [304]. And secondly, $\rho(E_\beta)$ is the density of states at the energy E_β.

[305]: Pershan (1967), 'Magneto-Optical Effects'

[304]: Bennett et al. (1965), 'Faraday Effect in Solids'

The quantitative description of the magneto-optical effects therefore relies on precise knowledge of the material's band structure and typically requires ab-initio calculations [306].

[306]: Oppeneer et al. (1992), '*Ab initio* calculated magneto-optical Kerr effect of ferromagnetic metals'

Phenomenological description

The microscopic understanding of the origin of magneto-optical effects and particularly the ability to model MOKE results based on band structures by ab-initio calculations developed quite late compared to the discovery and subsequent use of the effect as a characterisation technique. Consequently, an approach for a description purely based on classical principles of electromagnetism and optics was developed early on and is commonly used in magneto-optical studies. Both approaches essentially describe the magneto-optical interaction through the complex conductivity tensor $\hat{\sigma}$, which enters the wave equation

$$\nabla^2\mathbf{E} - \frac{\hat{\varepsilon}}{c^2} \cdot \frac{\partial^2}{\partial t^2}\mathbf{E} = 0 \tag{4.71}$$

describing the propagation of an electromagnetic wave with radial frequency ω in a non-charging medium with the complex permittivity $\hat{\varepsilon}$ linked to the complex conductivity $\hat{\sigma}$ via

$$\hat{\varepsilon} = i\frac{\hat{\sigma}}{\varepsilon_0 \omega} \tag{4.72}$$

with the imaginary unit i, and the vacuum permittivity ε_0.

The principal difference in the two approaches lies in the origin of the magnetisation-dependent complex permittivity $\hat{\varepsilon} = \hat{\varepsilon}(\mathbf{M})$ and the derivation of the resulting tensor elements: While the microscopic approach is based on quantum mechanical expressions of all involved interactions justifying the use of a magnetisation-dependent permittivity tensor and involving a calculation of resulting tensor elements from the material's band structure, the phenomenological description is based on a heuristic postulation of $\hat{\varepsilon} = \hat{\varepsilon}(\mathbf{M})$ and a derivation of the tensor shape from symmetry considerations based on the crystal lattice structure [307]. To this aim, it is convenient to expand the complex permittivity tensor as a Maclaurin series

[307]: Wettling (1976), 'Magneto-optics of ferrites'

$$\begin{aligned}\varepsilon_{ij}(\mathbf{M}) &= \varepsilon_{ij}^{(0)} + \sum_k \left[\frac{\partial \varepsilon_{ij}}{\partial M_k}\right]_{\mathbf{M}=0} M_k + \frac{1}{2}\sum_{k,l}\left[\frac{\partial^2 \varepsilon_{ij}}{\partial M_k \partial M_l}\right]_{\mathbf{M}=0} M_k M_l + \dots \\ &= \varepsilon_{ij}^{(0)} + \varepsilon_{ij}^{(1)} + \varepsilon_{ij}^{(2)} + \dots \end{aligned} \tag{4.73}$$

where $\varepsilon_{ij}^{(0)}$ are the magnetisation independent components of the permittivity tensor, i.e. for $\mathbf{M} = 0$, the $\varepsilon_{ij}^{(1)}$ is the linear magneto-optical tensor, i.e. linear in $\mathbf{M}$, and $\varepsilon_{ij}^{(2)}$ the second order tensor accounting for effects quadratic in $\mathbf{M}$ [308]. Higher order terms are neglected for the discussion in the present study, but can be analogously added if a description of higher order non-linearities is necessary.

[308]: Višnovský (1986), 'Magneto-optical permittivity tensor in crystals'

The dependence of the $\varepsilon_{ij}(\mathbf{M})$ is governed by the Onsager relation

$$\varepsilon_{ij}(\mathbf{M}) = \varepsilon_{ji}(-\mathbf{M}) \tag{4.74}$$

and $\varepsilon_{ij}^{(0)} = \varepsilon_{ji}^{(0)}$. The shape of the nonmagnetic part $\varepsilon_{ij}^{(0)}$ is determined solely by the symmetry of the crystal system and becomes diagonal for cubic systems with axes aligned with the Cartesian coordinate system, i.e. $\varepsilon^{(0)} = \varepsilon_d \cdot \hat{I}$ with unity matrix $\hat{I}$ and dielectric constant ε_d. The cubic system is the case with highest symmetry in the dielectric tensor $\varepsilon^{(0)}$ and tensors for all other crystal systems can be found in [308].

[308]: Višnovský (1986), 'Magneto-optical permittivity tensor in crystals'

Linear magneto-optical tensor

The second term of the complex permittivity tensor in equation 4.73 describes all phenomena which are linear in the magnetisation $\mathbf{M}$

$$\begin{aligned}\varepsilon_{ij}^{(1)}(\mathbf{M}) &= \sum_k \left[\frac{\partial \varepsilon_{ij}}{\partial M_k}\right]_{\mathbf{M}=0} M_k \\ &= \sum_k K_{ijk} M_k \end{aligned} \tag{4.75}$$

and again simplifies taking Onsager's principle as well as cubic crystal symmetries into account, resulting in only one free parameter $K := K_{ijk}$ for cubic

crystals. The linear magneto-optical tensor then has the shape

$$\varepsilon^{(1)}(\mathbf{M}) = \begin{bmatrix} 0 & KM_z & -KM_y \\ -KM_z & 0 & KM_x \\ KM_y & -KM_x & 0 \end{bmatrix} \tag{4.76}$$

for cubic lattices with axes aligned with the Cartesian coordinate system[43].

43: This choice of coordinate system is no loss of generality, since a simple transformation by adequate rotation matrices will yield the respective expression for a rotation of the crystal system with respect to the coordinate system, see for instance [308, 309].

[308]: Višnovský (1986), 'Magneto-optical permittivity tensor in crystals'
[309]: Hamrlová et al. (2013), 'Quadratic-in-magnetization permittivity and conductivity tensor in cubic crystals'

Quadratic magneto-optical tensor

The third term of the complex permittivity tensor in equation 4.73 accounts for all effects which are quadratic in $\mathbf{M}$

$$\begin{aligned} \varepsilon^{(2)}_{ij}(\mathbf{M}) &= \frac{1}{2}\sum_{k,l}\left[\frac{\partial^2 \varepsilon_{ij}}{\partial M_k \partial M_l}\right]_{\mathbf{M}=0} M_k M_l \\ &= \sum_{k,l} G_{ijkl} M_k M_l \end{aligned} \tag{4.77}$$

and for cubic crystals in the $m\bar{3}m$ Laue group (such as Heusler compounds) the tensor elements G_{ijkl} reduce to three free parameters

$$\begin{aligned} G_{11} &:= G_{iiii} \\ G_{12} &:= G_{iijj} \\ G_{44} &:= G_{ijij} \end{aligned} \tag{4.78}$$

with all other tensor elements becoming zero. This results in

$$\begin{aligned} \varepsilon^{(2)}(\mathbf{M}) = &\begin{bmatrix} G_{11}M_x^2 + G_{12}(M_y^2 + M_z^2) & 0 & 0 \\ 0 & G_{11}M_y^2 + G_{12}(M_x^2 + M_z^2) & 0 \\ 0 & 0 & G_{11}M_z^2 + G_{12}(M_x^2 + M_y^2) \end{bmatrix} \\ &+ \begin{bmatrix} 0 & 2G_{44}M_xM_y & 2G_{44}M_xM_z \\ 2G_{44}M_xM_y & 0 & 2G_{44}M_yM_z \\ 2G_{44}M_xM_z & 2G_{44}M_yM_z & 0 \end{bmatrix} \end{aligned} \tag{4.79}$$

for the quadratic magneto-optical tensor of the crystal again with cubic axes aligned with the coordinate system[40]. In an isotropic medium, the $2G_{44}$ transform to $G_{11} - G_{12}$ and therefore the difference $\Delta G = G_{11} - G_{12} - 2G_{44}$ is commonly used to quantify the magneto-optical anisotropy induced by quadratic magneto-optical effects [309].

[309]: Hamrlová et al. (2013), 'Quadratic-in-magnetization permittivity and conductivity tensor in cubic crystals'

Kerr angle and change of polarisation

The MOKE effect, i.e. the change of polarisation upon reflection from a magnetic material, is commonly expressed through the complex Kerr angle[44]

$$\Phi_{\mathrm{s/p}} = \theta_{\mathrm{s/p}} + i\ell_{\mathrm{s/p}} \tag{4.80}$$

where $\theta_{\mathrm{s/p}}$ is the Kerr rotation and $\ell_{\mathrm{s/p}}$ the Kerr ellipticity[45] for s and p polarised light respectively. The change of polarisation $\Phi_{\mathrm{s/p}}$ is related to the permittivity tensor elements by the analytical approximation [310]

$$\Phi_{\mathrm{s}} = A_{\mathrm{s}}\left(\varepsilon_{yx} - \frac{\varepsilon_{yx}\varepsilon_{zx}}{\varepsilon_d}\right) + B_{\mathrm{s}}\varepsilon_{zx} \tag{4.81}$$

$$\Phi_{\mathrm{p}} = -A_{\mathrm{p}}\left(\varepsilon_{xy} - \frac{\varepsilon_{xz}\varepsilon_{zy}}{\varepsilon_d}\right) + B_{\mathrm{s}}\varepsilon_{yz} \tag{4.82}$$

44: Sometimes also named *Kerr amplitude* instead, which is less common but also less easily confused with physical angles in the description of the effect or the related measurements.

45: The uncommon notation as $\ell_{\mathrm{s/p}}$ instead of the more common $\varepsilon_{\mathrm{s/p}}$ was introduced here to avoid confusion with the permittivity tensor elements.

[310]: Hamrle et al. (2007), 'Huge quadratic magneto-optical Kerr effect and magnetization reversal in the Co_2FeSi Heusler compound'

with the weighting optical factors $A_{s/p}$ and $B_{s/p}$ being even and odd functions of the angle of incidence. Considering the permittivity tensor series up to second order in the magnetisation $\mathbf{M}$, this results in [310]

$$\begin{aligned}\Phi_{s/p} = &\pm A_{s/p}\left(2G_{44} + \frac{\Delta G}{2}(1-\cos 4\phi) + \frac{K^2}{\varepsilon_d}\right)M_L M_T \\ &\mp A_{s/p}\frac{\Delta G}{2}\sin\phi(M_L^2 - M_T^2) \\ &\mp B_{s/p} K M_L \end{aligned} \tag{4.83}$$

with the longitudinal magnetisation component M_L in the film plane and the incidence plane of light, the transverse magnetisation component M_T in the film plane and perpendicular to the incidence plane of light and vanishing polar magnetisation component M_P perpendicular to the film plane. The angle ϕ describes the rotation of the principle cubic lattice axis [100] with respect to the direction $\mathbf{m}_L$.

Equation 4.83 notably shows that for an in-plane magnetised sample, three contributions are obtained, scaling differently with the magnetisation components: A single linear contribution $\Phi_{s/p}^{lin} = \mp B_{s/p} K M_L$ is obtained, which only depends on the linear magneto-optical tensor and is independent of the crystal orientation ϕ, making the linear MOKE effect isotropic upon sample rotation. Two different quadratic terms are obtained, one $\sim (M_L^2 - M_T^2)$ which is solely determined by the quadratic magneto-optical tensor through ΔG, and the other one $\sim M_L M_T$, which contains contributions from the quadratic as well as the linear magneto-optical tensor and thus even for $G_{ijkl} = 0$ a quadratic contribution proportional to K^2/ε_d remains. The effect described by the quadratic terms is commonly denoted as QMOKE, and the linear part will be explicitly denoted as linMOKE in this work to avoid any confusions[46]. Indeed, the linMOKE is often referred to purely as MOKE since in many cases isotropic magneto-optical behaviour is observed and thus non-linear terms in the complex permittivity are negligible. However, recent examples of significant non-linear effects in epitaxial thin films demonstrate the importance of second order terms in the complex permittivity tensor for specific cases [311–313]. In particular, notable non-linear magneto-optical contributions have been reported for various Heusler compounds, such as *X*MnSb with *X*={Co, Ni, Pt} [314–316], Co_2FeSi [74, 310] and especially Co_2Mn-based Heusler compounds [72, 82, 195, 317–323].

Analogies

The obtained signature of contributions in $\sim M_L$, $\sim M_L M_T$ and $\sim (M_L^2 - M_T^2)$ are not unique to magneto-optics in reflection as was the focus of above section, but apply to various settings: As already indicated above, a similar change in the polarisation of light can be observed upon transmission through a (sufficiently transparent) magnetised material. The linear effect in transmission is the above-named *Faraday effect*, sometimes also denoted as magnetic circular birefringence (MCD) [324] referring to the difference in the effective refraction indices for left- and right-circular polarised light. The quadratic effect in transmission is called the *Voigt effect*, which can be referred to as magnetic linear birefringence (MLD) analogously for s- and p-polarised light [324].

This analogy is not restricted to the visible range, as similar effects are observed in X-ray absorption spectroscopy. In fact, it is not even restricted to magneto-optics as with the complex conductivity tensor $\hat{\sigma}$ being linked to the the complex permittivity tensor $\hat{\varepsilon}$ by the expression $\hat{\sigma} = -i\varepsilon_0\omega\hat{\varepsilon}$ (see equation 4.72), similar

46: LMOKE is sometimes chosen as a denomination in the literature, but is misleading, since LMOKE commonly serves as a denomination for the MOKE measurement geometry along the longitudinal direction, see section 5.3 on page 106.

[311]: Osgood et al. (1995), 'Asymmetric magneto-optic response in epitaxial Fe(110)/Mo(110) thin films'
[312]: Osgood et al. (1997), 'Asymmetric magneto-optic response in anisotropic thin films'
[313]: Postava et al. (1997), 'Linear and quadratic magneto-optical measurements of the spin reorientation in epitaxial Fe films on MgO'
[314]: Carey et al. (1998), 'Asymmetric non-linear magneto-optic effects in PtMnSb thin films'
[315]: Kuz'min et al. (2008), 'Optical absorption and magnetooptical effects in the Heusler alloy NiMnSb'
[316]: Lobov et al. (2012), 'Optical and magnetooptical properties of Heusler alloys XMnSb (X = Co, Pt)'
[74]: Hamrle et al. (2007), 'Ion beam induced modification of exchange interaction and spin–orbit coupling in the Co_2FeSi Heusler compound'
[310]: Hamrle et al. (2007), 'Huge quadratic magneto-optical Kerr effect and magnetization reversal in the Co_2FeSi Heusler compound'
[72]: Gaier et al. (2008), 'Influence of the $L2_1$ ordering degree on the magnetic properties of Co_2MnSi Heusler films'
[82]: Silber et al. (2020), 'Scaling of quadratic and linear magneto-optic Kerr effect spectra with $L2_1$ ordering of Co_2MnSi Heusler compound'
[195]: Trudel et al. (2011), 'Effect of annealing on $Co_2FeAl_{0.5}Si_{0.5}$thin films: A magneto-optical and x-ray absorption study'
[317]: Muduli et al. (2008), 'Composition dependence of magnetic anisotropy and quadratic magnetooptical effect in epitaxial films of the Heusler alloy Co_2MnGe'
[318]: Muduli et al. (2009), 'Study of magnetic anisotropy and magnetization reversal using the quadratic magnetooptical effect in epitaxial $Co_xMn_yGe_z$ (111) films'
[319]: Trudel et al. (2010), 'Tandem magneto-optical Kerr effect magnetometer for the study of quadratic effects'
[320]: Trudel et al. (2010), 'Note: Probing quadratic magneto-optical Kerr effects with a dual-beam system'
[321]: Trudel et al. (2010), 'Magneto-optical investigation of epitaxial nonstoichiometric Co_2MnGe thin films'
[322]: Wolf et al. (2011), 'Quadratic magneto-optical Kerr effect in Co_2MnSi'
[323]: Liu et al. (2017), 'Linear and quadratic magneto-optical Kerr effect investigation of $Co_2Mn_{1.30}Si_{0.84}$ epitaxially grown on MgO'
[324]: Hubert et al. (1993), 'Magneto-optical sensitivity functions of thin-film systems'

magnetisation-dependence is observed in spintronics, where spin-charge-coupling is investigated for instance by electrical DC measurements [309]: Here, the anomalous Hall effect (AHE) has the linear $\sim M_L$ signature, the planar Hall effect (PHE) scales with $\sim M_L M_T$ and the anisotropic magnetoresistance (AMR) shows $\sim (M_L^2 - M_T^2)$. An overview of analogous effects is given in table 4.2.

[309]: Hamrlová et al. (2013), 'Quadratic-in-magnetization permittivity and conductivity tensor in cubic crystals'

Table 4.2: Categorisation of magneto-optical and related magnetotransport effects by detection technique and scaling with different powers of the magnetisation components. Table adapted from [309]. MO stands for "magneto-optical", DC for "direct current".

	$\sim M_L$	$\sim M_L M_T$	$\sim (M_L^2 - M_T^2)$
MO reflection	linMOKE	QMOKE	QMOKE
MO transmission	Faraday	Voigt	Voigt
DC conductivity	AHE	PHE	AMR

4.3.2 Brillouin light scattering

Brillouin light scattering (BLS) describes the inelastic scattering of light from collective excitations in a crystal system, i.e. acoustic waves in the lattice system or spin waves in the spin system. BLS is closely linked to the magneto-optical effects presented hereabove and is therefore briefly introduced at this point although for now only zero wavenumber spin waves (the spatially uniform oscillation or ferromagnetic resonance) have been introduced. A detailed knowledge of non-zero wavenumber spin waves is not necessary for the basic understanding of BLS introduced in this section and will be given later on in the third part of this thesis, which focuses on the work towards magnonic applications of Co_2Mn-based Heusler compounds.

Indeed, it is sufficient at this point to view the spin waves as a collective excitation of the ferromagnetic spin system, which results in a spatial modulation of the magnetisation, i.e. $\mathbf{M}(t) \Rightarrow \mathbf{M}(\mathbf{r}, t)$. Collective excitations with non-zero wavenumbers then result in a periodic spatial modulation of the complex permittivity tensor $\hat{\varepsilon}$ introduced above, i.e. $\hat{\varepsilon} \Rightarrow \hat{\varepsilon}(\mathbf{r}, t)$, which can be interpreted as an "effective oscillating and propagating optical grating" [310] resulting in a scattering of reflected light with a change of frequency and propagation direction. Consequently, a spatially uniform magnetisation, i.e. the static magnetisation in a ferromagnet as well as the spatially-uniform magnetisation oscillations at the ferromagnetic resonance, will not lead to any Brillouin light scattering. Still, near-zero wavenumber spin waves close to the FMR can already result in a detectable Brillouin light scattering allowing to probe quasi-FMR properties [325].

[310]: Hamrle et al. (2007), 'Huge quadratic magneto-optical Kerr effect and magnetization reversal in the Co_2FeSi Heusler compound'

[325]: Srinivasan et al. (1988), 'Brillouin light scattering detection of ferromagnetic resonance in thin films'

The BLS signal intensity is linked to the above introduced magneto-optical effects via the permittivity tensor and following the approach by Buchmeier *et al.* [326] and decomposing the ferromagnet into discrete sheets, the polarisation $\mathbf{P}_i$ of light in layer i

$$\mathbf{P}_i = \hat{\varepsilon}_i(M_S \delta \mathbf{m}_i) \cdot \mathbf{E}_i \tag{4.84}$$

is thus oscillating at a frequency $\omega_{light} \pm \omega_{SW}$ and determined by the permittivity tensor $\hat{\varepsilon}_i(M_S \delta \mathbf{m}_i(t))$ accounting for the magneto-optical interaction of a dynamic magnetisation $M_S \delta \mathbf{m}_i(t)$ induced by a spin wave with frequency ω_{SW} and the electric field of the light $\mathbf{E}_i$ at frequency ω_{light}. Analogously, the complex Kerr angle can be decomposed to a sum of MOKE contributions from layers i in the ferromagnet [326] and including quadratic terms as in equation 4.83, this yields[47]

[326]: Buchmeier et al. (2007), 'Intensity of Brillouin light scattering from spin waves in magnetic multilayers with noncollinear spin configurations'

47: Polar contributions are included in the linear term since the oscillating wave will introduce a small polar component even for an in-plane magnetised sample, but it's quadratic effect is assumed negligible just as higher order non-linear terms in any dynamic magnetisation component $M_S \delta m_i$.

$$\Phi_{\mathrm{s/p}}(t) = \sum_i \Delta d_i \cdot \Big[L_{\mathrm{s/p},i} \cdot \delta m_{\mathrm{L},i} + P_{\mathrm{s/p},i} \cdot \delta m_{\mathrm{P},i} + Q^{\mathrm{LL}}_{\mathrm{s/p},i} \cdot (\delta m^2_{\mathrm{L},i} - \delta m^2_{\mathrm{T},i}) + Q^{\mathrm{LT}}_{\mathrm{s/p},i} \cdot (\delta m_{\mathrm{L},i} \cdot \delta m_{\mathrm{T},i}) + O(\delta m_i^3) \Big] \tag{4.85}$$

with the layer thicknesses Δd_i, the (normalised) dynamic magnetisation components δm_i of the spin wave oscillating at ω_{SW} and the effective MOKE coefficients $L_{\mathrm{s/p},i}$ for longitudinal, $P_{\mathrm{s/p},i}$ for polar and $Q^{\mathrm{LL}}_{\mathrm{s/p},i}$, $Q^{\mathrm{LT}}_{\mathrm{s/p},i}$ for quadratic effects on s- and p-polarised light (in deg/m). The complex Kerr angle for (static) MOKE $\Phi_{\mathrm{s/p}}$ is here included and forms the time-independent part, i.e. $\Phi_{\mathrm{s/p}}(t) = \Phi_{\mathrm{s/p}} \sin(\omega_{\mathrm{SW}} \cdot t + \phi_{\mathrm{s/p}})$. The BLS intensity can be expressed in an analogous manner [326]

$$I^{\omega_{\mathrm{light}} \pm \omega_{\mathrm{SW}}}_{\mathrm{s/p}} = I_0 \cdot \left| \sum_i \Delta d_i \cdot \big[- L_{\mathrm{s/p},i} \cdot \delta m_{\mathrm{L},i} + P_{\mathrm{s/p},i} \cdot \delta m_{\mathrm{P},i} + Q^{\mathrm{LL}}_{\mathrm{s/p},i} \cdot (\delta m^2_{\mathrm{L},i} - \delta m^2_{\mathrm{T},i}) + Q^{\mathrm{LT}}_{\mathrm{s/p},i} \cdot (\delta m_{\mathrm{L},i} \cdot \delta m_{\mathrm{T},i}) \big] \right|^2 \tag{4.86}$$

where the sign of the longitudinal component is reversed for backscattered light [326]. The close relation between BLS intensity $I^{\omega_{\mathrm{light}} \pm \omega_{\mathrm{SW}}}_{\mathrm{s/p}}$ and complex Kerr angle $\Phi_{\mathrm{s/p}}$ is thus clearly apparent from above equations:

$$I^{\omega_{\mathrm{light}} \pm \omega_{\mathrm{SW}}}_{\mathrm{s/p}} \sim |\Phi_{\mathrm{s/p}}(t)|^2 \tag{4.87}$$

i.e. both depend on the same effective coefficients, but BLS can essentially be seen as "a quadratic form of MOKE" [296]. In the case of non-negligible quadratic MOKE effects, this denomination might be slightly misleading, as BLS shall not be understood as solely dependent on the quadratic magneto-optical tensor $\hat{\varepsilon}^{(2)}(\mathbf{M})$ (see equation 4.77). Indeed even for considerable quadratic magneto-optical effects in MOKE expressed by $\hat{\varepsilon}^{(2)}$, the corresponding signature in the BLS intensity can still be negligible over the usually much larger contributions originating from $\hat{\varepsilon}^{(1)}$ and thus it is often sufficient to express the BLS intensity as a function of the linear components only

$$I^{\omega_{\mathrm{light}} \pm \omega_{\mathrm{SW}}}_{\mathrm{s/p}} = I_0 \cdot \left| \sum_i \Delta d_i \cdot \big[- L_{\mathrm{s/p},i} \cdot \delta m_{\mathrm{L},i} + P_{\mathrm{s/p},i} \cdot \delta m_{\mathrm{P},i} \big] \right|^2$$

as is the case in the derivations in references [296, 326] where effects quadratic in magnetisation are postulated to be negligible, or partly in [327], where only cubic terms $\sim 2G_{44}M_{\mathrm{L}}$ are included in the quadratic part.

[326]: Buchmeier et al. (2007), 'Intensity of Brillouin light scattering from spin waves in magnetic multilayers with noncollinear spin configurations'

[296]: Hamrle et al. (2010), 'Analytical expression of the magneto-optical Kerr effect and Brillouin light scattering intensity arising from dynamic magnetization'

[296]: Hamrle et al. (2010), 'Analytical expression of the magneto-optical Kerr effect and Brillouin light scattering intensity arising from dynamic magnetization'

[326]: Buchmeier et al. (2007), 'Intensity of Brillouin light scattering from spin waves in magnetic multilayers with noncollinear spin configurations'

[327]: Cochran et al. (1988), 'Calculation of the intensity of light scattered from magnons in thin films'

4.4 Concluding remarks

In summary, this chapter provided an overview over basic concepts of magnetism forming the background for the subsequent discussion of experimental results in this second part of the thesis.

Firstly, an introduction of ferromagnets and the resulting magnetic hysteresis was given. This set the base for the subsequent analysis of magnetic hysteresis curves investigated in vibrating sample magnetometry measurements, the principles of which will be briefly introduced in the following chapter 5. An uncommon focus was set on the introduction of the cubic magnetocrystalline anisotropy up to the second order, which is due to this contribution being of significance throughout this work: In chapter 6, the strength of the cubic anisotropy is quantified in thin films, where the assumption of only a first order cubic anisotropy term was found to be insufficient to reproduce the experimental behaviour. Building on the description of anisotropies in this chapter, as well as the results that will be presented in chapter 6 of this part, the effects of the first and second order cubic anisotropy on the dispersion relation of propagating spin waves and the ellipticity of the precession will be detailed in chapter 8 in the third part of this work.

Secondly, the fundamental concept of magnetisation oscillations and magnetic damping were introduced, focusing on the spatially uniform (zero wavenumber) case of ferromagnetic resonance. The FMR was exploited throughout this work for the characterisation of the dynamic properties and key parameters that are crucial for the further investigations. A detailed description of the underlying experimental technique and subsequent data analysis will be given in the next chapter 5 and a FMR study on Co_2MnSi and Co_2MnAl thin films will be presented in chapter 6.

Finally, magneto-optical phenomena and their analogies were briefly discussed, and a motivation was given for the relation between magneto-optical signal intensities obtained from MOKE and BLS processes. This is of importance for the characterisation of the achievable magneto-optical signal strengths as will be presented in chapter 7.

Based on the theoretical foundations given in this chapter, the principles of the related experimental techniques will be introduced in the subsequent chapter 5, allowing for a discussion of the experimental results thereafter.

Methods: Magnetic and magneto-optical thin film characterisation

5

The present part of the work is devoted to the magnetic characterisation of the Co_2Mn-based Heusler thin films, and this chapter shall give the necessary details on the methods used to this aim. Precisely, the samples were investigated using vibrating sample magnetometry (VSM), ferromagnetic resonance (FMR) spectroscopy, magneto-optical Kerr effect (MOKE) magnetometry and conventional Brillouin light scattering spectroscopy (BLS) techniques, the technical concepts of which will be presented in the present chapter along with the procedure of the subsequent data treatment. Particular focus is set on the data analysis in the FMR section 5.2, where a thorough discussion of the background removal technique for (non-calibrated) broadband FMR data analyses potential systematically induced effects on the resonance lineshapes to avoid systematic errors in the later magnetic damping analysis.

5.1 VSM magnetometry . . . 93
Experimental technique . . 93
Data post-processing 95
5.2 FMR spectroscopy 97
BB-FMR setup 97
BB-FMR data analysis . . . 100
5.3 MOKE magnetometry . . 106
Experimental technique . . 106
linMOKE and QMOKE . . . 108
5.4 Conventional BLS 109
Experimental technique . . 109
Intensity analysis 110

5.1 Vibrating sample magnetometry (VSM)

Vibrating sample magnetometry (VSM) was developed in the 1950s [328] and is nowadays a standard technique for measuring the absolute magnetic moment of a sample. A simultaneous development of vibrating coil magnetometers (VCM) [329] was based on the opposite principle: here the sample is fixed and the recording coils oscillate. Although VCMs equally record the signal induced by the magnetic/magnetized sample, they are susceptible to pick up additional noise, e.g. signals originating from spatial inhomogeneities in the external field. Contrary to this, VSMs are insensitive to static magnetic inhomogeneities [330] and have therefore become widely used in modern research laboratories with implementations ranging from custom setups [331–333] to commercial devices [334, 335].

[328]: Van Oosterhout (1957), 'A rapid method for measuring coercive force and other ferromagnetic properties of very small samples'

[329]: Smith (1956), 'Development of a Vibrating-Coil Magnetometer'

[330]: Foner (1959), 'Versatile and Sensitive Vibrating-Sample Magnetometer'

[331]: El-Alaily et al. (2015), 'Construction and calibration of a low cost and fully automated vibrating sample magnetometer'

[332]: Lopez-Dominguez et al. (2018), 'A simple vibrating sample magnetometer for macroscopic samples'

[333]: Jordán et al. (2018), 'Detection of magnetic moment in thin films with a home-made vibrating sample magnetometer'

[334]: MicroSense (2023), *EasyVSM Brochure*

[335]: QuantumDesign (2024), *Vibrating Sample Magnetometer (VSM) Brochure*

5.1.1 Measurement principle and experimental setup

The working principle of a VSM is based on Faraday's law of induction: the periodically varying relative position of a sample in an external magnetic field with respect to a set of pickup coils leads to an induced voltage in the latter.

This induced voltage can be derived by laws of classical physics[1]: The magnetostatic potential $\mathbf{A}_{\text{pot}}$ of a magnetic dipole moment $\mathcal{M}$ is given by

$$\mathbf{A}_{\text{pot}}(\mathbf{r}) = \frac{\mu_0}{4\pi} \frac{\mathcal{M} \times \mathbf{r}}{|r|^3} \tag{5.1}$$

at any point $\mathbf{r}$, where the associated magnetic flux density is given by $\mathbf{B}(\mathbf{r}) = \nabla \times \mathbf{A}_{\text{pot}}(\mathbf{r})$. As the dipole is set to vibration, the magnetostatic potential becomes a function of time with the time varying component given by

$$\widetilde{\mathbf{A}}_{\text{pot}}(\mathbf{r}, t) = -A_{\text{vib}} \cdot \frac{\partial \mathbf{A}_{\text{pot}}(\mathbf{r})}{\partial \hat{\mathbf{e}}_z} \cdot e^{i\omega t} \tag{5.2}$$

where ω is the pulsation frequency, A_{vib} the pulsation amplitude and $\hat{\mathbf{e}}_z$ the unity vector along the vibration axis. Consequently, a modulation of the

1: Funnily enough, this application combines quite a few physical quantities that are typically labelled A across literature. This established notation shall be maintained here, but original indices are introduced in an attempt to help the attentive reader with the distinction of the different quantities.

magnetic flux described by the surface integral

$$\Phi_B(A_{rea}, t) = \iint_{A_{rea}} \nabla \times \widetilde{\mathbf{A}}_{pot}(\mathbf{r}, t)\, dA_{rea} \tag{5.3}$$

is obtained in a pickup coil of area A_{rea}, which induces a voltage

$$V_{ind}(t) \sim \frac{\partial}{\partial t}\Phi_B(A_{rea}, t) \tag{5.4}$$

in the pickup coils according to Faraday's law of induction. This voltage can be recorded in correlation with the sample position over time, e.g. by recording the position of a known reference sample on the same rod, oscillating through a set of reference coils [330], yielding a time/position dependent voltage waveform related to the magnetic moment of the sample under investigation.

Although the underlying principles are based on well-known laws of classical physics, the subsequent step of extracting the magnetic moment from the recorded voltage trace is not straightforward as the signal strongly depends on the setup geometries, in particular on the arrangement of the pickup coils and the axis of vibration, see e.g. [336]. In commercial VSM setups as used in this work, the conversion of the recorded voltage waveform into a corresponding magnetic moment is usually directly implemented taking into account all setup-specific geometries when fitting a theoretical response function to the recorded curves. This typically requires a calibration of the system with a reference sample of known magnetic moment [337, 338]. Therefore, the data treatment must involve a correction of the recorded moment considering all relevant differences between actual measurement and utilized calibration measurement, notably including the sample geometry [339, 340].

Setup specifications

The measurements presented in this thesis were mostly[2] acquired on a commercial setup by Quantum Design, i.e. a physical properties measurement system (PPMS) DynaCool base setup equipped with the VSM add-on option.

A schematic corresponding to the PPMS (DynaCool) VSM setup is shown in figure 5.1. The sample and pickup coils are positioned in a purged chamber detached from the closed cryo-cooling system hosting the electromagnet. This ensures the possible application of magnetic fields up to $\mu_0 H_{ext} = 9\,T$, while independently enabling a temperature in the sample chamber between 2 K and 400 K. The sample is mounted on a quartz sample holder and set to vibration by a linear motor. The vibration axis coincides with the axes of the pickup coils as well as the static magnetic field applied by the external electromagnet.

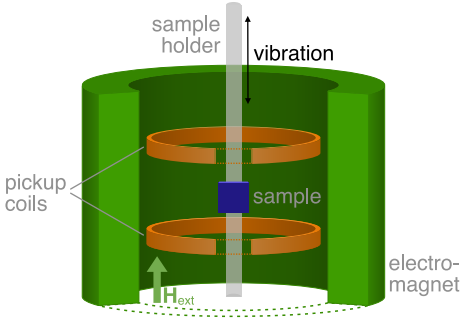

Figure 5.1: Schematic of the VSM setup (not to scale). The sample (blue) is placed upside down on a quartz sample holder (grey), which is vibrated along its long axis (black arrow). The vibration is driven by a linear motor (not shown). The oscillating magnetic sample induces a detectable voltage in the pickup coils (orange). The external magnetic field is provided by an electromagnet (green), capable of mounting up to $\mu_0 H_{ext} = 9\,T$.

[330]: Foner (1959), 'Versatile and Sensitive Vibrating-Sample Magnetometer'

[336]: Bernards et al. (1993), 'An improved detection coil system for a biaxial vibrating sample magnetometer'

[337]: QuantumDesign (2020), *VSM Application Note 1500-021*

[338]: QuantumDesign (), *VSM Application Note 1041-001*

[339]: Lindemuth et al. (2001), 'Finite sample size effects on the calibration of vibrating sample magnetometer'

[340]: QuantumDesign (2021), *SQUID VSM Application Note 1500-020*

2: In the course of the PhD work, various other VSM setups were used, precisely: Quantum Design PPMS VSM setups similar to the one described, a MicroSense VSM setup as well as Quantum Design MPMS3 SQUID VSM setups. Focus is set here on the PPMS DynaCool VSM, since the measurements presented in this thesis were primarily acquired on such a system. The working principles of the other setups are fairly similar. The difference between the PPMS VSM and PPMS DynaCool VSM lies mainly in the cryogenic cooling and the systems can be treated equally concerning the VSM application. The Quantum Design MPMS3 SQUID VSM setup is equipped with a superconducting quantum interference device in the detection unit, resulting in an order of magnitude higher sensitivity than the Quantum Design PPMS (DynaCool) VSM, otherwise the setups are comparable in specifications. The MicroSense VSM additionally allows for a sample rotation with the magnetic field applied in the film plane, but yields a lower measurement resolution than the PPMS setups. It was therefore mainly used for testing purposes.

Measurement procedure

The $M(H)$ measurements were performed at a temperature of $T = 300\,\mathrm{K}$ if not stated otherwise. The VSM was operated with a peak amplitude of $A_{\mathrm{VSM}} = 2\,\mathrm{mm}$ and a frequency of $f_{\mathrm{VSM}} = 40\,\mathrm{Hz}$, resulting in a maximum acceleration of $a_{\mathrm{VSM}} = 126.33\,\mathrm{m/s^2}$ and a maximum measurable moment of $\mathscr{M}_{\mathrm{max}} = 44.59\,\mathrm{mJ/T} = 44.59 \times 10^{-3}\,\mathrm{Am^2}$. The field was swept with a rate set to $r = 1\,\mathrm{mT/s}$, and data was acquired for an averaging time of $t_{\mathrm{avg}} = 1\,\mathrm{s}$ per field point during which the field was controlled in the driven mode.

A strict measurement procedure was followed for the VSM measurement series on each sample in order to reduce systematic errors:

1. A mark was scratched on the backside of the sample in order to indicate the [110] axis placed parallel to the external field and vibration axis[3].
2. The measurement noise arising from loose sample mounting [341] was reduced by a tight application of Kapton tape along the sample holder.
3. Every measurement was conducted as a hysteresis loop, i.e. full $M(H)$ cycle, in order to enable a proper background removal in the data post-processing (see below).[4]
4. An automated touchdown centring was performed at intervals of $\Delta t = 10\,\mathrm{min}$ in order to avoid a vertical positioning error during the measurement [344].
5. The comparability between different measurements was ensured by a setup demagnetising procedure: Prior to each $M(H)$ measurement, a saturation was forced by applying the maximal field $\mu_0 H_{\mathrm{ext}} = 9\,\mathrm{T}$ and followed by a demagnetisation to $\mu_0 H_{\mathrm{ext}} = 0\,\mathrm{T}$ at a rate of $r = 20\,\mathrm{mT/s}$ in the *oscillate* mode[5], in order to reduce varying field shifts due to different measurement/setup history (e.g. from vortices pinned in the superconducting coils from previous field applications).
6. The precision of the extracted parameters from in-plane hysteresis loops, particularly coercive field and saturation magnetisation, was maximised by recording a set of two $M(H)$ loops with different field ranges: the first one with a maximum field of $\mu_0 H_{\mathrm{ext}} = 20\,\mathrm{mT}$ for a high resolution measurement of the hysteresis loop opening without potential shifts due to vortices in the superconducting coils, and the second one with a maximum field of $\mu_0 H_{\mathrm{ext}} = 2\,\mathrm{T}$ for a precise determination of the saturation magnetisation and saturation field.

3: Note that prior to the first VSM measurement on each sample piece, the [110] direction was arbitrarily chosen as one axis parallel to the sample borders (since $[110]_{\mathrm{Co_2MnSi}} \parallel [100]_{\mathrm{MgO}}$). This choice was marked on the sample backside with a diamond pen. Therefore, the comparison of measurements along different $[hkl]$ is possible for one specific sample, but concerning the comparison between different samples, the results obtained from one sample along [110] may be equally compared to the results obtained from the other sample along [110] as well as $[\bar{1}10]$ due to the arbitrary choice of axes for each sample.

[341]: QuantumDesign (2010), *VSM Application Note 1500-009*

4: Importantly, this enables reducing the errors arising from the magnetic impurities in the MgO substrates [342, 343], particularly important in temperature dependent measurements as shown in a previous work [83].

[342]: Khalid et al. (2010), 'Ubiquity of ferromagnetic signals in common diamagnetic oxide crystals'

[343]: Li et al. (2013), 'Origin of room temperature ferromagnetism in MgO films'

[83]: Friedel (2021), *Thin film materials with ultralow damping for novel magnonic phenomena*

[344]: Quantum Design (2011), *Vibrating Sample Magnetometer (VSM) Option User's Manual, 5th edition, Part Number 1096-100, B0*

5: Precisely, the field set to oscillate around $\mu_0 H_{\mathrm{center}} = 0$ with a decreasing amplitude starting from $|\mu_0 H_{\mathrm{max}}| = 9\,\mathrm{T}$ and ending with $|\mu_0 H_0| = 0\,\mathrm{T}$

5.1.2 Data post-processing

As mentioned above, the recorded moment $\mathscr{M}_{\mathrm{rec}}$ (recorded in emu) needs to be corrected in a post-processing procedure in order to extract the magnetic moment related to the magnetic volume under investigation.

The post-processing corrections need to account for the differences between the measurement and the previous calibration concerning all relevant parameters which influence the induced voltage, i.e. pick-up coil geometry (sizes, spacing, windings/coil), sample shape (length along vibration axis, width perpendicular to vibration axis), positioning (radial and axial offsets) and vibration settings (frequency, amplitude).

Hence, a first post-processing step involved the calculation of suitable correction factors F_{corr} using the `VSMcoilcalc.exe`[6] tool provided by Quantum Design. The corrected moment is then given by

$$\mathscr{M}_{\mathrm{corr}}\left[\mathrm{Am^2}\right] = \mathscr{M}_{\mathrm{rec}}\left[\mathrm{emu}\right] \cdot 10^{-3} \cdot F_{\mathrm{corr}} \tag{5.5}$$

6: PPMS VSM Coilset Response Function Calculator (Oct. 14, 2003)

where the obtained correction factors were in the range of $F_{\text{corr}} = 1.005 - 1.008$ for the samples cut to squares of $\sim 4 \times 4\,\text{mm}^2$ in this work.

Secondly, a linear function was subtracted to account for the diamagnetic background from substrate, capping[7] and sample holder, the parameters of this diamagnetic contribution were determined by a linear regression BG of the data aquired at fields significantly above saturation (this depends on the material / sample and in the case of the studied Co_2Mn-based Heusler compounds in the field in-plane geometry, setting $|\mu_0 H_{\text{BG}}| > 1.0\,\text{T}$ is valid for all investigated samples).

Finally, the volume V_{mag} of the ferromagnetic material needs to be taken into account in order to calculate the magnetisation

$$M_{\text{meas}}\left[\frac{\text{kA}}{\text{m}}\right] = \frac{\mathcal{M}_{\text{corr}}\left[\text{Am}^2\right] - BG}{V_{\text{mag}}} \tag{5.6}$$

of the magnetic material, sometimes also indicated in μ_B/f.u., i.e. Bohr magneton per formula unit[8]. V_{mag} was determined from the thin film thickness multiplied by the area, measured using DinoLite digital microscopes.

Error specifications: For the VSM data evaluation, an error of $0.1\,\text{mm}^2$ was assumed on the sample area, 1 nm on the sample thickness, and the error of the correction factor F_{corr} estimated by calculation[9], typically amounting to approx. 2×10^{-3}.

Saturation magnetisation and saturation field

Saturation magnetisation M_{sat} and saturation field $\mu_0 H_{\text{sat}}$ were extracted from the in-plane $M(H)$ curves with the large field range ($\mu_0 H_{\text{max}} = 2\,\text{T}$): The saturation magnetisation was determined by averaging over $|M(|\mu_0 H| > 1\,\text{T})|$ for each in-plane $M(H)$ measurement. The error on the saturation magnetisation was determined by error propagation, taking into account the standard error on the measured moment recorded by the VSM, the error on the sample volume as well as the geometry correction factor. The saturation field was determined as the minimal absolute field value above which all absolute magnetisation values reach at least 98% of M_{sat} for each orientation with an error mainly determined by the field uncertainty (resolution) in the $M(H)$ measurements.

Hysteresis loop shape and in-plane anisotropy

The $M(H)$ measurements with the small field range ($\mu_0 H_{\text{max}} = 20\,\text{mT}$) were corrected with the corresponding geometry correction factors and the diamagnetic background correction obtained from the associated large-range $M(H)$ measurements. From these measurements, the loop shape, the remanence magnetisation and coercive field, as well as the loop closure field[10] were extracted.

7: Capping materials used in this work: Au, Al and Ti. Au is diamagnetic. Al and Ti are paramagnetic, but their oxides are diamagnetic. Since the Al and Ti capping layers are substantially oxidised and the non-oxidised part makes a relatively small volume contribution, a governing diamagnetic background was observed in all experiments.

8: Given by

$$M\left[\frac{\mu_B}{\text{f.u.}}\right] = M\left[\frac{\text{kA}}{\text{m}}\right] \cdot \frac{V_{\text{u.c.}}}{\mu_B \cdot N_{\text{f.u.}}} \tag{5.7}$$

where $V_{\text{u.c.}} = a^3$ is the volume of a unit cell with lattice parameter a and $N_{\text{f.u.}}$ the number of formula units per unit cell. $N_{\text{f.u.}} = 4$ for the Heusler compounds.

9: Correction factors were calculated for all combination of sample shapes with ±0.1 mm different lengths to the measured values. The maximum difference between all calculated correction factors was then used as an error.

10: The loop closure field signifies the absolute field value for fields above which the state of the sample's magnetisation is indifferent from the magnetic history, e.g. the field sweep direction in any field dependent measurement.

5.2 Ferromagnetic resonance (FMR) spectroscopy

Ferromagnetic resonance spectroscopy (FMR) is a powerful technique to study the characteristics of magnetisation dynamics in magnetic materials. The basic principle of FMR measurements is the resonant absorption of an alternating microwave field by the magnetic system of the sample. This resonant absorption is described by the dynamic susceptibility tensor

$$\hat{\chi}(\omega) = \frac{\gamma^2 M_S \mu_0}{(1+\alpha^2)\left[\omega_{res}^2 - \omega^2 + i\omega\cdot\Delta\omega_{res}\right]} \begin{pmatrix} \frac{\ell_{\varphi\varphi}}{M_S \sin^2(\theta_0)} + \frac{i\omega\alpha}{\gamma} & -\frac{\ell_{\theta\varphi}}{M_S \sin(\theta_0)} + \frac{i\omega}{\gamma} \\ -\frac{\ell_{\varphi\theta}}{M_S \sin(\theta_0)} - \frac{i\omega}{\gamma} & \frac{\ell_{\theta\theta}}{M_S} + \frac{i\omega\alpha}{\gamma} \end{pmatrix} \tag{5.8}$$

as introduced in chapter 4.2.2. Exemplary curves of the resulting real and imaginary part of the susceptibility parameter[11]

$$\chi_{\varphi\varphi}(\omega, H_{ext}) = \frac{\gamma\mu_0 M_S\left(\gamma\mu_0 H_{ext} + i\alpha\omega\right)}{(1+\alpha^2)\left[\omega_{res}^2 - \omega^2 + i\omega\cdot\Delta\omega_{res}\right]} = \frac{\omega_M(\omega_H + i\alpha\omega)}{(1+\alpha^2)\left[\omega_{res}^2 - \omega^2 + i\omega\cdot\Delta\omega_{res}\right]} \tag{5.10}$$

are shown in figure 5.2, calculated for typical values of a Co_2MnSi thin film. For $\omega \approx \omega_H$ and $\alpha \approx 0$, these curves can be approximated by Lorentz resonance curves [225] as is commonly used in data analysis for extracting the resonance frequency ω_{res} and resonance linewidth $\Delta\omega_{res}$. However, for materials with large saturation magnetisation as investigated in this work, the approximation by Lorentz resonance curves is imprecise and it is preferential to work with the susceptibility function given in equation 5.10.

Different experimental methods for probing the ferromagnetic resonance exist, which can be generally categorised by the static property: fixed-field measurements, often also referred to as *broadband-FMR (BB-FMR)* measurements as the microwave frequency is swept in this case [345, 346], and fixed-frequency measurements referred to as *field-sweep FMR* in this work, where the magnetic field is swept for fixed frequencies [263]. Given the dependence of the susceptibility tensor in equation 5.8 on the second derivatives of the total energy density, which is a function of the applied magnetic field, the fundamental difference between both measurement approaches is directly apparent: A spectroscopic experiment in the strict sense, i.e. with no perturbation of the probed magnetic state, is only realised in the BB-FMR approach [345] since the field-sweep FMR approach involves a variation in the energy of the system[12].

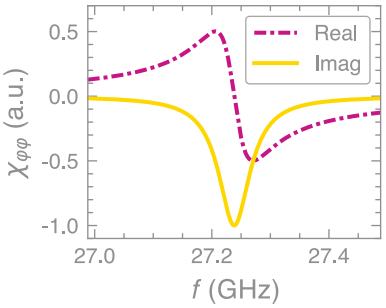

Figure 5.2: Calculated real and imaginary part of the normalised susceptibility tensor component $\chi_{\varphi\varphi}$ for the exemplary condition $\mu_0 M_S = 1.25\,T$, $\gamma = 28.75\,GHz/T$, $\mu_0 H_{ani} = 10\,mT$ and $\alpha = 0.001$ (assuming no non-Gilbert linewidth contribution), for an external field $\mu_0 H_{ext} = 500\,mT$.

11: Clearly, the susceptibility tensor given in equation 5.8 has the general form

$$\hat{\chi}(\omega) = \begin{pmatrix} \chi_{\varphi\varphi} & \chi_{\theta\varphi} \\ \chi_{\varphi\theta} & \chi_{\theta\theta} \end{pmatrix} \tag{5.9}$$

where the χ_{ij} are the susceptibility parameters linking the respective magnetisation component ($j = \varphi/\theta$ for in-plane / out-of-plane) to the harmonic pumping field components ($i = \varphi/\theta$ for in-plane / out-of-plane), see the derivation in chapter 4.2.2.

[225]: Gurevich et al. (1996), *Magnetization oscillations and waves*

[345]: Hoon et al. (1992), 'Field dependent rf absorption spectra of particulate magnetic recording materials'

[346]: Denysenkov et al. (2003), 'Broadband ferromagnetic resonance spectrometer'

[263]: Maksymov et al. (2015), 'Broadband stripline ferromagnetic resonance spectroscopy of ferromagnetic films, multilayers and nanostructures'

12: This is particularly important when investigating materials with magnetic textures, where a modification of the external field will directly imply a change in the magnetic configuration [347].

[347]: Schwarze et al. (2015), 'Universal helimagnon and skyrmion excitations in metallic, semiconducting and insulating chiral magnets'

5.2.1 Broadband-FMR: experimental setup and technique

Broadband-FMR measurement setups typically involve a vector network analyser (VNA) as a microwave source as well as a receiver [263]. In the rotational-field setup used in this work, a schematic of which is shown in figure 5.3, a Keysight N5225B PNA microwave network analyser providing a frequency range from 900 Hz to 50 GHz was used. Air cored coaxial radiofrequency (rf) cables with 2.4 mm dielectric diameter[13] were used to guide the microwave signal through end launch connectors to a coplanar waveguide (CPW), on which the sample was positioned. The external magnetic field was generated by a Caylar EA186 electromagnet equipped with a rotation base and variable pole shoe gap sizes allowing for a maximum field of up to ≈ 2.1 T. The applied field was recorded before and after each VNA measurement using a Lake Shore Cryotronics F41 teslameter equally attached to the rotation base.

For *in-plane FMR measurements (ip-FMR)*, i.e. with the magnetic field applied in the film plane, the sample holder hosting the full microwave circuit was fixed

13: For measurements which did not require the full frequency range, 2.92 mm cables were used providing lower losses for frequencies up to ≈ 25 GHz.

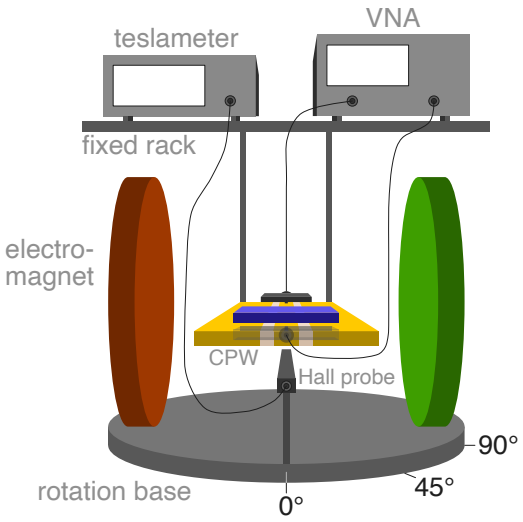

Figure 5.3: Schematic of the BB-FMR setup with rotating field option (not to scale). Electromagnet and Hall probe are mounted on a rotation base. The sample (blue) is placed upside down on the coplanar waveguide (yellow) mounted on a fixed sample holder. This setup geometry was used for measurements with the rotating field applied in the sample plane. For measurements with the field applied perpendicular to the film plane, a fixed CPW holder was mounted onto the rotation base (not shown).

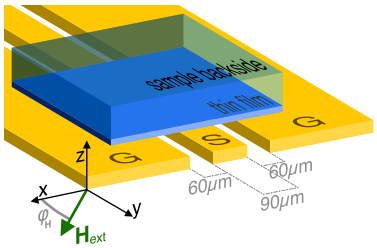

Figure 5.4: Schematic of the sample placed upside down on the CPW (not to scale). The field angle φ_H for in-plane rotational measurements is defined with respect to the x-axis perpendicular to the CPW line.

to a rack and decoupled from the rotation base, a sketch of this measurement configuration is shown in figure 5.3. Prior to each measurement, the sample holder hosting the microwave circuit was aligned at the rotation centre of the magnet rotation base. The Hall probe was centred at the sample position below the fixed sample holder (approx. 1 cm below the sample) in order to ensure free access upon rotation of the magnet.

For *out-of-plane FMR measurements (oop-FMR)*, i.e. with the static field applied perpendicular to the film plane, the CPW was centred in the field on a fixed mount attached to the magnet rotation base, and the Hall probe was positioned right next to the backside of the sample.

The sample was positioned upside down on the CPW, see figure 5.4, and kept in place with *Fixogum* glue applied across the backside. All utilised CPWs are impedance matched to 50 Ω and coated with a 1 − 1.5 µm thick layer of AZ5214E photo resist serving as a protective barrier to avoid scratches. To check on the presence of a significant radiative damping contribution, test measurements were performed with glass substrates of 150 µm or 200 µm thickness stacked between the CPW and the sample[14]. The absence of non-linear power processes was checked by analysing test measurements performed at various VNA output powers. Both tests were evaluated verifying unchanged resonance frequencies and resonance linewidths, and if not explicitly stated otherwise, the measurements shown in this thesis were performed without glass spacer and at 0 dBm (1 mW) VNA output power.

VNA measurements were carried out in transmission mode[15], i.e. each end of the CPW was connected (via end launch connectors and rf-cables) to one port of the VNA, probing the full scattering matrix

$$S = \begin{pmatrix} S_{11} & S_{12} \\ S_{21} & S_{22} \end{pmatrix} \tag{5.11}$$

of the microwave system. For every field, the VNA output frequency was swept allowing to record a spectral scan of the scattering matrix components' real and imaginary parts[16]. Each scattering parameter S_{xy} is described by $S_{xy} = V_{\text{meas}}/V_{\text{in}} \cdot e^{i\phi}$, i.e. the ratio of the voltage V_{meas} measured at VNA port $x = 1, 2$ to the voltage V_{in} inserted into the microwave circuit from VNA port $y = 1, 2$, multiplied by a delay factor accounting for an acquired phase ϕ. When loading the microwave circuit with a ferromagnetic sample, the measured voltage is modulated by the excited magnetisation precession [350]

14: As detailed in section 4.2.5 on page 82, radiative damping decreases with increasing spacing between sample and CPW.

15: It is equally possible to perform analogous measurements in reflection mode, as comparable sensitivities are typically reported for both modes see e.g. [348].

[348]: Counil et al. (2004), 'Spin wave contributions to the high-frequency magnetic response of thin films obtained with inductive methods'

16: Early versions of BB-FMR techniques involve the use of scalar network analysers, which do not allow for the decomposition in real and imaginary parts [345, 349].

[345]: Hoon et al. (1992), 'Field dependent rf absorption spectra of particulate magnetic recording materials'
[349]: Harward et al. (2011), 'A broadband ferromagnetic resonance spectrometer to measure thin films up to 70 GHz'

[350]: Maier-Flaig et al. (2018), 'Note: Derivative divide'

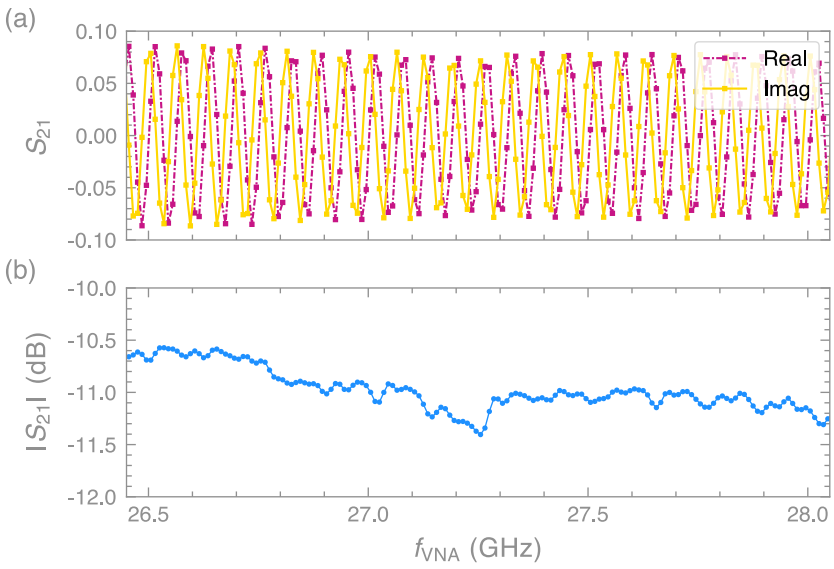

Figure 5.5: Exemplary raw S_{21} data around the ferromagnetic resonance point of a 20 nm Co_2MnSi thin film measured in the in-plane geometry at a static field of 500 mT. (a) Real and imaginary part and (b) magnitude of the complex S_{21} parameter. Little indication of the FMR induced resonant absorption of microwave power is visible. This data was acquired from the 20 nm Co_2MnSi thin film and is part of the measurements discussed in detail in chapter 6.

$$V_{\text{meas}}(\omega) = V^0_{\text{meas}}(\omega) \cdot [1 - i\omega A \cdot \chi(\omega, H_{\text{ext}})] \tag{5.12}$$

where the scaling factor A accounts for the coupling between the sample and the CPW, and $V^0_{\text{meas}}(\omega)$ denotes the measured voltage of the microwave circuit without the magnetic sample. The measured scattering parameter therefore contains a signal from the magnetic susceptibility showing the behaviour plotted above in figure 5.2, where under ideal circumstances the curve of the imaginary part corresponds to the typical absorption dip from the loss of microwave energy upon excitation of the FMR and the real part shows the related dispersion [351].

[351]: Kalarickal et al. (2006), 'Ferromagnetic resonance linewidth in metallic thin films'

Yet, the magnitude of the signal arising from the FMR is typically exceeded by the frequency dependent background signal of non-magnetic origin arising from variations in the impedance of the system [263], often fully masking the resonance curves. This is shown in figure 5.5 presenting a zoom-in on the raw data of a measurement corresponding to the calculated condition plotted in figure 5.2 above. The real and imaginary part of the complex S_{21} parameter exhibit oscillations governed by the frequency dependent phase $\phi(\omega)$, modulating the frequency dependent background $V^0_{\text{meas}}(\omega)$ which itself follows an exponential decay function as shown in figure 5.6.

[263]: Maksymov et al. (2015), 'Broadband stripline ferromagnetic resonance spectroscopy of ferromagnetic films, multilayers and nanostructures'

To limit the detection of the background signal arising from the parasitic magnetic distortions in the microwave setup, a pre-calibration of the microwave system is often performed in BB-FMR studies, typically done with a standardised calibration kit and connections by flexible microwave probes. Yet, a calibration does not circumvent the need for a background removal, as it only removes the background arising from the microwave components up to the probe tips, and hence cannot account for the microwave circuit between the probe contacts. In addition, the calibration approach introduces an additional source of error assuming the repeatability of the microwave connections at the probe tips. Moreover, the calibration is not guaranteed for long measurement durations due to the VNA's strong dependence on temperature stability [352].

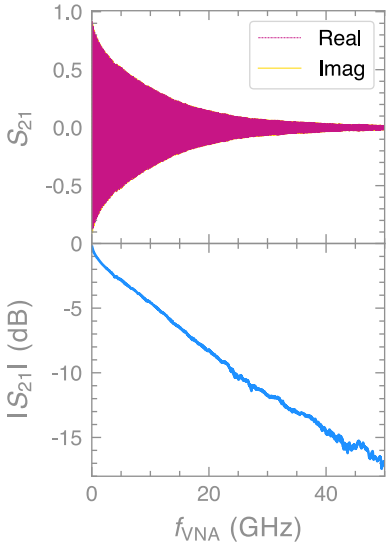

Figure 5.6: Full spectral data set, a cut-out of which is shown in figure 5.5, presenting the frequency dependent background $V^0_{\text{meas}}(\omega)$ of the complex S_{21} parameter.

[352]: Bystrov et al. (2022), 'Analysis of Vector Network Analyzer Thermal Drift Error'

Therefore, post-processing the recorded S-parameter data is a crucial step in extracting the magnetic susceptibility. This will be addressed in the following subsection.

5.2.2 Non-calibrated broadband-FMR: effect of the data analysis procedure on the resonance linewidth

This subsection will briefly present the results of a comparative study of various post-processing methods for the analysis of non-calibrated BB-FMR data.

Post-processing of the data acquired from BB-FMR measurements is commonly performed in studies throughout literature, see e.g. [264, 348, 350, 351, 353–357], aiming at accessing the signal related to the magnetic susceptibility and removing the above introduced complex frequency dependent background. Given the vast options for setup details and the measurement protocol[17], various data evaluation methods can be found in literature. Most commonly, a single S-parameter is investigated [350, 351, 354, 356, 357], but sophisticated protocols involving full scattering matrix measurements can yield precise corrections accounting for instance for microwave reflections[18] in the system [355]. Typical approaches rely on a pre-calibration followed by data corrections using separate reference measurements recorded at off-resonant fields [351, 357], or recorded with fields applied perpendicular to the CPW line (i.e. parallel to the x-direction in figure 5.4) [355, 356]. Yet in a recent note by Maier-Flaig *et al.* [350] a method for the analysis of BB-FMR measurements was introduced which neither requires a pre-calibration nor a separate reference measurement.

The various measurement protocols and data evaluation methods naturally trigger the question on the comparability and precision of the extracted parameters. Indeed, in a study by Bilzer *et al.* [355] the precise extraction of the ferromagnetic resonance frequency is found to be hardly influenced by the choice of data evaluation procedure, whereas a significant dependence has been reported for the extracted resonance linewidths, when comparing their own approach with the procedures proposed by Kalarickal *et al.* [351] and Kuanr *et al.* [264]. Differences in the extracted linewidths amount up to 10 % [355], making the choice of data evaluation crucial for the analysis of the resonance linewidth behaviour[19] especially when aiming to extract the magnetic damping.

In particular, an atypical non-Gilbert like resonance linewidth behaviour with the same signature as commonly attributed to inhomogeneous linewidth contributions [264, 348, 358], can be systematically introduced by the data post-processing especially when working with modulations of similar magnitude as the resonance linewidths of the system under investigation [350]. To avoid a false interpretation of potential erroneous features systematically introduced by the data post-processing, a brief comparative study was therefore carried out, evaluating the results from non-calibrated BB-FMR measurements through different post-processing methods. A focus is set on the comparison of the *derivative divide* method [350] to common off-resonant reference removal approaches similar to the ones employed in [351, 356, 357].

Methodology of the comparative evaluation

The study is performed on two test data sets both corresponding to typical S_{21} parameter data from BB-FMR measurements in a non-calibrated VNA setup: The first test data set is measured from a $Co_2MnSi/MgO/Al$ thin film sample[20]. The second test data set is artificially constructed, in order to compare the results extracted through the post-processing algorithm to the known parameters.

[264]: Kuanr et al. (2005), 'Narrowing of the frequency-linewidth in structured magnetic strips'
[348]: Counil et al. (2004), 'Spin wave contributions to the high-frequency magnetic response of thin films obtained with inductive methods'
[350]: Maier-Flaig et al. (2018), 'Note: Derivative divide'
[351]: Kalarickal et al. (2006), 'Ferromagnetic resonance linewidth in metallic thin films'
[353]: Barry (1986), 'A Broad-Band, Automated, Stripline Technique for the Simultaneous Measurement of Complex Permittivity and Permeability'
[354]: Pain et al. (1999), 'An improved permeameter for thin film measurements up to 6 GHz'
[355]: Bilzer et al. (2007), 'Vector network analyzer ferromagnetic resonance of thin films on coplanar waveguides'
[356]: Bilzer et al. (2008), 'Open-Circuit One-Port Network Analyzer Ferromagnetic Resonance'
[357]: Kennewell et al. (2010), 'Magnetization pinning at a Py/Co interface measured using broadband inductive magnetometry'

17: Calibration procedures, recording of unloaded circuit references, recording of off-resonant field references, measurement of single matrix parameters or full scattering matrix, ...

18: Microwave reflections typically occur at abrupt changes of the circuit parameters, e.g. cable connectors, contacts, CPW line borders (in the propagation direction), sample borders (in the propagation direction).

19: Naturally also coming with the need to specify the chosen data analysis procedure, which is sadly not always indicated [358].

[358]: Mosendz et al. (2006), 'Spin dynamics at low microwave frequencies in crystalline Fe ultrathin film double layers using co-planar transmission lines'

20: Sample S1.4 in table 2.1.

Three data processing approaches are applied to both data sets in order to isolate the signal originating from the magnetic susceptibility of the thin film under investigation from the background signal of non-magnetic origin. As detailed in above section 5.2.1, the recorded signal is described by

$$S_{21}(\omega, H_{\text{ext}}) = \frac{V_{\text{meas}}}{V_{\text{in}}} \cdot e^{i\phi} = \frac{V^0_{\text{meas}}(\omega) \cdot [1 - i\omega A \cdot \chi(\omega, H_{\text{ext}})]}{V_{\text{in}}} \cdot e^{i\phi(\omega)} \quad (5.13)$$

for a fixed field H_{ext}. Consequently, all approaches share the common feature of requiring the division by a second S_{21} spectrum[21] in order to remove the frequency dependent phase factor $e^{i\phi(\omega)}$ as well as the background signal $V^0_{\text{meas}}(\omega)/V_{\text{in}}$. The difference mainly lies in the choice of the reference spectrum, i.e. choosing a fixed reference or an equidistant moving reference method, as well as in the reference distance in the latter case.

The comparative study was thoroughly carried out by analysing 2080 spectra, spanning a field range[22] of $0 - 1.04\,\text{T}$, for each test data set and evaluating the best fits and subsequent fit results through the different applied approaches. The full data evaluation was carried out 10 times per data set: Twice for the derivative divide approach (using two different fit functions), and four times for each of the other approaches (using different off-resonant moving reference distances). The methods were evaluated with a particular attention on a potential resonance profile distortion determining the suitability of the procedures for a non-falsified magnetic damping analysis. As a main result of this comparative study, the *derivative divide* procedure is determined to be the best suitable approach for the further data treatment due to its superior background suppression linked to the maximal proximity of the reference[23]. However, the field step size set to $\Delta H = 1\,\text{mT}$ in the measurements is found to be a limiting issue for the analysis of the Co_2MnSi resonance linewidths through the *derivative divide* procedure. Hence, caution needs to be employed when interpreting the extracted resonance linewidths and as this is particularly relevant for the study in chapter 6, a detailed discussion on the peculiarities of the *derivative divide* procedure will be presented in the following[24].

21: Precisely, the background removal approaches follow the form $(S^A_{xy} - S^B_{xy})/S^C_{xy}$, where often $S^B_{xy} = S^C_{xy}$ is the reference and S^A_{xy} is the spectrum taken at the field of interest (but not always, see the derivative divide procedure on page 101).

22: Translates to a resonance frequency range of $\sim 0 - 45\,\text{GHz}$.

23: Concerning temporal drifts, as well as all other defining parameters.

24: More details on the construction of the test data set, the results from the other two approaches and the comparative evaluation can be found in the appendix chapter E.

Derivative divide background removal

Maier-Flaig *et al.* [350] introduced the *derivative divide* background removal method, where the corrected signal is described by

$$\mathrm{d_D}S_{21}(\omega, H) := \frac{S_{21}(\omega, H + \Delta H^{\pm}) - S_{21}(\omega, H - \Delta H^{\pm})}{S_{21}(\omega, H) \cdot \Delta H^{\pm}} \quad (5.14)$$

$$\approx -i\omega\tilde{A} \cdot \frac{\mathrm{d}\chi}{\mathrm{d}\omega} \quad (5.15)$$

where $\mathrm{d_D}$ stands for derivative divide and $\Delta H^{\pm}$ is the finite modulation field step width[25]. This method does not require a calibration prior to the measurement, and due to the moving reference procedure[26] is not sensitive to background drifts due to temperature fluctuations.

Note: For improved signal-to-noise ratios, the procedure can be modified to

$$\mathrm{d_D}S_{21}(\omega, H_{\text{ext}}) = \frac{\sum_{n=1}^{N} S_{21}(\omega, H_{\text{ext}} + n \cdot \Delta H^{\pm}) - \sum_{n=1}^{N} S_{21}(\omega, H_{\text{ext}} - n \cdot \Delta H^{\pm})}{S_{21}(\omega, H_{\text{ext}}) \cdot \sum_{n=1}^{N} n \cdot \Delta H^{\pm}} \quad (5.16)$$

extending equation 5.14 by the sums over N neighbouring spectra. This increases signal modulation and must not be used for extracting the linewidths[27].

[350]: Maier-Flaig et al. (2018), 'Note: Derivative divide'

25: To avoid confusion: No real field modulation is performed in the measurements. $\Delta H^{\pm}$ basically indicates the "reference distance" between the respective VNA spectra.

26: The term *moving reference* refers to the fact that the field difference between all considered spectra is kept constant. Contrary to this, *fixed reference* shall denote the use of a reference taken at a fixed field.

27: In this work, N was set to $N = 4$ only for the automated peak detection. $N = 1$ was set for the analysis (spectral $\mathrm{d_D}S_{21}$ curve fits) of the fundamental mode, corresponding exactly to equation 5.14. $N = 2$ was set for the spectral $\mathrm{d_D}S_{21}$ curve fits of higher order PSSW modes for an increased precision in the resonance position ω_{res} (no linewidth analysis for PSSWs).

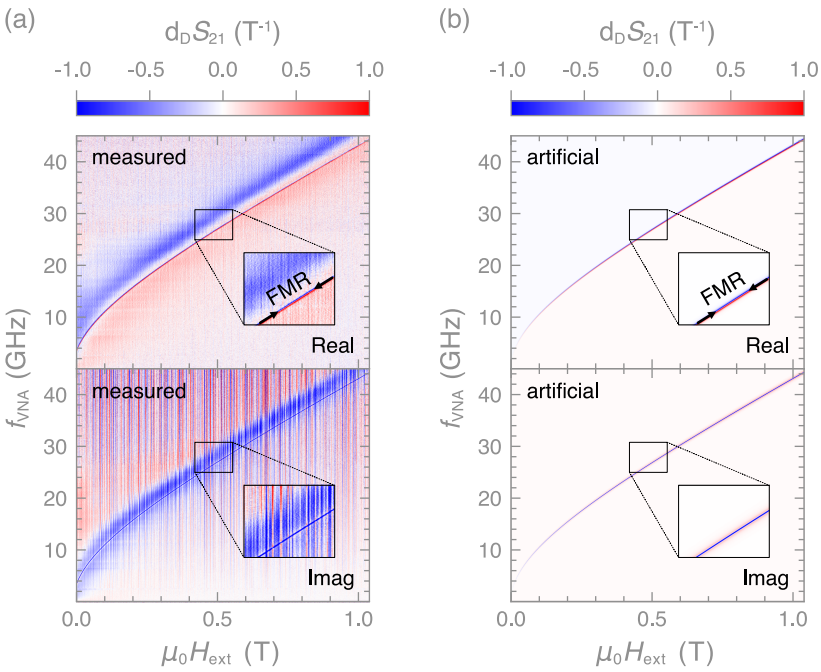

Figure 5.7: Full data sets of (a) the measured data and (b) the artificial test data after processing the S_{21} parameter with derivative divide [350] using a modulation amplitude of $\Delta H^{\pm} = 1\,\mathrm{mT}$ in equation 5.15. The narrow resonance is now clearly visible as opposed to the case of the raw data shown in figure E.4. In the measured data set, the resonance is shadowed by a broader background resonance, which does not appear in the artificial data set. An exemplary spectrum from each data set is shown in figure 5.9.

[350]: Maier-Flaig et al. (2018), 'Note: Derivative divide'

Figure 5.7 shows the resulting spectral data set after the derivative divide background removal procedure performed with a modulation[28] step size $\Delta H^{\pm} = 1\,\mathrm{mT}$ on the measured data (a) as well as the artificial test data (b). As can be seen in figure 5.7 (a), the procedure clearly removes the frequency dependent phase oscillation and a significant part of the background, resulting in an improved signal-to-noise ratio for the narrow FMR line pointed out in the inset. Yet, a broad field-dependent background remains, shadowing the resonance at higher frequencies.

28: This can be translated to a frequency modulation, as shown in figure 5.8.

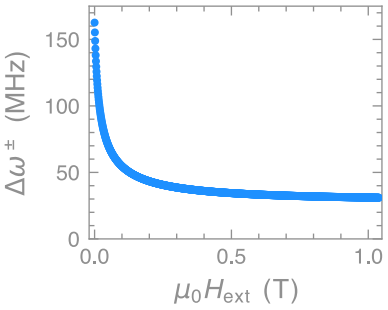

Figure 5.8: Frequency modulation amplitude $\Delta\omega^{\pm} = \Delta H^{\pm} \cdot \frac{\partial \omega_{res}}{\partial H_{ext}}$ corresponding to the fixed field modulation step size $\Delta H^{\pm} = 1\,\mathrm{mT}$ used in measured data as well as artificial test data. $\Delta\omega^{\pm}$ calculated for a Co_2MnSi sample with $\mu_0 M_S = 1.25\,\mathrm{T}$, $\gamma = 28.75\,\mathrm{GHz/T}$ and $\mu_0 H_{ani} = 10\,\mathrm{mT}$.

Exemplary spectra of both data sets are shown in figure 5.9 for an external field of $\mu_0 H_{ext} = 500\,\mathrm{mT}$[29], where the narrow sharp peaks correspond to the FMR signal. In the spectral plot of the measured data in figure 5.9 (a), the field-dependent background shows the shape of a broad resonance, which moves with the FMR and corresponds to the signal perceived as a blue shadow particularly in the real part in figure 5.7 (a). For the construction of the artificial test data shown in figure 5.9 (b), each spectrum was set to have the exact same background spectrum[30] and, consequently, the background is fully removed in all spectra as can be seen in figure 5.7 (b).

29: Matching the conditions in figure 5.2, figure 5.5, and figure 5.6.

30: See the data construction details on page 253.

[350]: Maier-Flaig et al. (2018), 'Note: Derivative divide'

Resonance curve fitting and parameter extraction

The ultimate goal of the FMR analysis is the extraction of the key parameters defining the magnetisation dynamics, for which the resonance frequency and linewidth need to be determined from each spectrum. Since this background removal approach does not work with off-resonant corrections but instead forms approximately the derivative of the spectra, the frequency derivative of the susceptibility function as given in equation 5.15 is an obvious choice for the resonance fit function. Yet, as pointed out in [350], the approximation of $d_D S_{21} \sim \frac{d\chi}{d\omega}$ as given in equation 5.15 is only true for small field steps, i.e. for $\Delta\omega^{\pm} = \Delta H^{\pm} \cdot \frac{\partial \omega_{res}}{\partial H_{ext}} \ll \Delta\omega_{res}$, otherwise the procedure will induce an over-modulation leading to a distortion of the resonance curves [350] and consequently resulting in an artificial enhancement of the extracted resonance linewidths [359].

[359]: Weiler et al. (2017), '*Supplemental information:* Helimagnon Resonances in an Intrinsic Chiral Magnonic Crystal'

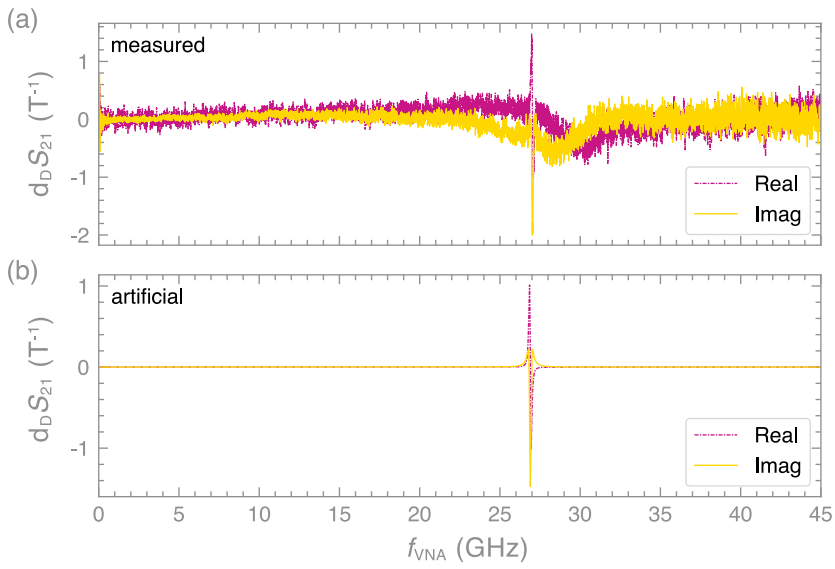

Figure 5.9: Exemplary derivative divide spectra for $\mu_0 H_{ext} = 500\,\mathrm{mT}$ of (a) the measured data and (b) the artificial test data. The phase oscillation and a significant part of the frequency dependent background present in the corresponding spectra of the raw data, see figures 5.5 and 5.6 on page 99, are removed. The remaining background in the measured data set has the signature of a broad resonance, while the background in the artificial test data set is fully removed.

Indeed, the consideration of the resonance curve distortion is of particular importance for samples with large saturation magnetisation and low magnetic damping (and low inhomogeneous linewidth), as is the case of the Co_2Mn-based Heusler compounds used in this work: For Co_2MnSi for instance, the modulation step size $\Delta H^{\pm} = 1\,\mathrm{mT}$ corresponds to a frequency modulation amplitude between approx. 25 MHz and 175 MHz for fields up to 1.04 T applied in the film plane, see figure 5.8.

To account for this resonance curve distortion in the case of $\Delta\omega^{\pm} \approx \Delta\omega_{res}$, Maier-Flaig *et al.* [350] suggest not to use the derivative of the susceptibility fitting a formula

$$\mathrm{d_D}S_{21}(\omega, H) = -i\omega\tilde{A} \cdot \mathrm{CDQ}(\omega, H_{ext}) \tag{5.17}$$

for a quantitative analysis of the $\mathrm{d_D}S_{21}$ spectra. $\mathrm{CDQ}(\omega, H_{ext})$ stands for the central difference quotient

$$\mathrm{CDQ}(\omega, H_{ext}) = \frac{\chi(\omega + \Delta\omega^{\pm}, H_{ext}) - \chi(\omega - \Delta\omega^{\pm}, H_{ext})}{2 \cdot \Delta\omega^{\pm}} \tag{5.18}$$

which is used instead of the frequency derivative of the susceptibility

$$\frac{\mathrm{d}\chi}{\mathrm{d}\omega}(\omega, H_{ext}) = \frac{\gamma\mu_0 M_S \left(2\gamma\mu_0 H_{ext} \cdot \omega + i\alpha\left(\omega_{res}^2 + \omega^2\right) - i\gamma\mu_0 H_{ext} \cdot \Delta\omega_{res}\right)}{(1+\alpha^2) \cdot \left[\omega_{res}^2 - \omega^2 + i\omega \cdot \Delta\omega_{res}\right]^2} \tag{5.19}$$

in equation 5.15. The qualitative difference between the resulting lineshapes is shown in figure 5.10, where the calculated real and imaginary part of the susceptibility $\chi(\omega, H_{ext})$ from equation 5.10, its derivative $\frac{\mathrm{d}\chi}{\mathrm{d}\omega}(\omega, H_{ext})$, as well as the central difference quotient $\mathrm{CDQ}(\omega, H_{ext})$ are compared. The CDQ line shape resembles the derivative of the susceptibility $\frac{\mathrm{d}\chi}{\mathrm{d}\omega}$, but yields a broader resonance width for the same parameters.

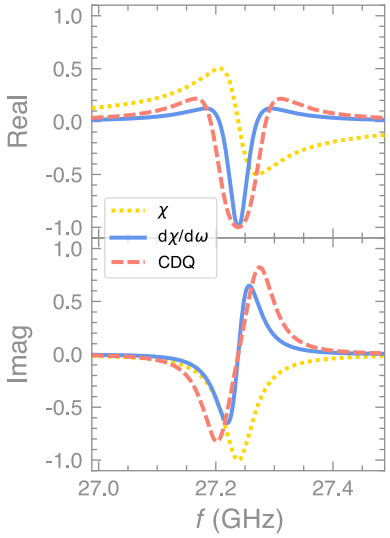

Figure 5.10: Calculated real and imaginary part of the normalised susceptibility function χ, its derivative $d\chi/d\omega$ and the central difference quotient CDQ. All curves calculated for the exemplary condition $\mu_0 M_S = 1.25\,\mathrm{T}$, $\gamma = 28.75\,\mathrm{GHz/T}$, $\mu_0 H_{ani} = 10\,\mathrm{mT}$, $\alpha = 0.001$ and $\Delta\omega_0 = 0$, for an external field $\mu_0 H_{ext} = 500\,\mathrm{mT}$.

Given the comparably large frequency modulation amplitude especially for small fields as seen in figure 5.8 and the rather narrow resonance curves, both fit functions were applied for a comparison on the measured data as well as the artificial data in this study.

Exemplary cut-outs of the data around the resonances for selected fields of $\mu_0 H_{ext} = 25\,\mathrm{mT}$, 50 mT and 500 mT are shown in figure 5.11 together with the respective fit curves. For an applied field of $\mu_0 H_{ext} = 500\,\mathrm{mT}$ as shown in

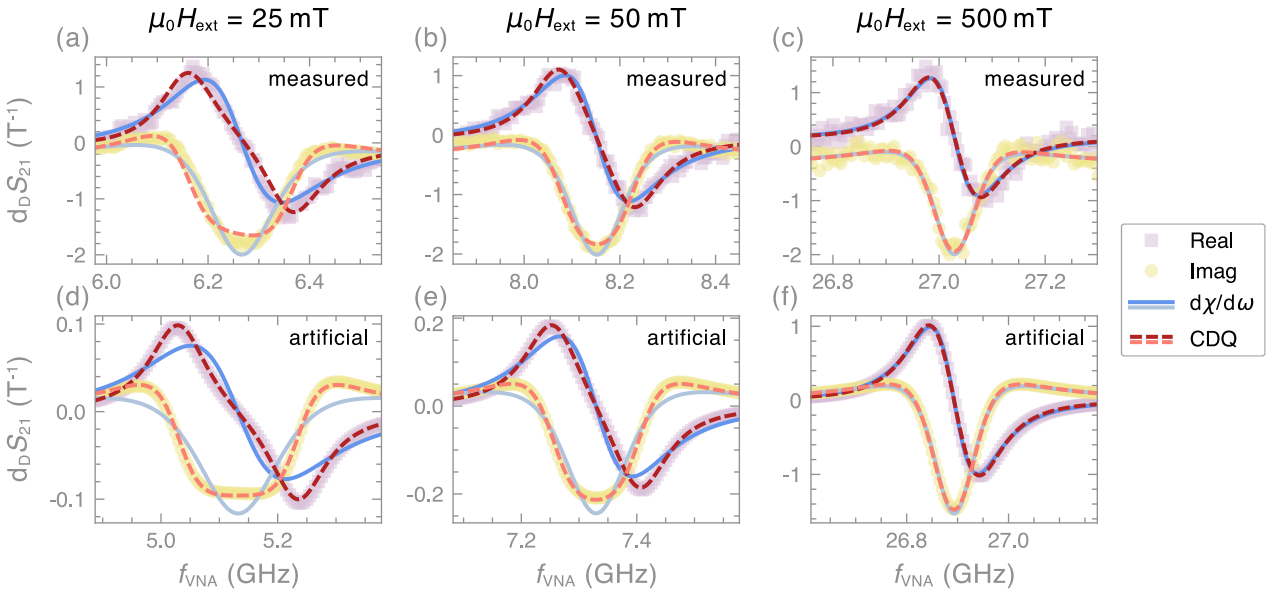

Figure 5.11: Exemplary fits of selected resonance curves in the measured as well as the artificial data set. Two fit functions are compared, i.e. equation 5.17 is used either with the central difference quotient (CDQ) from equation 5.18 (dashed red lines) or instead with the derivative of the susceptibility ($d\chi/d\omega$) equation 5.19 (straight blue lines). The functions are recalled in the margin on this page.

figure 5.11 (c) and (f), the data can be described by the function considering the derivative of the susceptibility and hardly any difference is obtained compared to the curves using the central difference quotient. Towards lower fields on the other hand, using $\mathrm{d}\chi/\mathrm{d}\omega$ becomes less suitable for describing the distorted data as is most prominent for $\mu_0 H_{\mathrm{ext}} = 25\,\mathrm{mT}$ in figure 5.11 (a) and (d), but the function using the central difference quotient does indeed account for the distortion and thus yields improved fits.

The parameters extracted with both fitting approaches on both data sets are shown in figure 5.12: (a) and (b) show the resonance frequencies (Kittel plots) obtained from the measured and artificial data set respectively, and the corresponding resonance linewidths are presented in (c) and (d). The choice of the fit function used on the derivative divide data clearly yields little influence on the extracted resonance frequency in figure 5.12 (a) and (b), which aligns with the conclusion drawn by Bilzer *et al.* [355] based on their comparison of FMR analysis approaches on calibrated FMR data.

[355]: Bilzer et al. (2007), 'Vector network analyzer ferromagnetic resonance of thin films on coplanar waveguides'

However, significant differences are obtained on the extracted resonance linewidths shown in figure 5.12 (c) and (d): Using the derivative of the susceptibility $\mathrm{d}\chi/\mathrm{d}\omega$ clearly yields erroneous linewidth results (blue data points) on both data sets, which mimick the $1/f$ behaviour of the frequency modulation amplitude[31] for frequencies below 20 GHz. As the artificial test data set was constructed to follow $\Delta\omega_{\mathrm{res}} = \alpha\gamma \cdot (2\,(H_{\mathrm{ext}} + H_{\mathrm{ani}}) + M_{\mathrm{S}}) + \Delta\omega_0$ with $\alpha = 7.5 \cdot 10^{-4}$ and $\Delta\omega_0 = 45\,\mathrm{MHz}$, the $1/f$ behaviour can clearly be identified as an effect of the post-processing i.e. the increasingly poor fit with obtained with $\mathrm{d}\chi/\mathrm{d}\omega$ towards small fields.

31: See discussion around figure 5.8 on page 102.

As proposed by Maier-Flaig *et al.* [350], the central difference quotient (CDQ) allows to account for the overmodulation and the improved fits in figure 5.11 yield more realistic results on the extracted data (red data points) in figure 5.12: The $1/f$ behaviour imposed by the modulation amplitude $\Delta\omega^{\pm}$ is not mimicked by the resonance linewidths extracted from the artificially constructed test data set in figure 5.12 (d). Still, a strange modulation is obtained in the measured data set even when using the CDQ (red data points) in figure 5.12 (c), which again coincides with the rise of the frequency modulation amplitude.

[350]: Maier-Flaig et al. (2018), 'Note: Derivative divide'

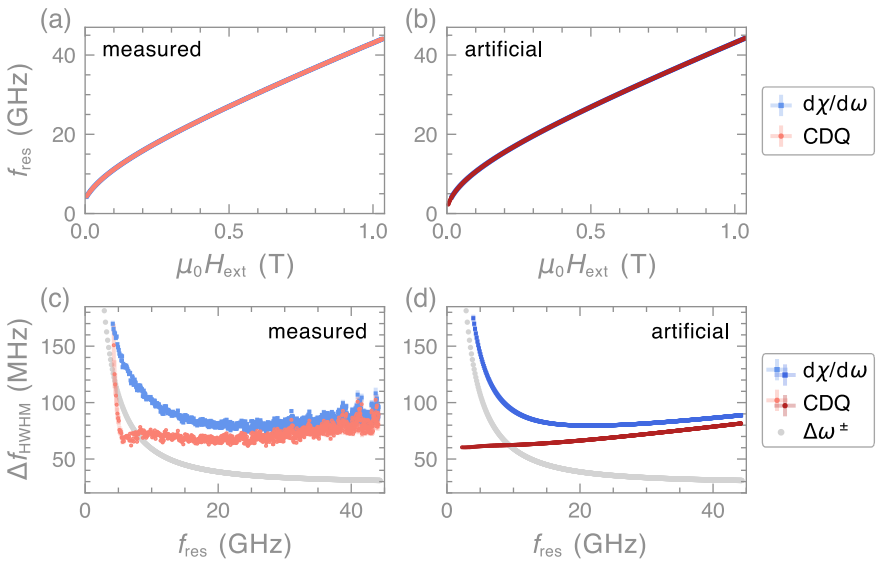

Figure 5.12: Results obtained from the derivative divide procedure for the measured data (a) and (c) as well as the artificial data (b) and (d). In addition, the modulation amplitude $\Delta\omega^{\pm} = \Delta H^{\pm} \cdot \frac{\partial \omega_{res}}{\partial H_{ext}}$ is shown in (c) and (d). The resonance curve distortion leads to clearly erroneous linewidth results when using the derivative of the susceptibility dχ/dω, which present a similar behaviour to the frequency modulation amplitude $\Delta\omega^{\pm}$, i.e. approximately a $1/f$ curve. The results obtained from using the central difference quotient (CDQ) yield more credible results on this scale, but a zoom-in shows unexpected behaviour for the CDQ too, as is presented in figure 5.13.

A zoom-in on the linewidth results from both data sets (regrouped by the fitting functions) is shown in figure 5.13, where additionally the set linewidth $\Delta\omega^{set}$ for the construction of the artificial data set is plotted in black for a comparison. Comparing the parameters extracted from the processed artificial data set (dark coloured blue/red points) to the artificially set linewidth $\Delta\omega^{set}$, the dχ/dω can clearly not reproduce the set linewidth even for the high frequency data (compare the dark blue points in figure 5.13 (a) with the black line), whereas the CDQ yields a decent reproduction (compare the dark red points with the black line in figure 5.13 (b)) especially for $f_{res} \gtrsim 25$ GHz. Yet for the smaller frequencies, particularly for $f_{res} \lesssim 20$ GHz, the zoom-in presented in figure 5.13 (b) still shows an unexpected modulation even for the use of the CDQ where the extracted resonance linewidths present a local maximum / shoulder. Again, the comparison with the artificially set linewidth (black line) allows to identify this as a feature originating from the data processing, which is underlined by the coincidence with the significant rise of the modulation frequency (light grey points in the background) in this frequency range.

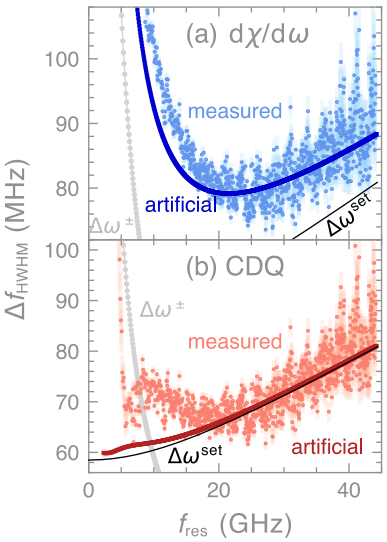

Figure 5.13: Zoom-in on the linewidth results presented in figure 5.12, regrouped by the fit function used with (a) the derivative of the susceptibility dχ/dω and (b) the central difference quotient CDQ results. As in figure 5.12, the bold colours correspond to the artificial data set, and the light colours correspond to the measured data set. The light grey points correspond to the modulation amplitude $\Delta\omega^{\pm}$. In addition, the artificially fixed linewidth $\Delta\omega^{set}$ is plotted as a black line.

In fact, the approximate "cut-off" frequency of $\sim 20-25$ GHz is not arbitrary but roughly corresponds to the frequency below which the resonance frequency in figure 5.12 (a/b) cannot be approximated by a linear function of the applied field anymore. As the derivative divide construction is based on the subtraction of spectra with fixed field steps, the non-linearity of the Kittel curve naturally yields an increasing modulation amplitude towards small fields. Additionally, the "problem" is enhanced by the naturally decreasing resonance linewidth for decreasing resonance frequencies[32], i.e. by the narrower resonance curves for lower fields.

Therefore, the effect of an overmodulation is of particular importance for the case of in-plane FMR data of materials with a large saturation magnetisation M_S and low magnetic damping, as narrow resonance linewidths can be expected with a significant non-linearity of the Kittel persisting over a large frequency range[33].

Nevertheless, the superior results on the background suppression make the derivative divide procedure the favourable approach for the further data analysis, especially for the high frequency data which principally is the most important for the extraction of the Gilbert damping parameter. Yet, it is noted that special caution needs to be employed for the interpretation of the inhomogeneous linewidth in the subsequent analysis in chapter 6.

32: At least for the linewidth contributions of viscous origin (Gilbert damping), scaling with the resonance frequency.

33: In principle, the modulation could be reduced by refining the field modulation step size, i.e. $\Delta H^{\pm}$. As the smallest modulation step possible for this measurement was already chosen here, i.e. $\Delta H^{\pm} = 1$ mT, the field step size would need to be further reduced. Yet when wanting to scan large field ranges (particularly for the materials with large M_S and low damping), this comes with the disadvantage of increasing the measurement time and the amount of collected data significantly.

5.3 Magneto-optical Kerr effect (MOKE) magnetometry

The magneto optical Kerr effect (MOKE), i.e. the change of the polarisation of light upon reflection from a magnetic sample as introduced in chapter 4.3, has been exploited for the study of various phenomena in magnetic materials since the eponymous reports by Kerr in the 1870s [293, 294]. In this work, the MOKE effect was mainly used in classical MOKE magnetometry, that is the investigation of the MOKE effect of the samples as a function of an externally applied magnetic field.

[293]: Kerr (1877), 'XLIII. *On rotation of the plane of polarization by reflection from the pole of a magnet*'
[294]: Kerr (1878), 'XXIV. *On reflection of polarized light from the equatorial surface of a magnet*'

5.3.1 Measurement principle and experimental setup

The measurement principle of MOKE magnetometry is fairly simple: The sample under investigation is placed in a magnetic field, and the change of polarisation of light[34] is recorded as a function of the applied field. To this aim, the incoming light is polarised, typically a linear polarisation is chosen, as then upon reflection on the magnetic sample a rotation and ellipticity are acquired. These can be measured from the change of the intensities of the reflected light decomposed along two orthogonal polarisation directions, and are in a first approximation[35] directly proportional to the magnetisation, thus the recording of the change of polarisation corresponds to a magnetometry measurement.

34: Light in the visible to infrared spectrum is typically used as the corresponding frequencies are in the THz range, and thus the irradiation does not excite magnetisation oscillations - at least in ferromagnetic samples where excitations of the magnetic system are typically in the GHz range (hence studied by microwave techniques as the FMR spectroscopy described above).

35: I.e. neglecting quadratic or higher order effects, see chapter 4.3 on pages 85-90.

MOKE magnetometry vs. VSM magnetometry

In MOKE magnetometry, hysteresis curves are recorded analogously to the VSM measurements described in section 5.1 above. Yet, contrary to VSM measurements, MOKE magnetometry is no absolute measure of the magnetic moment, but a measure of real and/or imaginary part of the complex Kerr amplitude

$$\Phi_{s/p} = \theta_{s/p} + i\ell_{s/p} \tag{5.20}$$

i.e. Kerr rotation $\theta_{s/p}$ and Kerr ellipticity[36] $\ell_{s/p}$ for s and p polarised light. As introduced in equations 4.80 and 4.83, these are functions of the magneto-optical tensor and therefore the measurements additionally depend on the utilised wavelength, crystal symmetry, and angle of observation. Moreover, as the direct proportionality $\Phi_{s/p} \sim M$ is only an approximation resulting from a series expansion, the hysteresis loops recorded in MOKE magnetometry can show additional symmetric and anti-symmetric contributions in the case of significant higher order magneto-optical effects.

36: The uncommon notation as $\ell_{s/p}$ instead of the more common $\varepsilon_{s/p}$ was introduced in chapter 4 on page 88 in order to avoid confusion with the permittivity tensor elements.

Setup geometry

The magneto-optical tensor[37] simplifies for an alignment of the magnetisation with the cartesian coordinate system defined by the incidence plane of light and the reflective sample surface. As a result, the setup geometries with an according field alignment are most common in MOKE studies and are usually indicated as LMOKE, TMOKE and PMOKE. A schematic of the three geometries is shown in figure 5.14: LMOKE and TMOKE denote the effects for the magnetisation lying in the film plane and oriented in (longitudinal) or perpendicular to (transverse) the incidence plane of light respectively, PMOKE stands for the polar effect where the magnetisation is pointing perpendicular

37: See equation 4.76 (p.88) for the linear effects and equation 4.79 (p.88) for the quadratic effects.

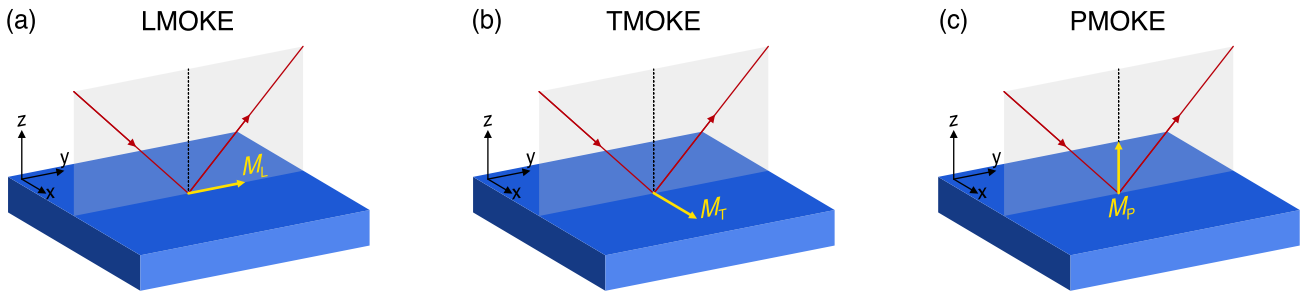

Figure 5.14: Characteristic MOKE geometries LMOKE, TMOKE and PMOKE, indicating the orientation of the magnetisation with respect to the reflective sample surface and the incidence plane of light: (a) longitudinal, (b) transverse and (c) polar orientation respectively. Figure inspired by a similar schematic in [102].

to the sample surface. The MOKE effect has a different signature for each geometry, notable determined by the magneto-optical tensor and the reflection matrix for *s* and *p* polarised light. The latter becomes diagonal for the transverse geometry, resulting in only an intensity change for p-polarised light and no influence on s-polarised light, while the longitudinal and polar geometry result in a mixing of the two components leading to a change of polarisation[38]. Therefore, LMOKE, TMOKE and PMOKE are often indicated as independent effects in literature, which is not to be confused with a different micromagnetic origin.

The measurements analysed in this work[39] were performed on a typical MOKE magnetometry setup, a schematic of which is shown in figure 5.15. The setup is mounted in the LMOKE geometry, i.e. the magnetic field provided by an electromagnet is aligned with the incidence plane of light. The sample is positioned on a rotatable plate centred in the magnetic field, allowing for a rotational study of the LMOKE as a function of the crystallographic orientation. The light is provided by a NKT photonics SuperK EXTREME supercontinuum laser, a tuneable laser providing output in a wavelength range of $\lambda \approx 550\,\text{nm} - 900\,\text{nm}$[40] which enables wavelength dependent magneto-optical studies. The laser beam is coupled into an optical rack mounted at an angle of incidence of 35° to the sample plane. A polariser and collimating lens are mounted on the optical rack, in order to focus the beam to the sample surface and obtain s-polarised light. After reflection from the sample, the beam is focused into a rotatable detection unit, consisting of a Wollaston prism and a 2-diode detector. The Wollaston prism separates the beam into two components of orthogonal polarisation with intensities I_1 and I_2 which are detected by the two photodiodes in the rotatable detection unit.

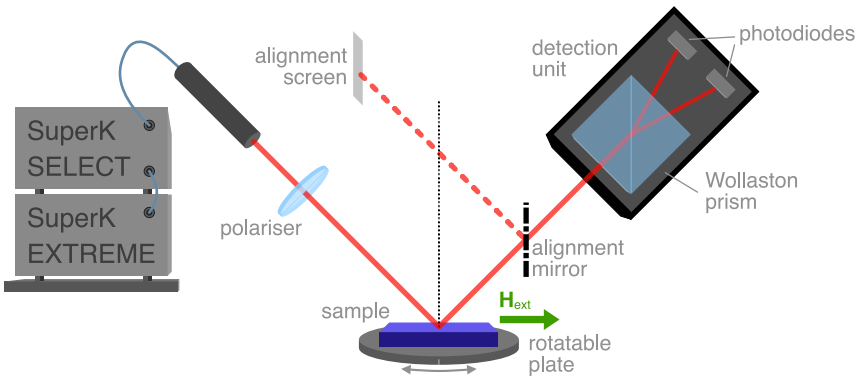

Figure 5.15: Simplified schematic of the setup used in this work (not to scale). For the alignment procedure, a mirror is inserted at the indicated position and hence the beam does not continue to the detection unit, but is reflected along the dashed line onto an alignment screen. Figure inspired by a similar schematic in [94].

[102]: Silber (2019), 'Quadratic magnetooptic Kerr effect spectroscopy of magnetic thin films with cubic crystal structure'

38: Further details can be found in [102], where table 1.1 lists the reflection matrices for the different geometries.

39: LMOKE measurements presented in this work were carried out by Nicolas Fermon from the école normale supérieure Paris-Saclay within the framework of a master research project [360] supervised by the author of this work. The analysis discussed in chapter 7 was carried out by the author of this work extending the analysis presented in [360].

[360]: Fermon (2023), *Etude des alliages de Heusler de type Co_2MnZ par diffusion Brillouin et effet Kerr magnéto-optique*

40: This SuperK EXTREME supercontinuum laser produces radiation in the range $\lambda \approx 450\,\text{nm} - 1800\,\text{nm}$ by non-linear broadening of seed pulses. Consequently, the output power is wavelength dependent and the output always contains a background radiation in the infrared (IR). In the setup, the laser is coupled into an optical fibre, which reduces the output power. Furthermore, the optical fibre is coupled to a NKT photonics SuperK SELECT filter module, which further reduces output power and suppresses the IR background. As a result, sufficient signal for the LMOKE studies in this work was obtained in the range of $\lambda \approx 550\,\text{nm} - 900\,\text{nm}$ only.

[94]: Gaier (2009), 'A study of exchange interaction, magnetic anisotropies, and ion beam induced effects in thin films of Co_2-based Heusler compounds'

Measurement procedure

In the course of a measurement, the normalised difference of the photodiode intensities

$$\frac{\Delta I}{I_1 + I_2} = \frac{I_1 - I_2}{I_1 + I_2} \tag{5.21}$$

is recorded as a function of the applied magnetic field. For $\Delta I \approx 0$, the normalised intensity difference is approximately proportional to the Kerr rotation[41] θ.

An alignment protocol was followed prior to all MOKE measurements:

1. The sample was aligned using the alignment beam path: A full rotation was performed and the reflection traced on a sheet of paper serving as the alignment screen indicated in figure 5.15. Typically, a circular or elliptical trace was obtained, indicating a misalignment of the center of rotation and the reflection point. The rotation plate was then iteratively aligned to minimise the deviation of the reflected beam.
2. The detection unit was adjusted automatically, rotating prior to each measurement such that $\Delta I = 0$ in order to ensure the approximation $\frac{\Delta I}{I_1+I_2} \approx \theta$ for the recorded signal.

41: In order to get information on the Kerr ellipticity $\ell_{s/p}$, one would need to introduce a quarter-wave retarder into the setup [102], but the Kerr ellipticity was irrelevant in the present work.

[102]: Silber (2019), 'Quadratic magnetooptic Kerr effect spectroscopy of magnetic thin films with cubic crystal structure'

5.3.2 Separation of linMOKE and QMOKE contributions

Multiple methods for the separation of linMOKE and QMOKE contributions have been proposed in recent studies [94, 310, 361–365]: the ROTMOKE method [361, 362], the 8 field method [310, 363], the separation based on field-dependent symmetry considerations [94, 364], and the rotating field method [365].

A quantitative separation of quadratic contributions is possible by the 8 field method [310, 363], yielding

$$\theta_{M_\mathrm{L}M_\mathrm{T}} = Q_a \cos 4\phi + Q_b \tag{5.22}$$

$$\theta_{M_\mathrm{L}^2 - M_\mathrm{T}^2} = Q_a \sin 4\phi \tag{5.23}$$

with quadratic Kerr amplitudes Q_a and Q_b, and the angle ϕ between the [100] direction and the plane of incidence of the incoming light. However, such a separation of the two contributions could not be achieved with the available setup as the method requires a possibility of rotation between the incidence plane of light and the applied magnetic field[42], whereas in the experimental setup used in this study a fixed LMOKE geometry was used.

In this work, symmetric and antisymmetric contributions were separated analogously to references [94, 364] by a simple symmetry consideration, i.e.

$$\theta_\mathrm{linMOKE} = \theta_\mathrm{asym} = \frac{\theta_\mathrm{inc}(H) - \theta_\mathrm{dec}(-H)}{2} \tag{5.24}$$

$$\theta_\mathrm{QMOKE} = \theta_\mathrm{sym} = \frac{\theta_\mathrm{inc}(H) + \theta_\mathrm{dec}(-H)}{2} \tag{5.25}$$

with $\theta_\mathrm{inc/dec}$ indicating the magnetisation loop branch for increasing and decreasing external field. Although not accessing the individual quadratic contributions for a quantitative analysis, this symmetry separation into linear and quadratic contributions in the final Kerr rotation still allows for an overall analysis of the quadratic MOKE effects, as will be discussed in chapter 7 of this thesis.

[94]: Gaier (2009), 'A study of exchange interaction, magnetic anisotropies, and ion beam induced effects in thin films of Co_2-based Heusler compounds'
[310]: Hamrle et al. (2007), 'Huge quadratic magneto-optical Kerr effect and magnetization reversal in the Co_2FeSi Heusler compound'
[361]: Mattheis et al. (1999), 'Separation of the Voigt Effect in Longitudinal Kerr Magnetometry'
[362]: Mattheis et al. (1999), 'Determination of the anisotropy field strength in ultra-thin magnetic films using longitudinal MOKE and a rotating field'
[363]: Postava et al. (2002), 'Anisotropy of quadratic magneto-optic effects in reflection'
[364]: Mewes et al. (2004), 'Separation of the first- and second-order contributions in magneto-optic Kerr effect magnetometry of epitaxial FeMn/NiFe bilayers'
[365]: Liang et al. (2015), 'Separation of linear and quadratic magneto-optic Kerr effects in ultra-thin Fe films using a rotating field method'

42: Typically achieved with a rotatable magnet or a vector magnetic field setup.

5.4 Conventional Brillouin light scattering (BLS)

As introduced in section 4.3.2 in the previous chapter, Brillouin light scattering (BLS) describes the inelastic scattering of light from collective excitations in a crystal system, i.e. acoustic waves in the lattice system or spin waves in the spin system[43]. In the particle picture, this can be described as the inelastic scattering event of a photon with incident frequency ω_{incident} and wavevector $\mathbf{k}_{\text{incident}}$ by a quasi particle with ω_{quasi} and $\mathbf{k}_{\text{quasi}}$, i.e. a phonon or a magnon in the solid. The process yields

$$\omega_{\text{scattered}} = \omega_{\text{incident}} \mp \omega_{\text{quasi}} \tag{5.26}$$

$$\mathbf{k}_{\text{scattered}} = \mathbf{k}_{\text{incident}} \mp \mathbf{k}_{\text{quasi}} \tag{5.27}$$

for the scattered photon, where the two cases correspond to the *Stokes* or *Anti-Stokes* process. These can be interpreted as the creation or annihilation of a quasi particle respectively, as illustrated in figure 5.16[44] [229].

43: As stated before, a detailed knowledge of spin waves is not necessary to introduce the technical aspects of conventional BLS experiments. Here, it is sufficient to understand that spin waves, as any other wave, can be described by a frequency ω and an associated wave vector $\mathbf{k}$, linked by a dispersion relation. For further details, see the third part of this work from page 151.

44: In principle, higher order processes exist, i.e. involving multiple magnons, yet the simple picture of one-magnon scattering is sufficient for the analysis of the BLS signal intensity measurements.

[229]: Rezende (2020), *Fundamentals of Magnonics*

5.4.1 Measurement principle and experimental setup

The BLS measurement principle is based on the relations given in equations 5.26 and 5.27: A precise determination of $\omega_{\text{scattered}}$ and $\mathbf{k}_{\text{scattered}}$ equates to an indirect measurement of the quasi particle involved in the scattering process. For this, multiple conditions need to be met in the experiment:

1. The incident photon's frequency ω_{incident} needs to be precisely known. While this would ideally be fixed by the use of a monochromatic light source, sufficient precision is typically achieved by using appropriate lasers capable of operating in a single-frequency mode with narrow spectral linewidth of less than 10 MHz [366].
2. A precise measurement of the scattered photon's frequency ω_{incident} is imperative. For this purpose, multi-pass tandem Fabry-Pérot interferometers (TFPIs) are used in modern setups [367], a schematic of which is shown in figure 5.17. TFPIs yield high spectral resolution and suppress higher order transmission modes, enabling a high resolution frequency analysis even for comparably weak BLS signals [366].
3. The BLS signal originating from scattering events involving magnons needs to be separated from the signal originating from scattering events with phonons (or vice versa). This is easily achieved by using a polarisation analyser in the reflected beam path: As a scattering with phonons does not yield a change of polarisation, but a scattering with magnons results in a polarisation rotation of 90°, the two cases are easily distinguishable [366–368].

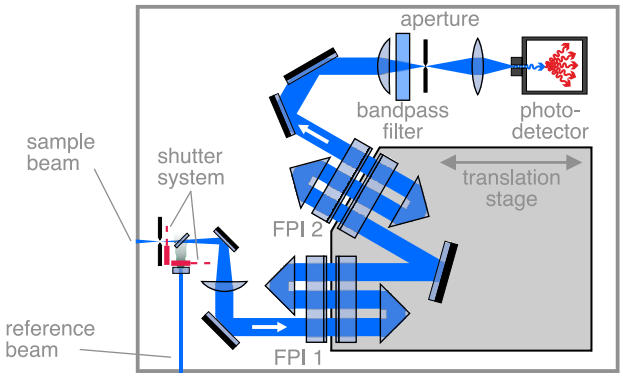

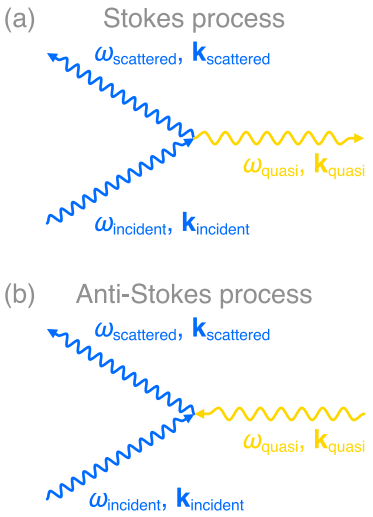

Figure 5.16: Schematic of (a) the Stokes process (creation of a quasi particle) corresponding to the minus sign in equations 5.26 and 5.27 and (b) Anti-Stokes process (annihilation of a quasi particle), corresponding to the plus sign respectively.

[366]: Sebastian et al. (2015), 'Micro-focused Brillouin light scattering'
[367]: Cochran (1994), '3.2 Light Scattering from Ultrathin Magnetic Layers and Bilayers'
[368]: Geilen (2022), 'Excitation of spin waves by magneto-elastic effects'

[369]: Heinz (2021), 'Nano-scaled yttrium iron garnet conduits for magnonic networks'

Figure 5.17: Schematic of a multi-pass tandem Fabry-Pérot interferometer (TFPI), consisting of two Fabry-Pérot interferometers (FPI) each passed thrice. The FPIs are mounted under an angle on a same translation stage. Figure taken from [369] and edited.

Thermal excitation

In order to obtain sufficient signal intensities, spin waves are often excited by external means, e.g. microwave antennae positioned on the sample surface similar to the excitation in FMR experiments. Yet, an external excitation is not always necessary, as the sensitivity is often sufficiently high to measure the signal arising from scattering with the thermally activated magnons: As boson quasiparticles, magnons follow the Bose-Einstein distribution

$$p(\omega) = \frac{1}{\exp(\frac{\hbar\omega - \mu}{k_B T}) - 1} \tag{5.28}$$

giving the occupation probability function for a magnon state with energy $E_{\text{magnon}} = \hbar\omega$ at a temperature T, where k_B is the Boltzmann constant and μ is the chemical potential. $\mu = 0$ in the thermodynamic equilibrium, and the temperature of the magnonic, phononic and electronic subsystem are then equal, i.e. given by the sample temperature. The associated average thermal energy $E_{\text{thermal}} = \frac{N}{2} k_B T = k_B T$ with $N = 2$ degrees of freedom is substantially larger than the magnon energies E_{magnon} for spin waves in the GHz range, resulting in a significant population of magnon states in the GHz range.

The absolute signal intensity obtained in a BLS experiment is related to the average thermal occupation of the spin wave modes and thus proportional[45] to the absolute temperature T [367]. Yet, a full analytical description is tedious and outside the scope of this work, where relative signal intensities will be compared, thus it is referred to [327, 367] for more details.

45: For GHz magnons at room temperature, the occupation probability can be approximated by the Rayleigh-Jeans distribution

$$p(\omega) = \frac{k_B T}{\hbar\omega} \tag{5.29}$$

yielding a direct proportionality of the population of a magnon state to the temperature and the inverse of its energy.

[327]: Cochran et al. (1988), 'Calculation of the intensity of light scattered from magnons in thin films'
[367]: Cochran (1994), '3.2 Light Scattering from Ultrathin Magnetic Layers and Bilayers'

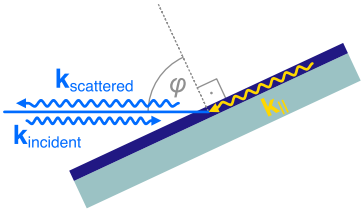

Figure 5.18: Schematic of the backscattering geometry. Figure inspired by a similar schematic in [370].

[370]: Brächer (2015), 'Parallel parametric amplification of spin waves in microstructures'

Setup and measurement protocol in this work

In this work, thermally excited spin waves were measured at room temperature using a conventional BLS system mounted in the backscattering geometry a schematic of which is shown in figure 5.18. In this case, the probed in-plane wavevector $k_{\parallel}$ is fixed by the angle of incidence φ through the relation

$$k_{\parallel} = \frac{4\pi \sin\varphi}{\lambda} \tag{5.30}$$

where λ is the laser wavelength. Measurements discussed in this work were performed[46] with lasers of wavelengths $\lambda = 457\,\text{nm}$ and $\lambda = 532\,\text{nm}$. Using angles of incidence of $\varphi = 2.5°$, quasi-FMR spin waves[47] were probed. The samples were placed in an external magnetic field, applied in the film plane perpendicular to the plane of incidence of light, i.e. in the *Damon-Eshbach geometry*. Prior to each measurement, the free spectral range of the TFPI was adapted by changing the offset mirror distance in order to achieve maximum resolution in the required frequency range [366].

46: BLS measurements with $\lambda = 457\,\text{nm}$ presented in chapter 7 were carried out by Nicolas Fermon from the école normale supérieure Paris-Saclay within the framework of a master research project [360] supervised by the author of this work. The analysis discussed in chapter 7 was carried out by the author of this work.

[360]: Fermon (2023), *Etude des alliages de Heusler de type Co_2MnZ par diffusion Brillouin et effet Kerr magnéto-optique*

47: The BLS process is based on the periodic modulation of the permittivity tensor and can be described as a phase grating moving with the phase velocity of the quasi particle, see section 4.3. The photons are diffracted and their frequency is Doppler-shifted, and consequently only propagating spin waves, i.e. with non-zero wavevector, can yield a frequency shift. Hence, the spatially uniform magnetisation oscillation of the FMR is not observable in BLS. Still, a quasi-FMR condition can be probed by working with near-zero wavenumber spin waves [325].

[325]: Srinivasan et al. (1988), 'Brillouin light scattering detection of ferromagnetic resonance in thin films'

[366]: Sebastian et al. (2015), 'Micro-focused Brillouin light scattering'

5.4.2 Data evaluation for the BLS intensity analysis

The BLS signal intensities were determined by fitting a Lorentzian peak function to the measured data. The integrated signal was normalised by the integrated reference signal, in order to exclude variations due to instabilities in the output laser power as the BLS signal is directly proportional to the applied laser power [366]. This normalisation also conveniently eliminates any influence from potential temporal drifts in the interferometer performance.

Magnetic properties of epitaxial Co_2MnSi and Co_2MnAl Heusler thin films

6

6.1 **Static properties** 111
Co_2MnSi film 112
Co_2MnAl film 114
Direct comparison 116
6.2 **Magnetisation dynamics** 118
Anisotropic FMR 121
Anisotropy interpretation 129
Linewidth analysis 133
6.3 **Conclusions** 136

This chapter is dedicated to the investigation of static and dynamic magnetic properties of Co_2Mn-based Heusler compounds by vibrating sample magnetometry (VSM) and ferromagnetic resonance spectroscopy (FMR) techniques. The focus is centred on two epitaxial thin film samples of the compounds Co_2MnSi and Co_2MnAl, both grown by MBE as detailed in chapter 2. This specific Co_2MnSi thin film was grown as part of the sample series presented in table 2.1 for the fabrication of future magnonic devices, for the design of which a thorough thin film characterisation is required. Additionally, the study of the Co_2MnSi thin film is complemented by a Co_2MnAl film with an analogous stack for a direct comparison. Indeed, the thin film characterisation presented in this chapter not only served as a preliminary study for the precise design of Co_2MnSi-based magnonic devices, but also as a preliminary study for future coupling investigations towards complex heterostructures made of Co_2MnSi/Co_2MnAl bilayers as will be pointed out in the outlook of this work.

The first section of this chapter will focus on the static magnetic properties of the compounds investigated by VSM, particularly the magnetic moment and the magnetic hysteresis. The second section of the chapter is centred around the microwave analysis of the FMR and a thorough extraction of the key parameters, i.e. the anisotropy constants, the gyromagnetic ratio, the Gilbert damping and the inhomogeneous linewidth, which determine the magnetisation dynamics in the materials. The final section of this chapter will summarise all characteristics and clearly define the standard parameters particularly for Co_2MnSi to be used throughout this work.

6.1 Static properties: Hysteresis, magnetic moment and saturation magnetisation

The static properties of the two Co_2Mn-based Heusler compounds were investigated by VSM. The main goal of these measurements was to precisely quantify the saturation magnetisation of the two compounds under investigation, Co_2MnSi and Co_2MnAl, since this parameter is of key importance throughout the work.

Additionally, the remanence magnetisation, coercive field and saturation field can be determined from the hysteresis curves and the comparison of the $M(H)$ measurements with the field aligned along distinct crystallographic orientations allows for a qualitative verification of the anisotropic effects[1] in the two compounds Co_2MnSi and Co_2MnAl.

The VSM measurements were performed as detailed in section 5.1. The external field was applied in the sample plane and $M(H)$ loops were recorded in four configurations with different orientations of the sample, i.e. with $[hkl] = [110], [010], [\bar{1}10], [\bar{1}00]$ parallel to the external field coinciding with the vibration axis. For each orientation, a set of two measurements with different field ranges as detailed in section 5.1 was performed in order to maximise the precision on the saturation magnetisation as well as to resolve the narrow loop opening.

1: For a precise quantitative VSM-analysis of the anisotropy in the film plane, a rotational measurement would need to be performed on a VSM setup with a rotation function. Instead, a rotational FMR measurement was performed in this work, as will be presented in section 6.2.1 of this chapter.

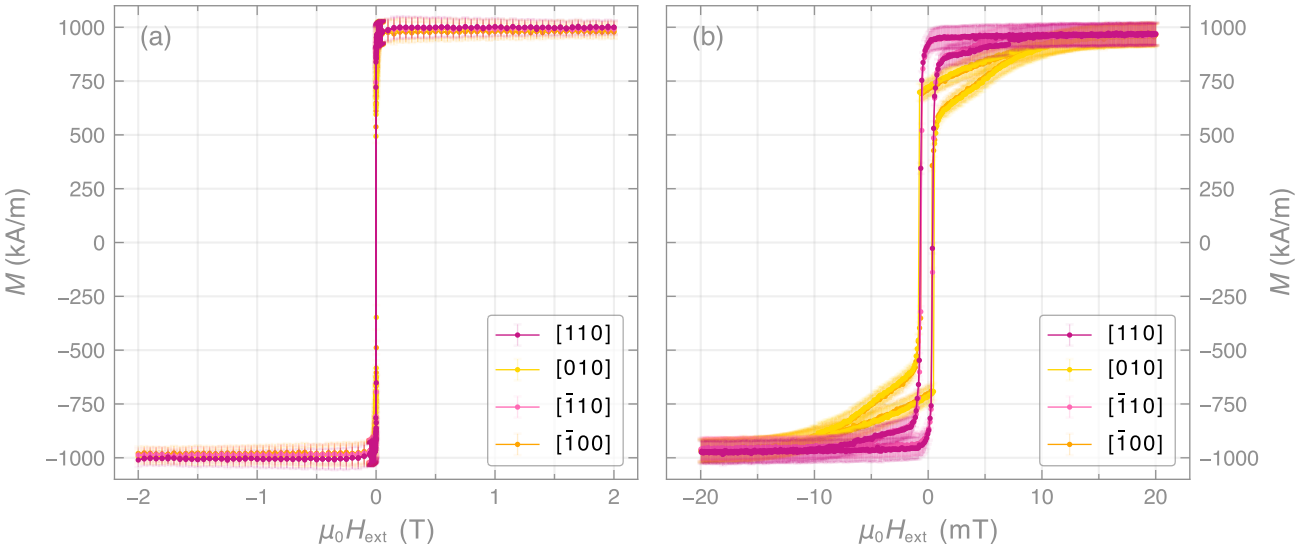

Figure 6.2: Hysteresis loops obtained from in-plane VSM measurements on the Co_2MnSi thin film (a) with a maximum field of $|\mu_0 H_{max}| = 2\,T$ and (b) with a maximum applied field of $|\mu_0 H_{max}| = 20\,mT$. The field was applied in the sample plane along the crystal directions as indicated.

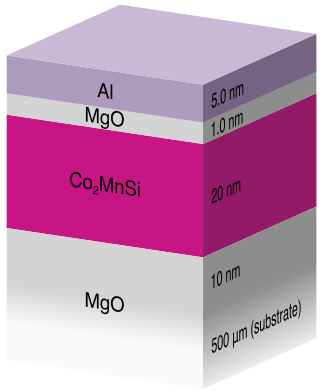

Figure 6.1: Schematic of the thin film stack of the Co_2MnSi sample investigated in this chapter.

6.1.1 Co_2MnSi film

A schematic illustration of the sample stack is shown in figure 6.1: The sample is part of the sample series presented in table 2.1 and was capped with an MgO/Al bilayer similar to the MgO/Ti bilayer capping of the sample described in section 9.1.1 for the study in chapter 10.

The hysteresis loops from the in-plane VSM measurements on the Co_2MnSi film are shown in figure 6.2 for both field ranges: The large field range measurements in figure 6.2 (a) with $|\mu_0 H_{max}| = 2\,T$ were used for the extraction of the saturation magnetisation and the saturation field. The small range measurements in figure 6.2 (b) with $|\mu_0 H_{max}| = 20\,mT$ were used for the analysis of the anisotropy effects on the remanence magnetisation, the coercive field and the loop closure field.

Saturation of Co_2MnSi

The saturation magnetisation was determined as[2]

$$M_S = (996 \pm 5)\,\frac{kA}{m} = (4.87 \pm 0.04)\,\frac{\mu_B}{f.u.} \tag{6.1}$$

which is slightly below the theoretically expected value of $M_{theory} = 4.94\,\mu_B/f.u.$ [114], but within the range of commonly reported values for Co_2MnSi [63, 71, 158] as listed in table 1.1: Typical values range from $4.78\,\mu_B/f.u. \approx 981\,kA/m$ [158] to $5.1\,\mu_B/f.u. \approx 1042\,kA/m$ [71]. The measured saturation magnetisation $M_S = 996 \pm 5\,kA/m$ is consistent with various samples studied throughout this thesis and therefore serves as the representative reference in this work.

Although a cubic anisotropy is expected from the Heusler lattice, hardly any directional variation was determined on the saturation field by above definition[3] and

$$\mu_0 H_{sat,\,IP} = (45 \pm 5)\,mT \tag{6.2}$$

was obtained as a saturation field of the Co_2MnSi film.

2: A cubic cell with the lattice constant $a = 0.566\,nm$ [71] and 4 formula units of Co_2MnSi per cell was assumed for the transformation from kA/m to μ_B/f.u. (with f.u. denoting *formula unit*).

[114]: Galanakis et al. (2002), 'Slater-Pauling behavior and origin of the half-metallicity of the full-Heusler alloys'

[63]: Webster (1971), 'Magnetic and chemical order in Heusler alloys containing cobalt and manganese'

[71]: Guillemard et al. (2020), 'Issues in growing Heusler compounds in thin films for spintronic applications'

[158]: Ritchie et al. (2003), 'Magnetic, structural, and transport properties of the Heusler alloys Co_2MnSi and NiMnSb'

3: The saturation field was defined as the absolute field value above which the measured magnetic moment consistently exceeds 98% of M_S.

In-plane anisotropy of Co_2MnSi

The small range hysteresis loops shown in figure 6.2 (b) clearly present a qualitative difference between the principal axes of the cubic lattice, i.e. $\langle 100\rangle_{Co_2MnSi}$, and the face diagonals, i.e. $\langle 110\rangle_{Co_2MnSi}$: A significant curvature is obtained along the [010] and $[\bar{1}00]$ directions, and hence the averaged remanence magnetisation increases from

$$M_R^{\langle 010\rangle}/M_S = (72 \pm 4)\% \tag{6.3}$$

for a field orientation along the principal lattice axes to

$$M_R^{\langle 110\rangle}/M_S = (90 \pm 4)\% \tag{6.4}$$

when changing the field direction to the face diagonals as is shown in figure 6.3 (a).

This allows for the following conclusions at this point:

1. The energy (density) for a field orientation along the $\langle 100\rangle_{Co_2MnSi}$ must be larger than the energy (density) for a field orientation along the $\langle 110\rangle_{Co_2MnSi}$. – This is often directly interpreted as an identification of the *hard axes* and the *easy axes* respectively. However, it is important to note that these terms are commonly used for the global maximum and respectively the global minimum of the associated energy density (here: magnetocrystalline), yet the identification of the global maxima/minima is not as trivial in the case of a cubic magnetocrystalline anisotropy, especially when a second order term comes into play.
2. It is correct to conclude that the first order cubic magnetocrystalline anisotropy constant K_{c1} must be negative, since this ratio of the respective energy densities can only be obtained for $K_{c1} < 0$, as detailed in table 4.1.
3. The identification of the magnetocrystalline anisotropy axes depends on the ratio between the first order and second order cubic anisotropy constants as listed in table 4.1:
   - If the second order cubic anisotropy is negligible, the $\langle 100\rangle_{Co_2MnSi}$ directions can be identified as *hard axes* and the $\langle 110\rangle_{Co_2MnSi}$ directions correspond to *medium axes* accordingly.
   - If the second order cubic anisotropy is non-negligible, the $\langle 100\rangle_{Co_2MnSi}$ directions can correspond to *hard axes* of the magnetocrystalline anisotropy and the $\langle 110\rangle_{Co_2MnSi}$ can then correspond to *medium axes* or *easy axes*. The $\langle 100\rangle_{Co_2MnSi}$ directions can, however, also correspond to *medium axes*, then the $\langle 110\rangle_{Co_2MnSi}$ must be *easy axes*.

Note that although it cannot be concluded from the VSM measurements at this point, the later FMR study will yield a negative second order cubic anisotropy constant and hence according to table 4.1 the $\langle 100\rangle_{Co_2MnSi}$ directions can be identified as global maxima of the magnetocrystalline energy density and thus *hard axes*, while the $\langle 110\rangle_{Co_2MnSi}$ directions correspond to a saddle point[4] and therefore to *medium axes* of the magnetocrystalline energy density.

The extracted coercive field does not present a consistent effect which can be attributed to a cubic anisotropy, but instead is found to be nearly constant within the error bars as shown in figure 6.3 (b). For all orientations, a sharp switching step is observed at small coercive fields

$$\mu_0 H_c \leq (0.7 \pm 0.2)\,\mathrm{mT} \tag{6.5}$$

in the small field range $M(H)$ curves shown in figure 6.2 (b).

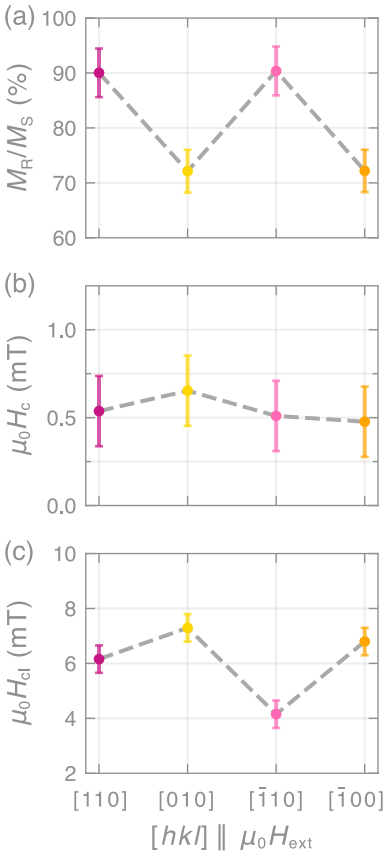

Figure 6.3: Results from the in-plane VSM measurements on the Co_2MnSi film: (a) the relative remanence magnetisation M_R/M_S, (b) the coercive field H_c and (c) the loop closure field H_{cl}.

4: A minimum only in the $(001)_{Co_2MnSi}$ plane.

However, a persistent hysteretic opening is observed and the loops only close for an applied field that is nearly an order of magnitude larger than the coercive field. The resulting appearance of *tails* in the hysteresis loops has been observed by previous studies of Co_2MnSi on MgO [83, 371], as well as other Co_2Mn-based Heusler compounds like Co_2MnGe where it is attributed to the pinning of magnetic moments at "defects that require higher fields to switch" [157]. In the investigated Co_2MnSi film with two adjacent MgO layers as illustrated in figure 6.1, the dislocations along the bottom and top interface of the Co_2MnSi layer (see chapter 3) are likely to act as such defects pinning the surrounding magnetic moments.

[83]: Friedel (2021), *Thin film materials with ultralow damping for novel magnonic phenomena*

[371]: Uemura et al. (2008), 'Epitaxial growth and characterization of Co_2MnSi thin films on GaAs with MgO interlayer'

[157]: Yang et al. (2002), 'Multistep magnetic switching in single-crystal (001) Co_2MnGe films'

The extracted loop closure field H_{cl} is presented in figure 6.3 (c), and clearly presents an anisotropic effect: Highest loop closure fields are obtained for the hard axes, i.e. $\langle 100 \rangle_{Co_2MnSi}$, and at the maximum loop closure field

$$\mu_0 H_{cl,max} = (7.3 \pm 0.5)\,\mathrm{T} \tag{6.6}$$

the magnetisation becomes independent of the field sweep history. This is of importance for the study in chapter 10, where the smallest applied field of $\mu_0 H_{ext} = 8.9\,\mathrm{mT}$ along an [110] direction corresponds to a reduced effective field of only $\mu_0 H_{eff} = 7.2\,\mathrm{mT}$ due to the demagnetisation contribution from the waveguide structure (see section 8.1.5), and hence is just enough to ensure an absence of strongly hysteretic effects in the study presented in chapter 10.

6.1.2 Co_2MnAl film

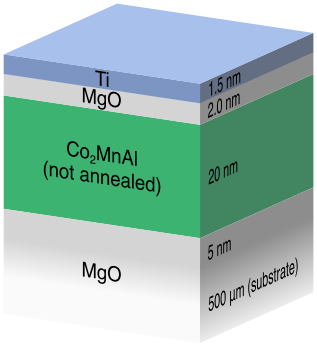

Figure 6.4: Schematic of the thin film stack of the Co_2MnAl sample investigated in this chapter.

A schematic illustration of the sample stack is shown in figure 6.4: The sample is part of the sample series presented in table 2.3 and was capped with an MgO/Ti bilayer capping. The Co_2MnAl film was not annealed, since the intention of this sample was to be a reference for a bilayer coupling study, as listed in chapter 2.

The hysteresis loops from the in-plane VSM measurements on the Co_2MnAl film are shown in figure 6.5 for both field ranges: Analogous to the Co_2MnSi film above, the large field range measurements in figure 6.5 (a) with $|\mu_0 H_{max}| = 2\,\mathrm{T}$ were used for the extraction of the saturation magnetisation and the saturation field. The small range measurements in figure 6.5 (b) with $|\mu_0 H_{max}| = 20\,\mathrm{mT}$ were used for the analysis of the anisotropy effects on the remanence magnetisation, the coercive field and the loop closure field.

Saturation of Co_2MnAl

Analogous to the above described analysis of the Co_2MnSi film, the saturation magnetisation was determined averaging over all measurements. The saturation magnetisation

$$M_S = (742 \pm 4)\,\frac{\mathrm{kA}}{\mathrm{m}} = (3.8 \pm 0.02)\,\frac{\mu_B}{\mathrm{f.u.}} \tag{6.7}$$

was extracted, which is slightly below the theoretical expectation of $4\,\mu_B/\mathrm{f.u.}$ from the Slater-Pauling rule [114]. The discrepancy is likely related to the Co_2MnAl film in this sample not being annealed: For a comparable annealed Co_2MnAl film[5], $M_S = 851\,\mathrm{kA/m}$ was determined for the saturation magnetisation in [71] as listed with the reference properties in table 1.1.

[114]: Galanakis et al. (2002), 'Slater-Pauling behavior and origin of the half-metallicity of the full-Heusler alloys'

5: Listed as sample "S2.1" in table 2.2 - grown in a previous study on the same system following the same growth protocol.

[71]: Guillemard et al. (2020), 'Issues in growing Heusler compounds in thin films for spintronic applications'

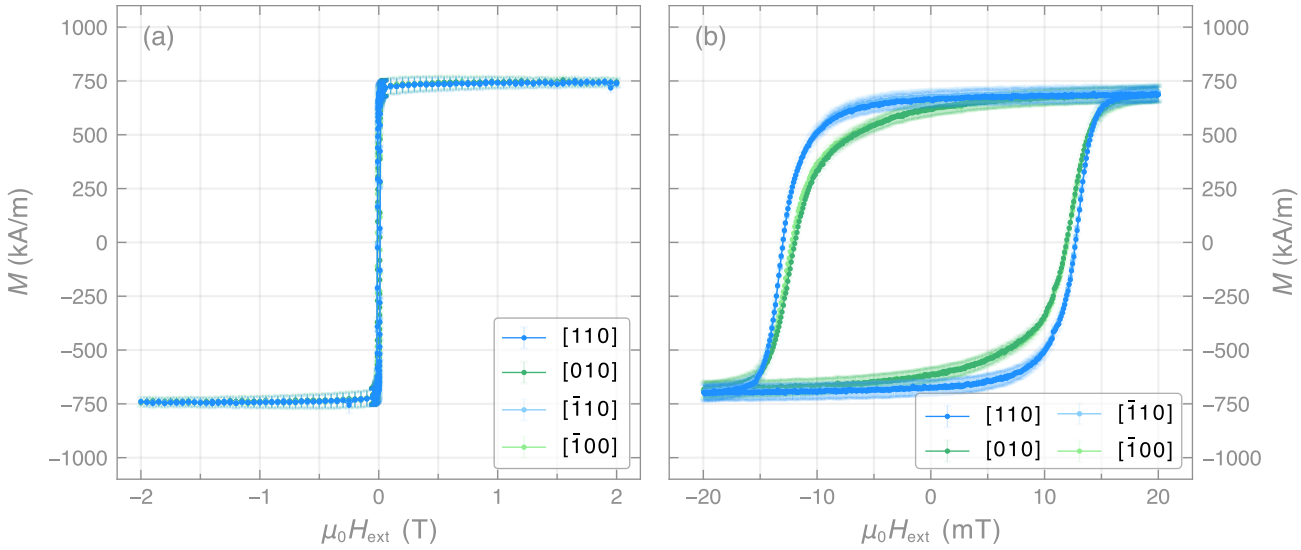

Figure 6.5: Hysteresis loops obtained from in-plane VSM measurements on the Co_2MnAl thin film (a) with a maximum field of $|\mu_0 H_{max}| = 2\,T$ and (b) with a maximum applied field of $|\mu_0 H_{max}| = 20\,mT$. The field was applied in the sample plane along the crystal directions as indicated.

The in-plane saturation field was found to be independent of the sample orientation like for the above discussed Co_2MnSi film. In comparison, the saturation field of the non-annealed Co_2MnAl film

$$\mu_0 H_{sat,\,IP} = (175 \pm 25)\,mT \tag{6.8}$$

is approximately 4 times larger than the saturation field from the Co_2MnSi film.

In-plane anisotropy of Co_2MnAl

Little difference is observed between the principal axes of the cubic lattice, i.e. $\langle 100\rangle_{Co_2MnAl}$, and the face diagonals of the cubic lattice, i.e. $\langle 110\rangle_{Co_2MnAl}$, in the small-range $M(H)$ loops in figure 6.5 (b). This is reflected in the remanence magnetisation changing from

$$M_R^{\langle 110\rangle}/M_S = (90 \pm 4)\% \tag{6.9}$$

only to

$$M_R^{\langle 010\rangle}/M_S = (83 \pm 4)\% \tag{6.10}$$

as shown in figure 6.6 (a). As for the Co_2MnSi film above, a negative first-order cubic anisotropy constant is expected (and will be confirmed in the subsequent rotational FMR study) since the $\langle 100\rangle_{Co_2MnAl}$ directions must correspond to a larger energy density than the $\langle 110\rangle_{Co_2MnAl}$ directions.

This anisotropic behaviour is also observed in the coercive fields obtained from the small-range VSM measurements, as shown in figure 6.6 (b). Largest values were obtained for a field alignment along the $\langle 110\rangle_{Co_2MnAl}$ directions, where

$$\mu_0 H_c^{\langle 110\rangle} = (12.9 \pm 0.5)\,mT \tag{6.11}$$

is of the same order of magnitude as observed in other studies, i.e. between $\mu_0 H_c \approx 15 - 26\,mT$ reported for epitaxial Co_2MnAl films on GaAs substrates [372] and $\mu_0 H_c \approx 2 - 6\,mT$ reported for sputtered Co_2MnAl films with different grain sizes[6] on SiO_2/Si (100) substrates [373].

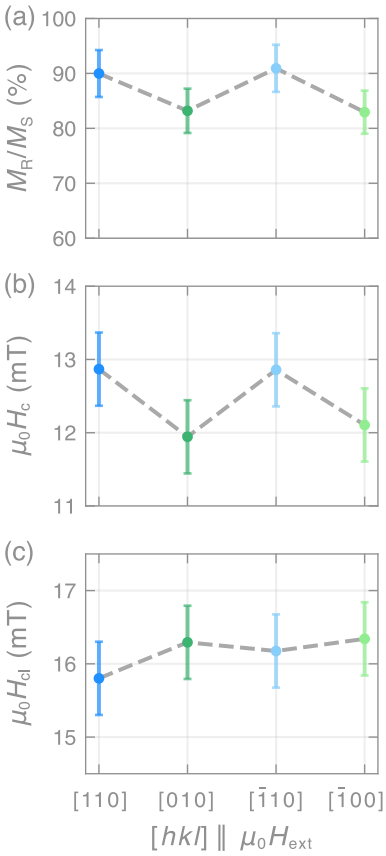

Figure 6.6: Results from the in-plane VSM measurements on the Co_2MnAl film: (a) the relative remanence magnetisation M_R/M_S, (b) the coercive field H_c and (c) the loop closure field H_{cl} are shown.

[372]: Liu et al. (2015), 'Static and dynamic magnetic properties of B2 ordered Co_2MnAl film epitaxially grown on GaAs'

6: The grain sizes of the sputtered Co_2MnAl films in [373] are correlated with the deposition temperature.

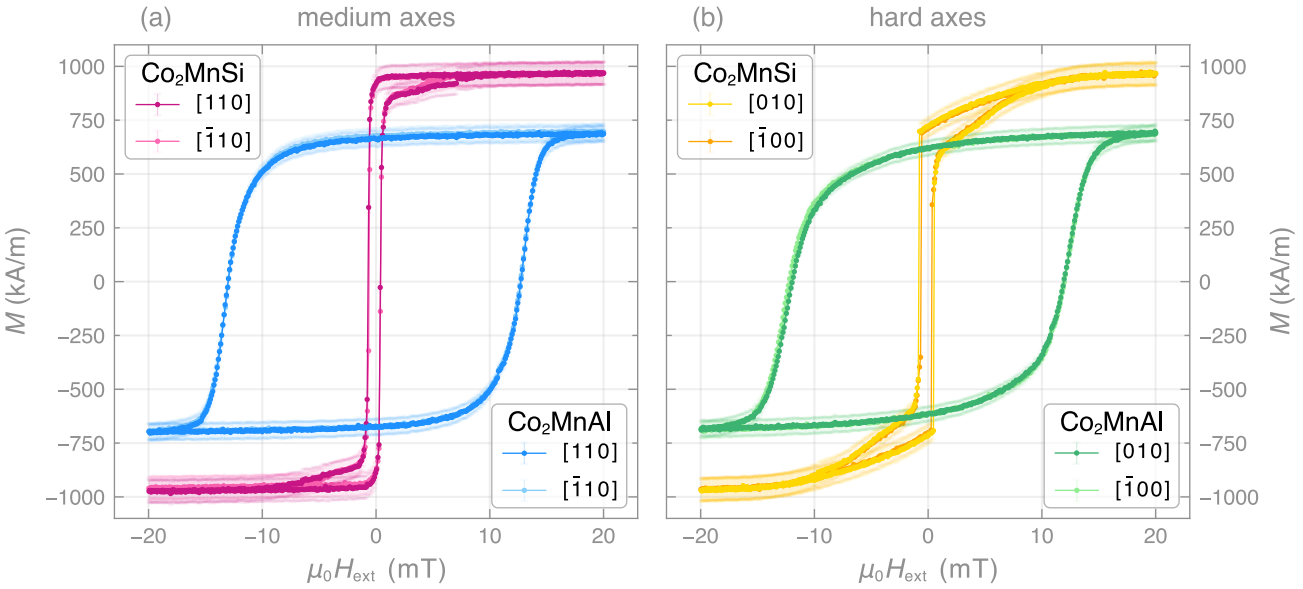

Figure 6.7: Comparison of the in-plane hysteresis loops obtained from the VSM measurements with a small field range (a maximum applied field of $|\mu_0 H_{max}| = 20\,\mathrm{mT}$) on the annealed Co_2MnSi thin film and the non-annealed Co_2MnAl thin film (a) with the field applied along the face diagonals of the cubic crystal lattice and (b) with the field applied along the principal axes of the lattice.

[373]: Barwal et al. (2018), 'Growth dependent magnetization reversal in Co_2MnAl full Heusler alloy thin films'

7: Recall that the identification of the axes is not possible only from these VSM measurements, but is a result from the subsequent FMR analysis, as was discussed above.

[114]: Galanakis et al. (2002), 'Slater-Pauling behavior and origin of the half-metallicity of the full-Heusler alloys'

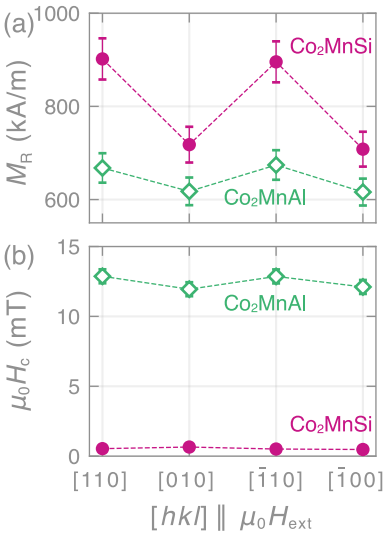

Figure 6.8: Comparison of (a) the remanence magnetisation and (b) the coercive field obtained from the VSM measurements on the Co_2MnSi and Co_2MnAl thin films.

[71]: Guillemard et al. (2020), 'Issues in growing Heusler compounds in thin films for spintronic applications'

[103]: Guillemard (2019), 'Half-metal magnets Heusler compounds for spintronics'

The loop closure field is hardly influenced by any anisotropic behaviour and approximately constant within error range as shown in figure 6.6 (c). No *tails* were observed in the $M(H)$ loops of the Co_2MnAl film and the maximum loop closure field for this sample is

$$\mu_0 H_{cl,max} = (16.3 \pm 0.5)\,\mathrm{mT} \quad . \tag{6.12}$$

6.1.3 Comparison of Co_2MnSi and Co_2MnAl

For a direct comparison, the hysteresis loops obtained from the two films in the small field-range VSM measurements are shown jointly in figure 6.7 (a) for a field orientation along the ⟨110⟩ directions corresponding to medium axes of the magnetocrystalline anisotropy[7] and (b) for a field orientation along the ⟨110⟩ directions corresponding to hard axes of the magnetocrystalline anisotropy respectively.

As expected from the Slater-Pauling rule [114] and the reference values listed in table 1.1, the saturation magnetisation $M_S = 996 \pm 5\,\mathrm{kA/m}$ obtained from the Co_2MnSi film is significantly larger than the saturation magnetisation $M_S = 742 \pm 4\,\mathrm{kA/m}$ from the Co_2MnAl film.

The most significant anisotropic effect is observed in the $M(H)$ curves on Co_2MnSi, resulting in a large drop of the remanence magnetisation as compared in figure 6.8 (a) to the results from Co_2MnAl.

The hysteresis loops obtained from the (non-annealed) Co_2MnAl film present larger loop openings, translating to coercive fields that are approximately an order of magnitude larger than the coercive fields obtained from the Co_2MnSi film as is compared in figure 6.8 (b). The hysteretic loop opening also persists for larger fields, resulting in an increase of the loop closure fields approximately by a factor of 2 as well as increased saturation fields which are approximately 4 times larger compared to the Co_2MnSi film.

Compared to the annealed Co_2MnAl film studied in [71, 103], the non-annealed Co_2MnAl film studied here presents a reduced saturation magnetisation of

$M_S = 742 \pm 4\,\mathrm{kA/m}$ compared to the $M_S = 851 \pm 4\,\mathrm{kA/m}$ (1.07 T) reported in [71]. Moreover, the hysteresis loops of the non-annealed film studied here present a significantly enlarged loop opening compared to the hysteresis loops of the annealed film reported in [103], where similar coercive fields for Co_2MnSi and Co_2MnAl are obtained[8]. The change in the properties is therefore attributed to the annealing step: The non-annealed film is likely to present chemical (dis)ordering domains, more defects or lattice distortions. The defects or grain boundaries can act as pinning centres and hence result in a creeping domain wall motion which can lead to a gradual switching process as observed in the hysteresis loops from the Co_2MnAl film in figure 6.7 and opposed to the sharp switching in the loops from the Co_2MnSi film. Moreover, in the case of defects or lattice distortions, the associated strain on the crystal lattice can significantly increase the anisotropy as has been reported for instance for the case of Co_2MnGa [374].

[71]: Guillemard et al. (2020), 'Issues in growing Heusler compounds in thin films for spintronic applications'

[103]: Guillemard (2019), 'Half-metal magnets Heusler compounds for spintronics'

8: See figure 2.31 on page 61 in [103].

[374]: Pechan et al. (2005), 'Remarkable strain-induced magnetic anisotropy in epitaxial Co2MnGa (001) films'

The annealed Co_2MnSi film and the non-annealed Co_2MnAl investigated in this work were studied for a comparison with epitaxial $Co_2MnSi/X/Co_2MnAl$ heterostructures, where an annealing of the upper layers risks an intermixing of the different compounds and is thus preferably omitted. In such multilayer systems, the above discussed significant increase in the coercive field, the loop closure field as well as the saturation field for the non-annealed top layer could result for instance in pinned domains being persistent over larger field ranges in the top layer (here: Co_2MnAl) than in the bottom (Co_2MnSi) layer, especially when the two layers are magnetically decoupled by an interlayer. Similar trilayer systems are for instance studied for applications of Co_2MnX-based magnetic tunnel junctions (MTJs) [193, 375] or spin valves [247, 376] e.g. for nanocontact vortex oscillators [80].

[193]: Kämmerer et al. (2004), 'Co_2MnSi Heusler alloy as magnetic electrodes in magnetic tunnel junctions'

[375]: Li et al. (2015), 'High-performance giant-magnetoresistance junction with *B* 2-disordered Heusler alloy based Co2MnAl/Ag/Co2MnAl trilayer'

[247]: Goripati et al. (2011), 'Bi-quadratic interlayer exchange coupling in $Co_2MnSi/Ag/Co_2MnSi$ pseudo spin-valve'

[376]: Yu et al. (2012), 'Transport and magnetic properties of the Co2MnSi/Al/Co2MnSi trilayer'

[80]: Létang et al. (2021), 'Nanocontact vortex oscillators based on Co_2MnGe pseudo spin valves'

All characteristics obtained from the VSM measurements are summarised in table 6.1, and will be recalled for comparison with the FMR results in the subsequent sections of this chapter.

Table 6.1: Summarised results from field-in-plane VSM measurements on the annealed $MgO/Co_2MnSi/MgO/Al$ thin film sample and the non-annealed $MgO/Co_2MnAl/MgO/Ti$ thin film sample: The extracted saturation magnetisation M_S, saturation field $\mu_0 H_{sat}$, remanence magnetisation M_R and relative remanence M_R/M_S, as well as the coercive field $\mu_0 H_c$ and the loop closure field $\mu_0 H_{cl}$ are listed.

	M_S (kA/m)	M_S (μ_B/f.u.)	$\mu_0 H_{sat}$ (mT)		M_R (kA/m)	M_R/M_S (%)	$\mu_0 H_c$ (mT)	$\mu_0 H_{cl}$ (mT)
Co_2MnSi	996 ± 5	4.87 ± 0.04	45 ± 5	⟨110⟩	899 ± 44	90 ± 4	0.5 ± 0.2	5.2 ± 0.5
				⟨100⟩	713 ± 38	72 ± 4	0.6 ± 0.2	7.0 ± 0.5
Co_2MnAl	742 ± 4	3.80 ± 0.3	175 ± 25	⟨110⟩	671 ± 32	90 ± 4	12.9 ± 0.5	16.0 ± 0.5
				⟨100⟩	617 ± 29	83 ± 4	12.0 ± 0.5	16.3 ± 0.5

6.2 Magnetisation dynamics

The magnetisation dynamics of the Co_2MnSi and Co_2MnAl thin film samples[9] were investigated by ferromagnetic resonance spectroscopy in order to determine the gyromagnetic ratio, the exchange stiffness, the effective magnetisation and the magnetic damping, as well as to quantify the effect of the anisotropy.

The FMR measurements presented in this chapter were performed on the rotational broadband FMR setup described in section 5.2.1 in the previous chapter. The sample was placed upside down on a coplanar waveguide (CPW) microwave antenna as sketched in figure 5.4 with the $[110]_{Co_2MnSi}$ direction parallel to the CPW axis.

Two types of measurements were performed:

1. Firstly, full-range FMR measurements were performed for a Kittel analysis at fixed orientations of the magnetic field along the high symmetry directions $\langle 100\rangle_{Co_2MnX}$ and $\langle 110\rangle_{Co_2MnX}$. For these measurements, the rotatable magnet was fixed at various positions in steps of 45° (see figure 5.3 and table 6.2). The magnetic field was varied from $H_{max} = 1.039\,T$ down to $H = 0\,T$ in steps of 1 mT then analogously for the opposite field direction (negative values), in order to ensure the validity of the macrospin approximation for the maximal range possible[10].
2. Secondly, rotational FMR measurements were carried out, where fixed fields of $H_{ext} = 0.5\,T$ and $H_{ext} = 0.2\,T$ were set and a full rotation was performed from $\mathbf{H}_{ext} \parallel [\bar{1}10]_{Co_2MnX}$ via $\mathbf{H}_{ext} \parallel [0\bar{1}0]_{Co_2MnX}$ and $\mathbf{H}_{ext} \parallel [100]_{Co_2MnX}$ to $\mathbf{H}_{ext} \parallel [\bar{1}10]_{Co_2MnX}$ in steps of 1°.

All measurements were carried out as frequency sweeps (with VNA settings $f_{min} = 50\,MHz$, $f_{max} = 50\,GHz$, and frequency step size 10 MHz), recording the real and imaginary part of the full scattering matrix ($S_{11}, S_{12}, S_{21}, S_{22}$) as described in section 5.2.1. The measurements were performed at room temperature ($T \approx 295\,K$) and at a fixed microwave excitation power[11].

Background subtraction and data overview

The analysis was performed on the S_{21} parameter, i.e. the parameter corresponding to the measurement in transmission from VNA Port 1 to VNA Port 2. The microwave background of non-magnetic origin was removed in a post-treatment following the derivative divide procedure [350] as given in equation 5.16, i.e.

$$\mathrm{d_D}S_{21}(\omega, H_{ext}) = \frac{\sum_{n=1}^{N} S_{21}(\omega, H_{ext} + n\cdot\Delta H^{\pm}) - \sum_{n=1}^{N} S_{21}(\omega, H_{ext} - n\cdot\Delta H^{\pm})}{S_{21}(\omega, H_{ext})\cdot\sum_{n=1}^{N} n\cdot\Delta H^{\pm}} \tag{6.13}$$

where the modulation step size $\Delta H^{\pm} = 1\,mT$ was set equal to the field step size of the recording. As detailed in section 5.2.2 on page 101, the averaging over the neighbouring N spectra was only used for the automated peak search and the fitting of the higher order PSSWs: $N = 4$ was set for the automated peak search, $N = 2$ was set for the fitting of the PSSW where only the resonance frequencies were extracted and no averaging ($N = 1$) was set for the fitting and analysis of the main resonance.

An overview of the post-processed data is shown in figure 6.9, where the 2D maps show the real part of the 2080 spectra recorded at each field orientation along the high symmetry directions (case 1 in above listing of the two measurement types performed).

9: The pieces investigated in VSM and FMR measurements are exactly the same for the non-annealed Co_2MnAl film, where first the VSM measurements and then the FMR measurements were performed on the same small $4\times4mm^2$ piece (RPTU identifier: RPTU0377), cut for the VSM measurements from the initial sample listed as "S3.1" (Growth identifier: Q230604) in table 2.3. For the annealed Co_2MnSi sample, a small $4\times4mm^2$ piece (RPTU identifier: RPTU0293) was investigated by VSM and a larger piece ($10\times10mm^2$) was investigated in FMR (RPTU identifier: RPTU0288), both pieces were cut from the same initial sample ($30\times30mm^2$) grown in MBE and listed as "S1.4" (Growth identifier: Q240212) in table 2.1.

Table 6.2: Resulting field alignment of the crystallographic axes in the FMR measurements for the different settings of the rotatable magnet in the setup presented in figure 5.3 with φ_{rot} defined as the angle between field direction and the direction perpendicular to the CPW axis as introduced in figure 5.4. The sample was placed such that the CPW axis coincides with $[110]_{Co_2MnX}$.

φ_{rot}	field setting
0°	$\mathbf{H}_{ext} \parallel [1\bar{1}0]_{Co_2MnX}$ $-\mathbf{H}_{ext} \parallel [\bar{1}10]_{Co_2MnX}$
45°	$\mathbf{H}_{ext} \parallel [\bar{1}00]_{Co_2MnX}$ $-\mathbf{H}_{ext} \parallel [100]_{Co_2MnX}$
90°	$\mathbf{H}_{ext} \parallel [\bar{1}\bar{1}0]_{Co_2MnX}$ $-\mathbf{H}_{ext} \parallel [110]_{Co_2MnX}$
135°	$\mathbf{H}_{ext} \parallel [0\bar{1}0]_{Co_2MnX}$ $-\mathbf{H}_{ext} \parallel [010]_{Co_2MnX}$

10: I.e. the field was always swept from saturation down to 0 T, see the related hysteresis loops in the VSM section 6.1 above.

11: An output power of 0 dBm was set at the VNA and due to losses in the microwave circuit (cables, connectors, ..) the excitation power at the sample is expected to be lower - but wasn't quantified as it is irrelevant in this work. Test measurements at different powers were performed to exclude nonlinear effects to the damping. Equally, test measurements with glass spacers between the sample and the CPW were performed to verify the absence of radiative damping effects.

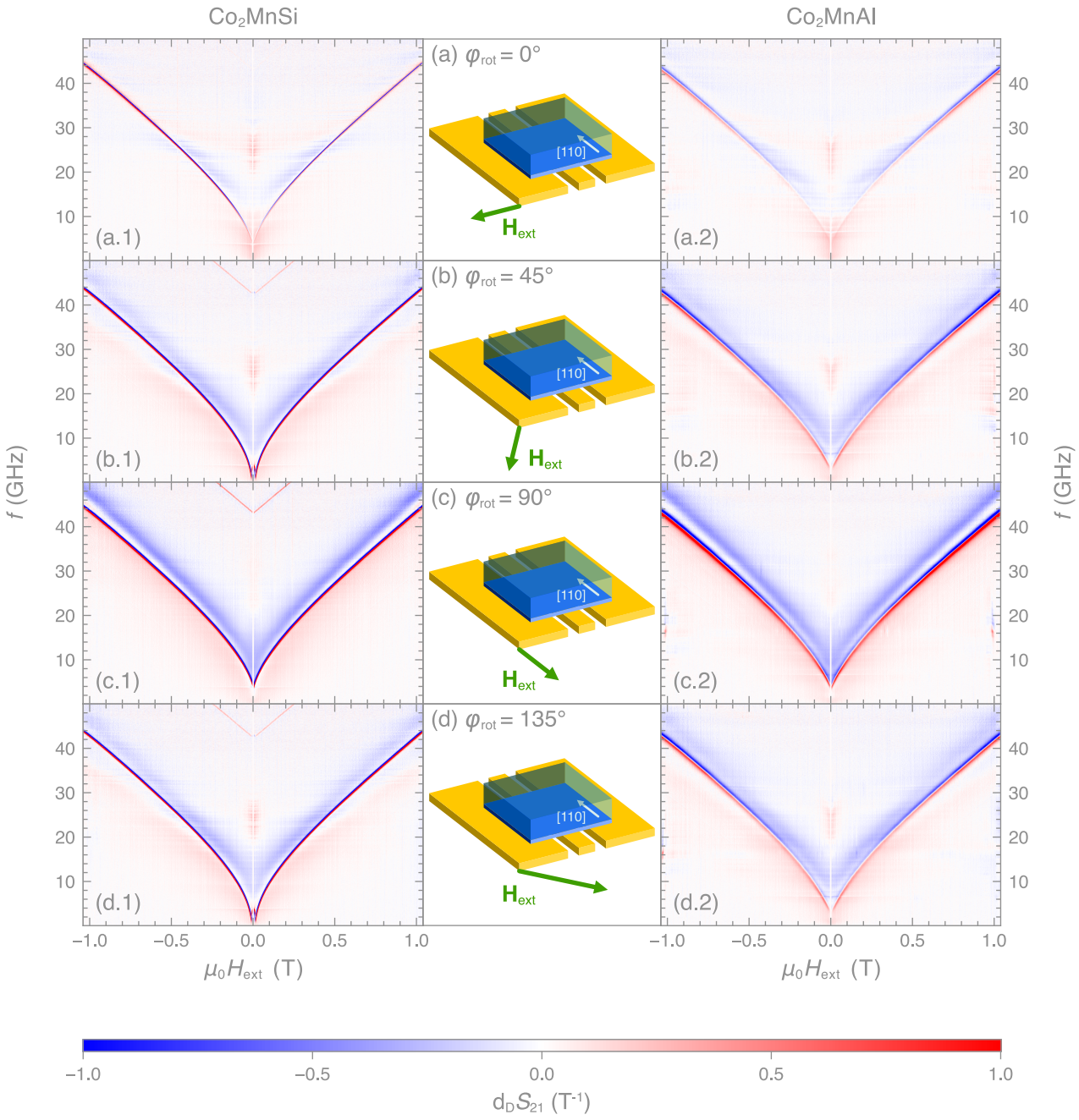

Figure 6.9: Real part of the signal after the background removal procedure using the *derivative divide* algorithm (with $N = 4$ in equation 5.16) from in-plane FMR measurements at different angles for (1) $Co_2MnSi/MgO/Al$ and (2) $Co_2MnAl/MgO/Ti$ for different orientations (a) - (b). Note that the resonance corresponds to the sign change in the real part, which in this colour scheme is represented by the narrow white line in between the red and blue parts, as was introduced in figure 5.7. The signal intensity is highest for (c) $\mathbf{H}_{ext} \parallel$ CPW for both samples, since the contribution of all components of the dynamic field is maximal in this case. A higher order PSSW was detected in the $Co_2MnSi/MgO/Al$ sample for (b.1) $\varphi_{rot} = 45°$, (c.1) $\varphi_{rot} = 90°$ and (d.1) $\varphi_{rot} = 135°$.

The recorded signal intensities in the 2D map plots for the different directions in figure 6.9 vary with the field orientation with respect to the CPW antenna: Independent of the sample under investigation, the highest signal intensities are obtained for the parallel alignment of the magnetic field and the CPW axis, corresponding to figure 6.9 (c), for which all oscillating microwave field components are perpendicular to the magnetisation direction and therefore the excitation is the most efficient. Analogously, the lowest signal intensities are obtained when the magnetic field is aligned perpendicular to the CPW axis, see figure 6.9 (a).

The anisotropy of the signal intensity is equally observed in the rotational

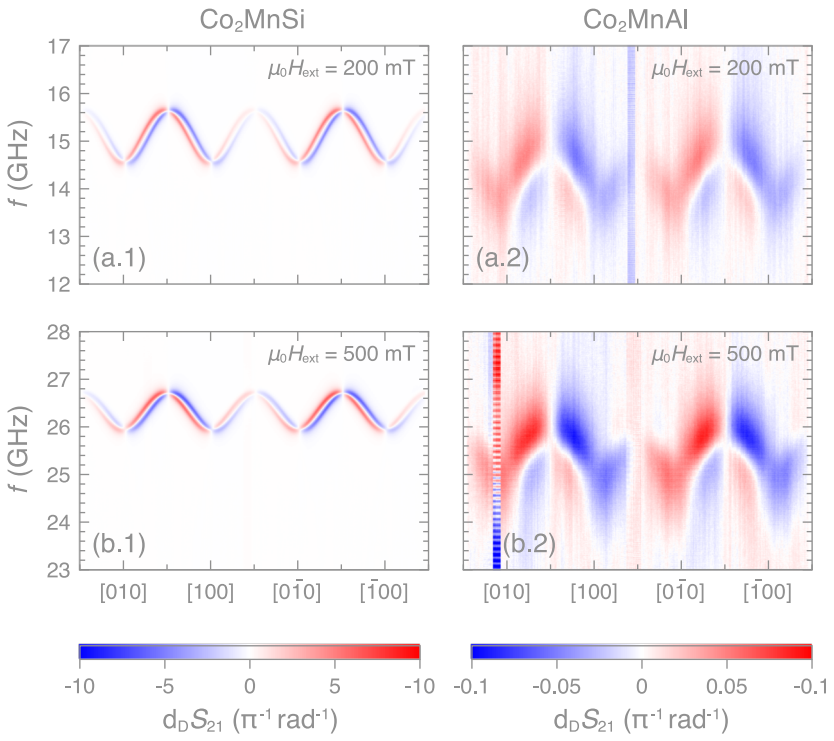

Figure 6.10: Real part of the signal after the background removal procedure using the *derivative divide* algorithm (with $N = 4$ in equation 5.16) from the rotational in-plane FMR measurements for (1) the $Co_2MnSi/MgO/Al$ sample and (2) the $Co_2MnAl/MgO/Ti$ sample measured at a fixed field of (a) $\mu_0 H_{ext} = 200\,mT$ and (b) $\mu_0 H_{ext} = 500\,mT$. Note that the resonance corresponds to the sign change in the real part, which in this color scheme is represented by the narrow white line in between the red and blue parts, as was introduced in figure 5.7. A cubic anisotropy can be clearly identified in both samples, although the poor signal-to-noise ratio in the Co_2MnAl film does not allow for a clear identification of the resonance positions for orientations approaching the perpendicular alignment of the CPW long axis and the external magnetic field.

measurements presented in figure 6.10: The signal fades for orientations towards $[\bar{1}10]$ and $[1\bar{1}0]$ which correspond to an alignment of the field perpendicular to the long axis of the CPW[12], and increases for orientations towards [110] and $[\bar{1}\bar{1}0]$, i.e. an alignment parallel to the long axis of the CPW antenna.

Consequently, the high order perpendicular standing spin wave mode (PSSW) detected in the measurements on the $Co_2MnSi/MgO/Al$ sample is best visible on the measurement with $\varphi_{rot} = 90°$ in figure 6.9 (c.1), but was also detected for $\varphi_{rot} = 45°$ and 135° in figures 6.9 (b.1) and (d.1). No PSSW was detected from the $Co_2MnAl/MgO/Ti$ sample, which is attributed to the generally lower signal intensity obtained from this sample[13].

As detailed in chapter 5, the spectral resonance parameters were fitted using the formula

$$\mathrm{d_D}S_{21}(\omega, H) = -i\omega\tilde{A} \cdot \mathrm{CDQ}(\omega, H_{ext}) \tag{6.14}$$

with the central difference quotient (CDQ) of the susceptibility[14] functions

$$\mathrm{CDQ}(\omega, H_{ext}) = \frac{\chi(\omega + \Delta\omega^{\pm}, H_{ext}) - \chi(\omega - \Delta\omega^{\pm}, H_{ext})}{2 \cdot \Delta\omega^{\pm}} \tag{6.15}$$

as proposed by Maier-Flaig *et al.* [350] to account for the resonance curve distortion for modulation step sizes $\Delta\omega^{\pm} = \Delta H^{\pm} \cdot \frac{\partial\omega_{res}}{\partial H_{ext}}$ close to the resonance linewidth $\Delta\omega_{res}$.

It is important to note that this data analysis procedure can result in systematic errors especially for modulation step sizes close to the resonance linewidth, which cannot fully be accounted for by the CDQ formula. Precisely, in this study an erroneous qualitative behaviour of the resonance linewidths[15] scaling approximately with $1/f$ was obtained for resonance frequencies below 25 GHz. However, for the high-frequency data, the procedure yields correct results and results in the best background suppression among the methods compared in section 5.2.2 and is therefore applied in this study.

12: See table 6.2 and figure 5.4 for the definition of the rotational angle in the experiment.

13: On the scales in figures 6.9 and 6.10 best seen in the latter: The intensity color scale had to be rescaled by two orders of magnitude in order to display the signal from all measurements.

14: In order to avoid an overparametrisation of the CDQ fit function, the saturation magnetisation (entering the susceptibility) was fixed to the values extracted from the VSM measurements as listed in table 6.1.
[350]: Maier-Flaig et al. (2018), 'Note: Derivative divide'

15: A detailed discussion of different data analysis approaches is presented in section 5.2.2, where the analysis of an artificial test data set allowed to prove the non-physical origin of this behaviour.

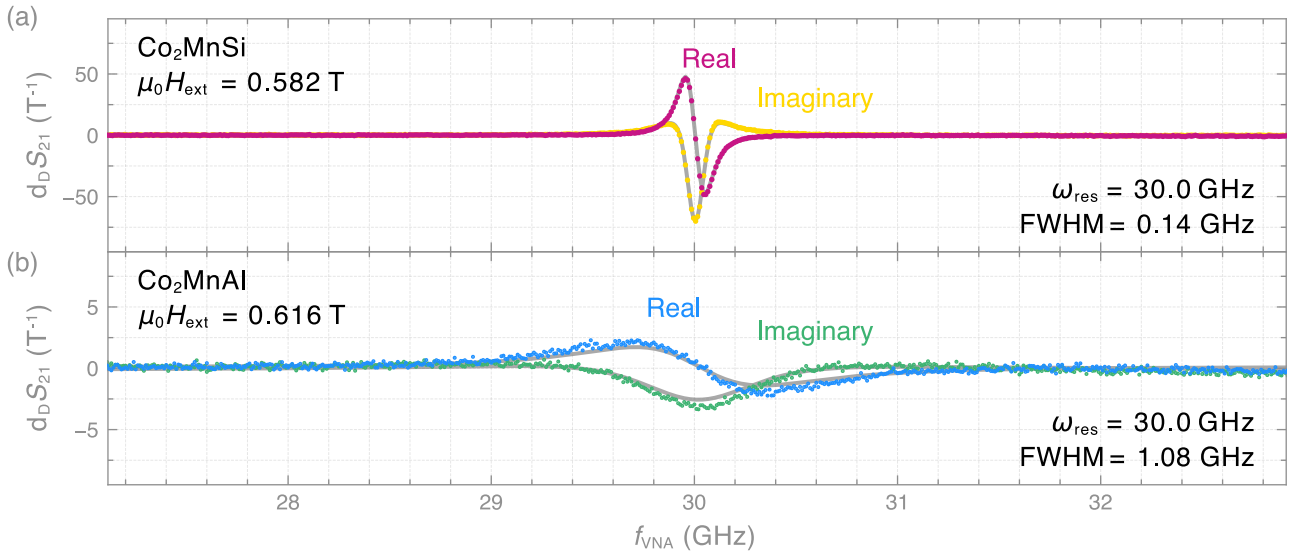

Figure 6.11: Real and imaginary part of the $d_D S_{21}$ signal (with $N = 1$ in equation 6.13) from in-plane FMR measurements with $\mathbf{H}_{ext} \parallel [\bar{1}\bar{1}0]$ corresponding to case (c) in figure 6.9. Resonance curves with $f_{res} = 30\,\text{GHz}$ are compared from (a) the $Co_2MnSi/MgO/Al$ sample and (b) the $Co_2MnAl/MgO/Ti$ sample. The dots indicate the data points and the grey lines correspond to the fitted curves using equation 6.14 with shared parameters between real and imaginary part. Co_2MnSi presents narrower resonance linewidths and larger signal intensities. The absence of side resonances or ripples is an indication for a predominance of one single chemical ordering phase and the desired 2:1:1 stoichiometry.

Two exemplary spectra with $f_{res} \approx 30\,\text{GHz}$ and the respective fit curves are presented in figure 6.11. The resonance curve in the spectrum from the Co_2MnSi thin film in figure 6.11 (a) clearly presents a narrower resonance linewidth and a larger signal amplitude compared to the spectrum obtained from the Co_2MnAl thin film in figure 6.11 (b). Moreover, in both samples no side resonances or ripples were obtained on the resonance curves, which is attributed to a decent 2:1:1 stoichiometry in the Heusler films and an indication for one predominant chemical (dis)ordering phase[16].

The spectral resonance curve fit with the CDQ formula as shown on the exemplary spectra in figure 6.11 was run on all 2080 spectra for each orientation of the field sweep measurements presented in figure 6.9 and was analogously performed on the spectral curves from the rotational measurements presented in figure 6.10. This allowed to extract the resonance frequency and linewidth[17] from each spectrum, which was followed by a subsequent filtering step to remove outliers.

6.2.1 Anisotropic FMR analysis

For the extraction of the defining factors from the FMR data, the multiple data sets from each sample were analysed jointly. As the derivation of the resonance expression following the Smit-Beljers approach in a spherical coordinate system is inconvenient when involving a cubic anisotropy [377], the analytical expression used in this anisotropy study was derived in a cubic coordinate system in consistency with the Kalinikos-Slavin formalism [378, 379] for the dispersion relation used in the third part of this work[18]. Details can be found in the appendix chapters C and D.

Procedure

For an in-plane magnetised thin film with a principal cubic lattice direction coinciding with the film normal, the formula for the anisotropic in-plane

16: A deviation from the 2:1:1 stoichiometry as well as the occurrence of domains of disorder in Co_2MnSi have been related in previous works [71, 76, 83] to the observation of side resonances in the FMR spectra.
[71]: Guillemard et al. (2020), 'Issues in growing Heusler compounds in thin films for spintronic applications'
[76]: Abdallah et al. (2017), 'Evolution of magnetic properties and damping coefficient of Co_2MnSi Heusler alloy with Mn/Si and Co/Mn atomic disorder'
[83]: Friedel (2021), *Thin film materials with ultralow damping for novel magnonic phenomena*

17: Note that the linewidth was not extracted from the rotational scans presented in figure 6.10, since the equidistant angular steps translate into a nonlinear frequency modulation and hence the linewidth is periodically modulated when applying the *derivative divide* algorithm on the rotational data set.

[377]: Baselgia et al. (1988), 'Derivation of the resonance frequency from the free energy of ferromagnets'
[378]: Kalinikos et al. (1986), 'Theory of dipole-exchange spin wave spectrum for ferromagnetic films with mixed exchange boundary conditions'
[379]: Kalinikos et al. (1990), 'The dipole-exchange spin wave spectrum for anisotropic ferromagnetic films with mixed exchange boundary conditions'

18: In this work, the approximative analytical formula from the Kalinikos-Slavin works [378, 379] is used, which for the in-plane FMR transforms to the Kittel function as does the Smit-Beljers approach.

ferromagnetic resonance reads[19]

$$\omega_{\mathrm{res}} = \sqrt{\left(\omega_{\mathrm{H}} + \omega_{\mathrm{exch}} + \omega_{\mathrm{M}} N_{yy}^{\mathrm{ani}}\right) \cdot \left(\omega_{\mathrm{H}} + \omega_{\mathrm{exch}} + \omega_{\mathrm{M}} + \omega_{\mathrm{M}} N_{xx}^{\mathrm{ani}}\right)} \tag{6.16}$$

with $\omega_{\mathrm{H}} = \gamma \mu_0 H_{\mathrm{ext}}$, $\omega_{\mathrm{exch}} = \gamma \frac{2A_{\mathrm{exch}}}{\mu_0 M_{\mathrm{S}}^2} \cdot \frac{n*\pi}{d}$ (with mode number n, exchange constant A_{exch} and film thickness d), $\omega_{\mathrm{M}} = \gamma \mu_0 M_{\mathrm{S}}$ and the anisotropy tensor elements N_{xx}^{ani} and N_{yy}^{ani} given by

$$N_{xx}^{\mathrm{ani}} = \frac{2K_{\mathrm{c1}}}{\mu_0 M_{\mathrm{S}}^2} + \frac{2K_{\mathrm{c2}}}{\mu_0 M_{\mathrm{S}}^2} \cdot \sin^2\left(\varphi_{100}\right) \cos^2\left(\varphi_{100}\right) - \frac{2K_{\mathrm{oop}}}{\mu_0 M_{\mathrm{S}}^2} \tag{6.17}$$

$$N_{yy}^{\mathrm{ani}} = \frac{2K_{\mathrm{c1}}}{\mu_0 M_{\mathrm{S}}^2} \cdot \left(1 - 6 \cdot \sin^2\left(\varphi_{100}\right) \cos^2\left(\varphi_{100}\right)\right) \tag{6.18}$$

where φ_{100} is the angle between the static magnetisation and the [100] axis of the crystal lattice[20] and the terms with K_{c1} and K_{c2} correspond to the cubic anisotropy contribution of the first and second order respectively, as derived in the appendix. Additionally, a potential out-of-plane uniaxial anisotropy described by K_{oop} with the anisotropy axis along the film normal is included in equation 6.17 to test for the presence of a perpendicular magnetic anisotropy in the Co_2MnSi film as had been determined in [91].

Clearly a fitting of these expressions involves quite some cross-correlation between the various parameters, even if the saturation magnetisation was set fixed[21]. Notably, the fit of the gyromagnetic ratio can partly compensate the results of the anisotropy terms, and especially the combination of a first and second order cubic anisotropy or a first order cubic anisotropy with the out-of-plane anisotropy are hardly distinguishable as is obvious from the terms in 6.17 and 6.18.

In an attempt to minimise the problem of over-parametrisation, the data analysis procedure was hence done in multiple steps:

1. First, the gyromagnetic ratio γ was determined from the high field (high frequency) resonance data of the fixed orientation measurements presented in figure 6.9, assuming negligible anisotropy for $\mu_0 H_{\mathrm{ext}} \geq 800\,\mathrm{mT}$.
2. Second, the anisotropy constants were determined from a fitting of equation 6.16 to the rotational data sets at fixed fields as were presented in figure 6.11. This was done in a joint fitting algorithm with shared parameters for both rotational scans at $\mu_0 H_{\mathrm{ext}} = 200\,\mathrm{mT}$ as well as $\mu_0 H_{\mathrm{ext}} = 500\,\mathrm{mT}$ using the fixed γ from the first step (and the fixed M_{S} from the VSM analysis). This anisotropy evaluation step was carried out for three assumption cases:
   a) the simplified case of only a first order cubic anisotropy, i.e. fitting K_{c1} and setting $K_{\mathrm{oop}} = K_{\mathrm{c2}} = 0$.
   b) the natural extension by a second order cubic anisotropy term, i.e. fitting K_{c1} and K_{c2}, but (still) no additional uniaxial anisotropies, i.e. $K_{\mathrm{oop}} = 0$.
   c) the verification of a first order cubic anisotropy K_{c1} combined with an out-of-plane anisotropy[22] K_{oop}, while setting $K_{\mathrm{c2}} = 0$.
3. Third, the entire data set was modelled using the determined anisotropy constants from the best fits in the different cases, for each of which the R^2 values were determined for the Kittel curves as well as the rotational data sets.

19: Note that the anisotropy tensor elements depend on the crystal orientation in the thin film geometry (i.e. the crystal orientation that is identical to the film normal) - and this also influences the factorisation of the terms in the resonance equation. This specific expression was derived for the out-of-plane direction aligning with a principal axis of the cubic lattice (here the [001] direction), see appendix chapter D.

20: Here, the [001] direction is identified as the film normal, then the [100] is in the film plane. The expressions are, however, equally true for an identification of [100] as the film normal, obviously then φ_{100} simply needs to be redefined as the in-plane angle, e.g. to [001].

[91]: Solano Córdova (2024), 'Temperature dependent spin wave study of magnetic properties and spin-polarized electron transport in $Fe_{1-X}V_X$ and Co_2MnSi epitaxial films'

21: In all fits, the saturaton magnetisation entering equation 6.16 in N_{xx}^{ani}, N_{yy}^{ani} and $\omega_{\mathrm{M}} = \gamma \mu_0 M_{\mathrm{S}}$ was set fixed to the value obtained from VSM measurements, as listed in table 6.1.

22: Commonly also referred to as perpendicular magnetic ansitropy (PMA).

Note that this approach involves the simplified assumption that the two contributions (second order cubic anisotropy with K_{c2} and PMA with K_{oop}) do not coexist[23].

Signature of K_{c2} vs. K_{oop}

At this point it is important to point out that only from the in-plane resonance data a qualitative distinction between the case of a first and second order cubic anisotropy term (here case (b) with K_{c1}, K_{c2}) and the case of a combination of first order cubic anisotropy with an out-of-plane uniaxial anisotropy[24] (here case (c) with K_{c1}, K_{oop}) is hardly possible for films with a principle crystal lattice axis coinciding with the film normal: Due to the similar signatures on the resonance frequency, suitable combinations of parameters can be found for both assumptions equally making up for the discrepancy in the simplified case (a).

This is not only a result from the fit results about to be discussed[25], but also clear from the anisotropy tensor element N_{xx}^{ani} in equation 6.17: As both anisotropy contributions only act on the out-of-plane component of the dynamic magnetisation[26], they enter in the same term in the resonance equation 6.16.

In the in-plane FMR case, the main difference between the two terms is the directional modulation on the contribution in K_{c2}, whereas the out-of-plane term with K_{oop} is uniform in the film plane. Precisely, the addition of the K_{c2} in equation 6.17 results in the addition of the term

$$\omega_M \cdot \frac{2K_{c2}}{\mu_0 M_S^2} \cdot \sin^2(\varphi_{100}) \cos^2(\varphi_{100}) \cdot \left(\omega_H + \omega_{exch} + \omega_M \frac{2K_{c1}}{\mu_0 M_S^2} \cdot \left(1 - 6 \cdot \sin^2(\varphi_{100}) \cos^2(\varphi_{100})\right) \right) \tag{6.19}$$

in the root in equation 6.16, when comparing to the case of a K_{c1} only. The addition of the PMA term with K_{oop} only yields an additional term

$$-\omega_M \cdot \frac{2K_{oop}}{\mu_0 M_S^2} \cdot \left(\omega_H + \omega_{exch} + \omega_M \frac{2K_{c1}}{\mu_0 M_S^2} \cdot \left(1 - 6 \cdot \sin^2(\varphi_{100}) \cos^2(\varphi_{100})\right) \right) \tag{6.20}$$

in the root.

Consequently, the second order cubic anisotropy introduces an angular dependence[27] in $4\varphi_{100}$ in addition to the $2\varphi_{100}$ modulation, which can principally result in a qualitative difference between the two cases. However, the dominance of the $4\varphi_{100}$ terms is only observable for a fixed M_S and γ at particular combinations of K_{c1}, K_{c2} and $\mu_0 H_{ext}$, whereas in most cases the in-plane anisotropy can be equally modelled with a combination of a (different) first order cubic anisotropy K_{c1} yielding the terms $\sim \sin^2(\varphi_{100}) \cos^2(\varphi_{100})$, and an out-of-plane term with K_{oop} then serving as a compensating offset[28]. In that case, the two anisotropies cannot be distinguished solely from the in-plane FMR data.

For a clear distinction between the two anisotropy contributions, additional data is necessary, ideally in the form of an out-of-plane measurement[29]: The second order cubic anisotropy does not yield a contribution to the magnetisation dynamics for an orientation along a principle cubic lattice axis. Hence for films where [001] corresponds to the film normal, like in this study, the

23: This is *per se* not true, as nothing prevents the two anisotropies from coexisting. It would, however, directly lead to an overparametrisation of the in-plane data, especially in cases where neither of the two terms is massively dominant over the others. As no such indication is given in the data sets in this study, the coexistence of K_{c2} and K_{oop} is neglected here for this simple practical reason.

24: Commonly also referred to as a perpendicular magnetic anisotropy (PMA) for cases where $K_{oop} > 0$ leads to a preferential out-of-plane alignment of the magnetisation.

25: See figure 6.12 (b) and (c) and the respective parameters in table 6.3

26: The x component in local coordinates. For a definition of the coordinate system, see figure 8.1.

27: As it features a term

$$-\gamma^2 \frac{24 K_{c1} K_{c2}}{M_S^2} \sin^4(\varphi_{100}) \cos^4(\varphi_{100}) \tag{6.21}$$

which cannot be modelled without the K_{c2}.

28: This is, in fact, the case in the present study on Co_2MnSi, as will be seen on the next pages.

29: Technically, the addition of various rotational in-plane measurements at other external fields is another possibility, since the terms including the external magnetic field differ in the two cases: As stated above, the use of K_{c1}, K_{c2} with $K_{oop} = 0$ yields an additional angular modulation that is multiplied with the Larmor frequency of the external magnetic field ω_H, whereas the use of K_{c1}, K_{oop} with $K_{c2} = 0$ results in an additional isotropic term only. Hence, the two could be principally distinguished in a larger rotational data set, however, this would be based on a pure quantitative evaluation of the fit match and the results presented hereafter suggest a large uncertainty margin on the rotational fits, making this approach unpreferable over the extension by an out-of-plane measurement. - Still, this addition of more in-plane rotational scans could be followed e.g. if out-of-plane measurements are technically impossible.

K_{c2} contribution and the PMA are easily distinguishable when combining the in-plane FMR study with an out-of-plane measurement.

Indeed, it is principally sufficient (for films with the film normal coinciding with a principal lattice axis) to do a single FMR measurement along an in-plane and another along an out-of-plane direction in order to conclude on the PMA and the first order cubic anisotropy simply from the symmetry of the anisotropy field contributions, as is for instance detailed in [91]. However, the in-plane direction must be chosen as a [100] direction to do so, since for a measurement along the [110] direction, the K_{c2} and K_{oop} contribution are mathematically equal resulting in an additional uncertainty[30] in the evaluation.

[91]: Solano Córdova (2024), 'Temperature dependent spin wave study of magnetic properties and spin-polarized electron transport in $Fe_{1-X}V_X$ and Co_2MnSi epitaxial films'

30: Note that, while the entire problem is here treated as if the two could not coexist, nothing prohibits a combination of the K_{oop} and K_{c2} contributions. Hence, the choice of the in-plane axis is significant for a correct evaluation of the K_{oop}.

This generalised conclusion is not only relevant to the specific case of [001] oriented films, but relevant to other thin film orientations of cubic crystals as well: Equal attention needs to be given for instance, when the film normal commonly corresponds to the [111] direction, as then the contribution of the second order cubic anisotropy and the K_{oop} are mathematically the same for the FMR in the out-of-plane geometry, and the contributions can only be distinguished by the different nature of the respective terms in the in-plane case. This might be of particular relevance for the thorough anisotropy analysis in YIG films for instance [380], where the film normal commonly corresponds to the [111] direction[31], especially with the rising interest in doped YIG for PMA applications.

[380]: Lee et al. (2016), 'Ferromagnetic resonance of a YIG film in the low frequency regime'

31: When grown on GGG(111) substrates [132].

[132]: Dubs et al. (2020), 'Low damping and microstructural perfection of sub-40nm-thin yttrium iron garnet films grown by liquid phase epitaxy'

Discussion of results from this study

The gyromagnetic ratio was determined to be 28.4±0.3 GHz/T for the Co_2MnSi sample and 28.9 ± 0.4 GHz/T for the Co_2MnAl sample, which are close to the free electron value and correspond to an electron Landé factor of $g = 2.03 \pm 0.02$ and $g = 2.06 \pm 0.03$ respectively.

Co_2MnSi

For the Co_2MnSi film, the rotational data points with the respective fit curves obtained for the best fit in the three cases are shown in the comparative figure 6.12 with the corresponding fit results given in table 6.3, where additionally an angular offset was added as a fit parameter to equations 6.16, 6.17 and 6.18 in order to account for a potential misalignment.

The simplest case (a) of a fit with only a first order cubic anisotropy term replicated the data sufficiently for field orientations parallel to the principal axes ⟨100⟩ of the Co_2MnSi lattice, as is presented in figure 6.12 (a.200mT) and 6.12 (a.500mT). However, for orientations along the face diagonals ⟨110⟩ of the cubic lattice, this simplified model resulted in an underestimation of the resonance frequency for both field values, hence suggesting the necessity of an inclusion of the second order term.

Yet, as detailed above, the second order cubic anisotropy cannot be easily distinguished from a perpendicular magnetic anisotropy in the given geometry, and the aforementioned ambiguity of the two cases is indeed observed for the data set from the Co_2MnSi film studied here.

Table 6.3: Fit parameters corresponding to the three cases shown in figure 6.12. Note that the errors on the K_{c2} and K_{oop} are comparable: Although the absolute error on the K_{oop} is significantly lower, it amounts to 54 % of the fit parameter and is thus comparable to the 51 % relative error obtained on the K_{c2}.

	γ $\left(\frac{\text{GHz}}{\text{T}}\right)$	K_{c1} $\left(\frac{\text{kJ}}{\text{m}^3}\right)$	K_{c2} $\left(\frac{\text{kJ}}{\text{m}^3}\right)$	K_{oop} $\left(\frac{\text{kJ}}{\text{m}^3}\right)$	φ_{offset} (°)
(a)		−7.9 ± 0.9	-	-	1.9 ± 1.9
(b)	28.4 ± 0.3	−8.1 ± 0.9	37.7 ± 19.4	-	1.9 ± 1.7
(c)		−9.2 ± 1.1	-	−7.1 ± 3.8	1.9 ± 1.7

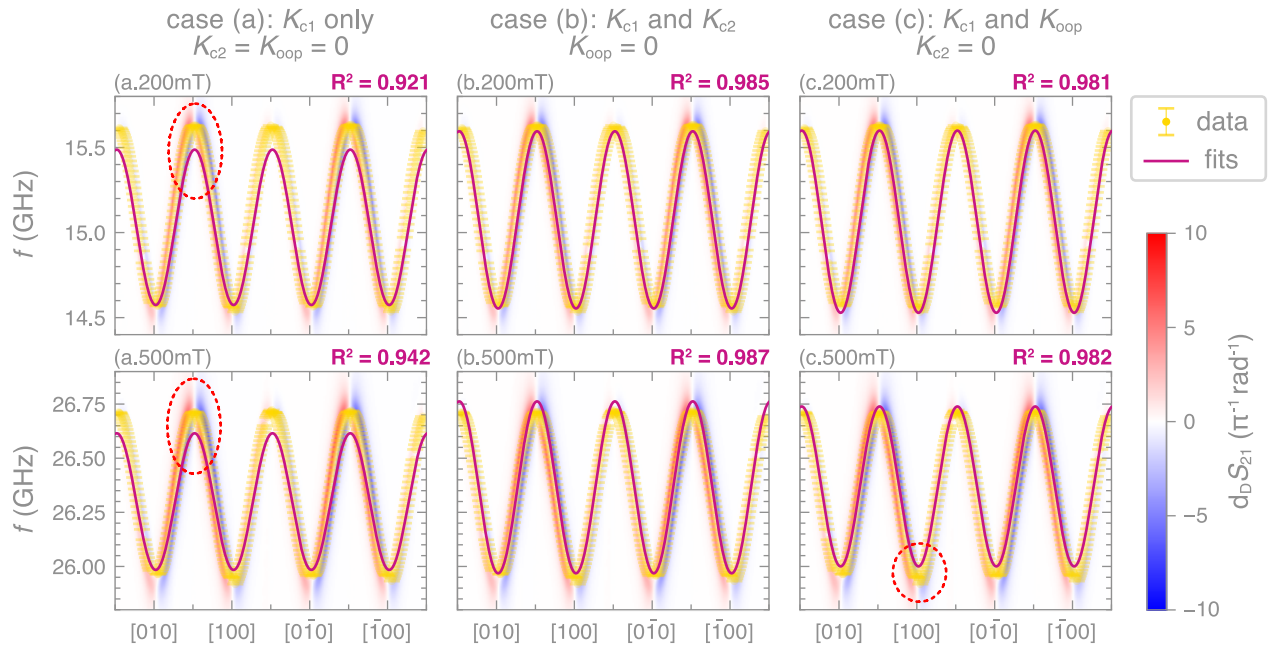

Figure 6.12: Results of the fits to the rotational data from the Co_2MnSi sample for the different cases listed above. The intensity maps from the derivative divide procedure are overlayed with the resonance data points obtained from the spectral resonance curve fitting (as shown in the examples in figure 6.11) and the fit curves from the analysis procedure with the three anisotropy approaches. The red dashed circles indicate the points of significant qualitative deviations between the fit and the resonance data. The R^2 values indicated above each subpanel were calculated to determine the quality of the fit to the data shown in the respective subpanel.

Consequently, both approaches yield suitable fit results which significantly improve the replication of the data along the ⟨110⟩ directions and present the aforementioned correlation between the parameters:

- Hardly any difference is obtained on the first order cubic anisotropy constant K_{c1} when adding the second order cubic anisotropy to the model (compare case (a) to case (b)), as the K_{c2} mainly acts on the orientations along the ⟨110⟩ directions along which it improves the fit.
- In the case of an additional K_{oop} instead of the K_{c2} on the other hand, the new term results in a uniform offset of the resonance frequencies, and the increase of the modulation amplitude is achieved by an increase of the K_{c1} value.

Moreover, the subsequent evaluation of the match with the Kittel curves listed in table 6.4 confirms the overall improvement when adding either K_{c2} or K_{oop}, where the average fit changes from $R^2 = 0.9958$ to $R^2 = 0.9966$ in both cases.

Hence, only the rotational fits presented in figure 6.12 give a slight indication towards a marginally better modelling with the second order cubic anisotropy, yet for a conclusion on the predominance of one assumption over the other, the in-plane data sets are clearly insufficient.

Table 6.4: Comparison of the R^2 values evaluating the match of the Kittel curves on the data from the Co_2MnSi film, each modelled with the best fit parameters from the three approaches as listed in table 6.3. Additionally, the average R^2 values of the Kittel fits are listed, and the R^2 values from the rotational fits are recalled.

φ_{rot} = $\mathbf{H}_{ext} \parallel$	−180° [1̄10]	−135° [010]	−90° [110]	−45° [100]	0° [1$\bar{1}$0]	45° [0$\bar{1}$0]	90° [$\bar{1}\bar{1}$0]	135° [$\bar{1}$00]	average Kittel	200 mT rot.	500 mT rot.
(a)	0.9935	0.9955	0.9930	0.9956	0.9969	0.9978	0.9960	0.9980	0.9958	0.9210	0.9421
(b)	0.9956	0.9953	0.9950	0.9954	0.9982	0.9977	0.9976	0.9978	0.9966	0.9851	0.9870
(c)	0.9953	0.9955	0.9948	0.9956	0.9980	0.9979	0.9974	0.9981	0.9966	0.9810	0.9818

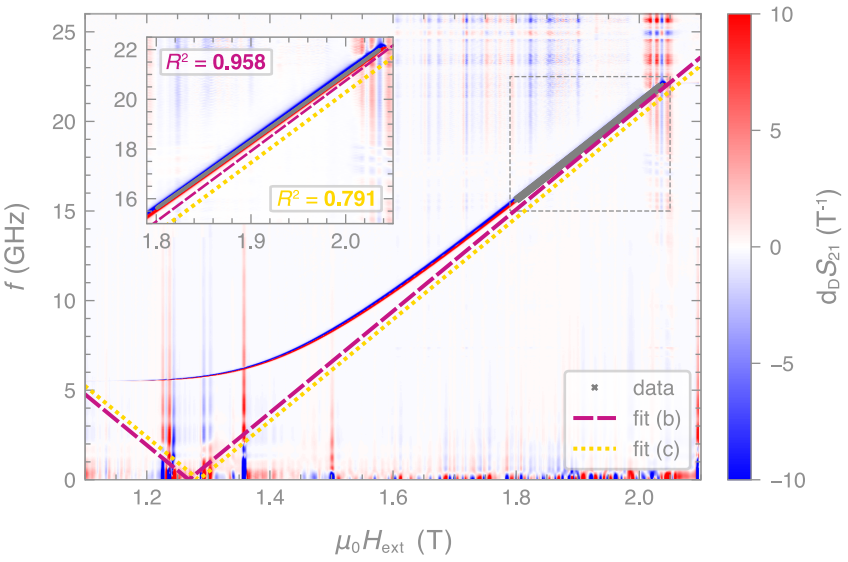

Figure 6.13: Fit results for case (b) and case (c) modelled to an out-of-plane data set from the same sample. The inset shows a zoom-in on the area marked by the dashed rectangle additionally indicating the obtained R^2 values evaluating the match of the two models to the high-field data, i.e. for $\mu_0 H_{ext} > 1.8\,\mathrm{T}$, for which the spectral resonance data positions (obtained from the automated spectral resonance curve fitting) are indicated by the grey cross markers.

The data sets were therefore complemented by an additional out-of-plane measurement, which is presented in figure 6.13 together with the respective resonance curves corresponding to the two modelling cases with the fit parameters as indicated in table 6.3. For the out-of-plane case, the resonance condition is given by

$$\omega_{res} = \omega_H + \omega_{exch} + \omega_M \cdot \left(\frac{2K_{c1}}{\mu_0 M_S^2} + \frac{2K_{oop}}{\mu_0 M_S^2} \right) - \omega_M \tag{6.22}$$

for a principal cubic lattice axis coinciding with the film normal, where the contribution of the second order cubic anisotropy cancels out. Consequently, the two assumptions corresponding to case (b) and (c) result in a qualitative difference and with the parameters listed in table 6.3 the corresponding match with the additional out-of-plane data set yielded $R^2 = 0.958$ for the case (b) with a first and second order cubic anisotropy term, whereas $R^2 = 0.791$ was obtained for the case (c) assuming a first order cubic anisotropy and an additional out-of-plane magnetic anisotropy.

The evaluation of the out-of-plane match thus gives an indication towards an improved description of the system by a first and second order anisotropy, yet the trace of the resonance in figure 6.13 was found to deviate from the expected linear behaviour described by equation 6.22 for quite large fields, which can be an indication for a misalignment of the rotational magnet with respect to the film normal, potentially falsifying the conclusion at this point. Moreover, the entire evaluation was carried out under the assumption of an exclusive presence of either a second order cubic anisotropy, or a perpendicular magnetic anisotropy, which is a significant simplification of the problem.

Therefore, the evaluation carried out in this work is interpreted as a strong indication towards a non-negligible second order cubic anisotropy in the Heusler compound Co_2MnSi, the implications of which will be discussed in the next section 6.2.2 jointly with the results from the evaluation of the C_2MnAl data presented hereafter.

Finally, the exchange constant was determined for both cases from a fit with equation 6.16, setting $n = 1$ and all other parameters to the values indicated in table 6.3, as well as the thickness to $d = 20\,\mathrm{nm}$ and the saturation magnetisation to the value from VSM measurements as before. This resulted in an extraction of $A_{exch} = (25.5 \pm 0.2)\,\mathrm{pJ/m}$ for the exchange constant in both

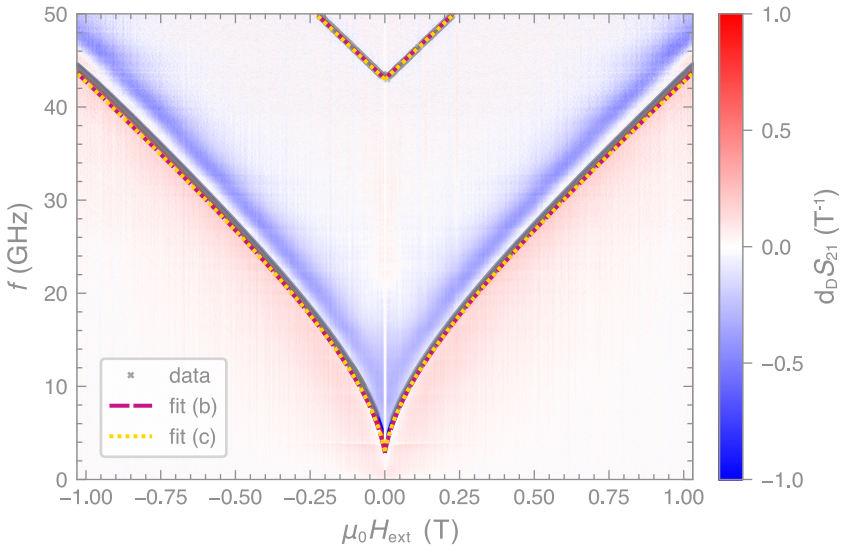

Figure 6.14: Final fit results for case (b) and case (c) shown on the exemplary data corresponding to panel (c.1) in figure 6.9, and to $\varphi_{rot} = 90°$ (positive field values) and $\varphi_{rot} = -90°$ (negative field values) in table 6.4. Hardly any difference is obtained between the curves corresponding to the two cases on this scale, as is expected from the similar R^2 values in table 6.4.

cases (b and c in table 6.3), which matches the exchange constants reported in other studies, e.g. $A_{exch} = 25.6 - 28.7\,pJ/m$ from FMR measurements [381] or $A_{exch} = (23.5 \pm 1)\,pJ/m$ from conventional Brillouin light scattering (BLS) measurements [153, 382] on sputtered Co_2MnSi films.

[381]: Belmeguenai et al. (2012), 'Structural and magnetic properties of Co_2MnSi thin films'

[153]: Kubota et al. (2009), 'Structure, exchange stiffness, and magnetic anisotropy of $Co_2MnAl_xSi_{1-x}$Heusler compounds'

[382]: Hamrle et al. (2009), 'Determination of exchange constants of Heusler compounds by Brillouin light scattering spectroscopy'

Co_2MnAl

For the Co_2MnAl film, the poor signal-to-noise ratio on the rotational data[32] didn't allow to perform the anisotropy analysis in the same way. Instead, the field sweeps along the high symmetry directions (as presented in figure 6.9) were used in the second step for the fitting of the model with the three assumptions (case a: K_{c1} only, case b: K_{c1} and K_{c2}, case c: K_{c1} and K_{oop}). The resulting best fit parameters are listed in table 6.5 with the respective average R^2 value and are plotted as functions of the rotational angle on top of the rotational data in figure 6.15. The related R^2 values for the individual curves are listed in table 6.6.

As for the Co_2MnSi film, the simplified case (a) assuming only a first order cubic anisotropy was insufficient to model the data from the Co_2MnAl film, where the main problem is the general reduction of the resonance frequencies for $K_{c1} < 0$ compared to $K_{c1} = 0$: For a negligible anisotropy, a decent match is achieved for the orientation along the principal lattice axes ⟨100⟩ with the saturation magnetisation taken fixed from VSM measurements as listed in table 6.1. Consequently, as the first order cubic anisotropy constant would need to be negative to achieve a modulation with frequency minima along these directions, the induced reduction of the resonance frequency requires a counteraction in the modelling either by an increased saturation magnetisation or the addition of an anisotropy contribution acting alike.

This is precisely the reason for the significantly improved fits when including either K_{c2} or K_{oop}, not only in the Kittel fit evaluation on the fixed orientation data listed in table 6.5, but also when comparing the fit results to the rotational data in figure 6.15: As both terms act like an effective out-of-plane contribution, the modelling with the fixed saturation magnetisation from the VSM measurements is improved in both cases.

However, the comparison with the rotational data sets in figure 6.15 indicates a potential overestimation of the K_{oop} contribution in case (c) and a better qualitative agreement seems to be achieved with the second order cubic anisotropy term, where remarkably still a negligible first order constant

32: Note that in figure 6.10, the data is presented with $N = 4$ and an averaging over 4 spectra in the derivative divide procedure to enhance the contrast on the colormap. However, the signal-to-noise ratio on the spectra for the resonance analysis is significantly poorer. Additionally, since the resonance curves on this data set are asymmetric (the resonance position corresponds to the white line indicating the sign change of the signal of each spectrum, but the signal above the resonance frequency is always significantly larger than the signal below the resonance frequency), often a falsified resonance position was obtained from the spectral resonance fits, hence making the further analysis impossible.

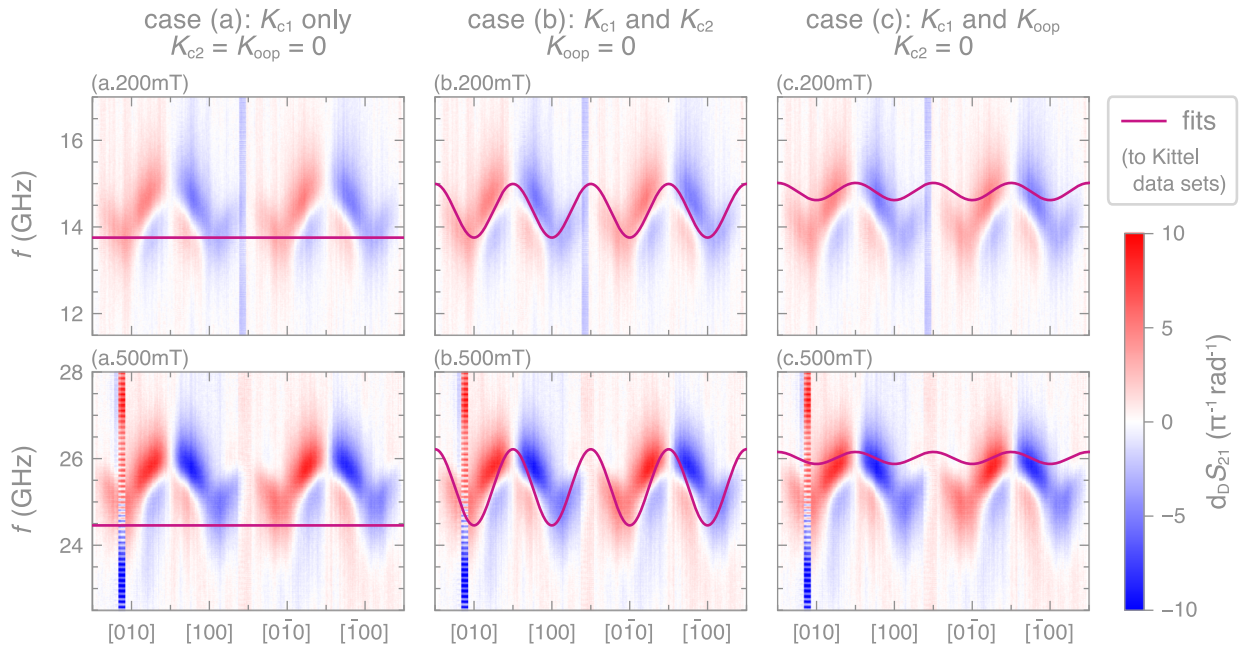

Figure 6.15: Results of the fits for the three different cases to the Kittel curve data from the Co_2MnAl sample, plotted as a function of the in-plane angle and displayed superposed with the rotational FMR data as intensity maps (where the resonance corresponds to the sign change).

Table 6.5: Fit parameters obtained from the modelling of the Kittel data along the high-symmetry directions. Due to the lack of angular points apart from the high symmetry directions, the φ_{offset} parameter was not used in the fitting procedure in this case.

	γ $\left(\frac{GHz}{T}\right)$	K_{c1} $\left(\frac{kJ}{m^3}\right)$	K_{c2} $\left(\frac{kJ}{m^3}\right)$	K_{oop} $\left(\frac{kJ}{m^3}\right)$	R^2 total
(a)		0 ± 0.35	-	-	0.9649
(b)	28.9 ± 0.4	0 ± 0.22	316.7 ± 4.4	-	0.9921
(c)		-2.63 ± 0.05	-	-74.6 ± 0.2	0.9995

$K_{c1} \approx 0$ is obtained and the anisotropic modulation can be entirely described by the second order term.

Given the significant difference between the modelling results in the two cases for this sample, a clear distinction is to be expected when complementing the data by an additional out-of-plane measurement. Yet, lacking the latter, no further conclusion can be drawn from the data at this point, and therefore the different implications of both cases will be discussed in the next subsection.

No higher order PSSWs were detected in the Co_2MnAl sample in this study, and hence the extraction of the exchange constant was impossible in the present work. However, a literature research yields consistently lower exchange parameters reported for Co_2MnAl compared to Co_2MnSi [153, 383], as listed in table 1.1. With $A_{exch} = (25.5 \pm 0.2)$ pJ/m for Co_2MnSi from this work being comparable to $A_{exch} = (23.5 \pm 1)$ pJ/m from [153], an exchange constant similar to $A_{exch} = (4.8 \pm 1)$ pJ/m reported in the same study for Co_2MnAl is expected, amounting to approximately 20 % of the parameter for Co_2MnSi.

[153]: Kubota et al. (2009), 'Structure, exchange stiffness, and magnetic anisotropy of $Co_2MnAl_xSi_{1-x}$Heusler compounds'
[383]: Umetsu et al. (2011), 'Spin Wave-Stiffness Constants of Half-Metallic Ferromagnets Co_2YZ (Y=Cr, Mn, and Fe, Z=Ga, Al, and Si) Heusler Alloys'

Table 6.6: Comparison of the R^2 values evaluating the match of the individual Kittel curves on the data from the Co_2MnAl film, each modelled with the best fit parameters (obtained from the joint fit on the entire data set) from the three approaches as listed in table 6.5.

φ_{rot} = $\mathbf{H}_{ext} \parallel$	−180° [$\bar{1}$10]	−135° [010]	−90° [110]	−45° [100]	0° [1$\bar{1}$0]	45° [0$\bar{1}$0]	90° [$\bar{1}\bar{1}$0]	135° [$\bar{1}$00]	average Kittel
(a)	0.9135	0.9835	0.9677	0.9811	0.9222	0.9877	0.9758	0.9878	0.9649
(b)	0.9997	0.9835	0.9985	0.9811	0.9993	0.9877	0.9993	0.9878	0.9921
(c)	0.9993	0.9991	0.9989	0.9997	0.9998	0.9995	0.9997	0.9996	0.9995

6.2.2 Anisotropy interpretation

The similarity between the second order cubic anisotropy and the out-of-plane magnetic anisotropy not only makes the distinction between both anisotropy contributions difficult (or even impossible when only analysing data along certain high symmetry directions), but naturally raises the question whether a thorough distinction is then even necessary and worth the effort[33]. The answer is certainly up to the individual case, and depends inter alia on the data at hand, the attainable precision based on the significance of the related distinct anisotropy effects, as well as the desired application use.

Different origins of the anisotropy energy contributions

A uniaxial magnetic anisotropy contribution perpendicular to the film plane is not intrinsic to the (undistorted) cubic lattice, but is typically growth induced e.g. by exploiting substrate-mismatch related strain resulting in lattice distortions from the cubic to an orthorhombic structure [188, 384, 385], or by utilising interface anisotropies in multilayer stacks [386, 387].

For a significant lattice distortion to result in an out-of-plane uniaxial anisotropy e.g. to introduce a PMA, the Co_2MnX compounds need to be grown on adequate seed layers or in superlattices for instance with Mn_3Ge as in [188]. For the growth on MgO(001) as in this study, little distortion is expected from the decent lattice match with the MgO(001) substrate [71]. Also, while a mismatch induced deformation was found on the MgO/Co_2MnSi interface as previously reported in [81, 83], the distortion affects the interface layers only and is esteemed insignificant compared to the majorly relaxed Co_2MnSi lattice especially for film thicknesses of 20 nm as in this work.

A potential origin of an out-of-plane anisotropy contribution in MgO/Co_2MnSi systems can also arise from the chemical nature of the interface with MgO, as was concluded based on a theoretical study in [388]: For the hypothetical case of five layers of Co_2MnSi on MgO, the reported DFT calculations yielded a different anisotropy induced by the possible chemical interface junctions. Precisely, a negative $K_{oop} = -397\,kJ/m^3$ (favouring an in-plane alignment) is found for a Co_2-layer adjacent to the MgO, whereas a negligible[34] $K_{oop} = 65\,kJ/m^3$ is listed for a MnSi-junction at the MgO/Co_2MnSi interface[35]. However, given the purely interfacial origin and the low film thickness in the calculations[36], the effect is expected to be significantly reduced or negligible for a 20 nm thick film as studied in this work.

The magnetocrystalline anisotropy generally arises from the spin-orbit coupling in the crystal lattice and thus mimics the intrinsic cubic lattice symmetry [389]. It is therefore principally independent of sample geometry factors such as the film thickness or orientation, as long as the lattice symmetry is not distorted. The second order contribution is typically neglected [72, 153, 160], but can be of significant influence as has for instance been reported for Co-substituted YIG [390].

In the Co_2Mn-based Heusler compounds, the main contribution to the magnetic moment stems from the Mn atoms [103, 117], which in the case of the $L2_1$ ordered Co_2MnSi film form a cubic sublattice as introduced in chapter 1 contributing with approximately $\sim 4\,\mu_B$ to the total magnetic moment. The Co atoms form another cubic sublattice, which is shifted by $(\frac{1}{4}, \frac{1}{4}, \frac{1}{4})$ in the unit cell with respect to the manganese lattice, hence the Co atoms are located on the body diagonal directions of the Mn lattice. This particular distribution of the magnetic atoms in the Heusler lattice could give rise to a significant second

33: In particular, such a question can quickly arise when the main interest in determining the anisotropy constants is for a later modelling of a practical application case, where often additional uncertainties e.g. from structuring additionally reduce precision and hence "only" a sufficient reproduction of the observed behaviour is sought.

[188]: Palin et al. (2023), 'Engineering of perpendicular magnetic anisotropy in half-metallic magnetic Heusler epitaxial thin films'

[384]: Maryško (1981), 'Ferromagnetic resonance relations in {110} garnet films with induced orthorhombic anisotropy'

[385]: Mellinger et al. (2020), 'Perpendicular magnetic anisotropy in conducting $NiCo_2O_4$ films from spin-lattice coupling'

[386]: Daalderop et al. (1992), 'Prediction and confirmation of perpendicular magnetic anisotropy in Co/Ni multilayers'

[387]: Beaujour et al. (2009), 'Ferromagnetic resonance linewidth in ultrathin films with perpendicular magnetic anisotropy'

[188]: Palin et al. (2023), 'Engineering of perpendicular magnetic anisotropy in half-metallic magnetic Heusler epitaxial thin films'

[71]: Guillemard et al. (2020), 'Issues in growing Heusler compounds in thin films for spintronic applications'

[81]: De Melo et al. (2021), 'Unveiling transport properties of Co_2MnSi Heusler epitaxial thin films with ultra-low magnetic damping'

[83]: Friedel (2021), *Thin film materials with ultralow damping for novel magnonic phenomena*

[388]: Munira et al. (2014), 'Achieving perpendicular anisotropy in half-metallic Heusler alloys for spin device applications'

34: Compared to the demagnetisation anisotropy constant $K_{demag} = \mu_0 M_S^2/2 \approx 630\,kJ/m^3$ for $M_S \approx 1000\,kA/m$.

35: In the simulation study, additionally a junction with an adjacent MnMn-layer is listed to yield $K_{oop} = 123\,kJ/m^3$ yet such a layer is more likely to arise in non-epitaxial growth like sputtering, and additionally no indication for a positive PMA-like out-of-plane anisotropy was observed in this work, hence this case is to be esteemed irrelevant in this discussion.

36: The simulated 5 layers of the Heusler film correspond to a film thickness of $d < 3$ nm.

[389]: Van Vleck (1937), 'On the Anisotropy of Cubic Ferromagnetic Crystals'

[72]: Gaier et al. (2008), 'Influence of the $L2_1$ ordering degree on the magnetic properties of Co_2MnSi Heusler films'

[153]: Kubota et al. (2009), 'Structure, exchange stiffness, and magnetic anisotropy of $Co_2MnAl_xSi_{1-x}$Heusler compounds'

[160]: Meng et al. (2017), 'Thickness dependence of magnetic anisotropy and intrinsic anomalous Hall effect in epitaxial Co_2MnAl film'

[390]: Maryško (1980), 'Ferromagnetic resonance relations in {111}-oriented garnet films'
[103]: Guillemard (2019), 'Half-metal magnets Heusler compounds for spintronics'
[117]: Kumar et al. (2024), 'Exploring the physical properties of Co_2MnSi full Heusler alloy'

[25]: Graf et al. (2011), 'Simple rules for the understanding of Heusler compounds'

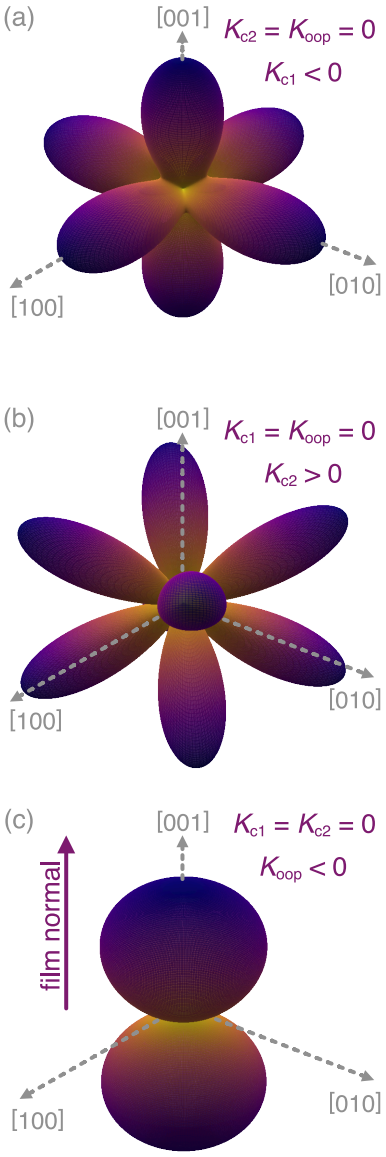

Figure 6.16: Illustration of (a) the first order cubic anisotropy (for negative K_{c1}), (b) the isolated second order cubic anisotropy (for positive K_{c2}) as well as (b) the out-of-plane magnetic anisotropy (for negative K_{oop}) as a surface plot. Note that the $K_{oop} < 0$ symmetry is the same as from the demagnetisation energy contribution - for $K_{oop} > 0$ the out-of-plane anisotropy would counteract the demagnetisation energy and favour an out-of-plane alignment for large K_{oop}, hence the common denomination as *perpendicular magnetic anisotropy (PMA)* for that case.

order anisotropy in the material in a simplified picture, aligning with the insignificant first order term but comparably large second order constant for the case of the B2 disordered Co_2MnAl film in this study, where the occupation on the Mn-sublattice is randomised with the Si-sublattice. Hence, the symmetry of the atomic distribution in the respective crystal lattices can be taken as another hint towards the presence of the second order cubic anisotropy rather than an out-of-plane anisotropy in the studied films. Yet it is important to note that the microscopic origin of the anisotropy formation is far more complex than a simple spatial distribution consideration, as the magnetic properties are determined by the hybridised atomic orbitals in play [25]. For pertinent conclusions on the potential origin of the second order cubic anisotropy term and the resulting interpretation of the magnetocrystalline anisotropy it would thus be necessary to perform a thorough theoretical modelling e.g. by DFT calculations.

Symmetry of the energy contributions

For an intuitive understanding of the difference between the anisotropy contributions, it is helpful to visualise the symmetries of the respective energy contributions as surface plots, as was already done in chapter 4 for the introduction of the cubic anisotropy.

Exemplary (normalised) surface plots corresponding to the relevant anisotropy energy terms in question are illustrated in figure 6.16: The first order cubic anisotropy in figure 6.16 (a) is recalled from figure 4.2 and shows the expected symmetry with maximal contributions for orientations along the principal crystal lattice directions. The second order uniaxial anisotropy in figure 6.16 (b) only yields energy contributions for orientations with a non-zero projection on all principal axes of the cubic crystal lattice, with a maximal effect for an orientation along the diagonal [111] of the lattice. Finally, the perpendicular magnetic anisotropy in figure 6.16 (c) mimics the demagnetisation energy symmetry for $K_{oop} < 0$, with a maximal contribution along the film normal and an isotropic behaviour for rotations around the film normal.

Given the symmetries shown in figure 6.16, it is clear that for a determination of an out-of-plane magnetic anisotropy term in a cubic system, particular attention needs to be given to the axes to be chosen for the evaluation. Ideally, the potential K_{oop} contribution in cubic crystals is determined (or ruled out) from a comparison of FMR measurements taken along the out-of-plane direction as well as an in-plane axis of equal crystallographic symmetry. However, this is not possible for all cases (e.g. for the out-of-plane axis coinciding with a [111] direction), and in those situations it can be necessary to perform rotational scans, potentially even at oblique angles.

For the case of the out-of-plane axis corresponding to a principal lattice axis, the problem luckily simplifies and the K_{oop} is clearly distinguishable from the first and second order cubic contributions by performing FMR measurements along e.g. the [100] direction in the film plane, as well as along the out-of-plane direction. Equally, the surface plots in figure 6.16 illustrate the ambiguity for a comparison of a measurement taken along the [110] direction in the film plane and another along the out-of-plane direction: Here, a combination of first and second order cubic anisotropy could yield the same result as the combination of a first order cubic term with an out-of-plane anisotropy.

Illustrations of the superpositions corresponding to the results obtained from the anisotropy analysis in this study are shown in figure 6.17.

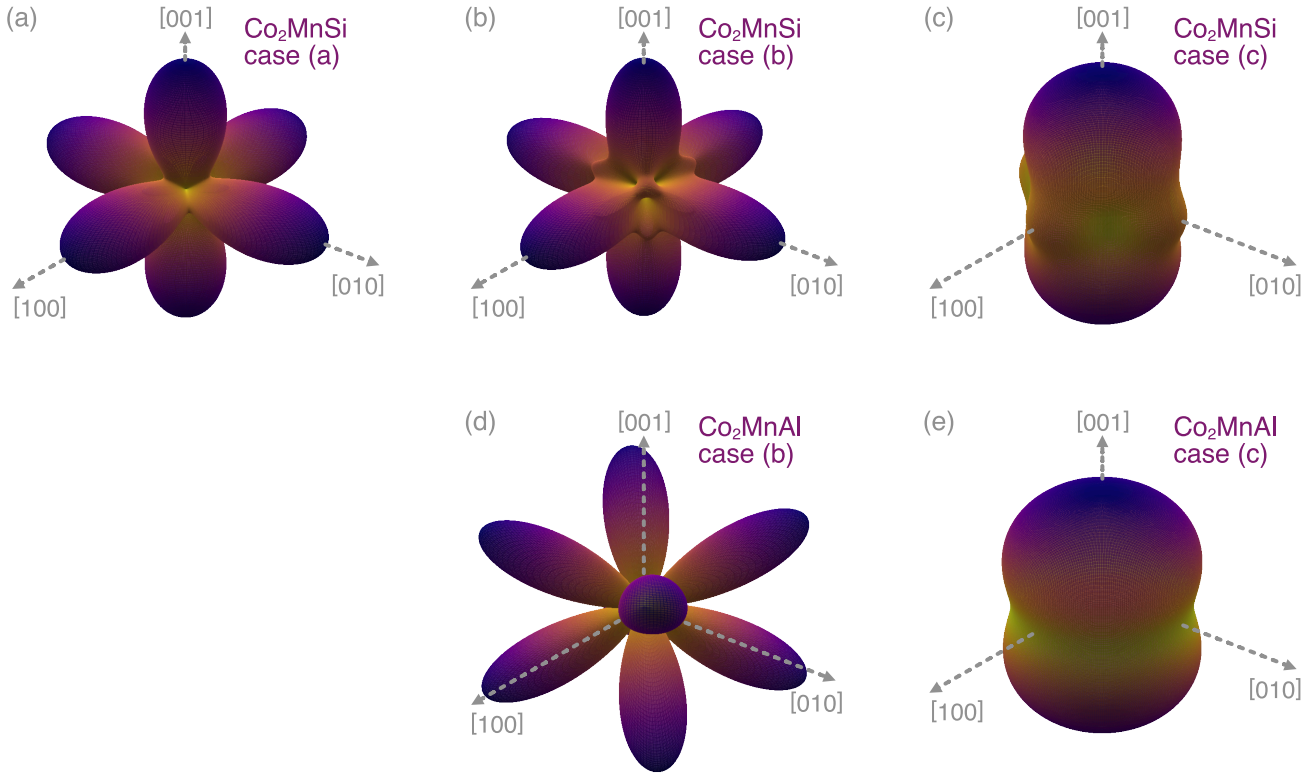

Figure 6.17: Illustration of the normalised energy surface plots corresponding to the anisotropy results obtained from the different fit model assumptions (case a: K_{c1} only, case b: K_{c1} and K_{c2}, case c: K_{c1} and K_{oop}) on the two samples: (a), (b) and (c) show the results obtained for Co_2MnSi corresponding to the normalised total anisotropy energy calculated from the parameters as listed in table 6.3 accordingly, (e) and (f) show the corresponding case for the Co_2MnAl sample obtained from the parameters as listed in table 6.5.

The energy surface plots in figure 6.17 notably illustrate the similar symmetry of the energy surfaces obtained in the model cases (b) with K_{c1} & K_{c2} and (c) with K_{c1} & K_{oop} for a rotation in the (001) plane: This is particularly obvious in the plots of the respective results obtained on Co_2MnSi shown in figure 6.17 (b) and (c), but also the case for Co_2MnAl, where the (001) plane is nearly isotropic.

Moreover, the surface plots for Co_2MnSi in figure 6.17 (b), (c) are an ideal example illustrating the importance of the in-plane axis choice for a determination of the K_{oop} contribution: Comparing a set of measurements along the [110] and [001] direction only cannot enable a distinction between the combination of K_{c1} and PMA (in figure 6.17 (c)) and the combination of the first and second order cubic anisotropy (in figure 6.17 (b)). Comparing the [100] and [001] direction, however, would allow for a conclusion on the presence of a K_{oop}, as K_{c2} does not contribute to either measurement.

Finally, the surface plots for Co_2MnAl in figure 6.17 (d), (e) are an ideal example showcasing the different impact of the two energy contributions on the out-of-plane case. This is particularly interesting when comparing the resulting change in the *effective magnetisation* M_{eff}[37]: In case (b), the maximal anisotropy field is obtained for an in-plane orientation along the ⟨110⟩ directions, for which the effective change in the magnetisation would be equal to

$$H_{Kc2}(\mathbf{M_0} \parallel [110]) = \frac{2K_{c2}}{\mu_0 M_S} \cdot \sin^2\left(\frac{\pi}{4}\right)\cos^2\left(\frac{\pi}{4}\right) \approx 170 \pm 2\,\frac{\mathrm{kA}}{\mathrm{m}} \tag{6.23}$$

$$\Rightarrow \mu_0 H_{Kc2} \approx 213 \pm 3\,\mathrm{mT} \tag{6.24}$$

for $K_{c2} = 316.7 \pm 4.4\,\mathrm{kA/m^3}$ which is comparable to the change in magnetisation

37: The effective magnetisation is commonly introduced to combine the contributions with the same signature as the demagnetisation term in one fit parameter (introduced in the model then in the place of the saturation magnetisation). Clearly, the contributions which can be combined into an effective magnetisation depend on the data sets available: If modelling the full space, essentially only PMA-like contributions can be accounted for as an effective magnetisation. However, when only comparing measurements along selected orientations, the effect of a reduced/increased magnetisation (or: the effect of K_{oop}) can be mimicked by other anisotropy contributions as well, as discussed just above.

by the combination of the out-of-plane anisotropy and the first order cubic anisotropy in case (c), where

$$H_{\mathrm{Kc1}} + H_{\mathrm{Koop}} = \frac{2K_{\mathrm{c1}}}{\mu_0 M_{\mathrm{S}}} + \frac{2K_{\mathrm{oop}}}{\mu_0 M_{\mathrm{S}}} \approx -165.6 \pm 0.5 \,\frac{\mathrm{kA}}{\mathrm{m}} \tag{6.25}$$

$$\Rightarrow \mu_0 \left(H_{\mathrm{Kc1}} + H_{\mathrm{Koop}}\right) = -208.2 \pm 0.6\,\mathrm{mT} \tag{6.26}$$

for $K_{\mathrm{c1}} = -2.63 \pm 0.05\,\mathrm{kA/m^3}$ and $K_{\mathrm{c2}} = -74.6 \pm 2.2\,\mathrm{kA/m^3}$ as listed in table 6.5. However, the two cases yield a significant difference for the out-of-plane geometry[38]: In case (c) the significant change in the effective magnetisation related to the PMA with $\mu_0 H_{\mathrm{Koop}} \approx 201.1 \pm 0.6\,\mathrm{mT}$ must be observed in any direction, whereas in case (b) the out-of-plane measurement is described by an effective magnetisation equal to the saturation magnetisation, i.e. no anisotropy influence affecting this geometry.

38: Unfortunately no corresponding out-of-plane was recorded in the course of this study, but given the significant difference of the anisotropy fields, a clear indication of the predominance of one term over the other (or a coexistence of the two) is to be expected.

This difference essentially allowed for the conclusion on the improved match with case (b) for the Co_2MnSi film based on the out-of-plane measurement presented in figure 6.13, where the *effective magnetisation* graphically corresponds to the point where $f = 0$ for the curves following the linear function in equation 6.22 and the related anisotropy fields for the Co_2MnSi film in the out-of-plane direction yield

$$H_{\mathrm{Kc1}} \approx -13 \pm 1 \,\frac{\mathrm{kA}}{\mathrm{m}} \Rightarrow \mu_0 H_{\mathrm{Kc1}} = -16 \pm 2\,\mathrm{mT} \tag{6.27}$$

for the case (b) with only a cubic anisotropy contribution $K_{\mathrm{c1}} = -8.1 \pm 0.9\,\mathrm{kJ/m^3}$ (since $K_{\mathrm{c2}} = 37.7 \pm 19.4\,\mathrm{kJ/m^3}$ does not contribute), and

$$H_{\mathrm{Kc1}} + H_{\mathrm{Koop}} \approx -26 \pm 6 \,\frac{\mathrm{kA}}{\mathrm{m}} \Rightarrow \mu_0 \left(H_{\mathrm{Kc1}} + H_{\mathrm{Koop}}\right) = -33 \pm 8\,\mathrm{mT} \tag{6.28}$$

for the case (c) with $K_{\mathrm{c1}} = -9.2 \pm 1.1\,\mathrm{kJ/m^3}$ and $K_{\mathrm{oop}} = -7.1 \pm 3.8\,\mathrm{kJ/m^3}$.

In general, the distinction between the different anisotropy terms is necessary for a decent prediction of the anisotropy effects along arbitrary directions, or the application to the modelling e.g. of microstructures fabricated from the same sample and the expected dispersion relations for propagating spin waves in such samples, as is central to the third part of the work. Moreover, in the prospect of multilayer coupling investigations for which the Co_2MnAl sample was produced as a reference film, the drastic difference between the two cases obtained in the Co_2MnAl film is of significant importance, highlighting the need for a thorough analysis of the anisotropy contributions[39].

39: And underlining the need to do an additional FMR measurement in the out-of-plane geometry to complement this study.

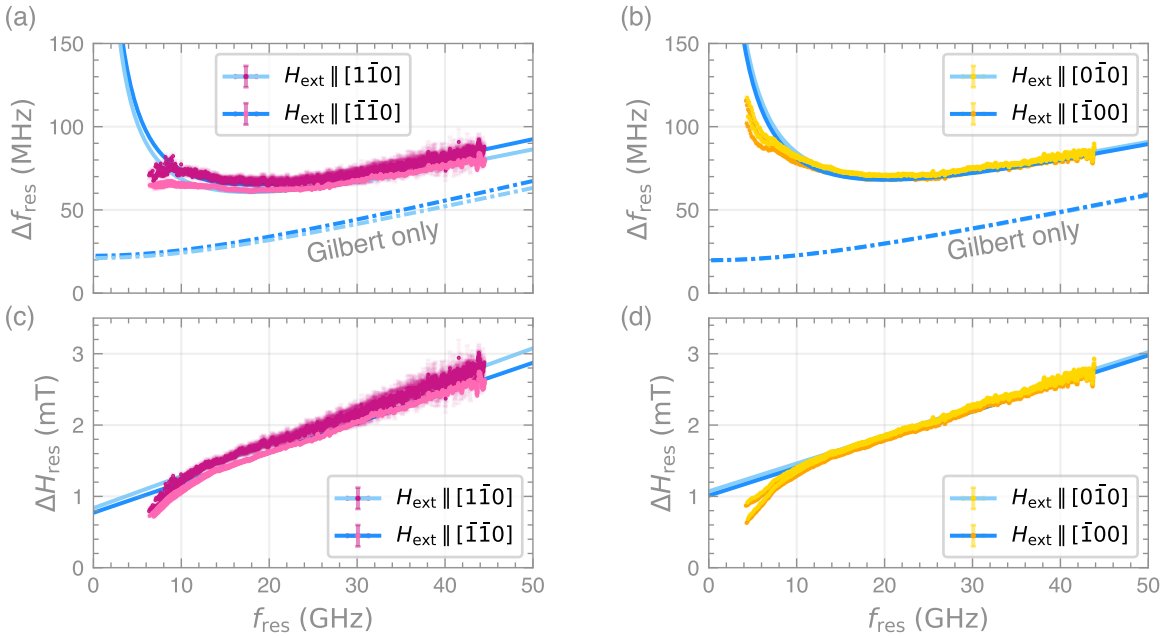

Figure 6.18: Resonance linewidths (HWHM) extracted from the spectral resonance curve fits from the Co_2MnSi film (a) for the field oriented along the ⟨110⟩ directions and (b) the ⟨100⟩ directions. A transformation to field linewidths is shown in (c) and (d) respectively. The blue lines correspond to the fit curves as described in the text, and the dashed lines correspond to the frequency linewidth that would be obtained from the respective Gilbert damping only (setting the non-Gilbert like terms described by the inhomogeneous linewidth to zero).

6.2.3 Linewidth analysis

The resonance linewidths Δf_{res} were extracted from the spectral resonance fits, examples of which were presented in figure 6.11. The extracted spectral resonance linewidths are shown in figure 6.18 (a) and (b) and were found to follow approximately a $1/f_{res}$ relation for resonance frequencies up to $\sim 20\,\mathrm{GHz}$, as was already seen in the methodical study in chapter 5. Such a behaviour can originate from a systematic error introduced by the modulation amplitude in the chosen data post-treatment approach, as was discussed on the case of an artificial data set in section 5.2.2. However, similar behaviour has been reported in other studies on the frequency linewidth in FMR experiments, see e.g. [264, 351, 391], where it was linked to large field inhomogeneities in the system.

[264]: Kuanr et al. (2005), 'Narrowing of the frequency-linewidth in structured magnetic strips'
[351]: Kalarickal et al. (2006), 'Ferromagnetic resonance linewidth in metallic thin films'
[391]: Silva et al. (1999), 'Inductive measurement of ultrafast magnetization dynamics in thin-film Permalloy'

Given the systematic introduction of a fixed $\Delta H^{\pm}$ by the data post-processing in the present study, a formulation of the inhomogeneous linewidth as a fixed field linewidth parameter ΔH_0 is chosen in this evaluation, as is common in field-swept FMR measurements, for which the resonance linewidth ΔH_{res} follows the simple linear expression

$$\mu_0 \Delta H_{res} = \mu_0 \Delta H_0 + \frac{F_{lw} \alpha \omega_{res}}{\gamma} \tag{6.29}$$

with the factor $F_{lw} = 1$ for the HWHM and $F_{lw} = 2$ for the FWHM. The study of the field linewidth from in-plane FMR thus allows to extract the damping parameter α from a simple linear regression, for which the frequency linewidths were transformed into field linewidths following [264]

[264]: Kuanr et al. (2005), 'Narrowing of the frequency-linewidth in structured magnetic strips'

$$\Delta H_{res} = \Delta \omega_{res} \cdot \left(\frac{\partial \omega_{res}}{\partial H_{ext}} \right)^{-1} \tag{6.30}$$

where the expression for the derivative $\frac{\partial \omega_{res}}{\partial H_{ext}}$ depends on the orientation and

Table 6.7: Inhomogeneous linewidth $\mu_0\Delta H_0$ and Gilbert damping parameter α from the linear fits for $f_{res} \geq 20\,GHz$ on the linewidths presented in figure 6.18 (c) and (d).

	easy axes			hard axes		
φ_{rot} $\mathbf{H}_{ext} \parallel$	0° $[1\bar{1}0]$	90° $[\bar{1}\bar{1}0]$	avg.	45° $[0\bar{1}0]$	135° $[\bar{1}00]$	avg.
$\alpha\ (10^{-3})$	1.27 ± 0.02	1.19 ± 0.02	1.23 ± 0.02	1.11 ± 0.02	1.11 ± 0.01	1.11 ± 0.01
$\mu_0\Delta H_0$ (mT)	0.84 ± 0.03	0.77 ± 0.02	0.80 ± 0.02	1.07 ± 0.02	1.01 ± 0.02	1.04 ± 0.02

the anisotropy terms entering the Kittel equation 6.16. Given the slightly better match with the combination of K_{c1} and K_{c2} in the anisotropy analysis, the extracted parameters as listed for case (b) in table 6.3 were used here[40] and the resulting field linewidths are shown in figure 6.18 (c) and (d) respectively.

The linear model given in equation 6.29 was then fitted to the data using only the data points for which $f_{res} \geq 20\,GHz$ for each setup orientation[41], for which the fit results are listed in table 6.7 and the corresponding fit curves are plotted as bold lines with the data in figure 6.18 (c) and (d).

The fit curves were transformed using the inverse relation from equation 6.30 in order to display the corresponding curves with the frequency linewidths in figure 6.18 (a) and (b). In addition, the frequency linewidths corresponding only to the Gilbert damping contribution of the parameters listed in table 6.7 are plotted as dashed lines in figure 6.18 (a) and (b) for comparison.

Four key conclusions can be drawn from the evaluation of the results shown in figure 6.18 and listed in table 6.7:

- A significant non-Gilbert-like linewidth contribution is observed when comparing the solid fit curves in figure 6.18 (a) and (b) with the dashed lines representing the part corresponding to only the Gilbert-like (viscous) damping contributions. The corresponding inhomogeneous linewidth parameters $\mu_0\Delta H_0$ are nearly equal to the field modulation step size $\Delta H^{\pm} = 1\,mT$ employed in the data post-processing procedure[42] and are therefore likely influenced by the spectral modulation introduced in the background removal procedure as discussed in chapter 5.
- The extracted Gilbert damping parameters are approximately three times larger than the ultralow value of $\alpha = 4.6 \times 10^{-4}$ reported in [64], but larger values closer to $\alpha = 1 \times 10^{-3}$ were equally found in other epitaxial films grown on the same setup as for instance reported in [81]. In particular, the extracted damping parameters of $\alpha \approx 1.1 - 1.2 \times 10^{-3}$ match the values determined on a comparable film (similar sample stack with MgO top and bottom interfaces) by José Solano in [91], which corresponds to the sample investigated in the third part of this work.
- An anisotropic Gilbert damping parameter is not ruled out, but cannot be confirmed either. Indeed, the extracted Gilbert damping parameters suggest an anisotropy of the viscous damping contributions with a consistent decrease by 10 % when comparing the [110] directions to the [100] directions. While this observation matches the report from other studies [392], the effect is suppressed in the investigated sample by the significant non-Gilbert-like contribution with a counteracting increase in the extracted inhomogeneous linewidth parameter, and hardly any directional difference is observed on the extracted resonance linewidths. Such non-Gilbert-like anisotropic magnetic damping can for instance originate from an angular-dependent two-magnon scattering at a rectangular network of misfit dislocations [209]. A signature of this

40: Note that as the measurements evaluated for the frequency linewidths not only correspond to the same directions, but are exactly the same measurements as evaluated before for the anisotropy analysis, where a similar match was obtained for case (b) and (c), the choice of one model cannot introduce an error at this point. (It would, however, introduce an falsified factor when evaluating e.g. measurements taken along an oblique direction.)

41: Corresponding to two data sets, e.g. $\varphi_{rot} = 45°$ and $\varphi_{rot} = -135°$ were recorded in the same setting by simply inverting the set field value as displayed in figure 6.9.

42: See the discussion around figure 5.8 on page 102.

[64]: Guillemard et al. (2019), 'Ultralow Magnetic Damping in Co_2Mn-Based Heusler Compounds'

[81]: De Melo et al. (2021), 'Unveiling transport properties of Co_2MnSi Heusler epitaxial thin films with ultra-low magnetic damping'

[91]: Solano Córdova (2024), 'Temperature dependent spin wave study of magnetic properties and spin-polarized electron transport in $Fe_{1-X}V_X$ and Co_2MnSi epitaxial films'

[392]: Yilgin et al. (2007), 'Anisotropic Intrinsic Damping Constant of Epitaxial Co_2MnSi Heusler Alloy Films'

[209]: Heinrich et al. (2004), 'Magnetic properties of NiMnSb(001) films grown on InGaAs/InP(001)'

process is a modulated resonance linewidth reflecting the symmetry of the defect network [210], which could fit to the lattice dislocations commonly observed at the MgO/Co_2MnSi interfaces [81, 83] due to the slight lattice misfit as detailed in section 3.2.2.

- The modulation step size of $\Delta H^{\pm} = 1\,\mathrm{mT}$ is too large for a thorough linewidth analysis and the overmodulation distorting the extracted resonance linewidth behaviour cannot be ruled out albeit the consideration via the CDQ function[43].

For the Co_2MnAl film, no sensible resonance linewidths could be extracted, which is attributed to the poor signal-to-noise ratio in the related measurements and was not further investigated.

[210]: Woltersdorf et al. (2004), 'Spin dynamics in ultrathin film structures with a network of misfit dislocations'

[81]: De Melo et al. (2021), 'Unveiling transport properties of Co_2MnSi Heusler epitaxial thin films with ultra-low magnetic damping'

[83]: Friedel (2021), *Thin film materials with ultralow damping for novel magnonic phenomena*

43: See the details given in section 5.2.2 on page 103.

6.3 Conclusions

This chapter presented an elaborate study of the static and dynamic properties in the Heusler compounds Co_2MnSi and Co_2MnAl[44] by means of vibrating sample magnetometry and ferromagnetic resonance spectroscopy.

The VSM study allowed for an extraction of the parameters defining the hysteresis loops and the results were summarised in table 6.1 on page 117. For the further study in this work, the most important result from the VSM measurements is certainly the extracted saturation magnetisation, particularly for Co_2MnSi, where for both compounds approximately the values expected from literature were reproduced. Moreover, the hysteresis curves presented an anisotropic signature in both cases, although more pronounced on the Co_2MnSi film.

This anisotropy was further investigated in FMR measurements, where a cubic anisotropy was observed in both compounds with the expected in-plane rotational signature corresponding to negative first order cubic anisotropy constants. Yet for both samples, a consideration of either a second order cubic or an out-of-plane uniaxial anisotropy contribution in addition to the first order cubic anisotropy was found to be necessary to achieve a correct description of the system[45]. The best matching results are summarised in tables 6.8 and 6.9.

The analysis of the data obtained from the Co_2MnSi film suggests a best description of the measured data by a combination of the first and second order cubic anisotropy with the anisotropy constants listed in table 6.3. In this case, the ratio of the anisotropy constants amounts to $K_{c2}/|K_{c1}| \approx 4.65$, which translates to an identification of the principal cubic lattice axes $\langle 100 \rangle$ as hard axes, and the face diagonals $\langle 110 \rangle$ as easy axes of the magnetocrystalline anisotropy energy as was introduced on page 71.

For the Co_2MnAl sample, an improved qualitative match with the rotational data also suggests a likely second order cubic anisotropy contribution, yet the low resonance amplitudes and relatively poor signal to noise ratio as well as the lack of an out-of-plane data set did not allow for any further conclusions. Moreover, the in-plane FMR data on the (non-annealed) Co_2MnAl film suggests a noteworthy increase of the effective magnetisation by approximately 200 mT, which underlines the importance of a further anisotropy analysis for the use as an intended reference sample.

The subsequent discussion of the symmetry implications arising from the different anisotropy terms emphasized the importance of a sensible measurement geometry when aiming for a distinction between the different terms, which is a generalised conclusion applicable to any cubic system, and of particular importance in the context of the growing interest in perpendicular magnetic anisotropy applications.

Finally, the resonance linewidths were briefly analysed yielding and an indication towards an anisotropic damping with a 10 % change and lowest values for a field application along the $\langle 100 \rangle$ directions (hard axes). However, while this matches similar observations reported in [392], it is counteracted in the present study by the change in the anisotropic inhomogeneous resonance linewidth which could be potentially attributed to an angular-dependent two-magnon scattering contribution related to the lattice dislocations at the interfaces. However, a distortion of the resonance linewidths due to the modulation from the data processing could not be ruled out to affect the analysis.

44: Not annealed.

Table 6.8: Characterisation results of the Co_2MnAl sample studied in this chapter, corresponding to sample S2.1 in table 2.2.

VSM		
$\mu_0 M_S$	742 ± 4	kA/m
	3.80 ± 0.3	μ_B/f.u.
FMR		
γ	28.9 ± 0.4	GHz/T
g	2.06 ± 0.03	
K_{c1}	0 ± 0.2	kJ/m^3
K_{c2}	316.7 ± 4.4	kJ/m^3

Table 6.9: Characterisation results of the Co_2MnSi sample studied in this chapter, corresponding to sample S1.4 in table 2.1.

VSM		
$\mu_0 M_S$	996 ± 5	kA/m
	4.87 ± 0.04	μ_B/f.u.
FMR		
γ	28.4 ± 0.3	GHz/T
g	2.03 ± 0.02	
K_{c1}	−8.1 ± 0.9	kJ/m^3
K_{c2}	37.7 ± 19.4	kJ/m^3
A_{exch}	25.5 ± 0.2	pJ/m
$\alpha_{[100]}$	1.11 ± 0.01	$\times 10^{-3}$
$\alpha_{[110]}$	1.23 ± 0.02	$\times 10^{-3}$

45: It is emphasized that while a combination of the two cannot be excluded it would overparametrise the system for the available data sets and was therefore not considered in the analysis.

[392]: Yilgin et al. (2007), 'Anisotropic Intrinsic Damping Constant of Epitaxial Co_2MnSi Heusler Alloy Films'

Magneto-optical signal from Co_2Mn-based Heusler thin films

7

7.1 linMOKE vs. QMOKE . . 137
Magnetic anisotropy 139
Magneto-optical anisotropy 140
7.2 Wavelength dependence in linMOKE and QMOKE . 142
7.3 BLS signal intensity . . . 145
7.4 Conclusions 147

A magneto-optical signal study was performed on series of Co_2MnX thin films with X={Al_xSi_{1-x}, Ge_xGa_{1-x}, Sn} in order to determine the suitability of these compounds for investigation with important techniques in magnonics, i.e. experiments with Brillouin light scattering (BLS) as well as experiments relying on the magneto-optical Kerr effect (MOKE).

The presented study in this chapter relates to a preliminary study [83] of BLS signal intensities from thermal spin waves in the same compounds, where a laser wavelength of $\lambda = 532\,\text{nm}$ was used and lowest signal intensities were obtained for half-metallic compounds Co_2MnSi and Co_2MnGe compared to other Heusler compounds of the series such as Co_2MnAl. Yet with higher interest in Co_2MnSi for low-damping applications, the motivation for the sequel in this work was to improve magneto-optical signal results by changing to a different wavelength.

Indeed, a recent study of the magneto-optical Kerr effect on epitaxial Co_2MnSi films by Silber *et al.* [82] reports a strong wavelength dependence of linear and quadratic magneto-optical tensor elements of Co_2MnSi in the range $\lambda = 225\,\text{nm} - 1550\,\text{nm}$ and indicates an increased effect for improved chemical ordering in the Heusler compound. With the magneto-optical tensor linking BLS intensity to the square of the complex Kerr angle as introduced in section 4.3, this is of particular significance for BLS measurements as well.

To study the linear and quadratic magneto-optical effects in the whole Co_2MnX thin film series in this thesis, the evolution of linear and quadratic magneto-optical signal was investigated as a function of the crystallographic orientation in LMOKE measurements performed with a tunable laser in the wavelength range $\lambda = 550\,\text{nm} - 900\,\text{nm}$. The results of the rotational study at $\lambda = 636\,\text{nm}$ reveal a significant QMOKE signature on the obtained hysteresis loops and the largest effect was indeed obtained from the compound Co_2MnSi as will be discussed in the first section of this chapter. Subsequently, a thorough angle-resolved wavelength-dependent study will be discussed comparing the results obtained from Co_2MnSi and Co_2MnAl for $\lambda = 550\,\text{nm} - 900\,\text{nm}$. Additionally, a second BLS study on thermally excited spin waves was performed in the Co_2MnX thin film series using a laser wavelength of $\lambda = 457\,\text{nm}$ and will be set into relation with the MOKE results and the previously obtained BLS signal intensities at $\lambda = 532\,\text{nm}$ in the third section of this chapter.

MOKE and BLS measurements presented in this chapter were performed within the framework of a master research project carried out by Nicolas Fermon from the école normale supérieure Paris-Saclay [360] which was supervised by the author of the present work.

[83]: Friedel (2021), *Thin film materials with ultralow damping for novel magnonic phenomena*

[82]: Silber et al. (2020), 'Scaling of quadratic and linear magneto-optic Kerr effect spectra with $L2_1$ ordering of Co_2MnSi Heusler compound'

[360]: Fermon (2023), *Etude des alliages de Heusler de type Co_2MnZ par diffusion Brillouin et effet Kerr magnéto-optique*

7.1 MOKE measurements and QMOKE signature

The Co_2MnX thin film series[1] with X={Al, Si, Ga, Sn} was investigated by MOKE magnetometry to study the magneto-optical signal and anisotropies of the films. Measurements were performed in the longitudinal MOKE geometry as described in chapter 5.3 using wavelengths in the range of $\lambda = 550\,\text{nm} - 900\,\text{nm}$ for various sample orientations in the external field.

1: See sample list in table 2.2.

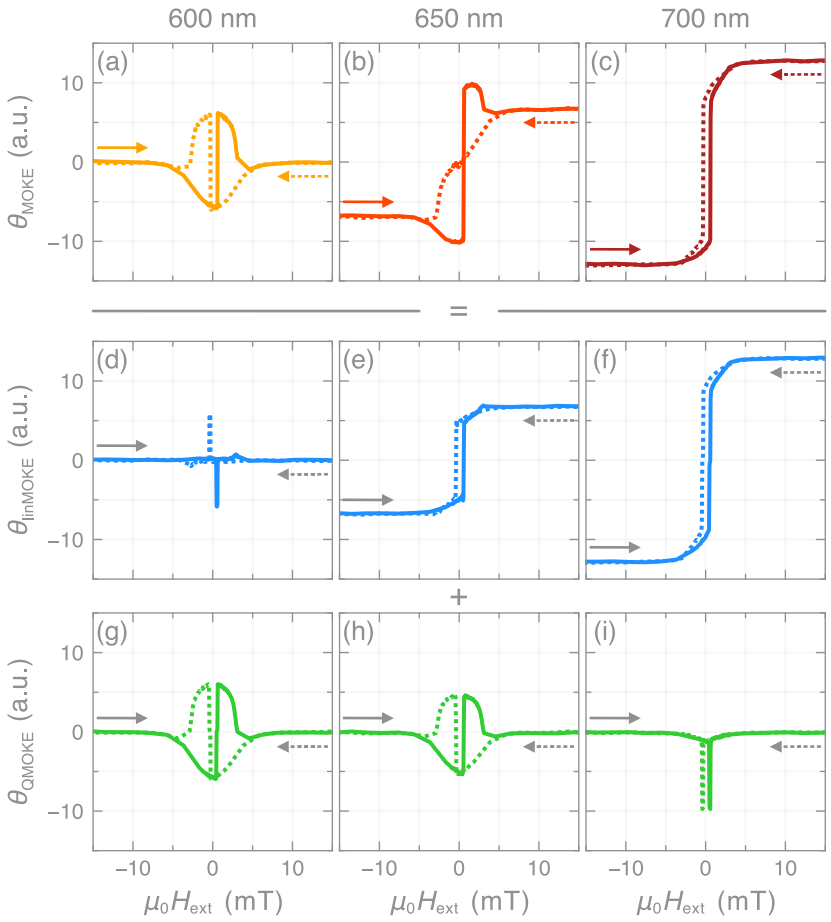

Figure 7.1: Exemplary hysteresis loops of the MOKE signal obtained from Co_2MnSi recorded along a hard axis with λ = 600 nm, 650 nm and 700 nm (a-c), all corresponding to red-tones in the visible spectrum. The MOKE signal was numerically separated into anti-symmetric linMOKE part shown in blue (d-f) and symmetric QMOKE part shown in green (g-i). Arrows indicate the field sweep direction. An analogous separation is used on the measurements at λ = 670 nm of sputtered Co_2MnSi films in a study of the $L2_1$ ordering degree in [72].

[72]: Gaier et al. (2008), 'Influence of the $L2_1$ ordering degree on the magnetic properties of Co_2MnSi Heusler films'

The recorded signal of each loop was corrected by a linear function of the elapsed time to account for a signal drift during the measurement resulting in a loop opening causing initial and final saturation signals to differ. Moreover, a linear field-dependent background correction was performed to remove the Faraday rotation signal originating from the gold capping layer. An exemplary measurement result of the Co_2MnSi film is shown in figure 7.1.

Figure 7.1 (a-c) show the Kerr rotation θ_{MOKE} obtained at λ = 600 nm, 650 nm and 700 nm respectively. Some hysteresis loops clearly present a symmetric and antisymmetric part upon field inversion, as is the case for λ = 600 nm and 650 nm in the given example, which correspond to linear and quadratic contributions to the MOKE signal as introduced in chapter 4.3.1.

The recorded signal was thus numerically separated into the linMOKE part

$$\theta_{linMOKE} = \theta_{asym} = \frac{\theta_{inc}(H) - \theta_{dec}(-H)}{2} \tag{7.1}$$

which is anti-symmetric upon field inversion, and the symmetric QMOKE part

$$\theta_{QMOKE} = \theta_{sym} = \frac{\theta_{inc}(H) + \theta_{dec}(-H)}{2} \tag{7.2}$$

as shown in figure 7.1 (d-f) as well as (g-i), respectively.

The three exemplary measurements shown in figure 7.1 present quite a peculiar selection: The measurement at λ = 600 nm in figure 7.1 (a, d, g) corresponds to a purely quadratic magneto-optical effect as the linear magneto-optical contribution vanishes. On the other hand, at λ = 700 nm in figure 7.1 (c, f, i), a negligible quadratic contribution is obtained, and the magneto-optical signal

is described by the linear effect. In between, at $\lambda = 650\,\text{nm}$ in figure 7.1 (b, e, h), a superposition of the two is obtained, and the effects are clearly in similar orders of magnitude.

The common linMOKE assumption, i.e. assuming that the MOKE can be described as a linear function of the magnetisation, can thus clearly not be applied to the case of Co_2MnSi - at least not to the entire spectral range. Instead, the above results show that the quadratic MOKE effect must be taken into account, and as a direct consequence the measurement geometry plays a significant role as well: Additionally to the magnetic anisotropy investigated in the previous chapter in Co_2MnSi and Co_2MnAl thin films, a magneto-optical anisotropy is added in the case of non-negligible QMOKE effects, since only the quadratic contributions in the complex Kerr angle

$$\begin{aligned}\Phi_{s/p} = \theta + i\varepsilon = &\pm A_{s/p}\left(2G_{44} + \frac{\Delta G}{2}(1-\cos 4\phi) + \frac{K^2}{\varepsilon_d}\right)M_L M_T \\ &\mp A_{s/p}\frac{\Delta G}{2}\sin\phi(M_L^2 - M_T^2) \\ &\mp B_{s/p} K M_L \end{aligned} \tag{7.3}$$

introduced in chapter 4 depend on the orientation angle ϕ between the principal axis [100] of the cubic lattice and the direction of the magnetic field.

The linear contribution on the other hand only depends on the longitudinal magnetisation projection $M_L(H)$ and indirectly on the wavelength through the linear magneto-optical tensor element K, but does not depend on the sample orientation. Only this contribution is therefore suitably for an analysis of the magnetic anisotropies in the sample. Its wavelength dependence is directly apparent when comparing the results for the three wavelengths in figure 7.1 (d-f) where a vanishing linear MOKE is observed at $\lambda = 600\,\text{nm}$ and the amplitude between saturation signals at positive and negative fields seems to increase for greater wavelengths in the selection.

The rotational dependence of the magneto-optical signal was therefore investigated by rotational MOKE magnetometry measurements at a fixed wavelength of $\lambda = 636\,\text{nm}$ for a full sample rotation in steps of 3°.

7.1.1 Magnetic anisotropy in the linMOKE

Although not of main interest in this magneto-optical study, the anisotropy of the linMOKE signal allowed to verify the magnetocrystalline anisotropy in the studied thin films. To this aim, the signal at remanence was extracted and normalised by the averaged saturation signal $|\theta_{\text{linMOKE}}(|H| \geq 20\,\text{mT})|$. The resulting normalised remanence is shown in figure 7.2.

Co_2MnAl and Co_2MnSi present the expected cubic anisotropy with hard axes along the principal crystal axes ⟨100⟩ and easy-like axes along the ⟨110⟩ directions as was also observed in VSM measurements on different Co_2MnAl and Co_2MnSi films analysed in the previous chapter 6.1.

Interestingly, the relative change of remanence signal observed in MOKE is similar for the three compounds Co_2MnAl, Co_2MnGa and Co_2MnSi, from $M_R \approx 100\,\%M_S$ along the easy(-like) axes to approximately $M_R \approx 70\,\%M_S$ along the hard axes. While the drop to $M_R \approx 70\,\%M_S$ matches the results on the Co_2MnSi film studied by VSM in chapter 6.1, it does not match the results obtained on the Co_2MnAl film studied by VSM.

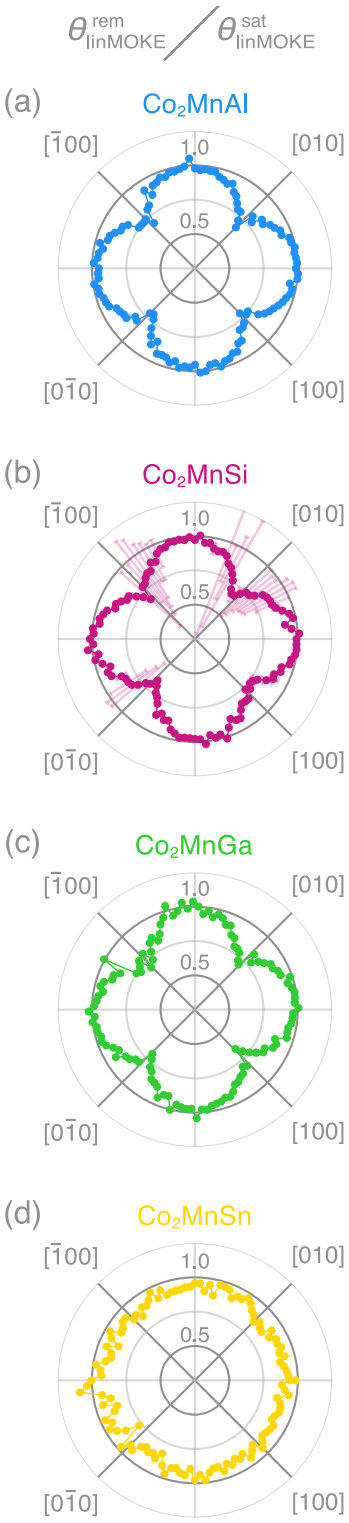

Figure 7.2: Normalised remanence signal from linMOKE loops, where $\theta^{\text{rem}}_{\text{linMOKE}} = \theta_{\text{linMOKE}}(H_{\text{ext}} = 0)$ and $\theta^{\text{sat}}_{\text{linMOKE}} = (|H_{\text{ext}}| > H_{\text{sat}})$, of the different Co_2MnX Heusler compounds (a-d) with $\lambda = 636\,\text{nm}$. Directions $[hkl]$ denote the crystal orientation parallel to the applied magnetic field and incident plane of light.

[103]: Guillemard (2019), 'Half-metal magnets Heusler compounds for spintronics'

2: See figure 2.31 on page 61 in [103].

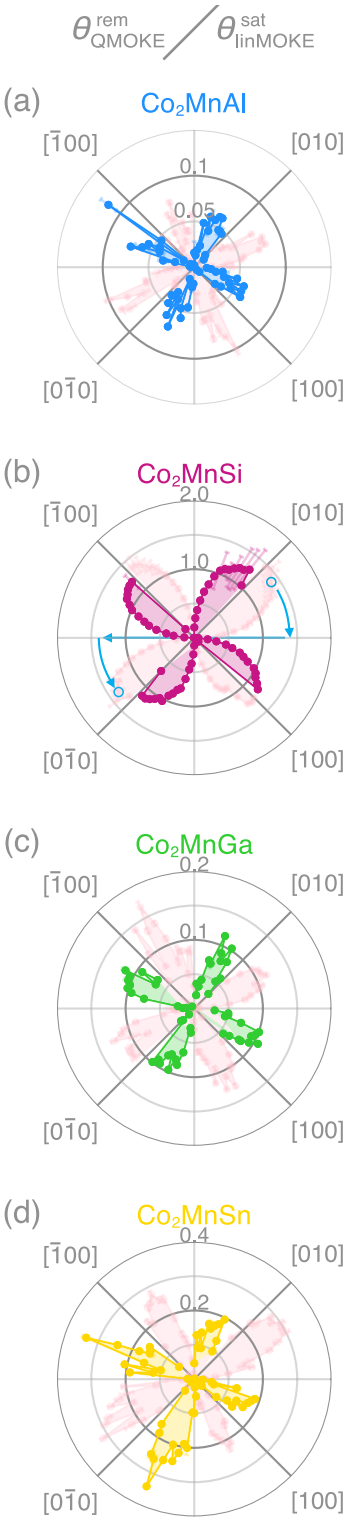

Figure 7.3: Dependence of the QMOKE signal at remanence normalised by the linMOKE signal in saturation as a function of crystal orientation $[hkl] \parallel \mathbf{H}_{ext}$ at $\lambda = 636\,nm$ for the different Co_2MnX films (a-d). Negative QMOKE remanence signal is shown in pink. Blue arrows in (b) show an exemplary directional switching towards the nearest easy-like axis, resulting in the sign change from one octant to the next.

This discrepancy might be related to the Co_2MnAl film studied by MOKE being annealed, whereas the Co_2MnAl film studied by VSM was not annealed (see the sample specifications in chapter 2). Indeed, the drop to $M_R \approx 70\,\%M_S$ obtained in this magneto-optical study is backed by VSM results reported in the original work [103] from which this sample series was obtained for the presented MOKE study: a significant drop to approximately $M_R \approx 70\,\%M_S$ is found in the reported VSM measurements for the Co_2MnAl film along the [100] direction[2].

Co_2MnSn is the only compound in the series which seems to be isotropic in remanence studied by linMOKE, see figure 7.2. This again confirms the results in the VSM study in [103], where indeed little anisotropy was found for Co_2MnSn as well.

7.1.2 Magneto-optical anisotropy in the QMOKE

In order to quantify the QMOKE contribution and its anisotropy, the QMOKE signal at remanence was extracted as well as the area of the loop opening, since a simple determination of the signal amplitude is prone to errors originating from noise: a random noise on the data can lead to false symmetric/anti-symmetric contributions that are negligible in the case of significant signal, but lead to false peaks in the amplitudes of the signals in the case of vanishing linMOKE or QMOKE, as is seen in the exemplary traces in figure 7.1 (d) and (i). The obtained results for each compound are shown in figures 7.3 and 7.4.

Co_2MnSi

Co_2MnSi was found to present largest relative QMOKE signal amplitudes, compare figure 7.3 (b) to (a, c, d), and is the only compound in the series to show a significant angle-dependent hysteretic behaviour of the quadratic MOKE contribution (loop area) in figure 7.4 (b).

The QMOKE was found to vanish for an orientation of the easy-like axes $\langle 110 \rangle$ along the magnetic field, and the QMOKE signal amplitude at zero field as well as the loop area were found to be maximal for an orientation of the hard axis $\langle 100 \rangle$ along the magnetic field. In the remanent signal amplitudes, the fourfold anisotropy is modulated by a change of sign in each octant resulting from a sign change in the transversal component of the magnetisation upon reorientation towards the nearest easy-like axis, i.e. the magnetisation trajectory indicated by the blue errors for one exemplary case in figure 7.3 (b) would change from 'clockwise-turn / flip / counterclockwise-turn' in the light pink octants (negative remanence values) to 'couterclockwise-turn / flip / clockwise-turn' if starting from a field orientation in one of the dark violet octants (positive remanence values).

An anisotropy analysis of the quadratic MOKE contribution, particularly comparing the signals obtained along the symmetry axes, allows for conclusions on the quadratic magneto-optical tensor elements:

In the $\langle 100 \rangle \parallel \mathbf{H} \Rightarrow \phi = 0°$, the term proportional to $\sim (M_L^2 - M_T^2)$ does not contribute, and the quadratic MOKE signal is entirely described by

$$\theta_{QMOKE}(\mathbf{H} \parallel \langle 100 \rangle) \sim \mathrm{Re}\left[\pm A_{s/p} \left(2G_{44} + \frac{K^2}{\varepsilon_d} \right) M_L M_T \right] \tag{7.4}$$

for the field aligned along the hard axes ⟨100⟩, i.e. the QMOKE contribution for a field orientation along the principle axes of the cubic lattice solely depends on three magneto-optical tensor elements ε_d, K and G_{44}.

For $\langle 110\rangle \parallel \mathbf{H} \Rightarrow \phi = 45°$, a vanishing QMOKE loop opening (area) is observed, thus the same curve is obtained for increasing and decreasing field branch (as is the case for instance in figure 7.1 (i)). This suggests that either longitudinal and transverse magnetisation change sign simultaneously, or that the term proportional to $\sim M_\mathrm{L} M_\mathrm{T}$ is not significant in this orientation. Assuming the prior and considering the nearly instant magnetisation switching observed in VSM measurements along this direction (see figure 6.2 and the relevant discussion in chapter 6.1), i.e. $M_\mathrm{T} \approx 0$, equally leads to a negligible contribution of the term in $\sim M_\mathrm{L} M_\mathrm{T}$. Hence in this case

$$\theta_\mathrm{QMOKE}(\mathbf{H} \parallel \langle 110\rangle) \sim \mathrm{Re}\left[A_{\mathrm{s/p}} \frac{\Delta G}{2} \frac{1}{\sqrt{2}} M_\mathrm{L}^2\right] \tag{7.5}$$

is obtained for the quadratic MOKE signal along the easy-like axes ⟨110⟩, i.e. if $M_\mathrm{T} \approx 0$ the QMOKE signal for a field orientation along the face diagonals of the cubic lattice depends on all three cubic magneto-optical tensor elements through $\Delta G = G_{11} - G_{12} - 2G_{44}$.

For orientations between these directions, the ΔG plays a role in both terms ($\sim M_\mathrm{L} M_\mathrm{T}$ and $\sim (M_\mathrm{L}^2 - M_\mathrm{T}^2)$) and hence the observed behaviour aligns with the interpretation of ΔG as the magneto-optical anisotropy parameter as introduced in section 4.3. However, a precise quantification of ΔG and G_{44} requires knowledge of the magneto-optical weighting factors $A_{\mathrm{s/p}}$, as well as the dielectric constant ε_d and the linear magneto-optical tensor element K for the same wavelength. Such a quantification cannot be achieved by the simple study of LMOKE as was performed in this work, but could be obtained from a more sophisticated approach as for instance in [102] utilising a MOKE setup with an additional field rotation possibility allowing to distinguish the symmetry of various contributions to the MOKE signal in different geometries.

Co_2MnAl, Co_2MnGa and Co_2MnSn

The compounds Co_2MnAl, Co_2MnGa and Co_2MnSn present much lower relative QMOKE amplitudes in remanence in figure 7.3 (a, c, d) and hardly any hysteretic behaviour is detected in the QMOKE signal as indicated by the negligible loop opening in figure 7.4 (a, c, d).

Moreover, the loop area is found to be isotropic, while the remanence signal is still found to present a similar symmetry to the behaviour observed in Co_2MnSi: A vanishing QMOKE signal is observed along the easy axes ⟨110⟩ and the remanent QMOKE signal changes sign in every quadrant. However, the absolute signal drops nearly equally towards the hard axes ⟨100⟩ as it does towards the easy-like axes, resulting in an eight-fold symmetry of the absolute signal at remanence contrary to the fourfold symmetry of the absolute signal observed in the case of Co_2MnSi.

This allows to conclude that the term in $\sim \sin\phi$ is hardly contributing to the QMOKE in these compounds, implying

$$\Delta G = G_{11} - G_{12} - 2G_{44} \approx 0 \tag{7.6}$$

for Co_2MnAl, Co_2MnGa and Co_2MnSn.

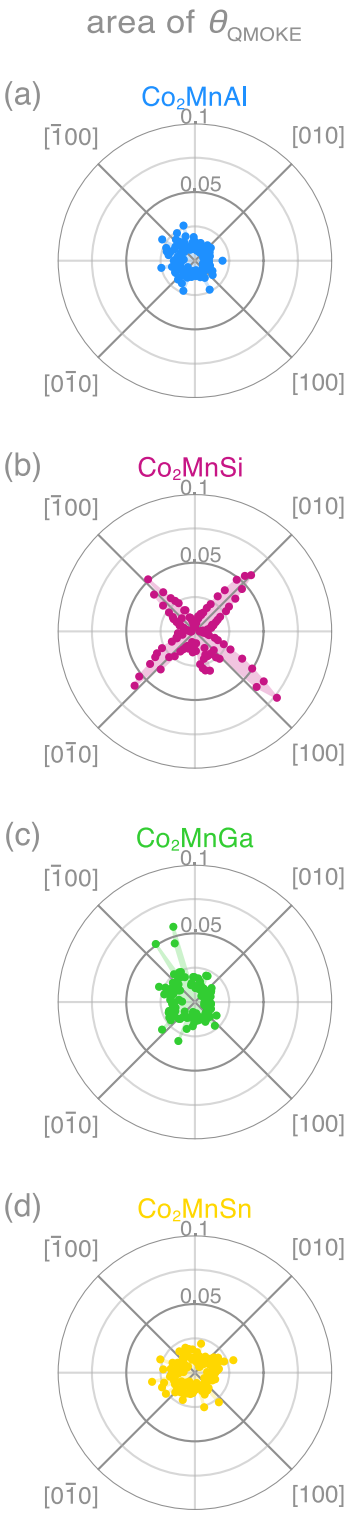

Figure 7.4: Area of the symmetric curves as a function of crystal orientation $[hkl] \parallel \mathbf{H}_\mathrm{ext}$ at $\lambda = 636\,\mathrm{nm}$ for the different Co_2MnX films (a-d). The shaded area has no other significance but to enhance the appearance of anisotropies in the plots. Only Co_2MnSi shows a significant anisotropic QMOKE hysteresis (area of the symmetric loops).

[102]: Silber (2019), 'Quadratic magnetooptic Kerr effect spectroscopy of magnetic thin films with cubic crystal structure'

The symmetry of the QMOKE does not allow for a distinction between a significant or insignificant quadratic MOKE tensor element G_{44} and a linear MOKE tensor element K, since both contribute to the remaining term $\sim (2G_{44} + \frac{K^2}{\varepsilon_d})M_L M_T$. However, the combination of ΔG and overall little normalised QMOKE amplitudes of less than 10, 15 and 30 % for Co_2MnAl, Co_2MnGa and Co_2MnSn respectively, allows to assume a negligible quadratic contribution of the magneto-optical tensor as opposed to Co_2MnSi where the quadratic magneto optical tensor results in an important QMOKE contribution of up to 150 %.

Consequently, the rotational study at $\lambda = 636\,\text{nm}$ allows to conclude on a negligible quadratic magneto-optical tensor and a governing linear magneto-optical effect in the case of Co_2MnAl, Co_2MnGa and Co_2MnSn, whereas a significant QMOKE contribution is related to an important quadratic magneto-optical tensor in Co_2MnSi at $\lambda = 636\,\text{nm}$.

7.2 Wavelength dependent study of Co_2MnSi and Co_2MnAl in MOKE

The wavelength dependence arising from the magneto-optical tensor's dependence on the material's band structure as introduced in section 4.3.1 was studied focusing on the two compounds Co_2MnAl and Co_2MnSi, which are the compounds of primary interest in this work. As introduced in chapter 1, these two compounds also represent the 'extrema' of the composition series not only in terms of significance of the previously studied QMOKE effect at $\lambda = 636\,\text{nm}$, but also in terms of crystalline ordering, from full B2 disorder in the Co_2MnAl film to full $L2_1$ order in the Co_2MnSi film, as well as the related spin polarisation, changing from 63 % in the Co_2MnAl film to 100 % in the Co_2MnSi film, as reported in the study by Guillemard *et al.* performed on the exact same samples [71]. For a list of all significant properties and reference values, see table 1.1.

[71]: Guillemard et al. (2020), 'Issues in growing Heusler compounds in thin films for spintronic applications'

For the wavelength dependent study of the MOKE response, the same LMOKE setup was used and tunable laser was set to various wavelengths in the range of $\lambda = 550\,\text{nm}$ to $\lambda = 900\,\text{nm}$ and in order to investigate the angular evolution of the QMOKE effect the sample was rotated scanning one quadrant with an angular resolution of 0.5°. The linMOKE and QMOKE signal was again separated by symmetry considerations as detailed above and the results obtained from the Co_2MnSi film are shown in figure 7.5.

In figure 7.5 (A) the linMOKE amplitude

$$A_{\text{linMOKE}} = \bar{\theta}_{\text{linMOKE}}(H \geq 20\,\text{mT}) - \bar{\theta}_{\text{linMOKE}}(H \leq -20\,\text{mT}) \tag{7.7}$$

is shown as a function of wavelength and crystal orientation in the external magnetic field. The independence of linMOKE on the crystal orientation is confirmed and a clear wavelength dependence is observed with a sign change between 590 nm and 610 nm where the linMOKE is found to vanish.

This is reflected by the normalised remanent QMOKE signal

$$\frac{\theta^{\text{rem}}_{\text{QMOKE}}}{A_{\text{linMOKE}}} = \frac{\theta^{\text{incr}}_{\text{QMOKE}}(0) + \theta^{\text{decr}}_{\text{QMOKE}}(0)}{2 \cdot A_{\text{linMOKE}}} \tag{7.8}$$

showing a particularly significant QMOKE contribution in the wavelength range where nearly vanishing linMOKE signal was obtained, see figure 7.5

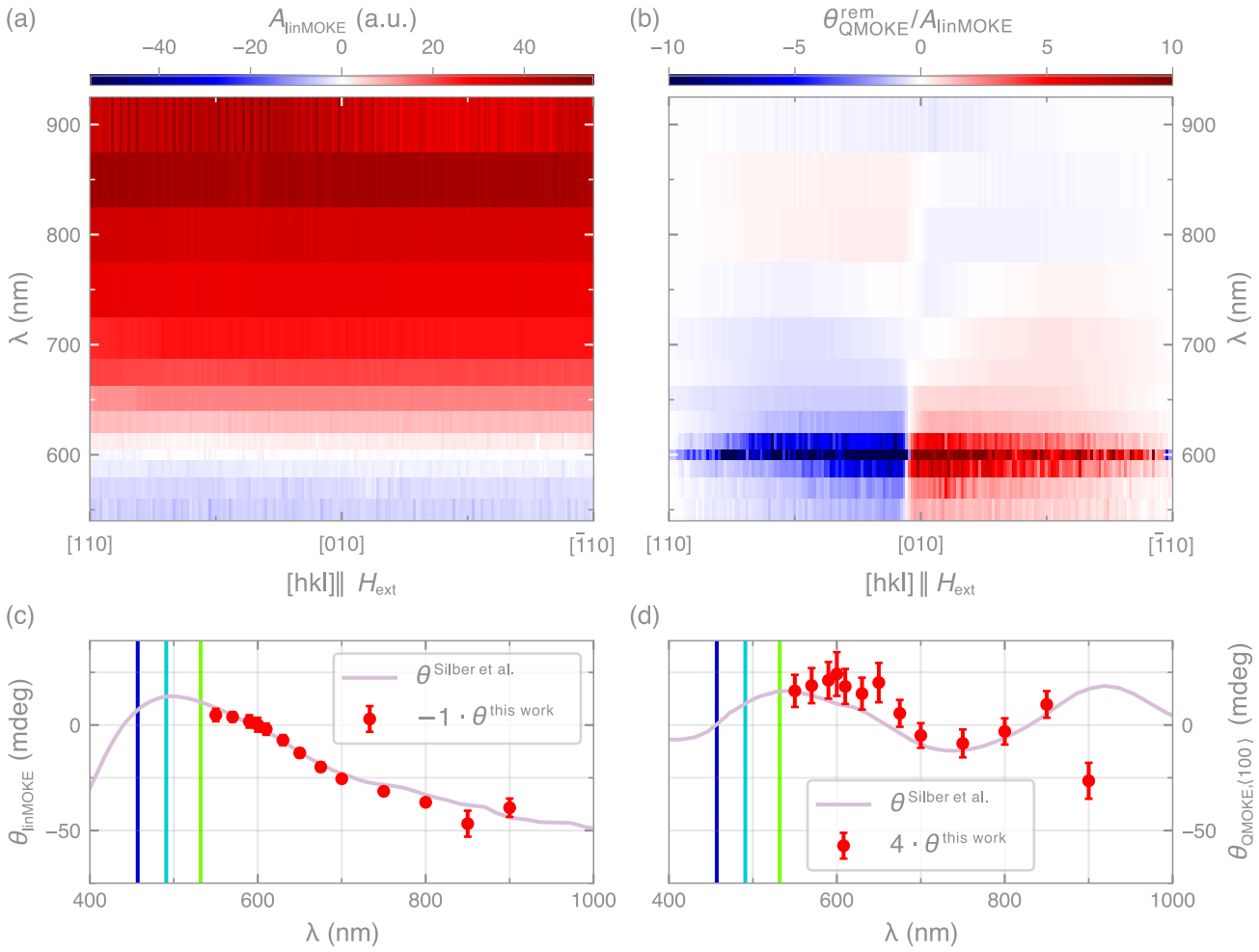

Figure 7.5: Angle-resolved wavelength dependence of the magneto-optical response from the Co_2MnSi film. (a) Amplitude of the linMOKE rotation measured as the difference of the Kerr rotation values in saturation. (b) QMOKE rotation signal in remanence normalised by the linMOKE amplitude. (c) Comparison of the linMOKE rotation data from Silber *et al.* [393] reported in [82] with the linMOKE amplitude average over all directional measurements in the present work. A match is obtained with a factor of -1 arising from a different choice of coordinate systems for the linMOKE definition. (d) Comparison of the QMOKE rotation along ⟨100⟩ at remanence from this work with the data from Silber *et al.* [393] reported in [82]. A match is obtained for a factor of 4 likely accounting for the difference of the extracted parameter, i.e. the remanence signal (this work) or the saturation signal (Silber *et al.*). Coloured vertical lines indicate the laser wavelengths available for the BLS labs in Kaiserslautern.

(b). The angular dependence of the QMOKE signal matches that observed at $\lambda = 636\,\mathrm{nm}$ and was discussed in detail in the previous section, but a sign change is observed at $\lambda = 800\,\mathrm{nm}$ and $850\,\mathrm{nm}$, where the relative QMOKE contribution is little compared to the significant linMOKE signal.

Indeed, maximum linMOKE signal is obtained for the largest wavelengths, and the wavelength dependence shown in figure 7.5 (c) matches the observation in the extensive study by Silber *et al.* [82] obtained with a more sophisticated MOKE spectroscopy approach[3] quite accurately. The factor −1 between the data in this work and the data reported by Silber *et al.* is related to a different coordinate definition for the linMOKE case.

Moreover, in figure 7.5 (d) an excellent agreement is found between the QMOKE rotation along ⟨100⟩ in remanence from the present study and the data reported in the study Silber *et al.* with a proportionality factor of 4 likely accounting for the different probing techniques: While the setup used by Silber *et al.* allows for an independent rotation of the magnetic field and the sample positioning, and thus enables the probing of quadratic MOKE contributions in saturation, the fixed LMOKE geometry in the case of the present study limits the quantification of QMOKE to a relative comparison of the remanence

[393]: Silber et al. (2020), *Longitudinal and quadratic magnetooptic Kerr effect spectra of Co_2MnSi Heusler compound*

[82]: Silber et al. (2020), 'Scaling of quadratic and linear magneto-optic Kerr effect spectra with $L2_1$ ordering of Co_2MnSi Heusler compound'

3: The setup used by Silber *et al.* in [82] allows to rotate the magnetic field as well as the sample independently, and therefore enables to probe different QMOKE contributions from each other which is not possible with the simpler setup used in the present study.

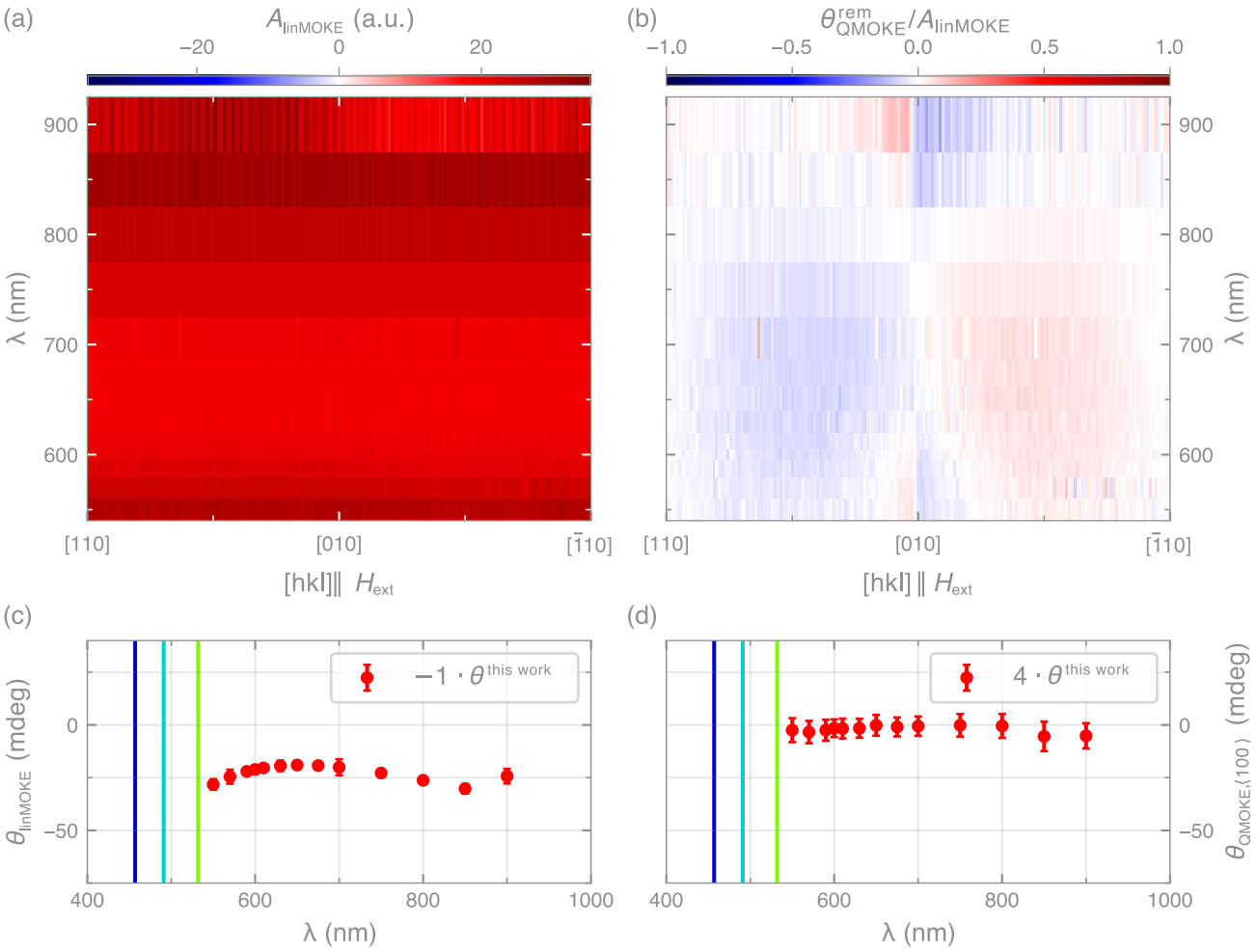

Figure 7.6: Angle-resolved wavelength dependence of the magneto-optical response from the Co_2MnAl film. (a) linMOKE amplitudes measured as the difference of the saturation values. (b) QMOKE signal in remanence normalised by the linMOKE amplitude. (c) Average linMOKE amplitude of all directions and (d) remanent QMOKE signal along the hard axis [010] vs. wavelength with the same scaling as previously used for Co_2MnSi in figure 7.5. Both show nearly constant behaviour in the investigated laser wavelength range. Coloured vertical lines indicate the BLS wavelengths as before in figure 7.5. This compound was not studied by Silber *et al.* [102].

Kerr rotation signals. Yet the quite accurate match of the Kerr rotation from both studies not only allows to validate the results obtained in this work, but also to extrapolate towards the wavelengths available in the BLS labs in Kaiserslautern, i.e. $\lambda = 457\,nm$, 491 nm and 532 nm, which are indicated by the coloured lines at the respective spectral positions: As both effects are relatively small, comparably little BLS signal is to be expected in this range[4].

In the case of Co_2MnAl, a roughly constant linMOKE signal is obtained in the whole wavelength range, as shown in figure 7.6 (a). Little change is also observed in the insignificant QMOKE signal shown in 7.6 (b). Contrary to the dispersive magneto-optical response from the Co_2MnSi film shown in figure 7.5, the investigated Co_2MnAl film presents hardly any wavelength dependence in the studied range as shown in figure 7.6 (c) and (d). This compound was not studied by Silber *et al.* [102], but for comparison the results are displayed with the same scaling factors as in figure 7.5. The roughly constant linMOKE amplitude of Co_2MnAl is comparable to that of Co_2MnSi at $\lambda = 700\,nm$ and in the entire spectral range between 550 nm and 700 nm, the amplitude of the Kerr rotation from Co_2MnSi is significantly lower than the Kerr rotation from Co_2MnAl. While an extrapolation to the BLS wavelengths is principally incorrect[5], the results suggest an improved BLS signal for Co_2MnAl at least for $\lambda = 550\,nm - 700\,nm$, nearly including the laser with $\lambda = 532\,nm$.

[102]: Silber (2019), 'Quadratic magnetooptic Kerr effect spectroscopy of magnetic thin films with cubic crystal structure'

4: It is important to note here that this does not mean that these wavelengths cannot be used at all for BLS investigations on Co_2MnSi: The BLS intensity is only proportional to the square of the complex Kerr angle, not equal, as pointed out in section 4.3.2. Therefore, very small Kerr angles do not directly equate to vanishing BLS signals, and indeed detectable BLS signal intensities could still be achieved for the laser wavelengths indicated here, see the discussion in the subsequent section.

5: As introduced in chapter 4, the wavelength-dependence of the magneto-optical tensor arises from the band structure of the material, and therefore ab-initio calculations are necessary for a modelling.

7.3 Signal intensity from thermal spin waves in conventional BLS

One of the main goals of this magneto-optical study was to identify the best wavelength to study spin waves by Brillouin light scattering (BLS) techniques in magnonic devices made of the Co_2MnX Heusler compounds. To this aim, the above discussed MOKE investigations allowed to identify the contributing magneto-optical effects and their wavelength dependence, which are linked to the BLS signal intensity through the complex Kerr angle, i.e.

$$I_{s/p}^{BLS} \sim |\Phi_{s/p}^{MOKE}|^2 = \theta_{s/p}^2 + \ell_{s/p}^2 \tag{7.9}$$

as introduced in chapter 4. Although the operating laser wavelengths in the experimental setups in Kaiserslautern do not overlap[6] with the reachable wavelengths in the tunable MOKE setup, an extrapolation of the observed behaviour is possible for Co_2MnSi based on the agreement with the results by Silber *et al.* [82] as detailed above. Yet, this only yields an estimation, since the signal intensities are related but not exactly equal, and additionally no such estimation could be done for any of the other compounds of the series.

Therefore, the BLS signal intensities were quantified by conventional BLS spectroscopy measurements of thermally excited spin waves[7], which were performed with a laser wavelength of $\lambda = 457\,\text{nm}$ and are compared to results collected at 532 nm from a previous study [83]. The BLS spectra were measured in a configuration where the external magnetic field was applied along an easy-like axis of the film plane, i.e. $\mathbf{H}_{ext} \parallel \langle 110 \rangle$, at 90° to the incidence plane of light, i.e. equally probing the reflected magneto-optical signal along an easy-axis like direction $\langle 110 \rangle$. Measurements were performed at 100 mT with 2.5° difference from normal incidence, probing the signal obtained from quasi-FMR spin waves and averaging over 40 000 spectra in a frequency range of $f_{BLS} = [-47.5\,\text{GHz}, 47.5\,\text{GHz}]$. Details on the experimental technique are given in section 5.4.

The BLS signal intensities from $\lambda = 457\,\text{nm}$ and $\lambda = 532\,\text{nm}$ are shown in figure 7.7 (a) and (b). The signal amplitudes from the obtained spectra were normalised by the integrated reference signal between $f_{BLS} = [-3\,\text{GHz}, 3\,\text{GHz}]$ to account for potential fluctuations of the applied laser output power within a measurement [366]. Still, this normalisation cannot account for all factors affecting the signal intensities particularly upon changing the wavelength:

- Firstly, there are naturally factors originating from the change in the experimental setup: The change of laser wavelength requires the swap of lasers in the setup and consequently a realignment which can differ from before. As a consequence, the resulting laser power arriving on the sample surface may be different even if adjusting the laser to equal reference outputs. Additionally, optical components like beam splitters etc. are typically optimised for specific wavelengths and might cause higher losses for one wavelength than the other, and equally the detector sensitivity can differ from one wavelength to the other.
- Secondly, there is an additional factor originating from the sample: the reflectivity/absorption coefficients are equally wavelength-dependent functions - not only for the Heusler film under investigation but as well for the gold capping layer.

As a result, a direct comparison of the (normalised) signal amplitudes from the measurement at one wavelength to the other does not make sense[8], but instead the distribution of normalised signal intensities will be discussed focusing

6: As mentioned above, the three wavelengths $\lambda = 457\,\text{nm}$, 491 nm and 532 nm are available for BLS setups in Kaiserslautern, whereas sufficient laser output power in the tunable MOKE setup could only be obtained for $\lambda > 550\,\text{nm}$.

[82]: Silber et al. (2020), 'Scaling of quadratic and linear magneto-optic Kerr effect spectra with $L2_1$ ordering of Co_2MnSi Heusler compound'

7: The study of the BLS signal intensity at this point only serves as a benchmark of feasibility and expectable magneto-optical signal intensities. To this aim, no precise knowledge of spin waves and their characteristics is necessary and it is sufficient to understand spin waves as a spatially varying oscillating magnetisation. The specification of thermal excitation indicates that this is the case where lowest signal intensities are to be expected. A more extensive introduction of spin waves is given in chapter 8 in the beginning of the third part of this thesis, which is itself dedicated towards applications also based on spin waves.

[83]: Friedel (2021), *Thin film materials with ultralow damping for novel magnonic phenomena*

[366]: Sebastian et al. (2015), 'Micro-focused Brillouin light scattering'

8: Indeed, significantly lower normalised signal amplitudes were obtained for the whole Co_2MnX series at $\lambda = 491\,\text{nm}$ compared to the previous measurements at $\lambda = 532\,\text{nm}$ (Measurements at $\lambda = 491\,\text{nm}$ were taken in the first half of 2023, measurements at $\lambda = 532\,\text{nm}$ in the first half of 2020, and the samples were fabricated in the second half of 2018 and 2019.). This is also reflected by the larger error bars arising from the lower signal-to-noise ratio in the measurements at $\lambda = 491\,\text{nm}$ albeit averaging over 40 000 scans, whereas only 1 000 spectra were averaged for the measurements at $\lambda = 532\,\text{nm}$ with improved signal-to-noise ratio resulting in smaller error bars in figure 7.7.

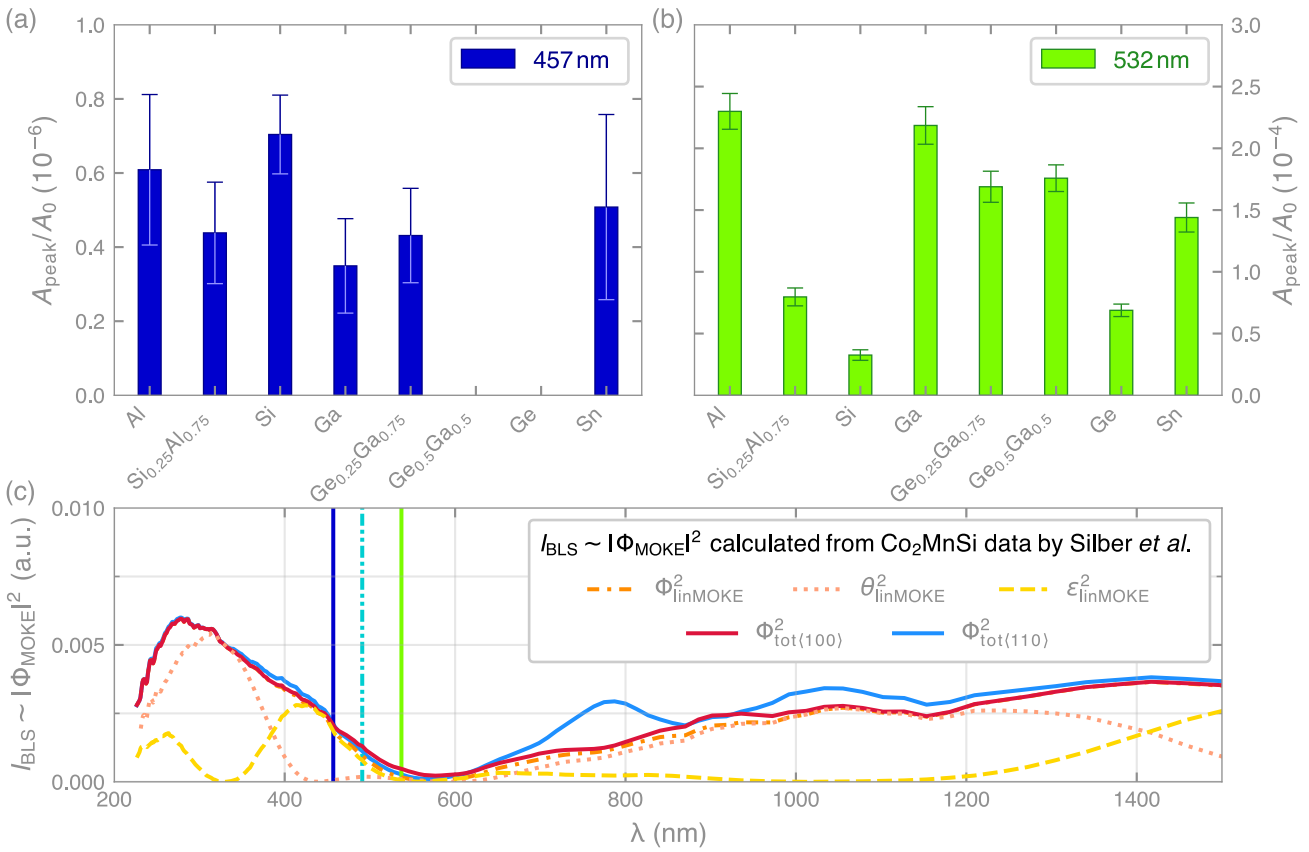

Figure 7.7: Normalised peak amplitude for the different Co_2MnX compounds from BLS spectra of thermal spin waves measured with (a) $\lambda = 457\,nm$ in this work and compared with (b) $\lambda = 532\,nm$ from a previous work [83]. Signal amplitudes obtained from the measurement with $\lambda = 457\,nm$ (a) are three orders of magnitude smaller than with $\lambda = 532\,nm$ (b). BLS signal was normalised by the integrated signal for $f_{BLS} = [-3\,GHz, 3\,GHz]$ for both wavelengths. (c) BLS signal intensity expectation for Co_2MnSi based on the squared Kerr angle calculated from linMOKE and QMOKE spectral data by Silber *et al.* [82, 393]. Vertical lines mark the BLS laser wavelengths $\lambda = 457\,nm$ and $\lambda = 532\,nm$ used in (a) and (b), as well as available but unused $\lambda = 491\,nm$ (dash-dotted).

thus on the comparison of relative signal differences between the different compounds measured at the same conditions.

Comparing the relative signal intensities obtained from the different compounds in the series, the difference between Co_2MnGa, $Co_2MnGe_xGa_{1-x}$, and Co_2MnSn is little for both wavelengths, whereas Co_2MnAl, $Co_2MnSi_xAl_{1-x}$, and Co_2MnSi show peculiar behaviour linked to the strongly wavelength-dependent Kerr angle of Co_2MnSi:

- The compounds Co_2MnSi and Co_2MnAl present a significant difference in the results at $\lambda = 532\,nm$ from [83], where a relatively poor signal was obtained from Co_2MnSi, but Co_2MnAl presented the strongest signal in the series, as is shown in figure 7.7 (b). For $\lambda = 457\,nm$, on the other hand, the two compounds yield approximately equal signal amplitudes within the error ranges, as can be seen in figure 7.7 (a).
- The quarternary compound $Co_2MnSi_{0.25}Al_{0.75}$ presents a similar behaviour to Co_2MnSi which translates to approximately equal results to Co_2MnSi and Co_2MnAl at $\lambda = 457\,nm$, and a significant drop compared to Co_2MnAl for $\lambda = 532\,nm$.

The behaviour of the BLS signal intensity can be reasoned from the square of the wavelength-dependent complex Kerr angles: The analysis of Co_2MnSi presented in the previous section showed an accurate match between the Kerr rotation results in the investigated sample and that of the independent study by Silber *et al.* [82]. Therefore, the evolution of the expected BLS signal intensity with the probing laser wavelength can be estimated based on their results

[83]: Friedel (2021), *Thin film materials with ultralow damping for novel magnonic phenomena*

[82]: Silber et al. (2020), 'Scaling of quadratic and linear magneto-optic Kerr effect spectra with $L2_1$ ordering of Co_2MnSi Heusler compound'

[393]: Silber et al. (2020), *Longitudinal and quadratic magnetooptic Kerr effect spectra of Co_2MnSi Heusler compound*

[82]: Silber et al. (2020), 'Scaling of quadratic and linear magneto-optic Kerr effect spectra with $L2_1$ ordering of Co_2MnSi Heusler compound'

for Kerr rotation and ellipticity, even though the MOKE wavelength range in this study did not overlap with the available BLS laser wavelengths. The resulting squared Kerr angle is shown in figure 7.7 (c), where linear MOKE contributions are shown in dashed and dotted curves, and the QMOKE was taken into consideration for an alignment of a hard axis along the external field, i.e. $\mathbf{H}_{\text{ext}} \parallel \langle 100 \rangle$ (solid red curve), as well as an easy axis along the external field, i.e. $\mathbf{H}_{\text{ext}} \parallel \langle 110 \rangle$ (solid blue curve). The spectral positions of the available BLS laser wavelengths are shown by vertical lines as before and it is directly apparent that lowest signal amplitudes are to be expected between $\sim 500\,\text{nm}$ and $\sim 600\,\text{nm}$, where the square of the complex Kerr angle is vanishing.

Indeed, the expected BLS intensity is mainly governed by the linMOKE which validates the common assumption of negligible quadratic magneto-optical effects discussed in chapter 4.3. In particular in the wavelength range from 400 nm to 550 nm of this study's BLS probing wavelengths, the BLS intensity is dominated by the linear Kerr ellipticity as the linear Kerr rotation yields a vanishing contribution as well. The behaviour in the wavelength range from 550 nm to 900 nm studied by MOKE in this work is contrary to that from BLS: Here, the linear Kerr angle is essentially given by the Kerr rotation as the linear Kerr ellipticity contribution is vanishing.

According to the spectral data from [82, 393], a significant QMOKE contribution is only to be expected when the incidence plane of light and the $\langle 110 \rangle$ directions coincide, which does not match the observation in the present study, where significant contributions where only obtained for an orientation of field (and angle of incidence) close to $\mathbf{H}_{\text{ext}} \parallel \langle 100 \rangle$. Instead, the results from the simplified QMOKE study in this work suggest a significant relative QMOKE contribution only at an incidence plane of light coinciding with the hard axis directions $\langle 100 \rangle$. Moreover, in this orientation a significant QMOKE signal was only observed at wavelengths around 570 nm to 630 nm and can result in detectable BLS intensities even though the BLS signal related to the linMOKE vanishes for these wavelengths.

[82]: Silber et al. (2020), 'Scaling of quadratic and linear magneto-optic Kerr effect spectra with $L2_1$ ordering of Co_2MnSi Heusler compound'
[393]: Silber et al. (2020), *Longitudinal and quadratic magnetooptic Kerr effect spectra of Co_2MnSi Heusler compound*

7.4 Conclusions and applicability of magneto-optical techniques to the study of Co_2Mn-based Heusler compounds

In summary, this chapter presented a brief magneto-optical study of various Co_2Mn-based Heusler compounds by standard longitudinal MOKE magnetometry as well as BLS spectroscopy, for both of which the signal amplitudes are linked to the complex Kerr angle $\Phi = \theta + i\ell$.

Co_2MnSi was the only sample presenting significant quadratic MOKE effect in the investigated Kerr rotation θ, which was found to be maximal for an incident light projection along a principal axis of the cubic lattice $\langle 100 \rangle$ corresponding to the hard axis in the investigated samples. Largest quadratic MOKE amplitudes were obtained between 550 nm and 650 nm and a sign change was found to appear between 700 nm and 850 nm. The linear MOKE effect was found to vanish at approximately 600 nm with the linMOKE rotation also presenting a sign change at this wavelength. The wavelength dependence of linMOKE as well as QMOKE rotation was found to match the results of an independent study [82].

[82]: Silber et al. (2020), 'Scaling of quadratic and linear magneto-optic Kerr effect spectra with $L2_1$ ordering of Co_2MnSi Heusler compound'

Co_2MnAl, Co_2MnGa and Co_2MnSn all showed insignificant QMOKE effects compared to the linMOKE signal, which are mainly related to the natural

appearance of a quadratic contribution arising from the linear magneto-optical tensor. Co_2MnAl was selected for a thorough comparison with Co_2MnSi in the wavelength-dependent study and the obtained evolution of the Kerr rotation from Co_2MnAl show hardly any QMOKE contribution and a nearly constant linMOKE rotation for $\lambda = 550\,\text{nm} - 900\,\text{nm}$.

Based on these results, the obtained BLS signal intensities were discussed: The relatively small BLS amplitude for Co_2MnSi at $\lambda = 532\,\text{nm}$ was found to be related to the vanishing complex Kerr angle, since $I_{BLS} \sim |\Phi|^2$. Indeed, Co_2MnSi as well as the related ternary compound $Co_2MnSi_{0.25}Al_{0.75}$ were found to show the largest difference in BLS intensities for $\lambda = 532\,\text{nm}$ and $\lambda = 457\,\text{nm}$ compared with the other compounds of the series.

This brief study of the magneto-optical response obtained from Co_2MnX with X={Al_xSi_{1-x}, Ge_xGa_{1-x}, Sn} has confirmed a complex magneto-optical behaviour in particular for the Heusler compound Co_2MnSi, where contrary to standard approaches the quadratic magneto-optical responses are not negligible and the wavelength dependence of the complex Kerr angle definitely suggests to choose probing wavelengths wisely.

For the available BLS laser wavelengths $\lambda = 457\,\text{nm}$, $\lambda = 491\,\text{nm}$ and $\lambda = 532\,\text{nm}$ in the BLS setups in Kaiserslautern, the wavelength dependence of the complex Kerr angle predicts best results from $\lambda = 457\,\text{nm}$ and worst from $\lambda = 532\,\text{nm}$. This is confirmed by the relative signal from Co_2MnSi being significantly lower than the other compounds in the BLS study at $\lambda = 532\,\text{nm}$ from 2020 [83] and being of the same order of magnitude as all other compounds in the study at $\lambda = 457\,\text{nm}$ in 2023. Finally, the importance of a setup optimisation in particular for operation this wavelength range of little expected Kerr angles is pointed out in relation to the direct comparison of normalised signal amplitudes from Co_2MnSi obtained at $\lambda = 532\,\text{nm}$ and $\lambda = 457\,\text{nm}$: albeit vanishing expected intensity from the Kerr angle at $\lambda = 532\,\text{nm}$, BLS spectra were successfully detected from Co_2MnSi at that wavelength and even required less averaging. It is thus possible to optimise external factors for a sufficient signal sensitivity, as discussed above. Additionally, it is noteworthy that the signal from thermal spin waves as investigated in this study is usually much lower than what is to be expected in typical magnonic studies with external excitation e.g. by antennae.

[83]: Friedel (2021), *Thin film materials with ultralow damping for novel magnonic phenomena*

Part III

Nonlinear magnonic spin transport in Co_2MnSi-based microstructures

Background: Concepts of spin dynamics in anisotropic microstructures

8

The third part of this thesis focuses on the investigation of magnonic spin transport phenomena and their characteristics in microstructures of the Co_2MnSi Heusler compound. In spintronic applications, spin transport is usually accompanied by a simultaneous charge transport in the form of a spin polarised current. On the other hand, the field of magnonics is centred around spin waves, which essentially form a spin transport mechanism that is independent of a charge current. The Co_2MnSi compound forms a very peculiar case for both: Its 100% spin polarisation yields fully spin polarised currents for spintronic applications, and the associated ultralow Gilbert damping promises long spin wave life times in magnonic devices.

Introduced in the previous part of the thesis, the phenomenological Landau-Lifshitz-Gilbert (LLG) equation is the fundamental equation for the description of collective magnetisation dynamics in this work and is central to this third part as well: Collective magnetisation oscillations and waves are its formal solutions and the special case of the spatially homogeneous precession, i.e. oscillation with zero wave vector, is the ferromagnetic resonance (FMR) which was a central focus topic in the previous part of this work. In the present part, the full set of solutions is of interest including the non-zero wave vector solutions, i.e. propagating magnetisation waves, called *spin waves* with the associated quasi-particles usually referred to as *magnons*.

The LLG is an intrinsically nonlinear equation [394] and as such can describe quite complex or even chaotic magnetisation dynamics [288, 395–400], but does not provide direct access to a general analytical solution. A commonly adopted approach for the description of spin wave modes is the linearisation of the LLG, as done in chapter 4 for the derivation of the FMR. Since this approximation is only valid for magnetisation dynamics close to equilibrium[1], it implies a classification into two distinct spin wave regimes:

- The term *linear spin waves* is commonly used for spin waves close to equilibrium, for which the linearisation of the LLG is a valid approximation.
- For *nonlinear spin waves*, the precession deviates substantially from the equilibrium magnetisation and the approximation does not hold anymore. Hence a different theoretical approach is necessary for the description of nonlinear spin wave phenomena, for instance by a Hamiltonian formalism approach [401, 402].

This classification is adopted in the present chapter in order to introduce the underlying concepts of linear and nonlinear spin wave dynamics, which are fundamental to the discussion of the experimental results later on. Similar to the previous theoretical background chapter 4, only a brief summary of the essential concepts will be given and it is referred to textbooks for a more comprehensive description, e.g. in [225, 227, 229, 403].

8.1 Linear spin waves 151
Dispersion relation 152
Limitations 153
Spin wave properties . . . 153
Anisotropy and ellipticity 155
Waveguide confinement . 161
8.2 Nonlinear spin waves . . 162
Suhl instabilities 162
Nonlinear frequency shift 164
Hamilton formalism . . . 165
Nonlinear Hamiltonian . 166
8.3 Concluding remarks . . . 169

8.1 Linear spin waves

Linear spin waves have been studied for nearly a century at this point, and many crucial advances have been achieved in the field by now. Notably, for the derivation of spin wave dispersion relations as solutions of the linearised

[394]: De Laire (2022), 'Recent results for the Landau–Lifshitz equation'

[288]: Suhl (1957), 'The theory of ferromagnetic resonance at high signal powers'
[395]: Rezende et al. (1990), 'Spin-wave instabilities, auto-oscillations, and chaos in yttrium-iron-garnet'
[396]: Álvarez et al. (2000), 'Quasiperiodicity, bistability, and chaos in the Landau-Lifshitz equation'
[397]: Bertotti et al. (2001), 'Nonlinear Magnetization Dynamics under Circularly Polarized Field'
[398]: He et al. (2007), 'Localized steady-state domain wall oscillators'
[399]: Petit-Watelot et al. (2012), 'Commensurability and chaos in magnetic vortex oscillations'
[400]: Manfrini et al. (2014), 'Propagation of magnetic vortices using nanocontacts as tunable attractors'

1: Close to equilibrium meaning with small precession angles, i.e. negligible dynamic amplitudes compared to the static magnetisation $\mathbf{M}_0$.

[401]: Krivosik et al. (2010), 'Hamiltonian formulation of nonlinear spin-wave dynamics'
[402]: Tyberkevych et al. (2020), *Vector Hamiltonian Formalism for Nonlinear Magnetization Dynamics*

[225]: Gurevich et al. (1996), *Magnetization oscillations and waves*
[227]: Stancil et al. (2009), *Spin waves*
[229]: Rezende (2020), *Fundamentals of Magnonics*
[403]: L'vov (1994), *Wave Turbulence under Parametric Excitation*

LLG, famous key studies include the derivation of spin wave dispersions in an infinite body by Herring and Kittel in the 1950s [404, 405], the derivation of analytical expressions for the dipolar[2] dispersion of spin waves in in-plane magnetised thin films by Damon and Eshbach in 1961 [406, 407] and the inclusion of the exchange energy in an approximative description by Kalinikos and Slavin in 1986 [378]. The latter was expanded in 1990 to include anisotropy terms [379] which is substantial to the case of Co_2MnSi microstructures studied in this thesis: The non-negligible influence of the cubic anisotropy is a key result of the thin film characterisation presented in chapter 6 and will be of importance for the spin wave dynamics of the propagating waves as well.

8.1.1 Dispersion relation for anisotropic thin films

The Kalinikos-Slavin dispersion relation for in-plane propagating spin waves in an anisotropic thin film is given by [379]

$$\omega_n^2 = (\omega_H + \omega_{exch}) \cdot \left(\omega_H + \omega_{exch} + \omega_M \left(F_{nn} + F_{nn}^{ani}\right)\right) \tag{8.1}$$

with the dipolar matrix elements[3] F_{nn} defined as

$$\begin{aligned} F_{nn} &= \sin^2(\theta_0) - P_{nn} \sin^2(\theta_0) \cos^2(\phi_k) \\ &+ P_{nn} \left(\cos^2(\theta_0) + \frac{\omega_M}{\omega_H + \omega_{exch}} (1 - P_{nn}) \sin^2(\phi_k) \sin^2(\theta_0)\right) \end{aligned} \tag{8.2}$$

and incorporating the anisotropy energy in

$$\begin{aligned} F_{nn}^{ani} &= N_{xx}^{ani} + N_{yy}^{ani} + \frac{\omega_M}{\omega_H + \omega_{exch}} \cdot \left(N_{xx}^{ani} N_{yy}^{ani} + N_{yy}^{ani} \sin^2(\theta_0) - \left(N_{xy}^{ani}\right)^2\right) \\ &+ P_{nn} \cdot \frac{\omega_M}{\omega_H + \omega_{exch}} \cdot \left(N_{yy}^{ani} \left(\cos^2(\phi_k) - \sin^2(\theta_0) \left(1 + \cos^2(\phi_k)\right)\right)\right) \\ &+ N_{xx}^{ani} \sin^2(\phi_k) - N_{xy}^{ani} \cos(\theta_0) \sin(2\phi_k)\Big) \end{aligned} \tag{8.3}$$

both depending on the matrix elements P_{nn} which simplify to[4]

$$P_{00}(k_{ip}) = 1 - \frac{1 - \exp(-k_{ip} \cdot d)}{k_{ip} \cdot d} \tag{8.4}$$

for the lowest order mode with mode number $n = 0$ and a homogeneous mode profile across the film thickness, i.e. $k_{ip} \cdot d \lesssim 1$. The gyrotropic frequencies $\omega_M = \gamma\mu_0 M_S$ and $\omega_H = \gamma\mu_0 H_{ext}$ are used as abbreviations to incorporate the saturation magnetisation and the external magnetic field respectively. Analogously, $\omega_{exch} = \gamma\mu_0 H_{exch} = \omega_M \lambda_{exch}^2 k_{n,tot}^2$ is used to include the exchange interaction, where the total wave vector for the mode number n

$$k_{n,tot}^2 = k_{ip}^2 + k_n^2 \quad \text{with} \quad k_n = \frac{n \cdot \pi}{d} \tag{8.5}$$

is defined by its in-plane component k_{ip} and its quantised component along the film normal k_n with the film thickness d, as introduced on page 79 in the section on perpendicular standing spin waves (PSSWs) in chapter 4.

θ_0 is the polar angle between the film normal and the equilibrium position of the magnetisation, and $\phi_k = \varphi_k - \varphi_0$ is the azimuthal angle between the in-plane projection of the equilibrium position of the magnetisation and the propagation direction of the spin waves. The precise choice of coordinates is shown in figure 8.1.

[404]: Herring et al. (1951), 'On the Theory of Spin Waves in Ferromagnetic Media'
[405]: Herring et al. (1952), 'The Theory of Spin Waves in Ferromagnetic Media'

2: Limited to spin wave wavelengths longer than the dipole-exchange length

$$\lambda_{exch} = \sqrt{\frac{2A_{exch}}{\mu_0 M_S^2}}$$

see equation 4.15 on page 69, as well as the related comment on the anisotropy-exchange length after equation 4.29 on page 73.

[406]: Damon et al. (1961), 'Magnetostatic modes of a ferromagnet slab'
[407]: Hurben et al. (1995), 'Theory of magnetostatic waves for in-plane magnetized isotropic films'

[378]: Kalinikos et al. (1986), 'Theory of dipole-exchange spin wave spectrum for ferromagnetic films with mixed exchange boundary conditions'

[379]: Kalinikos et al. (1990), 'The dipole-exchange spin wave spectrum for anisotropic ferromagnetic films with mixed exchange boundary conditions'

3: It seems like there are not enough letters in this alphabet to avoid absolutely all possible confusions in this thesis. F was chosen in chapter 4 as a mathematical symbol for the free energy, with the free energy density terms denoted as f, in order to avoid confusion with the permittivity ϵ or ε in the magneto-optical part of this work. Now, to facilitate comparison with the Kalinikos-Slavin publications [378, 379], the original formulation with terms F_{nn} is preferred for the dispersion relation. It is important to note, that the F_{nn} must not be confused with a free energy term of the system. Here, the indices n denote the mode numbers and will never denote angles (as introduced for the angular derivations $f_{\theta\varphi}$ before). It is therefore assumed that the distinction between the F_{nn} terms and the free energy terms F is uncomplicated and reasonable in this context.

4: A detailed description of the rather complicated expressions for the higher order P_{nn} is given in the appendix of [378] for pinned, unpinned and mixed boundary conditions at the film interfaces.

8.1.2 Limitations of the Kalinikos-Slavin approximation[5]

The Kalinikos-Slavin dispersion relation given in equation 8.1 was derived under the assumption of linear spin waves, i.e. where the magnetisation and the effective field can be decomposed into a static and a small dynamic part

$$\mathbf{M}(\mathbf{r},t) = \mathbf{M}_0(\mathbf{r}) + M_\mathrm{S}\delta\mathbf{m}(\mathbf{r},t) \tag{8.6}$$

$$\mathbf{H}(\mathbf{r},t) = \mathbf{H}^\mathrm{static}(\mathbf{r}) + \delta\mathbf{h}(\mathbf{r},t) \tag{8.7}$$

and thus, the linearisation of the LLG is a valid approximation.

Moreover, the magnetostatic Maxwell equations

$$\nabla \times \delta\mathbf{h} = 0 \tag{8.8}$$

$$\nabla \cdot \delta\mathbf{b} = \nabla \cdot \mu_0(\delta\mathbf{h} + M_\mathrm{S}\delta\mathbf{m}) = 0 \tag{8.9}$$

are assumed for the dynamic field $\delta\mathbf{h}$, the dynamic magnetisation $M_\mathrm{S}\delta\mathbf{m}$ and the corresponding magnetic flux density $\delta\mathbf{b}$. This assumption is limited to [227] spin wave wave vectors $\mathbf{k} \gg \omega/c$, i.e. which are significantly larger than the free space wave vector of a photon of equal energy.

Finally, the quantisation of the out-of-plane wave vector component k_n indicated in equation 8.5 clearly introduces *perpendicular standing spin wave* (PSSW) modes due to the break of translation symmetry, which are shifted to higher frequencies than the fundamental mode with $n = 0$. Yet, the separation of the PSSWs from the fundamental mode depends on the exchange constant A_exch as well as the film thickness d, and an insufficient separation e.g. for large film thicknesses can lead to a hybridisation of the modes, which is not considered in the Kalinikos-Slavin approximation[6]. Concerning the frequency dispersion relation $\omega(k)$ as given in equation 8.1, the approximation of non-hybridising modes is valid in this work, where $A_\mathrm{exch} \approx 20\,\mathrm{pJ/m}$, $M_\mathrm{S} \approx 1000\,\mathrm{kA/m}$ and $d = 20\,\mathrm{nm}$ leads to a sufficient separation of the PSSWs in the order of tens of GHz. Yet, an accurate description of the mode profiles is generally not achieved, and can be obtained for instance by typical micromagnetic simulations.

The Kalinikos-Slavin dispersion relation given in equation 8.1 is thus a valid approximation for the dispersion $\omega(k)$ of linear spin waves in this work.

8.1.3 Properties of spin waves in (isotropic) thin films

Before discussing the influence of the anisotropy contributions on the dispersion relation of spin waves in thin films in section 8.1.4, the implications of equation 8.1 for $F_{nn}^\mathrm{ani} = 0$, i.e. neglecting anisotropy, shall be discussed here for a brief familiarisation with the general properties of linear spin waves in isotropic[7] thin films.

Given the form of the spin wave dispersion in equation 8.1, the two extreme cases for small and large spin wave wave vectors $\mathbf{k}_{n,\mathrm{tot}}$ yield a clear difference in the expected behaviour, as can be seen in figure 8.2 (a):

- For small wave vectors $\mathbf{k}_{n,\mathrm{tot}}$, the exchange contribution in ω_exch becomes negligible and the dispersion is governed by the dipolar interaction entering in the term $\omega_\mathrm{M}F_{nn}$. Spin waves in this regime are therefore typically named *dipole-dominated* spin waves. The entire study in the third part of this thesis is carried out in this *dipole-dominated* regime[8].

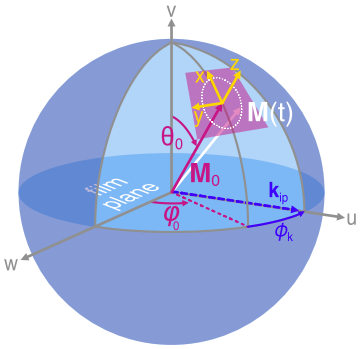

Figure 8.1: Definition of the global coordinates uvw and the dynamic (local) coordinates xyz used for the Kalinikos-Slavin dispersion relation 8.1 analogous to [233] and consistent with the coordinate definition in chapter 4 (figure 4.9). The radius of the sphere is given by M_S. $\mathbf{M}_0$ is the equilibrium position of the magnetisation, which corresponds to a minimum in f_tot and therefore coincides with the direction of the static effective field $\mathbf{H}_0$. $\hat{\mathbf{e}}_\mathrm{v}$ corresponds to the normal of the film plane, $\hat{\mathbf{e}}_\mathrm{u}$ corresponds to the propagation direction of the spin waves.

5: In this thesis, the term *Kalinikos-Slavin approximation* or *Kalinikos-Slavin dispersion* is always used to refer to the (approximative) dispersion relation formula given in equation 8.1. Note that this is an approximative formula is derived based on a couple of assumptions from the more general Kalinikos-Slavin theory as presented in [378, 379].

6: Precisely, the hybridisation is neglected in the approximative analytical formula given in equation 8.1, but is considered in the general Kalinikos-Slavin theory detailed in [378, 379] and can therefore be taken into account by a numerical implementation of the approach.

[233]: Henry et al. (2016), *Propagating spin-wave normal modes*

[227]: Stancil et al. (2009), *Spin waves*

[378]: Kalinikos et al. (1986), 'Theory of dipole-exchange spin wave spectrum for ferromagnetic films with mixed exchange boundary conditions'

[379]: Kalinikos et al. (1990), 'The dipole-exchange spin wave spectrum for anisotropic ferromagnetic films with mixed exchange boundary conditions'

7: Note that the shape anisotropy (demagnetisation energy arising from the dipolar coupling) is entering equation 8.1 in the F_{nn} and will be regarded here as well, as it is not an anisotropic property of the material but only arising from the sample shape and therefore present for all thin films.

8: Simply because the detectable wavevector is limited by the microscope objective of the microfocused BLS setup, see the description around equation 9.1 on page 175.

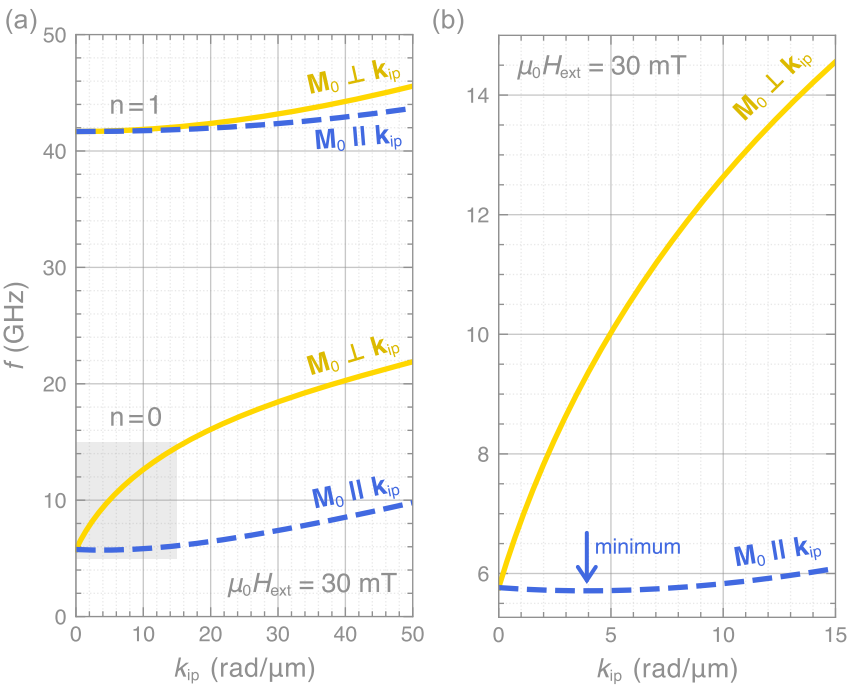

Figure 8.2: Exemplary spin wave dispersion relations neglecting anisotropy for a Co_2MnSi thin film with $M_S = 1058\,kA/m$, $\gamma = 28.54\,GHz/T$, $A_{exch} = 19.5\,pJ/m$ and $d = 20\,nm$ in the $\mathbf{k}_{ip} \perp \mathbf{M}_0$ geometry and the $\mathbf{k}_{ip} \parallel \mathbf{M}_0$ geometry for two different wavevector ranges in (a) and (b). The grey boxes in (a) indicate the range of the zoom-in shown in (b). Note that the FMR corresponds to $\mathbf{k}_{ip} = 0$ and, as a consequence of the *Backward-Volume spin waves* exhibiting a minimum for finite $\mathbf{k}_{ip}$ as indicated by the arrow in (b), the FMR does not correspond to the minimum frequency (*band bottom*) in the system. Note that the wavevector range is limited to the range up to $k_{ip} \cdot d \leq 1$ to satisfy the assumption of a homogeneous mode profile across the thickness.

- For large wave vectors $\mathbf{k}_{n,tot}$, the exchange contribution governs the dispersion relation in equation 8.1 and thus a characteristic quadratic dependency on the spin wave wave vector $\mathbf{k}_{n,tot}$ is obtained. Spin waves in this regime are referred to as *exchange-dominated* spin waves.

The transition between the two regimes is generally quantified by the aforementioned characteristic dipole-exchange length λ_{exch}, see in section 4.1.2.

For a non-negligible dipolar contribution, the spin wave dispersion becomes highly anisotropic even in the absence of any magnetocrystalline anisotropy: The dipolar matrix elements F_{nn} introduce a dependence of the dispersion relation on the polar angle θ_0 as well as on the azimuthal angle ϕ_k[9]. Exemplary dispersion relations for $\mathbf{k}_{n,ip} \leq 30\,rad/\mu m$ for the first two modes in the two high symmetry cases $\mathbf{k}_{ip} \perp \mathbf{M}_0$ and $\mathbf{k}_{ip} \parallel \mathbf{M}_0$ are shown in figure 8.2 (b).

In particular for the dipole-dominated fundamental spin wave modes (i.e. $n = 0$ in figure 8.2), the two high symmetry cases with $\mathbf{k}_{ip} \perp \mathbf{M}_0$ and $\mathbf{k}_{ip} \parallel \mathbf{M}_0$ yield distinctly different dispersion forms and mode profiles, linked to the thickness-induced quantisation of the wave vector and the propagation direction. The two geometries are therefore often distinguished with a reference to the fundamentally different behaviour in this regime, as was initially derived by Damon and Eshbach for the pure dipolar case (neglecting exchange[10]) [406, 407]. Precisely, the denomination as the *Damon-Eshbach (DE) geometry* and the *Backward-Volume (BV) geometry* for the two geometries $\mathbf{k}_{ip} \perp \mathbf{M}_0$ and $\mathbf{k}_{ip} \parallel \mathbf{M}_0$ have become popular within the research community.

The latter is linked to the peculiar feature of spin waves with $\mathbf{k}_{ip} \parallel \mathbf{M}_0$ typically exhibiting a negative group velocity in the low wavevector regime: For the pure dipolar case, the dispersion in this geometry would yield negative group velocities and thus the energy flow is oriented "backward" with respect to the phase front propagation[11]. For non-negligible exchange interactions as incorporated in the Kalinikos-Slavin dispersion shown in figure 8.2, the negative group velocities are only obtained for the dipole-dominated regime, and the increasing contribution of the exchange interaction with increasing $\mathbf{k}_{ip}$ leads to the formation of a global minimum for finite $\mathbf{k}_{ip}$. This can be seen in figure 8.2 (b) around $k_{ip} \approx 4\,rad/\mu m$, above which the exchange energy

9: A schematic of the geometric definitions is shown in figure 8.1: the polar angle θ_0 (of the equilibrium position of the magnetisation) and the azimuthal angle ϕ_k (between the projection of the magnetisation and the in-plane propagation direction of the spin waves).

10: In fact, in the purely dipolar case, the fundamental mode ($n = 0$) for $\mathbf{k}_{ip} \perp \mathbf{M}_0$ exhibits a maximal amplitude of the mode profile at the surfaces of the film, which decays exponentially to the centre. These waves are therefore also called *(magnetostatic) surface spin waves* (MSSWs). Yet, the exchange energy works against this effect and hence instead a uniform mode profile is considered instead in the Kalinikos-Slavin approach leading to equation 8.1.

[406]: Damon et al. (1961), 'Magnetostatic modes of a ferromagnet slab'
[407]: Hurben et al. (1995), 'Theory of magnetostatic waves for in-plane magnetized isotropic films'

11: The group velocity is given by the gradient of the spin wave dispersion, i.e. $\mathbf{v}_g = \nabla_{\mathbf{k}}\omega(\mathbf{k})$ [408], and as usual for a dispersive wave system indicates the direction and speed of the energy transport. The phase front propagation (direction and speed) is described by the phase velocity $\mathbf{v}_p = \mathbf{k}\,\omega(\mathbf{k})/\|\mathbf{k}\|^2$ [408].

[408]: Mahmoud et al. (2020), 'Introduction to spin wave computing'

governs and positive group velocities are obtained. This minimum is often referred to as the *band bottom* of the spin wave spectrum, since it defines the smallest attainable frequency in the system.

The *perpendicular standing spin wave* (PSSW) modes with $n > 0$ are clearly exchange-dominated given the small film thickness $d = 20\,\mathrm{nm}$ which yields short wave lengths of the standing wave with n nodes across the thickness, and hence the respective dispersion curve presents a quadratic signature for both geometries in figure 8.2.

8.1.4 Effective anisotropy tensors and their influence on the ellipticity of the precession

The incorporation of the anisotropy tensors in the Kalinikos-Slavin dispersion relation in equation 8.1 requires the precise definition of a suitable set of coordinate systems, for which similar coordinate definitions to [233] and [378, 379] were followed in this work[12] as illustrated in figure 8.3: A global coordinate system uvw with base vectors $\{\hat{\mathbf{e}}_u, \hat{\mathbf{e}}_v, \hat{\mathbf{e}}_w\}$ is used to describe the sample geometry, where the $\hat{\mathbf{e}}_v$ direction is chosen to point along the film normal, and the $\hat{\mathbf{e}}_u$ direction is chosen to coincide with the spin wave propagation direction. A dynamic coordinate system xyz is chosen such that $\hat{\mathbf{e}}_z \parallel \mathbf{M}_0$, i.e. the z axis is parallel to the equilibrium magnetisation $\mathbf{M}_0$, which reduces the three dimensional LLG to a set of only two coupled differential equations as detailed in section 4.2. The y axis is defined[13] perpendicular to the plane defined by $\mathbf{M}_0$ and the film normal $\hat{\mathbf{e}}_v$. Finally, a crystal coordinate system with base vectors $\{\hat{\mathbf{e}}_1, \hat{\mathbf{e}}_2, \hat{\mathbf{e}}_3\}$ is used to define the cubic anisotropy, as detailed in section 4.1.2 on page 69.

To use the expression given in equation 8.3, the effective total anisotropy tensor $\hat{N}^{\mathrm{ani}}$ must be expressed in the dynamic coordinates xyz and all relevant anisotropy terms must be taken into account, except of the anisotropy arising from the shape of the specimen: The dipolar energy giving rise to the associated demagnetisation tensor is already taken into account in the derivation of the Kalinikos-Slavin dispersion and enters the dipolar matrix elements F_{nn}. Building on the characterisation of the thin films presented in chapter 6, the relevant contributions for the effective total anisotropy tensor $\hat{N}^{\mathrm{ani}}$ in this work can be identified as:

- the cubic magnetocrystalline anisotropy up to second order, imposed by the crystal structure and hence easily defined in the crystal base $\{\hat{\mathbf{e}}_1, \hat{\mathbf{e}}_2, \hat{\mathbf{e}}_3\}$ with the constants as listed in table 6.9
- and a potential additional uniaxial anisotropy term, e.g. arising from a fabrication process for microstructures[14], which is easiest defined in the global base $\{\hat{\mathbf{e}}_u, \hat{\mathbf{e}}_v, \hat{\mathbf{e}}_w\}$.

Both were already formally introduced in section 4.1.2 and the expressions are detailed in the appendix chapter C. Therefore, only the explicit expressions corresponding to the most relevant geometries in this work will be recalled here to discuss their effect on the magnetisation oscillation trajectory.

Cubic anisotropy

For the case of an in-plane magnetised film along the [110] direction, i.e. $\mathbf{M}_0 \parallel [110]_{123}$ as will be the main interest in chapter 10, the cubic anisotropy

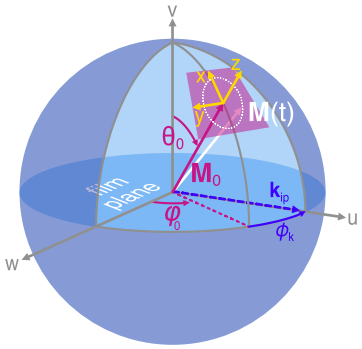

Figure 8.3: Recalling the schematic illustration of figure 8.1 for the definition of the global coordinates uvw and the dynamic (local) coordinates xyz used for the Kalinikos-Slavin dispersion relation 8.1 analogous to [233] and consistent with the coordinate definition in chapter 4 (figure 4.9). The radius of the sphere is given by M_S. $\mathbf{M}_0$ is the equilibrium position of the magnetisation, which corresponds to a minimum in f_{tot} and therefore coincides with the direction of the static effective field $\mathbf{H}_0$. $\hat{\mathbf{e}}_v$ corresponds to the normal of the film plane, $\hat{\mathbf{e}}_u$ corresponds to the propagation direction of the spin waves. The crystal coordinate system can be linked by defining the directions $[hkl]_{123}$ that coincide with $\hat{\mathbf{e}}_u$ and $\hat{\mathbf{e}}_v$, or by defining a polar and azimuthal angle, as shown in figure and deriving the corresponding transformation matrix as detailed in [227].

[227]: Stancil et al. (2009), *Spin waves*

[233]: Henry et al. (2016), *Propagating spin-wave normal modes*

[378]: Kalinikos et al. (1986), 'Theory of dipole-exchange spin wave spectrum for ferromagnetic films with mixed exchange boundary conditions'

[379]: Kalinikos et al. (1990), 'The dipole-exchange spin wave spectrum for anisotropic ferromagnetic films with mixed exchange boundary conditions'

12: Cleary, the choice of coordinates does not change anything but the formulation of the transformation matrices, which are necessary to rotate the terms into the dynamic system, in which the anisotropy tensors of the Kalinikos-Slavin dispersion relation in equation 8.1 are defined. These transformation matrices are easily calculated, which was done analogously to sections 3.6.2 and 3.6.3 in [227].

13: Note that in this point the convention used here differs from the coordinate definitions in [233], where the z axis is equally $\hat{\mathbf{e}}_z \parallel \mathbf{M}_0$, but the x axis is the one to be normal to the plane defined by $\mathbf{M}_0$ and the film normal. The reason for the choice in this work was to keep the Kalinikos-Slavin dispersion with the anisotropy tensor elements entering the F_{nn}^{ani} in equation 8.3 in its original form to avoid confusion.

14: Although, technically, the Kalinikos-Slavin approach deals with infinite thin films.

tensors simplify to

$$\hat{N}_{\mathrm{ani}}^{\mathrm{cub,110}} = \frac{2K_{\mathrm{c1}}}{\mu_0 M_{\mathrm{S}}^2}\begin{bmatrix}\frac{1}{2} & 1 & 0\\ 1 & \frac{1}{2} & 0\\ 0 & 0 & 1\end{bmatrix}_{123} + \frac{2K_{\mathrm{c2}}}{\mu_0 M_{\mathrm{S}}^2}\begin{bmatrix}0 & 0 & 0\\ 0 & 0 & 0\\ 0 & 0 & \frac{1}{4}\end{bmatrix}_{123} \tag{8.10}$$

while for the high-symmetry direction $\mathbf{M}_0 \parallel [100]_{123}$, the second order cubic anisotropy vanishes, and the cubic anisotropy tensor reads

$$\hat{N}_{\mathrm{ani}}^{\mathrm{cub,100}} = \frac{2K_{\mathrm{c1}}}{\mu_0 M_{\mathrm{S}}^2}\begin{bmatrix}0 & 0 & 0\\ 0 & 1 & 0\\ 0 & 0 & 1\end{bmatrix}_{123} \tag{8.11}$$

in that case.

Consequently, for $\mathbf{M}_0 \parallel \langle 100\rangle$ the cubic anisotropy induces an isotropic dynamic effective field acting in the plane perpendicular to $\mathbf{M}_0 \parallel \langle 100\rangle$, which is defined by[15]

$$\delta\mathbf{h}_{\mathrm{ani}}^{\mathrm{cub,100}} = -\frac{2K_{\mathrm{c1}}}{\mu_0 M_{\mathrm{S}}}\delta\mathbf{m} \tag{8.13}$$

and affects the precession angle and frequency, but does not distort the precession trajectory. This field basically (de)stabilises the precession around this equilibrium axis depending on the sign of the anisotropy constant K_{c1}[16].

For $\mathbf{M}_0 \parallel \langle 110\rangle$ on the other hand, an anisotropic dynamic effective field is obtained, which for $\delta\mathbf{m} \perp \mathbf{M}_0$ is expressed in the local coordinates xyz as[17]

$$\delta\mathbf{h}_{\mathrm{ani}}^{\mathrm{cub,110}} = -\frac{2K_{\mathrm{c1}}}{\mu_0 M_{\mathrm{S}}}\begin{bmatrix}1 & 0\\ 0 & -\frac{1}{2}\end{bmatrix}_{xy}\cdot\delta\mathbf{m} - \frac{2K_{\mathrm{c2}}}{\mu_0 M_{\mathrm{S}}}\begin{bmatrix}\frac{1}{4} & 0\\ 0 & 0\end{bmatrix}_{xy}\cdot\delta\mathbf{m} \tag{8.16}$$

and thus, depending on the ratio of the constants K_{c1} and K_{c2}, leads to an elliptical distortion of the precession elongated along $x = [001]_{123}$ for hard axes along the principal lattice axes (and elongated along $y = [1\bar{1}0]_{123}$ for easy axes), or to a uniform contribution (around the precession axis) for $K_{\mathrm{c1}} = -K_{\mathrm{c2}}/2$.

With the anisotropy constants $K_{\mathrm{c1}} = -8.1\,\mathrm{kJ/m^3}$ and $K_{\mathrm{c2}} = 37.7\,\mathrm{kJ/m^3}$ for Co_2MnSi thin films from the results listed in table 6.9, one obtains

$$\delta\mathbf{h}_{\mathrm{ani}}^{\mathrm{cub,110}} = -\frac{2}{\mu_0 M_{\mathrm{S}}}\begin{bmatrix}-1.3\,\frac{\mathrm{kJ}}{\mathrm{m^3}} & 0\\ 0 & 4.1\,\frac{\mathrm{kJ}}{\mathrm{m^3}}\end{bmatrix}_{xy}\cdot\delta\mathbf{m} \tag{8.17}$$

and therefore the cubic magnetocrystalline anisotropy alone[18] induces an elliptic precession around $\mathbf{M}_0 \parallel \langle 110\rangle$ with roughly a factor of −3 difference between the two symmetry axes x and y of the elliptical trajectory.

For comparison[19], the demagnetisation field can be expressed in analogy[20] as

$$\mathbf{H}_{\mathrm{demag}} = -\frac{2K_{\mathrm{demag}}}{\mu_0 M_{\mathrm{S}}}\begin{bmatrix}1 & 0 & 0\\ 0 & 0 & 0\\ 0 & 0 & 0\end{bmatrix}_{xyz}\cdot\mathbf{m} \tag{8.18}$$

for a thin film with the film normal along the x axis in the local coordinates xyz. The effective anisotropy constant is given by $K_{\mathrm{demag}} = \mu_0 M_{\mathrm{S}}^2/2$, which for $M_{\mathrm{S}} \approx 1000\,\mathrm{kA/m}$ yields $K_{\mathrm{demag}} \approx 600\,\mathrm{kJ/m^3}$.

In the sample geometry in this work, the cubic anisotropy thus counteracts the elliptical trajectory induced by the demagnetisation field[21] as illustrated in figure 8.4, but only with approximately two orders of magnitude difference in the strength of the contribution.

15: Precisely, one would obtain

$$\delta\mathbf{h}_{\mathrm{ani}}^{\mathrm{cub,100}} = -\frac{2K_{\mathrm{c1}}}{\mu_0 M_{\mathrm{S}}}\begin{bmatrix}1 & 0 & 0\\ 0 & 1 & 0\\ 0 & 0 & 0\end{bmatrix}_{xyz}\cdot\delta\mathbf{m} \tag{8.12}$$

but since $\delta\mathbf{m} \perp \mathbf{M}_0$, the field component $\delta\mathbf{h}_{\mathrm{ani}}^{\mathrm{cub,100}}$ along the z direction is also zero and thus $\delta\mathbf{h}_{\mathrm{ani}}^{\mathrm{cub,100}} = -\frac{2K_{\mathrm{c1}}}{\mu_0 M_{\mathrm{S}}}\delta\mathbf{m}$.

16: For positive K_{c1} (easy axes along the $\langle 100\rangle$ directions if $K_{\mathrm{c2}} = 0$, else see the identifications in table 4.1 on page 71), the precession cone will get narrower, and the field corresponds thus to an effective Zeeman-like field contribution, i.e. it acts like an enhancement of the external field and stabilises the precession. For the case of negative K_{c1} (accordingly hard axes along the $\langle 100\rangle$ directions if $K_{\mathrm{c2}} = 0$), the anisotropy field opens the precession cone and destabilises the precession.

17: Again, one would obtain

$$\delta\mathbf{h}_{\mathrm{ani}}^{\mathrm{cub,110}} = -\frac{2K_{\mathrm{c1}}}{\mu_0 M_{\mathrm{S}}}\begin{bmatrix}1 & 0 & 0\\ 0 & -\frac{1}{2} & 0\\ 0 & 0 & \frac{3}{2}\end{bmatrix}_{xyz}\cdot\delta\mathbf{m} \tag{8.14}$$

$$-\frac{2K_{\mathrm{c2}}}{\mu_0 M_{\mathrm{S}}}\begin{bmatrix}\frac{1}{4} & 0 & 0\\ 0 & 0 & 0\\ 0 & 0 & 0\end{bmatrix}_{xyz}\cdot\delta\mathbf{m} \tag{8.15}$$

but since $\delta\mathbf{m} \perp \mathbf{M}_0$, the field component $\delta\mathbf{h}_{\mathrm{ani}}^{\mathrm{cub,110}}$ along the z direction is zero.

18: I.e. disregarding the demagnetisation energy, which normally is the main factor inducing an elliptical precession.

19: Note that this comparative conclusion is the only point in the entire discussion of the implications of the cubic anisotropy, for which the knowledge about the sample shape is relevant and an identification of the out-of-plane direction is necessary.

20: See equation 4.15 and the discussion thereafter.

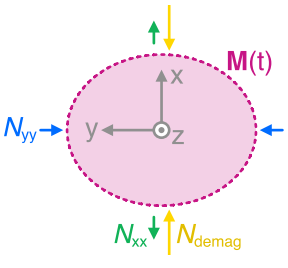

Figure 8.4: Schematic illustration of the anisotropy effect on the magnetisation trajectory for the case given in equation 8.17, compared to the demagnetisation impact as in equation 8.18. Arrows are not to scale.

21: And hence - although presenting a different origin and signature (in the anisotropy tensor / field) - yields a similar result as would be obtained with a (weak) perpendicular magnetic anisotropy (PMA) term.

Potential uniaxial anisotropy contribution

For an additional uniaxial anisotropy term induced by the structuring process to fabricate a waveguide for instance[22], the anisotropy symmetry axis is most likely to coincide with the long axis of the structure along which a translation invariance is given. In this case[23], $\theta_a = 90°$ and $\varphi_a = 0°$, which simplifies the anisotropy tensor to

$$\hat{N}_{\text{ani}}^{\text{uni}} = -\frac{2K_{u1}}{\mu_0 M_S^2}\begin{bmatrix}1&0&0\\0&0&0\\0&0&0\end{bmatrix}_{uvw} - \frac{12K_{u2}}{\mu_0 M_S^2}\begin{bmatrix}\sin^2\theta_0\sin^2\varphi_0&0&0\\0&0&0\\0&0&0\end{bmatrix}_{uvw} \tag{8.19}$$

with the polar and azimuthal angles θ_0 and φ_0 defining the equilibrium position of the magnetisation[24] as indicated in figure 8.3.

Effect on the Kalinikos-Slavin dispersion relation of thin films

After the explicit definition of the anisotropy tensors and the transition matrices between the different coordinate systems, the respective components of the tensors defined in the local coordinate system and generally indexed as

$$\hat{N}_{\text{ani}} = \begin{bmatrix}N_{xx}^{\text{ani}}&N_{xy}^{\text{ani}}&N_{xz}^{\text{ani}}\\N_{yx}^{\text{ani}}&N_{yy}^{\text{ani}}&N_{yz}^{\text{ani}}\\N_{zx}^{\text{ani}}&N_{zy}^{\text{ani}}&N_{zz}^{\text{ani}}\end{bmatrix}_{xyz} \tag{8.20}$$

can be inserted into the approximative Kalinikos-Slavin dispersion relation given in equation 8.1.

For an in-plane magnetised thin film, i.e. $\theta_0 = 90°$, the dispersion relation from equation 8.1 for the lowest mode number $n = 0$ is given by[25]

$$\omega_{n=0}^2 = (\omega_H + \omega_{\text{exch}}) \cdot \left(\omega_H + \omega_{\text{exch}} + \omega_M \left(F_{00} + F_{00}^{\text{ani}}\right)\right) \tag{8.21}$$

and drastically simplifies for the two high symmetry cases $\mathbf{k}_{ip} \perp \mathbf{M}_0$ and $\mathbf{k}_{ip} \parallel \mathbf{M}_0$ (DE and BV geometry[26] respectively), for which the dipole matrix elements F_{00} read[27]

$$F_{00,\text{DE}} = 1 + P_{00}\left(1 - P_{00}\right) \cdot \frac{\omega_M}{\omega_H + \omega_{\text{exch}}} \tag{8.22}$$

$$F_{00,\text{BV}} = 1 - P_{00} \tag{8.23}$$

and the anisotropy matrix elements read

$$\begin{aligned} F_{00,\text{DE}}^{\text{ani}} &= N_{xx}^{\text{ani}} + N_{yy}^{\text{ani}} + \frac{\omega_M}{\omega_H + \omega_{\text{exch}}} \cdot \left(N_{xx}^{\text{ani}} N_{yy}^{\text{ani}} + N_{yy}^{\text{ani}} - \left(N_{xy}^{\text{ani}}\right)^2\right) \\ &\quad + P_{00} \cdot \frac{\omega_M}{\omega_H + \omega_{\text{exch}}} \cdot \left(N_{xx}^{\text{ani}} - N_{yy}^{\text{ani}}\right) \end{aligned} \tag{8.24}$$

$$F_{00,\text{BV}}^{\text{ani}} = N_{xx}^{\text{ani}} + N_{yy}^{\text{ani}} + \frac{\omega_M}{\omega_H + \omega_{\text{exch}}} \cdot \left(N_{xx}^{\text{ani}} N_{yy}^{\text{ani}} + N_{yy}^{\text{ani}} - \left(N_{xy}^{\text{ani}}\right)^2\right) \quad . \tag{8.25}$$

The effects of the different anisotropy terms on the Kalinikos-Slavin dispersion are illustrated in figure 8.5 for an exemplary case corresponding to the geometry at the core of chapter 10, where the propagation direction is given by $[110]_{123}$ and the film normal is $[001]_{123}$ in the crystal base $\{\hat{\mathbf{e}}_1, \hat{\mathbf{e}}_2, \hat{\mathbf{e}}_3\}$. Additionally, a potential uniaxial anisotropy contribution along the propagation direction is considered[28]. In this case, the above derived anisotropy tensor elements

22: See the discussion around equation 4.26.

23: Assuming the spin waves propagate in the film plane along the long axis of the waveguide, which is per se the core idea of a waveguide.

24: For $\mathbf{M}_0 \perp \hat{\mathbf{e}}_u$ these are $\theta_0 = 90°$ and $\varphi_0 = 0°$, and thus the second order uniaxial anisotropy yields no contribution when the equilibrium position and the anisotropy symmetry axis coincide.

25: With

$$\omega_H = \gamma\mu_0 H_{\text{ext}}$$
$$\omega_{\text{exch}} = \gamma\mu_0 H_{\text{exch}} = \lambda_{\text{exch}}^2 k_{n,\text{tot}}^2$$
$$\omega_M = \gamma\mu_0 M_S$$

as introduced above.

26: As introduced on page 155, DE refers to "Damon-Eshbach" ($\mathbf{k}_{ip} \perp \mathbf{M}_0$, and thus $\varphi_0 = 0°$ and $\phi_k = 90°$) and BV refers to "Backward-Volume" ($\mathbf{k}_{ip} \parallel \mathbf{M}_0$, with $\varphi_0 = 0°$ and $\phi_k = 90°$).

27: Recalling equation 8.4 here:

$$P_{00}\left(k_{ip}\right) = 1 - \frac{1 - \exp\left(-k_{ip} \cdot d\right)}{k_{ip} \cdot d}$$

for completeness.

28: To account for potential structuring effects or alike.

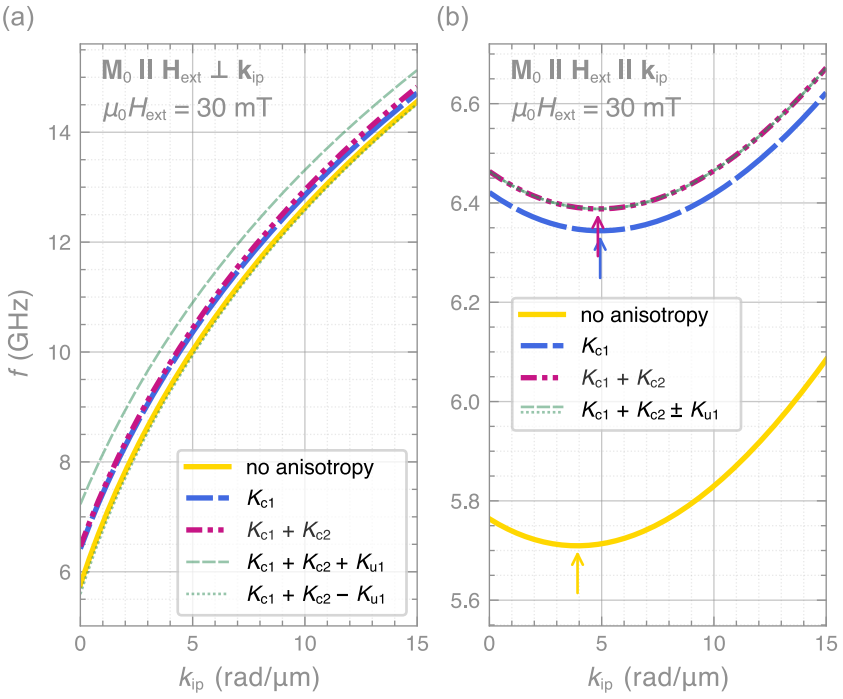

Figure 8.5: Spin wave dispersion relations of the fundamental mode $n = 0$ calculated with the approximative Kalinikos-Slavin formula for (a) an external field applied in the film plane, perpendicular to the propagation direction and (b) an external field applied along the propagation direction, each for different considerations of the anisotropy terms. The arrows in (b) indicate the minimum of the respective curve. The cubic anisotropy constants were set to $K_{c1} = -8.1\,\mathrm{kJ/m^3}$ and $K_{c2} = 37.7\,\mathrm{kJ/m^3}$ as was the result in chapter 6. The dashed green line with $K_{u1} = 5\,\mathrm{kJ/m^3}$ corresponds to an easy axis along the propagation direction, the dotted green line with $K_{u1} = -5\,\mathrm{kJ/m^3}$ corresponds to a hard axis respectively. The external field was set to $\mu_0 H_{ext} = 30\,\mathrm{mT}$ for all. As before in figure 8.2, the material parameters were set for a thin film with $M_S = 1058\,\mathrm{kA/m}$, $\gamma = 28.54\,\mathrm{GHz/T}$, $A_{exch} = 19.5\,\mathrm{pJ/m}$ and $d = 20\,\mathrm{nm}$, which corresponds to the sample investigated in chapter 10.

yield

$$N^{ani}_{xx,DE} = N^{ani}_{xx,BV} = \frac{2}{\mu_0 M_S}\left(K_{c1} + \frac{1}{4}K_{c2}\right) \tag{8.26}$$

$$N^{ani}_{xy,DE} = N^{ani}_{xy,BV} = 0 \tag{8.27}$$

as well as

$$N^{ani}_{yy,DE} = -\frac{2}{\mu_0 M_S}\left(\frac{1}{2}K_{c1} + K_{u1}\right) \tag{8.28}$$

$$N^{ani}_{yy,BV} = -\frac{2}{\mu_0 M_S}\left(\frac{1}{2}K_{c1}\right) \quad . \tag{8.29}$$

in the local coordinate system xyz, as listed in table D.1. Clearly, the uniaxial anisotropy along the propagation direction does not affect the Backward-Volume dispersion.

The resulting dispersion relations for different combinations of anisotropy constants are shown for the DE ($\mathbf{H}_{ext} \perp \mathbf{k}_{ip}$) geometry in figure 8.5 (a) and the BV ($\mathbf{H}_{ext} \parallel \mathbf{k}_{ip}$) geometry in figure 8.5 (b). Here, the cubic anisotropy constants $K_{c1} = -8.1\,\mathrm{kJ/m^3}$ and $K_{c1} = 37.7\,\mathrm{kJ/m^3}$ are taken from the FMR investigations in chapter 6 as summarised in table 6.9 and in order to illustrate the effect of the potential additional uniaxial anisotropy along the propagation direction, an arbitrary $K_{u1} = \pm 5\,\mathrm{kJ/m^3}$ is set. As expected from symmetry considerations, or simply from equation 8.28, the additional uniaxial anisotropy does not contribute in the BV ($\mathbf{H}_{ext} \parallel \mathbf{k}_{ip}$) geometry[29] and only for the DE ($\mathbf{H}_{ext} \perp \mathbf{k}_{ip}$) geometry, it simply leads to a shift to smaller (larger) k_{ip} for an easy (hard) axis along the propagation direction: see the dashed (dotted) light green lines in figure 8.5 (a).

For the Damon-Eshbach ($\mathbf{H}_{ext} \perp \mathbf{k}_{ip}$) geometry illustrated in figure 8.5 (a), the first order cubic anisotropy clearly leads to a shift of the original dispersion relation to higher frequencies in the shown wavevector range. The effect only persists for $k_{ip} \leq 30\,\mathrm{rad/\mu m}$, as seen when evaluating the difference to the isotropic dispersion as plotted in figure 8.6 (a), and is marginally[30]

29: As the equilibrium position of the magnetisation coincides with $\mathbf{H}_{ext}$ and therefore coincides with the anisotropy symmetry axis, the effect on the two perpendicular components is zero as is described by the tensors given in equation 8.19.

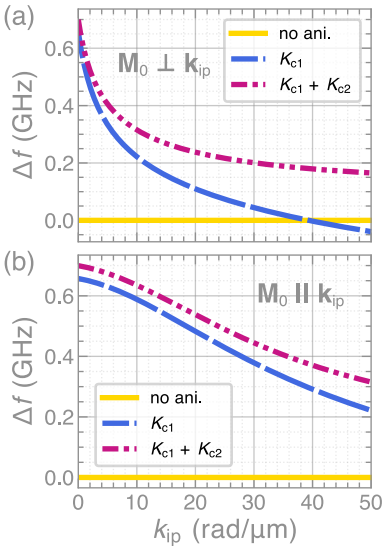

Figure 8.6: The cubic anisotropy induced frequency shift on the (a) DE and (b) BV dispersion, calculated as the difference between the respective dispersion and the isotropic function. Note that the wavevector range is chosen to cover the range up to $k_{ip} \cdot d \leq 1$ as in figure 8.2 (a), which includes the range in figure 8.5.

30: The effect would be stronger with stronger anisotropy constants, and particularly with a larger difference or factor between K_{c1} and K_{c2} - as was for instance found for the non-annealed Co_2MnAl sample, as listed in table 6.8.

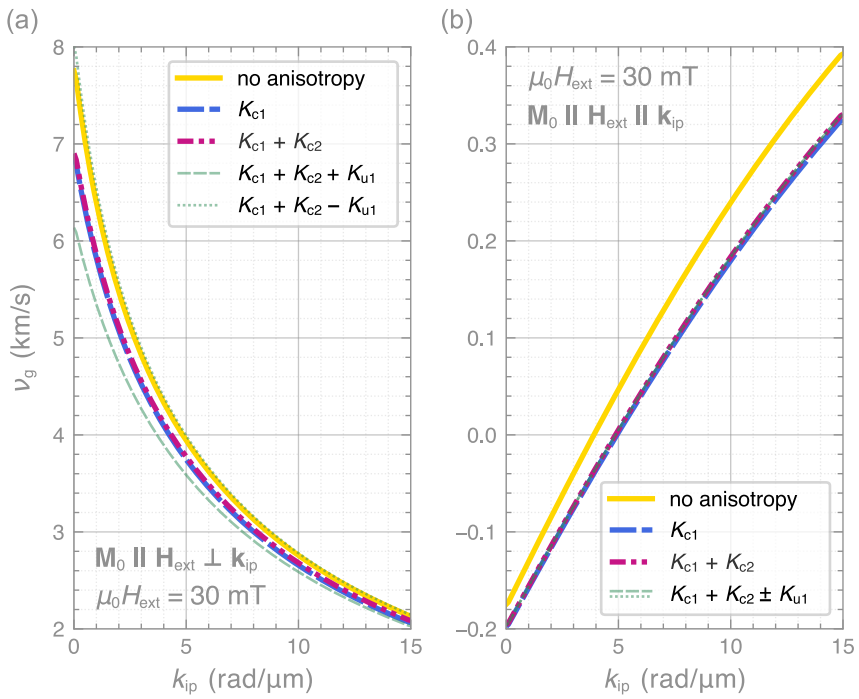

Figure 8.7: Group velocities corresponding to the spin wave dispersion relations shown in figure 8.5 (a) and (b). The zero crossing in (b) indicates the minimum in the disperion relations as pointed out by the arrows in figure 8.5 (b), and thus illustrates the observed k_{ip} shift of the band bottom.

strengthened (beyond $k_{ip} \gtrsim 30\,\mathrm{rad/\mu m}$ counteracted) by the second order cubic anisotropy. The absolute anisotropy induced frequency shift is not constant in k_{ip}, but decreases with the wavevector as shown in figure 8.6 (a) which directly translates to a general reduction of the group velocity

$$\nu_g = \frac{\partial \omega}{\partial k} \tag{8.30}$$

as is shown accordingly in figure 8.7 (a). Also, the two contributions clearly scale different with the wavevector: While for small k_{ip} the second order cubic anisotropy is hardly relevant, its relative contribution increases with increasing k_{ip}. This principally yields a counteracting effect on the group velocity as can be seen in figure 8.8 (a).

Yet, the anisotropy induced frequency shift becomes increasingly negligible with increasing k_{ip} as is shown in figure 8.9 (a) and linked to the strongly increasing spin wave frequencies in the Damon-Eshbach geometry: The anisotropy yields an upshift of the spin wave frequency by $\sim 12\%$ for $k_{ip} = 0$, which drops below $\sim 5\%$ already for $k_{ip} \approx 1\,\mathrm{rad/\mu m}$ and below $\sim 2\%$ for $k_{ip} \approx 15\,\mathrm{rad/\mu m}$. Moreover, as the relative impact of the frequency shift decreases drastically, the change of the group velocities becomes marginal, particularly for $k_{ip} \gtrsim 5\,\mathrm{rad/\mu m}$ as shown in figure 8.8 (a).

For the Backward-Volume ($\mathbf{H}_{ext} \parallel \mathbf{k}_{ip}$) geometry illustrated in figure 8.5 (b), the first order cubic anisotropy also leads to a shift of the dispersion relation to higher frequencies and the shift is again slightly increased by the second order cubic anisotropy, as shown in figure 8.8 (b). This is already apparent in figure 8.5 (b), linked to the generally "flatter" dispersion in this wavevector range[31]. Hence, the relative increase of the spin wave frequency in the Backward-Volume geometry is significant over a longer wavevector range than for the Damon-Eshbach geometry as shown in figure 8.9 (b): An increase of the frequency by $\gtrsim 10\%$ is obtained for wavevectors up to $k_{ip} \approx 10\,\mathrm{rad/\mu m}$ for the first order cubic anisotropy alone and up to $k_{ip} \approx 15\,\mathrm{rad/\mu m}$ for the inclusion of the second order cubic anisotropy, and drops below $\sim 5\%$ only for $k_{ip} \gtrsim 30\,\mathrm{rad/\mu m}$ and $k_{ip} \gtrsim 36\,\mathrm{rad/\mu m}$ respectively.

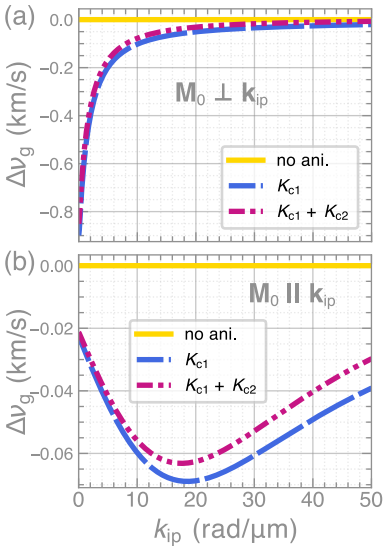

Figure 8.8: The cubic anisotropy induced reduction of the group velocity on the (a) DE and (b) BV dispersion, calculated as the difference between the respective dispersion and the isotropic function. Note that the wavevector range is chosen to cover the range up to $k_{ip} \cdot d \leq 1$ as in figure 8.2 (a), which includes the range in figure 8.5.

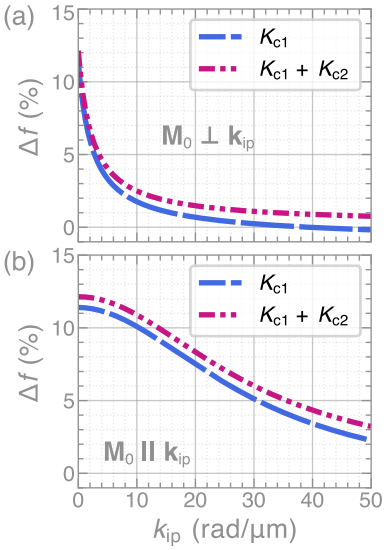

Figure 8.9: The relative anisotropy induced frequency shift on the (a) DE and (b) BV dispersion, corresponding to figure 8.6.

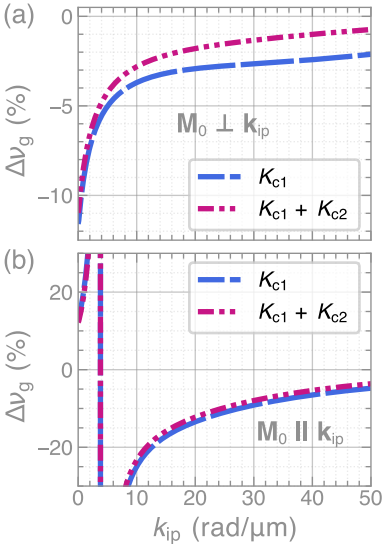

Figure 8.10: The relative anisotropy induced group velocity shift on the (a) DE and (b) BV dispersion, corresponding to figure 8.8. The divergence in (b) is due to the zero crossing at $k_{ip} \approx 4\,\mathrm{rad/\mu m}$ in the isotropic case (see the yellow line in figure 8.7 (b)) based on which the relative shift is evaluated.

31: And the related different scaling of the plot. See both geometries on the same scale in figure 8.2.

32: As pointed out in in figure 8.5 (b), where the minima are indicated by the respective arrow beneath each curve. Also seen on the shift of the corresponding zero crossing in figure 8.7 (b).

33: Studied in chapter 6, see table 6.8 on page 136.

Consequently, the related reduction of the group velocity in the Backward-Volume geometry is more significant than in the Damon-Eshbach geometry in the relative strength of the effect as well as the concerned wavevector range, compare figure 8.10 (a) and (b). The anisotropy therefore basically extends the "backward" propagation range. Moreover, the change of the group velocity does not monotonously decay as is the case in the Damon-Eshbach geometry, but instead yields a maximal absolute change between $k_{ip} \approx 15 - 25\,\mathrm{rad/\mu m}$ as seen in figure 8.8, while the relative impact of the change in figure 8.10 (b) naturally diverges around the band bottom with zero group velocity.

It is noted that in both geometries, Damon-Eshbach and Backward-Volume, the decrease of the group velocity induced by the first order cubic anisotropy is principally counteracted by the different wavevector dependence of the second order term, as seen in figure 8.8 and in figure 8.10. This is linked to the different wavevector dependence of two contributions in the dispersion relation as seen in figure 8.6. Yet the effect is marginal for the constants used here, and even negligible for the wavevector range $k_{ip} \lesssim 15\,\mathrm{rad/\mu m}$. A measure is for instance the significant shift of the dispersion minimum to greater in-plane wavevectors by $\Delta k_{ip} \approx 1\,\mathrm{rad/\mu m}$ (corresponding to $\sim 25\%$ of the isotropic minimum position), which is hardly counteracted by the second order contribution[32]. The distinct signature of the two contributions could, however, be of relevance for cases with a greater difference between the constants, and an extreme case would be e.g. the non-annealed Co_2MnAl film[33] with $K_{c1} \approx 0$ and $K_{c2} \approx 317\,\mathrm{kJ/m^3}$.

In summary, this analysis of the cubic anisotropy effects for a spin wave propagation along the crystal [110] direction leads to the following conclusions:

- The first order cubic anisotropy with negative K_{c1} alone (hard axes along the principal lattice directions ⟨100⟩) yields a shift of the dispersion relation along both geometries.
- The frequency shift induced by the negative K_{c1} is not constant in k_{ip}, but decreases with increasing k_{ip} for both geometries. It therefore results in a general reduction of the group velocities.
- For the DE geometry, the frequency shift is only significant for very small wavevectors, here $k_{ip} \lesssim 2\,\mathrm{rad/\mu m}$, as it rapidly becomes negligible due to the strong increase of the spin wave frequencies. Equally, the group velocity is hardly changed for larger wavevectors.
- For the BV geometry, the frequency shift is significant over a larger wavevector range linked to the relatively "flat" dispersion, particularly for $k_{ip} \leq 15\,\mathrm{rad/\mu m}$. This results in a significant shift of the in-plane wavevector corresponding to the band bottom (minimum frequency in the BV geometry) and a non-negligible reduction of the group velocities.
- The additional consideration of a second order term can principally enhance or counteract some effects of the first order term, yet the strength of this effect depends on the difference between the two constants.
- In particular for the investigated combination of constants as are the result from chapter 6, i.e. $K_{c1} = -8.1\,\mathrm{kJ/m^3}$ and $K_{c2} = 37.7\,\mathrm{kJ/m^3}$, the most significant impact of the second order cubic anisotropy is the additional increase of the spin wave frequency in the BV geometry.

Hence, the negligence of the second order cubic anisotropy term is considered a valid approximation for the modelling of the dispersion relation in the DE geometry for the further studies in this thesis. Yet, especially for the analysis of the nonlinear dynamics introduced in section 8.2, the second order term can be relevant e.g. for the identification of scattering partners, or for the estimation of the instability ranges based on the band bottom frequency.

8.1.5 Demagnetisation and width modes in waveguides

The lateral confinement in waveguides yields an additional demagnetisation contribution leading to a change in the shape anisotropy compared to the thin film case, as well as an additional quantisation of the respective wave vector component which results in the formation of width modes [409, 410].

For the Damon-Eshbach geometry[34], an approximative analytical expression of the resulting demagnetisation field was derived by Joseph and Schlömann [411] as a correction to the external field applied perpendicular to the waveguide, i.e. resulting in an inhomogeneous effective internal field

$$H_{\text{eff}}(z) = H_{\text{ext}} - N_{zz}^{\text{demag}}(z)\, M_{\text{S}} \tag{8.31}$$

which is a function of the position z along the transversal direction where $z = 0$ corresponds to the position at the centre of the waveguide and where the inhomogeneity is expressed by the demagnetisation tensor element in the z direction[35] given by [412]

$$N_{zz}^{\text{demag}}(z) = \frac{1}{\pi}\left(\arctan\left(\frac{d}{2z+b}\right) - \arctan\left(\frac{d}{2z-b}\right)\right) \tag{8.32}$$

with the thickness d and the width b of the waveguide[36]. For a waveguide with the cross section given by $d = 20\,\text{nm}$ and $b = 10\,\mu\text{m}$ and with the magnetisation of the material given by $M_{\text{S}} \approx 1000\,\text{kA/m}$ as corresponds to the case in chapter 10, this results in a field correction of $H_{\text{eff}}(z = 0) \approx H_{\text{ext}} - 1.5\,\text{mT}$ at the centre of the waveguide. Due to the strongly inhomogeneous field, the expression of the dispersion relation becomes a function of the position within the waveguide which complicates the analytical expression of the wave vector quantisation and thus the waveguide width modes [97].

For the Backward-Volume geometry, the static magnetisation is aligned along the long axis of the waveguide and can be approximated as homogeneous. Consequently, demagnetisation fields are only obtained for the dynamic component of the magnetisation $\delta\mathbf{m}$ and are strongest at the edges of the waveguide, resulting in a dipolar pinning. The quantisation of the wave vector along the width direction $\hat{\mathbf{e}}_{\text{w}}$ is then obtained analogously to the quantisation along the thickness in equation 8.5, which results in the total wave vector for a mode with the thickness mode number n and the width mode number m

$$\mathbf{k} = k_{\text{u/z}}\hat{\mathbf{e}}_{\text{z}} + \frac{n\pi}{d}\hat{\mathbf{e}}_{\text{x}} + \frac{m\pi}{b_{\text{eff}}}\hat{\mathbf{e}}_{\text{y}} \tag{8.33}$$

$$= k_{\text{u/z}}\hat{\mathbf{e}}_{\text{u}} + \frac{n\pi}{d}\hat{\mathbf{e}}_{\text{v}} + \frac{m\pi}{b_{\text{eff}}}\hat{\mathbf{e}}_{\text{w}} \tag{8.34}$$

expressed as a function of an effective waveguide width [97]

$$b_{\text{eff}} = b \cdot \left(\frac{D_{\text{pin}}}{D_{\text{pin}} - 2}\right) \tag{8.35}$$

which is determined by the dipolar pinning parameter $D_{\text{pin}} = \frac{2\pi\,\frac{b}{d}}{1+2\ln\frac{b}{d}}$ and thus by the aspect ratio b/d of the waveguide cross section. For a device like the one studied in chapter 10 with $d = 20\,\text{nm}$ and $b = 10\,\mu\text{m}$, this results in an effective width of $b_{\text{eff}} \approx 10.09\,\mu\text{m}$, hence the correction is negligible[37].

A more detailed description of the confinement consequences on the spin wave dynamics in rectangular elements is given in [412]. However, due to the increased complication of the micromagnetic problem, the spin wave dynamics

[409]: Kostylev et al. (2007), 'Dipole-exchange propagating spin-wave modes in metallic ferromagnetic stripes'
[410]: Demokritov (2019), *Spin Wave Confinement*

34: The propagation direction is considered along the long axis of the waveguide, and in consistency with above definitions the Damon-Eshbach geometry then corresponds to the case of the waveguide being magnetised perpendicular to its long axis, while the Backward-Volume geometry refers to the case of the waveguide being magnetised along its long axis.

[411]: Joseph et al. (1965), 'Demagnetizing Field in Nonellipsoidal Bodies'

35: As the waveguide axis corresponds to the propagation direction chosen as u in the convention in figure 8.1 and figure 8.3, the Damon-Eshbach geometry corresponds to a field applied along the w (or $-w$) direction, then the relation between local coordinates xyz and global coordinates uvw is simply $\hat{\mathbf{e}}_{\text{x}} \parallel \hat{\mathbf{e}}_{\text{v}}$, $\hat{\mathbf{e}}_{\text{y}} \parallel -\hat{\mathbf{e}}_{\text{u}}$ and $\hat{\mathbf{e}}_{\text{z}} \parallel \hat{\mathbf{e}}_{\text{w}}$ (or $\hat{\mathbf{e}}_{\text{y}} \parallel \hat{\mathbf{e}}_{\text{u}}$ and $\hat{\mathbf{e}}_{\text{z}} \parallel -\hat{\mathbf{e}}_{\text{w}}$).

[412]: Bayer et al. (2006), 'Chapter 2: Spin-Wave Excitations in Finite Rectangular Elements'

36: Precisely, in the global coordinate system uvw, d corresponds to the extent along the $\hat{\mathbf{e}}_{\text{v}}$ direction, whereas b is the extent along the direction $\hat{\mathbf{e}}_{\text{w}}$. While it is more intuitive and probably common to use w for the width, the choice of b instead of w is deliberately made here in order to avoid confusion with the global coordinate w.

[97]: Pirro (2014), 'Lineare und nichtlineare Spinwelleninteraktionen in magnetischen Mikrostrukturen'

37: Just calculated for comparison. The study in chapter 10 is carried out in the Damon-Eshbach geometry.

[412]: Bayer et al. (2006), 'Chapter 2: Spin-Wave Excitations in Finite Rectangular Elements'

in such confined structures are usually calculated with the help of micromagnetic simulations employing a discretisation of the sample typically based on a finite-difference or finite-element method. Common recent micromagnetic simulation codes include for instance MuMax3 [413], SWIIM [233] or TetraX [414–416], yet not all of those simulation codes are currently suitable for the simulation of second order cubic anisotropy effects.

[413]: Vansteenkiste et al. (2014), 'The design and verification of MuMax3'
[233]: Henry et al. (2016), *Propagating spin-wave normal modes*
[414]: Körber et al. (2022), *TetraX*
[415]: Körber et al. (2021), 'Finite-element dynamic-matrix approach for spin-wave dispersions in magnonic waveguides with arbitrary cross section'
[416]: Körber et al. (2022), 'Finite-element dynamic-matrix approach for propagating spin waves'

8.2 Nonlinear spin waves

At this point it is recalled that the LLG is an inherently nonlinear equation. The peculiar features arising from this inherent nonlinearity are omitted when linearising the LLG, which involves the separation into a static part $M_S\mathbf{m}_0$ and a small dynamic part $\delta\mathbf{m}$ of the magnetisation, the higher order terms of which $\mathcal{O}\left(\delta\mathbf{m}^2\right)$ are assumed to be negligible. This linearisation allows for an analytical solution e.g. for the calculation of the spin wave dispersion as above, yet the described linear spin waves are only valid solutions for very small oscillations $\delta\mathbf{m}$. Consequently, for oscillation amplitudes beyond the validity of the linearisation, the approach fails to describe the (nonlinear) features of the magnetisation dynamics, such as multi-magnon scattering and the related damping effects [86], or the appearance of nonlinear frequency shifts [417].

To account for the nonlinear spin wave dynamics, an approximative method can consist of the application of corrections in higher order of $\delta\mathbf{m}$ to the solutions of the linearised LLG, which has the advantage of building on the already developed formalism. Yet, the corrections typically need to be formulated specifically for the problem in question and the approach can be fairly cumbersome, see e.g. chapter 9 in [225]. Therefore, a different approach based on a Hamiltonian formalism has recently gained increasing popularity [225, 227, 229, 291, 401–403, 418].

In this section on nonlinear spin waves, the relevant phenomena will first be introduced giving an overview of the implications and motivating the need for the Hamiltonian formalism. Key concepts of this formalism will be briefly outlined to establish a foundation for the discussion of predominantly nonlinear spin wave dynamics in chapter 10. For more comprehensive treatments of nonlinear magnonic phenomena, see for example in textbooks [225, 227, 229] or the PhD theses [97, 370]. The structure in the following subsections 8.2.1-8.2.4 is inspired by the discussion in [97].

[86]: Pirro et al. (2014), 'Non-Gilbert-damping Mechanism in a Ferromagnetic Heusler Compound Probed by Nonlinear Spin Dynamics'
[417]: Weiss (1958), 'Microwave and Low-Frequency Oscillation Due to Resonance Instabilities in Ferrites'
[225]: Gurevich et al. (1996), *Magnetization oscillations and waves*
[227]: Stancil et al. (2009), *Spin waves*
[229]: Rezende (2020), *Fundamentals of Magnonics*
[291]: Dobin et al. (2004), 'Intrinsic nonlinear ferromagnetic relaxation (invited)'
[401]: Krivosik et al. (2010), 'Hamiltonian formulation of nonlinear spin-wave dynamics'
[402]: Tyberkevych et al. (2020), *Vector Hamiltonian Formalism for Nonlinear Magnetization Dynamics*
[403]: L'vov (1994), *Wave Turbulence under Parametric Excitation*
[418]: Verba et al. (2019), 'Hamiltonian formalism for nonlinear spin wave dynamics under antisymmetric interactions'

8.2.1 Multi-magnon scattering and Suhl instabilities

The aforementioned interactions of spin wave modes through their dynamic effective fields can be interpreted as elastic scattering processes in the particle picture, which need to obey energy and momentum conservation.

The interest in such multi-magnon scattering sparked with the analysis of "anomalous effects in the microwave absorption of ferromagnets at high signal powers" [288] by Suhl in 1957. Since then, the multi-magnon scattering processes have been investigated in various contexts e.g. for their effects on the relaxation of spin wave modes [86, 291, 419–421], the consequent effects on the magnetisation switching [422], or the resulting formation of magnon Bose-Einstein condensates as macroscopic quantum states [423–426]. With the rising interest in neuromorphic computing and quantum computing approaches, these nonlinear scattering effects and their implications have become of increasing importance for the development of unconventional

[225]: Gurevich et al. (1996), *Magnetization oscillations and waves*
[227]: Stancil et al. (2009), *Spin waves*
[229]: Rezende (2020), *Fundamentals of Magnonics*
[97]: Pirro (2014), 'Lineare und nichtlineare Spinwelleninteraktionen in magnetischen Mikrostrukturen'
[370]: Brächer (2015), 'Parallel parametric amplification of spin waves in microstructures'
[288]: Suhl (1957)
[86]: Pirro et al. (2014)
[291]: Dobin et al. (2004)
[419]: Olson et al. (2007)
[420]: Nembach et al. (2011)
[421]: Schultheiss et al. (2012)
[422]: Livesey et al. (2007)
[423]: Nikuni et al. (2000)
[424]: Giamarchi et al. (2008)
[425]: Schneider et al. (2020)
[426]: Schneider et al. (2021)

magnonic devices promising a tunability e.g. by device geometries [427], surface acoustic waves [428], spin currents [60] or rapid cooling [429].

The most relevant processes are of lowest order in the number of particles (spin wave modes) involved. With increasing number of involved scattering partners, the processes become less important in their contribution to the total energy of the system[38]. It is therefore often sufficient to consider the first two processes, i.e. three-magnon and four-magnon scattering[39].

A schematic illustration of exemplary three-magnon and four-magnon scattering processes is shown in figure 8.11. Other configurations[40] exist, yet the depictions in figure 8.11 (a) and (b) correspond to the configurations which lead to the phenomenon of the *first order* and *second order (Suhl) instability* respectively, describing the scattering of directly excited modes[41] (primary magnons) into secondary spin wave modes:

- The *first order Suhl instability* refers to the resonant three-magnon scattering process, where one primary magnon splits into two secondary magnons as illustrated in figure 8.11 (a). The energy conservation

$$\omega_A = \omega_B + \omega_C \tag{8.36}$$

  directly implies $\omega_A \geq 2 \cdot \omega_{min}$, where ω_{min} corresponds to the minimal spin wave frequency in the system, i.e. the band bottom.
- The *second order Suhl instability* refers to the resonant four-magnon scattering process similar to the one illustrated in figure 8.11 (b): The scattering of two primary magnons into two secondary magnons yields

$$\omega_A + \omega_B = 2 \cdot \omega_A = \omega_C + \omega_D \tag{8.37}$$

  for the energy conservation, for which the trivial solution $\omega_A = \omega_C = \omega_D$ always yields possible scattering partners (which can still differ in $\mathbf{k}$).

In consequence, the excitation spectra yield a parameter range, where the first order Suhl instability is forbidden and therefore only a second order Suhl instability[42] can lead to an energy loss of the directly excited spin waves. An estimation for the case of this study is shown in figure 8.12, where additionally the isotropic case is traced for comparison.

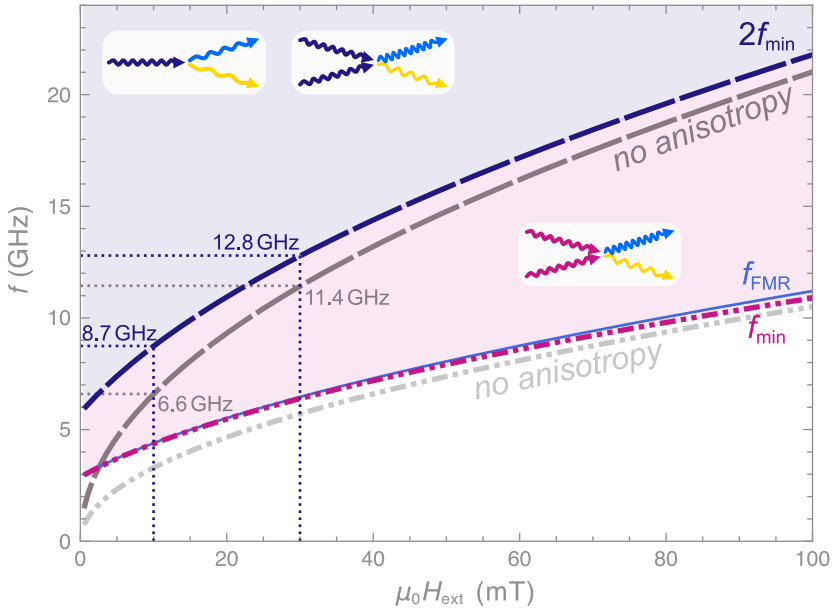

[427]: Mohseni et al. (2021)
[428]: Geilen et al. (2025)
[60]: Hache et al. (2023)
[429]: Breitbach et al. (2023)

38: The Hamiltonian of the total energy of the magnetic system can be developed in terms of different orders in the amount of modes involved. More details will be given in subsection 8.2.3.

39: Note that the two-magnon scattering is bound to defects and does not obey momentum conservation, see page 40. It is therefore not one of the intrinsic nonlinear scattering mechanisms, albeit the misleading naming and its appearance alongside multi-magnon scattering analyses notably in various discussions on the damping enhancement effect.

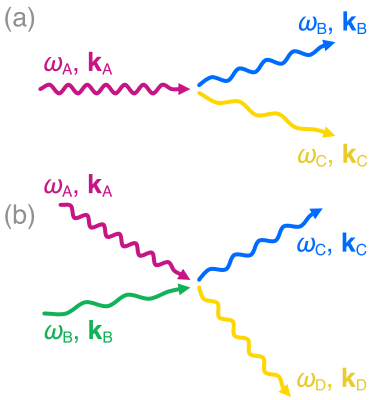

Figure 8.11: Schematic illustration of (a) an exemplary three-magnon scattering process and (b) an exemplary four-magnon scattering process.

40: E.g. the confluence of two magnons into one instead of the process depicted in figure 8.11 (a), or e.g. the splitting of one primary magnon into three secondary magnons instead of figure 8.11 (b).

[97]: Pirro (2014), 'Lineare und nichtlineare Spinwelleninteraktionen in magnetischen Mikrostrukturen'

Figure 8.12: Estimation of the instability ranges based on the dispersion relation given in equation 8.1 for a Co_2MnSi film magnetised along the [110] direction, with $M_S = 1058\,kA/m$, $\gamma = 28.54\,GHz/T$, $A_{exch} = 19.5\,pJ/m$, $K_{c1} = -8.1\,kJ/m^3$, $K_{c2} = 37.7\,kJ/m^3$ and $d = 20\,nm$. The grey curves labelled with "no anisotropy" correspond to the same calculation but for $K_{c1} = K_{c2} = 0$. The vertical, tinily dotted lines correspond to the external fields used in chapter 10: For external fields $\mu_0 H_{ext} = 10\,mT$ and $30\,mT$, the first order Suhl instability can only be observed for excitation frequencies above $2 \cdot f_{min} \approx 8.7\,GHz$ and $12.8\,GHz$ respectively, and particularly for small fields the frequency shift due to the anisotropy contributions is significant. Figure after [97].

The band bottom is nearly identical to the FMR frequency and the excitation frequencies below which it is impossible to find scattering partners for a first oder Suhl instability yield 8.7 GHz and 12.8 GHz for external fields $\mu_0 H_{\text{ext}} = 10\,\text{mT}$ and 30 mT as used in the study presented in chapter 10. The limit for the first order instability is larger than for zero anisotropy due to the anisotropy-induced shift to higher frequencies as observed in figure 8.5[43].

8.2.2 Nonlinear frequency shift

Right after the analysis of spin wave instabilities in the form of multi-magnon scattering by Suhl in 1957 [288], the "anharmonic response" [417] of the FMR in the form of a nonlinear frequency shift was reported and analysed in relation to the occurrence of Suhl instabilities [290]. In analogy to the phenomenon observed on the resonance of a classical pendulum, the effect is often called *foldover* effect especially in studies focusing on the characteristic deformation of the resonance curve, or also referred to in the context of the resulting *bistability* [430–434].

Intuitively, the effect can be described as motivated on page 162: Due to the self-interaction of the spin wave modes through their effective fields, the increasing precession amplitudes obtained when driving the magnetisation at increasing excitation powers lead to an increasing change in the related self-induced effective field, which acts again as a perturbation on the system. Thus, the increase in the spin wave amplitudes is correlated with a shift of the dispersion relation of the spin wave modes as will be relevant in chapter 10.

For weakly nonlinear excitations, the change of the dispersion relation can be expressed as a correction to the linear solution by

$$\widetilde{\omega}_{\mathbf{k}}(t) = \omega_{\mathbf{k}}(t) + \Delta\omega_{\mathbf{k}}(t) \tag{8.38}$$

for a spin wave with wave vector $\mathbf{k}$, where the nonlinear shift

$$\Delta\omega_{\mathbf{k}}(t) = \widetilde{W}_{\mathbf{kk},\mathbf{kk}} \cdot |c_{\mathbf{k}}(t)|^2 \tag{8.39}$$

is defined by the complex spin wave amplitudes $c_{\mathbf{k}}(t)$ as well as the coupling coefficient $\widetilde{W}_{\mathbf{kk},\mathbf{kk}}$ accounting for the self-interaction of the spin waves modes [401]. The sign of the matrix elements $\widetilde{W}_{\mathbf{kk},\mathbf{kk}}$ clearly determines the direction of the frequency shift and a precise description of the coupling coefficients $\widetilde{W}_{\mathbf{kk},\mathbf{kk}}$ can be derived in the Hamiltonian formalism for nonlinear spin wave dynamics [401, 402], which for instance allows to reproduce the frequency foldover effect on the FMR response [402].

Apart from the foldover effect on the FMR and the resulting bistability of the dynamic response in a certain pumping frequency range, nonlinear frequency shifts have recently been studied extensively in relation to the nonlinear dynamics observed in spintronic oscillators [130, 435–443]: The nonlinear shifts can result in oscillation frequencies below the FMR [439], are crucial for the accurate description of the oscillation linewidth in spin-torque nano-oscillators [437], can lead to the formation of a magnon soliton mode governing the nonlinear auto-oscillations in spin-Hall nano-oscillators [435], can assist the synchronisation of the multiple oscillators [441, 442] and can be driven by spin currents [443]. A thorough understanding of the nonlinear magnetisation dynamics is therefore not only important for nonlinear spin wave applications, but highly desirable for the development of efficient hybrid magnonic-spintronic devices as well.

41: E.g. pumped by a microwave antenna field.

42: Assuming negligible contributions from higher order scattering processes.

43: Note that for $K_{c1} = -8.1\,\text{kJ/m}^3$ and $K_{c2} = 0$, i.e. the case of K_{c1} only in figure 8.5, a slight reduction to 8.6 GHz and 12.7 GHz.

[288]: Suhl (1957)
[417]: Weiss (1958)
[290]: Schlömann et al. (1960)
[430]: Zhang et al. (1986)
[431]: Chen et al. (1989)
[432]: Fetisov et al. (1999)
[433]: Fetisov et al. (2004)
[434]: Slobodianiuk et al. (2019)
[401]: Krivosik et al. (2010), 'Hamiltonian formulation of nonlinear spin-wave dynamics'
[402]: Tyberkevych et al. (2020), *Vector Hamiltonian Formalism for Nonlinear Magnetization Dynamics*
[130]: Slavin et al. (2009), 'Nonlinear Auto-Oscillator Theory of Microwave Generation by Spin-Polarized Current'
[435]: Slavin et al. (2005), 'Spin Wave Mode Excited by Spin-Polarized Current in a Magnetic Nanocontact is a Standing Self-Localized Wave Bullet'
[436]: Rezende et al. (2006), 'Magnon excitation by spin-polarized direct currents in magnetic nanostructures'
[437]: Kim et al. (2008), 'Generation Linewidth of an Auto-Oscillator with a Nonlinear Frequency Shift'
[438]: Dussaux et al. (2012), 'Field dependence of spin-transfer-induced vortex dynamics in the nonlinear regime'
[439]: Ranjbar et al. (2014), 'CoFeB-Based Spin Hall Nano-Oscillators'
[440]: Demidov et al. (2014), 'Synchronization of spin Hall nano-oscillators to external microwave signals'
[441]: Locatelli et al. (2015), 'Efficient Synchronization of Dipolarly Coupled Vortex-Based Spin Transfer Nano-Oscillators'
[442]: Li et al. (2018), 'Selective control of vortex polarities by microwave field in two robustly synchronized spin-torque nano-oscillators'
[443]: Divinskiy et al. (2019), 'Controllable excitation of quasi-linear and bullet modes in a spin-Hall nano-oscillator'

8.2.3 Hamilton formalism for spin wave dynamics

Motivated by an interest in the analysis of the nonlinear phenomena observed on the FMR at high excitation powers, the use of a Hamiltonian formalism was proposed in 1959 [289]. This formalism has since become a widespread approach[44] for the treatment of nonlinear spin wave dynamics [291, 401–403, 418, 437, 444], which in its most recent vectorised form allows for a description of highly non-uniform ground states like vortices or skyrmions [402].

The Hamiltonian approach consists of several general steps, and following the derivation in [401, 402], these are in short[45]:

1. An expression of the Hamiltonian operator $\mathscr{H}$ of the magnetic system to include all terms considered in the total energy density ℓ_{tot}, i.e.[46]

$$\mathscr{H} = \int_V \ell_{\text{tot}}\, dV \tag{8.40}$$

   which is cast to frequency units for convenience: $|\gamma|\mathscr{H}/M_S V \rightarrow \mathcal{U}$ [401].
2. A transformation to canonically conjugated variables, which separates the static and dynamic contribution of the magnetisation vector. For the classical Hamiltonian approach, this is given by the transformation introduced by Schlömann [289, 401]

$$\alpha_\perp(\mathbf{r},t) = a(\mathbf{r},t)\sqrt{2 - a(\mathbf{r},t)\,a^*(\mathbf{r},t)} \tag{8.41}$$
$$\alpha_0(\mathbf{r},t) = 1 - a(\mathbf{r},t)\,a^*(\mathbf{r},t) \tag{8.42}$$

   linking the direction cosines $\alpha_\perp$ and α_0 of the magnetisation to the canonical variables a and a^*, which allow to transform the equations of motion into a set of classical Hamiltonian equations[47]

$$i\frac{da(\mathbf{r},t)}{dt} = \frac{\delta\mathcal{U}}{\delta a^*(\mathbf{r},t)} \quad \text{and} \quad -i\frac{da^*(\mathbf{r},t)}{dt} = \frac{\delta\mathcal{U}}{\delta a(\mathbf{r},t)} \quad . \tag{8.44}$$

   This transformation is sometimes also referred to as the *Holstein-Primakoff transformation*, referring to the analogy to the quantum mechanical version given in [445].
3. A Fourier plane-wave expansion of the canonical variables[48]

$$a(\mathbf{r},t) = \sum_{\mathbf{k}} a_{\mathbf{k}}(t)\, e^{i\mathbf{k}\cdot\mathbf{r}} \tag{8.45}$$

   where the $a_{\mathbf{k}}(t)$ and $a^*_{\mathbf{k}}(t)$ correspond to the complex amplitudes of the plane waves with wave vector $\mathbf{k}$. As the $a_{\mathbf{k}}(t)$ and $a^*_{\mathbf{k}}(t)$ do not correspond to the eigenmodes of the system for elliptical magnetisation precession trajectories [97], an additional transformation called *Bogoliubov transformation* to a new set of canonical variables $b_{\mathbf{k}}(t)$ and $b^*_{\mathbf{k}}(t)$ is necessary which diagonalise the system and correspond to the complex spin wave amplitudes [227].
4. An expansion of the Hamiltonian as a Taylor series in their powers

$$\mathcal{U}\left(b_{\mathbf{k}}(t), b^*_{\mathbf{k}}(t)\right) = \sum_n \mathcal{U}^{(n)} \approx \sum_n^4 \mathcal{U}^{(n)} + \mathcal{O}\left(\mathcal{U}^{(5)}\right) \tag{8.46}$$

   which yields a polinomial form sorted by the number n of spin waves involved in the related contribution.

Precisely, this formalism leads to an expansion which sorts the contributions by their nature: $\mathcal{U}^{(0)}$ is the ground state of the system and does not contribute to

[289]: Schlömann (1959), 'Fine Structure in the Decline of the Ferromagnetic Resonance Absorption with Increasing Power Level'

44: As stated in the introduction of this chapter, the main other approach is to use the LLG in its linearised form and come up with correction terms to the effective field to account for the nonlinear effects [401].

[291]: Dobin et al. (2004), 'Intrinsic nonlinear ferromagnetic relaxation (invited)'

[401]: Krivosik et al. (2010), 'Hamiltonian formulation of nonlinear spin-wave dynamics'

[402]: Tyberkevych et al. (2020), *Vector Hamiltonian Formalism for Nonlinear Magnetization Dynamics*

[403]: L'vov (1994), *Wave Turbulence under Parametric Excitation*

[418]: Verba et al. (2019), 'Hamiltonian formalism for nonlinear spin wave dynamics under antisymmetric interactions'

[437]: Kim et al. (2008), 'Generation Linewidth of an Auto-Oscillator with a Nonlinear Frequency Shift'

[444]: Zakharov et al. (1975), 'Spin-wave turbulence beyond the parametric excitation threshold'

45: For a detailed description it is highly recommendable to read [227, 401–403], or the concise summary in [97].

46: Here, it should be noted that following the common derivations, e.g. in [401, 402, 418], the cubic anisotropy is typically excluded for simplicity, since its incorporation would lead to "more complicated expressions for all linear and nonlinear coefficients" [402]. As discussed above, one of the results in the previous part of this thesis is the non-negligible cubic anisotropy in the Co_2MnSi systems, so this assumption is likely to yield wrong results for the case of this work. Yet, since it is not used for a quantitative analysis, but only introduced here for a qualitative description, the derivations in [401, 402] are followed at this point.

47: In the vector Hamiltonian formalism, the transformation is achieved by a Lambert azimuthal equal-area projection

$$\mathbf{m} = \left(1 - \frac{|\mathbf{s}|^2}{2}\right)\cdot\mathbf{m}_0 + \sqrt{1 - \frac{|\mathbf{s}|^2}{4}}\cdot\mathbf{s} \tag{8.43}$$

with the *spin excitation vector* $\mathbf{s}$ defining the mapping of the spherical problem onto a plane $\mathbf{s}$ under conservation of the area, as commonly used in cartography [402]. The Hamiltonian equation is then expressed in terms of $\mathbf{s}$.

[445]: Holstein et al. (1940), 'Field Dependence of the Intrinsic Domain Magnetization of a Ferromagnet'

48: In the vector Hamiltonian approach, the Hamiltonian is directly expanded in powers of the *spin excitation vector* $\mathbf{s}$ [402].

[97]: Pirro (2014), 'Lineare und nichtlineare Spinwelleninteraktionen in magnetischen Mikrostrukturen'

[227]: Stancil et al. (2009), *Spin waves*

the time-dependent spin-wave dynamics, $\mathcal{U}^{(1)}$ describes the time-dependent pumping by transverse fields, $\mathcal{U}^{(2)} = \sum_{\mathbf{k}} \omega_{\mathbf{k}} b^*_{\mathbf{k}}(t)\, b_{\mathbf{k}}(t)$ describes the linear response of the system with dispersions $\omega_{\mathbf{k}}$, $\mathcal{U}^{(3)}$ represents the three-wave processes, $\mathcal{U}^{(4)}$ the four-wave processes and higher orders are typically omitted as their contribution is negligible for most systems [401].

[401]: Krivosik et al. (2010), 'Hamiltonian formulation of nonlinear spin-wave dynamics'

8.2.4 Nonlinear dynamics in the Hamiltonian

In order to obtain a description of the above introduced nonlinear effects, i.e. the first and second order Suhl instabilities as well as the nonlinear frequency shift, clearly the nonlinear contributions to $\mathcal{U}$ need to be evaluated: $\mathcal{U}^{(3)}$ and $\mathcal{U}^{(4)}$. Following the convention of the scalar Hamiltonian approach, the implications will be outlined briefly in the following two subsections. For a detailed analysis it is referred to [401] and [97].

[401]: Krivosik et al. (2010), 'Hamiltonian formulation of nonlinear spin-wave dynamics'
[97]: Pirro (2014), 'Lineare und nichtlineare Spinwelleninteraktionen in magnetischen Mikrostrukturen'

The third-order contribution $\mathcal{U}^{(3)}$ takes the form [401]

$$\begin{aligned}\mathcal{U}^{(3)} = &\sum_{\mathbf{k}_1\mathbf{k}_2\mathbf{k}_3} \left(V^*_{\mathbf{k}_1\mathbf{k}_2,\mathbf{k}_3} b_{\mathbf{k}_1} b_{\mathbf{k}_2} b^*_{\mathbf{k}_3} + c.c.\right) \delta\left(\mathbf{k}_1 + \mathbf{k}_2 - \mathbf{k}_3\right) \\ &+ \frac{1}{3} \sum_{\mathbf{k}_1\mathbf{k}_2\mathbf{k}_3} \left(U^*_{\mathbf{k}_1\mathbf{k}_2\mathbf{k}_3} b_{\mathbf{k}_1} b_{\mathbf{k}_2} b_{\mathbf{k}_3} + c.c.\right) \delta\left(\mathbf{k}_1 + \mathbf{k}_2 + \mathbf{k}_3\right)\end{aligned} \tag{8.47}$$

and the fourth-order contribution $\mathcal{U}^{(4)}$ can be written as

$$\begin{aligned}\mathcal{U}^{(4)} = &\frac{1}{2} \sum_{\mathbf{k}_1\mathbf{k}_2\mathbf{k}_3\mathbf{k}_4} \left(W_{\mathbf{k}_1\mathbf{k}_2,\mathbf{k}_3\mathbf{k}_4} b_{\mathbf{k}_1} b_{\mathbf{k}_2} b^*_{\mathbf{k}_3} b^*_{\mathbf{k}_4} + c.c.\right) \delta\left(\mathbf{k}_1 + \mathbf{k}_2 - \mathbf{k}_3 - \mathbf{k}_4\right) \\ &+ \sum_{\mathbf{k}_1\mathbf{k}_2\mathbf{k}_3\mathbf{k}_4} \left(G^*_{\mathbf{k}_1\mathbf{k}_2\mathbf{k}_3,\mathbf{k}_4} b_{\mathbf{k}_1} b_{\mathbf{k}_2} b_{\mathbf{k}_3} b^*_{\mathbf{k}_4} + c.c.\right) \delta\left(\mathbf{k}_1 + \mathbf{k}_2 + \mathbf{k}_3 - \mathbf{k}_4\right) \\ &+ \frac{1}{4} \sum_{\mathbf{k}_1\mathbf{k}_2\mathbf{k}_3\mathbf{k}_4} \left(R^*_{\mathbf{k}_1\mathbf{k}_2\mathbf{k}_3\mathbf{k}_4} b_{\mathbf{k}_1} b_{\mathbf{k}_2} b_{\mathbf{k}_3} b_{\mathbf{k}_4} + c.c.\right) \delta\left(\mathbf{k}_1 + \mathbf{k}_2 + \mathbf{k}_3 + \mathbf{k}_4\right)\end{aligned} \tag{8.48}$$

where the time dependencies have been abbreviated as $b_{\mathbf{k}_i} := b_{\mathbf{k}_i}(t)$, the abbreviation $c.c.$ stands for *complex conjugate* and the sequences of subscripts $\mathbf{k}_i$ in the coupling coefficients $U^*_{\mathbf{k}_1\mathbf{k}_2\mathbf{k}_3}$, $V^*_{\mathbf{k}_1\mathbf{k}_2,\mathbf{k}_3}$, $W_{\mathbf{k}_1\mathbf{k}_2,\mathbf{k}_3\mathbf{k}_4}$, $G^*_{\mathbf{k}_1\mathbf{k}_2\mathbf{k}_3,\mathbf{k}_4}$ and $R^*_{\mathbf{k}_1\mathbf{k}_2\mathbf{k}_3\mathbf{k}_4}$ are interchangeable within the groups split by the comma separator.

Multi-magnon interactions

[401]: Krivosik et al. (2010), 'Hamiltonian formulation of nonlinear spin-wave dynamics'

The precise form of the coupling coefficients can be looked up in [401]. For the qualitative introduction here, only the form of the respective terms in the third- and fourth-order Hamiltonian contributions $\mathcal{U}^{(3)}$ and $\mathcal{U}^{(4)}$ is of relevance:

- The $V_{\mathbf{k}_1\mathbf{k}_2,\mathbf{k}_3}$ and $V^*_{\mathbf{k}_1\mathbf{k}_2,\mathbf{k}_3}$ terms in equation 8.47 describe three magnon scattering processes which obey the momentum conservation $\mathbf{k}_1 + \mathbf{k}_2 = \mathbf{k}_3$ imposed by the Kronecker delta function. In the particle picture, this corresponds to a splitting of one magnon into two magnons, or to a confluence of two into one.
- Analogously, the $U_{\mathbf{k}_1\mathbf{k}_2\mathbf{k}_3}$ and $U^*_{\mathbf{k}_1\mathbf{k}_2\mathbf{k}_3}$ terms in equation 8.47 represent processes in which three magnons with $\mathbf{k}_1 + \mathbf{k}_2 + \mathbf{k}_3 = 0$ interact.
- In the fourth-order contribution $\mathcal{U}^{(4)}$, the terms with $W_{\mathbf{k}_1\mathbf{k}_2,\mathbf{k}_3\mathbf{k}_4}$ and $W^*_{\mathbf{k}_1\mathbf{k}_2,\mathbf{k}_3\mathbf{k}_4}$ correspond to scattering processes of two magnons $\mathbf{k}_1, \mathbf{k}_2$ into two other magnons $\mathbf{k}_3, \mathbf{k}_4$. These interactions are typically the governing four-magnon processes.

- Finally, the terms with $G_{\mathbf{k}_1\mathbf{k}_2\mathbf{k}_3,\mathbf{k}_4}$ and $G^*_{\mathbf{k}_1\mathbf{k}_2\mathbf{k}_3,\mathbf{k}_4}$ represent the splitting of one magnon into three or the confluence of three magnons into one, and the terms with $R_{\mathbf{k}_1\mathbf{k}_2\mathbf{k}_3\mathbf{k}_4}$ and $R^*_{\mathbf{k}_1\mathbf{k}_2\mathbf{k}_3\mathbf{k}_4}$ correspond to the interaction of four magnons analogous to the terms with $U_{\mathbf{k}_1\mathbf{k}_2\mathbf{k}_3}$ and $U^*_{\mathbf{k}_1\mathbf{k}_2\mathbf{k}_3}$. These four-magnon processes are typically negligible[49].

49: Negligible, because the products of the corresponding complex spin wave amplitudes $b_\mathbf{k}$ lead to high-frequency variations in $\exp(2i\omega t)$, while the nonlinear spin wave dynamics are typically described by the low-frequency envelope functions of the system [401].

The additional requirement to obey the energy conservation yields parameter ranges, in which only the three-magnon processes are forbidden, while there is no exclusion range for the four-magnon interaction with $\omega_1 + \omega_2 = \omega_3 + \omega_4$. As was discussed above in subsection 8.2.1, this is the case for the fields applied in the investigations presented in chapter 10.

In literature, the processes are often denoted as *resonant* or *nonresonant* referring to the possibility of fulfilling energy and momentum conservation, or not.

Virtual magnon states or cascaded processes

Although the energy conservation excludes the three-magnon processes in some cases, these situations do not allow for a simple assumption of $\mathcal{U}^{(3)} \approx 0$ since the nonresonant three-magnon interactions can lead to a significant four-magnon scattering contribution. An intuitive picture is given by the idea of a *virtual magnon state*: Pairs of (nonresonant) three-magnon processes can yield an effective four magnon process, i.e. a confluence process of two magnons into a virtual magnon, accompanied by a splitting process of the virtual magnon into two other magnons. These combinations of two three-magnon processes are sometimes also referred to as *cascaded processes* [422].

[422]: Livesey et al. (2007), 'Parametric spin wave excitation and cascaded processes during switching in thin films'

To account for[50] these interactions in the description of the four-magnon terms, it is required to transform the system to yet another set of canonical variables, i.e. $b_\mathbf{k}(t), b^*_\mathbf{k}(t) \longrightarrow c_\mathbf{k}(t), c^*_\mathbf{k}(t)$, which still diagonalise the linear response in $\mathcal{U}^{(2)} = \sum_\mathbf{k} \omega_\mathbf{k} c^*_\mathbf{k}(t) c_\mathbf{k}(t)$. These then allow to incorporate pairs of three-magnon processes into the fourth order Hamiltonian contribution

$$\begin{aligned}\mathcal{U}^{(4)} = \frac{1}{2} \sum_{\mathbf{k}_1\mathbf{k}_2\mathbf{k}_3\mathbf{k}_4} \left(\widetilde{W}_{\mathbf{k}_1\mathbf{k}_2,\mathbf{k}_3\mathbf{k}_4} c_{\mathbf{k}_1} c_{\mathbf{k}_2} c^*_{\mathbf{k}_3} c^*_{\mathbf{k}_4} + c.c.\right) \delta(\mathbf{k}_1 + \mathbf{k}_2 - \mathbf{k}_3 - \mathbf{k}_4) \\ + \mathcal{O}\left(G_{\mathbf{k}_1\mathbf{k}_2\mathbf{k}_3,\mathbf{k}_4} + R_{\mathbf{k}_1\mathbf{k}_2\mathbf{k}_3\mathbf{k}_4} + c.c.\right)\end{aligned} \tag{8.49}$$

50: In [401, 418], this step is referred to as an "elimination" of the nonresonant three-magnon terms.
[401]: Krivosik et al. (2010), 'Hamiltonian formulation of nonlinear spin-wave dynamics'
[418]: Verba et al. (2019), 'Hamiltonian formalism for nonlinear spin wave dynamics under antisymmetric interactions'

where the new coupling coefficient for symmetric[51] four-magnon processes

$$\widetilde{W}_{\mathbf{k}_1\mathbf{k}_2,\mathbf{k}_3\mathbf{k}_4} = W_{\mathbf{k}_1\mathbf{k}_2,\mathbf{k}_3\mathbf{k}_4} + T_{\mathbf{k}_1\mathbf{k}_2,\mathbf{k}_3\mathbf{k}_4} \tag{8.50}$$

51: Symmetric in terms of spin waves created / destroyed, i.e. $(\mathbf{k}_1\mathbf{k}_2) \longrightarrow (\mathbf{k}_3\mathbf{k}_4)$.

basically adds a three-magnon correction $T_{\mathbf{k}_1\mathbf{k}_2,\mathbf{k}_3\mathbf{k}_4}$ to the original four-magnon coupling coefficients $W_{\mathbf{k}_1\mathbf{k}_2,\mathbf{k}_3\mathbf{k}_4}$. The three-magnon correction $T_{\mathbf{k}_1\mathbf{k}_2,\mathbf{k}_3\mathbf{k}_4}$ consists of six different additions corresponding to combinations of $V^*_{\mathbf{k}_1\mathbf{k}_2,\mathbf{k}_3} \cdot V_{\mathbf{k}_1\mathbf{k}_2,\mathbf{k}_3}$ and $U^*_{\mathbf{k}_1\mathbf{k}_2\mathbf{k}_3} \cdot U_{\mathbf{k}_1\mathbf{k}_2\mathbf{k}_3}$ for all possible configurations and, like for the other coupling coefficients, the precise expressions can be looked up in [401].

[401]: Krivosik et al. (2010), 'Hamiltonian formulation of nonlinear spin-wave dynamics'

While the precise expressions of the coupling coefficients are irrelevant at this point, it is important to note that any energy transfer represented by scattering processes which do not conserve the number of magnons, must be mediated by the dipolar interaction. Hence, the three-magnon coupling coefficients, and consequently the three-magnon correction coefficients $T_{\mathbf{k}_1\mathbf{k}_2,\mathbf{k}_3\mathbf{k}_4}$ must be proportional to the saturation magnetisation M_S and therefore a significant contribution can be expected for Co_2MnSi with $M_S \approx 1000\,\mathrm{kA/m}$ [86, 401].

[86]: Pirro et al. (2014), 'Non-Gilbert-damping Mechanism in a Ferromagnetic Heusler Compound Probed by Nonlinear Spin Dynamics'
[401]: Krivosik et al. (2010), 'Hamiltonian formulation of nonlinear spin-wave dynamics'

Suhl instabilities and threshold behaviour

The terms corresponding to the *first order Suhl instability* introduced in subsection 8.2.1, can thus be clearly identified as the processes with coupling coefficients $V^*_{\mathbf{k}_1\mathbf{k}_2,\mathbf{k}_3}$. The *second order Suhl instability*, however, is described by the $\widetilde{W}_{\mathbf{k}_1\mathbf{k}_2,\mathbf{k}_3\mathbf{k}_4}$, and hence can include contributions from the four-magnon processes described by the initial terms with $W^*_{\mathbf{k}_1\mathbf{k}_2,\mathbf{k}_3\mathbf{k}_4}$ and $W_{\mathbf{k}_1\mathbf{k}_2,\mathbf{k}_3\mathbf{k}_4}$, as well as contributions from the three-magnon correction $T_{\mathbf{k}_1\mathbf{k}_2,\mathbf{k}_3\mathbf{k}_4}$.

[225]: Gurevich et al. (1996), *Magnetization oscillations and waves*
[288]: Suhl (1957), 'The theory of ferromagnetic resonance at high signal powers'

The Suhl instabilities are threshold processes [225, 288] and a significant population of the secondary spin wave modes $c_{\mathbf{k}_1}$ and $c_{\mathbf{k}_2}$ can be observed only when the primary spin wave amplitude $c_{\mathbf{k}_0}$ exceeds a critical amplitude

$$c^{\text{krit,1st}}_{\mathbf{k}_0} = \frac{\sqrt{\eta_1\eta_2}}{2|V_{\mathbf{k}_0,\mathbf{k}_1\mathbf{k}_2}|} \quad \text{or} \quad c^{\text{krit,2nd}}_{\mathbf{k}_0} = \sqrt{\frac{\sqrt{\eta_1\eta_2}}{|\widetilde{W}_{\mathbf{k}_0\mathbf{k}_0,\mathbf{k}_1\mathbf{k}_2}|}} \tag{8.51}$$

[401]: Krivosik et al. (2010), 'Hamiltonian formulation of nonlinear spin-wave dynamics'

for the first and second order Suhl instability respectively, as derived in [401]. The η_i are the relaxation coefficients of the secondary spin wave modes, and hence a significant population of these modes above the thermal excitation is only achieved when the transfer into the secondary modes exceeds the dissipation due to their damping [97].

[97]: Pirro (2014), 'Lineare und nichtlineare Spinwelleninteraktionen in magnetischen Mikrostrukturen'

The naming as *instabilities* refers to their instable nature: Once the spin wave amplitudes $c_{\mathbf{k}_1}$ and $c_{\mathbf{k}_2}$ of the secondary modes are significant, the processes self-enhance since the nonlinear coupling terms in the corresponding Hamiltonian contributions contain product terms of the spin wave amplitudes of all scattering partners. Thus, the energy transfer is negligible as long as both secondary modes are hardly populated, but increases exponentially once the critical threshold is surpassed. Yet, these modes can be subject to nonlinear scattering as well, and for large secondary spin wave amplitudes the decay into tertiary modes can result in a limitation to the rise of $c_{\mathbf{k}_1}$ and $c_{\mathbf{k}_2}$.

Self-induced nonlinear frequency shift

[401]: Krivosik et al. (2010), 'Hamiltonian formulation of nonlinear spin-wave dynamics'

The self-induced nonlinear frequency shift observed for instance in the FMR experiments at high signal amplitudes is equally described by the coupling coefficients $\widetilde{W}_{\mathbf{k}_1\mathbf{k}_2,\mathbf{k}_3\mathbf{k}_4}$ as can be derived in the Hamiltonian formalism [401]: Setting all $\mathbf{k}$ equal, the self-interaction Hamiltonian is obtained and given by

$$\mathcal{U}_{\text{self}} \approx \sum_{\mathbf{k}} \omega_{\mathbf{k}} c^*_{\mathbf{k}}(t)\, c_{\mathbf{k}}(t) + \frac{1}{2}\sum_{\mathbf{k}} \left(\widetilde{W}_{\mathbf{k}\mathbf{k},\mathbf{k}\mathbf{k}} c_{\mathbf{k}} c_{\mathbf{k}} c^*_{\mathbf{k}} c^*_{\mathbf{k}}\right) \tag{8.52}$$

where the static contribution $\mathcal{U}^{(0)}$ representing the ground state, and the pumping term $\mathcal{U}^{(1)}$ describing the direct excitation are omitted since they cannot contribute to the nonlinear response of the system. The Hamiltonian equations 8.44 then yield the equation of motion

$$i\frac{dc_{\mathbf{k}}(t)}{dt} = \frac{\partial \mathcal{U}}{\partial c^*_{\mathbf{k}}(t)} \approx \left(\omega_{\mathbf{k}} + \widetilde{W}_{\mathbf{k}\mathbf{k},\mathbf{k}\mathbf{k}}|c_{\mathbf{k}}(t)|^2\right)\cdot c_{\mathbf{k}}(t) \tag{8.53}$$

for a spin wave mode with complext amplitude $c_{\mathbf{k}}(t)$. Hence, a harmonic oscillation with nonlinear frequency

$$\widetilde{\omega}_{\mathbf{k}} = \omega_{\mathbf{k}} + \widetilde{W}_{\mathbf{k}\mathbf{k},\mathbf{k}\mathbf{k}}|c_{\mathbf{k}}(t)|^2 \tag{8.54}$$

is obtained, describing the nonlinear frequency shift as was introduced in subsection 8.2.2.

The nonlinear frequency shift clearly does not present any criticality or threshold behaviour, but given equation 8.54 simply scales proportionally to the intensity $|c_{\mathbf{k}}(t)|^2$ of the spin wave under investigation.

8.3 Concluding remarks

This chapter has introduced some fundamental concepts of linear and nonlinear magnetisation dynamics with a focus on the topics of relevance for the subsequent chapters.

Section 8.1 of this chapter was focused on the concepts of linear spin waves. Here, the approximative Kalinikos-Slavin dispersion relation for in-plane magnetised anisotropic thin films was briefly introduced and the incorporation of the anisotropy terms was discussed in detail. The section resulted in some major conclusions for the subsequent analysis:

- For a Co_2MnSi film in a sample geometry corresponding to the case studied in chapter 10, the cubic anisotropy with constants taken from the FMR characterisation in chapter 6 was shown to yield a frequency shift on the dispersion relation, which generally decreases for increasing wavevector k_{ip}.
- The anisotropy induced frequency shift was found to be of significance for the Damon-Eshbach geometry only for very small wavevectors $k_{\mathrm{ip}} \lesssim 2\,\mathrm{rad}/\mu\mathrm{m}$, above which the change is $\lesssim 5\%$.
- The most important impact of the cubic anisotropy was found on the Backward-Volume geometry, and for $k_{\mathrm{ip}} \lesssim 30\,\mathrm{rad}/\mu\mathrm{m}$ the cubic anisotropy it not only yields frequency shifts by $\gtrsim 5\%$, but also a related drop of the group velocity by $\gtrsim 10\%$, as well as a consequent shift of the band bottom minimum to larger k_{ip}.

As a consequence, the consideration of the pure first order cubic anisotropy (and negligence of a second order contribution) is assumed to be a valid approximation for the Damon-Eshbach dispersion. Yet, it is noted that caution needs to be employed for quantitative analyses, particularly of the nonlinear effects potentially involving scattering partners with other propagation directions.

Section 8.2 of this chapter gave an overview of the relevant concepts of nonlinear spin wave dynamics. First, mutli-magnon scattering processes were introduced as a form of nonlinear energy conversion within the magnetic system, of which the first and second order Suhl instabilities form a special case concerning the energy conversion from a directly pumped mode into secondary spin wave modes. Furthermore, the phenomenon of the nonlinear frequency shift was introduced, which can result in a shift of the dispersion relation depending on the self-interaction coefficients $\widetilde{W}_{\mathbf{kk},\mathbf{kk}}$ and the amplitude of the spin waves. These coefficients can be derived within the Hamiltonian formalism for nonlinear spin wave dynamics, the concepts of which were introduced in the third subsection.

- For a Co_2MnSi film in a sample geometry corresponding to the case studied in chapter 10, the anisotropy-induced shift of the dispersion relation was found to result in threshold frequencies of 8.7 GHz and 12.8 GHz which need to be exceeded for the occurrence of the first order Suhl instability at external fields of 10 mT and 30 mT, respectively.

- Even though the first order Suhl instability is nonresonant for the investigated fields, the cascade of two nonresonant three-magnon processes via a virtual magnon state results in an effective four-magnon process, and thus three-magnon interactions need to be accounted for in the description of four-magnon scattering terms. The three-magnon correction is expected to be significant due to the large saturation magnetisation of the Heusler compound Co_2MnSi.
- The Suhl instabilities are threshold processes, which self-enhance above a critical primary spin wave amplitude leading to an expected exponential rise in the secondary spin wave amplitudes.
- The self-induced nonlinear frequency shift is not a threshold process, and is expected to scale proportionally to the spin wave amplitude.

These implications are important for the study of spin waves in anisotropic, micro-sized, half-metallic Co_2MnSi waveguides, and will be central to the discussion presented in chapter 10.

Methods: Probing spin wave dynamics in half-metallic microstructures

9

In this third part of the work, linear and nonlinear spin wave dynamics were investigated in a half-metallic Co_2MnSi waveguide, the underlying theoretical concepts of which were described in the previous chapter. In this methodological chapter, the sample geometry and the experimental methods will be introduced: The investigated waveguide is part of a spin wave Doppler shift device [43, 91] fabricated from a Co_2MnSi thin film, as will be detailed in section 9.1. The spin wave dynamics were probed by microfocused Brillouin light scattering μBLS, a powerful magneto-optical technique which is based on the same principle as the conventional BLS technique introduced in chapter 5 as will be described in the subsequent section 9.2.

9.1 Sample specifications . . 171
Stack and structure 171
Device geometry 173
9.2 Microfocused Brillouin light scattering (μBLS) . . 175
Time-resolution 176

9.1 Sample specifications and device geometry

The investigated spin wave Doppler shift device is result of a collaboration with the *Institut de physique et chimie des matériaux de Strasbourg (IPCMS)* in Strasbourg, France, in the framework of the *ANR MARIN (ANR-20-CE24-0012)* project. In this frame, a thin film sample was fabricated and characterised at the IJL in Nancy, France, in the course of the present thesis. The patterning of the microsized devices was then carried out by José Solano in the framework of his PhD thesis at the IPCMS in Strasbourg, France [91].

9.1.1 Thin film stack and structural properties

The thin film stack was grown on a $30 \times 30\,mm^2$ large, single-side polished MgO (001) substrate of 500 μm thickness. After outgassing the substrate at a temperature of $T_{pyro} \approx 730°C$[1], a 10 nm thick buffer layer was deposited at the same temperature in order to cover contaminations and smoothen the substrate surface. Next, the 20 nm thick Co_2MnSi film was deposited at a temperature of $T_{pyro} \approx 365°C$ and subsequently annealed at $T_{pyro} \approx 630°C$. After cool-down, the capping bi-layer was deposited at ambient temperature, consisting of a 8.5 nm thick MgO layer, followed by a 4.5 nm thick Ti layer. This specific sample stack with the MgO/Ti capping bi-layer was chosen in order to provide a Co_2MnSi thin film with maximal similarity of top and bottom interfaces for the spin wave Doppler shift experiments in [91]. A schematic illustration of the final sample stack is shown in figure 9.1.

Details on the general growth method and the protocol followed for every sample in this thesis are specified in chapter 2. The growth of the specific sample in this study differed to the general procedure in this thesis in only two points:

1. At the time of the growth of this sample, Ti was not available in the MBE system described in section 2.1.1 in which all samples in this thesis were grown. The sample was therefore transferred into a different MBE system for the deposit of the final capping layer, the *MBE Oxydes*. This setup is equally attached to the aforementioned TUBE facility, i.e. connected to the principal MBE setup in this work by an ultrahigh vacuum chamber allowing for a direct sample transfer.

[43]: Vlaminck et al. (2008), 'Current-Induced Spin-Wave Doppler Shift'
[91]: Solano Córdova (2024), 'Temperature dependent spin wave study of magnetic properties and spin-polarized electron transport in $Fe_{1-X}V_X$ and Co_2MnSi epitaxial films'

[91]: Solano Córdova (2024), 'Temperature dependent spin wave study of magnetic properties and spin-polarized electron transport in $Fe_{1-X}V_X$ and Co_2MnSi epitaxial films'

1: The indicated temperatures were measured with a pyrometer, which was set to an arbitrary emissivity of 0.85 for the entire process.

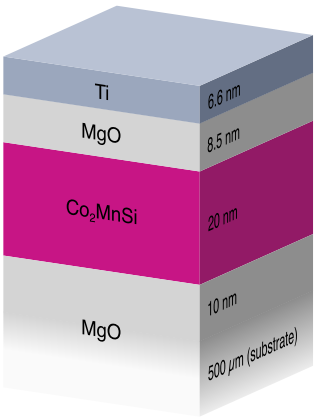

Figure 9.1: Schematic of the thin film stack fabricated for the patterning of the Doppler shift device structures. Note that the indicated thickness of the Ti layer is larger than the deposited thickness: While 4.5 nm nominated thickness were deposited, later HRTEM experiments revealed an inflation of approximately half of the Ti layer due to oxidation, yielding a total thickness of 6.6 nm as indicated in this illustration.

2. As this was the first sample fabricated with such a bi-layer capping, the proper coverage of the bi-layer stack was briefly verified with two Auger measurements performed in-situ: a first one prior to the deposit of the capping bi-layer, and a second one directly after the completion of the entire stack. The setup used for these characterisation measurements is equally attached to the TUBE facility. The spectral peaks related to Co, Mn and Si vanished after the deposited capping bi-layer, confirming a decent coverage[2].

2: See figure 2.10 on page 27 and the related discussion.

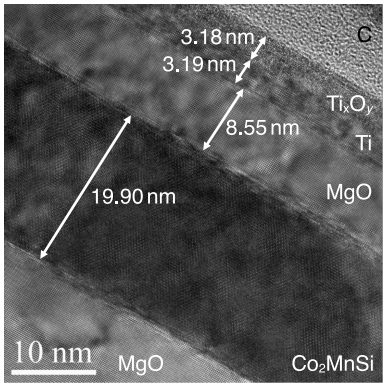

Figure 9.2: HRTEM micrograph of a cross section of the thin film sample. The altered structure in the top part of the Ti layer is linked to the partial oxidation of the Ti film. Details about the sample growth and capping layer are given in chapters 2 and 3.

Summary of structural properties

A FIB-cut cross section of the sample was extensively investigated in TEM as detailed in chapter 3. An exemplary HRTEM micrograph is shown in figure 9.2 and at this point only a summary of the specific observations that are of relevance for the further investigation of spin waves in the microstructured waveguide is given:

- **Partial oxidation of the capping layer:** The Ti capping layer was found to be partly oxidised, leading to a greater total thickness than intended, i.e. ~ 6.6 nm as opposed to the deposited 4.5 nm. HRTEM micrographs revealed a consistent separation of the partly oxidised Ti layer into two sub-layers, i.e. a Ti/TiO_x bilayer, with approximately the same thickness of ~ 3.2 nm each. The complete coverage as concluded by in-situ Auger spectroscopy was confirmed by the observation of a homogeneous thin film stack in HRTEM/STEM, see figure 3.13 on page 43 and the follwowing discussion.
- **Structural defects along the interfaces:** No structural defects were observed in the volume of the thin film, but atomic plane dislocations were found along the bottom interface as well as the top interface. These dislocations are linked to the slight lattice mismatch between the two materials and the associated deformation was found to relax towards the center of the film. Less dislocations were found along the top interface, which was linked to a lattice adaptation in the top MgO layer.
- **Predominant $L2_1$ ordering:** The intensity patterns from HAADF-STEM measurements revealed a predominant $L2_1$ ordering, but irregular appearances of domains with an intensity pattern linked to B2 disorder were detected. These B2-like[3] domains were found to be mostly located in proximity of the bottom interface with the MgO buffer layer.

Implications: Firstly, the partial oxidation of the Ti layer could hint towards an instability of the capping upon exposure to air or oxygen-rich environments. The samples were therefore stored in dissicators when not used for experiments. However, unchanged properties were obtained even roughly two years after growth, leading to the conclusion that the partial oxidation might as well have passivised the capping. Secondly, the unequal distribution of dislocations at the interfaces and the additional appearance of potential B2 disorder also mostly located towards the bottom interface imply the expectation of a higher contribution of defect-induced scattering at the bottom interface compared to the the top interface. Hence, not only the aforementioned[4] enhanced non-reciprocity of the surface spin waves upon field inversion is to be expected, but also a non-uniformity of the damping parameter cannot be excluded when investigating the propagating spin waves.

3: Note that while the appearance of the $L2_1$ intensity pattern is unambiguous in the HAADF-STEM experiments along the $[110]_{Co_2MnSi}$ axis, the appearance of the B2 intensity pattern is not as clearly interpretable: It can indeed be linked to a B2 disorder in the investigated region of the cross section (full randomisation of the Mn and Si sublattices). Yet, such an intensity pattern can equally appear when the Mn/Si columns are for instance exactly separated into two parts along the transmission direction. This would not correspond to a full randomisation but rather to an appearance of $L2_1$ order shifted by half a lattice cell in the middle of the cross section, e.g. along one atomic plane. The latter case could effectively be imagined as two $L2_1$-ordered domains, which are "phase shifted" by π and aligned "behind each other" in the transmission direction of the electron beam, resulting in the same intensity pattern as the B2 structure. Given the atomic plane dislocations due to the lattice mismatch as well as the confirmed 100 % spin polarisation in the waveguide, this second interpretation is not very unrealistic in the present study.

4: See the final discussion of the dislocation analysis in subsection 3.2.2 on page 43.

9.1.2 Spin wave Doppler shift device

As mentioned above, the microfabrication into spin wave Doppler shift devices was carried out by José Solano at the IPCMS in Strasbourg, France. The spin wave Doppler shift devices essentially consist of a microsized Co_2MnSi waveguide with two microwave antennas patterned on top, which are isolated from the waveguide by a sputtered SiO_2 layer. Additionally, four electrical contacts are etched approximately half-way through the Co_2MnSi layer and are located towards the ends of the waveguide. These are not used in the present study, but principally allow for an injection of a current into the waveguide.

Details of the sophisticated fabrication process are given in [91] and are shortly recalled here with the steps directly attacking the Co_2MnSi highlighted in bold:

1. Step: **Laser lithography for a patterning of the film into waveguides.**
   - First, the lithography is carried out in order to cover selected areas Co_2MnSi film by a protective resist mask, outlining the (future) waveguides.
   - Next, an **Ar^+ ion beam etching (IBE)** process is used in order to remove the Co_2MnSi outside of the designated waveguides.
2. Step: Sputtering of a SiO_2 insulation layer for electrical insulation.
3. Step: Laser lithography for a localised removal of the SiO_2 at the contact points for DC contacts[5].
4. Step: **Laser lithography for the patterning of the DC contacts.**
   - The protective resist mask this time exposes only the area of the intended DC contacts and covers the rest of the structure.
   - Again, an **Ar^+ ion beam etching (IBE)** process is used for etching into the waveguide where the SiO_2 was already removed[6], i.e. etching through the capping layers as well as **"roughly [through] half the ferromagnetic [layer]"** [91].
   - A Ti/Au bilayer is then deposited by e^--beam evaporation and followed by a lift-off step.
5. Step: Electron lithography for a patterning of the Ti/Au microwave antennas.

Hence, in the course of this sophisticated device fabrication procedure only the two ion beam etching (IBE) steps involved a direct attack on the Co_2MnSi. The effects of IBE on the crystal structure of $L2_1$-ordered Co_2MnSi thin films was investigated in a structural study in this thesis and is presented in chapter 3.3: The structural properties of the Co_2MnSi were found to be hardly influenced by the IBE process, and in particular a persistent $L2_1$ order was found even within the edges of the waveguide structures with maximal exposure to the ion milling. It is therefore assumed here that the spin wave Doppler shift device fabrication does not deteriorate the properties of the Co_2MnSi in this study.

The structured microwave antennas present a resistance of $R = 65\,\Omega \pm 0.1\,\Omega$ [91] and consist of meanders of coplanar waveguides designed for a specific excitation spectrum, which presents an excitation maximum at $k_1 = 3.9\,\mathrm{rad}/\mu\mathrm{m}$ and at $k_2 = 1.6\,\mathrm{rad}/\mu\mathrm{m}$ as shown in figure 9.3 [91].

An illustration of the final structure is shown in figure 9.4, with the relevant geometry details given in the top-view in figure 9.4 (a) and the final stack details illustrated in the cross-section view in figure 9.4 (b). As cited above, the intention in the fabrication procedure is to etch the DC contacts approximately half into the Co_2MnSi layer, and given the aforementioned resistance of the structural properties to the IBE process, a spin wave propagation could be

[91]: Solano Córdova (2024), 'Temperature dependent spin wave study of magnetic properties and spin-polarized electron transport in $Fe_{1-X}V_X$ and Co_2MnSi epitaxial films'

5: This step is done to "unbury" the Co_2MnSi/MgO/Ti stack at the desired locations for the DC contact points, and involves a reactive ion etching (RIE) step for a targeted localised etching process of the SiO_2. As the Co_2MnSi is still protected by the MgO/Ti capping, and since the waveguide will anyway be etched at these DC contact positions in the next step, it is assumed here that this RIE step does not have any impact on the dynamics in the Co_2MnSi.

6: To be precise, this step also etches the SiO_2 covering the bare substrate in the defined area where the contacts will be deposited.

[91]: Solano Córdova (2024), 'Temperature dependent spin wave study of magnetic properties and spin-polarized electron transport in $Fe_{1-X}V_X$ and Co_2MnSi epitaxial films'

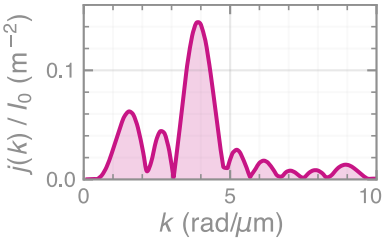

Figure 9.3: Antenna excitation efficiency presenting two maxima at $k_1 = 3.9\,\mathrm{rad}/\mu\mathrm{m}$ and at $k_2 = 1.6\,\mathrm{rad}/\mu\mathrm{m}$ as defined by the Fourier transform of the current density corresponding to the CPW antennas in the investigated device. Calculation by J. Solano "assuming a uniform current density in the strands of the antennas" [91]. Figure adapted from [91].

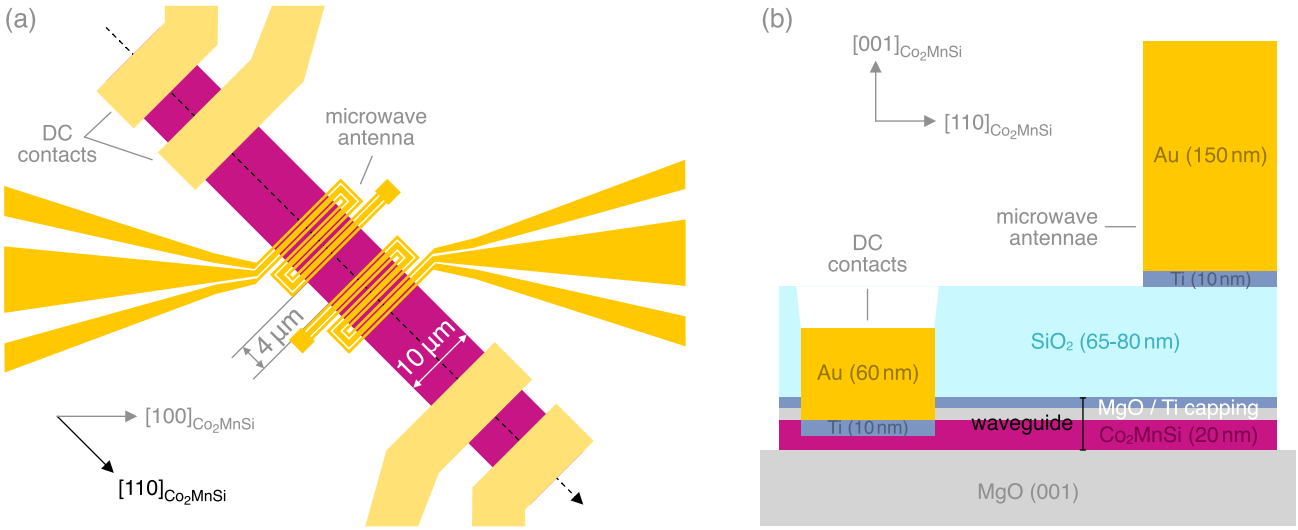

Figure 9.4: Illustration of the device geometry: (a) top view of the device consisting of a wave guide, four DC contacts and two patterned CPW antennas and (b) schematic cross section of the final stack (not to lateral scale). Schematic in (a) based on a lithography design by J. Solano [91].

[91]: Solano Córdova (2024), 'Temperature dependent spin wave study of magnetic properties and spin-polarized electron transport in $Fe_{1-x}V_x$ and Co_2MnSi epitaxial films'

Table 9.1: Relevant characterisation results of the sample studied in chapter 10, taken from tables 4.1 (= 4.2), 4.4 and 4.6 in [91]. $\mu_0 M_{\text{eff}}^{\text{IP}}$ and $\mu_0 M_{\text{eff}}^{\text{OOP}}$ from an internal communication.

VSM		
$\mu_0 M_S$	1.33 ± 0.02	T
	1058 ± 16	kA/m
FMR		
$\mu_0 M_{\text{eff}}^{\text{IP}}$	1.23 ± 0.02	T
	979 ± 16	kA/m
$\mu_0 M_{\text{eff}}^{\text{OOP}}$	1.26 ± 0.02	T
	1003 ± 16	kA/m
$\mu_0 M_{\text{eff}}$	1.25 ± 0.02	T
	995 ± 16	kA/m
K_{c1}	-5.4 ± 0.2	kJ/m^3
$K_{s,\text{total}}$	0.48 ± 0.04	kJ/m^2
A_{exch}	19.7 ± 0.5	pJ/m
γ	28.54 ± 0.1	GHz/T
α_{IP}	1.2 ± 0.1	$\times 10^{-3}$
α_{OOP}	1.0 ± 0.1	$\times 10^{-3}$
PSWS		
$K_{s,\text{top}}$	0.24 ± 0.04	kJ/m^2
$K_{s,\text{bottom}}$	0.24 ± 0.04	kJ/m^2

expected even behind the DC contacts. Yet, test measurements carried out in the course of the µBLS study in this thesis could not detect any spin wave signal behind the DC contacts. The entire study presented in chapter 10 is therefore carried out between one contacted microwave-antenna and the closest DC contact.

The sample was thoroughly characterised by J. Solano for the study in [91] by (SQUID) VSM, FMR and propagating spin wave spectroscopy (PSWS) characterisation measurements and the relevant parameters of this sample are summarised in table 9.1. The broadband FMR measurements were performed on a thin film piece in two field configurations: One measurement with the external field applied perpendicular to the film plane, i.e. along the [001] direction, and one with the field applied in the film plane along an easy-like (medium) axis, i.e. along a [110] direction. Only a first-order cubic anisotropy constant was determined and no second-order cubic anisotropy was considered. Additionally, the surface anisotropy $K_{s,\text{total}}$ arising from top and bottom interface with MgO was determined, for which equal contributions were obtained from the two interfaces ($K_{s,\text{top}}$ and $K_{s,\text{bottom}}$ respectively).

It is important to note that a determination of the second-order cubic anisotropy is hardly possible from an FMR analysis in consideration of only two field directions as in [91] ([110] and [001]), especially when accounting for an additional uniaxial perpendicular magnetic anisotropy (PMA): As is clear from the considerations and anisotropy tensors derived in section 8.1.4 (see especially equation 8.16), the second order uniaxial anisotropy only gives a contribution to the out-of-plane component of the dynamic magnetisation for a field alignment along the [110] crystal direction, whereas it does not give any contribution for a field applied along the [001] direction. Hence, the qualitative contribution when regarding these two selected directions is similar to the effect of a PMA with $K_{u,\text{perp}}$, as was instead considered in [91] to account for the difference between M_{eff} from the FMR measurements and M_S from the VSM measurements resulting in $K_{u,\text{perp}} = 3 \pm 17\,\text{kJ/m}^3$.

Consequently, while the characterisation from the thorough FMR analysis in [91] was taken as a reference for the analysis in chapter 10, a potential second-order cubic anisotropy contribution cannot be excluded and was therefore considered as a second case in addition to the constants summarised in table in 9.1 for the analysis presented in chapter 10.

9.2 Microfocused Brillouin light scattering (μBLS)

The spin wave dynamics in the sample were probed by microfocused Brillouin light scattering (μBLS) spectroscopy, a detailed description of which is given in [366]. The underlying principle is exactly the same as introduced in section 5.4 for the conventional Brillouin light scattering: The inelastic scattering of light from spin waves causes a frequency shift, which is measured by a high-resolution multi-pass tandem Fabry-Pérot interferometer (TFPI).

[366]: Sebastian et al. (2015), 'Microfocused Brillouin light scattering'

The fundamental difference between the two techniques is the use of a microscope objective[7] focusing the probing laser beam onto the sample. This adaptation results in three important implications:

7: The microscope objective used in this study is a Zeiss 100× HD-DIC, with a numerical aperture of $NA = 0.75$ and a working distance of 4 mm [366].

1. The focus yields a spatial resolution of a few hundred nm [366], allowing for the desired space-resolved investigation of the spin waves in the microsized waveguide.
2. The maximal detectable wave vector is defined by the numerical aperture of the microscope [366, 369] entering equation 5.30 from page 110, i.e.

$$k_{\mathrm{ip,max}} = \frac{4\pi \sin \varphi_{\mathrm{max}}}{\lambda} \quad \text{with} \quad \varphi_{\mathrm{max}} = \arcsin\left(\frac{NA}{\widetilde{n}}\right) \tag{9.1}$$

   with the numerical aperture NA of the microscope objective and the refractive index $\widetilde{n}$ of the surrounding medium. For this study with $\lambda = 491\,\mathrm{nm}$, $NA = 0.75$ and $\widetilde{n} \approx 1$ (air), the maximal detectable wave vector is $k_{\mathrm{ip,max}} \approx 19\,\mathrm{rad/\mu m}$.
3. And, in relation to the previous point, the focus-cone from the microscope objective clearly results in a loss of the wave vector resolution, as spin waves of all wave vectors $0 < k_{\mathrm{ip}} \leq k_{\mathrm{ip,max}}$ are probed simultaneously.

[366]: Sebastian et al. (2015), 'Microfocused Brillouin light scattering'
[369]: Heinz (2021), 'Nano-scaled yttrium iron garnet conduits for magnonic networks'

A schematic illustration of the (optical part of the) μBLS setup is shown in figure 9.5. The setup consists of two main beam paths: A probing beam path using the laser beam for the measurement of the spin wave dynamics, and an illuminating beam path for the microscope image. The sample is placed on a motorised xyz-stage, which is coupled to a software stabilising the xy-positioning based on unique features in the microscope image. Additionally, part of the reflected beam is coupled into a photodiode, allowing for an autofocus routine to control the z-positioning. For the measurement, the reference beam for the TFPI is decoupled at the beginning of the optical beam path, and together with the sample beam guided into the interferometer, a schematic of which is shown in figure 5.17 on page 109.

The sample stage is centred in an external magnetic field, provided by an electromagnet (not shown in above figure). Additionally, an external microwave-source is connected to a pico-probe fixed on the sample stage, which allows to contact one of the CPW antennas for the spin wave excitation in the waveguide.

The automation software *thaTEC:OS*[8] was used to control the microwave circuit, the data acquisition via the TFPI, the sample stabilisation coupled to the microscope image, as well as the autofocus routine.

8: Software by *THATec Innovation GmbH*.

At this point it shall be noted that magneto-optical signal anisotropies as were central to chapter 7 and particularly detected on the Co_2MnSi films[9] are assumed to be negligible in μBLS experiments, where the aforementioned focus-cone of the microscope objective yields an illumination of the sample (and probing of the reflected signal) from all directions simultaneously.

9: See the discussion from page 137.

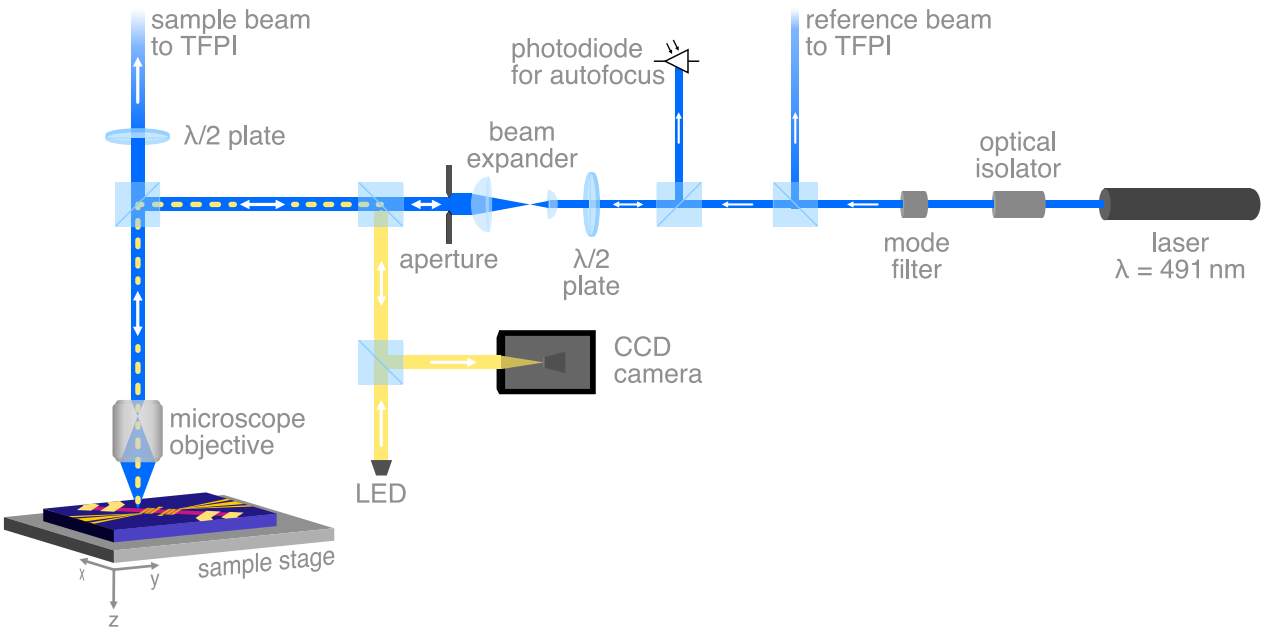

Figure 9.5: Schematic illustration of the μBLS setup, only showing the optical part. Image not to scale. The optical beam path corresponding to the probing laser beam is depicted in blue, the illuminating beam path for the microscope image is depicted in yellow and the overlap of the two is marked by the yellow dotted line superpositioned with the blue beam path. The laser beam passes multiple beam splitter: First, a reference beam is decoupled for the operation of the TFPI. The measurement is carried out in reflection and the reflected sample beam as well as the reference beam are coupled into the TFPI, a schematic illustration of which is shown in figure 5.17 on page 109. Part of the reflected probing beam is split and guided into a photodiode allowing for an autofocus routine during the measurement, which controls the z-positioning of the sample stage. Additionally, the illumination from a LED is coupled into the beam path and allows for a sample image on the CCD camera, which is used for the sample stabilisation in the xy-plane. Not shown: The sample stage is centred in an external magnetic field provided by an electro-magnet, and a CPW antenna on the sample is connected to an electrical microwave circuit to control the spin wave excitation. Figure based on corresponding illustrations in [100, 368].

[100]: Meyer (2017), 'Spin Orbit Torque Driven Spin Wave Dynamics in Microstructured Heusler Magnon Conduits'
[368]: Geilen (2022), 'Excitation of spin waves by magneto-elastic effects'

9.2.1 Time-resolved μBLS measurements

To study the temporal evolution of the spin wave intensities, the setup is adapted to perform measurements in a time-of-flight experiment [366, 369, 370]. To do so, a pulse generator and a switch are added into the microwave circuit and coupled to the data acquisition software. This additional adaptation of the setup enables a study of the temporal evolution of the spin wave intensities, and is used in this work for instance to determine the temporal onset of the nonlinear scattering into secondary spin wave modes, as will be discussed in chapter 10.

[366]: Sebastian et al. (2015), 'Micro-focused Brillouin light scattering'
[369]: Heinz (2021), 'Nano-scaled yttrium iron garnet conduits for magnonic networks'
[370]: Brächer (2015), 'Parallel parametric amplification of spin waves in microstructures'

Details on the time-resolved technique are equally given in [366]. Essentially, the time-delay between the excitation pulse and the intensity detected by the photodetector in the TFPI are recorded simultaneously and are correlated to the equally recorded mirror spacing of the TFPI, which defines the spin wave frequency corresponding to the signal. The measurements are thus carried out in a stroboscopic manner and it is averaged over multiple repetitions.

[366]: Sebastian et al. (2015), 'Micro-focused Brillouin light scattering'

It is important to note that the time resolution of the measurements is not simply given by the time resolution of the microwave circuit, but altered by the time-delay acquired due to the finite travel time of the photons within the TFPI. This travel time can reach up to several nanoseconds [370] and depends on the mirror reflectivity for the utilised laser wavelength, as well as the mirror spacing - thus the time resolution implies a trade-off with the frequency resolution. In result, sharp temporal features especially at very short time scales compared to the travel time of the photons in the TFPI can appear broadened, as is discussed in detail in [370].

[370]: Brächer (2015), 'Parallel parametric amplification of spin waves in microstructures'

Nonlinear spin waves in a microsized half-metallic Co_2MnSi waveguide

10

This chapter presents first investigations exploring the spin wave excitation and propagation in microstructured half-metallic Co_2MnSi waveguides. The study is the result of a collaboration with the *Institut de physique et chimie des matériaux de Strasbourg (IPCMS)* in Strasbourg, France, initiated in the framework of the *ANR MARIN (ANR-20-CE24-0012)* project.

Spin wave excitation spectra were investigated by micro-focused Brillouin light scattering spectroscopy (μBLS) in a microsized epitaxial Co_2MnSi waveguide of 10 μm width, structured from the sample S1.1 listed in table 2.1 on page 29. The device specifications are detailed in section 9.1 in the previous chapter. The exact same device had already been studied in the PhD work of José Solano [91], where notably the half-metallicity of Co_2MnSi is concluded to persist even in this microstructured device as was experimentally confirmed by spin wave Doppler shift experiments.

The magnetocrystalline anisotropy[1] analysis on comparable Co_2MnSi films has shown interesting symmetry effects as discussed in chapters 6 and 8. Therefore, particular attention is drawn to the device orientation used in this study: The propagation axis of the selected waveguide corresponds to the $[110]_{Co_2MnSi}$ direction, and the out-of-plane axis to $[001]_{Co_2MnSi}$ like in all samples in this thesis. All measurements for the study presented in this chapter 10 were carried out in the Damon-Eshbach geometry, i.e. $\mathbf{M}_0 \parallel \mathbf{H}_{ext} \perp \mathbf{k}_{ip}$. Given the cubic symmetry of the system with $K_{c1} < 0$ for Co_2MnSi, the propagation direction as well as the magnetisation direction correspond to an in-plane energy minimum of the magnetocrystalline anisotropy[2] which yields a few implications as detailed in chapter 8: For small magnetisation oscillations around this axis (as opposed to the highly symmetric $[100]_{Co_2MnSi}$ direction), the anisotropy energy presents only a partial rotation symmetry which results in an effect on the ellipticity of the precession, partially (but marginally for the constants here) counteracting the ellipticity induced by the demagnetisation energy. Moreover, the spin wave dispersion and correlated group velocities are affected by the anisotropy contribution, notably yielding a shift of the band bottom to higher frequencies and larger in-plane wavevectors, and consequently increasing the nonlinear Suhl instability thresholds.

These sample specifications are of major importance in this chapter 10 for two reasons: Firstly, an onset of nonlinear spin wave dynamics is observed at record-low microwave powers for a metallic magnonic device[3], as low as $P_{rf} = -11\,\mathrm{dBm} = 0.08\,\mathrm{mW}$ at the antenna excitation maximum, which is primarily related to the low damping and large magnetisation in the half-metallic Co_2MnSi waveguide. Secondly, even for rather small external fields of $\mu_0 H_{ext} \approx 9\,\mathrm{mT}$, no indications for a first order Suhl instability (a three magnon process) are detected but only signatures of second order Suhl instabilities are obtained, which is primarily linked to the anisotropy-induced upshift of the instability frequency thresholds with the increased band bottom frequencies.

This first explorative study is therefore dedicated particularly to the onset of nonlinear dynamics in the half-metallic Co_2MnSi device in view of a further exploitation for applications at the intersection of magnonics and spintronics. Throughout the evaluation, a comparison will be drawn to a similar study in [86, 97] on a non-epitaxial $Co_2Mn_{0.6}Fe_{0.4}Si$ waveguide of comparable parameters[4] but negligible anisotropy, equally in the Damon-Eshbach geometry.

10.1 Excitation spectra 178
Overview 178
Direct excitation 181
10.2 2nd order Suhl instability onset 183
Frequency dependency . 186
Power dependency 188
Time-resolved onset . . . 199
10.3 Conclusion 202

[91]: Solano Córdova (2024), 'Temperature dependent spin wave study of magnetic properties and spin-polarized electron transport in $Fe_{1-X}V_X$ and Co_2MnSi epitaxial films'

1: As noted on page 175, the magneto-optical anisotropy is disregarded in this μBLS study, reasoned by the focus-cone of the microscope objective yielding a fully rotational illumination (and probing).

2: Which depending on the second order cubic anisotropy contribution can be identified as either a medium or an easy axis (of the magnetocrystalline anisotropy energy) as indicated in table 4.1 on page 71: If $K_{c2} = 0$, as assumed in the characterisation in [91] the results of which are listed in table 9.1 on page 174, this in-plane minimum is a medium axis and the global minima of the cubic anisotropy energy are along the ⟨111⟩ directions. If $K_{c2} > 9/4 \cdot |K_{c1}|$, as is found on the other Co_2MnSi sample studied in chapter 6 the results of which are listed in table 6.9 on page 136, the in-plane minimum is a global minimum and corresponds to an easy axis of the energy landscape.

3: See the detailed discussion further in the chapter: It is noted that a direct comparison between studies on different setups and devices is limited due to the change in the absorption by the respective microwave circuits (notably the losses related to the impedance matching of the patterned antennas). Nevertheless, an onset at such low absolute microwave powers has not been observed in metallic structures in any study reported in literature to the best of my knowledge.

[86]: Pirro et al. (2014), 'Non-Gilbert-damping Mechanism in a Ferromagnetic Heusler Compound Probed by Nonlinear Spin Dynamics'
[97]: Pirro (2014), 'Lineare und nichtlineare Spinwelleninteraktionen in magnetischen Mikrostrukturen'

4: $M_S = 1003\,\mathrm{kA/m}$, $A_{exch} = 13\,\mathrm{pJ/m}$, $\alpha = 3 \times 10^{-3}$, $w = 5\,\mu\mathrm{m}$, $d = 30\,\mathrm{nm}$

10.1 Spin wave excitation spectra

Spin waves were excited in the waveguide using a microwave source[5] connected to one of the CPW antennas, as detailed in chapter 9. The applied microwave powers were in the range of $P_{rf} = -40\,\text{dBm}$ to $P_{rf} = 0\,\text{dBm}$, i.e. $P_{rf} = 0.1\,\mu\text{W}$ to $P_{rf} = 1\,\text{mW}$, and no measurement was performed with $P_{rf} > 1\,\text{mW}$ in order to avoid damages to the antenna[6]. The measurements were carried out by space-resolved μBLS as described in section 9.2 with external magnetic fields of $\mu_0 H_{ext} = 8.9\,\text{mT}$, $\mu_0 H_{ext} = 30.8\,\text{mT}$ and $\mu_0 H_{ext} = 63.7\,\text{mT}$ applied perpendicular to the waveguide.

For these fixed fields, excitation frequency sweeps at fixed microwave power settings, as well as excitation power sweeps at fixed frequencies were carried out for the investigation of the inductive excitation of spin waves and particularly the onset of nonlinear processes. Prior to the more in-depth analysis in the following subsections, the observed spectral characteristics and the underlying dependencies will first be introduced for an overview.

10.1.1 Overview of detected spectral characteristics

An exemplary overview of the observed phenomena investigated in the course of this study is given in figure 10.1. The intensity map in figure 10.1 (a) shows the detected spin wave spectra as a function of the microwave excitation frequency obtained at the maximal applied power of $P_{rf} = 0\,\text{dBm} = 1\,\text{mW}$ at an external magnetic field of $|\mu_0 H_{ext}| = 8.9\,\text{mT}$, for which several distinct characteristics can be made out already prior to a detailed analysis:

1. A direct excitation of primary spin waves with $f_{BLS} = f_{rf}$ is obtained as labelled in figure 10.1 (a). For excitation frequencies outside of the areas highlighted by dashed lines in the anti-Stokes part of the spectra, no secondary nonlinear spin waves were detected and only the directly excited spin wave modes are observed.
2. An additional indirect excitation of discrete modes is obtained for excitation frequencies approximately in the range of $5.5 \lesssim f_{rf} \lesssim 6.5\,\text{GHz}$, an exemplary spectrum of which is shown in figure 10.1 (b). Precisely, in this regime the direct excitation $f_{BLS} = f_{rf}$ and the excitation of the higher harmonic $f_{BLS} = 2f_{rf}$ are observed, and additionally two nonlinear spin wave modes are observed as indicated by the rectangular area in figure 10.1 (a) as well as the annotated arrows in (b). These two modes neither correspond to a higher harmonic of the microwave source, nor to a mixing thereof[7], but instead are excited by nonlinear scattering processes as introduced in section 8.2.
3. Another indirect excitation range presenting a broad spectrum of detected spin wave modes is obtained for excitation frequencies around $7.5 \lesssim f_{rf} \lesssim 8.5\,\text{GHz}$, as highlighted by the dashed oval in the Anti-Stokes part of the intensity map shown in figure 10.1 (a). An exemplary spectrum is shown in figure 10.1 (c), where the area marked as "broad scattering" in (a) presents as a consistent increase of the detected background signal as indicated, but no distinct spin wave modes can be made out.
4. The constant spectral features obtained for all spectra are identified as laser modes[8] as indicated in figure 10.1 (a), and can be disregarded.

As introduced in chapter 8, the nonlinear scattering into secondary spin wave modes is generally only observable above critical excitation power thresholds, below which the dissipation of the secondary modes governs the dynamics and therefore no significant population can be obtained.

5: For the first measurement series carried out in this study, an amplifier was additionally present in the setup, amplifying the generated microwave signal by 30 dB. For later measurements, particularly when changing to the time resolution, the amplifier was removed. Therefore, it is important to note that to facilitate the comparison, the indicated powers P_{rf} in this thesis **always** correspond to the **total applied power** unless explicitly stated otherwise. I.e. in the case of the combination of microwave generator and amplifier, the indicated $P_{rf} = -40\,\text{dBm}$ means that $P_{rf} = -70\,\text{dBm}$ was set on the source and the 30 dB amplification are considered. For later measurements, the amplifier was removed and the indicated $P_{rf} = -40\,\text{dBm}$ corresponds to the power set on the source. It was generally verified whether the nonlinear modes correspond to harmonic frequencies (potentially originating from the amplification or the source itself) or a mixing thereof, in order to avoid a wrongful interpretation of the signal for modes which do not correspond to the set direct excitation.

6: Potentially a bit paranoid, but such damage is normally not reversible, and this exact device was not only matching the specific geometry requests for the present study, but also to my information the best characterised device (aka "the baby") on which the most measurements had been performed by J. Solano in the framework of his PhD thesis [91]. Other devices had been fabricated by J. Solano in the same lithography process, but with different device geometries (e.g. changing the crystal orientation of the waveguide, the antenna / contact spacing, etc.), and also were not as extensively characterised. Hence, to allow for a reproduction of measurements and particularly a correlation of results from both studies, this sample was handled with extra care. (Not meaning to imply the other samples in this thesis were not handled with care.)

7: I.e. these spin wave modes do not correspond to $f_{BLS} = f_{rf}$, $2f_{rf}$ or $f_{BLS} = 3/2 f_{rf}$, see the sidenote above.

8: Clearly identifiable since higher order PSSWs cannot be observed in this low frequency range, see the exemplary spin wave dispersion in figure 8.2 on page 154.

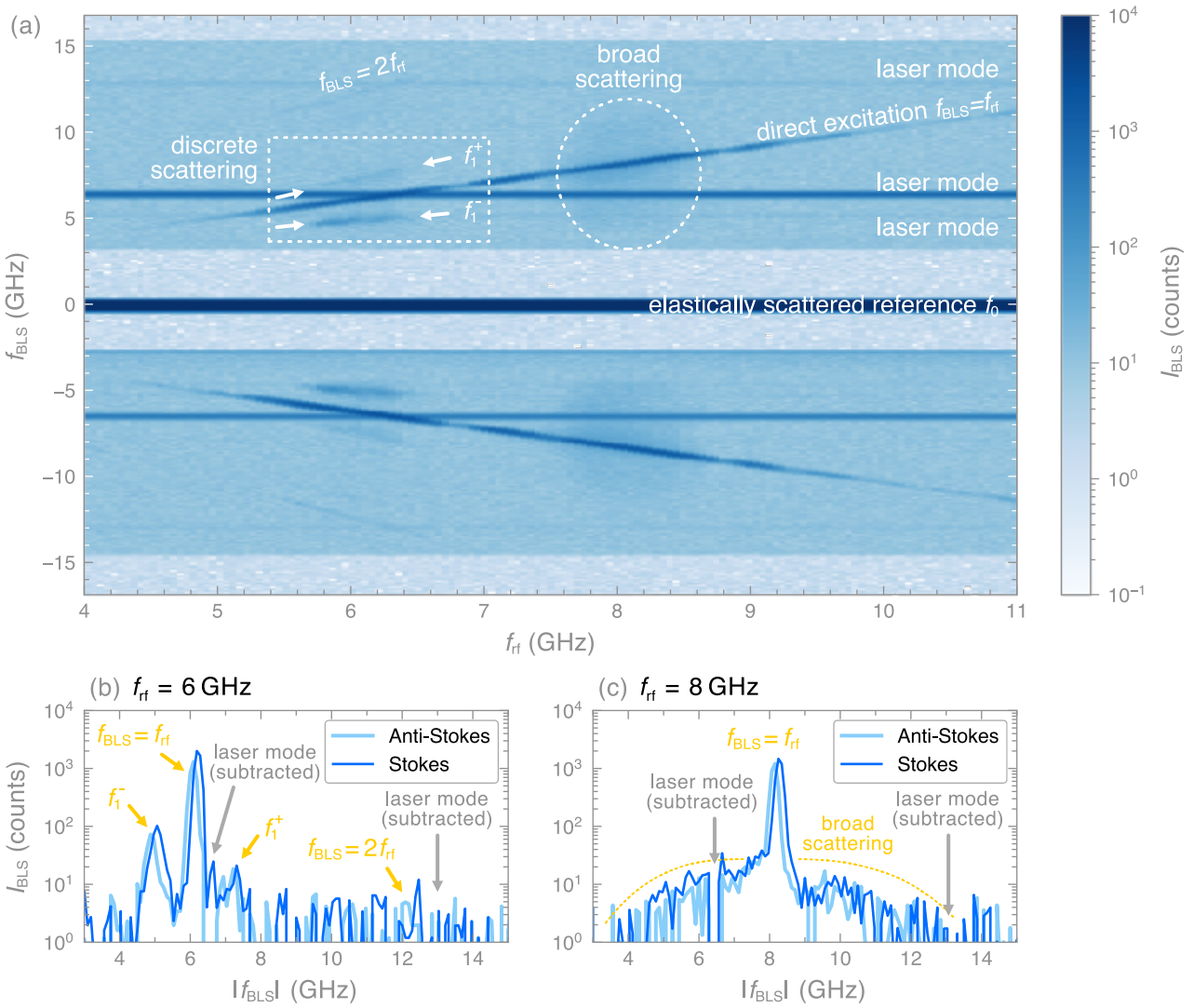

Figure 10.1: Excitation spectra recorded in the Damon-Eshbach geometry at a distance of ~ 2 µm to the microwave antenna (CPW) in an external magnetic field of $|\mu_0 H_{set}| = 8.9$ mT and with an applied microwave power of $P_{rf} = 0$ dBm = 1 mW, which corresponds to the maximal power applied in the entire study.

(a): 2D intensity map of the raw BLS intensity spectra (I_{BLS} vs. f_{BLS} as measured) as a function of the microwave excitation frequency f_{rf}.

(b) and (c): Exemplary BLS intensity spectra I_{BLS} vs. f_{BLS} for selected excitation frequencies of $f_{rf} = 6$ GHz and $f_{rf} = 8$ GHz respectively, where an averaged background was subtracted to remove the laser mode peaks.

The 2D map in (a) presents an overview of the different excitation regimes detected for this set of parameters, where annotations are only made in the anti-Stokes part (positive frequency shifts) to allow for an undisturbed comparison in the Stokes-part (negative frequency shifts) of the spectral intensity map. Two distinct nonlinear excitation regimes are detected here: A discrete scattering is observed in the excitation frequency regime 5.5 GHz $\lesssim f_{rf} \lesssim$ 6.5 GHz as highlighted by the rectangular box, for which distinct modes are detected in the intensity spectra as shown exemplarily in (b) for the excitation frequency $f_{rf} = 6$ GHz. A broad scattering is observed in the excitation frequency regime 7.5 GHz $\lesssim f_{rf} \lesssim$ 8.5 GHz as highlighted by the oval curve, and can be identified as well in the corresponding spectral plots, one of which is exemplarily shown in (c) for the excitation frequency $f_{rf} = 8$ GHz.

The appearance of the nonlinear excitation processes is therefore linked to the effective excitation power, which is a function of the applied microwave power, as well as the excited wavevector[9] imposed by the design of the CPW antennas, as introduced in section 9.1. This wavevector-dependence translates to a frequency-dependent excitation efficiency of the spin wave modes, which is linked to the antenna excitation spectrum via the spin wave dispersion relation introduced in chapter 8. Moreover, due to the link being given by the spin wave dispersion relation, the onset of the nonlinear scattering processes is not only a function of the excitation frequency, but naturally also depends on the applied magnetic field, which yields a shift of the spin wave frequencies[10].

9: See figure 9.3 on page 173. Or figure 10.3 on page 181 in section 10.1.2 hereafter.

10: See e.g. the approximative analytical dispersion relation from the Kalinikos-Slavin theory for linear spin waves in anisotropic films, as introduced in equations 8.1 to 8.5 on page 152.

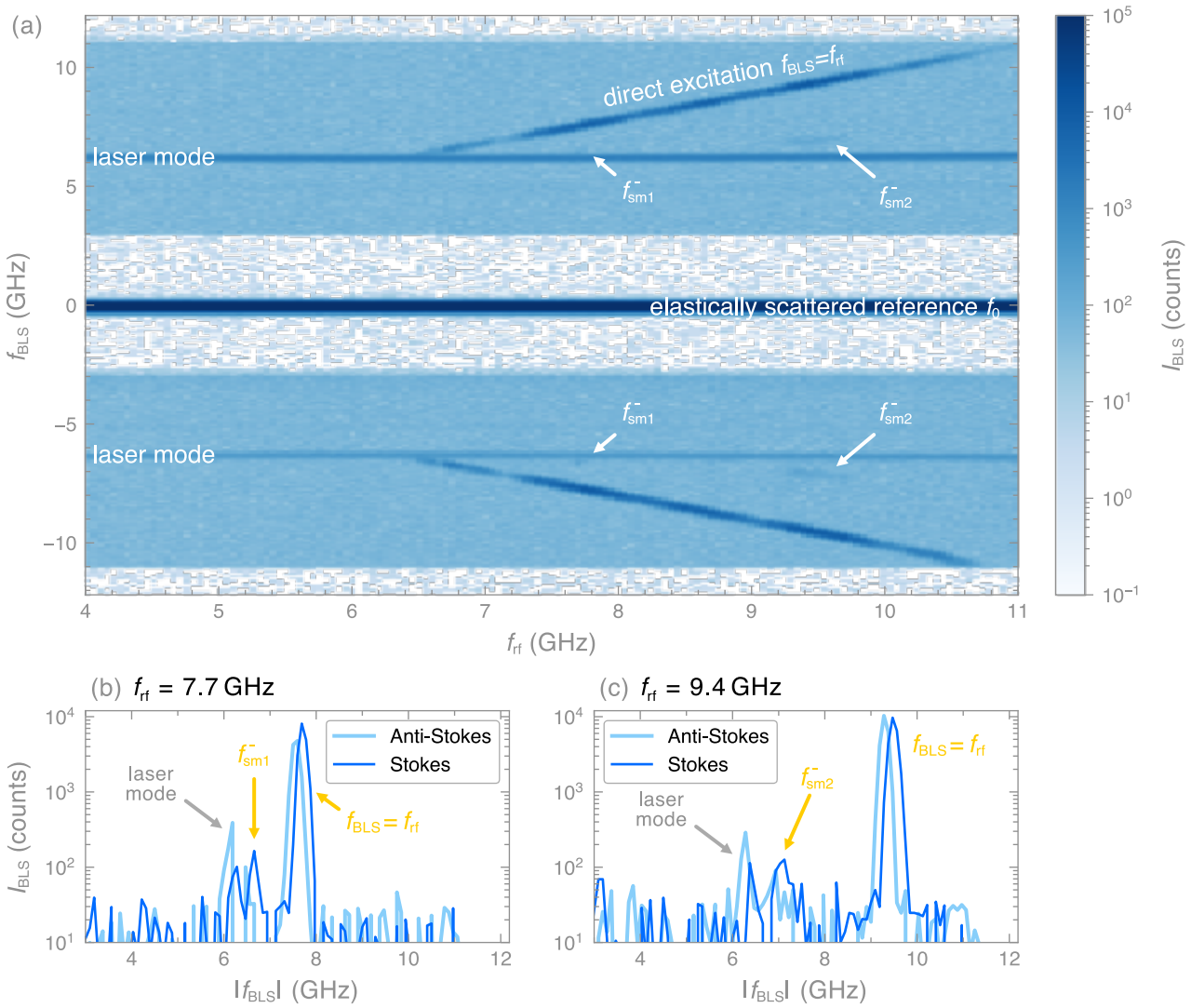

Figure 10.2: Excitation spectra recorded in the Damon-Eshbach geometry at a distance of ~ 2 µm to the microwave antenna (CPW) in an external magnetic field of $|\mu_0 H_{set}| = 30.8\,\text{mT}$ and with an applied microwave power of $P_{rf} = -10\,\text{dBm} = 0.1\,\text{mW}$, presented in analogy to figure 10.1.

(a): 2D intensity map of the raw BLS intensity spectra (I_{BLS} vs. f_{BLS} as measured) as a function of the microwave excitation frequency f_{rf}.

(b) and (c): Exemplary BLS intensity spectra I_{BLS} vs. f_{BLS} for selected excitation frequencies of $f_{rf} = 7.7\,\text{GHz}$ and $f_{rf} = 9.4\,\text{GHz}$ respectively, where an averaged background was subtracted to remove the laser mode peaks.

These dependencies are directly apparent in a comparison with another exemplary overview mapping for the case of $P_{rf} = -10\,\text{dBm} = 0.1\,\text{mW}$ and $|\mu_0 H_{ext}| = 30.8\,\text{mT}$, as is presented analogously in figure 10.2.

Firstly, again two separate frequency ranges are identified, where an indirect population of secondary magnon modes is observed with this low scattering threshold[11]. In both measurements, these frequency ranges correlate with the maxima in the direct excitation intensity, i.e. for $f_{BLS} = f_{rf}$, and are therefore related to the antenna excitation maxima, the frequency of which is a function of the external magnetic field as imposed by the dispersion relation.

Secondly, as opposed to the case in figure 10.1, no broad scattering is observed in figure 10.2 but only a scattering into discrete modes. A further analysis of excitation power sweeps at fixed frequencies shows a broad scattering indeed also for $|\mu_0 H_{set}| = 30.8\,\text{mT}$ at $f_{rf} \approx 9\,\text{GHz}$, but only for $P_{rf} > -10\,\text{dBm} = 0.1\,\text{mW}$. This observation thus again underlines the excitation power dependence of the processes involved.

11: It is pointed out that this measurement at $P_{rf} = -10\,\text{dBm} = 0.1\,\text{mW}$ is an example for the low nonlinear instability thresholds in this sample, as remarked in the introduction to this chapter, since an indirect population of secondary magnon modes is detected already in this overview.

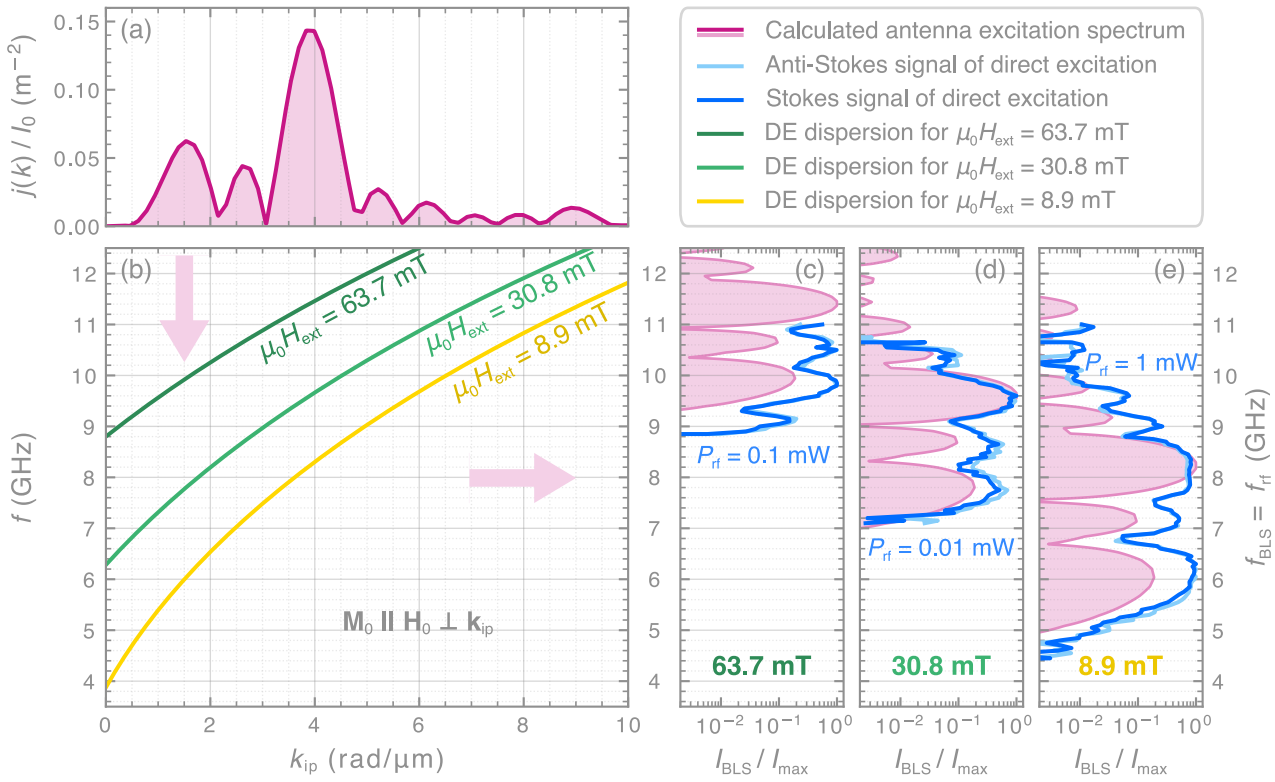

Figure 10.3: Correlation between the spectral antenna excitation efficiency (a) and the direct excitation spectra for $|\mu_0 H_{ext}|$ = 63.7 mT (c), $|\mu_0 H_{ext}|$ = 30.8 mT (d) and $|\mu_0 H_{ext}|$ = 8.9 mT (e), via the dispersion relation (b). The curves in (c,d,e) are normalised on the maximal value. The dispersion curves are calculated with the approximative Kalinikos-Slavin formula given in equation 8.1, with the device parameters as listed in table 9.1 on page 174 but neglecting the surface anisotropy. *DE dispersion* stands for "Damon-Eshbach dispersion", i.e. recalls the $\mathbf{M_0} \parallel \mathbf{H_{ext}} \perp \mathbf{k_{ip}}$ geometry. The direct excitation spectra in (e) for $|\mu_0 H_{ext}|$ = 8.9 mT correspond to the measurement shown in figure 10.1.

10.1.2 Antenna excitation and dispersion relation

The wavevector dependence of the antenna excitation efficiency and the field dependence as introduced by the dispersion relation hence play a crucial role for the further analysis. Therefore, the first step in this study consists of an evaluation of the direct excitation itself, involving the mapping of the calculated antenna spectrum to the measured direct excitation spectra via the spin wave dispersion relation.

To this aim, the direct excitation is extracted from the spin wave spectra recorded in radiofrequency sweep measurements, two examples of which were shown in figures 10.1 and 10.2 before: For a fixed applied field and fixed microwave power[12], the excitation frequency f_{rf} was set in steps of Δf_{rf} = 50 MHz with the frequency ranging

- for $|\mu_0 H_{ext}|$ = 8.9 mT → from f_{rf} = 4 GHz to f_{rf} = 11 GHz
- for $|\mu_0 H_{ext}|$ = 30.8 mT → from f_{rf} = 3 GHz to f_{rf} = 11 GHz
- for $|\mu_0 H_{ext}|$ = 63.7 mT → from f_{rf} = 8 GHz to f_{rf} = 11 GHz

and for each fixed excitation frequency f_{rf} a full BLS spectrum was recorded[13]. The direct excitation is then extracted as a line with $f_{BLS} = f_{rf}$ and a width of 9 frequency channels[14], i.e. tracing $f_{BLS} = f_{rf} \pm \Delta f^{\pm}_{BLS}$ with $\Delta f^{\pm}_{BLS}$ = 375 MHz for $|\mu_0 H_{ext}|$ = 8.9 mT and 30.8 mT, and $\Delta f^{\pm}_{BLS}$ = 300 MHz for $|\mu_0 H_{ext}|$ = 63.7 mT. To subtract the static background and the laser modes, a parallel line[15] is analogously extracted and subtracted from the direct excitation spectra.

Figure 10.3 presents the mapping of the antenna excitation spectrum from figure 9.3 to the direct excitation spectra extracted from the full radiofrequency sweep measurement with the lowest applied microwave power for each

12: Note that the microwave power is a crucial factor here, due to the nonlinear frequency shift affecting the extracted spectra (notably shifting the spectral position of the maxima to lower frequencies), as will be addressed on the next page. Yet, these measurements also (primarily) served for a mapping of the nonlinear phenomena to identify the ranges of interest for further measurements, for which clearly large microwave powers need to be applied. Sadly, the massive measurement duration (linked to the comparably poor magneto-optical signal from the Co_2MnSi compound - see chapter 7) did not allow for many of those full f_{rf} sweep measurements. The applied powers, for which such full f_{rf} sweeps were recorded, are:

- 8.9 mT → P_{rf} = 0 dBm
- 30.8 mT → P_{rf} = −10, −20 dBm
- 63.7 mT → P_{rf} = −10 dBm

13: Precisely, 120-800 BLS spectra were accumulated for each averaged spectrum to obtain a sufficient signal to noise ratio.

14: Note that this is a second factor affecting the extracted spectra, notably yielding a reduced separation of the maxima.

15: Naturally shifted in f_{rf} to ensure the correct background removal for f_{BLS}. The shift was chosen for each measurement individually to ensure no overlap with any spectral feature (i.e. the signal from nonlinear secondary modes).

field value[16]: The k-vactor dependent antenna spectrum in figure 10.3 (a) is transformed to a frequency dependence via the dispersion relation in figure 10.3 (b). Finally, the amplitude values are squared and normalised for the comparison in figure 10.3 (c), (d) and (e) to the normalised intensities of the direct excitation extracted from the measured BLS spectra.

Note that the match of the mapped spectra can only be evaluated on a qualitative base, explicitly neglecting the (mis)match of the intensities but only focusing on the spectral position of the maxima, since particularly the rather complicated, frequency dependent BLS detection function[17] is completely neglected in the simplified mapping here. Considering this, a fairly decent match is obtained for the three spectra in figure 10.3 (c - e), particularly concerning the approximate spectral position of the three main maxima with the lowest k_{ip}.

Still, it can be noted that all observable deviations[18], particularly in figure 10.3 (e, f) for $f_{BLS}\,(30.8\,\mathrm{mT}) \gtrsim 10\,\mathrm{GHz}$ and $f_{BLS}\,(8.9\,\mathrm{mT}) \gtrsim 9\,\mathrm{GHz}$, systematically show an overestimation of the frequencies in the mapped antenna spectrum (pink area) to the detected excitation spectra (blue curves). In principle, the self-induced nonlinear frequency shift described by $\widetilde{\omega}_{\mathbf{k}}(t) = \omega_{\mathbf{k}}(t) + \Delta\omega_{\mathbf{k}}(t)$ with $\Delta\omega_{\mathbf{k}}(t) = \widetilde{W}_{\mathbf{kk,kk}} \cdot |c_{\mathbf{k}}(t)|^2$ for a spin wave with wave vector $\mathbf{k}$ as introduced in chapter 8 particularly on pages 164 and 168 can yield exactly this effect: A negative nonlinear frequency shift is expected for the Co_2MnSi Heusler compound in the Damon-Eshbach geometry, and as this phenomenon is not a threshold process, the population of the pumped spin wave mode generally yields a shift of the dispersion to lower frequencies for all excitation powers[19].

Yet it is non-recommendable to jump to hasty conclusions here, since various other factors come into play, where particularly an uncertainty on the material parameters ultimately determining the dispersion relation can yield a deviation in the mapping, notably an underestimation of the cubic anisotropy for instance. Equally measurement errors, such as an uncertainty of the field setting or the sample positioning, can yield similar shifts of the dispersion. Moreover, it is worthy to recall the dispersion model is only an approximation and especially neglects waveguide width modes, the excitation of which could also distort the detected direct excitation spectrum. In short, the problem is absolutely over-parametrised to draw any conclusion based on the slight deviations in the mapping.

For $|\mu_0 H_{ext}| = 30.8\,\mathrm{mT}$, two full excitation frequency sweep measurements were carried out with different applied microwave powers[20] and the two (normalised) direct excitation spectra are compared in figure 10.4. Note that all spectra are normalised on the maximal intensity (at $f_{rf} \approx 9.55\,\mathrm{GHz}$ for all). Comparing the set of Stokes and Anti-Stokes spectra for the two applied microwave powers, an indication for an increase of the relative intensity of all three minor maxima, i.e. at $f_{rf} \approx 7.75\,\mathrm{GHz}$, 8.65 GHz and 10.3 GHz is observed, but a clear frequency shift cannot be resolved within the detection limit[21]. Nevertheless, it can be noted that the increase of the intensity detected at the minima between excitation maxima, i.e. at $f_{rf} \approx 8.2\,\mathrm{GHz}$, 9.05 GHz and 10.1 GHz is a strong indication for a nonlinear broadening of the spectrum: If the power increase would only yield a simple intensity increase in the spectrum, the normalisation should result in the same separation of the maxima.

Consequently, the one main conclusion to draw from this direct excitation analysis, specifically in prospect of the further analysis in this chapter, is the generally adequate reproduction of the direct excitation spectra by the calculated dispersion curves, particularly for $k_{ip} \lesssim 5\,\mathrm{rad/\mu m}$ at applied fields of $|\mu_0 H_{ext}| = 30.8\,\mathrm{mT}$ and $|\mu_0 H_{ext}| = 8.9\,\mathrm{mT}$. It is noted that the deviation for

16: The direct excitation (blue curves) in figure 10.3 (e) corresponds to the measurement shown in figure 10.1.

17: See the brief motivation in chapter 4 where the BLS intensity is linked to the dynamic magnetisation components, for more details it is referred to [296, 326, 327, 446, 447].

18: Again: only evaluating the spectral position of the features, not the intensity!

19: Note that the shift is still (indirectly) excitation power dependent: Although no threshold needs to be overcome, the phenomenon does scale with the applied power entering via the spin wave intensity.

20: I.e. one with $P_{rf} = -10\,\mathrm{dBm} = 0.1\,\mathrm{mW}$ as shown in figure 10.2, and a second with $P_{rf} = -20\,\mathrm{dBm} = 0.01\,\mathrm{mW}$, the direct excitation trace of which is used in figure 10.3 (d)

21: Here mostly defined by the combination of the poor magneto-optical signal from the Heusler compound, and the averaging, i.e. the amount of accumulated spectra (number of TFPI scans) recorded for the same conditions.

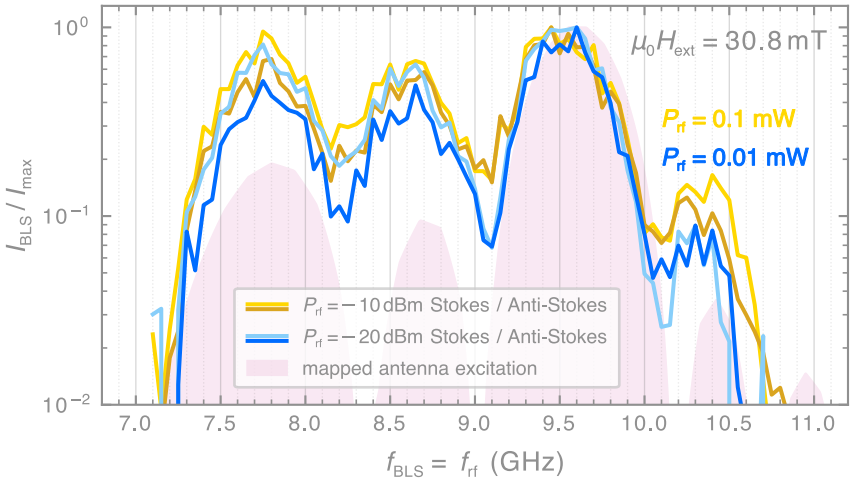

Figure 10.4: Comparison of the normalised direct excitation spectra at $|\mu_0 H_{ext}| = 30.8\,mT$ for $P_{rf} = -10\,dBm = 0.1\,mW$ (yellow) and $P_{rf} = -20\,dBm = 0.01\,mW$ (blue). The yellow lines for $P_{rf} = -10\,dBm = 0.1\,mW$ were extracted from the measurement presented in figure 10.2, where a population of indirectly excited secondary magnon modes is observed. The blue lines for $P_{rf} = -20\,dBm = 0.01\,mW$ correspond to the measurement also plotted in figure 10.3 (d). The direct excitation spectra in this figure are a central point in the further analysis and will be recalled in figures 10.5 and 10.14.

$k_{ip} \gtrsim 5\,rad/\mu m$ is rather insignificant for the further study in this work: As shown in figures 10.1 and 10.2, the main areas of interest for the further investigation of the nonlinear processes lie below the corresponding frequencies $f_{BLS}(30.8\,mT) = 10\,GHz$ and $f_{BLS}(8.9\,mT) = 9\,GHz$. Hence, in a first approximation the analytical Kalinikos-Slavin dispersion can be used in this range. The second conclusion is to note a likely non-negligible nonlinear frequency shifting effect even at the fairly low microwave powers employed in this study, an effect of which is seen in the study presented hereafter, where a related enhancement of the excitation is seen for a pumping frequency just below the excitation spectrum[22].

22: Precisely, at $f_{rf} = 7.15\,GHz$ which corresponds to the lower border of the mapped/measured excitation spectrum in figure 10.4.

10.2 2nd order Suhl instability onset

Contrary to the self-induced nonlinear frequency shift, the Suhl instabilities are threshold processes and only occur when the population of the directly excited primary mode exceeds a critical amplitude as introduced on page 168. Consequently, a specific threshold power is expected for the onset of the scattering from the directly excited primary mode into secondary magnon modes. A signature of such processes was already detected in the initial excitation frequency sweep measurements presented in figure 10.1 for $|\mu_0 H_{ext}| = 8.9\,mT$ and $P_{rf} = 0\,dBm$ and in figure 10.2 with $|\mu_0 H_{ext}| = 30.8\,mT$ and $P_{rf} = -10\,dBm$, which already allowed for a qualitative conclusion of the threshold being overcome in both cases for the excitation frequencies corresponding to the antenna excitation maxima.

Additionally, it is recalled that the first order Suhl instability[23] can only occur for excitation frequencies which are larger than twice the band bottom, i.e. $f_{rf} \geq 2 \cdot f_{min}$. This process is therefore not only power dependent, but also field and frequency dependent, as was shown in the calculation in figure 8.12. For an applied field of $\mu_0 H_{ext} \approx 30\,mT$, already the (hypothetical) isotropic Co_2MnSi case[24] yields a threshold of $2 f_{min} = 11.4\,GHz$. Additionally, the magnetocrystalline anisotropy contributions for the Co_2MnSi compound in this geometry, i.e. with $\mathbf{M}_0 \parallel [110]_{Co_2MnSi}$, increase the threshold frequency further and given the thorough analysis of the device in [91], no surprising counteracting anisotropy contributions are to be expected. Consequently, no first order Suhl instability processes can be involved in the scattering detected in the measurements at $|\mu_0 H_{ext}| = 30.8\,mT$ as all excitation frequencies are lower than the isotropic threshold, i.e. $f_{rf} < 11.4\,GHz$.

23: As introduced on page 163, the first order Suhl instability process corresponds to the resonant three magnon process where one primary (directly excited) magnon splits into two secondary magnons. The second order Suhl process is a four magnon scattering process, where two primary magnons scatter into two secondary magnons. Scattering partners for the latter can always be found, and therefore no exclusion regime exists for this process (obviously only frequencies above the band bottom can be populated, and energy and momentum conservation need to be validated).

24: I.e. calculating the dispersion for Co_2MnSi parameters but neglecting any anisotropy terms (except of the shape anisotropy due to the demagnetisation term, of course).

[91]: Solano Córdova (2024), 'Temperature dependent spin wave study of magnetic properties and spin-polarized electron transport in $Fe_{1-X}V_X$ and Co_2MnSi epitaxial films'

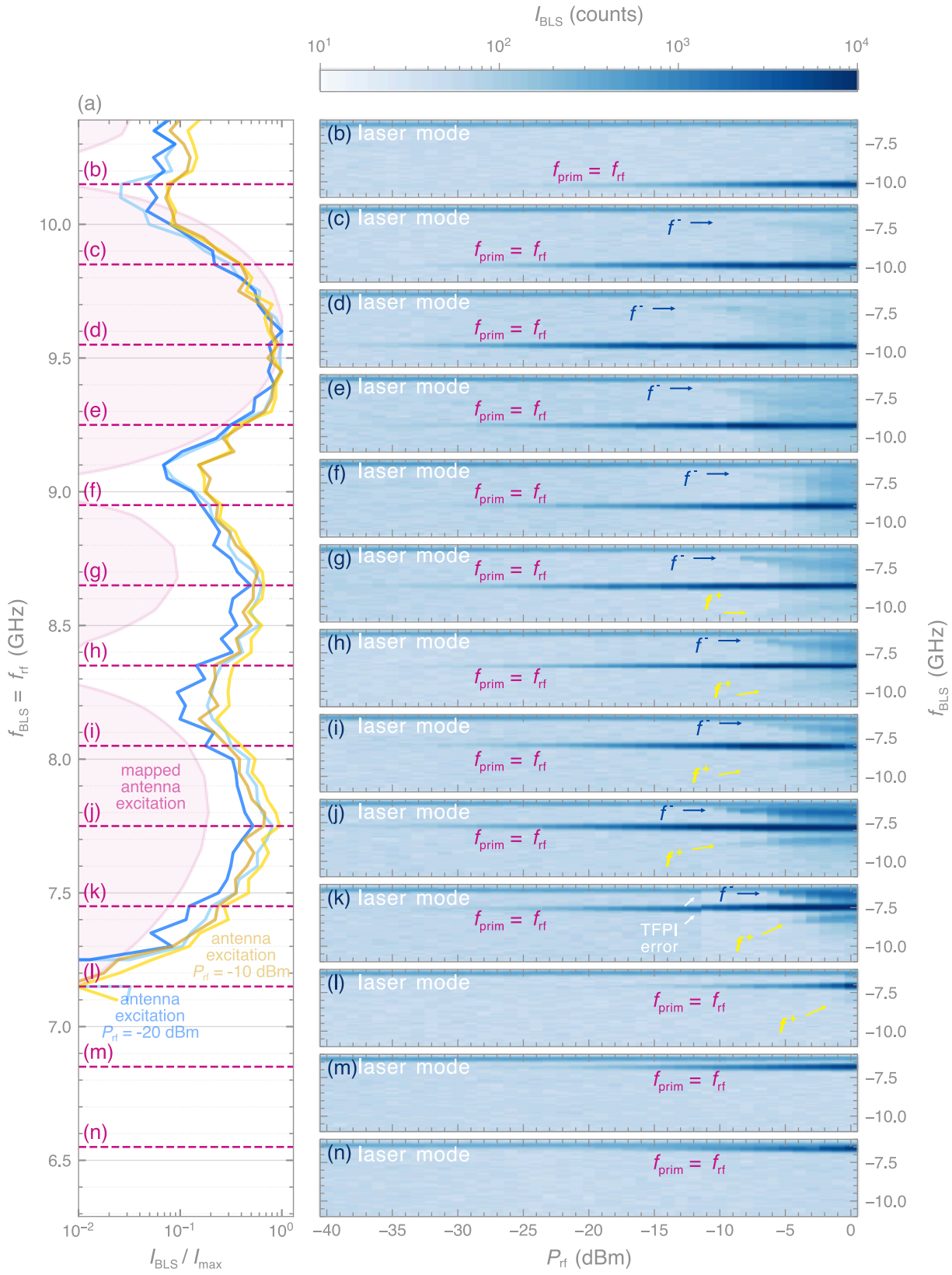

Figure 10.5: Excitation power sweep measurements at $|\mu_0 H_{ext}| = 30.8$ mT measured at the same position as before, i.e. ~ 2 µm from the CPW antenna at the centre of the 10 µm wide Co_2MnSi waveguide. The direct excitation plot in (a) is recalled from figure 10.4, where additional dashed pink horizontal lines indicate the excitation frequencies corresponding to (b-m). The colormaps in (b-m) present the Stokes part of the recorded BLS spectra as a function of the applied microwave power which was swept from $P_{rf} = -40$ dBm to $P_{rf} = 0$ dBm. The direct excitation is marked as f_{prim} for *primary mode*. Note that for the measurement presented as case (k) with $f_{rf} = 7.45$ GHz, an automation error during the TFPI data acquisition caused a measurement interruption, which is the reason for the abrupt frequency shift at the indicated position. From the restart, the measurement ran smoothly again and the onset of the nonlinear scattering processes is undisturbed by the measurement error.

For the measurements in an applied field of $|\mu_0 H_{\text{ext}}| = 8.9\,\text{mT}$, however, the anisotropy does play a crucial role for the exclusion or potential presence of the first order Suhl instability, since the hypothetical isotropic Co_2MnSi here yields $2f_{\text{min}} = 6.6\,\text{GHz}$, which is exactly between the two scattering regimes identified in figure 10.1.

Therefore, a first investigation is focused on the critical threshold power for the second order Suhl instability onset at $|\mu_0 H_{\text{ext}}| = 30.8\,\text{mT}$. To this aim, various excitation power sweeps were recorded at selected excitation frequencies from $f_{\text{rf}} = 6.55\,\text{GHz}$ to $f_{\text{rf}} = 10.15\,\text{GHz}$ in steps of $\Delta f_{\text{rf}} = 0.3\,\text{GHz}$, and the Stokes part of the resulting BLS spectra is presented[25] as an overview in figure 10.5. This frequency range corresponds to the range of $0\,\text{rad}/\mu\text{m} \lesssim k_{\text{ip}} \lesssim 5\,\text{rad}/\mu\text{m}$ of the dispersion plotted in figure 10.3 (b), and hence covers the first three main maxima of the antenna spectrum. For comparison, the excitation spectra from figure 10.4 are recalled in figure 10.5 (a) and the fixed frequencies are marked as dashed lines. The power was set from $P_{\text{rf}} = -40\,\text{dBm} = 10^{-4}\,\text{mW}$ to $P_{\text{rf}} = 0\,\text{dBm} = 1\,\text{mW}$ in steps of $\Delta P_{\text{rf}} = 1\,\text{dB}$ and for the further analysis it is important to recall that this does not correspond to a linear power increase, but to a logarithmic scaling[26] of the applied microwave powers.

Prior to the detailed analysis, different excitation and instability regimes can be already identified in the overview in figure 10.5: As shown in figure 10.5 (a), the probed spectral range by the fixed frequencies (dashed horizontal lines) in the power sweep measurements covers not only the three excitation maxima, but in addition two frequencies well below the minimum of the antenna spectrum, i.e. with $f_{\text{rf}} < 7\,\text{GHz}$, are probed in figure 10.5 (m, n). Also, the case in figure 10.5 (l) corresponds to the frequency just at the minimum of the mapped and measured antenna excitation spectra with $f_{\text{rf}} = 7.15\,\text{GHz}$. Similarly, the maximal frequency $f_{\text{rf}} = 10.15\,\text{GHz}$ in figure 10.5 (b) corresponds to a spectral position just above the main excitation maxima, and the detected population onset again shifts to higher powers, compared to e.g. the measurement just below at $f_{\text{rf}} = 9.85\,\text{GHz}$ in figure 10.5 (c).

For the excitation with f_{rf} outside or at the boundaries of the three excitation maxima, i.e. for $f_{\text{rf}} = 10.15\,\text{GHz}$ in figure 10.5 (b) as well as $f_{\text{rf}} \leq 7.15\,\text{GHz}$ in figure 10.5 (n - l), rather large microwave powers are necessary to yield a detectable population at $f_{\text{prim}} = f_{\text{rf}}$ compared to the frequencies f_{rf} corresponding to the main excitation maxima, i.e. with $7.45\,\text{GHz} \leq f_{\text{rf}} \leq 9.85\,\text{GHz}$ in figure 10.5 (k - c). In relation to this, no clear population of secondary modes is observed for these frequencies, precisely only for $f_{\text{rf}} = 7.15\,\text{GHz}$ a faint[27] onset is visible at $P_{\text{rf}} \approx -1\,\text{dBm}$ as indicated in figure 10.5 (l).

For the excitation where f_{rf} coincides with the main three excitation maxima, on the other hand, i.e. for $7.45\,\text{GHz} \leq f_{\text{rf}} \leq 9.85\,\text{GHz}$ in figure 10.5 (k - c), a population of secondary magnon modes is clearly detected, where two different regimes can be made out: For $7.45\,\text{GHz} \leq f_{\text{rf}} \leq 8.65\,\text{GHz}$ in figure 10.5 (k - g), a symmetric appearance of two modes around the primary frequency is observed and labelled as f^- for the secondary magnons with $|f| = f_{\text{rf}} - \Delta f$ and f^+ for the secondary magnons with $|f| = f_{\text{rf}} + \Delta f$. The difference between the secondary modes and the primary mode increases with increasing excitation frequency, and for a fixed excitation frequency, the increasing power leads to an increased intensity on the secondary magnon modes as well as a spectral shift towards the central excitation frequency. For $8.95\,\text{GHz} \leq f_{\text{rf}} \leq 9.85\,\text{GHz}$ in figure 10.5 (f - c), also an initial scattering into a defined secondary mode f^- is detected[28] as marked, but a rapid spectral broadening with increasing power makes the mode untraceable.

25: Note that always the full BLS spectra, i.e. the Stokes and Anti-Stokes part, were recorded but only the Stokes part between $f_{\text{BLS}} = -6\,\text{GHz}$ and $f_{\text{BLS}} = -11\,\text{GHz}$ is shown for clarity. The Anti-Stokes part shows generally the same spectral features in the μBLS measurements.

26: The unit conversion is very common in radiotechnology: The dBm unit stands for *decibel-milliwatts* and indicates absolute power levels which are referenced to 1 mW, i.e.

$$P[\text{mW}] = 1\,\text{mW} \cdot 10^{P[\text{dBm}]/10\,\text{dBm}} \tag{10.1}$$

and hence

$$P[\text{dBm}] = 10\,\text{dBm} \cdot \log_{10}\left(\frac{P[\text{mW}]}{1\,\text{mW}}\right). \tag{10.2}$$

for the conversion between the two units. The relative difference of absolute power levels in dBm is a dimensionless measure and indicated in dB (decibel): It corresponds to the ratio of two power levels in mW, specifically

$$P[\text{dBm}] + \Delta P[\text{dB}] = P[\text{mW}] \cdot 10^{\Delta P[\text{dB}]/10} \tag{10.3}$$

and hence the step $\Delta P_{\text{rf}} = 1\,\text{dB}$ corresponds to a factor of $10^{\Delta P_{\text{rf}}/10} \approx 1.26$ or an increase by $\sim 26\,\%$ per step.

27: As in figure 10.5 (l) for $f_{\text{rf}} = 7.15\,\text{GHz}$. Depending on the screen/printer contrast the faint signal might not be identifiable in the colormaps. However, the population of the indicated secondary mode f^+ is clearly observable when plotting the individual spectra from this power mapping. This case will be discussed in detail later on.

28: Note that for the measurements with $8.95\,\text{GHz} \leq f_{\text{rf}} \leq 9.85\,\text{GHz}$ in figure 10.5 (f - c) the secondary mode f^+ drifts out of the detection range and cannot be identified anymore. This does not mean that a scattering into this mode is not happening.

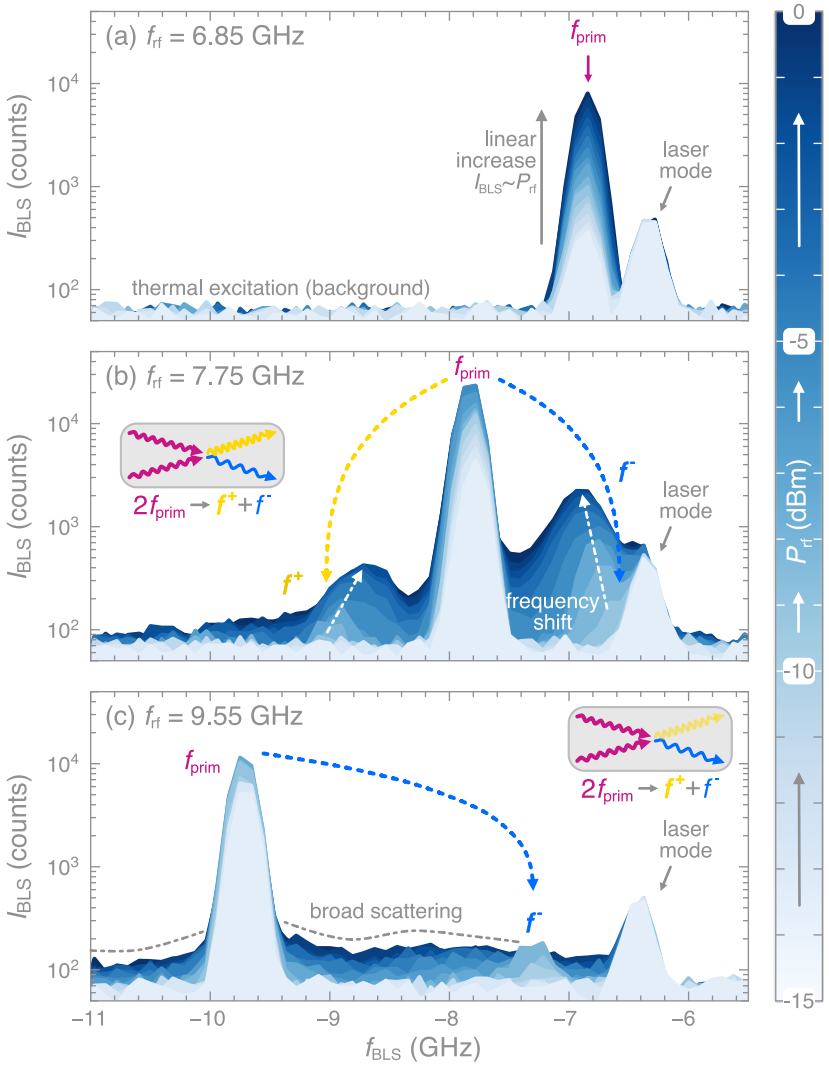

Figure 10.6: Stokes part of the recorded BLS spectra (raw, no background subtraction) for $P_{rf} \geq -15\,\text{dBm} \approx 32\,\mu\text{W}$ at three fixed excitation frequencies (a) $f_{rf} = 6.85\,\text{GHz}$, (b) $f_{rf} = 7.75\,\text{GHz}$ and (c) $f_{rf} = 9.55\,\text{GHz}$, each corresponding to one of the three characteristic regimes described in the main text. The spectra are stacked towards the back with increasing power and with a joint colourcode as indicated by the colourbar. The anti-Stokes shows principally the same behaviour (see microscope implications in section 9.2) and was therefore ommitted here. In (a) a linear excitation regime is observed. In (b) a scattering into two distinct modes is observed, which shift towards the central frequency for further power increase. In (c) a scattering into a distinct mode is observed, but subsequently a broad scattering resulting in a broadened background increase is observed.

10.2.1 Frequency dependency

For each regime, the recorded spectra of an exemplary case are shown in figure 10.6, where the characteristics are clearly identifiable:

1. For $f_{rf} = 6.85\,\text{GHz}$ in figure 10.6 (a), the excitation frequency is below the antenna excitation spectrum[29] and the power increase simply leads to a constant intensity increase on the direct excitation f_{prim}.
2. The case of $f_{rf} = 7.75\,\text{GHz}$ in figure 10.6 (b) corresponds approximately to the first local maximum of the antenna spectrum and consistently, the intensity at f_{prim} is already for $P_{rf} = -15\,\text{dBm}$ significantly larger than for $f_{rf} = 6.85\,\text{GHz}$ in (a)[30]. Above a critical amplitude $c^{krit,2nd}$, here reached at an excitation power $P_{rf} = -9\,\text{dBm}$[31], the second order Suhl instability sets in as indicated in the BLS spectra in figure 10.6 (b). The underlying four magnon process yields a population of secondary magnon modes f^+ and f^-, where the energy conservation $2 \cdot f_{prim} = f^+ + f^-$ yields a symmetric position around the primary (directly excited) mode f_{prim}. With increasing excitation power, the intensity of the secondary modes increases and a broadening of the peaks is observed accompanied by a frequency shift of the secondary magnon modes towards the central f_{prim} as marked in the BLS spectra in figure 10.6 (b).
3. The case of $f_{rf} = 9.55\,\text{GHz}$ in figure 10.6 (c) corresponds to the global

29: Compare to case (m) in figure 10.5.

30: Note that a direct comparison of the intensities at different frequencies is only possible in a limited way, due to the various frequency dependencies in the system as mentioned before.

31: In fact, for $P_{rf} = -10\,\text{dBm}$ a shoulder is already detected on the laser mode in the Stokes and anti-Stokes signal and corresponds to the onset of f^-, but is difficult to evaluate and additionally the population of f^+ is nearly indifferentiable from the thermal background at that power.

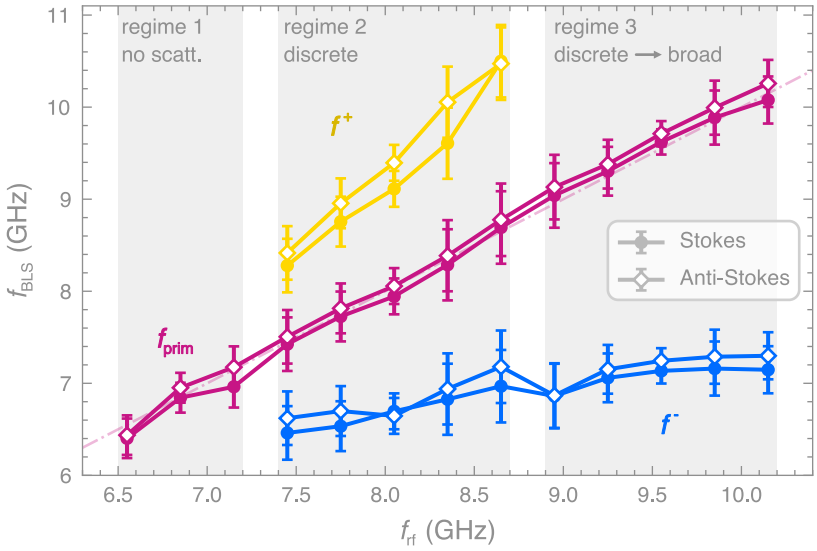

Figure 10.7: Tracing of the direct excitation f_{prim} as well as the secondary modes f^+ and f^- at the critical onset as a function of the applied microwave frequency f_{rf}. Note that the critical power corresponding to each set $\{f^-, f_{\text{prim}}, f^+\}$ shown in this figure is not the same for all f_{rf} mainly due to the antenna excitation characteristics. The frequencies were determined by a fit of a Lorentzian function to the respective spectral peak.

maximum of the antenna spectrum. Again, an initial scattering into a well defined secondary magnon mode[32] f^- is observed at a critical amplitude $c^{\text{krit,2nd}}$, here reached for $P_{\text{rf}} = -11\,\text{dBm}$ as indicated in the BLS spectra in figure 10.6 (c). With increasing power, the secondary magnon mode shows a slight shift and a peak broadening as observed in case (b). However, unlike in case (b), a super critical behaviour rapidly sets in: For $P_{\text{rf}} \geq -8\,\text{dBm}$ only a broadly increased background is observed as indicated in the BLS spectra in figure 10.6 (c), and a secondary magnon mode is not well defined anymore.

32: Note that a population of the corresponding f^+ could not be measured withing the detection range

The observed broadening with increasing excitation powers beyond the critical threshold, i.e. above the onset of the secondary modes f^+ and f^-, can originate from the further instability of the directly excited primary mode f_{prim}, i.e. reaching a further critical threshold for additional scattering partner combinations, or from a subsequent (secondary) instability of the populated secondary modes f^+ and f^-, resulting in a scattering cascade [422, 427].

[422]: Livesey et al. (2007), 'Parametric spin wave excitation and cascaded processes during switching in thin films'
[427]: Mohseni et al. (2021), 'Controlling the Nonlinear Relaxation of Quantized Propagating Magnons in Nanodevices'

As mentioned above for the exemplary spectra for $f_{\text{rf}} = 7.75\,\text{GHz}$ in figure 10.6 (b), the symmetric splitting of the secondary modes f^+ and f^- around the primary excitation $f_{\text{prim}}$is a signature of the energy conservation in the underlying four-magnon scattering mechanism, i.e.

$$2 \cdot f_{\text{prim}} = f^+ + f^- \tag{10.4}$$

as introduced in chapter 8 on page 163. The onset frequencies of all (detected) secondary modes as a function of the excitation frequency are shown in figure 10.7, and are found to verify the energy conservation in the regime 2, as can be seen by the overlapping frequency differences in figure 10.8. It is noted that while this is also expected in the regime 3, it cannot be verified as f^+ is not withing the detection range in this case.

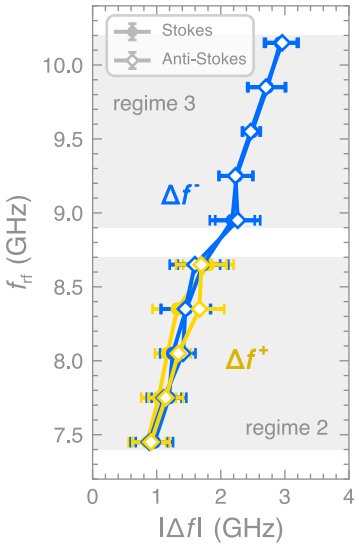

Figure 10.8: Frequency difference at the onset of the secondary modes f^+ and f^- to the respective primary mode f_{prim}, i.e. $\Delta f^- = f^- - f_{\text{prim}}$ and $\Delta f^+ = f^+ - f_{\text{prim}}$.

In comparison with the aforementioned comparable study on the non-epitaxial $Co_2Mn_{0.6}Fe_{0.4}Si$ waveguide of similar parameters[33] but negligible anisotropy [97], a different behaviour is observed: In [97], a population of a *dominant critical mode* is identified, i.e. a population of a fixed mode in the dispersion relation independent of the excitation frequency. The phenomenon is attributed either to a superior coupling to the underlying four magnon scattering mechanism, or to a particularly small relaxation coefficient for this mode (or both). In the study in [97], the dominant mode is identifiable by a constant $f^-(f_{\text{rf}})$ signature

33: $M_S = 1003\,\text{kA/m}$, $A_{\text{exch}} = 13\,\text{pJ/m}$, $\alpha = 3 \times 10^{-3}$, $w = 5\,\mu\text{m}$, $d = 30\,\text{nm}$

[97]: Pirro (2014), 'Lineare und nichtlineare Spinwelleninteraktionen in magnetischen Mikrostrukturen'
[97]: Pirro (2014), 'Lineare und nichtlineare Spinwelleninteraktionen in magnetischen Mikrostrukturen'

observed at $\mu_0 H_{ext} = 48\,\mathrm{mT}$, with an additional confirmation by the scaling for different external fields[34].

In the present study, a constant f^- behaviour attributable to a *dominant critical mode* could not be confirmed for the critical onset frequencies in figure 10.7. This might be an effect of the selective wavevector excitation with the given antenna geometry, as the four-magnon scattering process not only needs to conserve energy, but also momentum. Indeed, while in [97] a 1 µm wide stripline antenna with a (rather broad) maximum at $k = 0$ was utilised, the meander shaped CPW antenna in this study yields a refined wavevector selection and particularly $k \gtrsim 0.5\,\mu\mathrm{m}$ as shown in figure 10.3. In particular, the excitation imposing a wavenumber $k > 0$ in combination with the probing spot being at a distance of $\sim 2\mu$m from the antenna, implies in a first approximation that the excited spin waves travel away from the antenna[35], which notably excludes a scattering into the Backward-Volume modes ($\mathbf{k} \parallel H_{ext}$) due to the non-validation of the momentum conservation. However, a precise identification of the potential scattering partners is rather complicated, since particularly the waveguide width modes yield a zoo of potential scattering partners, and is further complicated by the proximity of the DC contacts of the spin wave Doppler shift device[36] from which a backreflection cannot be excluded and cause further mode interference in the system. Indeed, a time resolved test measurement confirmed a propagation with little losses until the DC contacts, and additionally a first modelling attempt by Solano *et al.* reported in [91] for a similar device (but simulated for an excitation frequency of 19 GHz and an applied field of 118 mT) notably reports a confinement-induced self-focusing effect similar to previous reports in [448, 449] which is generally related to the interference of multiple modes in the waveguide.

Hence, a rather extensive micromagnetic modelling and experimental verification of the width modes and confinement effects, e.g. by an areal mapping by space resolved µBLS, is required for an attempt to identify potential scattering partners. While this is outside the scope of this preliminary, rather explorative study[37], an analysis of the power dependence in the system and particularly a determination of the power threshold for the onset of the nonlinear processes is quantifiable, which is not only interesting for a potential future exploitation of the Heusler compound in nonlinear magnonic devices, but equally for the knowledge of the limitation e.g. for analytical descriptions which are mostly developed for the linear dynamics[38].

10.2.2 Power dependency

From the above identification of different characteristic regimes[39] it can already be anticipated that the specific antenna excitation spectrum in the investigated device is a major factor throughout this study, notably governing the frequency dependence of the critical threshold power as well as the further observations in the supercritical regime.

For the analysis of the power dependency and notably the extraction of the critical threshold, the intensity of the different spectral features is extracted as a function of the applied microwave power for all spectra. For an improved comparison, the measurements corresponding to figure 10.6 will continue to serve as exemplary cases in the following, and particularly the respective power traces are shown in figure 10.9 for comparison. It is noted that, even if not shown, all other measurements of this data set, an overview over which was given in 10.5, are treated equally and will be referred to in the text.

34: See figure 7.6 in [97]. Note that f_{prim}, f^- and f^+ are named f_0, f_1 and f_2 in [97].

35: Neglecting a potential backreflection, see the next sentences.

36: The probing spot is at ~ 2 µm distance to the CPW antenna border and at ~ 13 µm distance to the DC contact border. See the (scaled) device geometry in figure 9.4 (a).

[448]: Demidov et al. (2007), 'Self-focusing of spin waves in Permalloy microstripes'
[449]: Demidov et al. (2008), 'Mode interference and periodic self-focusing of spin waves in permalloy microstripes'

37: Note that due to the rather poor magneto-optical signal from the Co_2MnSi Heusler compound, quite long measurement times were already necessary for the data acquisition presented in this study: The measurements presented in this chapter blocked the µBLS for a total duration of ~ 2 months. (And the setup time was efficiently used! Certainly primarily motivated by the urge to explore nonlinear dynamics in the Heusler compound, but also partly by the enormous demand for setup time on this system at the time of the study not allowing for significant idle times.) A spatial mapping with sufficient width points for an evaluation of potential confinement effects could not be performed and will require a future measurement (in a rather long session).

38: At this point of the thesis sufficiently discussed, yet just in case it is especially referred to chapter 4 for the linearisation of the fundamental LLG equation of motion, and chapter 8 for a brief introduction of spin waves in the linear and nonlinear regime.

39: Note that regime 1 corresponds to the forced excitation below the main antenna spectrum, regime 2 coincides with the first two local maxima, and regime 3 coincides with the global maximum.

To extract the intensity traces from all measurements, the background is first removed by subtracting the average of the 5 spectra recorded at the lowest applied microwave powers, i.e. for $P_{rf} \leq -35\,\mathrm{dBm}$[40]. The accumulated signal is then extracted within $|f_{BLS}| = f_{rf} \pm 350\,\mathrm{MHz}$ for the direct excitation, and accordingly $6.6\,\mathrm{GHz} < |f_{BLS}| < f_{rf} - 350\,\mathrm{MHz}$ as well as $f_{rf} + 350\,\mathrm{MHz} < |f_{BLS}| < 11\,\mathrm{GHz}$ for the extraction of all scattered signal to lower and higher frequencies, where the boundaries at 6.6 GHz and 11 GHz are set to avoid an influence of the laser mode or the limit of the TFPI scanning region of interest[41]. Finally, the extracted signal is normalised on the number of frequency channels which were included in the accumulation for each trace, to allow for a relative intensity comparison between the different traces.

40: Except of the cases, where a non-thermal signal is already detected below $P_{rf} \leq -35\,\mathrm{dBm}$, of course: Especially for 10.9 (b) and (c) which correspond to a maximum in the antenna excitation spectrum, an onset of the population well below $P_{rf} = -35\,\mathrm{dBm}$ is detected (note that this corresponds to an applied power of $P_{rf} \approx 300\,\mathrm{nW}$), hence making the background removal difficult. In these cases only the first spectrum is used, which has the disadvantage of a poorer background estimation and thus results in an increased noise particularly on the secondary modes.

41: Within the region of interest (ROI), the TFPI stage scanning speed is reduced to increase the counting time / signal accumulation per channel. The speed change at the borders of the ROI can yield a frequency shift and is therefore avoided (anyway the poor signal outside of the ROI is irrelevant).

Linear intensity scaling and expected drop at the instability onset

Note that in all power traces in figure 10.9 and later on, the intensity as well as the power are scaled logarithmically. Consequently, a linear appearing feature in figure 10.9 is accurately described by $\log_{10}(I_{BLS}(P_{rf})) = a \cdot \log_{10}(P_{rf}) + \log_{10}(b)$ and hence transforms to

$$I_{BLS}(P_{rf}) = b \cdot P_{rf}^{a} \tag{10.5}$$

where the proportionality factor b is a non-trivial expression depending not only on the antenna excitation efficiency, but also the BLS detection efficiency [97] and a quantitative evaluation is not of interest in this study. The exponent[42] a is a function of the applied microwave power, as is clearly seen for the cases (b, c) in figure 10.9. Essentially, $a = 1$ for the direct excitation of primary magnons in the linear regime. Consequently, a deviation from this linear scaling at large pumping powers can be linked to an onset of nonlinear processes.

[97]: Pirro (2014), 'Lineare und nichtlineare Spinwelleninteraktionen in magnetischen Mikrostrukturen'

42: Or "the slope a", if thinking in the double logarithmic scaling as in figure 10.9. From now on simply denoted as *scaling factor*.

Indeed, a linear behaviour is observed in figure[43] 10.9 (a) for $f_{rf} = 6.85\,\mathrm{GHz}$, where no secondary modes are detected in the corresponding spectra in figure 10.6. As expected, a deviation from the linear behaviour is observed in figure 10.9 (b, c) especially in the power range marked by the grey background, within which the signal of the secondary modes is above the thermal noise.

43: Printed on the next page for a more convenient comparison with the subsequent figure especially for the printed manuscript, where no hyperlinks allow to "jump" between figures.

In addition to this expected behaviour for a second order Suhl instability onset, two interesting features are to be pointed out here: First, a *pre-drop* is observed as pointed out by the green arrows in figure 10.9 (b, c), i.e. a drop in the intensity increase of the primary magnon mode before the intensity of the secondary modes rises above the thermal level. This is in principle not surprising, as similar features were observed in other studies [97, 427]. However, it needs to be noted that such a pre-drop[44] cannot be related to the energy dissipation by a scattering into the secondary modes f^+ and f^-, but instead is a signature for an additional, "hidden" process. Second, while for a second order Suhl instability the intensity increase of the primary mode above the critical threshold is expected to drop due to the energy transfer into the secondary modes, $I(f_{prim})$ is still expected to rise with a reduced scaling factor a [403], and not expected to decrease as in figure 10.9 (b) or stagnate as in figure 10.9 (c). Thus, this is another sign for an additional, "hidden" process limiting the population of the primary mode.

[97]: Pirro (2014), 'Lineare und nichtlineare Spinwelleninteraktionen in magnetischen Mikrostrukturen'
[427]: Mohseni et al. (2021), 'Controlling the Nonlinear Relaxation of Quantized Propagating Magnons in Nanodevices'

44: Not a common/fixed terminology, but will be used throughout this analysis.

[403]: L'vov (1994), *Wave Turbulence under Parametric Excitation*

Therefore, these two points are relevant to address in more detail prior to the determination of a critical power threshold.

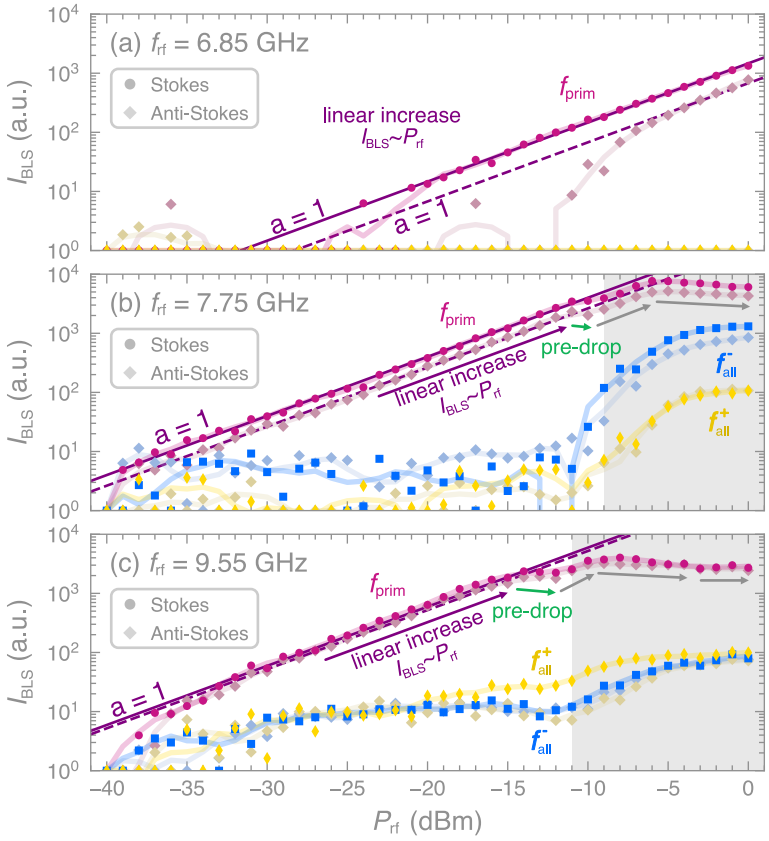

Figure 10.9: Spectral intensity traces extracted from the measurements at (a) f_{rf} = 6.85 GHz, (b) f_{rf} = 7.75 GHz and (c) f_{rf} = 9.55 GHz, for which the selected high-power spectra are shown in figure 10.6. The circles in bold colours show the data from the Stokes signal, the diamonds in muted colours show the data from the corresponding Anti-Stokes signal. The grey background boxes indicates the nonlinear power range within which the signal of all secondary traces is clearly above the thermal threshold level, precisely $P_{rf} \geq -9$ dBm for (b) and $P_{rf} \geq -11$ dBm for (c). The faint lines connecting the data points are a guide to the eye and were created using a Savitzky-Golay smoothing[47]. The traces show the accumulated data within $|f_{prim}| = f_{rf} \pm 350$ MHz, and 6.6 GHz $< |f_{all}^-| < f_{rf} - 350$ MHz and $f_{rf}+350$ MHz $< |f_{all}^+| <$ 11 GHz. The signal for every trace is normalised on the number of TPFI channels involved (frequency range covered). Prior to the extraction of the intensity traces, the background is removed, for which the average of the (a) 5, (b, c) 1 spectra with the lowest applied microwave powers is subtracted. The purple lines indicate a linear scaling, i.e. with the coefficient $a = 1$ in equation 10.5. The green and grey arrows in (b, c) indicate a deviation from the linear behaviour.

47: Hardly relevant if only considering the lines as a guide to the eye, but still it is specified that the Savitzky-Golay filter essentially is a kind of low-pass filter [450] and removes high frequency noise from data, and therefore used here for "smoothened" lines as guides. At each point, a least squares fit with a polynomial of higher order is performed - here a 3rd order polynomial was used within a window size of 7 data points (i.e. ±3 around the central point). Note that the smoothening cannot be used for an evaluation, since some features as for instance the *pre-drop* are at risk to be "smoothened" out.

[450]: Savitzky et al. (1964), 'Smoothing and Differentiation of Data by Simplified Least Squares Procedures.'

45: As the spin wave amplitude increases, the precession cone around the equilibrium axis "opens" and hence the projection M_z on the equilibrium axis deviates increasingly from M_S. As pointed out before, this notably implies a limitation of descriptions based on the linearisation of the LLG, but also gives rise to the self-induced nonlinear shift mentioned next.

46: Can be understood as a change in the self-induced effective field, as introduced in section 8.2.2 on page 164.

[97]: Pirro (2014), 'Lineare und nichtlineare Spinwelleninteraktionen in magnetischen Mikrostrukturen'

[427]: Mohseni et al. (2021), 'Controlling the Nonlinear Relaxation of Quantized Propagating Magnons in Nanodevices'

48: See the brief introduction of the technique on page 175.

***Pre-drop:* Instability of f_{prim} before the detected onset of $f^{\pm}$**

A reduction of the intensity scaling with the applied pumping power compared to the linear regime can have two generalised origins: (1) a decreased efficiency of the excitation mechanism, as well as (2) a dissipation of the energy away from the excited mode e.g. by multi-magnon scattering mechanisms (and of course, a combination of both). While the general classification seems rather simple, the underlying mechanisms can become arbitrarily complex not only on the side of the dissipation channels. Factors reducing the pumping efficiency by the antenna can be e.g. the enlarged precession cone yielding a reduced magnetisation projection M_z[45] to couple to the pumping antenna field. In relation, clearly also the increasing self-induced frequency shift with increasing precession cone[46] comes into play. Other effects can be an altered impedance of the device due to the excitation of magnon modes, or simply an increased heating and hence larger ohmic resistance of the structure.

Yet, especially the heating and the reduced coupling to the pumping field are expected to yield a rather continuous build-up of the deviation as is observed for large excitation frequencies in the comparative study in [97]. Here, instead, an abrupt drop is identified in most power traces, as indicated in the representative traces in figure 10.9 (b, c).

A similar behaviour has been reported by Mohseni *et al.* [427], where micromagnetic simulations were used to link the observation to a first "invisible" four-magnon scattering process into secondary modes which conserve the frequency: As the μBLS yields no wavevector resolution[48], a population of such secondary modes is impossible to distinguish from the direct excitation in the spectra. However, depending on the related wavevector, the modes can present a reduced BLS detection efficiency compared to the primary mode, and consequently result in the observed intensity drop at the corresponding

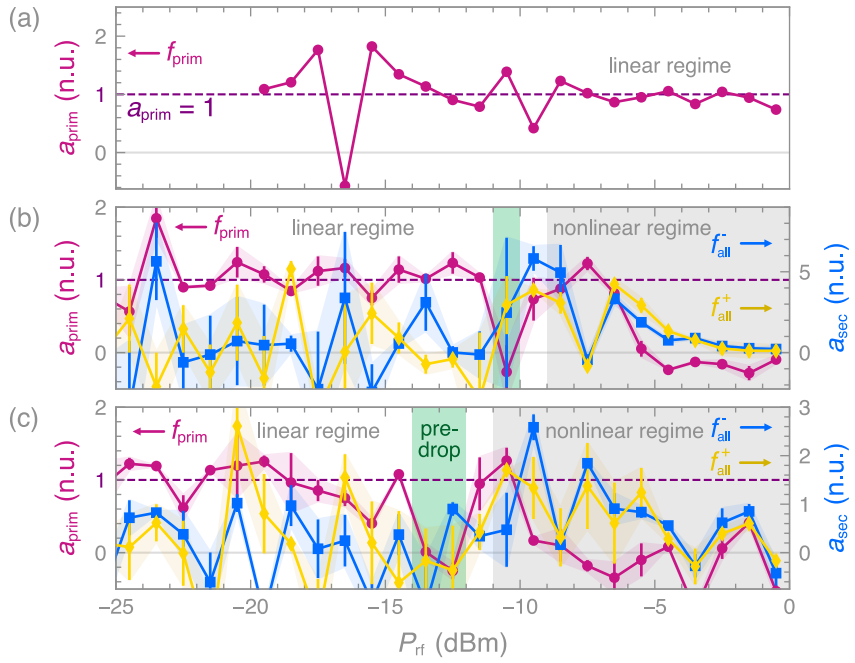

Figure 10.10: Extraction of the scaling factor $a = \frac{\log_{10}(I_{BLS})}{\log_{10}(P_{rf})}$ from the power traces shown in figure 10.9 for the directly excited primary magnon mode f_{prim}, and for the signal above and below, i.e. f^+_{all} and f^-_{all}, for (a) $f_{rf} = 6.85\,GHz$, (b) $f_{rf} = 7.75\,GHz$ and (c) $f_{rf} = 9.55\,GHz$. The linear regime corresponds to $a_{prim} = 1$ as indicated by the purple dashed line. The "(n.u.)" stands for *(no unit)*. Note that for (a) only the Stokes part is shown, while for (b) and (c) the slope parameter was extracted from Stokes and Anti-Stokes and the data in the figure corresponds to the average (to reduce noise). The shaded area in the same colour represents the difference between the Stokes and Anti-Stokes parameters, and is taken as an estimation for the error on each point. The grey background boxes are the same as in figure 10.9. The green background boxes indicate the pre-drop, corresponding to the first major deviation from the linear scaling. It is noted that while this can be easily made out in case (b), the rather noisy a parameters in case (c) require a correlation with the direct power traces in figure 10.9 (c) for a conclusion.

frequency. The study in [427] was performed in the Backward-Volume geometry and measured directly under the excitation antenna position[49], and the described process is essentially a feature of the BV dispersion relation yielding more than one possible wavevector for a given frequency. Although this is not directly transferable to the present study carried out in the Damon-Eshbach geometry and with a defined propagation direction as mentioned above, potential scattering partners for a similar frequency conserving "invisible" process could for instance involve the aforementioned waveguide width modes.

49: Measuring through the transparent sample backside, of course.

In principle, the evaluation of the scaling factor $a = \log_{10}(I_{BLS})/\log_{10}(P_{rf})$ is a neat way to identify the onset of an instability on the driven primary mode, simply by evaluating the point of a deviation from the linear scaling $I_{BLS}(P_{rf}) \sim P_{rf}$, i.e. the deviation from $a = 1$, as is remarkably successful in the analogous study in [97] on the (non-epitaxial) $Co_2Mn_{0.6}Fe_{0.4}Si$ waveguide mentioned before. Particularly, in the reference study in [97], the detailed evaluation of these scaling factor traces allows to exclude a cascaded scattering[50] and attribute the phenomenon to a reduced pumping efficiency notably related to a heating of the structure as mentioned above.

50: A cascaded event of a primary four magnon scattering into "invisible" modes at wavevectors outside of the detection range (invisible as the detection in µBLS is limited by the microwave aperture), which then (upon becoming instable themselves) in a secondary four magnon process scatter into the detected secondary modes f^+ and f^-. Hence, an effective four magnon scattering signature is observed within the detection range, but does not need to conserve momentum.

An attempt for an analogous scaling factor evaluation is presented in figure 10.10, again corresponding to the cases of the previous figures, i.e. the scaling parameters extracted from the power traces shown in the previous figure 10.9 are shown. Clearly, the signal to noise ratio proves insufficient for the analysis to rely only on the scaling factor a, yet it can be discussed in a joint evaluation with the power traces in figure 10.9 and the raw spectra in 10.6.

First, it is noted that the scaling of the primary excited mode f_{prim} in the linear regime in figure 10.10 (a) with $f_{rf} = 6.85\,GHz$ as well as in figure 10.10 (b) with $f_{rf} = 7.75\,GHz$ is rather stable around $a_{prim} = 1$. In the second case, the scaling factor a_{prim} therefore allows to identify the pre-drop behaviour as marked by the arrows in figure 10.9 (b): The scaling factor abruptly drops from $a_{prim} = 1$ to $a_{prim} < 0$ between $P_{rf} = -11\,dBm$ and $P_{rf} = -10\,dBm$ as is highlighted in figure 10.10 (b) by the green box, and subsequently an increase again to $a_{prim} = 1$ is observed between $P_{rf} = -10\,dBm$ and $P_{rf} = -8\,dBm$ which coincides with the onset of the detected population in the secondary

modes f^+ and f^- marked by the grey background like in figure 10.9 (b). Finally, a decrease is observed, where notably a drop below 0 is observed and $a_{\text{prim}} < 0$ is consistently maintained for $P_{\text{rf}} > -5\,\text{dBm}$, which corresponds to the aforementioned unexpected decrease[51].

51: Will be addressed on the following pages. The phenomenon is likely due to a combination of effects, notably including the self-induced nonlinear shift.

Concerning the scaling factors a_{sec} of the secondary magnon modes in figure 10.10 (b), an increased $a_{\text{sec}} \approx 2.5$ is noted to coincide with the green highlighted box between $P_{\text{rf}} = -11\,\text{dBm}$ and $P_{\text{rf}} = -10\,\text{dBm}$, which might raise the question on the pertinence and accuracy of the pre-drop identification. Yet, a verification of the respective spectra shows no identifiable intensity of the secondary modes for $P_{\text{rf}} < -9\,\text{dBm}$, and in general it is remarked that this change between $P_{\text{rf}} = -11\,\text{dBm}$ and $P_{\text{rf}} = -10\,\text{dBm}$ is on the order of the fluctuations which are equally observed in the thermal noise, i.e. for $P_{\text{rf}} \ll -11\,\text{dBm}$ on a_{sec} in the frequency ranges of f^+ and f^-. Moreover, the error bars indicate a large discrepancy between a_{sec} extracted from Stokes and Anti-Stokes, which further underlines the likeliness of a noise effect. In relation, it is noted that the laser mode is unfortunately close to the evaluation boundary[52] at 6.6 GHz and hence, although expected to be rather stable, a potential fluctuation or a drift can yield a similar increase of the detected intensity[53]. Therefore, instead of the scaling factor a_{sec}, it is decided to rely on the identification of a clear intensity above the thermal level ($f_{\text{rf}} = 7.45\,\text{GHz}$ and $f_{\text{rf}} = 7.75\,\text{GHz}$ in combination with a significant deformation of the laser mode [54]) in the respective BLS spectra for the determination of the population onset in f^+ and f^-. Nevertheless, once the intensity of the nonlinear modes is significantly above the thermal level, rather neat scaling factor traces are also obtained on a_{sec}, where a saturation of the intensity of the secondary modes is identified by $a_{\text{sec}} \approx 0$ for $P_{\text{rf}} > -3\,\text{dBm}$. Remarkably, although the population of the secondary modes stagnates, still a decrease is observed on the intensity of the primary mode as indicated by $a_{\text{prim}} < 0$.

52: Set right at the border of the laser mode to allow for an analysis particularly of the data with $f_{\text{rf}} \leq 8.35\,\text{GHz}$.

53: Zooming in, a slight drift might indeed be identified in the spectra in figure 10.6 (b).

54: A shoulder on the laser mode peak, which can be identified as f^-, typically coinciding with the onset of the above-thermal-level intensity of f^+.

Similar features can be identified in the case of $f_{\text{rf}} = 9.55\,\text{GHz}$, yet the rather enormous noise on the order of the feature strength makes an interpretation of the scaling parameter in figure 10.10 (c) strongly reliant on the simultaneous comparison with the power traces in figure 10.9 (c) and the spectra in figure 10.6 (c). Indeed, the pre-drop can be identified again with an abrupt drop of the scaling factor from $a_{\text{prim}} \approx 1$ to $a_{\text{prim}} < 0$ between $P_{\text{rf}} = -14\,\text{dBm}$ and $P_{\text{rf}} = -12\,\text{dBm}$, which coincides with the prominent feature on the intensity trace in figure 10.9 (c). Moreover, contrary to case (b), the significant rise of a_{sec} indeed now only starts with the shaded grey background, underlining a potential effect of the noise or fluctuating laser mode on the previous case (b). While the continuous $a_{\text{prim}} < 1$ for $P_{\text{rf}} = -18\,\text{dBm}$ to $-15\,\text{dBm}$ might imply a steady/gradual decrease from lower powers[55], it is noted that the scaling factors $a_{\text{prim}} > 1$ for $P_{\text{rf}} = -22\,\text{dBm}$ to $-19\,\text{dBm}$ have the counteracting effect, and hence the fluctuation of a_{prim} for $P_{\text{rf}} < -15\,\text{dBm}$ essentially showcases the noise on the data in figure 10.9 (c). Finally, above the population onset of the secondary mode[56] f^- at $P_{\text{rf}} = -11\,\text{dBm}$, the intensity scaling parameter a_{prim} of the primary mode is again found to drop consistently, and in particular from the point of a maximal a_{sec} between $P_{\text{rf}} = -10\,\text{dBm}$ and $P_{\text{rf}} = -9\,\text{dBm}$ yields $a_{\text{prim}} \lesssim 0$.

55: This would show in a gradual decrease from the linear slope, with a "rounding" effect on the intensity trace.

56: Recall that the corresponding f^+ is out of the detection range in this case.

These observations of $a_{\text{prim}} < 0$ at high pumping powers can be an indication for an onset of an instability of the secondary modes themselves, leading to a further energy redistribution within the magnonic system. In relation, it can be noted that indeed also an increase of the background is observed in the spectra for these large powers, which can be seen in figure 10.6 (b) for instance for frequencies $|f_{\text{BLS}}| \gtrsim 9.2\,\text{GHz}$. Yet, albeit a self-enhancement of the instability processes is expected above the critical threshold, it is pointed out

again that a continuous decrease on the intensity-power trace of the primary mode is not expected for the second order Suhl instability in the critical regime. The observations are thus unlikely attributable to an instability process of the secondary modes f^+ and f^- alone, but likely additional contributions to a further reduction of the intensity increase at f_{prim}.

Concerning this, it is recalled again that the continuous decrease of the intensity on the primary mode implies a governing efficiency of the energy dissipation away from f_{prim} over the population increase by the pumping power. In principle, this can be a signature of an unlocked damping channel, e.g. in the form of a very efficient multi-scattering cascade[57], or a further instability involving a scattering from the primary mode to invisible scattering partners. However, a conclusion is not trivial in this system, since various other effects can reduce the pumping efficiency with increasing applied power, notably the increased nonlinear shift and reduced coupling efficiency due to the increasing precession cone, as well as impedance changes or ohmic losses, as pointed out at the beginning of this section.

Hence, although the evaluation of the scaling factor $a = \frac{\log_{10}(I_{\mathrm{BLS}})}{\log_{10}(P_{\mathrm{rf}})}$ is found to be insufficient for a determination of the instability threshold, it is not irrelevant in this study as it brings attention to the potential importance of the self-induced nonlinear shift particularly for the nonlinear dynamics at large[58] powers in this system.

57: Used as a terminology in literature for a combination of multiple subsequent multi-magnon scattering processes, notably used for instance for a thermalisation of a magnon BEC [422, 427, 451, 452].

[422]: Livesey et al. (2007), 'Parametric spin wave excitation and cascaded processes during switching in thin films'
[427]: Mohseni et al. (2021), 'Controlling the Nonlinear Relaxation of Quantized Propagating Magnons in Nanodevices'
[451]: Kreil et al. (2018), 'From Kinetic Instability to Bose-Einstein Condensation and Magnon Supercurrents'
[452]: Sobucki et al. (2025), 'Goos–Hänchen shift of inelastically scattered spin-wave beams and cascade nonlinear magnon processes'

58: In this study. Note that this is still lower than the applied microwave powers e.g. in [86, 427].

[86]: Pirro et al. (2014), 'Non-Gilbert-damping Mechanism in a Ferromagnetic Heusler Compound Probed by Nonlinear Spin Dynamics'
[427]: Mohseni et al. (2021), 'Controlling the Nonlinear Relaxation of Quantized Propagating Magnons in Nanodevices'

Signature of nonlinear shift

For an evaluation of the significance of the nonlinear shift over the other listed effects, the two measurements at the excitation frequencies $f_{\mathrm{rf}} = 7.15\,\mathrm{GHz}$ and $f_{\mathrm{rf}} = 8.05\,\mathrm{GHz}$ are of particular interest: As was already pointed out at the beginning of the analysis, $f_{\mathrm{rf}} = 7.15\,\mathrm{GHz}$ corresponds to an excitation frequency quite exactly at the lower boundary of the measured and mapped excitation spectra. And $f_{\mathrm{rf}} = 8.05\,\mathrm{GHz}$ is an analogously interesting case, as it corresponds to a frequency just below the first minimum in the measured excitation spectra, see the recalled spectral position in relation to the antenna excitation spectrum in figure 10.11. The two related intensity traces are shown in figure 10.12 in analogy to the intensity traces in figure 10.9.

In the case in figure 10.12 (a) for $f_{\mathrm{rf}} = 7.15\,\mathrm{GHz}$, i.e. the fixed excitation frequency just below the main antenna spectrum, a deviation from the linear increase is observed, but instead of a drop, an enforced increase with $a_{\mathrm{prim}} \gg 1$ is obtained for $P_{\mathrm{rf}} > -3\,\mathrm{dBm}$. Shortly after this, for $P_{\mathrm{rf}} = -1\,\mathrm{dBm}$, an intensity of a secondary magnon mode f^+ above the thermal level is detectable as marked by the grey background. This is a strong signature for the self-induced nonlinear shift: As the dispersion relation shifts to lower frequencies, the excitation with the frequency $f_{\mathrm{rf}} = 7.15\,\mathrm{GHz}$ becomes increasingly efficient, and the intensity increase is therefore not only driven by the applied power, but also by the effective pumping efficiency increase related to this frequency shift.

Moreover, it is remarkable that the effect persists over a power range from $P_{\mathrm{rf}} = -3\,\mathrm{dBm} \approx 0.5\,\mathrm{mW}$ to $P_{\mathrm{rf}} = 0\,\mathrm{dBm} = 1\,\mathrm{mW}$. As pointed out above, the self-induced nonlinear shift is linked to the opening of the precession cone, which in return also reduces the coupling strength to the antenna field. Yet, clearly, the efficiency gain from the excitation maximum shifting towards the fixed frequency $f_{\mathrm{rf}} = 7.15\,\mathrm{GHz}$ governs over the pumping reduction linked to the increased oscillation amplitude.

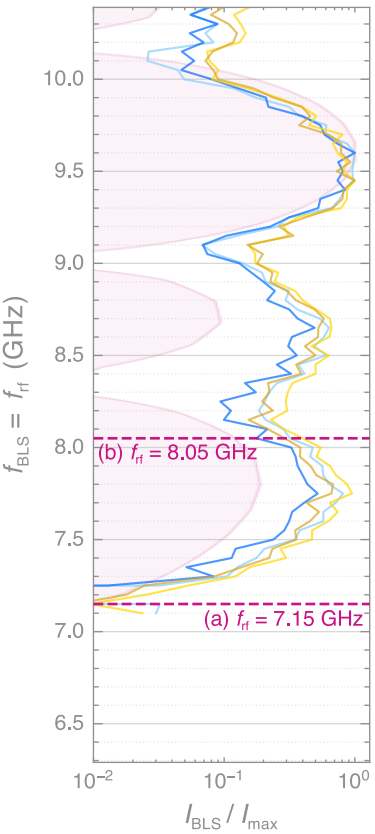

Figure 10.11: Spectral position of the two excitation frequencies (a) $f_{\mathrm{rf}} = 7.15\,\mathrm{GHz}$ and (b) $f_{\mathrm{rf}} = 8.05\,\mathrm{GHz}$ discussed in this subsection.

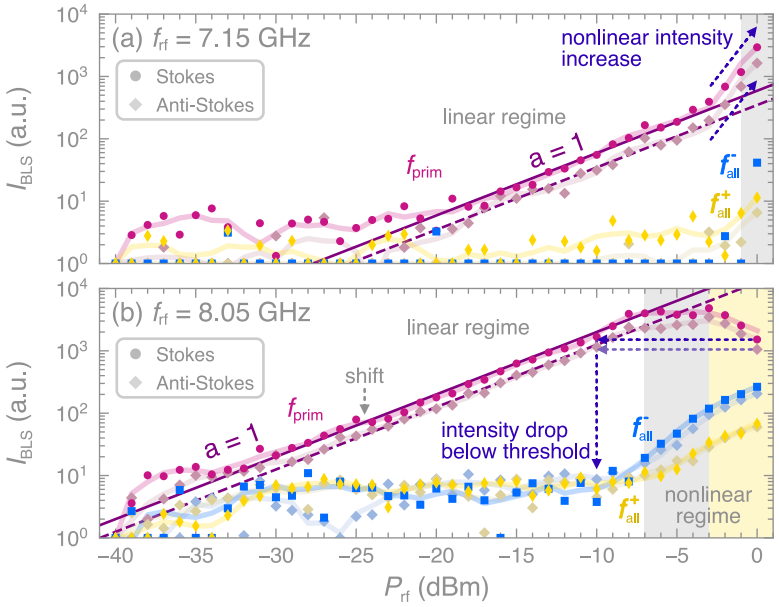

Figure 10.12: Indications for a nonlinear shift in the power traces for (a) f_{rf} = 7.15 GHz and (b) f_{rf} = 8.05 GHz, which approximately correspond to the upper and lower limit of the first excitation maximum, as seen in figure 10.5, were it corresponds to cases (l) and (i) respectively. As in all precedent figures, the grey background boxes highlight the power range, in which a population of f^+ and/or f^- is identified in the BLS spectra. The additional yellow background box in (b) highlights the range in which a drastic intensity drop is reached. The purple arrows indicate in (a) the significant nonlinear intensity increase, and in (b) relate the final intensity of f_{prim} at P_{rf} = 0 dBm to the linear regime, showing that I_{prim} (0 dBm) corresponds to intensities, and thus pumping powers, significantly below the critical threshold. Note that due to the proximity of the laser mode, f^- could not be read out for the Anti-Stokes part in case (a).

In analogy, the case figure 10.12 (b) for f_{rf} = 8.05 GHz corresponds to an "opposite" example, and yields more complex intensity traces: As the excitation power is increased, a first deviation from the linear regime is observed at the critical threshold power P_{rf} = −7 dBm, which coincides with the onset of the scattering into the secondary magnon modes f^+ and f^- as is again marked by the grey background. With a further power increase, the intensity first approximately stagnates[59], and then again from P_{rf} = −3 dBm ≈ 0.5 mW drastically decreases with $a_{prim} \ll 0$ as is highlighted by the yellow background. In this regime, i.e. $P_{rf} > -3$ dBm, still an increase of the intensity in the secondary modes is observed, yet clearly with a reduced a_{sec} compared to the grey highlighted area with −7 dBm < P_{rf} < −3 dBm, hence the pumping rate into the secondary modes reduces and does not account for the significant drop in the intensity of the primary mode. Remarkably, the intensity drops to a value I_{prim} (0 dBm) ≈ I_{prim} (−10 dBm), which is significantly below the critical power threshold and yields a reduction by a factor ∼ 2 compared to the intensity at the critical threshold I_{prim} (−7 dBm) which coincides with the power ratio between P_{rf} = −3 dBm ≈ 0.5 mW to P_{rf} = 0 dBm = 1 mW.

59: Except of one data point. A zoom-in on this data set is shown in figure 10.13.

Considering the spectral position of f_{rf} = 8.05 GHz on the antenna excitation spectrum, this can again be linked to the increasing influence of the nonlinear shift, here shifting the antenna spectrum such that a reduction of the effective pumping power is obtained for the fixed excitation frequency f_{rf} = 8.05 GHz. However, it must be noted that with the increased nonlinear shift and in general increased scattering and nonlinearities in the system, a broadening of the antenna spectrum is also expectable as discussed in subsection 10.1.2 around figure 10.4, and hence the minimum might not be sufficiently well-defined to account for the intensity drop. As mentioned above, it is possible that additionally further scattering processes come into play, redistributing the energy to other modes in the system which can be out of the detection range. Equally, an impedance change due to the increasing excitation of the magnonic system cannot be excluded. Yet, the consistent observation over a power range from P_{rf} = −3 dBm ≈ 0.5 mW to P_{rf} = 0 dBm = 1 mW is interpreted as an indication for a rather insignificant heating induced ohmic resistance increase.

Hence, although the precise underlying effects are certainly much more complex than the rather simple picture described above, the observations can

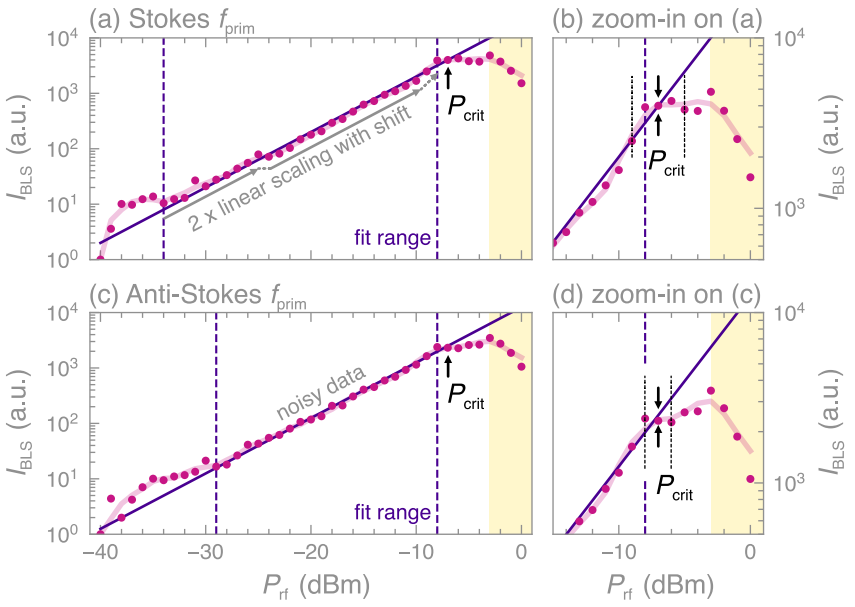

Figure 10.13: Extraction of the critical threshold power P_{crit} from the deviation of the data compared to a slope with $a = 1$ for (a) the Stokes part, for which a zoom-in on the extraction region is given in (b), and for (c) the Anti-Stokes part with the corresponding zoom-in in (d). As annotated in the zoom-in subplots in (b) and (d), P_{crit} is read out as the "last power on the line", i.e. the power above which the data consistently deviates from the linear scaling, which is indicated by the black arrows in the two cases. The error on the value is determined by the noise around the point: The dashed black lines indicate the error interval $P_{crit} \pm \Delta P_{crit}$, where ΔP_{crit} is set as the distance to the next clear deviation from the linear scaling. Naturally, the minimal read out error is $\Delta P_{crit} = 1\,\mathrm{dB}$. Additionally a few annotations are made and will be discussed in the text: The yellow background highlights the area of constant decrease in all subplots. The grey arrows in (a) trace the slope which seems to present a shift at $P_{rf} = -24\,\mathrm{dBm}$.

be interpreted as a clear indication for a significant self-induced nonlinear shift. Consequently, it can be concluded that the characteristical antenna spectrum plays a major role, not only defining the critical power threshold but also the further supercritical behaviour of the system.

Critical threshold power and onset of f^+ and f^-

Based on the results from the above discussion, two relevant threshold power levels are identified in this study: The power, from which the directly excited magnon mode deviates from the linear scaling $I_{prim} \sim P_{rf}$, as well as the power, from which an onset of the secondary magnon modes f^+ and/or f^- is detected in the BLS spectra. As the identification of the thresholds based on the scaling parameter a was rather unsuccessful with the data in this study, a different approach is employed here.

Firstly, for the determination of the critical threshold power, the individual power traces from the Stokes and the Anti-Stokes signal of the direct excitation f_{prim} are instead evaluated by "fitting" a linear function with a slope of $a = 1$ to the data[60] and reading out the power value for each power trace, from which a significant/continuous deviation from this line is observable. Particularly for excitation frequencies outside of the main two maxima, the error by this procedure is increased due to the increased noise on the power traces and is therefore individually estimated based on the noise around the extraction point and the proximity of the next clearer feature. An example is given in figure 10.13 for the case of $f_{rf} = 8.05\,\mathrm{GHz}$, which corresponds to the excitation just at the upper limit of the first antenna excitation maximum[61]. Secondly, the onset of the secondary modes f^+ and f^- is determined differently: A Lorentzian peak function is fitted to the secondary modes, mainly in order to determine the spectral position as were shown in figure 10.7, and to trace the shifting modes in the second characteristic regime, as will be discussed hereafter. The onset is in this case simply determined as the lowest power, from which a sufficient signal is obtained in the spectra for a successful fitting of the secondary mode peaks.

The extracted critical threshold and onset powers from Stokes and Anti-Stokes are averaged and shown as a function of the excitation frequency in figure 10.14,

60: As the slope is fixed, this might seem counter-intuitive and the term "fitting" certainly appears wrong, but the variable parameters are still the offset and also the limitation of the fit range (data selection boundaries).

61: Compare to case (i) in figure 10.5, or case (b) in figures 10.11 and 10.12 just before.

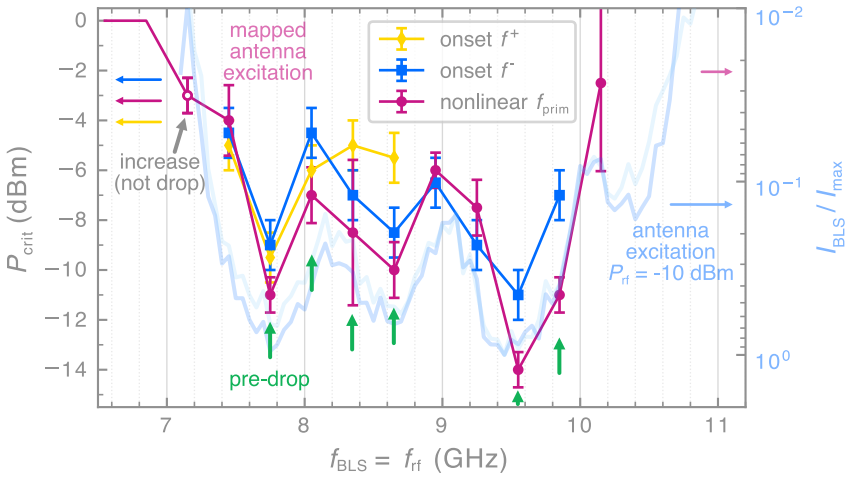

Figure 10.14: Critical power threshold from the nonlinear scaling of the direct excitation of f_{prim}, as well as the onset of the detected nonlinear modes labelled as f^+ and f^- as defined in figure 10.6, as a function of the fixed excitation frequency. In the background, the antenna spectrum from figure 10.4 is recalled. Note that except of the point marked by the unfilled circle for f_{rf} = 7.15 GHz, all thresholds of f_{prim} correspond to a subsequent drop of the intensity scaling, or even a decrease. Only for f_{rf} = 7.15 GHz an increase is detected instead, which is linked to the nonlinear shift of the antenna excitation spectrum.

where in addition the mapped and excited antenna spectra from figure 10.4 are recalled for comparison. It is noted, that the smallest error bars as for instance on the point at f_{rf} = 7.15 GHz are simply related to the power resolution, whereas the larger error bars, e.g. for f_{rf} = 10.15 GHz are related to a significant noise in the read-out range. Nevertheless, the general behaviour clearly mimics the excitation efficiency spectrum defined by the antenna geometry, where the lowest threshold and onset powers coincide with the main antenna maxima. Moreover, the pre-drop shows here as a reduced nonlinear threshold power read-out from f_{prim} (pink circles) compared to the secondary population onset (yellow diamonds, blue squares) and as pointed out by the green arrows is not only observed in the three power traces for f_{rf} = 7.75 GHz, 8.05 GHz and 9.55 GHz discussed in detail above, but also (within the resolution) for f_{rf} = 8.35 GHz, 8.65 GHz, 9.85 GHz, all falling within the main excitation range.

The lowest critical threshold power and nonlinear population onset in f^- are obtained for an excitation coinciding with the global antenna excitation maximum at f_{rf} = 9.55 GHz: Here, the deviation from the linear scaling is observed for powers as low as $P_{rf} = -14$ dBm ≈ 40 µW[62], and a significant population of the secondary magnon mode f^- is detectable for $P_{rf} = -11$ dBm ≈ 80 µW. For $P_{rf} < -11$ dBm, no other point in the probed spectral range is found to exhibit an instability.

For $P_{rf} \geq -11$ dBm ≈ 80 µW, a nonlinear power scaling is equally detected for the second excitation maximum with f_{rf} = 7.75 GHz with a clear onset of the secondary modes at $P_{rf} \approx -9$ dBm ≈ 126 µW. Additionally, also the excitation at f_{rf} = 9.85 GHz becomes nonlinear at $P_{rf} \geq -11$ dBm ≈ 80 µW, but an onset of the secondary modes is only observed at $P_{rf} \approx -7$ dBm ≈ 200 µW, which might be linked to the significantly increased wavevector yielding different scattering partners and different coupling efficiencies for the underlying four magnon scattering process.

For $P_{rf} \geq -9$ dBm ≈ 126 µW, the excitation is found to exhibit nonlinear signatures already for 5 excitation frequencies, and ultimately, for $P_{rf} \geq -2$ dBm ≈ 630 µW, the entire excitation range $7.45 \leq f_{rf} \leq 10.15$ GHz is found to exhibit nonlinear dynamics.

As mentioned before, such low instability thresholds are not known to have been reported in any previous report on a metallic magnonic sample system. In particular, in most studies the critical power threshold above P = 0 dBm = 1 mW: In the reference study in [97] on a similar, but non-epitaxial $Co_2Mn_{0.6}Fe_{0.4}Si$ waveguide of comparable parameters the minimal

62: See figure 10.14 for the errors, which are omitted in the text for an improved readability.

[97]: Pirro (2014), 'Lineare und nichtlineare Spinwelleninteraktionen in magnetischen Mikrostrukturen'

reported critical threshold power[63] is $P^{\text{crit}} = 0\,\text{dBm} = 1\,\text{mW}$, and in a $Ni_{81}Fe_{19}$ waveguide studied in a similar configuration in [421], even larger microwave powers are applied for an instability onset, where $P^{\text{crit}} \gtrsim 12\,\text{dBm} \approx 16\,\text{mW}$ is reported[64]. It needs to be acknowledged, that a direct comparison of absolute values between different studies is principally incorrect, not only because the different antenna and device geometries yield different excitation characteristics, but also since technical factors such as the device/antenna impedance matching as well as the losses in the microwave setup additionally come into play. Nevertheless, the nonlinear dynamics at applied microwave powers which are more than an order of magnitude below the commonly reported values for metallic systems certainly underlines the potential in the half-metallic Co_2MnSi compound for nonlinear magnonic applications.

63: For $\mu_0 H_{\text{ext}} = 48\,\text{mT}$ and $f_{\text{rf}} = 8.25\,\text{GHz}$.

[421]: Schultheiss et al. (2012), 'Direct observation of nonlinear four-magnon scattering in spin-wave microconduits'

64: Based on the observable features in the colormaps in the publication [421] and a cross-reading in the related PhD thesis [453]. For $\mu_0 H_{\text{ext}} = 51\,\text{mT}$ and $f_{\text{rf}} \approx 7.8\,\text{GHz}$.

[453]: Schultheiß (2010), 'Kohärenz und Dämpfungsverhalten von Spinwellen in magnetischen Mikrostrukturen'

In relation, particularly the study by Hache *et al.* [60] is of interest, where the nonlinear dynamics in a $Pt/Co_{60}Fe_{60}B_{20}$ waveguide are investigated as a function of the injected spin current[65]: In the absence of a spin current, the authors report a purely linear operation for an applied microwave power of $P_{\text{rf}} = -5\,\text{dBm}$, while the application of a 6 mA enables a significant population of four secondary magnon modes. Yet, in the $Pt/Co_{60}Fe_{60}B_{20}$ system, the effective damping is comparably poor with $\alpha = 0.016$ on the reference thin film [60]. Given the confirmed half-metallicity by J. Solano [91] even in the microstructured waveguide investigated here, as well as the already much reduced damping and the (certainly related) nonlinear threshold powers determined in the present study, an even superior performance can be expected when using the half-metallic Co_2MnSi as a base for similar applications.

[60]: Hache et al. (2023), 'Control of Four-Magnon Scattering by Pure Spin Current in a Magnonic Waveguide'

65: Generated by spin Hall effect in the Pt layer, transferred to the $Co_{60}Fe_{60}B_{20}$, where the resulting spin orbit torque (SOT) counteracts the Gilbert damping torque, and hence yields an effective damping reduction lowering the threshold of the nonlinear dynamics.

[91]: Solano Córdova (2024), 'Temperature dependent spin wave study of magnetic properties and spin-polarized electron transport in $Fe_{1-X}V_X$ and Co_2MnSi epitaxial films'

Additionally, the device-specific excitation characteristics especially the combination of the refined antenna excitation spectrum with the significant nonlinear shift detailed above could yield further peculiar features: Nonlinear shifts are already exploited in various ways, e.g. for an conversion of dipolar spin waves to exchange spin waves by exploiting the shift as the excited spin waves travel out of the excitation region [454] and equally for an erasing of spin waves by shifting out of the resonant dispersion [58]. In relation, in particular the above discussed frequency dependent excitation power dynamics could be exploitable as a frequency selective element for a nonlinear functionality in magnonic circuits, where for an operation below the excitation spectrum a drastic increase of the intensity is observed above a threshold power, while for an operation below a local minimum the device yields a self-capping effect with an intensity decrease to pre-nonlinear-threshold levels. This could be of interest for a frequency selective, nonlinear limiting functionality for the pumping into unconventional magnonic computing circuits.

[454]: Wang et al. (2023), 'Deeply nonlinear excitation of self-normalized short spin waves'

[58]: Breitbach et al. (2024), 'Nonlinear erasing of propagating spin-wave pulses in thin-film Ga'

Indeed, the results are not only interesting for a device operation relying on this specific antenna characteristic, but similarly the critical thresholds can be overcome by exploiting a coupling into nonlinear ring resonators for a self-enhancement of the spin wave intensity [54, 455, 456]. In such devices, the frequency selectivity is given by the device geometry and hence similar to the above antenna excitation, an operation just below, or just above the maximal transmission condition of the ring resonator could yield an analogous drastic enhancement or self-capping threshold behaviour for the transmitted spin wave amplitudes. Such frequency selective amplitude-dependent transmission characteristics are notably of interest for the exploitation in artificial neural networks [53, 56] and are mostly studied in YIG based systems [54, 455, 456] due to the superior spin wave propagation compared to common CoFeB ($Co_{60}Fe_{60}B_{20}$) or permalloy ($Ni_{81}Fe_{19}$) devices. Again, the half-metallic Co_2MnSi could yield a desirable functionality: Not only an improvement compared to the poor properties of the common metals can be expected, but the possibility

[54]: Wang et al. (2020), 'A nonlinear magnonic nano-ring resonator'

[455]: Odintsov et al. (2024), 'Lateral and vertical spin-wave transport in a multimode magnonic ring coupler'

[456]: Vilsmeier et al. (2025), *Spin wave propagation in a ring-shaped magnonic waveguide*

[53]: Brächer et al. (2018), 'An analog magnon adder for all-magnonic neurons'

[56]: Fripp et al. (2023), 'Nonlinear chiral magnonic resonators: Toward magnonic neurons'

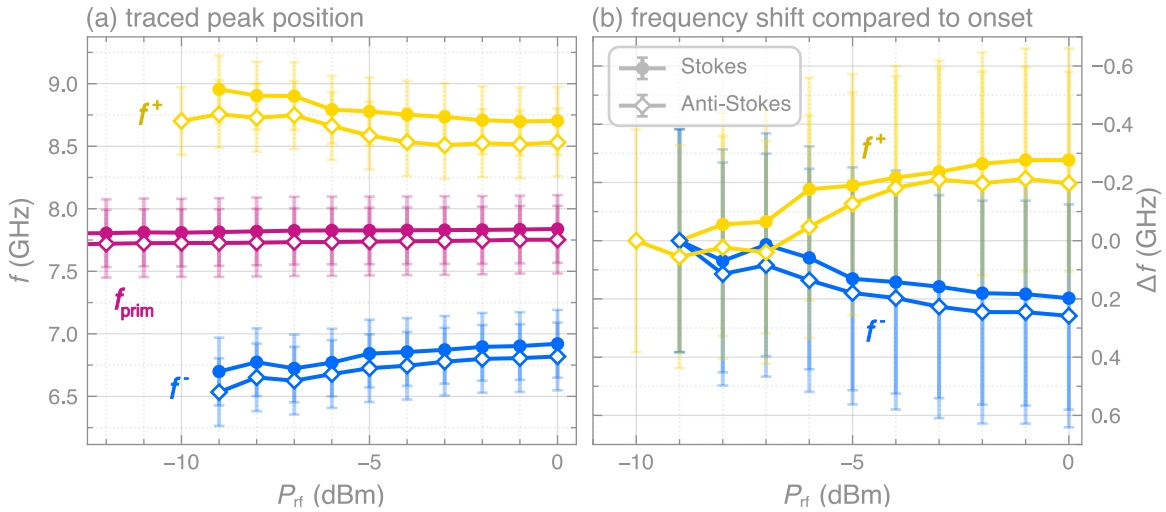

Figure 10.15: Frequency shift of the secondary modes in the supercritical regime at $f_{rf} = 7.75\,\text{GHz}$ in (a) observable in the tracing of the spectral position of the different modes, and in (b) quantified as $\Delta f^{\pm} = |f^{\pm}(P_{onset}) - f^{pm}(P_{rf})|$ where P_{onset} is the onset power as determined above and plotted in figure 10.14. This excitation frequency at $f_{rf} = 7.75\,\text{GHz}$ corresponds to an excitation at the first local antenna maximum, see figure 10.5 (j) and 10.14. The corresponding spectra are shown in figure 10.6 (b) and the power trace is shown in figure 10.9 (b). Note that the general down-shift of the anti-Stokes frequency is a technical asymmetry related to the TFPI scanning direction [453] and does not indicate a physical asymmetry of the four magnon scattering process.

of a spin current induced spin wave Doppler shift [43, 91] introduces an additional parameter compared to the insulating YIG based devices[66].

First supercritical regime and frequency shift

In view of such a device operation, also the observed stability of the scattering into distinct secondary magnon modes in the second frequency excitation regime, i.e. for $7.45\,\text{GHz} \leq f_{rf} \leq 8.65\,\text{GHz}$, pointed out at the beginning of the analysis is another interesting feature: As is clear from the overview in figure 10.5 (g - k), the secondary magnon modes f^+ and f^- are traceable over the entire applied power range and particularly for the excitation at $f_{rf} = 7.75\,\text{GHz}$ over a power range of up to $\Delta P_{rf} = 10\,\text{dB}$, i.e. an increase of one order of magnitude in the pumping power.

The intensity mapping in figure 10.5 (g - k) as well as the BLS spectra in figure 10.6 (b) for the exemplary case with $f_{rf} = 7.75\,\text{GHz}$ also show a nonlinear frequency shift of the secondary modes after the onset, and as mentioned above the fitting of a Lorentzian peak allows for an extraction of the frequency as is shown in figure 10.15 again on the example of $f_{rf} = 7.75\,\text{GHz}$. In the comparative study in [97], the extracted supercritical frequency shift is a linear function of the applied microwave power, and is modeled by a linear relation to the reduction of the magnetisation projection M_z on the equilibrium axis. In the present study, no clear linear behaviour is observed which is not only attributed to the massive error bars in figure 10.15 linked to the poor signal to noise ratio, but also a feature of the peculiar antenna geometry modulating the effective pumping power due to the above discussed nonlinear shift of the defined excitation spectrum, ultimately resulting in a modification of the linear scaling of the magnetisation projection with the applied excitation power. Nevertheless, the stability of the scattering into distinct secondary modes in this frequency range again underlines the potential for an operation similar to the study in [60], not only by a potential injection of spin currents, but similarly by an enhancement e.g. within the transmission condition of the potential aforementioned ring resonator.

[453]: Schultheiß (2010), 'Kohärenz und Dämpfungsverhalten von Spinwellen in magnetischen Mikrostrukturen'

[43]: Vlaminck et al. (2008), 'Current-Induced Spin-Wave Doppler Shift'

[91]: Solano Córdova (2024), 'Temperature dependent spin wave study of magnetic properties and spin-polarized electron transport in $Fe_{1-X}V_X$ and Co_2MnSi epitaxial films'

66: In principle, a similar Doppler frequency shift phenomenon can be induced by introducing surface acoustic waves as a moving Bragg grating for spin wave scattering in YIG [457], yet in that case the exploitation is limited to the operation in a narrow frequency range, linked to the matching condition to the phonon dispersion.

[457]: Chumak et al. (2010), 'Reverse Doppler effect of magnons with negative group velocity scattered from a moving Bragg grating'

[97]: Pirro (2014), 'Lineare und nichtlineare Spinwelleninteraktionen in magnetischen Mikrostrukturen'

[60]: Hache et al. (2023), 'Control of Four-Magnon Scattering by Pure Spin Current in a Magnonic Waveguide'

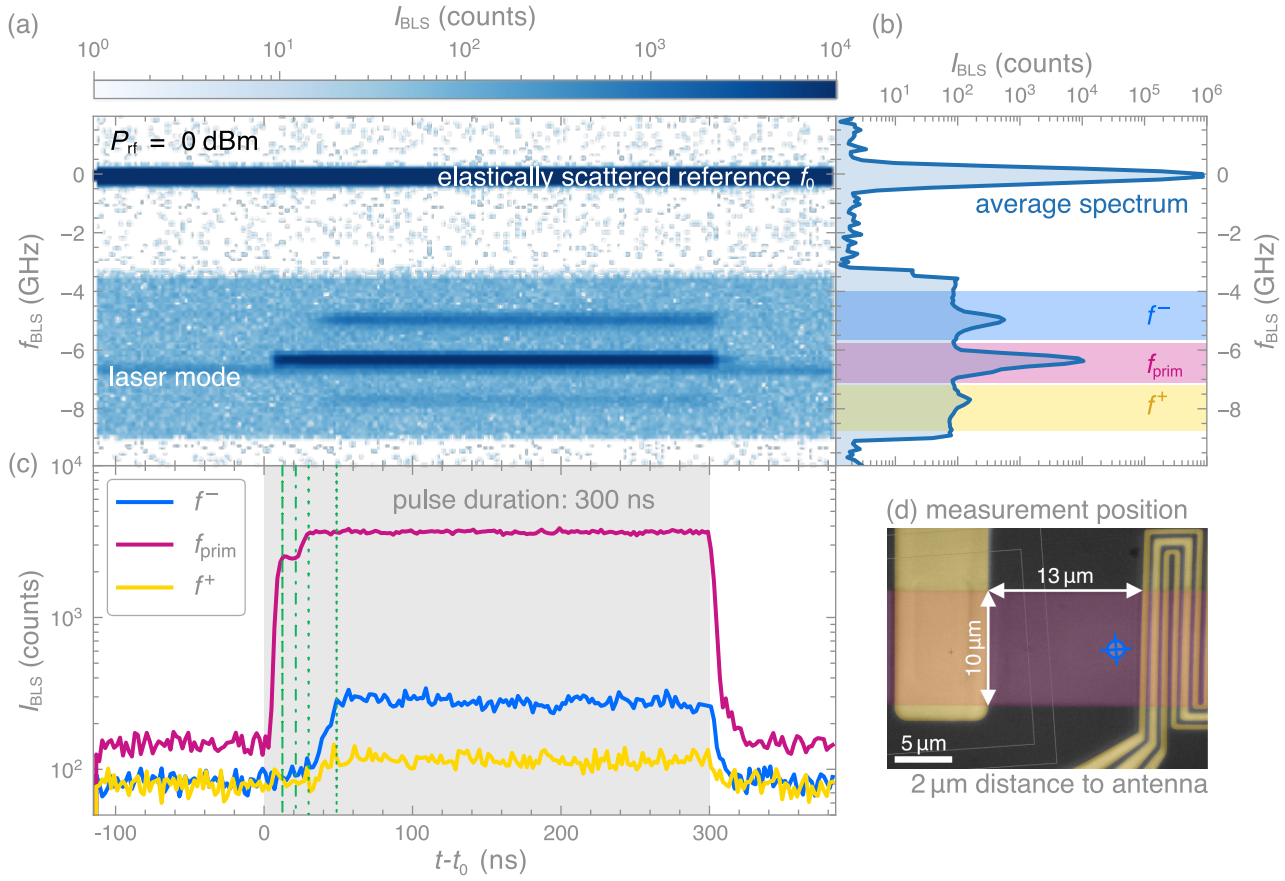

Figure 10.16: Overview of the time resolved µBLS measurements at an applied field $|\mu_0 H_{ext}|$ = 8.9 mT and a fixed excitation frequency f_{rf} = 6.25 GHz for the example at P_{rf} = 0 dBm. The time resolved BLS spectra (a) were recorded in 50 repetitions of 100 scans with a frequency range of −9.9 GHz ≲ f_{BLS} ≲ 1.9 GHz and a time resolution of Δt = 2 ns. Prior to the time trace extraction, the spectra are normalised on the elastically scattered reference f_0. The time traces of the direct excitation f_{prim} and the secondary modes f^+ and f^- are read out by averaging the signal within the spectral ranges highlighted in (b) in the averaged spectrum over all t, i.e. −8.75 GHz ≤ f^+ ≤ −7.2 GHz, −7.1 GHz ≤ f_{prim} ≤ −5.75 GHz and −5.65 GHz ≤ f^- ≤ −4.0 GHz, and normalising on the number of channels involved. Note that for the direct excitation f_{prim}, the laser mode is generously included to avoid fluctuation issues. The resulting time traces are shown in (c), where additionally the microwave pulse is marked by the grey background and green dashed lines are added for a facilitated comparison. The tinted optical microscope image in (d) shows the measurement position (blue target) on the Co_2MnSi waveguide (pink tinted) at a ∼ 2 µm distance to the antenna border (gold tinted meander CPW on the right side). The automated optical stage stabilisation was anchored on the DC contact (gold tinted on the left side) within the search range marked by the faint white rectangular outlines.

10.2.3 Time-resolved instability onset

To further investigate the behaviour at the critical threshold and instability onset, time resolved µBLS measurements can be carried out. This is particularly interesting for the excitation at the maxima of the antenna, where the above discussed *pre-drop* opened the question on other invisible scattering processes.

In order to avoid a disturbance due to the laser modes coinciding with the secondary mode f^-, a smaller external field of $\mu_0 H_{ext} \approx 8.9$ mT was chosen for this kind of investigation. Consequently, a fixed excitation frequency f_{rf} = 6.25 GHz had to be selected for the excitation at the first antenna maximum. The applied microwave power is again set from P_{rf} = −40 dBm to P_{rf} = 0 dBm and a microwave pulse duration of Δt_{pulse} = 300 ns is set with the pulse generator[67]. An exemplary overview of the recorded data for one applied power is shown in figure 10.16, where the subsequent time trace extraction is detailed in the description.

The extracted time traces at P_{rf} = 0 dBm in figure 10.16 (c) already show the

67: See the brief description of the setup alteration for the time resolution in section 9.2.

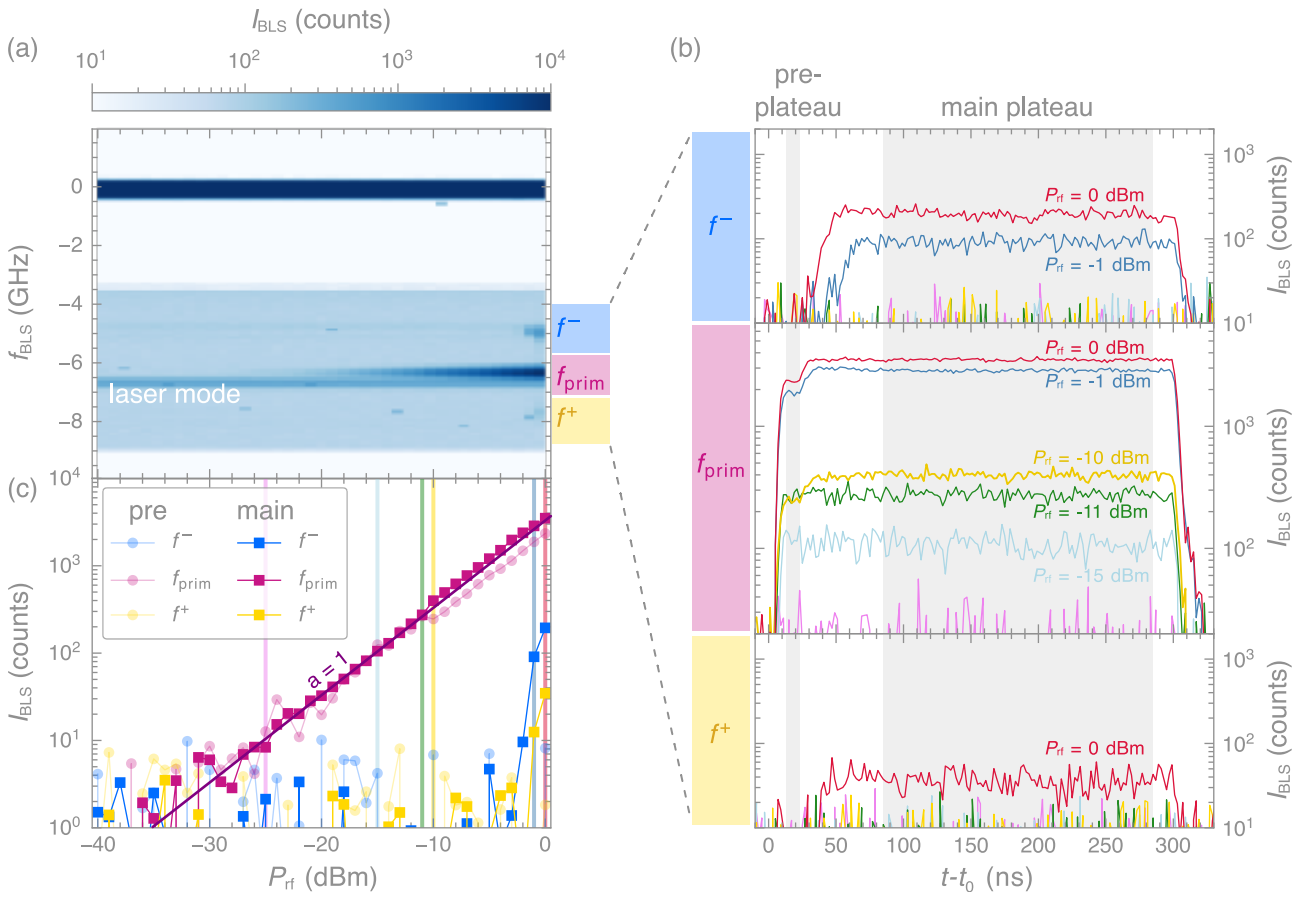

Figure 10.17: Power dependence of the pre-plateau and the main plateau in the time resolved μBLS measurements at an applied field $|\mu_0 H_{ext}| = 8.9\,\text{mT}$ and a fixed excitation frequency $f_{rf} = 6.25\,\text{GHz}$. The overview mapping in (a) shows the accumulated spectra for each power, where an onset of the secondary modes is only observed for $P_{rf} \geq -1\,\text{dBm}$. Selected time traces are shown in (b) for the three extraction ranges f_{prim}, f^+ and f^-. For the intensity traces at all microwave powers (also the ones not shown in (b)), the pre-plateau intensity is read out by averaging the signal in the narrow interval highlighted by the narrow grey background in (b), and the main plateau intensity is read out in the broad range accordingly. The resulting pre-plateau and main plateau intensities are traced for all three modes as a function of the applied microwave power in (c), where the bold markers indicate the main plateau intensity and the markers with reduced opacity indicate the pre-plateau intensity. Additionally, the linear scaling with $a = 1$ is marked by the purple line and the vertical lines in (c) indicate the position of the respecitve time traces in (b). Significant pre-plateau intensities are only obtained on f_{prim} (although traced for all modes), and a difference to the main plateau intensities is only observed for $P_{rf} \geq -10\,\text{dBm}$.

main features of interest, where vertical dashed lines are indicated at the relevant positions for a facilitated comparison: Shortly after the application of the microwave pulse[68] at t_0, the intensity on the direct excitation f_{prim} rises, and reaches a first pre-plateau, before the intensity of the secondary modes f^+ and f^- exceeds the thermal level. After a short stagnation at this pre-plateau, the intensity of the primary mode rises further. With the onset of the secondary modes f^+ and f^-, the intensity of the direct excitation f_{prim} again stagnates.

The formation of this pre-plateau is traced as a function of the microwave power as is shown in figure 10.17. Clearly, significant pre-plateau intensities are only obtained on f_{prim}, and a difference to the main plateau intensities is only observed for $P_{rf} \geq -10\,\text{dBm}$. Hence, the process giving rise to the pre-plateau sets in between $P_{rf} \geq -11\,\text{dBm} \approx 80\,\mu\text{W}$ and $P_{rf} \geq -10\,\text{dBm} = 100\,\mu\text{W}$. However, a significant intensity of the secondary modes f^+ and f^- is only observed for $P_{rf} \geq -1\,\text{dBm} \approx 800\,\mu\text{W}$. The abrupt formation of the pre-plateau at applied powers which are nearly an order of magnitude lower than the detected population of the secondary modes f^+ and f^- is another sign for an invisible/hidden scattering process with a lower critical threshold than the process involving the secondary modes f^+ and f^-. An underlying process could involve a frequency conserving scattering to higher order width modes,

68: Note that an absolute measurement of t_0 is hardly possible, but the pulse duration is fixed and the pulse window indicated in figure 10.16 (c) is hence determined by the abrupt decrease of the intensity when switching off. This was done in the measurement at $P_{rf} = 0\,\text{dBm}$ with highest signal to noise ratio, and the same t_0 was then applied to all recorded data.

similar to the phenomenon in [427]. Yet, a precise determination is rather complex not only due to the expectable width modes and interferences, but also for the antenna excitation characteristics in combination with the significant nonlinear shift, as discussed in detail above. Nevertheless, these measurements again highlight the low nonlinear threshold on the direct excitation, i.e. an onset of (invisible) nonlinear processes for applied microwave powers as low as $P_{\mathrm{rf}} \geq -10\,\mathrm{dBm} = 0.1\,\mathrm{mW}$.

[427]: Mohseni et al. (2021), 'Controlling the Nonlinear Relaxation of Quantized Propagating Magnons in Nanodevices'

Remarkably, at the onset from $P_{\mathrm{rf}} = -11\,\mathrm{dBm}$ to $P_{\mathrm{rf}} = -10\,\mathrm{dBm}$, the intensity in the pre-plateau drops abruptly, as can be seen in figure 10.17 (c), and simultaneously the signal from the main plateau abruptly shifts up. Subsequently, both continue to rise again with $a = 1$ (parallel to the purple line), where only for $P_{\mathrm{rf}} \geq -1\,\mathrm{dBm}$ the main plateau intensity starts to deviate from the linear scaling linked to the onset of the population in f^+ and f^-. This highlights the importance of the timescale on the nonlinear dynamics, where the abrupt increase of the main plateau could be due to an effective impedance improvement of the microwave device with the onset of the scattering into the "hidden" modes, which consequently would result in an improved microwave absorption from the direct excitation, and hence a an abrupt up-shift of the intensity of the direct excitation.

Especially with the promising results from the nanostructuring study presented in chapter 3, a further investigation of the nonlinear dynamics and their time-sensitive behaviour could be particularly interesting in similar[69] nanosized Co_2MnSi waveguides with a width of $w \approx 50\,\mathrm{nm}$, where the significantly increased width mode separation is expected to drastically facilitate the modelling and identification of the underlying processes.

69: I.e. analogously fabricated. Obviously, the study in chapter 3 was of a destructive nature and the structures cannot be used for a magnonic experiment anymore.

10.3 Conclusion

In summary, this preliminary explorative study of the nonlinear spin wave dynamics in the microsized spin wave Doppler shift device allowed for various conclusions which underline the potential of the half-metallic Co_2MnSi Heusler compound for further magnonic applications.

First, in relation to the magneto-optical study in chapter 7, a significant noise is observed throughout the study in the present chapter arising from the generally poor magneto-optical signal from this compound in the visible range. Similar, a rather poor magneto-optical signal-to-noise ratio from this material was equally seen in BLS spectra in previous studies from the magnetism group in Kaiserslautern [72, 382], certainly one of the reasons for the subsequent deviation towards the $Co_2Mn_{0.6}Fe_{0.4}Si$ compound in later studies [84, 86, 87]. Hence, albeit the relatively low magneto-optical signal and related long data acquisition times, the successful investigation by μBLS with $\lambda = 491\,\text{nm}$ presented in this chapter can be constated as a proof of hope for an exploitation of future half-metallic Co_2MnSi-based magnonic devices to be measured by μBLS.

Second, in this preliminary study no signature of three-magnon scattering processes could be observed. In particular for the smallest applied field at $\mu_0 H_{\text{ext}} \approx 8.9\,\text{mT}$, this is an indication for the significant impact of the cubic anisotropy increasing the cut-off frequency for the three-magnon scattering discussed around figure 8.12 in chapter 8. Concerning this, in particular the non-annealed Co_2MnAl yielding a governing second order cubic anisotropy contribution in chapter 6 might be an interesting case to study in similar conditions to further explore the effects of the K_{c2} term[70].

Third, the power dependent investigation of the second order Suhl instability onset yields multiple conclusions:

- The spectral repartition of the nonlinear excitation thresholds in this device is mainly defined by the antenna characteristics. Specifically, the critical threshold powers mimic the selective antenna excitation efficiency spectrum and remarkably low critical power thresholds down to $P_{\text{rf}} = -11\,\text{dBm} \approx 80\,\mu\text{W}$ are obtained at the maximal excitation efficiency. While it is underlined that a direct comparison between studies on different samples and setups is rather insignificant, these record-low power thresholds are attributed to the impressive properties of the half-metallic Co_2MnSi compared to e.g. the similar $Co_2Mn_{0.6}Fe_{0.4}Si$ [86, 97], and highlight the potential for further applications to exploit the nonlinear magnetisation dynamics in Co_2MnSi.
- Due to the defined wavevector selective excitation efficiency, the nonlinear shift is found to yield a remarkable gain when shifting into the maximum, and analogously a remarkable drop when shifting out. The latter case yields a kind of self-capping behaviour.
- A drop of the intensity prior to the onset of the detected secondary modes is identified, which is likely related to the exhibition of a pre-plateau in the time resolved measurements. Both are an indication towards invisible scattering processes redistributing the energy away from the directly excited primary mode into secondary modes that are not detectable, potentially due to an underlying frequency conserving process involving the higher order width modes. Yet, various other factors come into play and a certain conclusion requires further investigations.
- The time-resolved instability shows an improved absorption of the pumping power with the onset of the secondary modes and points towards an

[72]: Gaier et al. (2008), 'Influence of the $L2_1$ ordering degree on the magnetic properties of Co_2MnSi Heusler films'
[382]: Hamrle et al. (2009), 'Determination of exchange constants of Heusler compounds by Brillouin light scattering spectroscopy'
[84]: Sebastian et al. (2012), 'Low-damping spin-wave propagation in a micro-structured $Co_2Mn_{0.6}Fe_{0.4}Si$ Heusler waveguide'
[86]: Pirro et al. (2014), 'Non-Gilbert-damping Mechanism in a Ferromagnetic Heusler Compound Probed by Nonlinear Spin Dynamics'
[87]: Sebastian et al. (2015), 'All-optical characterisation of the spintronic Heusler compound $Co_2Mn_{0.6}Fe_{0.4}Si$'

70: Similar calculations as in chapter 8 for an applied field of 30 mT along the [110] direction, yield an impact on the precession ellipticity amounting to ~ 23% of the demagnetisation strength, and an increase of up to 18% of the spin wave frequencies notably for large wavevectors ($k_{\text{ip}} \approx 100\,\text{rad}/\mu\text{m}$). Naturally, this must yield a significant impact on the nonlinear dynamics in this direction. And as the K_{c2} term cannot affect the magnetisation along the [100] direction, a rather significant qualitative difference can be expected if the anisotropy is indeed this high (recall the rather noisy data set in chapter 8 from this compound).

[86]: Pirro et al. (2014), 'Non-Gilbert-damping Mechanism in a Ferromagnetic Heusler Compound Probed by Nonlinear Spin Dynamics'
[97]: Pirro (2014), 'Lineare und nichtlineare Spinwelleninteraktionen in magnetischen Mikrostrukturen'

impedance change potentially improving the power absorption of the device. This highlights the importance of time-resolved investigations for further insights into the nonlinear processes at play.

As is discussed in detail in the main part of this chapter, these results are particularly promising for a further exploitation of the half-metallic Co_2MnSi for nonlinear magnetisation dynamics: In particular, the combination of the remarkably low critical power thresholds obtained in this study, and the proven spin polarisation in the same device from the study in [91] yield a great motivation for further investigations and two discussed examples include exploiting the spin polarisation of injected currents to further drive the nonlinear behaviour in relation to [60], or going for a frequency-selective nonlinear self-enhancement by coupling to magnonic ring resonators [54] and potentially towards an application of the drastic nonlinear shift induced self-enhancement/self-capping behaviour for neural magnonic circuits.

Finally, in particular in combination with the impeccable nanofabrication results from chapter 3 and in combination with the exploitable spin polarisation [91], this study highlights the great potential in the half-metallic compound especially for applications at the intersection between magnonics and spintronics and hence strongly motivates the interest in further experimental investigations particularly in nanosized magnonic-spintronic devices.

[91]: Solano Córdova (2024), 'Temperature dependent spin wave study of magnetic properties and spin-polarized electron transport in $Fe_{1-X}V_X$ and Co_2MnSi epitaxial films'

[60]: Hache et al. (2023), 'Control of Four-Magnon Scattering by Pure Spin Current in a Magnonic Waveguide'

[54]: Wang et al. (2020), 'A nonlinear magnonic nano-ring resonator'

Conclusion and perspectives

The main objective of this thesis was to investigate the half-metallic Heusler compound Co_2MnSi in view of nonlinear magnonic and spintronic applications. As outlined in the introduction, the motivation is linked to the very timely interest in nonlinear dynamics for unconventional computing approaches [42, 51, 52] and the promising potential in the Co_2MnSi compound, notably enabled by the recent experimental demonstration of the half-metallicity [69, 70] opening new *realistic* perspectives on an exploitable full spin polarisation in epitaxial $L2_1$-ordered Co_2MnSi films [64].

[42]: Flebus et al. (2024)
[51]: Grollier et al. (2020)
[52]: Marrows et al. (2024)
[69]: Jourdan et al. (2014)
[70]: Andrieu et al. (2016)
[64]: Guillemard et al. (2019)

With this overarching goal, various main questions were identified at the beginning of this work[1] and principally defined the roadmap for the main part of this thesis:

1: See the introduction on page 3.

- How are the crucial structural properties affected by a typical nanofabrication process?
- What is the signature of the cubic anisotropy and its impact on the expectable spin wave properties?
- Can the magneto-optical signal be optimised by an adequate choice of parameters for a detection by BLS and μBLS?
- Can the expectable low nonlinear threshold be confirmed? What are the characteristics of the nonlinear spin wave dynamics?

The elaborate analysis of these points has led to main conclusions on the major implications within and beyond the context of this work, which not only consolidate the great interest for a use of half-metallic Co_2MnSi in future magnonic and spintronic applications, but importantly have opened various questions to address in future research projects.

This section briefly recalls the most significant results and implications, regrouped by the above four questions, and will close the thesis with a summarising general conclusion in the end.

Nanofabrication and structural characteristics

Nanofabrication preserves impeccable $L2_1$-order.[2]
A successful defect-less nanofabrication preserving the $L2_1$-order even at the etched borders of the patterned nanosized waveguides was confirmed by a transmission electron microscopy study. The defect-less downscaling is successful down to the smallest intended waveguide widths $w \approx 50\,\text{nm}$. The significance of this result is not only underlined by the important impact of structural defects on the spin wave dynamics reported in [77], but also in context with the cruciality of the $L2_1$-order for the full spin polarisation, these results make the dream of half-metallic Co_2MnSi nanostructures a realistic perspective for hybrid spintronic-magnonic applications.

2: See chapter 3, section 3.3 from page 46.

[77]: Mantion et al. (2022)

Nanofabrication yields auto-formed passivised oxidation barrier.[3]
A welcome passivised oxidation barrier in the form of a Si-containing amorphous oxide layer is found to cover the etched borders of all structures across samples. Astonishingly, in the case of the MgO/Al capping, a similar layer seems to have partly replaced the Mg in the capping. The analysis points towards an auto-formation process during the milling step, likely involving the adhesion promoter hexamethyldisilazane (HMDS) which is elsewhere

3: See chapter 3, section 3.3 from page 46.

employed in ion beam induced CVD processes as a precursor for an amorphous SiCN film deposition [223]. Further chemical analyses would be necessary for more insight into the underlying process, and could be of great interest in view of a potential future exploitation as a reliable auto-protection.

[223]: Yoshimura et al. (2021)

Dislocation network along $[110]_{Co_2MnSi}$ *at the MgO/Co₂MnSi interface.*[4]
Edge dislocations are determined along the MgO/Co_2MnSi interface in agreement with previous studies [81, 83] and the analysis in this work points towards an orientation along $[110]_{Co_2MnSi}$ (or $[100]_{MgO}$). The identification of the repartition is important as such dislocations can act as domain pinning centres, yield a directional inhomogeneous damping contribution [209, 210] and affect the magneto-electrical transport properties [81]. Yet, importantly, the dislocations are not found to yield a direct impact on the $L2_1$ ordering in the adjacent Co_2MnSi.

4: See chapter 3, section 3.2.2 from page 39.

[81]: De Melo et al. (2021)
[83]: Friedel (2021)

[209]: Heinrich et al. (2004)
[210]: Woltersdorf et al. (2004)

Cubic anisotropy

Non-negligible cubic anisotropy points towards second order contribution.[5]
A non-negligible cubic anisotropy with first and second order contributions of opposite sign is determined in a Co_2MnSi as well as a Co_2MnAl thin film, mainly by a rotational FMR study. In both cases, the combination of K_{c1} and K_{c2} results in an identification of the ⟨100⟩ axes as hard axes (maxima) and the ⟨110⟩ axes as easy axes (minima) of the magnetocrystalline anisotropy. For (001)-plane thin films, the second order anisotropy symmetry principally yields a contribution similar to an out-of-plane anisotropy for $M_S \parallel \langle 110 \rangle$, but does not have any impact for $M_S \parallel \langle 100 \rangle$. The resulting directional change of M_{eff} might be particularly relevant for the coupling in Co_2Mn-based Heusler multilayers.

5: See chapter 6 from page 111.

Cubic anisotropy impacts ellipticity of the magnetisation trajectory.[6]
The cubic anisotropy can principally yield a directionally dependent distortion of the elliptical precession trajectory, which for (001)-oriented thin films is maximal for the $M_S \parallel \langle 110 \rangle$ orientation, and zero for the $M_S \parallel \langle 100 \rangle$ orientation. For $M_S \parallel \langle 110 \rangle$ as studied in this work[7], the cubic anisotropy can reinforce ($K_{c1/2} > 0$) or counteract ($K_{c1/2} < 0$) the demagnetisation-induced ellipticity of the magnetisation precession. In Co_2MnSi the second order contribution[8] counteracts the first, yielding a negligible effect on the ellipticity of the precession, whereas for the (non-annealed) Co_2MnAl a reinforcement of the demagnetisation-induced ellipticity by 23% is to be expected[9]. Such a *directional enforcement of the ellipticity* could be interesting to explore in view of parallel parametric pumping processes, which principally allow for a frequency and mode selective spin wave amplification [458, 459]: Here, such an additional anisotropy-induced directional dependence of the precession trajectory could yield a further tuning parameter.

6: See chapter 8 from page 151.

7: For completeness: For $M_S \parallel \langle 100 \rangle$, the cubic anisotropy acts like an effective Zeeman-like term and with $K_{c1} < 0$ opens the precession cone (destabilises the precession, hence increases nonlinearity). This is generally true, independent of the film orientation.

8: With the saturation magnetisation $M_S \approx 1000\,\mathrm{kA/m}$ and the anisotropy constants $K_{c1} = -8.1\,\mathrm{kJ/m^3}$ and $K_{c2} = 37.7\,\mathrm{kJ/m^3}$ from chapter 6.

9: With the saturation magnetisation $M_S \approx 740\,\mathrm{kA/m}$ and the anisotropy constants $K_{c1} \approx 0$ and $K_{c2} \approx 317\,\mathrm{kJ/m^3}$ from chapter 6.

[458]: Brächer et al. (2017)
[459]: Heinz et al. (2022)

Cubic anisotropy impacts dispersion and instability ranges.[10]
Unsurprisingly, the cubic anisotropy yields a shift of the dispersion relation, which for $M_S \parallel \langle 100 \rangle$ is simply Zeeman-like (and only depends on K_{c1}), whereas for $M_S \parallel \langle 110 \rangle$ the wave vector dependence of the first and second order cubic anisotropy terms are of different nature: The first order mainly affects the dipolar spin waves, and the second order yields an increased impact on higher k_{ip}. In the case of Co_2MnSi, the impact of the second order cubic anisotropy is found to be negligible over the first order contribution, and a significant shift ($\Delta f \geq 5\%$) of the Damon-Eshbach dispersion ($M_S \perp \mathbf{k}_{ip}$) is only obtained for $k_{ip} \lesssim 1\,\mathrm{rad/\mu m}$, whereas for the Backward-Volume dispersion ($M_S \parallel \mathbf{k}_{ip}$) it affects $k_{ip} \lesssim 30\,\mathrm{rad/\mu m}$. The most important direct

10: See chapter 8 from page 151.

consequence is a shift of the band bottom (dispersion minimum) to larger wave vectors and higher frequencies, which yields an increase of the frequency threshold for the first order Suhl instability process.

Second order cubic anisotropy impacts exchange spin waves for $M_S \parallel \langle 110 \rangle$.
The Co_2MnAl film with $K_{c1} \approx 0$ and $K_{c2} \approx 317\,kJ/m^3$ in principle[11] yields an extreme case for the study of the second order cubic anisotropy term, and analogous calculations indicate the most significant impact for exchange-dominated spin waves. Precisely, the obtained frequency shift is minimal for $k_{ip} \rightarrow 0$ with $\Delta f \approx 0.5\,GHz$ in both geometries, and increases with increasing wave vector, where the largest relative impact on the calculated frequencies is obtained with $\Delta f \approx 18\%$ for $k_{ip} \approx 100\,rad/\mu m$. While such large wave vectors are completely out of the detection range in standard μBLS, and hence not further investigated in this study, the recently demonstrated Mie-resonance-enhancement for the μBLS detection [460] can extend the measurable wavevector ranges and could potentially[12] allow to verify the relevance and explore further implications of such seemingly important second order cubic anisotropy terms on the exchange spin wave spectra.

Unclear linewidth anisotropy highlights need for thorough data curation.[13]
The linewidth anisotropy in the Co_2MnSi film was equally investigated in the rotational FMR study. And while a directional variance of ~ 10% is obtained on the Gilbert damping parameter[14] is in principle in agreement with other reports on an anisotropic damping in the compound [392], the effect is in this study found to be counteracted by the inhomogeneous linewidth contribution. Here, the inhomogeneous linewidth contribution is found to arise mainly from the combination of the measurement resolution and the data treatment procedure, as is thoroughly evaluated in a comparative data processing study. Therefore, no clear indication for or against an anisotropic damping (and more importantly anisotropic linewidth) can be concluded within this study, and the study highlights the need for a thorough data curation especially for cases with large saturation magnetisation and narrow resonance linewidths linked to a small Gilbert damping parameter as is the case for Co_2MnSi.

11: It is recalled that a rather large noise importantly affected the evaluation of this sample in chapter 6, and hence this must be taken more as a hypothetical case to be verified.

[460]: Wojewoda et al. (2023)

12: It needs to be noted that the technique requires a pattering of Silicon nanoresonator discs on the sample, and hence in such an attempt particular caution will need to be given to a potential introduction of further (e.g. strain-induced) anisotropy contributions linked to the nanoresonator patterning.

13: See chapter 5, section 5.2.2 from page 100, as well as chapter 6, section 6.2.3 from page 133.

14: With $\alpha = (1.23 \pm 0.02) \times 10^{-3}$ for the easy axes $[110]_{Co_2MnSi}$ and $\alpha = (1.11 \pm 0.02) \times 10^{-3}$ for the hard axes $[100]_{Co_2MnSi}$, as determined in chapter 6, section 6.2.3 from page 133.

[392]: Yilgin et al. (2007)

Magneto-optical signal intensity

linMOKE and QMOKE signal shows orientation and wavelength dependence.[15]
For Co_2MnSi, the magneto-optical signal study in the frame of a master research project [360] yields a significant quadratic MOKE (QMOKE) contribution for $\lambda = 550\,nm - 600\,nm$ with a vanishing linear MOKE (linMOKE) around 600 nm, which is generally in agreement with other studies in [72, 82]. For the compounds Co_2MnAl, Co_2MnGa and Co_2MnSn, on the other hand, the QMOKE is found to be insignificant at $\lambda = 636\,nm$ and hence a wavelength dependence was only further investigated for Co_2MnAl, yielding a nearly constant linMOKE and vanishing QMOKE in the entire probing range for $\lambda = 550\,nm - 900\,nm$.

15: See chapter 7 from page 137.

[360]: Fermon (2023)

[72]: Gaier et al. (2008)
[82]: Silber et al. (2020)

Kerr angle yields qualitative implications for BLS detection.[16]
In principle, the correlation between the BLS signal intensity and the complex Kerr angle allows for a first estimation of a possible spin wave detection by BLS. Yet, setup optimisation factors play a crucial role, and hence the correlation is more suitable to identify near-zero-intensity ranges to be avoided (for Co_2MnSi around $\lambda = 550\,nm - 600\,nm$) than to predict best intensities. Moreover, it is pointed out that the magneto-optical anisotropy is not translated to μBLS due to the circular illumination cone from the microscope objective, but could

16: See chapter 7 from page 137.

impact measurements for k-resolved BLS, where the magneto-optical setup geometry indeed features one incidence plane of light.

Successful investigation in μBLS proves feasibility of future studies.[17]
Only few BLS studies on Co_2MnSi are known from the early 2000s [72, 153, 382], after which the magnonics community shifted towards the better detectable $Co_2Mn_{0.6}Fe_{0.4}Si$ [84–88]. After a correlation attempt in the composition dependent studies in relation with chapter 7 of this work [83, 360], the study presented in chapter 10 is one of the first reported μBLS studies on a Co_2MnSi structure together with [90] proving the technical feasibility of investigations relying on the detection technique. Nevertheless, comparably large data acquisition times are to be expected for a sufficient signal to noise ratio.

17: See chapter 10 from page 177.

[72]: Gaier et al. (2008)
[153]: Kubota et al. (2009)
[382]: Hamrle et al. (2009)
[84]: Sebastian et al. (2012)
[85]: Sebastian et al. (2013)
[86]: Pirro et al. (2014)
[87]: Sebastian et al. (2015)
[88]: Sebastian et al. (2016)
[83]: Friedel (2021)
[360]: Fermon (2023)
[90]: Mantion et al. (2024)

Nonlinear spin waves in half-metallic Co_2MnSi

Nonlinear spin wave dynamics were investigated in a spin wave Doppler shift device fabricated by J. Solano [91] at the IPCMS in Strasbourg, France, within a collaboration in the frame of the *ANR MARIN (ANR-20-CE24-0012)* project.

[91]: Solano Córdova (2024)

Low nonlinear threshold obtained in half-metallic Co_2MnSi device.
Remarkably low critical power thresholds down to $P_{rf} = -11$ dBm ≈ 80 μW are obtained at the maximal excitation efficiency, here for the operation at $\mu_0 H_{ext} \approx 30.8$ mT with $f_{rf} = 9.55$ GHz. While it is underlined that a direct comparison between studies on different samples and setups is rather insignificant, these record-low power thresholds are attributed to the impressive properties of the half-metallic Co_2MnSi especially compared to e.g. the similar[18] $Co_2Mn_{0.6}Fe_{0.4}Si$ [86, 97]. These results not only highlight the potential of the half-metallic Co_2MnSi for nonlinar magnonic applications, but in combination with the experimentally confirmed 100% spin polarisation in this device [91] yield a great motivation for an exploitation in hybrid spintronic and magnonic applications, e.g. making use of a spin current injection for an additional control of the nonlinear thresholds in [60].

18: $Co_2Mn_{0.6}Fe_{0.4}Si$ waveguide in [86, 97]:
$M_S = 1003$ kA/m,
$A_{exch} = 13$ pJ/m,
$\alpha = 3 \times 10^{-3}$,
$w = 5$ μm,
$d = 30$ nm.
Co_2MnSi waveguide here [91]:
$M_S = 1058$ kA/m,
$A_{exch} = 19.5$ pJ/m,
$\alpha = 1 \times 10^{-3}$,
$w = 10$ μm,
$d = 20$ nm.
[86]: Pirro et al. (2014)
[97]: Pirro (2014)
[60]: Hache et al. (2023)

Nonlinear shift yields frequency-selective characteristic.
In addition to the low nonlinear thresholds, the self-induced nonlinear shift is found to yield a remarkable intensity gain when shifting into an excitation maximum, and analogously a remarkable drop when shifting out. The study therefore also presents a great potential for a frequency selective self-enhancement/self-capping behaviour, and promises a similar functionality using nonlinear ring resonators for a self-enhancement of the spin wave intensity [54, 455, 456]. Such frequency selective amplitude-dependent transmission characteristics are sought-after for artificial neural networks [53, 56] and currently mostly explored in YIG. Here, the results from this exploratory study consolidate the great potential for Co_2MnSi-based nonlinear magnonic structures and additionally motivate for an exploration of further device functionalities linked to the possibility of a fully polarised spin current application as opposed to the insulating YIG.

[54]: Wang et al. (2020)
[455]: Odintsov et al. (2024)
[456]: Vilsmeier et al. (2025)
[53]: Brächer et al. (2018)
[56]: Fripp et al. (2023)

Indications for invisible processes highlights need for further investigations.
A drop of the intensity at even lower powers than corresponding to the onset of the detected secondary modes is identified, i.e. down to $P_{rf} = -14$ dBm ≈ 40 μW for the conditions mentioned hereabove. This is likely correlated with the exhibition of a pre-plateau detected in time resolved measurements. Both are an indication towards invisible scattering processes, potentially similar to the observations in [427]. A further study of nonlinear threshold processes is proposed to be carried out in nanosized half-metallic Co_2MnSi waveguides, where the significantly increased width mode separation

[427]: Mohseni et al. (2021)

is expected to drastically facilitate the modelling and identification of the underlying scattering processes.

Summarising remarks

In summary, the exploration of the half-metallic Heusler compound Co_2MnSi in this thesis has proven a great potential for bridging the gap between spintronic functionality and magnonic application. Particularly the demonstrated promising exploitability of nonlinear spin wave characteristics in combination with the defect-less $L2_1$-order-preserving nanofabrication opens great perspectives for an integration of half-metallic Co_2MnSi-based structures into nanoscale hybrid magnonic-spintronic circuits.

In relation, various potential future directions have been outlined, where in particular an exploitation of the self-induced nonlinear frequency shift in combination with the full spin polarisation for an additional current control functionality is pointed out as a promising next step.

Additionally, the investigations towards this overarching goal opened a few principle questions on the implications of a potential second order cubic anisotropy term, which in (001) oriented films yields a principal similarity with an out-of-plane anisotropy modulated by an in-plane orientation dependence. This might be an interesting topic to address for a further exploration of the expectable characteristics notably concerning the coupling in multilayers, or a potential angular modulation of the parametric pumping efficiency.

Finally, to come back to the first page of this thesis, the results from this work and notably in combination with the 100% spin polarisation confirmed by J. Solano in [91] certainly consolidate the interest for applications at the intersection between spintronics and magnonics, with the presented preliminary studies kick-starting the field of half-metal magnonics. Beyond this, the presented results also underline the possibility of exploiting epitaxial, half-metallic Co_2MnSi devices as a realistic experimental model system paving the way for fundamental full spin polarisation studies, even at the nanoscale.

[91]: Solano Córdova (2024), 'Temperature dependent spin wave study of magnetic properties and spin-polarized electron transport in $Fe_{1-X}V_X$ and Co_2MnSi epitaxial films'

Appendix

A

RHEED image sequences of the entire growth process

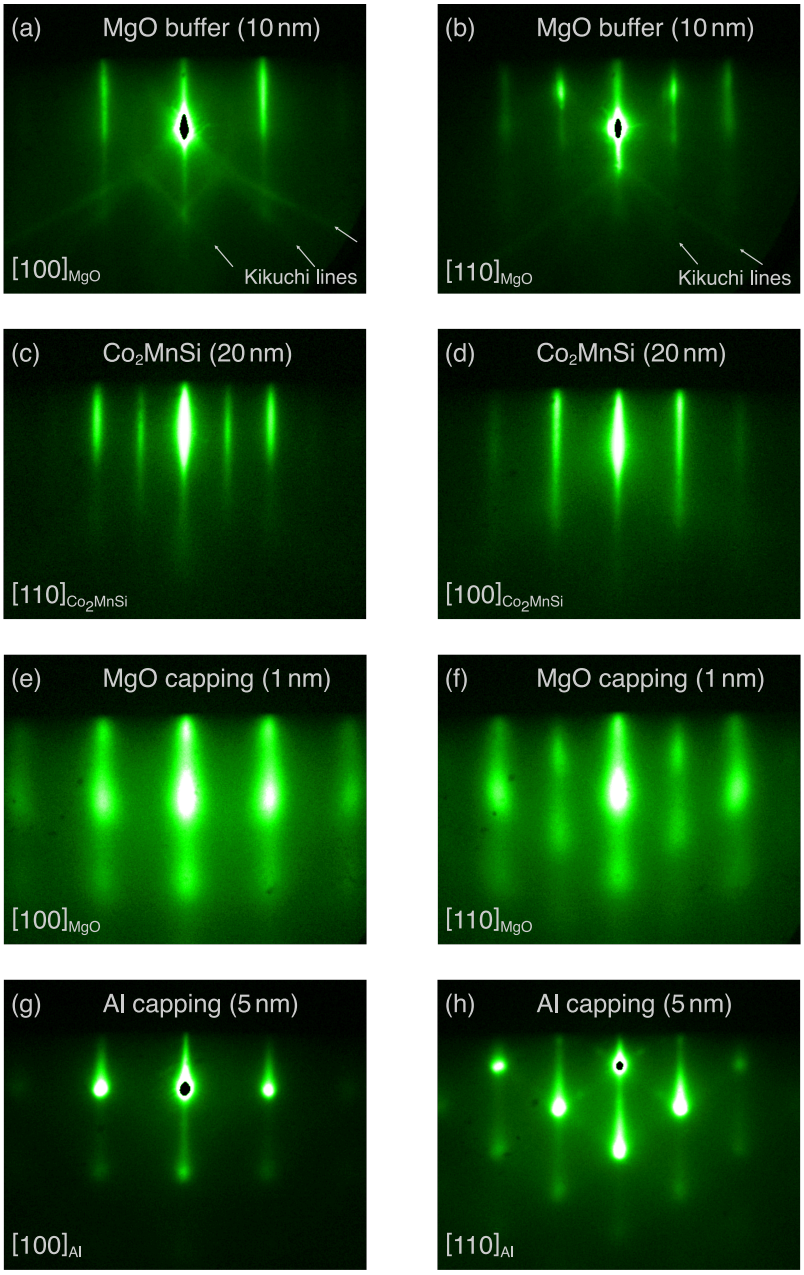

Figure A.1: RHEED image sequence of the entire process from sample Q240212.

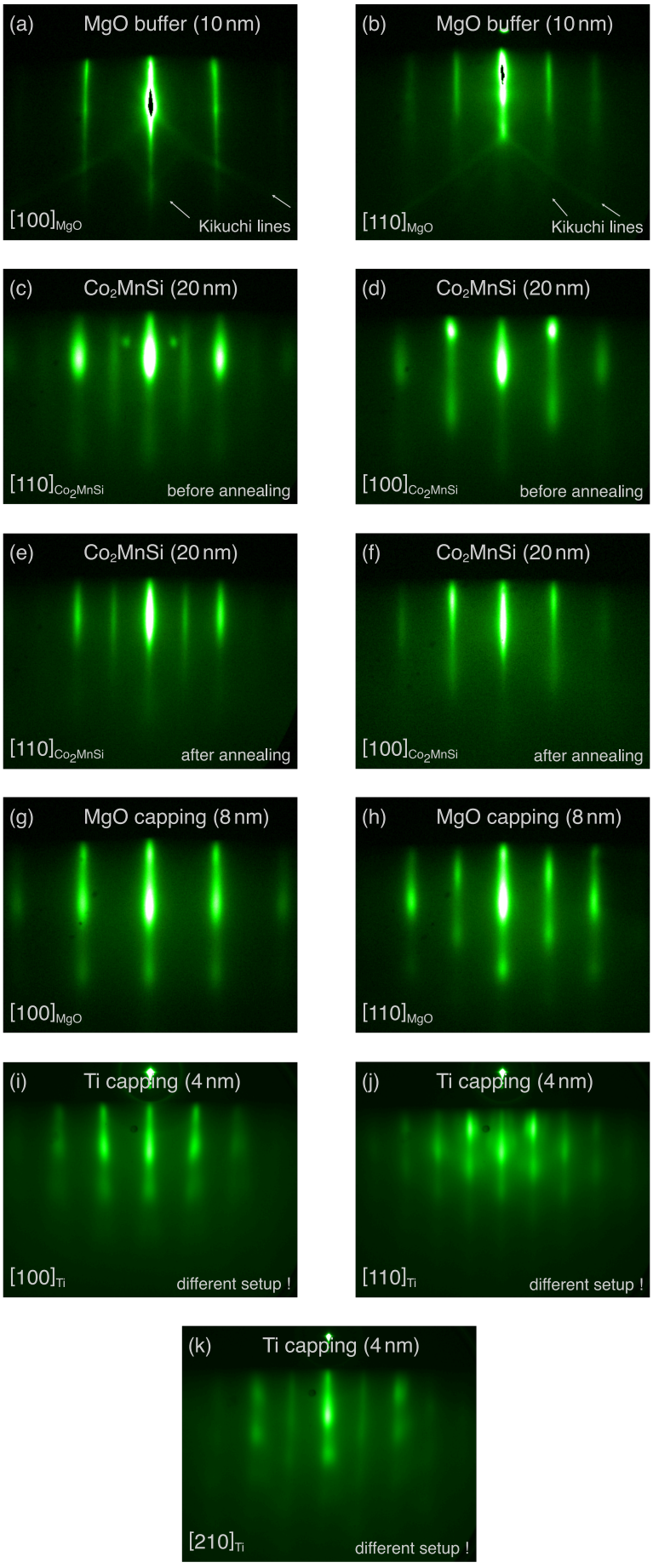

Figure A.2: RHEED image sequence of the entire process from sample Q220102.

B

Further EDXS mapping of the structured samples

B.1 Non-Structured Co_2MnSi / MgO / Al – Test-Sample S1.3 (Q240208)

Two EDXS cartography measurements were taken at two sites on the sample and are shown in figure B.1 and B.2.

In both measurements, a clear bottom interface between the detected intensities from the Heusler compound elements Co, Mn and Si and the buffer layer elements Mg and O is observed.

The top interface was found to be well defined only where the bilayer capping was sufficiently thick: While the MgO capping layer was found to be a homogeneous thin film (which gave only very little signal due to the small thickness of only 0.6 nm), the Al capping was found to be inhomogeneous and seems to have grown in islands, which are partly oxidised at the exposed surfaces.

In the proximity of the gaps between the islands, Si as well as O were detected outside of the Heusler layer. This suggests the formation of a silicon oxide where the capping layer coverage is insufficient. Below the islands where the capping thickness is larger, the Heusler layer was found to be intact and well protected showing no sign of impurity penetration or other faults. In between the islands, Pt was detected very close to / at the interface to the MgO or Silicon Oxide implying the insufficient coverage by the Al layer (islands).

It was therefore concluded that the MgO/Al bilayer capping works in principle, but the capping layer thicknesses need to be slightly increased for a complete protection of the Heusler layer. The deposited thicknesses in this sample were $d_{\mathrm{MgO}} = 0.6\,\mathrm{nm}$ and $d_{\mathrm{Al}} = 3\,\mathrm{nm}$, and based on the decent protection beneath the islands it was concluded that a deposit of $d_{\mathrm{MgO}} = 1\,\mathrm{nm}$ and $d_{\mathrm{Al}} = 5\,\mathrm{nm}$ should yield a sufficiently thick capping across the sample for a complete protection of the film (which was confirmed after imaging the next sample, see section B.2).

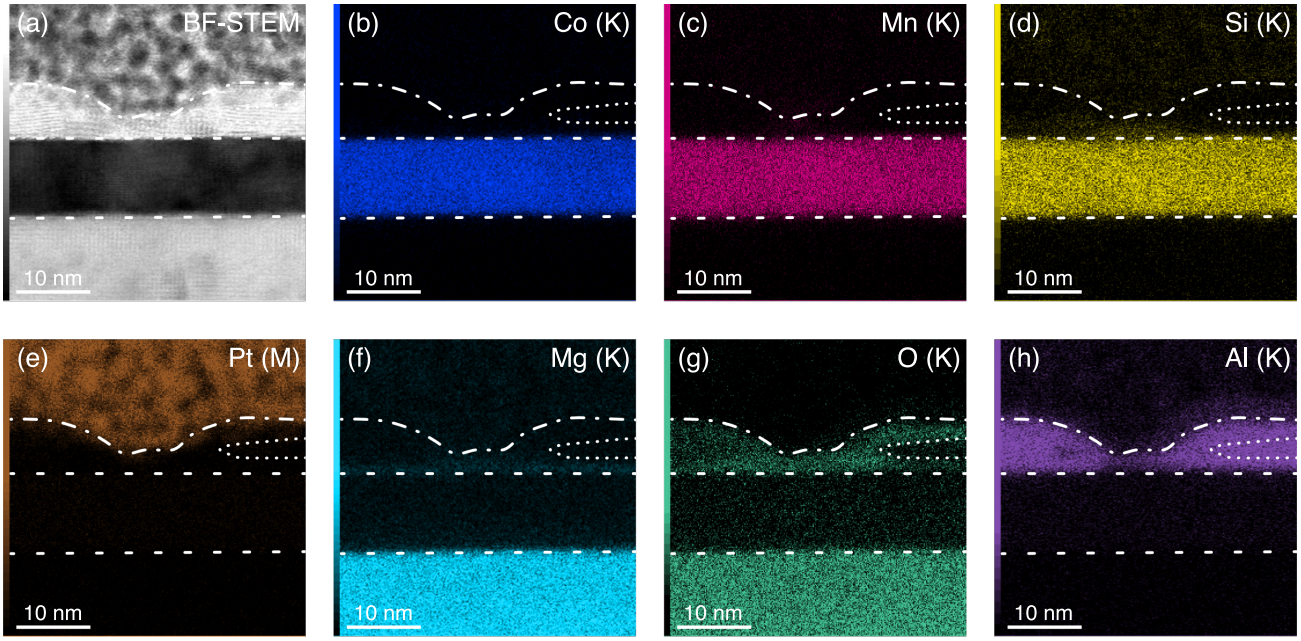

Figure B.1: EDXS elemental mapping of the $Co_2MnSi/MgO/Al$ thin film stack corresponding to sample S1.3 (Q240208) in table 2.1:
(a) BF-STEM micrograph captured before the spectral mapping,
(b-d) mapping of the Heusler compound elements Co, Mn and Si,
(e) mapping of the deposited Pt from the FIB process,
(f-h) mapping of the substrate and capping elements Mg, O, Al.
The dashed lines were added as guides for the comparison of the different elemental maps.

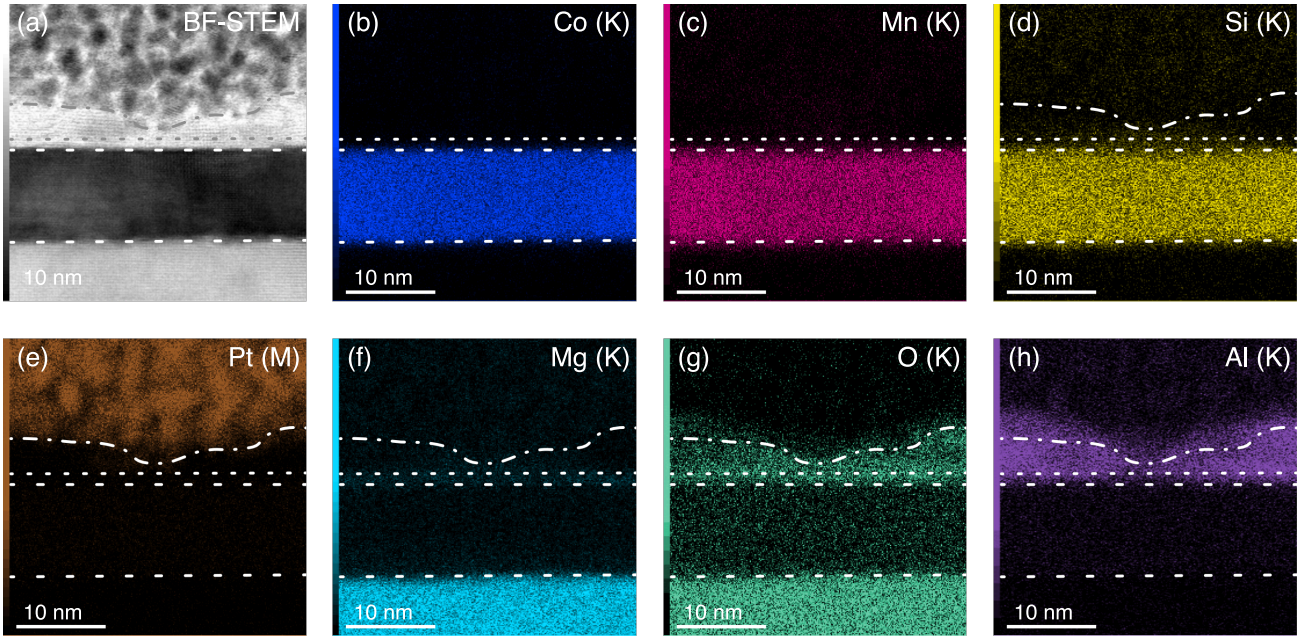

Figure B.2: EDXS elemental mapping of the $Co_2MnSi/MgO/Al$ thin film stack corresponding to sample S1.3 (Q240208) in table 2.1:
(a) BF-STEM micrograph captured before the spectral mapping,
(b-d) mapping of the Heusler compound elements Co, Mn and Si,
(e) mapping of the deposited Pt from the FIB process,
(f-h) mapping of the substrate and capping elements Mg, O, Al.
The dashed lines were added as guides for the comparison of the different elemental maps.

B.2 Non-Structured Co_2MnSi / MgO / Al – Sample S1.4 (Q240212)

Two EDXS cartography measurements were taken at two sites on the sample and are shown in figure B.3 and B.4.

In both measurements, a clear interface between the detected intensities from the Heusler compound elements Co, Mn and Si and the capping layer elements Mg, O and Al was observed, as is indicated by the dashed lines. However, occasional irregularities were found along the bottom interface as seen for instance in figure B.3, where locally the Heusler compound was found to penetrate into the MgO suggesting an inhomogeneity of the MgO buffer layer.

The adjacent MgO capping layer was found to be homogeneous and intact. Also, the Heusler layer underneath does not show any signs of impurity penetration towards the top of the film, and neither any signs of an oxidation gradient - the homogeneous intensity attributed to O which is detected across the entire film in subplot (g) in figures B.3 and B.4 does not imply an O penetration through the capping, but is more likely to be due to a partial oxidation of the lamella surface when transferring the sample from the FIB setup to the TEM setup, or an overlap of the O spectral features with either the Co, Mn or Si spectra.

The measurements thus indicate a successful protection of the Co_2MnSi film by the capping layer.

This is albeit the large surface roughness of the Al layer, which has not formed a homogeneous film but seems to have grown in islands. The exposed surface of the Al layer (islands) seems to have oxidised, as is clear from the close-up on one island in figure B.3 (compare the subplots in (g) and (h) corresponding to O and Al). Still, the entire surface seems to be covered with some (oxidised) Al, as the Pt is not found to reach the MgO layer (see subplot (e) in figure B.3 and B.4).

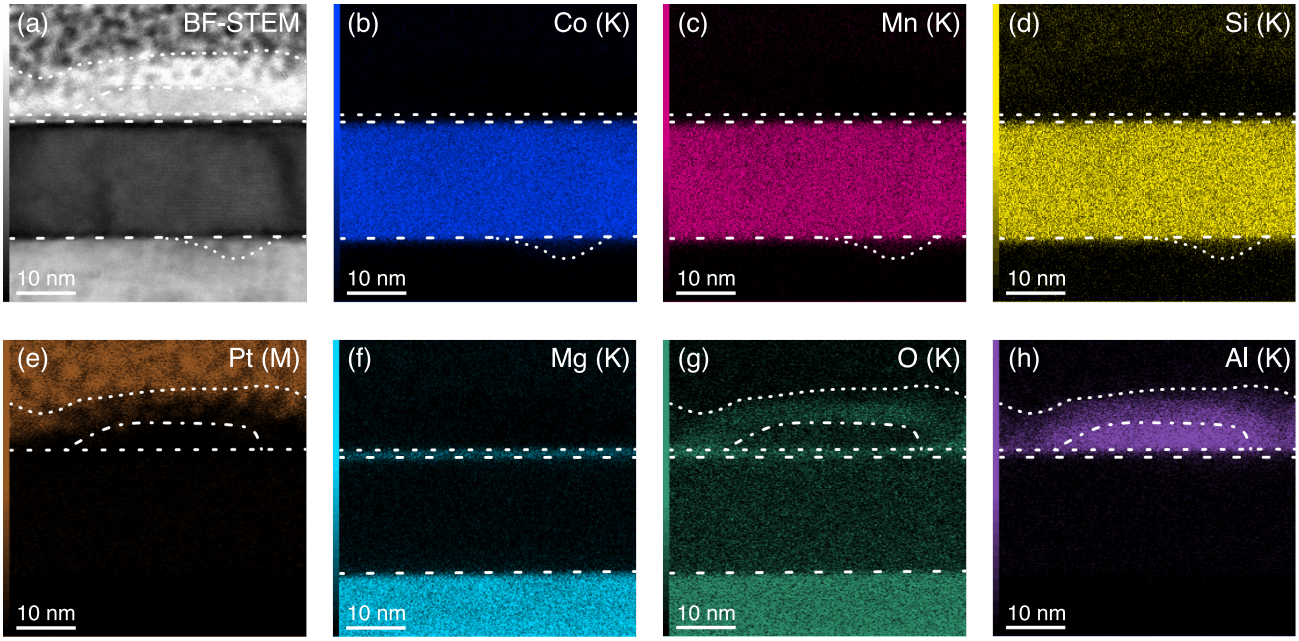

Figure B.3: EDXS elemental mapping of the Co_2MnSi/MgO/Al thin film stack corresponding to sample S1.4 (Q240212) in table 2.1, another piece of which was structured (see figures 3.1, 3.25, B.5 and B.6):
(a) BF-STEM micrograph captured before the spectral mapping,
(b-d) mapping of the Heusler compound elements Co, Mn and Si,
(e) mapping of the deposited Pt from the FIB process,
(f-h) mapping of the substrate and capping elements Mg, O, Al.
The dashed lines were added as guides for the comparison of the different elemental maps.

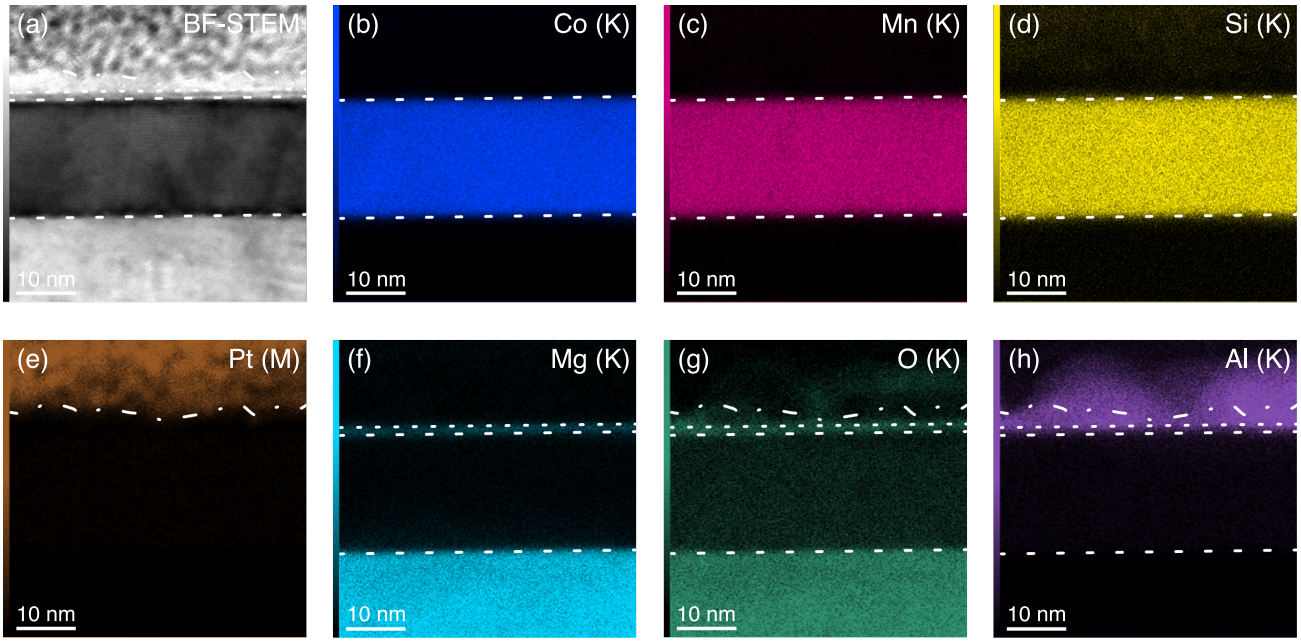

Figure B.4: EDXS elemental mapping of the $Co_2MnSi/MgO/Al$ thin film stack corresponding to sample S1.4 (Q240212) in table 2.1, another piece of which was structured (see figures 3.1, 3.25, B.5 and B.6):
(a) BF-STEM micrograph captured before the spectral mapping,
(b-d) mapping of the Heusler compound elements Co, Mn and Si,
(e) mapping of the deposited Pt from the FIB process,
(f-h) mapping of the substrate and capping elements Mg, O, Al.
The dashed lines were added as guides for the comparison of the different elemental maps.

B.3 Structured Co_2MnSi / MgO / Al – Sample S1.4 (Q240212)

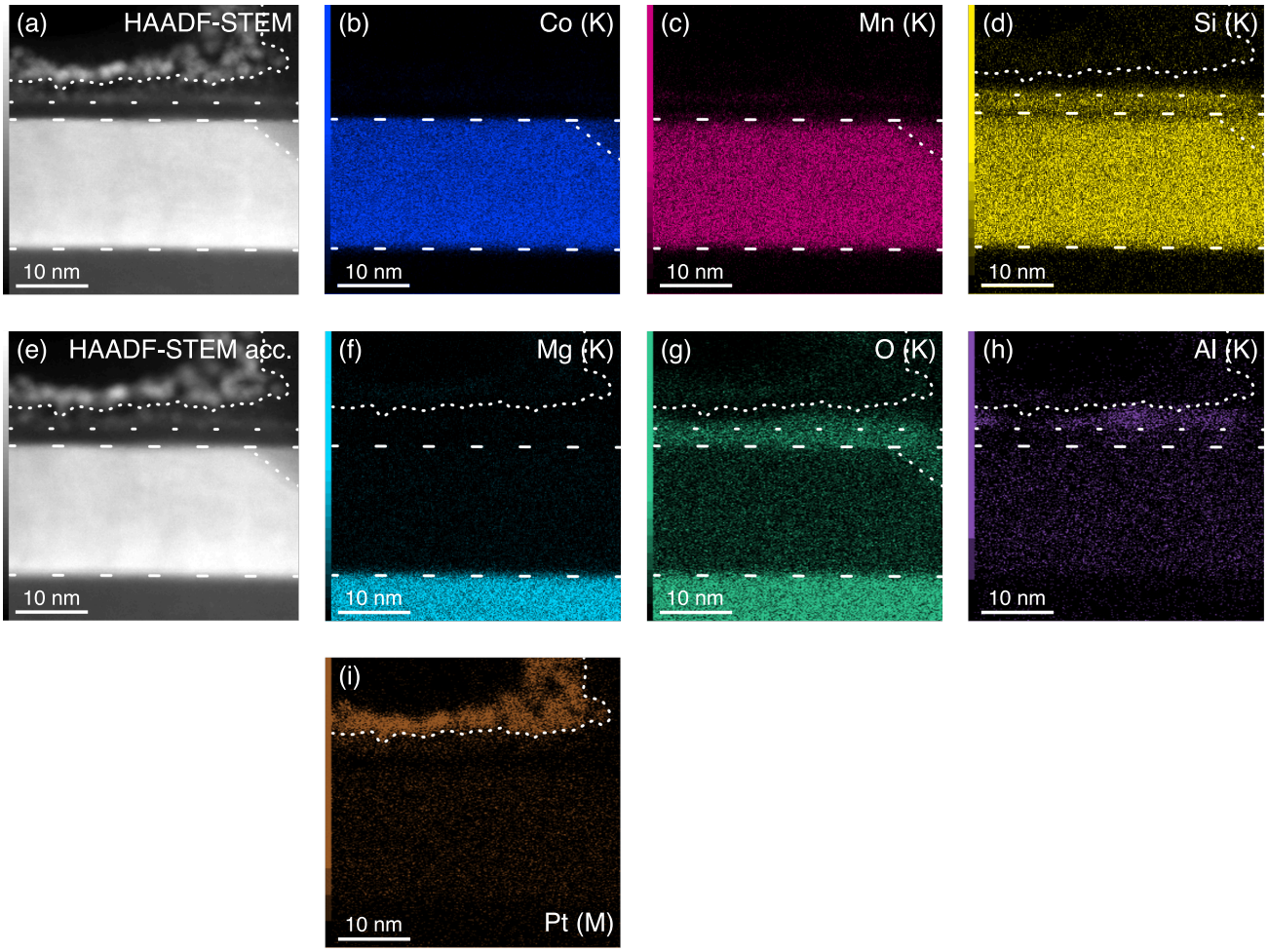

Figure B.5: EDXS elemental mapping of a waveguide edge from the structured Co_2MnSi/MgO/Al film from sample S1.4 (Q240212) in table 2.1: (a) HAADF-STEM micrograph captured before the spectral mapping, (b-d) mapping of the Heusler compound elements Co, Mn and Si (e) accumulated HAADF-STEM micrograph showing no signs of shift or drifting during the process, (f-h) mapping of the substrate and capping elements Mg, O, Al, (i) mapping of the deposited Pt from the FIB process. The investigated waveguide is part of the array on the lamella presented in figure 3.1. The dashed lines were added as guides for the comparison of the different elemental maps. The Al layer seems not to be continuous. Hardly any Mg is detected in the capping. The oxidised sample capping is not in direct contact with the Pt (compare (d), (g) and (h) to (i)), as additionally a C layer was deposited before loading the sample into the FIB setup to avoid charging effects, but the C was not mapped.

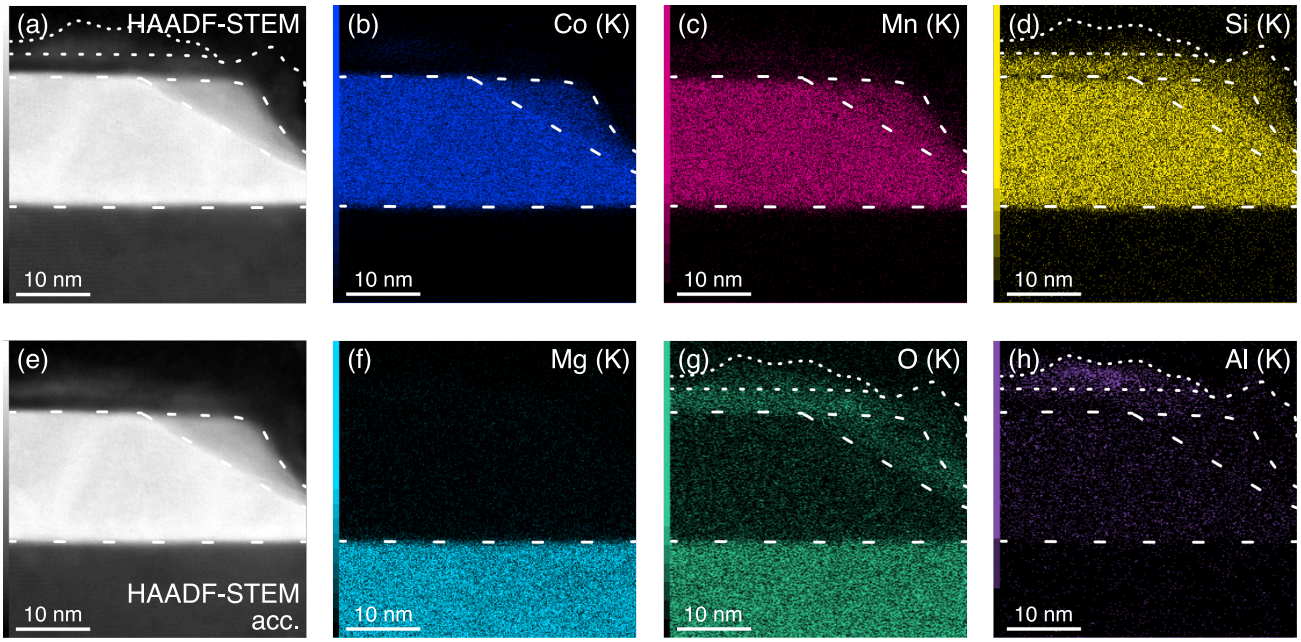

Figure B.6: EDXS elemental mapping of a waveguide edge from the structured $Co_2MnSi/MgO/Al$ film from sample S1.4 (Q240212) in table 2.1: (a) HAADF-STEM micrograph captured before the spectral mapping, (b-d) mapping of the Heusler compound elements Co, Mn and Si (e) accumulated HAADF-STEM micrograph showing no signs of shift or drifting during the process (f-h) mapping of the substrate and capping elements Mg, O, Al. The investigated waveguide is part of the array on the lamella presented in figure 3.1. The dashed lines were added as guides for the comparison of the different elemental maps.

C

Anisotropy - energy, fields and tensors

a.k.a. excercises in geometry

C.1 Cubic anisotropy energy (density)

The definition of the cubic anisotropy energy (density) is here recalled from the main text on page 69 and thereafter:

As introduced in the main part on page 69 and thereafter cubic lattice symmetry imposes two conditions on the magnetocrystalline anisotropy:

1. The magnetisation reversal along any crystal axis must not affect the anisotropy energy, thus imposing a function of even powers of the direction cosines m_i, where the symmetry axes $i = 1, 2, 3$ coincide with the principal axes of the cubic lattice.
2. The indifference to an interchange of any two crystal axes must be ensured, which implies a function of at least fourth order* of the direction cosines m_i [224].

The common form of the cubic magnetocrystalline anisotropy energy density meets these criteria and reads

$$\ell_{\text{ani,cubic}} = K_{\text{c1}}(m_1^2 m_2^2 + m_2^2 m_3^2 + m_3^2 m_1^2) + K_{\text{c2}} m_1^2 m_2^2 m_3^2 + \ldots \tag{C.1}$$

with the first and second order cubic anisotropy constants K_{c1} and K_{c2} in J/m^3 [224, 227]. An identification of the magnetic easy and hard axes is possible, but not trivial for the cubic anisotropy case: When taking the second order term into account, the identification of the magnetic easy and hard axes depends not only on the sign of the two constants but also their ratio as is given in table 4.1 on page 71 in the main part.

C.2 Anisotropy field and anisotropy tensors

The general expression of the cubic anisotropy field is obtained as the functional derivative [227] of the energy density and was given in equation 4.20 as

$$\mathbf{H}_{\text{ani,cub}} = -\frac{1}{\mu_0}\frac{\delta \ell_{\text{ani,cubic}}}{\delta \mathbf{M}} \tag{C.2}$$

$$= -\frac{2K_{\text{c1}}}{\mu_0 M_{\text{S}}} \sum_i \left(m_i \sum_{j \neq i} m_j^2 \right) \hat{\mathbf{e}}_i - \frac{2K_{\text{c2}}}{\mu_0 M_{\text{S}}} \sum_i \left(m_i \prod_{j \neq i} m_j^2 \right) \hat{\mathbf{e}}_i \tag{C.3}$$

where the m_i, m_j are the projections of the normalised vector field $\mathbf{m}(\mathbf{r}, t) = \frac{\mathbf{M}(\mathbf{r},t)}{M_{\text{S}}}$ defined in equation 4.2 on the crystal symmetry axes $i, j = 1, 2, 3$.

* Since the second order term $o \cdot m_1^2 + p \cdot m_2^2 + q \cdot m_3^2$ with any factors o, p, q and the interchangeability requirement imposing $o = p = q$, reduces to the term $m_1^2 + m_2^2 + m_3^2 = 1$, from which no anisotropy can arise.

C.2.1 Separation in a static part and a dynamic perturbation part

As stated on page 71, a tensor representation analogous to the demagnetisation tensor in equation 4.16 can be convenient to account for the distortion of the oscillation due to the anisotropy field. An approximative form can be derived by expressing the magnetisation $\mathbf{M}(\mathbf{r},t)$ as a combination of a static equilibrium component $\mathbf{M}_0(\mathbf{r})$ and a small dynamic perturbation $\delta\mathbf{m}(\mathbf{r},t)$, explicitly written as

$$\mathbf{M}(\mathbf{r},t) = \mathbf{M}_0(\mathbf{r}) + M_\mathrm{S}\delta\mathbf{m}(\mathbf{r},t) \tag{C.4}$$

for the magnetisation and

$$\mathbf{m}(\mathbf{r},t) = \mathbf{m}_0(\mathbf{r}) + \delta\mathbf{m}(\mathbf{r},t) \tag{C.5}$$

for the normalised vector field analogous to equation 4.2.

The magnetocrystalline anisotropy field can then be analogously written as a combination of a static equilibrium component and a dynamic perturbation, i.e.

$$\mathbf{H}_\mathrm{ani,cub} = \mathbf{H}^\mathrm{static}_\mathrm{ani,cub} + \delta\mathbf{h}_\mathrm{ani,cub} \tag{C.6}$$

where the static part $\mathbf{H}^\mathrm{static}_\mathrm{ani,cub}$ only depends on the equilibrium magnetisation $\mathbf{M}_0$ and its projections M_{0i} on the crystal axes $i = 1,2,3$ and can be written as

$$\mathbf{H}^\mathrm{static}_\mathrm{ani,cub} = -\frac{2K_\mathrm{c1}}{\mu_0 M_\mathrm{S}^4}\begin{pmatrix} M_{01}\cdot(M_\mathrm{S}^2 - M_{01}^2) \\ M_{02}\cdot(M_\mathrm{S}^2 - M_{02}^2) \\ M_{03}\cdot(M_\mathrm{S}^2 - M_{03}^2)\end{pmatrix} - \frac{2K_\mathrm{c2}}{\mu_0 M_\mathrm{S}^6}\begin{pmatrix} M_{01}\cdot M_{02}^2\cdot M_{03}^2 \\ M_{02}\cdot M_{03}^2\cdot M_{01}^2 \\ M_{03}\cdot M_{01}^2\cdot M_{02}^2\end{pmatrix} \tag{C.7}$$

or

$$\mathbf{H}^\mathrm{static}_\mathrm{ani,cub} = -\frac{2K_\mathrm{c1}}{\mu_0 M_\mathrm{S}}\begin{pmatrix} m_{01}\cdot(1 - m_{01}^2) \\ m_{02}\cdot(1 - m_{02}^2) \\ m_{03}\cdot(1 - m_{03}^2)\end{pmatrix} - \frac{2K_\mathrm{c2}}{\mu_0 M_\mathrm{S}}\begin{pmatrix} m_{01}\cdot m_{02}^2\cdot m_{03}^2 \\ m_{02}\cdot m_{03}^2\cdot m_{01}^2 \\ m_{03}\cdot m_{01}^2\cdot m_{02}^2\end{pmatrix} \tag{C.8}$$

and the dynamic part $\delta\mathbf{h}_\mathrm{ani,cub}$ depends on the equilibrium magnetisation $\mathbf{m}_0(\mathbf{r})$ as well as the dynamic perturbation $\delta\mathbf{m}(\mathbf{r},t)$. Keeping only terms of the lowest order in the dynamic perturbation $\delta\mathbf{m}$ allows to express the dynamic part of the anisotropy field as a linear function of the dynamic magnetisation perturbation $\delta\mathbf{m}$, i.e.

$$\delta\mathbf{h}_\mathrm{ani,cub} = -\hat{N}^\mathrm{cub}_\mathrm{ani}\cdot M_\mathrm{S}\delta\mathbf{m} = -\left(\hat{N}^\mathrm{c1}_\mathrm{ani} + \hat{N}^\mathrm{c2}_\mathrm{ani}\right)\cdot M_\mathrm{S}\delta\mathbf{m} \tag{C.9}$$

where the anisotropy tensor $\hat{N}^\mathrm{cub}_\mathrm{ani} = \hat{N}^\mathrm{c1}_\mathrm{ani} + \hat{N}^\mathrm{c2}_\mathrm{ani}$ depends on the cubic anisotropy constants K_c1 and K_c2 and contains the directional dependence of the anisotropy terms on the orientation in the crystal lattice.

As introduced on page 71 and 72, these tensors are easily defined in the crystal coordinates, in which they read

$$\hat{N}^\mathrm{c1}_\mathrm{ani} = \frac{2K_\mathrm{c1}}{\mu_0 M_\mathrm{S}^4}\begin{bmatrix} M_\mathrm{S}^2 - M_{01}^2 & 2M_{01}M_{02} & 2M_{01}M_{03} \\ 2M_{01}M_{02} & M_\mathrm{S}^2 - M_{02}^2 & 2M_{02}M_{03} \\ 2M_{01}M_{03} & 2M_{02}M_{03} & M_\mathrm{S}^2 - M_{03}^2\end{bmatrix}_{123} \tag{C.10}$$

$$= \frac{2K_\mathrm{c1}}{\mu_0 M_\mathrm{S}^2}\begin{bmatrix} 1 - m_{01}^2 & 2m_{01}m_{02} & 2m_{01}m_{03} \\ 2m_{01}m_{02} & 1 - m_{02}^2 & 2m_{02}m_{03} \\ 2m_{01}m_{03} & 2m_{02}m_{03} & 1 - m_{03}^2\end{bmatrix}_{123} \tag{C.11}$$

for the first order cubic anisotropy and

$$\hat{N}^\mathrm{c2}_\mathrm{ani} = \frac{2K_\mathrm{c2}}{\mu_0 M_\mathrm{S}^6}\begin{bmatrix} M_{02}^2\cdot M_{03}^2 & 2M_{01}M_{02}M_{03}^2 & 2M_{01}M_{02}^2M_{03} \\ 2M_{01}M_{02}M_{03}^2 & M_{03}^2\cdot M_{01}^2 & 2M_{01}^2M_{02}M_{03} \\ 2M_{01}M_{02}^2M_{03} & 2M_{01}^2M_{02}M_{03} & M_{01}^2\cdot M_{02}^2\end{bmatrix}_{123} \tag{C.12}$$

$$= \frac{2K_\mathrm{c2}}{\mu_0 M_\mathrm{S}^2}\begin{bmatrix} m_{02}^2\cdot m_{03}^2 & 2m_{01}m_{02}m_{03}^2 & 2m_{01}m_{02}^2m_{03} \\ 2m_{01}m_{02}m_{03}^2 & m_{03}^2\cdot m_{01}^2 & 2m_{01}^2m_{02}m_{03} \\ 2m_{01}m_{02}^2m_{03} & 2m_{01}^2m_{02}m_{03} & m_{01}^2\cdot m_{02}^2\end{bmatrix}_{123} \tag{C.13}$$

for the second order cubic anisotropy term. The index $[\ldots]_{123}$ denotes the expression of the tensor in the crystal coordinate system with base vectors $\{\hat{\mathbf{e}}_1, \hat{\mathbf{e}}_2, \hat{\mathbf{e}}_3\}$ as introduced on page 155.

C.2.2 Anisotropy tensor $\hat{N}_{\mathrm{ani}}$ and tensor elements $N_{\mathrm{xx}}, N_{\mathrm{xy}}, N_{\mathrm{yy}}$ etc.

In this thesis, tensors are generally denoted by a hat, e.g. $\hat{N}_{\mathrm{ani}}$. The tensor elements are referred to by the indices, as it is commonly used for matrix indexing. This is in fact mostly used in the context of the approximative analytical dispersion relation derived by Kaliniko and Slavin in [378, 379] as introduced on page 152 and thereafter, in which the different directional anisotropy contributions are incorporated via the respective tensor elements expressed in the local (dynamic) coordinate system xyz, see figure 8.1 as well as the description on page 155.

Precisely, the tensor elements are indexed as

$$\hat{N}_{\mathrm{ani}} = \begin{bmatrix} N_{xx}^{\mathrm{ani}} & N_{xy}^{\mathrm{ani}} & N_{xz}^{\mathrm{ani}} \\ N_{yx}^{\mathrm{ani}} & N_{yy}^{\mathrm{ani}} & N_{yz}^{\mathrm{ani}} \\ N_{zx}^{\mathrm{ani}} & N_{zy}^{\mathrm{ani}} & N_{zz}^{\mathrm{ani}} \end{bmatrix}_{\mathrm{xyz}} \tag{C.14}$$

in the local (dynamic) coordinate system, which can be calculated from the local coordinates following

$$\hat{N}_{\mathrm{ani}} = \begin{bmatrix} N_{xx}^{\mathrm{ani}} & N_{xy}^{\mathrm{ani}} & N_{xz}^{\mathrm{ani}} \\ N_{yx}^{\mathrm{ani}} & N_{yy}^{\mathrm{ani}} & N_{yz}^{\mathrm{ani}} \\ N_{zx}^{\mathrm{ani}} & N_{zy}^{\mathrm{ani}} & N_{zz}^{\mathrm{ani}} \end{bmatrix}_{\mathrm{xyz}} = \hat{T}_{123\to xyz} \cdot \begin{bmatrix} N_{11}^{\mathrm{ani}} & N_{12}^{\mathrm{ani}} & N_{13}^{\mathrm{ani}} \\ N_{21}^{\mathrm{ani}} & N_{22}^{\mathrm{ani}} & N_{23}^{\mathrm{ani}} \\ N_{31}^{\mathrm{ani}} & N_{32}^{\mathrm{ani}} & N_{33}^{\mathrm{ani}} \end{bmatrix}_{123} \cdot \hat{T}_{123\to xyz}^{\mathrm{T}} \tag{C.15}$$

with an appropriate transformation matrix [227]

$$\hat{T}_{123\to xyz} = \begin{bmatrix} \hat{\mathbf{e}}_x \cdot \hat{\mathbf{e}}_1 & \hat{\mathbf{e}}_x \cdot \hat{\mathbf{e}}_2 & \hat{\mathbf{e}}_x \cdot \hat{\mathbf{e}}_3 \\ \hat{\mathbf{e}}_y \cdot \hat{\mathbf{e}}_1 & \hat{\mathbf{e}}_y \cdot \hat{\mathbf{e}}_2 & \hat{\mathbf{e}}_y \cdot \hat{\mathbf{e}}_3 \\ \hat{\mathbf{e}}_z \cdot \hat{\mathbf{e}}_1 & \hat{\mathbf{e}}_z \cdot \hat{\mathbf{e}}_2 & \hat{\mathbf{e}}_z \cdot \hat{\mathbf{e}}_3 \end{bmatrix} \tag{C.16}$$

and its transposed form $\hat{T}_{123\to xyz}^{\mathrm{T}}$.

Transformation matrices

The **transformation between the global coordinates** uvw **and the dynamic coordinates** xyz is then easily achieved by defining $\hat{\mathbf{e}}_{\mathrm{z}} = \frac{\mathbf{M}_{0,uvw}}{M_{\mathrm{S}}}$ as described above, which allows to calculate the dynamic base as[†]

$$\hat{\mathbf{e}}_{\mathrm{y}} = \frac{\hat{\mathbf{e}}_{\mathrm{z}} \times \hat{\mathbf{e}}_{\mathrm{v}}}{\|\hat{\mathbf{e}}_{\mathrm{z}} \times \hat{\mathbf{e}}_{\mathrm{v}}\|} \quad \text{and} \quad \hat{\mathbf{e}}_{\mathrm{x}} = \frac{\hat{\mathbf{e}}_{\mathrm{y}} \times \hat{\mathbf{e}}_{\mathrm{z}}}{\|\hat{\mathbf{e}}_{\mathrm{y}} \times \hat{\mathbf{e}}_{\mathrm{z}}\|} \tag{C.17}$$

[†] Clearly, this definition only works for cases where the equilibrium position $\mathbf{M}_{0,uvw} \nparallel \hat{\mathbf{e}}_{\mathrm{v}}$, which is not an issue for in-plane magnetised thin films as studied here.

which can be expressed in the above defined angles[‡] θ_0, φ_0 to define the transformation matrix

$$\hat{T}_{uvw\to xyz} = \begin{bmatrix} \frac{-\sin\theta_0\cos\theta_0\sin\varphi_0}{\sin^2\theta_0} & 1 & \frac{-\sin\theta_0\cos\theta_0\cos\varphi_0}{\sin^2\theta_0} \\ \frac{-\sin\theta_0\cos\varphi_0}{\sqrt{\sin^2\theta_0}} & 0 & \frac{\sin\theta_0\sin\varphi_0}{\sqrt{\sin^2\theta_0}} \\ \sin\theta_0\sin\varphi_0 & \cos\theta_0 & \sin\theta_0\cos\varphi_0 \end{bmatrix} \tag{C.21}$$

between the global coordinates uvw and the dynamic coordinates xyz.

A static **transformation matrix between the crystal base and the global base** is easily defined by indicating the crystal axes $[h_\mathrm{u}, k_\mathrm{u}, l_\mathrm{u}]$ and $[h_\mathrm{v}, k_\mathrm{v}, l_\mathrm{v}]$ which coincide with the propagation direction $\hat{\mathbf{e}}_\mathrm{u}$ and the film normal $\hat{\mathbf{e}}_\mathrm{v}$ respectively. This corresponds to expressing the global base vectors $\hat{\mathbf{e}}_\mathrm{u}, \hat{\mathbf{e}}_\mathrm{v}$ in the crystal base $\{\hat{\mathbf{e}}_1, \hat{\mathbf{e}}_2, \hat{\mathbf{e}}_3\}$ and the transformation matrix is in this case easily expressed as

$$\hat{T}_{123\to uvw} = \begin{bmatrix} \frac{h_\mathrm{u}}{\sqrt{h_\mathrm{u}^2+k_\mathrm{u}^2+l_\mathrm{u}}} & \frac{k_\mathrm{u}}{\sqrt{h_\mathrm{u}^2+k_\mathrm{u}^2+l_\mathrm{u}}} & \frac{l_\mathrm{u}}{\sqrt{h_\mathrm{u}^2+k_\mathrm{u}^2+l_\mathrm{u}}} \\ \frac{h_\mathrm{v}}{\sqrt{h_\mathrm{v}^2+k_\mathrm{v}^2+l_\mathrm{v}}} & \frac{k_\mathrm{v}}{\sqrt{h_\mathrm{v}^2+k_\mathrm{v}^2+l_\mathrm{v}}} & \frac{l_\mathrm{v}}{\sqrt{h_\mathrm{v}^2+k_\mathrm{v}^2+l_\mathrm{v}}} \\ \frac{k_\mathrm{u}l_\mathrm{v}-l_\mathrm{u}k_\mathrm{v}}{\mathrm{norm_w}} & \frac{l_\mathrm{u}h_\mathrm{u}-h_\mathrm{u}l_\mathrm{v}}{\mathrm{norm_w}} & \frac{h_\mathrm{u}k_\mathrm{v}-k_\mathrm{u}h_\mathrm{v}}{\mathrm{norm_w}} \end{bmatrix} \tag{C.22}$$

where $\mathrm{norm_w} = \sqrt{(k_\mathrm{u}l_\mathrm{v} - l_\mathrm{u}k_\mathrm{v})^2 + (l_\mathrm{u}h_\mathrm{u} - h_\mathrm{u}l_\mathrm{v})^2 + (h_\mathrm{u}k_\mathrm{v} - k_\mathrm{u}h_\mathrm{v})^2}$ was introduced as an abbreviation. However, this fixed-orientation approach is useful only for such cases, where an explicit crystal geometry is regarded.

For more general cases, e.g. when investigating an angular dependence, it is convenient to define a rotatable expression of the transformation matrix. To do so, one can define sets of polar and azimuthal rotation angles θ and φ, analogous to θ_0 and φ_0 for the equilibrium position of the magnetisation. Let θ_3 and φ_3 be the the polar and azimuthal angles of the [001] direction, as well as θ_1 and φ_1 the polar and azimuthal angles of the [100] direction, with the azimuthal angles defined with respect to the propagation direction $\hat{\mathbf{e}}_\mathrm{u}$. This corresponds to an expression of the crystal base vectors $\hat{\mathbf{e}}_2, \hat{\mathbf{e}}_3$ in the global base $\{\hat{\mathbf{e}}_\mathrm{u}, \hat{\mathbf{e}}_\mathrm{v}, \hat{\mathbf{e}}_\mathrm{w}\}$, see the general forms in the footnote[§] from which the transformation $\hat{T}_{123\to uvw}$ is easily written in its general form, but due to its rather lengthy form omitted from being printed here.

[‡] Explicitely, one can write

$$\hat{\mathbf{e}}_z = \begin{pmatrix} \sin\theta_0\sin\varphi_0 \\ \cos\theta_0 \\ \sin\theta_0\cos\varphi_0 \end{pmatrix}_{\mathrm{uvw}} \tag{C.18}$$

then

$$\hat{\mathbf{e}}_\mathrm{y} = \frac{1}{\sqrt{\sin^2\theta_0}} \begin{pmatrix} -\sin\theta_0\cos\varphi_0 \\ 0 \\ \sin\theta_0\sin\varphi_0 \end{pmatrix}_{\mathrm{uvw}} \tag{C.19}$$

and

$$\hat{\mathbf{e}}_\mathrm{x} = \frac{1}{\sin^2\theta_0} \begin{pmatrix} -\sin\theta_0\cos\theta_0\sin\varphi_0 \\ \sin^2\theta_0 \\ \sin\theta_0\cos\theta_0\cos\varphi_0 \end{pmatrix}_{\mathrm{uvw}} \tag{C.20}$$

[§] With the sets of polar and azimuthal angles (θ_3, φ_3) and (θ_1, φ_1), the base vectors can be expressed as

$$\hat{\mathbf{e}}_3 = \begin{pmatrix} \sin\theta_3\cos\varphi_3 \\ \cos\theta_3 \\ \sin\theta_3\sin\varphi_3 \end{pmatrix}_{\mathrm{uvw}} \tag{C.23}$$

and

$$\hat{\mathbf{e}}_1 = \begin{pmatrix} \sin\theta_1\cos\varphi_1 \\ \cos\theta_1 \\ \sin\theta_1\sin\varphi_1 \end{pmatrix}_{\mathrm{uvw}} \tag{C.24}$$

and therefore

$$\hat{\mathbf{e}}_2 = \frac{\hat{\mathbf{e}}_3 \times \hat{\mathbf{e}}_1}{\|\hat{\mathbf{e}}_3 \times \hat{\mathbf{e}}_1\|} \tag{C.25}$$

where $\hat{\mathbf{e}}_2$ is not explicitly written for space reasons.

In this thesis, the crystal $[001]_{123}$ direction is always defined[¶] along the film normal $\hat{\mathbf{e}}_v$, hence $\theta_3 = 0$ and $\theta_1 = \pi/2$. Hence, the rotation matrix from crystal coordinates to the global base reads

$$\hat{T}_{123\to uvw} = \begin{bmatrix} \cos\varphi_1 & \sin\varphi_1 & 0 \\ 0 & 0 & 1 \\ \sin\varphi_1 & -\cos\varphi_1 & 0 \end{bmatrix} \tag{C.26}$$

which corresponds to a rotation in the film plane with the angle φ_1 (defined between the crystal $[100]_{123}$ direction and the propagation axis u as mentioned above). Moreover, the investigations in chapter 10 focus on a fixed propagation direction along the crystal direction $[110]_{123}$, which further simplifies the rotation matrix (i.e. $\varphi_1 = \pi/4$ and thus $\sin\varphi_1 = \cos\varphi_1 = \frac{1}{\sqrt{2}}$).

These transformation matrices can thus be used to derive a general expression of the anisotropy tensor (elements), e.g. in order to get a rotational dependence of the anisotropy fields for the rotational FMR, or a generalised form for the incorporation in the Kalinikos-Slavin dispersion relation (approximative analytical formula).

C.3 General angular dependence of the cubic anisotropy tensor (in the crystal base)

In the crystal coordinate system, an angular dependence of the anisotropy expressions can be easily introduced by an expression of the equilibrium position of the magnetisation in terms of an angle φ_{100} between the $\hat{\mathbf{e}}_1 = [100]_{123}$ axis of the crystal coordinate system and the equlibrium position of the magnetisation $\mathbf{M}_0(\mathbf{r})$ and an angle θ_{001} between the $\hat{\mathbf{e}}_3 = [001]_{123}$ axis of the crystal coordinate system and the magnetisation $\mathbf{M}_0(\mathbf{r})$. Clearly, this corresponds to a simple expression of the magnetisation in spherical coordinates as is typically used in various other cases as well. The projections m_{01}, m_{02}, m_{03} of the normalised magnetisation $\mathbf{m}_0(\mathbf{r})$ on the crystal axes with base vectors $\{\hat{\mathbf{e}}_1, \hat{\mathbf{e}}_2, \hat{\mathbf{e}}_3\}$ are then expressed as

$$m_{01} = \frac{M_{01}}{M_S} = \cos(\varphi_{100})\sin(\theta_{001}) \tag{C.27}$$

$$m_{02} = \frac{M_{02}}{M_S} = \sin(\varphi_{100})\sin(\theta_{001}) \tag{C.28}$$

$$m_{03} = \frac{M_{03}}{M_S} = \cos(\theta_{001}) \tag{C.29}$$

with the two angles $\varphi_{100} \in [0, 2\pi]$ and $\theta_{001} \in [0, \pi]$.

C.3.1 The cubic anisotropy tensor and its symmetries in the crystal coordinates

First order cubic anisotropy tensor in the crystal coordinates

According to equation C.11, the first order cubic anisotropy tensor is expressed as

$$\hat{N}_{\text{ani}}^{\text{c1}} = \frac{2K_{\text{c1}}}{\mu_0 M_S^2} \begin{bmatrix} 1-m_{01}^2 & 2m_{01}m_{02} & 2m_{01}m_{03} \\ 2m_{01}m_{02} & 1-m_{02}^2 & 2m_{02}m_{03} \\ 2m_{01}m_{03} & 2m_{02}m_{03} & 1-m_{03}^2 \end{bmatrix}_{123} \tag{C.30}$$

[¶] Simply fixed by the growth direction, ultimately defined by the choice of the MgO(001) substrate.

and therefore yields the tensor elements

$$N_{11}^{\mathrm{ani,c1}} = \frac{2K_{\mathrm{c1}}}{\mu_0 M_{\mathrm{S}}^2} \cdot \left(1 - \cos^2\left(\varphi_{100}\right) \sin^2\left(\theta_{001}\right)\right) \tag{C.31}$$

$$N_{22}^{\mathrm{ani,c1}} = \frac{2K_{\mathrm{c1}}}{\mu_0 M_{\mathrm{S}}^2} \cdot \left(1 - \sin^2\left(\varphi_{100}\right) \sin^2\left(\theta_{001}\right)\right) \tag{C.32}$$

$$N_{33}^{\mathrm{ani,c1}} = \frac{2K_{\mathrm{c1}}}{\mu_0 M_{\mathrm{S}}^2} \cdot \left(1 - \cos^2\left(\theta_{001}\right)\right) \tag{C.33}$$

for the diagonal elements as well as

$$N_{12}^{\mathrm{ani,c1}} = N_{21}^{\mathrm{ani,c1}} = \frac{2K_{\mathrm{c1}}}{\mu_0 M_{\mathrm{S}}^2} \cdot 2 \cdot \sin\left(\varphi_{100}\right) \cos\left(\varphi_{100}\right) \sin^2\left(\theta_{001}\right) \tag{C.34}$$

$$N_{13}^{\mathrm{ani,c1}} = N_{31}^{\mathrm{ani,c1}} = \frac{2K_{\mathrm{c1}}}{\mu_0 M_{\mathrm{S}}^2} \cdot 2 \cdot \cos\left(\varphi_{100}\right) \sin\left(\theta_{001}\right) \cos\left(\theta_{001}\right) \tag{C.35}$$

$$N_{23}^{\mathrm{ani,c1}} = N_{32}^{\mathrm{ani,c1}} = \frac{2K_{\mathrm{c1}}}{\mu_0 M_{\mathrm{S}}^2} \cdot 2 \cdot \sin\left(\varphi_{100}\right) \sin\left(\theta_{001}\right) \cos\left(\theta_{001}\right) \tag{C.36}$$

for the off-diagonal elements in the crystal base coordinates.

Second order cubic anisotropy tensor in the crystal coordinates

Analogously, the second order cubic anisotropy tensor from equation C.13 is expressed as

$$\hat{N}_{\mathrm{ani}}^{\mathrm{c2}} = \frac{2K_{\mathrm{c2}}}{\mu_0 M_{\mathrm{S}}^2} \begin{bmatrix} m_{02}^2 \cdot m_{03}^2 & 2m_{01}m_{02}m_{03}^2 & 2m_{01}m_{02}^2m_{03} \\ 2m_{01}m_{02}m_{03}^2 & m_{03}^2 \cdot m_{01}^2 & 2m_{01}^2m_{02}m_{03} \\ 2m_{01}m_{02}^2m_{03} & 2m_{01}^2m_{02}m_{03} & m_{01}^2 \cdot m_{02}^2 \end{bmatrix}_{123} \tag{C.37}$$

and therefore yields the tensor elements

$$N_{11}^{\mathrm{ani,c2}} = \frac{2K_{\mathrm{c2}}}{\mu_0 M_{\mathrm{S}}^2} \cdot \sin^2\left(\varphi_{100}\right) \sin^2\left(\theta_{001}\right) \cos^2\left(\theta_{001}\right) \tag{C.38}$$

$$N_{22}^{\mathrm{ani,c2}} = \frac{2K_{\mathrm{c2}}}{\mu_0 M_{\mathrm{S}}^2} \cdot \cos^2\left(\varphi_{100}\right) \sin^2\left(\theta_{001}\right) \cos^2\left(\theta_{001}\right) \tag{C.39}$$

$$N_{33}^{\mathrm{ani,c2}} = \frac{2K_{\mathrm{c2}}}{\mu_0 M_{\mathrm{S}}^2} \cdot \sin^2\left(\varphi_{100}\right) \cos^2\left(\varphi_{100}\right) \sin^4\left(\theta_{001}\right) \tag{C.40}$$

for the diagonal elements as well as

$$N_{12}^{\mathrm{ani,c2}} = N_{21}^{\mathrm{ani,c2}} = \frac{2K_{\mathrm{c2}}}{\mu_0 M_{\mathrm{S}}^2} \cdot 2 \cdot \sin\left(\varphi_{100}\right) \cos\left(\varphi_{100}\right) \sin^2\left(\theta_{001}\right) \cos^2\left(\theta_{001}\right) \tag{C.41}$$

$$N_{13}^{\mathrm{ani,c2}} = N_{31}^{\mathrm{ani,c2}} = \frac{2K_{\mathrm{c2}}}{\mu_0 M_{\mathrm{S}}^2} \cdot 2 \cdot \sin^2\left(\varphi_{100}\right) \cos\left(\varphi_{100}\right) \sin^3\left(\theta_{001}\right) \cos\left(\theta_{001}\right) \tag{C.42}$$

$$N_{23}^{\mathrm{ani,c2}} = N_{32}^{\mathrm{ani,c2}} = \frac{2K_{\mathrm{c2}}}{\mu_0 M_{\mathrm{S}}^2} \cdot 2 \cdot \sin\left(\varphi_{100}\right) \cos^2\left(\varphi_{100}\right) \sin^3\left(\theta_{001}\right) \cos\left(\theta_{001}\right) \tag{C.43}$$

for the off-diagonal elements in the crystal base coordinates.

Symmetry observations of the magnetocrystalline anisotropy (independent of the sample geometry)

From the general expression of the anisotropy tensors, a few implications can be constated without a specification of any sample geometry or local coordinate system. Note that these are pure magnetocrystalline effects and solely

dependent on the orientation of the equilibrium position in the crystal lattice, hence independent of the field geometry with respect to the global structure (or thin film) geometry under investigation.

General observations are:

- The off-diagonal elements $N_{ab}^{\mathrm{ani,c1}}$ of the first order tensor become zero when the projection of the magnetisation on either of the corresponding axes a, b is zero, i.e. $M_{0a} = 0$ or $M_{0b} = 0$.
- All off-diagonal elements $N_{ab}^{\mathrm{ani,c2}}$ of the second order tensor become zero when any projection M_{01}, M_{02}, M_{03} of the equilibrium magnetisation on a principle lattice axis is zero.
- If not all signs of the projections M_{01}, M_{02}, M_{03} are the same, the signs of the off-diagonal elements in both tensors change at the positions of the minority sign, e.g. if only M_{02} is positive (and equally if only M_{02} is negative), then the signs of $N_{12}^{\mathrm{ani}}, N_{21}^{\mathrm{ani}}, N_{23}^{\mathrm{ani}}$ and N_{32}^{ani} change.
- The sign of the diagonal elements of both tensors is always equal to the sign imposed by the respective anisotropy constant, independent of (the sign of) the different projections M_{01}, M_{02}, M_{03} of the equilibrium position on the crystal axes.

Examples of the resulting tensors for some common equilibrium orientations [100], [110], [111], [112]

Case 1: An alignment of the equilibrium position along a principle axis of the cubic lattice:

- $\mathbf{M}_0 \parallel i_a \hat{\mathbf{e}}_a$ for $a \in \{1, 2, 3\}$ and $i_a \in \{1, -1\}$:
  1. The corresponding diagonal element $N_{aa}^{\mathrm{ani,c1}}$ of the first order cubic anisotropy tensor vanishes, and the other two tensor elements become $N_{bb}^{\mathrm{ani,c1}} = \frac{2K_{\mathrm{c1}}}{\mu_0 M_{\mathrm{S}}^2}$ for $a \neq b \in \{1, 2, 3\}$.
  2. The off-diagonal elements of the first order cubic anisotropy tensor all vanish.
  3. The second order cubic anisotropy tensor vanishes entirely.
- An example is the alignment of $\mathbf{M}_0 \parallel [100]_{123}$, which results in

$$\hat{N}_{\mathrm{ani}} = \hat{N}_{\mathrm{ani}}^{\mathrm{c1}} + \hat{N}_{\mathrm{ani}}^{\mathrm{c2}} = \frac{2K_{\mathrm{c1}}}{\mu_0 M_{\mathrm{S}}^2} \begin{bmatrix} 0 & 0 & 0 \\ 0 & 1 & 0 \\ 0 & 0 & 1 \end{bmatrix}_{123} + \frac{2K_{\mathrm{c2}}}{\mu_0 M_{\mathrm{S}}^2} \begin{bmatrix} 0 & 0 & 0 \\ 0 & 0 & 0 \\ 0 & 0 & 0 \end{bmatrix}_{123} \tag{C.44}$$

$$\Rightarrow \hat{N}_{\mathrm{ani}} = \frac{1}{\mu_0 M_{\mathrm{S}}^2} \begin{bmatrix} 0 & 0 & 0 \\ 0 & 2K_{\mathrm{c1}} & 0 \\ 0 & 0 & 2K_{\mathrm{c1}} \end{bmatrix}_{123} \tag{C.45}$$

  for the cubic anisotropy tensor in the crystal base coordinate system $\{\hat{\mathbf{e}}_1, \hat{\mathbf{e}}_2, \hat{\mathbf{e}}_3\}$.

Case 2: An alignment of the equilibrium position along a face diagonal of the cubic unit cell:

- $\mathbf{M}_0 \parallel i_a \cdot \hat{\mathbf{e}}_a + i_b \cdot \hat{\mathbf{e}}_b$ for $a, b \in \{1, 2, 3\}$ and $a \neq b$, and $i_a, i_b \in \{1, -1\}$:
  1. The corresponding two diagonal elements of the first order cubic anisotropy tensor become $N_{aa}^{\mathrm{ani,c1}} = N_{bb}^{\mathrm{ani,c1}} = \frac{2K_{\mathrm{c1}}}{\mu_0 M_{\mathrm{S}}^2} \cdot \frac{1}{2}$. The other diagonal element $N_{cc}^{\mathrm{ani,c1}}$ with $c \neq a, b$ yields $N_{cc}^{\mathrm{ani,c1}} = \frac{2K_{\mathrm{c1}}}{\mu_0 M_{\mathrm{S}}^2}$.
  2. The off-diagonal elements of the first order cubic anisotropy tensor vanish for the components which contain the index $p \neq i, j$. The other two off-diagonal elements yield $|N_{ij}^{\mathrm{ani,c1}}| = \frac{2K_{\mathrm{c1}}}{\mu_0 M_{\mathrm{S}}^2}$ and the sign is given by the sign of $i_a \cdot i_b$.
  3. The diagonal element $N_{pp}^{\mathrm{ani,c2}}$ with $p \neq i, j$ of the second order cubic anisotropy tensor yields $N_{pp}^{\mathrm{ani,c2}} = \frac{2K_{\mathrm{c2}}}{\mu_0 M_{\mathrm{S}}^2} \cdot \frac{1}{4}$. All other elements of the second order cubic anisotropy tensor are zero.
- An example is the alignment of $\mathbf{M}_0 \parallel [110]_{123}$, which results in

$$\hat{N}_{\mathrm{ani}} = \hat{N}_{\mathrm{ani}}^{\mathrm{c1}} + \hat{N}_{\mathrm{ani}}^{\mathrm{c2}} = \frac{2K_{\mathrm{c1}}}{\mu_0 M_{\mathrm{S}}^2} \begin{bmatrix} \frac{1}{2} & 1 & 0 \\ 1 & \frac{1}{2} & 0 \\ 0 & 0 & 1 \end{bmatrix}_{123} + \frac{2K_{\mathrm{c2}}}{\mu_0 M_{\mathrm{S}}^2} \begin{bmatrix} 0 & 0 & 0 \\ 0 & 0 & 0 \\ 0 & 0 & \frac{1}{4} \end{bmatrix}_{123} \tag{C.46}$$

$$\Rightarrow \hat{N}_{\mathrm{ani}} = \frac{1}{\mu_0 M_{\mathrm{S}}^2} \begin{bmatrix} K_{\mathrm{c1}} & 2K_{\mathrm{c1}} & 0 \\ 2K_{\mathrm{c1}} & K_{\mathrm{c1}} & 0 \\ 0 & 0 & 2K_{\mathrm{c1}} + \frac{1}{2}K_{\mathrm{c2}} \end{bmatrix}_{123} \tag{C.47}$$

for the cubic anisotropy tensor in the crystal base coordinate system $\{\hat{\mathbf{e}}_1, \hat{\mathbf{e}}_2, \hat{\mathbf{e}}_3\}$.

- Another example is the alignment of $\mathbf{M}_0 \parallel [1\bar{1}0]_{123}$, which results in

$$\hat{N}_{\text{ani}} = \hat{N}^{\text{c1}}_{\text{ani}} + \hat{N}^{\text{c2}}_{\text{ani}} = \frac{2K_{\text{c1}}}{\mu_0 M_{\text{S}}^2} \begin{bmatrix} \frac{1}{2} & -1 & 0 \\ -1 & \frac{1}{2} & 0 \\ 0 & 0 & 1 \end{bmatrix}_{123} + \frac{2K_{\text{c2}}}{\mu_0 M_{\text{S}}^2} \begin{bmatrix} 0 & 0 & 0 \\ 0 & 0 & 0 \\ 0 & 0 & \frac{1}{4} \end{bmatrix}_{123} \tag{C.48}$$

$$\Rightarrow \hat{N}_{\text{ani}} = \frac{1}{\mu_0 M_{\text{S}}^2} \begin{bmatrix} K_{\text{c1}} & -2K_{\text{c1}} & 0 \\ -2K_{\text{c1}} & K_{\text{c1}} & 0 \\ 0 & 0 & 2K_{\text{c1}} + \frac{1}{2}K_{\text{c2}} \end{bmatrix}_{123} \tag{C.49}$$

for the cubic anisotropy tensor in the crystal base coordinate system $\{\hat{\mathbf{e}}_1, \hat{\mathbf{e}}_2, \hat{\mathbf{e}}_3\}$.

Case 3: An alignment of the equilibrium position along a body diagonal of the cubic unit cell:

- $\mathbf{M}_0 \parallel i_a \cdot \hat{\mathbf{e}}_a + i_b \cdot \hat{\mathbf{e}}_b + i_c \cdot \hat{\mathbf{e}}_c$ for $a, b, c \in \{1, 2, 3\}$ and $a \neq b \neq c$ with $i_a, i_b, i_c \in \{1, -1\}$:
  1. All elements of the first order cubic anisotropy tensor become $N^{\text{ani,c1}}_{ab} = \frac{2K_{\text{c1}}}{\mu_0 M_{\text{S}}^2} \cdot \frac{2}{3}$ for $a, b \in \{1, 2, 3\}$.
  2. All diagonal elements $N^{\text{ani,c2}}_{aa}$ of the second order cubic anisotropy tensor become $|N^{\text{ani,c2}}_{aa}| = \frac{2K_{\text{c2}}}{\mu_0 M_{\text{S}}^2} \cdot \frac{1}{6}$.
  3. All off-diagonal elements of the second order cubic anisotropy tensor become $|N^{\text{ani,c2}}_{ab}| = \frac{2K_{\text{c2}}}{\mu_0 M_{\text{S}}^2} \cdot \frac{2}{6}$ for $a, b \in \{1, 2, 3\}$ and $a \neq b$.
- An example is the alignment of $\mathbf{M}_0 \parallel [111]_{123}$, which results in

$$\hat{N}_{\text{ani}} = \hat{N}^{\text{c1}}_{\text{ani}} + \hat{N}^{\text{c2}}_{\text{ani}} = \frac{2K_{\text{c1}}}{\mu_0 M_{\text{S}}^2} \cdot \frac{2}{3} \cdot \begin{bmatrix} 1 & 1 & 1 \\ 1 & 1 & 1 \\ 1 & 1 & 1 \end{bmatrix}_{123} + \frac{2K_{\text{c2}}}{\mu_0 M_{\text{S}}^2} \cdot \frac{1}{6} \cdot \begin{bmatrix} 1 & 2 & 2 \\ 2 & 1 & 2 \\ 2 & 2 & 1 \end{bmatrix}_{123} \tag{C.50}$$

$$\Rightarrow \hat{N}_{\text{ani}} = \frac{1}{\mu_0 M_{\text{S}}^2} \cdot \frac{1}{3} \cdot \begin{bmatrix} 4K_{\text{c1}} + K_{\text{c2}} & 4K_{\text{c1}} + 2K_{\text{c2}} & 4K_{\text{c1}} + 2K_{\text{c2}} \\ 4K_{\text{c1}} + 2K_{\text{c2}} & 4K_{\text{c1}} + K_{\text{c2}} & 4K_{\text{c1}} + 2K_{\text{c2}} \\ 4K_{\text{c1}} + 2K_{\text{c2}} & 4K_{\text{c1}} + 2K_{\text{c2}} & 4K_{\text{c1}} + K_{\text{c2}} \end{bmatrix}_{123} \tag{C.51}$$

for the cubic anisotropy tensor in the crystal base coordinate system $\{\hat{\mathbf{e}}_1, \hat{\mathbf{e}}_2, \hat{\mathbf{e}}_3\}$.

- Another example is the alignment of $\mathbf{M}_0 \parallel [1\bar{1}1]_{123}$, which results in

$$\hat{N}_{\text{ani}} = \hat{N}^{\text{c1}}_{\text{ani}} + \hat{N}^{\text{c2}}_{\text{ani}} = \frac{2K_{\text{c1}}}{\mu_0 M_{\text{S}}^2} \cdot \frac{2}{3} \cdot \begin{bmatrix} 1 & -1 & 1 \\ -1 & 1 & -1 \\ 1 & -1 & 1 \end{bmatrix}_{123} + \frac{2K_{\text{c2}}}{\mu_0 M_{\text{S}}^2} \cdot \frac{1}{6} \cdot \begin{bmatrix} 1 & -2 & 2 \\ -2 & 1 & -2 \\ 2 & -2 & 1 \end{bmatrix}_{123} \tag{C.52}$$

$$\Rightarrow \hat{N}_{\text{ani}} = \frac{1}{\mu_0 M_{\text{S}}^2} \cdot \frac{1}{3} \cdot \begin{bmatrix} 4K_{\text{c1}} + K_{\text{c2}} & -(4K_{\text{c1}} + 2K_{\text{c2}}) & 4K_{\text{c1}} + 2K_{\text{c2}} \\ -(4K_{\text{c1}} + 2K_{\text{c2}}) & 4K_{\text{c1}} + K_{\text{c2}} & -(4K_{\text{c1}} + 2K_{\text{c2}}) \\ 4K_{\text{c1}} + 2K_{\text{c2}} & -(4K_{\text{c1}} + 2K_{\text{c2}}) & 4K_{\text{c1}} + K_{\text{c2}} \end{bmatrix}_{123} \tag{C.53}$$

for the cubic anisotropy tensor in the crystal base coordinate system $\{\hat{\mathbf{e}}_1, \hat{\mathbf{e}}_2, \hat{\mathbf{e}}_3\}$. The same tensor is obtained for $\mathbf{M}_0 \parallel [\bar{1}1\bar{1}]_{123}$.

Case 4: An alignment of the equilibrium position along a YIG-typical axis $[\bar{1}\bar{1}2]$*:*

- In YIG wafers on GGG, the $[\bar{1}\bar{1}2]$ direction corresponds usually to an in-plane orientation perpendicular to the small flat of the wafer [227]. When the equilibrium position is aligned along this direction, i.e. $\mathbf{M}_0 \parallel -1 \cdot \hat{\mathbf{e}}_1 - 1 \cdot \hat{\mathbf{e}}_2 + 2 \cdot \hat{\mathbf{e}}_3$, the anisotropy tensor becomes

$$\hat{N}_{\text{ani}} = \hat{N}^{\text{c1}}_{\text{ani}} + \hat{N}^{\text{c2}}_{\text{ani}} = \frac{2K_{\text{c1}}}{\mu_0 M_{\text{S}}^2} \cdot \frac{1}{6} \cdot \begin{bmatrix} 5 & 2 & -4 \\ 2 & 5 & -4 \\ -4 & -4 & 2 \end{bmatrix}_{123} + \frac{2K_{\text{c2}}}{\mu_0 M_{\text{S}}^2} \cdot \frac{1}{36} \cdot \begin{bmatrix} 4 & 8 & -4 \\ 8 & 4 & -4 \\ -4 & -4 & 1 \end{bmatrix}_{123} \tag{C.54}$$

$$\Rightarrow \hat{N}_{\text{ani}} = \frac{1}{\mu_0 M_{\text{S}}^2} \cdot \frac{1}{18} \cdot \begin{bmatrix} 30K_{\text{c1}} + 4K_{\text{c2}} & 12K_{\text{c1}} + 8K_{\text{c2}} & -24K_{\text{c1}} - 8K_{\text{c2}} \\ 12K_{\text{c1}} + 8K_{\text{c2}} & 30K_{\text{c1}} + 4K_{\text{c2}} & -24K_{\text{c1}} - 8K_{\text{c2}} \\ -24K_{\text{c1}} - 4K_{\text{c2}} & -24K_{\text{c1}} - 4K_{\text{c2}} & 12K_{\text{c1}} + 1K_{\text{c2}} \end{bmatrix}_{123} \tag{C.55}$$

in the crystal base coordinate system $\{\hat{\mathbf{e}}_1, \hat{\mathbf{e}}_2, \hat{\mathbf{e}}_3\}$. Clearly, the same tensor is obtained for $\mathbf{M}_0 \parallel [11\bar{2}]$.

- For an alignment along [112] or $[\bar{1}\bar{1}\bar{2}]$, the tensor becomes

$$\hat{N}_{\text{ani}} = \frac{1}{\mu_0 M_S^2} \cdot \frac{1}{18} \cdot \begin{bmatrix} 30K_{c1} + 4K_{c2} & 12K_{c1} + 8K_{c2} & 24K_{c1} + 8K_{c2} \\ 12K_{c1} + 8K_{c2} & 30K_{c1} + 4K_{c2} & 24K_{c1} + 8K_{c2} \\ 24K_{c1} + 4K_{c2} & 24K_{c1} + 4K_{c2} & 12K_{c1} + 1K_{c2} \end{bmatrix}_{123} \tag{C.56}$$

  in the crystal base coordinate system $\{\hat{\mathbf{e}}_1, \hat{\mathbf{e}}_2, \hat{\mathbf{e}}_3\}$.

C.3.2 The transition to local (dynamic) coordinates

Definition of the local coordinates based on the equilibrium position

In the Kalinikos-Slavin papers [378, 379] the magnetisation dynamics are described for anisotropic thin films and expressed in a local coordinate system, defined such that the z direction coincides with the equilibrium position of the magnetisation $\mathbf{M}_0(\mathbf{r})$ and the y direction is the perpendicular direction which is always in the film plane.

In this work, the film normal always corresponds to the $[001]_{123}$ direction and therefore the local coordinate system is easily expressed as‖

$$\hat{\mathbf{e}}_x = \begin{pmatrix} -\cos(\varphi_{100})\cos(\theta_{001}) \\ -\sin(\varphi_{100})\cos(\theta_{001}) \\ \sin(\theta_{001}) \end{pmatrix}_{123} \quad \text{and} \quad \hat{\mathbf{e}}_y = \begin{pmatrix} \sin(\varphi_{100}) \\ -\cos(\varphi_{100}) \\ 0 \end{pmatrix}_{123} \quad \text{and} \quad \hat{\mathbf{e}}_z = \begin{pmatrix} \cos(\varphi_{100})\sin(\theta_{001}) \\ \sin(\varphi_{100})\sin(\theta_{001}) \\ \cos(\theta_{001}) \end{pmatrix}_{123} \tag{C.57}$$

which results in the expression of the transformation matrix

$$\hat{T}_{123\to xyz} = \begin{bmatrix} -\cos(\varphi_{100})\cos(\theta_{001}) & -\sin(\varphi_{100})\cos(\theta_{001}) & \sin(\theta_{001}) \\ \sin(\varphi_{100}) & -\cos(\varphi_{100}) & 0 \\ \cos(\varphi_{100})\sin(\theta_{001}) & \sin(\varphi_{100})\sin(\theta_{001}) & \cos(\theta_{001}) \end{bmatrix} \tag{C.58}$$

and its transpose

$$\hat{T}^{\mathrm{T}}_{123\to xyz} = \begin{bmatrix} -\cos(\varphi_{100})\cos(\theta_{001}) & \sin(\varphi_{100}) & \cos(\varphi_{100})\sin(\theta_{001}) \\ -\sin(\varphi_{100})\cos(\theta_{001}) & -\cos(\varphi_{100}) & \sin(\varphi_{100})\sin(\theta_{001}) \\ \sin(\theta_{001}) & 0 & \cos(\theta_{001}) \end{bmatrix} \tag{C.59}$$

as simple functions of the two angles $\varphi_{100} \in [0, 2\pi]$ and $\theta_{001} \in [0, \pi]$ defining the equilibrium position of the magnetisation in the crystal coordinate system.

Transformation of the tensor elements

The transformation of the tensor elements with

$$\hat{N}_{\mathrm{ani}} = \begin{bmatrix} N^{\mathrm{ani}}_{xx} & N^{\mathrm{ani}}_{xy} & N^{\mathrm{ani}}_{xz} \\ N^{\mathrm{ani}}_{yx} & N^{\mathrm{ani}}_{yy} & N^{\mathrm{ani}}_{yz} \\ N^{\mathrm{ani}}_{zx} & N^{\mathrm{ani}}_{zy} & N^{\mathrm{ani}}_{zz} \end{bmatrix}_{\mathrm{xyz}} = \hat{T}_{123\to xyz} \cdot \begin{bmatrix} N^{\mathrm{ani}}_{11} & N^{\mathrm{ani}}_{12} & N^{\mathrm{ani}}_{13} \\ N^{\mathrm{ani}}_{21} & N^{\mathrm{ani}}_{22} & N^{\mathrm{ani}}_{23} \\ N^{\mathrm{ani}}_{31} & N^{\mathrm{ani}}_{32} & N^{\mathrm{ani}}_{33} \end{bmatrix}_{123} \cdot \hat{T}^{\mathrm{T}}_{123\to xyz} \tag{C.60}$$

yields

$$\begin{aligned} N^{\mathrm{ani}}_{xx} = &-\cos(\varphi_{100})\cos(\theta_{001}) \cdot \left(-N^{\mathrm{ani}}_{11} \cdot \cos(\varphi_{100})\cos(\theta_{001}) - N^{\mathrm{ani}}_{12} \cdot \sin(\varphi_{100})\cos(\theta_{001}) + N^{\mathrm{ani}}_{13} \cdot \sin(\theta_{001})\right) \\ &-\sin(\varphi_{100})\cos(\theta_{001}) \cdot \left(-N^{\mathrm{ani}}_{21} \cdot \cos(\varphi_{100})\cos(\theta_{001}) - N^{\mathrm{ani}}_{22} \cdot \sin(\varphi_{100})\cos(\theta_{001}) + N^{\mathrm{ani}}_{23} \cdot \sin(\theta_{001})\right) \\ &+\sin(\theta_{001}) \cdot \left(-N^{\mathrm{ani}}_{31} \cdot \cos(\varphi_{100})\cos(\theta_{001}) - N^{\mathrm{ani}}_{32} \cdot \sin(\varphi_{100})\cos(\theta_{001}) + N^{\mathrm{ani}}_{33} \cdot \sin(\theta_{001})\right) \end{aligned} \tag{C.61}$$

(C.62)

and

$$\begin{aligned} N^{\mathrm{ani}}_{xy} = &-\cos(\varphi_{100})\cos(\theta_{001}) \cdot \left(N^{\mathrm{ani}}_{11} \cdot \sin(\varphi_{100}) - N^{\mathrm{ani}}_{12} \cdot \cos(\varphi_{100})\right) \\ &-\sin(\varphi_{100})\cos(\theta_{001}) \cdot \left(N^{\mathrm{ani}}_{21} \cdot \sin(\varphi_{100}) - N^{\mathrm{ani}}_{22} \cdot \cos(\varphi_{100})\right) \\ &+\sin(\theta_{001}) \cdot \left(N^{\mathrm{ani}}_{31} \cdot \sin(\varphi_{100}) - N^{\mathrm{ani}}_{32} \cdot \cos(\varphi_{100})\right) \end{aligned} \tag{C.63}$$

‖ Attention shall be given here: This choice of local coordinates leads to the later identification of the anisotropy tensor elements N^{ani}_{xx}, N^{ani}_{xy} and N^{ani}_{yy} to be used in the Kalinikos-Slavin formalism. - This choice of coordinates does not directly imply a uselessness for other cases: The following tensor elements might still be easily transformed into other local coordinates, e.g. Henry *et al.* simply rotate the x-y coordinates in [233] compared to the ones defined in the Kalinikos-Slavin papers, and thus N^{ani}_{xx} and N^{ani}_{yy} simply need to be swapped. Moreover, the cubic axes [100], [010] and [001] are symmetrically equal, so the coordinates work equally for any other out-of-plane definition coinciding with a principal lattice axis.

and

$$\begin{aligned} N_{xz}^{\mathrm{ani}} = &-\cos\left(\varphi_{100}\right)\cos\left(\theta_{001}\right)\cdot\left(N_{11}^{\mathrm{ani}}\cdot\cos\left(\varphi_{100}\right)\sin\left(\theta_{001}\right)+N_{12}^{\mathrm{ani}}\cdot\sin\left(\varphi_{100}\right)\sin\left(\theta_{001}\right)+N_{13}^{\mathrm{ani}}\cdot\cos\left(\theta_{001}\right)\right)\\ &-\sin\left(\varphi_{100}\right)\cos\left(\theta_{001}\right)\cdot\left(N_{21}^{\mathrm{ani}}\cdot\cos\left(\varphi_{100}\right)\sin\left(\theta_{001}\right)+N_{22}^{\mathrm{ani}}\cdot\sin\left(\varphi_{100}\right)\sin\left(\theta_{001}\right)+N_{23}^{\mathrm{ani}}\cdot\cos\left(\theta_{001}\right)\right)\\ &+\sin\left(\theta_{001}\right)\cdot\left(N_{31}^{\mathrm{ani}}\cdot\cos\left(\varphi_{100}\right)\sin\left(\theta_{001}\right)+N_{32}^{\mathrm{ani}}\cdot\sin\left(\varphi_{100}\right)\sin\left(\theta_{001}\right)+N_{33}^{\mathrm{ani}}\cdot\cos\left(\theta_{001}\right)\right) \end{aligned} \tag{C.64}$$

and

$$\begin{aligned} N_{yx}^{\mathrm{ani}} = &\sin\left(\varphi_{100}\right)\cdot\left(-N_{11}^{\mathrm{ani}}\cdot\cos\left(\varphi_{100}\right)\cos\left(\theta_{001}\right)-N_{12}^{\mathrm{ani}}\cdot\sin\left(\varphi_{100}\right)\cos\left(\theta_{001}\right)+N_{13}^{\mathrm{ani}}\cdot\sin\left(\theta_{001}\right)\right)\\ &-\cos\left(\varphi_{100}\right)\cdot\left(-N_{21}^{\mathrm{ani}}\cdot\cos\left(\varphi_{100}\right)\cos\left(\theta_{001}\right)-N_{22}^{\mathrm{ani}}\cdot\sin\left(\varphi_{100}\right)\cos\left(\theta_{001}\right)+N_{23}^{\mathrm{ani}}\cdot\sin\left(\theta_{001}\right)\right) \end{aligned} \tag{C.65}$$

and

$$\begin{aligned} N_{yy}^{\mathrm{ani}} = &\sin\left(\varphi_{100}\right)\cdot\left(N_{11}^{\mathrm{ani}}\cdot\sin\left(\varphi_{100}\right)-N_{12}^{\mathrm{ani}}\cdot\cos\left(\varphi_{100}\right)\right)\\ &-\cos\left(\varphi_{100}\right)\cdot\left(N_{21}^{\mathrm{ani}}\cdot\sin\left(\varphi_{100}\right)-N_{22}^{\mathrm{ani}}\cdot\cos\left(\varphi_{100}\right)\right) \end{aligned} \tag{C.66}$$

and

$$\begin{aligned} N_{yz}^{\mathrm{ani}} = &\sin\left(\varphi_{100}\right)\cdot\left(N_{11}^{\mathrm{ani}}\cdot\cos\left(\varphi_{100}\right)\sin\left(\theta_{001}\right)+N_{12}^{\mathrm{ani}}\cdot\sin\left(\varphi_{100}\right)\sin\left(\theta_{001}\right)+N_{13}^{\mathrm{ani}}\cdot\cos\left(\theta_{001}\right)\right)\\ &-\cos\left(\varphi_{100}\right)\cdot\left(N_{21}^{\mathrm{ani}}\cdot\cos\left(\varphi_{100}\right)\sin\left(\theta_{001}\right)+N_{22}^{\mathrm{ani}}\cdot\sin\left(\varphi_{100}\right)\sin\left(\theta_{001}\right)+N_{23}^{\mathrm{ani}}\cdot\cos\left(\theta_{001}\right)\right) \end{aligned} \tag{C.67}$$

and

$$\begin{aligned} N_{zx}^{\mathrm{ani}} = &\cos\left(\varphi_{100}\right)\sin\left(\theta_{001}\right)\cdot\left(-N_{11}^{\mathrm{ani}}\cdot\cos\left(\varphi_{100}\right)\cos\left(\theta_{001}\right)-N_{12}^{\mathrm{ani}}\cdot\sin\left(\varphi_{100}\right)\cos\left(\theta_{001}\right)+N_{13}^{\mathrm{ani}}\cdot\sin\left(\theta_{001}\right)\right)\\ &+\sin\left(\varphi_{100}\right)\sin\left(\theta_{001}\right)\cdot\left(-N_{21}^{\mathrm{ani}}\cdot\cos\left(\varphi_{100}\right)\cos\left(\theta_{001}\right)-N_{22}^{\mathrm{ani}}\cdot\sin\left(\varphi_{100}\right)\cos\left(\theta_{001}\right)+N_{23}^{\mathrm{ani}}\cdot\sin\left(\theta_{001}\right)\right)\\ &+\cos\left(\theta_{001}\right)\cdot\left(-N_{31}^{\mathrm{ani}}\cdot\cos\left(\varphi_{100}\right)\cos\left(\theta_{001}\right)-N_{32}^{\mathrm{ani}}\cdot\sin\left(\varphi_{100}\right)\cos\left(\theta_{001}\right)+N_{33}^{\mathrm{ani}}\cdot\sin\left(\theta_{001}\right)\right) \end{aligned} \tag{C.68}$$

and

$$\begin{aligned} N_{zy}^{\mathrm{ani}} = &\cos\left(\varphi_{100}\right)\sin\left(\theta_{001}\right)\cdot\left(N_{11}^{\mathrm{ani}}\cdot\sin\left(\varphi_{100}\right)-N_{12}^{\mathrm{ani}}\cdot\cos\left(\varphi_{100}\right)\right)\\ &+\sin\left(\varphi_{100}\right)\sin\left(\theta_{001}\right)\cdot\left(N_{21}^{\mathrm{ani}}\cdot\sin\left(\varphi_{100}\right)-N_{22}^{\mathrm{ani}}\cdot\cos\left(\varphi_{100}\right)\right)\\ &+\cos\left(\theta_{001}\right)\cdot\left(N_{31}^{\mathrm{ani}}\cdot\sin\left(\varphi_{100}\right)-N_{32}^{\mathrm{ani}}\cdot\cos\left(\varphi_{100}\right)\right) \end{aligned} \tag{C.69}$$

and

$$\begin{aligned} N_{zz}^{\mathrm{ani}} = &\cos\left(\varphi_{100}\right)\sin\left(\theta_{001}\right)\cdot\left(N_{11}^{\mathrm{ani}}\cdot\cos\left(\varphi_{100}\right)\sin\left(\theta_{001}\right)+N_{12}^{\mathrm{ani}}\cdot\sin\left(\varphi_{100}\right)\sin\left(\theta_{001}\right)+N_{13}^{\mathrm{ani}}\cdot\cos\left(\theta_{001}\right)\right)\\ &+\sin\left(\varphi_{100}\right)\sin\left(\theta_{001}\right)\cdot\left(N_{21}^{\mathrm{ani}}\cdot\cos\left(\varphi_{100}\right)\sin\left(\theta_{001}\right)+N_{22}^{\mathrm{ani}}\cdot\sin\left(\varphi_{100}\right)\sin\left(\theta_{001}\right)+N_{23}^{\mathrm{ani}}\cdot\cos\left(\theta_{001}\right)\right)\\ &+\cos\left(\theta_{001}\right)\cdot\left(N_{31}^{\mathrm{ani}}\cdot\cos\left(\varphi_{100}\right)\sin\left(\theta_{001}\right)+N_{32}^{\mathrm{ani}}\cdot\sin\left(\varphi_{100}\right)\sin\left(\theta_{001}\right)+N_{33}^{\mathrm{ani}}\cdot\cos\left(\theta_{001}\right)\right) \end{aligned} \tag{C.70}$$

for the tensor elements in the local base xyz.

The lengthy expressions are slightly simplified by the symmetry of the cubic anisotropy imposing $N_{ij}^{\mathrm{ani}} = N_{ji}^{\mathrm{ani}}$ for $i, j = 1, 2, 3$, which leads to

$$\begin{aligned} N_{xx}^{\mathrm{ani}} = &N_{11}^{\mathrm{ani}}\cdot\cos^2\left(\varphi_{100}\right)\cos^2\left(\theta_{001}\right)+N_{22}^{\mathrm{ani}}\cdot\sin^2\left(\varphi_{100}\right)\cos^2\left(\theta_{001}\right)+N_{33}^{\mathrm{ani}}\cdot\sin^2\left(\theta_{001}\right)\\ &+2\cdot N_{12}^{\mathrm{ani}}\cdot\sin\left(\varphi_{100}\right)\cos\left(\varphi_{100}\right)\cos^2\left(\theta_{001}\right)-2\cdot N_{13}^{\mathrm{ani}}\cdot\cos\left(\varphi_{100}\right)\sin\left(\theta_{001}\right)\cos\left(\theta_{001}\right)\\ &-2\cdot N_{23}^{\mathrm{ani}}\cdot\sin\left(\varphi_{100}\right)\sin\left(\theta_{001}\right)\cos\left(\theta_{001}\right) \end{aligned} \tag{C.71}$$

$$N_{yy}^{\mathrm{ani}} = N_{11}^{\mathrm{ani}}\cdot\sin^2\left(\varphi_{100}\right)+N_{22}^{\mathrm{ani}}\cdot\cos^2\left(\varphi_{100}\right)-2\cdot N_{12}^{\mathrm{ani}}\cdot\sin\left(\varphi_{100}\right)\cos\left(\varphi_{100}\right) \tag{C.72}$$

$$\begin{aligned} N_{zz}^{\mathrm{ani}} = &N_{11}^{\mathrm{ani}}\cdot\cos^2\left(\varphi_{100}\right)\sin^2\left(\theta_{001}\right)+N_{22}^{\mathrm{ani}}\cdot\sin^2\left(\varphi_{100}\right)\sin^2\left(\theta_{001}\right)+N_{33}^{\mathrm{ani}}\cdot\cos^2\left(\theta_{001}\right)\\ &+2\cdot N_{12}^{\mathrm{ani}}\cdot\sin\left(\varphi_{100}\right)\cos\left(\varphi_{100}\right)\sin^2\left(\theta_{001}\right)+2\cdot N_{13}^{\mathrm{ani}}\cdot\cos\left(\varphi_{100}\right)\sin\left(\theta_{001}\right)\cos\left(\theta_{001}\right)\\ &+2\cdot N_{23}^{\mathrm{ani}}\cdot\sin\left(\varphi_{100}\right)\sin\left(\theta_{001}\right)\cos\left(\theta_{001}\right) \end{aligned} \tag{C.73}$$

for the diagonal elements as well as

$$\begin{aligned} N_{xy}^{\text{ani}} &= N_{xy}^{\text{ani}} \\ &= -N_{11}^{\text{ani}} \cdot \sin\left(\varphi_{100}\right) \cos\left(\varphi_{100}\right) \cos\left(\theta_{001}\right) + N_{22}^{\text{ani}} \cdot \sin\left(\varphi_{100}\right) \cos\left(\varphi_{100}\right) \cos\left(\theta_{001}\right) \\ &\quad + N_{12}^{\text{ani}} \cdot \left(\cos^2\left(\varphi_{100}\right) - \sin^2\left(\varphi_{100}\right)\right) \cos\left(\theta_{001}\right) + N_{13}^{\text{ani}} \cdot \sin\left(\varphi_{100}\right) \sin\left(\theta_{001}\right) - N_{23}^{\text{ani}} \cdot \cos\left(\varphi_{100}\right) \sin\left(\theta_{001}\right) \end{aligned} \tag{C.74}$$

$$\begin{aligned} N_{xz}^{\text{ani}} &= N_{zx}^{\text{ani}} \\ &= -N_{11}^{\text{ani}} \cdot \cos^2\left(\varphi_{100}\right) \sin\left(\theta_{001}\right) \cos\left(\theta_{001}\right) - N_{22}^{\text{ani}} \cdot \sin^2\left(\varphi_{100}\right) \sin\left(\theta_{001}\right) \cos\left(\theta_{001}\right) + N_{33}^{\text{ani}} \sin\left(\theta_{001}\right) \cos\left(\theta_{001}\right) \\ &\quad - 2 \cdot N_{12}^{\text{ani}} \cdot \sin\left(\varphi_{100}\right) \cos\left(\varphi_{100}\right) \sin\left(\theta_{001}\right) \cos\left(\theta_{001}\right) \\ &\quad + N_{13}^{\text{ani}} \cdot \cos\left(\varphi_{100}\right) \left(\sin^2\left(\theta_{001}\right) - \cos^2\left(\theta_{001}\right)\right) + N_{23}^{\text{ani}} \cdot \sin\left(\varphi_{100}\right) \left(\sin^2\left(\theta_{001}\right) - \cos^2\left(\theta_{001}\right)\right) \end{aligned} \tag{C.75}$$

$$\begin{aligned} N_{yz}^{\text{ani}} &= N_{zy}^{\text{ani}} \\ &= N_{11}^{\text{ani}} \cdot \sin\left(\varphi_{100}\right) \cos\left(\varphi_{100}\right) \sin\left(\theta_{001}\right) - N_{22}^{\text{ani}} \cdot \sin\left(\varphi_{100}\right) \cos\left(\varphi_{100}\right) \sin\left(\theta_{001}\right) \\ &\quad + N_{12}^{\text{ani}} \cdot \left(\sin^2\left(\varphi_{100}\right) - \cos^2\left(\varphi_{100}\right)\right) \sin\left(\theta_{001}\right) + N_{13}^{\text{ani}} \cdot \sin\left(\varphi_{100}\right) \cos\left(\theta_{001}\right) - N_{23}^{\text{ani}} \cdot \cos\left(\varphi_{100}\right) \cos\left(\theta_{001}\right) \end{aligned} \tag{C.76}$$

for the off-diagonal elements.

First order cubic anisotropy tensor: crystal → local base

$$\begin{aligned}
N_{xx}^{\mathrm{ani,c1}} &= N_{11}^{\mathrm{ani,c1}} \cdot \cos^2\left(\varphi_{100}\right)\cos^2\left(\theta_{001}\right) + N_{22}^{\mathrm{ani,c1}} \cdot \sin^2\left(\varphi_{100}\right)\cos^2\left(\theta_{001}\right) + N_{33}^{\mathrm{ani,c1}} \cdot \sin^2\left(\theta_{001}\right) \\
&\quad + 2 \cdot N_{12}^{\mathrm{ani,c1}} \cdot \sin\left(\varphi_{100}\right)\cos\left(\varphi_{100}\right)\cos^2\left(\theta_{001}\right) - 2 \cdot N_{13}^{\mathrm{ani,c1}} \cdot \cos\left(\varphi_{100}\right)\sin\left(\theta_{001}\right)\cos\left(\theta_{001}\right) \\
&\quad - 2 \cdot N_{23}^{\mathrm{ani,c1}} \cdot \sin\left(\varphi_{100}\right)\sin\left(\theta_{001}\right)\cos\left(\theta_{001}\right) \qquad \text{(C.77)} \\
&= \frac{2K_{\mathrm{c1}}}{\mu_0 M_{\mathrm{S}}^2} \cdot \left(1 - \cos^2\left(\varphi_{100}\right)\sin^2\left(\theta_{001}\right)\right) \cdot \cos^2\left(\varphi_{100}\right)\cos^2\left(\theta_{001}\right) \\
&\quad + \frac{2K_{\mathrm{c1}}}{\mu_0 M_{\mathrm{S}}^2} \cdot \left(1 - \sin^2\left(\varphi_{100}\right)\sin^2\left(\theta_{001}\right)\right) \cdot \sin^2\left(\varphi_{100}\right)\cos^2\left(\theta_{001}\right) \\
&\quad + \frac{2K_{\mathrm{c1}}}{\mu_0 M_{\mathrm{S}}^2} \cdot \left(1 - \cos^2\left(\theta_{001}\right)\right) \cdot \sin^2\left(\theta_{001}\right) \\
&\quad + 2 \cdot \frac{2K_{\mathrm{c1}}}{\mu_0 M_{\mathrm{S}}^2} \cdot 2 \cdot \sin\left(\varphi_{100}\right)\cos\left(\varphi_{100}\right)\sin^2\left(\theta_{001}\right) \cdot \sin\left(\varphi_{100}\right)\cos\left(\varphi_{100}\right)\cos^2\left(\theta_{001}\right) \\
&\quad - 2 \cdot \frac{2K_{\mathrm{c1}}}{\mu_0 M_{\mathrm{S}}^2} \cdot 2 \cdot \cos\left(\varphi_{100}\right)\sin\left(\theta_{001}\right)\cos\left(\theta_{001}\right) \cdot \cos\left(\varphi_{100}\right)\sin\left(\theta_{001}\right)\cos\left(\theta_{001}\right) \\
&\quad - 2 \cdot \frac{2K_{\mathrm{c1}}}{\mu_0 M_{\mathrm{S}}^2} \cdot 2 \cdot \sin\left(\varphi_{100}\right)\sin\left(\theta_{001}\right)\cos\left(\theta_{001}\right) \cdot \sin\left(\varphi_{100}\right)\sin\left(\theta_{001}\right)\cos\left(\theta_{001}\right) \qquad \text{(C.78)} \\
&= \frac{2K_{\mathrm{c1}}}{\mu_0 M_{\mathrm{S}}^2} \cdot \Bigg(\cos^2\left(\varphi_{100}\right)\cos^2\left(\theta_{001}\right) - \cos^4\left(\varphi_{100}\right)\sin^2\left(\theta_{001}\right)\cos^2\left(\theta_{001}\right) + \sin^2\left(\varphi_{100}\right)\cos^2\left(\theta_{001}\right) \\
&\quad - \sin^4\left(\varphi_{100}\right)\sin^2\left(\theta_{001}\right)\cos^2\left(\theta_{001}\right) + \sin^2\left(\theta_{001}\right) - \cos^2\left(\theta_{001}\right)\sin^2\left(\theta_{001}\right) \\
&\quad + 4 \cdot \sin^2\left(\varphi_{100}\right)\cos^2\left(\varphi_{100}\right)\sin^2\left(\theta_{001}\right)\cos^2\left(\theta_{001}\right) - 4 \cdot \cos^2\left(\varphi_{100}\right)\sin^2\left(\theta_{001}\right)\cos^2\left(\theta_{001}\right) \\
&\quad - 4 \cdot \sin^2\left(\varphi_{100}\right)\sin^2\left(\theta_{001}\right)\cos^2\left(\theta_{001}\right) \Bigg) \qquad \text{(C.79)} \\
&= \frac{2K_{\mathrm{c1}}}{\mu_0 M_{\mathrm{S}}^2} \cdot \Bigg(1 - \cos^4\left(\varphi_{100}\right)\sin^2\left(\theta_{001}\right)\cos^2\left(\theta_{001}\right) - \sin^4\left(\varphi_{100}\right)\sin^2\left(\theta_{001}\right)\cos^2\left(\theta_{001}\right) \\
&\quad - 5\sin^2\left(\theta_{001}\right)\cos^2\left(\theta_{001}\right) + 4 \cdot \sin^2\left(\varphi_{100}\right)\cos^2\left(\varphi_{100}\right)\sin^2\left(\theta_{001}\right)\cos^2\left(\theta_{001}\right) \Bigg) \qquad \text{(C.80)} \\
&= \frac{2K_{\mathrm{c1}}}{\mu_0 M_{\mathrm{S}}^2} \cdot \Bigg(1 + \sin^2\left(\theta_{001}\right)\cos^2\left(\theta_{001}\right) \cdot \Big(- \cos^4\left(\varphi_{100}\right) - \sin^4\left(\varphi_{100}\right) - 5 + 4 \cdot \sin^2\left(\varphi_{100}\right)\cos^2\left(\varphi_{100}\right) \Big) \Bigg) \\
&\qquad \text{(C.81)} \\
\Rightarrow N_{xx}^{\mathrm{ani,c1}} &= \frac{2K_{\mathrm{c1}}}{\mu_0 M_{\mathrm{S}}^2} \cdot \left(1 - \frac{3}{4}\sin^2\left(\theta_{001}\right)\cos^2\left(\theta_{001}\right) \cdot \Big(7 + \cos\left(4\varphi_{100}\right) \Big) \right) \qquad \text{(C.82)}
\end{aligned}$$

$$\begin{aligned}
N_{yy}^{\mathrm{ani,c1}} &= N_{11}^{\mathrm{ani,c1}} \cdot \sin^2\left(\varphi_{100}\right) + N_{22}^{\mathrm{ani,c1}} \cdot \cos^2\left(\varphi_{100}\right) - 2 \cdot N_{12}^{\mathrm{ani,c1}} \cdot \sin\left(\varphi_{100}\right)\cos\left(\varphi_{100}\right) \qquad \text{(C.83)} \\
&= \frac{2K_{\mathrm{c1}}}{\mu_0 M_{\mathrm{S}}^2} \cdot \left(1 - \cos^2\left(\varphi_{100}\right)\sin^2\left(\theta_{001}\right)\right) \cdot \sin^2\left(\varphi_{100}\right) + \frac{2K_{\mathrm{c1}}}{\mu_0 M_{\mathrm{S}}^2} \cdot \left(1 - \sin^2\left(\varphi_{100}\right)\sin^2\left(\theta_{001}\right)\right) \cdot \cos^2\left(\varphi_{100}\right) \\
&\quad - 2 \cdot \frac{2K_{\mathrm{c1}}}{\mu_0 M_{\mathrm{S}}^2} \cdot 2 \cdot \sin\left(\varphi_{100}\right)\cos\left(\varphi_{100}\right)\sin^2\left(\theta_{001}\right) \cdot \sin\left(\varphi_{100}\right)\cos\left(\varphi_{100}\right) \qquad \text{(C.84)} \\
\Rightarrow N_{yy}^{\mathrm{ani,c1}} &= \frac{2K_{\mathrm{c1}}}{\mu_0 M_{\mathrm{S}}^2} \cdot \Big(1 - 6 \cdot \sin^2\left(\varphi_{100}\right)\cos^2\left(\varphi_{100}\right)\sin^2\left(\theta_{001}\right) \Big) \qquad \text{(C.85)}
\end{aligned}$$

$$
\begin{aligned}
N_{zz}^{\mathrm{ani,c1}} &= N_{11}^{\mathrm{ani,c1}} \cdot \cos^2\left(\varphi_{100}\right) \sin^2\left(\theta_{001}\right) + N_{22}^{\mathrm{ani,c1}} \cdot \sin^2\left(\varphi_{100}\right) \sin^2\left(\theta_{001}\right) + N_{33}^{\mathrm{ani,c1}} \cdot \cos^2\left(\theta_{001}\right) \\
&\quad + 2 \cdot N_{12}^{\mathrm{ani,c1}} \cdot \sin\left(\varphi_{100}\right) \cos\left(\varphi_{100}\right) \sin^2\left(\theta_{001}\right) + 2 \cdot N_{13}^{\mathrm{ani,c1}} \cdot \cos\left(\varphi_{100}\right) \sin\left(\theta_{001}\right) \cos\left(\theta_{001}\right) \\
&\quad + 2 \cdot N_{23}^{\mathrm{ani,c1}} \cdot \sin\left(\varphi_{100}\right) \sin\left(\theta_{001}\right) \cos\left(\theta_{001}\right) \qquad \text{(C.86)} \\
&= \frac{2K_{\mathrm{c1}}}{\mu_0 M_{\mathrm{S}}^2} \cdot \left(1 - \cos^2\left(\varphi_{100}\right) \sin^2\left(\theta_{001}\right)\right) \cdot \cos^2\left(\varphi_{100}\right) \sin^2\left(\theta_{001}\right) \\
&\quad + \frac{2K_{\mathrm{c1}}}{\mu_0 M_{\mathrm{S}}^2} \cdot \left(1 - \sin^2\left(\varphi_{100}\right) \sin^2\left(\theta_{001}\right)\right) \cdot \sin^2\left(\varphi_{100}\right) \sin^2\left(\theta_{001}\right) \\
&\quad + \frac{2K_{\mathrm{c1}}}{\mu_0 M_{\mathrm{S}}^2} \cdot \left(1 - \cos^2\left(\theta_{001}\right)\right) \cdot \cos^2\left(\theta_{001}\right) \\
&\quad + 2 \cdot \frac{2K_{\mathrm{c1}}}{\mu_0 M_{\mathrm{S}}^2} \cdot 2 \cdot \sin\left(\varphi_{100}\right) \cos\left(\varphi_{100}\right) \sin^2\left(\theta_{001}\right) \cdot \sin\left(\varphi_{100}\right) \cos\left(\varphi_{100}\right) \sin^2\left(\theta_{001}\right) \\
&\quad + 2 \cdot \frac{2K_{\mathrm{c1}}}{\mu_0 M_{\mathrm{S}}^2} \cdot 2 \cdot \cos\left(\varphi_{100}\right) \sin\left(\theta_{001}\right) \cos\left(\theta_{001}\right) \cdot \cos\left(\varphi_{100}\right) \sin\left(\theta_{001}\right) \cos\left(\theta_{001}\right) \\
&\quad + 2 \cdot \frac{2K_{\mathrm{c1}}}{\mu_0 M_{\mathrm{S}}^2} \cdot 2 \cdot \sin\left(\varphi_{100}\right) \sin\left(\theta_{001}\right) \cos\left(\theta_{001}\right) \cdot \sin\left(\varphi_{100}\right) \sin\left(\theta_{001}\right) \cos\left(\theta_{001}\right) \qquad \text{(C.87)} \\
&= \frac{2K_{\mathrm{c1}}}{\mu_0 M_{\mathrm{S}}^2} \cdot \Bigg(\cos^2\left(\varphi_{100}\right) \sin^2\left(\theta_{001}\right) - \cos^4\left(\varphi_{100}\right) \sin^4\left(\theta_{001}\right) + \sin^2\left(\varphi_{100}\right) \sin^2\left(\theta_{001}\right) - \sin^4\left(\varphi_{100}\right) \sin^4\left(\theta_{001}\right) \\
&\quad + \cos^2\left(\theta_{001}\right) - \cos^4\left(\theta_{001}\right) + 4 \cdot \sin^2\left(\varphi_{100}\right) \cos^2\left(\varphi_{100}\right) \sin^4\left(\theta_{001}\right) \\
&\quad + 4 \cdot \cos^2\left(\varphi_{100}\right) \sin^2\left(\theta_{001}\right) \cos^2\left(\theta_{001}\right) + 4 \cdot \sin^2\left(\varphi_{100}\right) \sin^2\left(\theta_{001}\right) \cos^2\left(\theta_{001}\right) \Bigg) \qquad \text{(C.88)} \\
&= \frac{2K_{\mathrm{c1}}}{\mu_0 M_{\mathrm{S}}^2} \cdot \Bigg(1 - \cos^4\left(\varphi_{100}\right) \sin^4\left(\theta_{001}\right) - \sin^4\left(\varphi_{100}\right) \sin^4\left(\theta_{001}\right) - \cos^4\left(\theta_{001}\right) \\
&\quad + 4 \cdot \sin^2\left(\varphi_{100}\right) \cos^2\left(\varphi_{100}\right) \sin^4\left(\theta_{001}\right) + 4 \cdot \sin^2\left(\theta_{001}\right) \cos^2\left(\theta_{001}\right) \Bigg) \qquad \text{(C.89)} \\
\Rightarrow N_{zz}^{\mathrm{ani,c1}} &= \frac{2K_{\mathrm{c1}}}{\mu_0 M_{\mathrm{S}}^2} \cdot 4 \sin^2\left(\theta_{001}\right) \cdot \left(\sin^2\left(\varphi_{100}\right) \cos^2\left(\varphi_{100}\right) \sin^2\left(\theta_{001}\right) + \cos^2\left(\theta_{001}\right) \right) \qquad \text{(C.90)}
\end{aligned}
$$

$$N_{xy}^{\mathrm{ani,c1}} = -N_{11}^{\mathrm{ani,c1}} \cdot \sin\left(\varphi_{100}\right)\cos\left(\varphi_{100}\right)\cos\left(\theta_{001}\right) + N_{22}^{\mathrm{ani,c1}} \cdot \sin\left(\varphi_{100}\right)\cos\left(\varphi_{100}\right)\cos\left(\theta_{001}\right)$$
$$+ N_{12}^{\mathrm{ani,c1}} \cdot \left(\cos^2\left(\varphi_{100}\right) - \sin^2\left(\varphi_{100}\right)\right)\cos\left(\theta_{001}\right) + N_{13}^{\mathrm{ani,c1}} \cdot \sin\left(\varphi_{100}\right)\sin\left(\theta_{001}\right) - N_{23}^{\mathrm{ani}} \cdot \cos\left(\varphi_{100}\right)\sin\left(\theta_{001}\right) \tag{C.91}$$

$$= -\frac{2K_{\mathrm{c1}}}{\mu_0 M_{\mathrm{S}}^2} \cdot \left(1 - \cos^2\left(\varphi_{100}\right)\sin^2\left(\theta_{001}\right)\right) \cdot \sin\left(\varphi_{100}\right)\cos\left(\varphi_{100}\right)\cos\left(\theta_{001}\right)$$
$$+ \frac{2K_{\mathrm{c1}}}{\mu_0 M_{\mathrm{S}}^2} \cdot \left(1 - \sin^2\left(\varphi_{100}\right)\sin^2\left(\theta_{001}\right)\right) \cdot \sin\left(\varphi_{100}\right)\cos\left(\varphi_{100}\right)\cos\left(\theta_{001}\right)$$
$$+ \frac{2K_{\mathrm{c1}}}{\mu_0 M_{\mathrm{S}}^2} \cdot 2 \cdot \sin\left(\varphi_{100}\right)\cos\left(\varphi_{100}\right)\sin^2\left(\theta_{001}\right) \cdot \left(\cos^2\left(\varphi_{100}\right) - \sin^2\left(\varphi_{100}\right)\right)\cos\left(\theta_{001}\right)$$
$$+ \frac{2K_{\mathrm{c1}}}{\mu_0 M_{\mathrm{S}}^2} \cdot 2 \cdot \cos\left(\varphi_{100}\right)\sin\left(\theta_{001}\right)\cos\left(\theta_{001}\right) \cdot \sin\left(\varphi_{100}\right)\sin\left(\theta_{001}\right)$$
$$- \frac{2K_{\mathrm{c1}}}{\mu_0 M_{\mathrm{S}}^2} \cdot 2 \cdot \sin\left(\varphi_{100}\right)\sin\left(\theta_{001}\right)\cos\left(\theta_{001}\right) \cdot \cos\left(\varphi_{100}\right)\sin\left(\theta_{001}\right) \tag{C.92}$$

$$= \frac{2K_{\mathrm{c1}}}{\mu_0 M_{\mathrm{S}}^2} \cdot \Bigg(-\sin\left(\varphi_{100}\right)\cos\left(\varphi_{100}\right)\cos\left(\theta_{001}\right) + \sin\left(\varphi_{100}\right)\cos^3\left(\varphi_{100}\right)\sin^2\left(\theta_{001}\right)\cos\left(\theta_{001}\right)$$
$$+ \sin\left(\varphi_{100}\right)\cos\left(\varphi_{100}\right)\cos\left(\theta_{001}\right) - \sin^3\left(\varphi_{100}\right)\cos\left(\varphi_{100}\right)\sin^2\left(\theta_{001}\right)\cos\left(\theta_{001}\right)$$
$$+ 2 \cdot \sin\left(\varphi_{100}\right)\cos\left(\varphi_{100}\right)\sin^2\left(\theta_{001}\right)\cos\left(\theta_{001}\right) \cdot \left(\cos^2\left(\varphi_{100}\right) - \sin^2\left(\varphi_{100}\right)\right)$$
$$+ 2 \cdot \sin\left(\varphi_{100}\right)\cos\left(\varphi_{100}\right)\sin^2\left(\theta_{001}\right)\cos\left(\theta_{001}\right)$$
$$- 2 \cdot \sin\left(\varphi_{100}\right)\cos\left(\varphi_{100}\right)\sin^2\left(\theta_{001}\right)\cos\left(\theta_{001}\right) \Bigg) \tag{C.93}$$

$$= \frac{2K_{\mathrm{c1}}}{\mu_0 M_{\mathrm{S}}^2} \cdot \Bigg(\sin\left(\varphi_{100}\right)\cos\left(\varphi_{100}\right)\sin^2\left(\theta_{001}\right)\cos\left(\theta_{001}\right) \cdot \left(\cos^2\left(\varphi_{100}\right) - \sin^2\left(\varphi_{100}\right)\right)$$
$$+ 2 \cdot \sin\left(\varphi_{100}\right)\cos\left(\varphi_{100}\right)\sin^2\left(\theta_{001}\right)\cos\left(\theta_{001}\right) \cdot \left(\cos^2\left(\varphi_{100}\right) - \sin^2\left(\varphi_{100}\right)\right) \Bigg) \tag{C.94}$$

$$\Rightarrow N_{xy}^{\mathrm{ani,c1}} = \frac{2K_{\mathrm{c1}}}{\mu_0 M_{\mathrm{S}}^2} \cdot 3 \cdot \sin\left(\varphi_{100}\right)\cos\left(\varphi_{100}\right)\sin^2\left(\theta_{001}\right)\cos\left(\theta_{001}\right) \cdot \left(\cos^2\left(\varphi_{100}\right) - \sin^2\left(\varphi_{100}\right)\right) \tag{C.95}$$

$$
\begin{aligned}
N_{xz}^{\mathrm{ani,c1}} &= -N_{11}^{\mathrm{ani,c1}} \cdot \cos^2\left(\varphi_{100}\right) \sin\left(\theta_{001}\right) \cos\left(\theta_{001}\right) - N_{22}^{\mathrm{ani,c1}} \cdot \sin^2\left(\varphi_{100}\right) \sin\left(\theta_{001}\right) \cos\left(\theta_{001}\right) + N_{33}^{\mathrm{ani,c1}} \sin\left(\theta_{001}\right) \cos\left(\theta_{001}\right) \\
&\quad - 2 \cdot N_{12}^{\mathrm{ani,c1}} \cdot \sin\left(\varphi_{100}\right) \cos\left(\varphi_{100}\right) \sin\left(\theta_{001}\right) \cos\left(\theta_{001}\right) \\
&\quad + N_{13}^{\mathrm{ani,c1}} \cdot \cos\left(\varphi_{100}\right) \left(\sin^2\left(\theta_{001}\right) - \cos^2\left(\theta_{001}\right)\right) + N_{23}^{\mathrm{ani,c1}} \cdot \sin\left(\varphi_{100}\right) \left(\sin^2\left(\theta_{001}\right) - \cos^2\left(\theta_{001}\right)\right) \qquad \text{(C.96)} \\
&= -\frac{2K_{\mathrm{c1}}}{\mu_0 M_{\mathrm{S}}^2} \cdot \left(1 - \cos^2\left(\varphi_{100}\right) \sin^2\left(\theta_{001}\right)\right) \cdot \cos^2\left(\varphi_{100}\right) \sin\left(\theta_{001}\right) \cos\left(\theta_{001}\right) \\
&\quad - \frac{2K_{\mathrm{c1}}}{\mu_0 M_{\mathrm{S}}^2} \cdot \left(1 - \sin^2\left(\varphi_{100}\right) \sin^2\left(\theta_{001}\right)\right) \cdot \sin^2\left(\varphi_{100}\right) \sin\left(\theta_{001}\right) \cos\left(\theta_{001}\right) \\
&\quad + \frac{2K_{\mathrm{c1}}}{\mu_0 M_{\mathrm{S}}^2} \cdot \left(1 - \cos^2\left(\theta_{001}\right)\right) \sin\left(\theta_{001}\right) \cos\left(\theta_{001}\right) \\
&\quad - 2 \cdot \frac{2K_{\mathrm{c1}}}{\mu_0 M_{\mathrm{S}}^2} \cdot 2 \cdot \sin\left(\varphi_{100}\right) \cos\left(\varphi_{100}\right) \sin^2\left(\theta_{001}\right) \cdot \sin\left(\varphi_{100}\right) \cos\left(\varphi_{100}\right) \sin\left(\theta_{001}\right) \cos\left(\theta_{001}\right) \\
&\quad + \frac{2K_{\mathrm{c1}}}{\mu_0 M_{\mathrm{S}}^2} \cdot 2 \cdot \cos\left(\varphi_{100}\right) \sin\left(\theta_{001}\right) \cos\left(\theta_{001}\right) \cdot \cos\left(\varphi_{100}\right) \left(\sin^2\left(\theta_{001}\right) - \cos^2\left(\theta_{001}\right)\right) \\
&\quad + \frac{2K_{\mathrm{c1}}}{\mu_0 M_{\mathrm{S}}^2} \cdot 2 \cdot \sin\left(\varphi_{100}\right) \sin\left(\theta_{001}\right) \cos\left(\theta_{001}\right) \cdot \sin\left(\varphi_{100}\right) \left(\sin^2\left(\theta_{001}\right) - \cos^2\left(\theta_{001}\right)\right) \qquad \text{(C.97)} \\
&= \frac{2K_{\mathrm{c1}}}{\mu_0 M_{\mathrm{S}}^2} \cdot \Bigg(- \cos^2\left(\varphi_{100}\right) \sin\left(\theta_{001}\right) \cos\left(\theta_{001}\right) + \cos^4\left(\varphi_{100}\right) \sin^3\left(\theta_{001}\right) \cos\left(\theta_{001}\right) \\
&\quad - \sin^2\left(\varphi_{100}\right) \sin\left(\theta_{001}\right) \cos\left(\theta_{001}\right) + \sin^4\left(\varphi_{100}\right) \sin^3\left(\theta_{001}\right) \cos\left(\theta_{001}\right) \\
&\quad + \sin\left(\theta_{001}\right) \cos\left(\theta_{001}\right) - \sin\left(\theta_{001}\right) \cos^3\left(\theta_{001}\right) \\
&\quad - 4 \cdot \sin^2\left(\varphi_{100}\right) \cos^2\left(\varphi_{100}\right) \sin^3\left(\theta_{001}\right) \cos\left(\theta_{001}\right) \\
&\quad + 2 \cdot \cos^2\left(\varphi_{100}\right) \sin\left(\theta_{001}\right) \cos\left(\theta_{001}\right) \cdot \left(\sin^2\left(\theta_{001}\right) - \cos^2\left(\theta_{001}\right)\right) \\
&\quad + 2 \cdot \sin^2\left(\varphi_{100}\right) \sin\left(\theta_{001}\right) \cos\left(\theta_{001}\right) \cdot \left(\sin^2\left(\theta_{001}\right) - \cos^2\left(\theta_{001}\right)\right) \Bigg) \qquad \text{(C.98)} \\
&= \frac{2K_{\mathrm{c1}}}{\mu_0 M_{\mathrm{S}}^2} \cdot \Bigg(\sin\left(\theta_{001}\right) \cos\left(\theta_{001}\right) \cdot \Big(\cos^4\left(\varphi_{100}\right) \sin^2\left(\theta_{001}\right) + \sin^4\left(\varphi_{100}\right) \sin^2\left(\theta_{001}\right) - \cos^2\left(\theta_{001}\right) \\
&\quad - 4 \cdot \sin^2\left(\varphi_{100}\right) \cos^2\left(\varphi_{100}\right) \sin^2\left(\theta_{001}\right) + 2\sin^2\left(\theta_{001}\right) - 2\cos^2\left(\theta_{001}\right) \Big) \Bigg) \qquad \text{(C.99)} \\
&= \frac{2K_{\mathrm{c1}}}{\mu_0 M_{\mathrm{S}}^2} \cdot \Bigg(\sin\left(\theta_{001}\right) \cos\left(\theta_{001}\right) \cdot \Big(- 3\cos^2\left(\theta_{001}\right) \\
&\quad + \sin^2\left(\theta_{001}\right) \Big[\cos^4\left(\varphi_{100}\right) + \sin^4\left(\varphi_{100}\right) - 4 \cdot \sin^2\left(\varphi_{100}\right) \cos^2\left(\varphi_{100}\right) + 2 \Big] \Big) \Bigg) \qquad \text{(C.100)} \\
\Rightarrow N_{xz}^{\mathrm{ani,c1}} &= \frac{2K_{\mathrm{c1}}}{\mu_0 M_{\mathrm{S}}^2} \cdot \sin\left(\theta_{001}\right) \cos\left(\theta_{001}\right) \cdot \left(-3\cos^2\left(\theta_{001}\right) + \frac{3}{4} \sin^2\left(\theta_{001}\right) \cdot \left(\cos\left(4\varphi_{100}\right) + 3\right)\right) \qquad \text{(C.101)}
\end{aligned}
$$

$$N_{yz}^{\mathrm{ani,c1}} = N_{11}^{\mathrm{ani,c1}} \cdot \sin\left(\varphi_{100}\right)\cos\left(\varphi_{100}\right)\sin\left(\theta_{001}\right) - N_{22}^{\mathrm{ani,c1}} \cdot \sin\left(\varphi_{100}\right)\cos\left(\varphi_{100}\right)\sin\left(\theta_{001}\right)$$
$$+ N_{12}^{\mathrm{ani,c1}} \cdot \left(\sin^2\left(\varphi_{100}\right) - \cos^2\left(\varphi_{100}\right)\right)\sin\left(\theta_{001}\right) + N_{13}^{\mathrm{ani,c1}} \cdot \sin\left(\varphi_{100}\right)\cos\left(\theta_{001}\right) - N_{23}^{\mathrm{ani,c1}} \cdot \cos\left(\varphi_{100}\right)\cos\left(\theta_{001}\right) \tag{C.102}$$

$$= \frac{2K_{\mathrm{c1}}}{\mu_0 M_{\mathrm{S}}^2} \cdot \left(1 - \cos^2\left(\varphi_{100}\right)\sin^2\left(\theta_{001}\right)\right) \cdot \sin\left(\varphi_{100}\right)\cos\left(\varphi_{100}\right)\sin\left(\theta_{001}\right)$$
$$- \frac{2K_{\mathrm{c1}}}{\mu_0 M_{\mathrm{S}}^2} \cdot \left(1 - \sin^2\left(\varphi_{100}\right)\sin^2\left(\theta_{001}\right)\right) \cdot \sin\left(\varphi_{100}\right)\cos\left(\varphi_{100}\right)\sin\left(\theta_{001}\right)$$
$$+ \frac{2K_{\mathrm{c1}}}{\mu_0 M_{\mathrm{S}}^2} \cdot 2 \cdot \sin\left(\varphi_{100}\right)\cos\left(\varphi_{100}\right)\sin^2\left(\theta_{001}\right) \cdot \left(\sin^2\left(\varphi_{100}\right) - \cos^2\left(\varphi_{100}\right)\right)\sin\left(\theta_{001}\right)$$
$$+ \frac{2K_{\mathrm{c1}}}{\mu_0 M_{\mathrm{S}}^2} \cdot 2 \cdot \cos\left(\varphi_{100}\right)\sin\left(\theta_{001}\right)\cos\left(\theta_{001}\right) \cdot \sin\left(\varphi_{100}\right)\cos\left(\theta_{001}\right)$$
$$- \frac{2K_{\mathrm{c1}}}{\mu_0 M_{\mathrm{S}}^2} \cdot 2 \cdot \sin\left(\varphi_{100}\right)\sin\left(\theta_{001}\right)\cos\left(\theta_{001}\right) \cdot \cos\left(\varphi_{100}\right)\cos\left(\theta_{001}\right) \tag{C.103}$$

$$= \frac{2K_{\mathrm{c1}}}{\mu_0 M_{\mathrm{S}}^2}\Bigg(\sin\left(\varphi_{100}\right)\cos\left(\varphi_{100}\right)\sin\left(\theta_{001}\right) - \sin\left(\varphi_{100}\right)\cos^3\left(\varphi_{100}\right)\sin^3\left(\theta_{001}\right)$$
$$- \sin\left(\varphi_{100}\right)\cos\left(\varphi_{100}\right)\sin\left(\theta_{001}\right) + \sin^3\left(\varphi_{100}\right)\cos\left(\varphi_{100}\right)\sin^3\left(\theta_{001}\right)$$
$$+ 2 \cdot \sin\left(\varphi_{100}\right)\cos\left(\varphi_{100}\right)\sin^3\left(\theta_{001}\right) \cdot \left(\sin^2\left(\varphi_{100}\right) - \cos^2\left(\varphi_{100}\right)\right)$$
$$+ 2 \cdot \sin\left(\varphi_{100}\right)\cos\left(\varphi_{100}\right)\sin\left(\theta_{001}\right)\cos^2\left(\theta_{001}\right)$$
$$- 2 \cdot \sin\left(\varphi_{100}\right)\cos\left(\varphi_{100}\right)\sin\left(\theta_{001}\right)\cos^2\left(\theta_{001}\right)\Bigg) \tag{C.104}$$

$$\Rightarrow N_{yz}^{\mathrm{ani,c1}} = \frac{2K_{\mathrm{c1}}}{\mu_0 M_{\mathrm{S}}^2} \cdot 3 \cdot \sin\left(\varphi_{100}\right)\cos\left(\varphi_{100}\right)\sin^3\left(\theta_{001}\right) \cdot \left(\sin^2\left(\varphi_{100}\right) - \cos^2\left(\varphi_{100}\right)\right) \tag{C.105}$$

Result: First order cubic anisotropy tensor in the local base

In total, this coordinate transformation results in the first order anisotropy tensor

$$\hat{N}_{\text{ani,c1}} = \begin{bmatrix} N_{xx}^{\text{ani,c1}} & N_{xy}^{\text{ani,c1}} & N_{xz}^{\text{ani,c1}} \\ N_{yx}^{\text{ani,c1}} & N_{yy}^{\text{ani,c1}} & N_{yz}^{\text{ani,c1}} \\ N_{zx}^{\text{ani,c1}} & N_{zy}^{\text{ani,c1}} & N_{zz}^{\text{ani,c1}} \end{bmatrix}_{\text{xyz}} \tag{C.106}$$

with

$$N_{xx}^{\text{ani,c1}} = \frac{2K_{\text{c1}}}{\mu_0 M_{\text{S}}^2} \cdot \left(1 - \frac{3}{4}\sin^2\left(\theta_{001}\right)\cos^2\left(\theta_{001}\right) \cdot \left(7 + \cos\left(4\varphi_{100}\right)\right)\right) \tag{C.107}$$

$$N_{yy}^{\text{ani,c1}} = \frac{2K_{\text{c1}}}{\mu_0 M_{\text{S}}^2} \cdot \left(1 - 6 \cdot \sin^2\left(\varphi_{100}\right)\cos^2\left(\varphi_{100}\right)\sin^2\left(\theta_{001}\right)\right) \tag{C.108}$$

$$N_{zz}^{\text{ani,c1}} = \frac{2K_{\text{c1}}}{\mu_0 M_{\text{S}}^2} \cdot 4\sin^2\left(\theta_{001}\right) \cdot \left(\sin^2\left(\varphi_{100}\right)\cos^2\left(\varphi_{100}\right)\sin^2\left(\theta_{001}\right) + \cos^2\left(\theta_{001}\right)\right) \tag{C.109}$$

for the diagonal elements and

$$N_{xy}^{\text{ani,c1}} = \frac{2K_{\text{c1}}}{\mu_0 M_{\text{S}}^2} \cdot 3 \cdot \sin\left(\varphi_{100}\right)\cos\left(\varphi_{100}\right)\sin^2\left(\theta_{001}\right)\cos\left(\theta_{001}\right) \cdot \left(\cos^2\left(\varphi_{100}\right) - \sin^2\left(\varphi_{100}\right)\right) \tag{C.110}$$

$$N_{xz}^{\text{ani,c1}} = \frac{2K_{\text{c1}}}{\mu_0 M_{\text{S}}^2} \cdot \sin\left(\theta_{001}\right)\cos\left(\theta_{001}\right) \cdot \left(-3\cos^2\left(\theta_{001}\right) + \frac{3}{4}\sin^2\left(\theta_{001}\right) \cdot \left(\cos\left(4\varphi_{100}\right) + 3\right)\right) \tag{C.111}$$

$$N_{yz}^{\text{ani,c1}} = \frac{2K_{\text{c1}}}{\mu_0 M_{\text{S}}^2} \cdot 3 \cdot \sin\left(\varphi_{100}\right)\cos\left(\varphi_{100}\right)\sin^3\left(\theta_{001}\right) \cdot \left(\sin^2\left(\varphi_{100}\right) - \cos^2\left(\varphi_{100}\right)\right) \tag{C.112}$$

for the off-diagonal elements in the xyz base.

Second order cubic anisotropy tensor: crystal → local base

$$\begin{aligned}
N_{xx}^{\mathrm{ani,c2}} &= N_{11}^{\mathrm{ani,c2}} \cdot \cos^2\left(\varphi_{100}\right)\cos^2\left(\theta_{001}\right) + N_{22}^{\mathrm{ani,c2}} \cdot \sin^2\left(\varphi_{100}\right)\cos^2\left(\theta_{001}\right) + N_{33}^{\mathrm{ani,c2}} \cdot \sin^2\left(\theta_{001}\right) \\
&\quad + 2 \cdot N_{12}^{\mathrm{ani,c2}} \cdot \sin\left(\varphi_{100}\right)\cos\left(\varphi_{100}\right)\cos^2\left(\theta_{001}\right) - 2 \cdot N_{13}^{\mathrm{ani,c2}} \cdot \cos\left(\varphi_{100}\right)\sin\left(\theta_{001}\right)\cos\left(\theta_{001}\right) \\
&\quad - 2 \cdot N_{23}^{\mathrm{ani,c2}} \cdot \sin\left(\varphi_{100}\right)\sin\left(\theta_{001}\right)\cos\left(\theta_{001}\right) \qquad \text{(C.113)} \\
&= \frac{2K_{\mathrm{c2}}}{\mu_0 M_{\mathrm{S}}^2} \cdot \sin^2\left(\varphi_{100}\right)\sin^2\left(\theta_{001}\right)\cos^2\left(\theta_{001}\right) \cdot \cos^2\left(\varphi_{100}\right)\cos^2\left(\theta_{001}\right) \\
&\quad + \frac{2K_{\mathrm{c2}}}{\mu_0 M_{\mathrm{S}}^2} \cdot \cos^2\left(\varphi_{100}\right)\sin^2\left(\theta_{001}\right)\cos^2\left(\theta_{001}\right) \cdot \sin^2\left(\varphi_{100}\right)\cos^2\left(\theta_{001}\right) \\
&\quad + \frac{2K_{\mathrm{c2}}}{\mu_0 M_{\mathrm{S}}^2} \cdot \sin^2\left(\varphi_{100}\right)\cos^2\left(\varphi_{100}\right)\sin^4\left(\theta_{001}\right) \cdot \sin^2\left(\theta_{001}\right) \\
&\quad + 2 \cdot \frac{2K_{\mathrm{c2}}}{\mu_0 M_{\mathrm{S}}^2} \cdot 2 \cdot \sin\left(\varphi_{100}\right)\cos\left(\varphi_{100}\right)\sin^2\left(\theta_{001}\right)\cos^2\left(\theta_{001}\right) \cdot \sin\left(\varphi_{100}\right)\cos\left(\varphi_{100}\right)\cos^2\left(\theta_{001}\right) \\
&\quad - 2 \cdot \frac{2K_{\mathrm{c2}}}{\mu_0 M_{\mathrm{S}}^2} \cdot 2 \cdot \sin^2\left(\varphi_{100}\right)\cos\left(\varphi_{100}\right)\sin^3\left(\theta_{001}\right)\cos\left(\theta_{001}\right) \cdot \cos\left(\varphi_{100}\right)\sin\left(\theta_{001}\right)\cos\left(\theta_{001}\right) \\
&\quad - 2 \cdot \frac{2K_{\mathrm{c2}}}{\mu_0 M_{\mathrm{S}}^2} \cdot 2 \cdot \sin\left(\varphi_{100}\right)\cos^2\left(\varphi_{100}\right)\sin^3\left(\theta_{001}\right)\cos\left(\theta_{001}\right) \cdot \sin\left(\varphi_{100}\right)\sin\left(\theta_{001}\right)\cos\left(\theta_{001}\right) \qquad \text{(C.114)} \\
&= \frac{2K_{\mathrm{c2}}}{\mu_0 M_{\mathrm{S}}^2} \cdot \Bigg(\sin^2\left(\varphi_{100}\right)\cos^2\left(\varphi_{100}\right)\sin^2\left(\theta_{001}\right)\cos^4\left(\theta_{001}\right) + \sin^2\left(\varphi_{100}\right)\cos^2\left(\varphi_{100}\right)\sin^2\left(\theta_{001}\right)\cos^4\left(\theta_{001}\right) \\
&\quad + \sin^2\left(\varphi_{100}\right)\cos^2\left(\varphi_{100}\right)\sin^6\left(\theta_{001}\right) + 4 \cdot \sin^2\left(\varphi_{100}\right)\cos^2\left(\varphi_{100}\right)\sin^2\left(\theta_{001}\right)\cos^4\left(\theta_{001}\right) \\
&\quad - 4 \cdot \sin^2\left(\varphi_{100}\right)\cos^2\left(\varphi_{100}\right)\sin^4\left(\theta_{001}\right)\cos^2\left(\theta_{001}\right) - 4 \cdot \sin^2\left(\varphi_{100}\right)\cos^2\left(\varphi_{100}\right)\sin^4\left(\theta_{001}\right)\cos^2\left(\theta_{001}\right) \Bigg) \\
&\qquad \text{(C.115)} \\
&= \frac{2K_{\mathrm{c2}}}{\mu_0 M_{\mathrm{S}}^2} \cdot \sin^2\left(\varphi_{100}\right)\cos^2\left(\varphi_{100}\right) \cdot \left(6\sin^2\left(\theta_{001}\right)\cos^4\left(\theta_{001}\right) + \sin^6\left(\theta_{001}\right) - 8\sin^4\left(\theta_{001}\right)\cos^2\left(\theta_{001}\right)\right) \\
&\qquad \text{(C.116)} \\
\Rightarrow N_{xx}^{\mathrm{ani,c2}} &= \frac{2K_{\mathrm{c2}}}{\mu_0 M_{\mathrm{S}}^2} \cdot \sin^2\left(\varphi_{100}\right)\cos^2\left(\varphi_{100}\right) \cdot \left(6\sin^2\left(\theta_{001}\right) - 20\sin^4\left(\theta_{001}\right) + 15\sin^6\left(\theta_{001}\right)\right) \qquad \text{(C.117)}
\end{aligned}$$

$$\begin{aligned}
N_{yy}^{\mathrm{ani,c2}} &= N_{11}^{\mathrm{ani,c2}} \cdot \sin^2\left(\varphi_{100}\right) + N_{22}^{\mathrm{ani,c2}} \cdot \cos^2\left(\varphi_{100}\right) - 2 \cdot N_{12}^{\mathrm{ani,c2}} \cdot \sin\left(\varphi_{100}\right)\cos\left(\varphi_{100}\right) \qquad \text{(C.118)} \\
&= \frac{2K_{\mathrm{c2}}}{\mu_0 M_{\mathrm{S}}^2} \cdot \sin^2\left(\varphi_{100}\right)\sin^2\left(\theta_{001}\right)\cos^2\left(\theta_{001}\right) \cdot \sin^2\left(\varphi_{100}\right) \\
&\quad + \frac{2K_{\mathrm{c2}}}{\mu_0 M_{\mathrm{S}}^2} \cdot \cos^2\left(\varphi_{100}\right)\sin^2\left(\theta_{001}\right)\cos^2\left(\theta_{001}\right) \cdot \cos^2\left(\varphi_{100}\right) \\
&\quad - 2 \cdot \frac{2K_{\mathrm{c2}}}{\mu_0 M_{\mathrm{S}}^2} \cdot 2 \cdot \sin\left(\varphi_{100}\right)\cos\left(\varphi_{100}\right)\sin^2\left(\theta_{001}\right)\cos^2\left(\theta_{001}\right) \cdot \sin\left(\varphi_{100}\right)\cos\left(\varphi_{100}\right) \qquad \text{(C.119)} \\
&= \frac{2K_{\mathrm{c2}}}{\mu_0 M_{\mathrm{S}}^2} \cdot \Big(\sin^4\left(\varphi_{100}\right)\sin^2\left(\theta_{001}\right)\cos^2\left(\theta_{001}\right) + \cos^4\left(\varphi_{100}\right)\sin^2\left(\theta_{001}\right)\cos^2\left(\theta_{001}\right) \\
&\quad - 4 \cdot \sin^2\left(\varphi_{100}\right)\cos^2\left(\varphi_{100}\right)\sin^2\left(\theta_{001}\right)\cos^2\left(\theta_{001}\right) \Big) \qquad \text{(C.120)} \\
&= \frac{2K_{\mathrm{c2}}}{\mu_0 M_{\mathrm{S}}^2} \cdot \sin^2\left(\theta_{001}\right)\cos^2\left(\theta_{001}\right) \cdot \left(\sin^4\left(\varphi_{100}\right) + \cos^4\left(\varphi_{100}\right) - 4 \cdot \sin^2\left(\varphi_{100}\right)\cos^2\left(\varphi_{100}\right)\right) \qquad \text{(C.121)} \\
\Rightarrow N_{yy}^{\mathrm{ani,c2}} &= \frac{2K_{\mathrm{c2}}}{\mu_0 M_{\mathrm{S}}^2} \cdot \sin^2\left(\theta_{001}\right)\cos^2\left(\theta_{001}\right) \cdot \left(\frac{3}{4}\cos\left(4\varphi_{100}\right) + \frac{1}{4}\right) \qquad \text{(C.122)}
\end{aligned}$$

$$
\begin{aligned}
N_{zz}^{\mathrm{ani,c2}} &= N_{11}^{\mathrm{ani,c2}} \cdot \cos^2\left(\varphi_{100}\right) \sin^2\left(\theta_{001}\right) + N_{22}^{\mathrm{ani,c2}} \cdot \sin^2\left(\varphi_{100}\right) \sin^2\left(\theta_{001}\right) + N_{33}^{\mathrm{ani,c2}} \cdot \cos^2\left(\theta_{001}\right) \\
&\quad + 2 \cdot N_{12}^{\mathrm{ani,c2}} \cdot \sin\left(\varphi_{100}\right) \cos\left(\varphi_{100}\right) \sin^2\left(\theta_{001}\right) + 2 \cdot N_{13}^{\mathrm{ani,c2}} \cdot \cos\left(\varphi_{100}\right) \sin\left(\theta_{001}\right) \cos\left(\theta_{001}\right) \\
&\quad + 2 \cdot N_{23}^{\mathrm{ani,c2}} \cdot \sin\left(\varphi_{100}\right) \sin\left(\theta_{001}\right) \cos\left(\theta_{001}\right) \qquad \text{(C.123)} \\
&= \frac{2K_{\mathrm{c2}}}{\mu_0 M_{\mathrm{S}}^2} \cdot \sin^2\left(\varphi_{100}\right) \sin^2\left(\theta_{001}\right) \cos^2\left(\theta_{001}\right) \cdot \cos^2\left(\varphi_{100}\right) \sin^2\left(\theta_{001}\right) \\
&\quad + \frac{2K_{\mathrm{c2}}}{\mu_0 M_{\mathrm{S}}^2} \cdot \cos^2\left(\varphi_{100}\right) \sin^2\left(\theta_{001}\right) \cos^2\left(\theta_{001}\right) \cdot \sin^2\left(\varphi_{100}\right) \sin^2\left(\theta_{001}\right) \\
&\quad + \frac{2K_{\mathrm{c2}}}{\mu_0 M_{\mathrm{S}}^2} \cdot \sin^2\left(\varphi_{100}\right) \cos^2\left(\varphi_{100}\right) \sin^4\left(\theta_{001}\right) \cdot \cos^2\left(\theta_{001}\right) \\
&\quad + 2 \cdot \frac{2K_{\mathrm{c2}}}{\mu_0 M_{\mathrm{S}}^2} \cdot 2 \cdot \sin\left(\varphi_{100}\right) \cos\left(\varphi_{100}\right) \sin^2\left(\theta_{001}\right) \cos^2\left(\theta_{001}\right) \cdot \sin\left(\varphi_{100}\right) \cos\left(\varphi_{100}\right) \sin^2\left(\theta_{001}\right) \\
&\quad + 2 \cdot \frac{2K_{\mathrm{c2}}}{\mu_0 M_{\mathrm{S}}^2} \cdot 2 \cdot \sin^2\left(\varphi_{100}\right) \cos\left(\varphi_{100}\right) \sin^3\left(\theta_{001}\right) \cos\left(\theta_{001}\right) \cdot \cos\left(\varphi_{100}\right) \sin\left(\theta_{001}\right) \cos\left(\theta_{001}\right) \\
&\quad + 2 \cdot \frac{2K_{\mathrm{c2}}}{\mu_0 M_{\mathrm{S}}^2} \cdot 2 \cdot \sin\left(\varphi_{100}\right) \cos^2\left(\varphi_{100}\right) \sin^3\left(\theta_{001}\right) \cos\left(\theta_{001}\right) \cdot \sin\left(\varphi_{100}\right) \sin\left(\theta_{001}\right) \cos\left(\theta_{001}\right) \qquad \text{(C.124)} \\
&= \frac{2K_{\mathrm{c2}}}{\mu_0 M_{\mathrm{S}}^2} \cdot \Bigg(\sin^2\left(\varphi_{100}\right) \cos^2\left(\varphi_{100}\right) \sin^4\left(\theta_{001}\right) \cos^2\left(\theta_{001}\right) + \sin^2\left(\varphi_{100}\right) \cos^2\left(\varphi_{100}\right) \sin^4\left(\theta_{001}\right) \cos^2\left(\theta_{001}\right) \\
&\quad + \sin^2\left(\varphi_{100}\right) \cos^2\left(\varphi_{100}\right) \sin^4\left(\theta_{001}\right) \cos^2\left(\theta_{001}\right) \\
&\quad + 4 \cdot \sin^2\left(\varphi_{100}\right) \cos^2\left(\varphi_{100}\right) \sin^4\left(\theta_{001}\right) \cos^2\left(\theta_{001}\right) \\
&\quad + 4 \cdot \sin^2\left(\varphi_{100}\right) \cos^2\left(\varphi_{100}\right) \sin^4\left(\theta_{001}\right) \cos^2\left(\theta_{001}\right) \\
&\quad + 4 \cdot \sin^2\left(\varphi_{100}\right) \cos^2\left(\varphi_{100}\right) \sin^4\left(\theta_{001}\right) \cos^2\left(\theta_{001}\right) \Bigg) \qquad \text{(C.125)} \\
\Rightarrow N_{zz}^{\mathrm{ani,c2}} &= \frac{2K_{\mathrm{c2}}}{\mu_0 M_{\mathrm{S}}^2} \cdot 15 \cdot \sin^2\left(\varphi_{100}\right) \cos^2\left(\varphi_{100}\right) \sin^4\left(\theta_{001}\right) \cos^2\left(\theta_{001}\right) \qquad \text{(C.126)}
\end{aligned}
$$

$$
\begin{aligned}
N_{xy}^{\mathrm{ani,c2}} &= -N_{11}^{\mathrm{ani,c2}} \cdot \sin\left(\varphi_{100}\right) \cos\left(\varphi_{100}\right) \cos\left(\theta_{001}\right) + N_{22}^{\mathrm{ani,c2}} \cdot \sin\left(\varphi_{100}\right) \cos\left(\varphi_{100}\right) \cos\left(\theta_{001}\right) \\
&\quad + N_{12}^{\mathrm{ani,c2}} \cdot \left(\cos^2\left(\varphi_{100}\right) - \sin^2\left(\varphi_{100}\right)\right) \cos\left(\theta_{001}\right) + N_{13}^{\mathrm{ani,c2}} \cdot \sin\left(\varphi_{100}\right) \sin\left(\theta_{001}\right) \\
&\quad - N_{23}^{\mathrm{ani,c2}} \cdot \cos\left(\varphi_{100}\right) \sin\left(\theta_{001}\right) \qquad \text{(C.127)} \\
&= -\frac{2K_{\mathrm{c2}}}{\mu_0 M_{\mathrm{S}}^2} \cdot \sin^2\left(\varphi_{100}\right) \sin^2\left(\theta_{001}\right) \cos^2\left(\theta_{001}\right) \cdot \sin\left(\varphi_{100}\right) \cos\left(\varphi_{100}\right) \cos\left(\theta_{001}\right) \\
&\quad + \frac{2K_{\mathrm{c2}}}{\mu_0 M_{\mathrm{S}}^2} \cdot \cos^2\left(\varphi_{100}\right) \sin^2\left(\theta_{001}\right) \cos^2\left(\theta_{001}\right) \cdot \sin\left(\varphi_{100}\right) \cos\left(\varphi_{100}\right) \cos\left(\theta_{001}\right) \\
&\quad + \frac{2K_{\mathrm{c2}}}{\mu_0 M_{\mathrm{S}}^2} \cdot 2 \cdot \sin\left(\varphi_{100}\right) \cos\left(\varphi_{100}\right) \sin^2\left(\theta_{001}\right) \cos^2\left(\theta_{001}\right) \cdot \left(\cos^2\left(\varphi_{100}\right) - \sin^2\left(\varphi_{100}\right)\right) \cos\left(\theta_{001}\right) \\
&\quad + \frac{2K_{\mathrm{c2}}}{\mu_0 M_{\mathrm{S}}^2} \cdot 2 \cdot \sin^2\left(\varphi_{100}\right) \cos\left(\varphi_{100}\right) \sin^3\left(\theta_{001}\right) \cos\left(\theta_{001}\right) \cdot \sin\left(\varphi_{100}\right) \sin\left(\theta_{001}\right) \\
&\quad - \frac{2K_{\mathrm{c2}}}{\mu_0 M_{\mathrm{S}}^2} \cdot 2 \cdot \sin\left(\varphi_{100}\right) \cos^2\left(\varphi_{100}\right) \sin^3\left(\theta_{001}\right) \cos\left(\theta_{001}\right) \cdot \cos\left(\varphi_{100}\right) \sin\left(\theta_{001}\right) \qquad \text{(C.128)} \\
&= \frac{2K_{\mathrm{c2}}}{\mu_0 M_{\mathrm{S}}^2} \cdot \Bigg(-\sin^3\left(\varphi_{100}\right) \cos\left(\varphi_{100}\right) \sin^2\left(\theta_{001}\right) \cos^3\left(\theta_{001}\right) \\
&\quad + \sin\left(\varphi_{100}\right) \cos^3\left(\varphi_{100}\right) \sin^2\left(\theta_{001}\right) \cos^3\left(\theta_{001}\right) \\
&\quad + 2 \cdot \sin\left(\varphi_{100}\right) \cos\left(\varphi_{100}\right) \sin^2\left(\theta_{001}\right) \cos^3\left(\theta_{001}\right) \cdot \left(\cos^2\left(\varphi_{100}\right) - \sin^2\left(\varphi_{100}\right)\right) \\
&\quad + 2 \cdot \sin^3\left(\varphi_{100}\right) \cos\left(\varphi_{100}\right) \sin^4\left(\theta_{001}\right) \cos\left(\theta_{001}\right) \\
&\quad - 2 \cdot \sin\left(\varphi_{100}\right) \cos^3\left(\varphi_{100}\right) \sin^4\left(\theta_{001}\right) \cos\left(\theta_{001}\right) \Bigg) \qquad \text{(C.129)} \\
&= \frac{2K_{\mathrm{c2}}}{\mu_0 M_{\mathrm{S}}^2} \cdot \Bigg(3 \cdot \sin\left(\varphi_{100}\right) \cos\left(\varphi_{100}\right) \sin^2\left(\theta_{001}\right) \cos^3\left(\theta_{001}\right) \cdot \left(\cos^2\left(\varphi_{100}\right) - \sin^2\left(\varphi_{100}\right)\right) \\
&\quad - 2 \cdot \sin\left(\varphi_{100}\right) \cos\left(\varphi_{100}\right) \sin^4\left(\theta_{001}\right) \cos\left(\theta_{001}\right) \left(\cos^2\left(\varphi_{100}\right) - \sin^2\left(\varphi_{100}\right)\right) \Bigg) \qquad \text{(C.130)} \\
\Rightarrow N_{xy}^{\mathrm{ani,c2}} &= \frac{2K_{\mathrm{c2}}}{\mu_0 M_{\mathrm{S}}^2} \cdot \sin\left(\varphi_{100}\right) \cos\left(\varphi_{100}\right) \sin\left(\theta_{001}\right) \cos\left(\theta_{001}\right) \\
&\qquad \cdot \left(\cos^2\left(\varphi_{100}\right) - \sin^2\left(\varphi_{100}\right)\right) \cdot \left(3 \cdot \sin\left(\theta_{001}\right) \cos^2\left(\theta_{001}\right) - 2 \cdot \sin^3\left(\theta_{001}\right)\right) \qquad \text{(C.131)}
\end{aligned}
$$

$$
\begin{aligned}
N_{xz}^{\mathrm{ani,c2}} &= -N_{11}^{\mathrm{ani,c2}} \cdot \cos^2\left(\varphi_{100}\right) \sin\left(\theta_{001}\right) \cos\left(\theta_{001}\right) - N_{22}^{\mathrm{ani,c2}} \cdot \sin^2\left(\varphi_{100}\right) \sin\left(\theta_{001}\right) \cos\left(\theta_{001}\right) + N_{33}^{\mathrm{ani,c2}} \sin\left(\theta_{001}\right) \cos\left(\theta_{001}\right) \\
&\quad - 2 \cdot N_{12}^{\mathrm{ani,c2}} \cdot \sin\left(\varphi_{100}\right) \cos\left(\varphi_{100}\right) \sin\left(\theta_{001}\right) \cos\left(\theta_{001}\right) \\
&\quad + N_{13}^{\mathrm{ani,c2}} \cdot \cos\left(\varphi_{100}\right) \left(\sin^2\left(\theta_{001}\right) - \cos^2\left(\theta_{001}\right)\right) + N_{23}^{\mathrm{ani,c2}} \cdot \sin\left(\varphi_{100}\right) \left(\sin^2\left(\theta_{001}\right) - \cos^2\left(\theta_{001}\right)\right) \quad \text{(C.132)} \\
&= -\frac{2K_{\mathrm{c2}}}{\mu_0 M_{\mathrm{S}}^2} \cdot \sin^2\left(\varphi_{100}\right) \sin^2\left(\theta_{001}\right) \cos^2\left(\theta_{001}\right) \cdot \cos^2\left(\varphi_{100}\right) \sin\left(\theta_{001}\right) \cos\left(\theta_{001}\right) \\
&\quad - \frac{2K_{\mathrm{c2}}}{\mu_0 M_{\mathrm{S}}^2} \cdot \cos^2\left(\varphi_{100}\right) \sin^2\left(\theta_{001}\right) \cos^2\left(\theta_{001}\right) \cdot \sin^2\left(\varphi_{100}\right) \sin\left(\theta_{001}\right) \cos\left(\theta_{001}\right) \\
&\quad + \frac{2K_{\mathrm{c2}}}{\mu_0 M_{\mathrm{S}}^2} \cdot \sin^2\left(\varphi_{100}\right) \cos^2\left(\varphi_{100}\right) \sin^4\left(\theta_{001}\right) \sin\left(\theta_{001}\right) \cos\left(\theta_{001}\right) \\
&\quad - 2 \cdot \frac{2K_{\mathrm{c2}}}{\mu_0 M_{\mathrm{S}}^2} \cdot 2 \cdot \sin\left(\varphi_{100}\right) \cos\left(\varphi_{100}\right) \sin^2\left(\theta_{001}\right) \cos^2\left(\theta_{001}\right) \cdot \sin\left(\varphi_{100}\right) \cos\left(\varphi_{100}\right) \sin\left(\theta_{001}\right) \cos\left(\theta_{001}\right) \\
&\quad + \frac{2K_{\mathrm{c2}}}{\mu_0 M_{\mathrm{S}}^2} \cdot 2 \cdot \sin^2\left(\varphi_{100}\right) \cos\left(\varphi_{100}\right) \sin^3\left(\theta_{001}\right) \cos\left(\theta_{001}\right) \cdot \cos\left(\varphi_{100}\right) \left(\sin^2\left(\theta_{001}\right) - \cos^2\left(\theta_{001}\right)\right) \\
&\quad + \frac{2K_{\mathrm{c2}}}{\mu_0 M_{\mathrm{S}}^2} \cdot 2 \cdot \sin\left(\varphi_{100}\right) \cos^2\left(\varphi_{100}\right) \sin^3\left(\theta_{001}\right) \cos\left(\theta_{001}\right) \cdot \sin\left(\varphi_{100}\right) \left(\sin^2\left(\theta_{001}\right) - \cos^2\left(\theta_{001}\right)\right) \quad \text{(C.133)} \\
&= \frac{2K_{\mathrm{c2}}}{\mu_0 M_{\mathrm{S}}^2} \cdot \Bigg(- \sin^2\left(\varphi_{100}\right) \cos^2\left(\varphi_{100}\right) \sin^3\left(\theta_{001}\right) \cos^3\left(\theta_{001}\right) \\
&\quad - \sin^2\left(\varphi_{100}\right) \cos^2\left(\varphi_{100}\right) \sin^3\left(\theta_{001}\right) \cos^3\left(\theta_{001}\right) \\
&\quad + \sin^2\left(\varphi_{100}\right) \cos^2\left(\varphi_{100}\right) \sin^5\left(\theta_{001}\right) \cos\left(\theta_{001}\right) \\
&\quad - 4 \cdot \sin^2\left(\varphi_{100}\right) \cos^2\left(\varphi_{100}\right) \sin^3\left(\theta_{001}\right) \cos^3\left(\theta_{001}\right) \\
&\quad + 2 \cdot \sin^2\left(\varphi_{100}\right) \cos^2\left(\varphi_{100}\right) \sin^3\left(\theta_{001}\right) \cos\left(\theta_{001}\right) \cdot \left(\sin^2\left(\theta_{001}\right) - \cos^2\left(\theta_{001}\right)\right) \\
&\quad + 2 \cdot \sin^2\left(\varphi_{100}\right) \cos^2\left(\varphi_{100}\right) \sin^3\left(\theta_{001}\right) \cos\left(\theta_{001}\right) \cdot \left(\sin^2\left(\theta_{001}\right) - \cos^2\left(\theta_{001}\right)\right) \quad \text{(C.134)} \\
&= \frac{2K_{\mathrm{c2}}}{\mu_0 M_{\mathrm{S}}^2} \cdot \Bigg(\sin^2\left(\varphi_{100}\right) \cos^2\left(\varphi_{100}\right) \sin^5\left(\theta_{001}\right) \cos\left(\theta_{001}\right) \\
&\quad - 6 \cdot \sin^2\left(\varphi_{100}\right) \cos^2\left(\varphi_{100}\right) \sin^3\left(\theta_{001}\right) \cos^3\left(\theta_{001}\right) \\
&\quad + 4 \cdot \sin^2\left(\varphi_{100}\right) \cos^2\left(\varphi_{100}\right) \sin^3\left(\theta_{001}\right) \cos\left(\theta_{001}\right) \cdot \left(\sin^2\left(\theta_{001}\right) - \cos^2\left(\theta_{001}\right)\right) \Bigg) \quad \text{(C.135)} \\
\Rightarrow N_{xz}^{\mathrm{ani,c2}} &= \frac{2K_{\mathrm{c2}}}{\mu_0 M_{\mathrm{S}}^2} \cdot \sin^2\left(\varphi_{100}\right) \cos^2\left(\varphi_{100}\right) \sin^3\left(\theta_{001}\right) \cos\left(\theta_{001}\right) \cdot \left(\sin^2\left(\theta_{001}\right) + 2 \cdot \left(2\sin^2\left(\theta_{001}\right) - 5\cos^2\left(\theta_{001}\right)\right)\right) \quad \text{(C.136)}
\end{aligned}
$$

$$
\begin{aligned}
N_{yz}^{\mathrm{ani,c2}} &= N_{11}^{\mathrm{ani,c2}} \cdot \sin\left(\varphi_{100}\right) \cos\left(\varphi_{100}\right) \sin\left(\theta_{001}\right) - N_{22}^{\mathrm{ani}} \cdot \sin\left(\varphi_{100}\right) \cos\left(\varphi_{100}\right) \sin\left(\theta_{001}\right) \\
&\quad + N_{12}^{\mathrm{ani,c2}} \cdot \left(\sin^2\left(\varphi_{100}\right) - \cos^2\left(\varphi_{100}\right)\right) \sin\left(\theta_{001}\right) \\
&\quad + N_{13}^{\mathrm{ani,c2}} \cdot \sin\left(\varphi_{100}\right) \cos\left(\theta_{001}\right) - N_{23}^{\mathrm{ani,c2}} \cdot \cos\left(\varphi_{100}\right) \cos\left(\theta_{001}\right) \qquad \text{(C.137)} \\
&= \frac{2K_{\mathrm{c2}}}{\mu_0 M_{\mathrm{S}}^2} \cdot \sin^2\left(\varphi_{100}\right) \sin^2\left(\theta_{001}\right) \cos^2\left(\theta_{001}\right) \cdot \sin\left(\varphi_{100}\right) \cos\left(\varphi_{100}\right) \sin\left(\theta_{001}\right) \\
&\quad - \frac{2K_{\mathrm{c2}}}{\mu_0 M_{\mathrm{S}}^2} \cdot \cos^2\left(\varphi_{100}\right) \sin^2\left(\theta_{001}\right) \cos^2\left(\theta_{001}\right) \cdot \sin\left(\varphi_{100}\right) \cos\left(\varphi_{100}\right) \sin\left(\theta_{001}\right) \\
&\quad + \frac{2K_{\mathrm{c2}}}{\mu_0 M_{\mathrm{S}}^2} \cdot 2 \cdot \sin\left(\varphi_{100}\right) \cos\left(\varphi_{100}\right) \sin^2\left(\theta_{001}\right) \cos^2\left(\theta_{001}\right) \cdot \left(\sin^2\left(\varphi_{100}\right) - \cos^2\left(\varphi_{100}\right)\right) \sin\left(\theta_{001}\right) \\
&\quad + \frac{2K_{\mathrm{c2}}}{\mu_0 M_{\mathrm{S}}^2} \cdot 2 \cdot \sin^2\left(\varphi_{100}\right) \cos\left(\varphi_{100}\right) \sin^3\left(\theta_{001}\right) \cos\left(\theta_{001}\right) \cdot \sin\left(\varphi_{100}\right) \cos\left(\theta_{001}\right) \\
&\quad - \frac{2K_{\mathrm{c2}}}{\mu_0 M_{\mathrm{S}}^2} \cdot 2 \cdot \sin\left(\varphi_{100}\right) \cos^2\left(\varphi_{100}\right) \sin^3\left(\theta_{001}\right) \cos\left(\theta_{001}\right) \cdot \cos\left(\varphi_{100}\right) \cos\left(\theta_{001}\right) \qquad \text{(C.138)} \\
&= \frac{2K_{\mathrm{c2}}}{\mu_0 M_{\mathrm{S}}^2} \cdot \Bigg(\sin^3\left(\varphi_{100}\right) \cos\left(\varphi_{100}\right) \sin^3\left(\theta_{001}\right) \cos^2\left(\theta_{001}\right) \\
&\quad - \sin\left(\varphi_{100}\right) \cos^3\left(\varphi_{100}\right) \sin^3\left(\theta_{001}\right) \cos^2\left(\theta_{001}\right) \\
&\quad + 2 \cdot \sin\left(\varphi_{100}\right) \cos\left(\varphi_{100}\right) \sin^3\left(\theta_{001}\right) \cos^2\left(\theta_{001}\right) \cdot \left(\sin^2\left(\varphi_{100}\right) - \cos^2\left(\varphi_{100}\right) \right) \\
&\quad + 2 \cdot \sin^3\left(\varphi_{100}\right) \cos\left(\varphi_{100}\right) \sin^3\left(\theta_{001}\right) \cos^2\left(\theta_{001}\right) \\
&\quad - 2 \cdot \sin\left(\varphi_{100}\right) \cos^3\left(\varphi_{100}\right) \sin^3\left(\theta_{001}\right) \cos^2\left(\theta_{001}\right) \Bigg) \qquad \text{(C.139)} \\
\Rightarrow N_{yz}^{\mathrm{ani,c2}} &= \frac{2K_{\mathrm{c2}}}{\mu_0 M_{\mathrm{S}}^2} \cdot 5 \cdot \sin\left(\varphi_{100}\right) \cos\left(\varphi_{100}\right) \sin^3\left(\theta_{001}\right) \cos^2\left(\theta_{001}\right) \cdot \left(\sin^2\left(\varphi_{100}\right) - \cos^2\left(\varphi_{100}\right) \right) \qquad \text{(C.140)}
\end{aligned}
$$

Result: Second order cubic anisotropy tensor in the local base

In total, this coordinate transformation results in the second order anisotropy tensor

$$\hat{N}_{\mathrm{ani,c2}} = \begin{bmatrix} N_{xx}^{\mathrm{ani,c2}} & N_{xy}^{\mathrm{ani,c2}} & N_{xz}^{\mathrm{ani,c2}} \\ N_{yx}^{\mathrm{ani,c2}} & N_{yy}^{\mathrm{ani,c2}} & N_{yz}^{\mathrm{ani,c2}} \\ N_{zx}^{\mathrm{ani,c2}} & N_{zy}^{\mathrm{ani,c2}} & N_{zz}^{\mathrm{ani,c2}} \end{bmatrix}_{\mathrm{xyz}} \tag{C.141}$$

with

$$N_{xx}^{\mathrm{ani,c2}} = \frac{2K_{\mathrm{c2}}}{\mu_0 M_{\mathrm{S}}^2} \cdot \sin^2\left(\varphi_{100}\right) \cos^2\left(\varphi_{100}\right) \cdot \left(6\sin^2\left(\theta_{001}\right) - 20\sin^4\left(\theta_{001}\right) + 15\sin^6\left(\theta_{001}\right)\right) \tag{C.142}$$

$$N_{yy}^{\mathrm{ani,c2}} = \frac{2K_{\mathrm{c2}}}{\mu_0 M_{\mathrm{S}}^2} \cdot \sin^2\left(\theta_{001}\right) \cos^2\left(\theta_{001}\right) \cdot \left(\frac{3}{4}\cos\left(4\varphi_{100}\right) + \frac{1}{4}\right) \tag{C.143}$$

$$N_{zz}^{\mathrm{ani,c2}} = \frac{2K_{\mathrm{c2}}}{\mu_0 M_{\mathrm{S}}^2} \cdot 15 \cdot \sin^2\left(\varphi_{100}\right) \cos^2\left(\varphi_{100}\right) \sin^4\left(\theta_{001}\right) \cos^2\left(\theta_{001}\right) \tag{C.144}$$

for the diagonal elements and

$$\begin{aligned} N_{xy}^{\mathrm{ani,c2}} = \frac{2K_{\mathrm{c2}}}{\mu_0 M_{\mathrm{S}}^2} &\cdot \sin\left(\varphi_{100}\right) \cos\left(\varphi_{100}\right) \sin\left(\theta_{001}\right) \cos\left(\theta_{001}\right) \\ &\cdot \left(\cos^2\left(\varphi_{100}\right) - \sin^2\left(\varphi_{100}\right)\right) \cdot \left(3 \cdot \sin\left(\theta_{001}\right) \cos^2\left(\theta_{001}\right) - 2 \cdot \sin^3\left(\theta_{001}\right)\right) \end{aligned} \tag{C.145}$$

$$N_{xz}^{\mathrm{ani,c2}} = \frac{2K_{\mathrm{c2}}}{\mu_0 M_{\mathrm{S}}^2} \cdot \sin^2\left(\varphi_{100}\right) \cos^2\left(\varphi_{100}\right) \sin^3\left(\theta_{001}\right) \cos\left(\theta_{001}\right) \cdot \left(\sin^2\left(\theta_{001}\right) + 2 \cdot \left(2\sin^2\left(\theta_{001}\right) - 5\cos^2\left(\theta_{001}\right)\right)\right) \tag{C.146}$$

$$N_{yz}^{\mathrm{ani,c2}} = \frac{2K_{\mathrm{c2}}}{\mu_0 M_{\mathrm{S}}^2} \cdot 5 \cdot \sin\left(\varphi_{100}\right) \cos\left(\varphi_{100}\right) \sin^3\left(\theta_{001}\right) \cos^2\left(\theta_{001}\right) \cdot \left(\sin^2\left(\varphi_{100}\right) - \cos^2\left(\varphi_{100}\right)\right) \tag{C.147}$$

for the off-diagonal elements in the xyz base.

C.3.3 The resulting cubic anisotropy tensor in the local coordinates

Consequently, in the local coordinate system defined by

$$\hat{\mathbf{e}}_x = \begin{pmatrix} -\cos\left(\varphi_{100}\right)\cos\left(\theta_{001}\right) \\ -\sin\left(\varphi_{100}\right)\cos\left(\theta_{001}\right) \\ \sin\left(\theta_{001}\right) \end{pmatrix}_{123} \quad \text{and} \quad \hat{\mathbf{e}}_y = \begin{pmatrix} \sin\left(\varphi_{100}\right) \\ -\cos\left(\varphi_{100}\right) \\ 0 \end{pmatrix}_{123} \quad \text{and} \quad \hat{\mathbf{e}}_z = \begin{pmatrix} \cos\left(\varphi_{100}\right)\sin\left(\theta_{001}\right) \\ \sin\left(\varphi_{100}\right)\sin\left(\theta_{001}\right) \\ \cos\left(\theta_{001}\right) \end{pmatrix}_{123} \tag{C.148}$$

with $\hat{\mathbf{e}}_z \parallel \mathbf{M}_0$ and $\hat{\mathbf{e}}_y \perp [001]_{123}$, the cubic anisotropy tensor reads

$$\hat{N}_{\text{ani}} = \hat{N}_{\text{ani}}^{\text{c1}} + \hat{N}_{\text{ani}}^{\text{c2}} = \begin{bmatrix} N_{xx}^{\text{ani,c1}} & N_{xy}^{\text{ani,c1}} & N_{xz}^{\text{ani,c1}} \\ N_{yx}^{\text{ani,c1}} & N_{yy}^{\text{ani,c1}} & N_{yz}^{\text{ani,c1}} \\ N_{zx}^{\text{ani,c1}} & N_{zy}^{\text{ani,c1}} & N_{zz}^{\text{ani,c1}} \end{bmatrix}_{\text{xyz}} + \begin{bmatrix} N_{xx}^{\text{ani,c2}} & N_{xy}^{\text{ani,c2}} & N_{xz}^{\text{ani,c2}} \\ N_{yx}^{\text{ani,c2}} & N_{yy}^{\text{ani,c2}} & N_{yz}^{\text{ani,c2}} \\ N_{zx}^{\text{ani,c2}} & N_{zy}^{\text{ani,c2}} & N_{zz}^{\text{ani,c2}} \end{bmatrix}_{\text{xyz}} = \begin{bmatrix} N_{xx}^{\text{ani}} & N_{xy}^{\text{ani}} & N_{xz}^{\text{ani}} \\ N_{yx}^{\text{ani}} & N_{yy}^{\text{ani}} & N_{yz}^{\text{ani}} \\ N_{zx}^{\text{ani}} & N_{zy}^{\text{ani}} & N_{zz}^{\text{ani}} \end{bmatrix}_{\text{xyz}} \tag{C.149}$$

with the matrix elements

$$\begin{aligned} N_{xx}^{\text{ani}} = N_{xx}^{\text{ani,c1}} + N_{xx}^{\text{ani,c2}} &= \frac{2K_{\text{c1}}}{\mu_0 M_{\text{S}}^2} \cdot \left(1 - \frac{3}{4}\sin^2\left(\theta_{001}\right)\cos^2\left(\theta_{001}\right) \cdot \left(7 + \cos\left(4\varphi_{100}\right)\right)\right) \\ &\quad + \frac{2K_{\text{c2}}}{\mu_0 M_{\text{S}}^2} \cdot \sin^2\left(\varphi_{100}\right)\cos^2\left(\varphi_{100}\right) \cdot \left(6\sin^2\left(\theta_{001}\right) - 20\sin^4\left(\theta_{001}\right) + 15\sin^6\left(\theta_{001}\right)\right) \end{aligned} \tag{C.150}$$

$$\begin{aligned} N_{yy}^{\text{ani}} = N_{yy}^{\text{ani,c1}} + N_{yy}^{\text{ani,c2}} &= \frac{2K_{\text{c1}}}{\mu_0 M_{\text{S}}^2} \cdot \left(1 - 6 \cdot \sin^2\left(\varphi_{100}\right)\cos^2\left(\varphi_{100}\right)\sin^2\left(\theta_{001}\right)\right) \\ &\quad + \frac{2K_{\text{c2}}}{\mu_0 M_{\text{S}}^2} \cdot \sin^2\left(\theta_{001}\right)\cos^2\left(\theta_{001}\right) \cdot \left(\frac{3}{4}\cos\left(4\varphi_{100}\right) + \frac{1}{4}\right) \end{aligned} \tag{C.151}$$

$$\begin{aligned} N_{zz}^{\text{ani}} = N_{zz}^{\text{ani,c1}} + N_{zz}^{\text{ani,c2}} &= \frac{2K_{\text{c1}}}{\mu_0 M_{\text{S}}^2} \cdot 4\sin^2\left(\theta_{001}\right) \cdot \left(\sin^2\left(\varphi_{100}\right)\cos^2\left(\varphi_{100}\right)\sin^2\left(\theta_{001}\right) + \cos^2\left(\theta_{001}\right)\right) \\ &\quad + \frac{2K_{\text{c2}}}{\mu_0 M_{\text{S}}^2} \cdot 15 \cdot \sin^2\left(\varphi_{100}\right)\cos^2\left(\varphi_{100}\right)\sin^4\left(\theta_{001}\right)\cos^2\left(\theta_{001}\right) \end{aligned} \tag{C.152}$$

on the diagonal positions and the matrix elements

$$N_{xy}^{\text{ani}} = N_{xy}^{\text{ani,c1}} + N_{xy}^{\text{ani,c2}} = \frac{2K_{\text{c1}}}{\mu_0 M_{\text{S}}^2} \cdot 3 \cdot \sin\left(\varphi_{100}\right) \cos\left(\varphi_{100}\right) \sin^2\left(\theta_{001}\right) \cos\left(\theta_{001}\right) \cdot \left(\cos^2\left(\varphi_{100}\right) - \sin^2\left(\varphi_{100}\right)\right) + \frac{2K_{\text{c2}}}{\mu_0 M_{\text{S}}^2} \cdot \sin\left(\varphi_{100}\right) \cos\left(\varphi_{100}\right) \sin\left(\theta_{001}\right) \cos\left(\theta_{001}\right) \cdot \left(\cos^2\left(\varphi_{100}\right) - \sin^2\left(\varphi_{100}\right)\right) \cdot \left(3 \cdot \sin\left(\theta_{001}\right) \cos^2\left(\theta_{001}\right) - 2 \cdot \sin^3\left(\theta_{001}\right)\right) \tag{C.153}$$

$$N_{xz}^{\text{ani}} = N_{xz}^{\text{ani,c1}} + N_{xz}^{\text{ani,c2}} = \frac{2K_{\text{c1}}}{\mu_0 M_{\text{S}}^2} \cdot \sin\left(\theta_{001}\right) \cos\left(\theta_{001}\right) \cdot \left(-3\cos^2\left(\theta_{001}\right) + \frac{3}{4}\sin^2\left(\theta_{001}\right) \cdot \left(\cos\left(4\varphi_{100}\right) + 3\right)\right) + \frac{2K_{\text{c2}}}{\mu_0 M_{\text{S}}^2} \cdot \sin^2\left(\varphi_{100}\right) \cos^2\left(\varphi_{100}\right) \sin^3\left(\theta_{001}\right) \cos\left(\theta_{001}\right) \cdot \left(\sin^2\left(\theta_{001}\right) + 2 \cdot \left(2\sin^2\left(\theta_{001}\right) - 5\cos^2\left(\theta_{001}\right)\right)\right) \tag{C.154}$$

$$N_{yz}^{\text{ani}} = N_{yz}^{\text{ani,c1}} + N_{yz}^{\text{ani,c2}} = \frac{2K_{\text{c1}}}{\mu_0 M_{\text{S}}^2} \cdot 3 \cdot \sin\left(\varphi_{100}\right) \cos\left(\varphi_{100}\right) \sin^3\left(\theta_{001}\right) \cdot \left(\sin^2\left(\varphi_{100}\right) - \cos^2\left(\varphi_{100}\right)\right) + \frac{2K_{\text{c2}}}{\mu_0 M_{\text{S}}^2} \cdot 5 \cdot \sin\left(\varphi_{100}\right) \cos\left(\varphi_{100}\right) \sin^3\left(\theta_{001}\right) \cos^2\left(\theta_{001}\right) \cdot \left(\sin^2\left(\varphi_{100}\right) - \cos^2\left(\varphi_{100}\right)\right) \tag{C.155}$$

at the off-diagonal positions.

C.4 Uniaxial anisotropy energy (density)

The inclusion of an additional uniaxial anisotropy term can be necessary for structured samples e.g. to account for anisotropy contributions for instance induced by the structuring process (see the discussion around equation 4.26).

The uniaxial anisotropy field given in equation 4.28 reads**

$$\mathbf{H}_{\text{ani,uni}} = \frac{2K_{\text{u1}}}{\mu_0 M_{\text{S}}} m_{\text{a}} \hat{\mathbf{e}}_{\text{a}} + \frac{4K_{\text{u2}}}{\mu_0 M_{\text{S}}} m_{\text{a}}^3 \hat{\mathbf{e}}_{\text{a}} + \ldots \tag{C.156}$$

and like the cubic anisotropy field can be expressed as a function of the projection m_{a} of the normalised vector field $\mathbf{m}(\mathbf{r}, t) = \frac{\mathbf{M}_0(\mathbf{r})}{M_{\text{S}}} + \delta\mathbf{m}(\mathbf{r}, t)$ on the ainsotropy symmetry axis a.

Contrary to the cubic anisotropy, this uniaxial anisotropy is easily defined in the global coordinate system uvw by attributing a set of polar and azimuthal angles to the alignment of the uniaxial anisotropy axis. The anisotropy field can be rewritten as

$$\mathbf{H}_{\text{ani,uni}} = \frac{2K_{\text{u1}}}{\mu_0 M_{\text{S}}} \hat{P}_{\text{ani}}^{\text{uni}} \cdot \mathbf{m} + \frac{4K_{\text{u2}}}{\mu_0 M_{\text{S}}} \left(\hat{P}_{\text{ani}}^{\text{uni}} \cdot \mathbf{m}\right)^3 + \ldots \tag{C.157}$$

with the projection matrix

$$\hat{P}_{\text{ani}}^{\text{uni}} = \begin{bmatrix} \sin^2\theta_{\text{a}} \cos^2\varphi_{\text{a}} & \frac{\sin^2 2\theta_{\text{a}}}{2} \cos^2\varphi_{\text{a}} & \sin^2\theta_{\text{a}} \frac{\sin^2 2\varphi_{\text{a}}}{2} \\ \frac{\sin^2 2\theta_{\text{a}}}{2} \cos^2\varphi_{\text{a}} & \cos^2\theta_{\text{a}} & \frac{\sin^2 2\theta_{\text{a}}}{2} \sin^2\varphi_{\text{a}} \\ \sin^2\theta_{\text{a}} \frac{\sin^2 2\varphi_{\text{a}}}{2} & \frac{\sin^2 2\theta_{\text{a}}}{2} \sin^2\varphi_{\text{a}} & \sin^2\theta_{\text{a}} \sin^2\varphi_{\text{a}} \end{bmatrix}_{uvw} \tag{C.158}$$

** Note that the notation of the uniaxial anisotropy axis has been changed compared to equation 4.28: Here, the anisotropy axis is denoted by the indices a (was u before) in order to avoid confusion with the global coordinate system uvw.

obtained by the external tensor product of the anisotropy symmetry axis $\hat{\mathbf{e}}_\mathrm{a}$, which is defined by the polar angle θ_a towards the axis v and the azimuthal angle φ_a towards the propagation direction u. As before, the static and dynamic parts of the anisotropy field can be obtained by using $\mathbf{m}(\mathbf{r},t) = \mathbf{m}_0(\mathbf{r}) + \delta\mathbf{m}(\mathbf{r},t)$ and keeping only the first order terms in $\delta\mathbf{m}(\mathbf{r},t)$, which results in

$$\mathbf{H}^\mathrm{static}_\mathrm{ani,uni} = \frac{2K_\mathrm{u1}}{\mu_0 M_\mathrm{S}} \hat{P}^\mathrm{uni}_\mathrm{ani} \cdot \mathbf{m}_0 + \frac{4K_\mathrm{u2}}{\mu_0 M_\mathrm{S}} \left(\hat{P}^\mathrm{uni}_\mathrm{ani} \cdot \mathbf{m}_0\right)^3 \tag{C.159}$$

for the static part and

$$\delta\mathbf{h}_\mathrm{ani,uni} = \frac{2K_\mathrm{u1}}{\mu_0 M_\mathrm{S}} \hat{P}^\mathrm{uni}_\mathrm{ani} \cdot \delta\mathbf{m} + \frac{12K_\mathrm{u2}}{\mu_0 M_\mathrm{S}} \left(\hat{P}^\mathrm{uni}_\mathrm{ani} \cdot \mathbf{m}_0\right)^2 \cdot \hat{P}^\mathrm{uni}_\mathrm{ani} \cdot \delta\mathbf{m} \tag{C.160}$$

$$=: -\left(\hat{N}^\mathrm{u1}_\mathrm{ani} + \hat{N}^\mathrm{u2}_\mathrm{ani}\right) \cdot M_\mathrm{S}\delta\mathbf{m} =: -\hat{N}^\mathrm{uni}_\mathrm{ani} \cdot M_\mathrm{S}\delta\mathbf{m} \tag{C.161}$$

for the dynamic part with the anisotropy tensor

$$\hat{N}^\mathrm{uni}_\mathrm{ani} = -\frac{2K_\mathrm{u1}}{\mu_0 M_\mathrm{S}^2} \hat{P}^\mathrm{uni}_\mathrm{ani} - \frac{12K_\mathrm{u2}}{\mu_0 M_\mathrm{S}^2} \left(\hat{P}^\mathrm{uni}_\mathrm{ani} \cdot \mathbf{m}_0\right)^2 \cdot \hat{P}^\mathrm{uni}_\mathrm{ani} \tag{C.162}$$

defined by the projection matrix $\hat{P}^\mathrm{uni}_\mathrm{ani}$.

For a unaxial anisotropy term induced by the structuring process to fabricate a waveguide for instance, the anisotropy symmetry axis is most likely to coincide with the long axis of the structure along which a translation invariance is given. In this case[††], $\theta_\mathrm{a} = 90°$ and $\varphi_\mathrm{a} = 0°$, which simplifies the anisotropy tensor to

$$\hat{N}^\mathrm{uni}_\mathrm{ani} = -\frac{2K_\mathrm{u1}}{\mu_0 M_\mathrm{S}^2} \begin{bmatrix} 1 & 0 & 0 \\ 0 & 0 & 0 \\ 0 & 0 & 0 \end{bmatrix}_{uvw} - \frac{12K_\mathrm{u2}}{\mu_0 M_\mathrm{S}^2} \begin{bmatrix} \sin^2\theta_0 \sin^2\varphi_0 & 0 & 0 \\ 0 & 0 & 0 \\ 0 & 0 & 0 \end{bmatrix}_{uvw} \tag{C.163}$$

with the polar and azimuthal angles θ_0 and φ_0 defining the equilibrium position of the magnetisation[‡‡] as indicated in figure 8.3.

[††] Assuming the spin waves propagate in the film plane along the long axis of the waveguide, which is per se the core idea of a waveguide.

[‡‡] For $\mathbf{M}_0 \perp \hat{\mathbf{e}}_u$ these are $\theta_0 = 90°$ and $\varphi_0 = 0°$, and thus the second order uniaxial anisotropy yields no contribution when the equilibrium position and the anisotropy symmetry axis coincide.

D

Kalinikos-Slavin dispersion formula and FMR

D.1 Recalling the Kalinikos-Slavin dispersion (approximative analytical formula)

The Kalinikos-Slavin dispersion relation for in-plane propagating spin waves in an anisotropic thin film is given by [379]

$$\omega_n^2 = (\omega_\mathrm{H} + \omega_\mathrm{exch}) \cdot \left(\omega_\mathrm{H} + \omega_\mathrm{exch} + \omega_\mathrm{M}\left(F_{nn} + F_{nn}^\mathrm{ani}\right)\right) \tag{D.1}$$

with the dipolar matrix elements* F_{nn} defined as

$$\begin{aligned} F_{nn} = {} & \sin^2\theta_0 - P_{nn}\sin^2\theta_0\cos^2\phi_k \\ & + P_{nn}\left(\cos^2\theta_0 + \frac{\omega_\mathrm{M}}{\omega_\mathrm{H}+\omega_\mathrm{exch}}\left(1-P_{nn}\right)\sin^2\phi_k\sin^2\theta_0\right) \end{aligned} \tag{D.2}$$

and incorporating the anisotropy energy in

$$\begin{aligned} F_{nn}^\mathrm{ani} = {} & N_{xx}^\mathrm{ani} + N_{yy}^\mathrm{ani} + \frac{\omega_\mathrm{M}}{\omega_\mathrm{H}+\omega_\mathrm{exch}} \cdot \left(N_{xx}^\mathrm{ani}N_{yy}^\mathrm{ani} + N_{yy}^\mathrm{ani}\sin^2\theta_0 - \left(N_{xy}^\mathrm{ani}\right)^2\right) \\ & + P_{nn} \cdot \frac{\omega_\mathrm{M}}{\omega_\mathrm{H}+\omega_\mathrm{exch}} \cdot \left(N_{yy}^\mathrm{ani}\left(\cos^2\phi_k - \sin^2\theta_0\left(1+\cos^2\phi_k\right)\right)\right. \\ & \left. + N_{xx}^\mathrm{ani}\sin^2\phi_k - N_{xy}^\mathrm{ani}\cos\theta_0\sin 2\phi_k\right) \end{aligned} \tag{D.3}$$

both depending on the matrix elements P_{nn} which simplify to†

$$P_{00}\left(k_\mathrm{ip}\right) = 1 - \frac{1-\exp\left(-k_\mathrm{ip}\cdot d\right)}{k_\mathrm{ip}\cdot d} \tag{D.4}$$

for the lowest order mode with mode number $n = 0$ and $k_\mathrm{ip}\cdot d \lesssim 1$. The gyrotropic frequencies $\omega_\mathrm{M} = \gamma M_\mathrm{S}$ and $\omega_\mathrm{H} = \gamma H_\mathrm{ext}$ are used as abbreviations to incorporate the saturation magnetisation and the external magnetic field respectively. Analogously, $\omega_\mathrm{exch} = \gamma H_\mathrm{exch} = \lambda_\mathrm{exch}^2 k_{n,\mathrm{tot}}^2$ is used to include the exchange interaction, where the total wave vector for the mode number n

$$k_{n,\mathrm{tot}}^2 = k_\mathrm{ip}^2 + k_n^2 \quad \text{with} \quad k_n = \frac{n\cdot\pi}{d} \tag{D.5}$$

is defined by its in-plane component k_ip and its quantised component along the film normal k_n with the film thickness d, as introduced on page 79 in the section on perpendicular standing spin waves (PSSWs) in chapter 4.

* It seems like there are not enough letters in this alphabet to avoid absolutely all possible confusions in this thesis. F was chosen in chapter 4 as a mathematical symbol for the free energy, with the free energy density terms denoted as f, in order to avoid confusion with the permittivity ϵ or ε in the magneto-optical part of this work. Now, to facilitate comparison with the Kalinikos-Slavin publications [378, 379], the original formulation with terms F_{nn} is preferred for the dispersion relation. It is important to note, that the F_{nn} must not be confused with a free energy term of the system. Here, the indices n denote the mode numbers and will never denote angles (as introduced for the angular derivations $f_{\theta\varphi}$ before). It is therefore assumed that the distinction between the F_{nn} terms and the free energy terms F is uncomplicated and reasonable in this context.

† A detailed description of the rather complicated expressions for the higher order P_{nn} is given in the appendix of [378] for pinned, unpinned and mixed boundary conditions at the film interfaces.

D.2 The case of the FMR: $n = 0$ and $k_{\mathrm{ip}} \to 0$.

Then

$$P_{00}\left(k_{\mathrm{ip}} \to 0\right) = 0 \tag{D.6}$$

and

$$F_{00} = \sin^2 \theta_0 \tag{D.7}$$

and

$$F_{00}^{\mathrm{ani}} = N_{xx}^{\mathrm{ani}} + N_{yy}^{\mathrm{ani}} + \frac{\omega_{\mathrm{M}}}{\omega_{\mathrm{H}} + \omega_{\mathrm{exch}}} \cdot \left(N_{xx}^{\mathrm{ani}} N_{yy}^{\mathrm{ani}} + N_{yy}^{\mathrm{ani}} \sin^2 \theta_0 - \left(N_{xy}^{\mathrm{ani}} \right)^2 \right) \tag{D.8}$$

for the terms listed above.

In-plane FMR: $\theta_0 = 90°$.

Then

$$F_{00} = 1 \tag{D.9}$$

and

$$F_{00}^{\mathrm{ani}} = N_{xx}^{\mathrm{ani}} + N_{yy}^{\mathrm{ani}} + \frac{\omega_{\mathrm{M}}}{\omega_{\mathrm{H}} + \omega_{\mathrm{exch}}} \cdot \left(N_{xx}^{\mathrm{ani}} N_{yy}^{\mathrm{ani}} + N_{yy}^{\mathrm{ani}} - \left(N_{xy}^{\mathrm{ani}} \right)^2 \right) \tag{D.10}$$

for the terms listed above.

This simplifies the Kalinikos-Slavin formula from equation D.1 to

$$\omega_{\mathrm{IP-FMR}}^2 = (\omega_{\mathrm{H}} + \omega_{\mathrm{exch}}) \cdot \left(\omega_{\mathrm{H}} + \omega_{\mathrm{exch}} + \omega_{\mathrm{M}} \left(1 + N_{xx}^{\mathrm{ani}} + N_{yy}^{\mathrm{ani}} \right) + \frac{\omega_{\mathrm{M}}^2}{\omega_{\mathrm{H}} + \omega_{\mathrm{exch}}} \left(N_{xx}^{\mathrm{ani}} N_{yy}^{\mathrm{ani}} + N_{yy}^{\mathrm{ani}} - \left(N_{xy}^{\mathrm{ani}} \right)^2 \right) \right) \tag{D.11}$$

for the FMR in the in-plane magnetised thin film.

Negligible anisotropy

For negligible anisotropy ($F_{00}^{\mathrm{ani}} = 0$), the Kalinikos-Slavin formula from equation D.11 transforms to

$$\omega_{\mathrm{IP-FMR}}^2 = (\omega_{\mathrm{H}} + \omega_{\mathrm{exch}}) \cdot (\omega_{\mathrm{H}} + \omega_{\mathrm{exch}} + \omega_{\mathrm{M}}) \tag{D.12}$$

which corresponds to the Kittel equation

$$\omega_{\mathrm{FMR}} = \sqrt{(\omega_{\mathrm{H}} + \omega_{\mathrm{exch}}) \cdot (\omega_{\mathrm{H}} + \omega_{\mathrm{exch}} + \omega_{\mathrm{M}})} \tag{D.13}$$

as introduced in section 4.2.

Non-negligible anisotropy

For a non-negligible anisotropy, the anisotropy tensor elements N_{xx}^{ani}, N_{xy}^{ani} and N_{yy}^{ani} defined in the local coordinate system need to be considered.

In many descriptions, the anisotropy is often incorporated in the FMR formula (Kittel equation) by an anisotropy contribution aligned with the demagnetisation field, and an anisotropy contribution perpendicular to that, resulting in the factorised formula

$$\omega_{\mathrm{IP-FMR}}^2 = \left(\omega_{\mathrm{H}} + \omega_{\mathrm{exch}} + \omega_{\mathrm{ani},y}\right) \cdot \left(\omega_{\mathrm{H}} + \omega_{\mathrm{exch}} + \omega_{\mathrm{M}} + \omega_{\mathrm{ani},x}\right) \tag{D.14}$$

with $\omega_{\mathrm{ani},x} = -\gamma \mu_0 H_{\mathrm{ani},x}$ and $\omega_{\mathrm{ani},y} = \gamma \mu_0 H_{\mathrm{ani},y}$ for the two anisotropy contributions analogous to $\omega_{\mathrm{M}} = -\gamma \mu_0 H_{\mathrm{demag}}$ for the demagnetisation term.

This factorisation of the equation D.11 into field contributions in x and y directions is always possible by deriving the roots of equation D.11 for instance with the p-q formula for quadratic equations:

$$\omega^2_{\mathrm{IP-FMR}} = (\omega_\mathrm{H} + \omega_\mathrm{exch}) \cdot \left(\omega_\mathrm{H} + \omega_\mathrm{exch} + \omega_\mathrm{M} \left(1 + N^\mathrm{ani}_{xx} + N^\mathrm{ani}_{yy}\right) + \frac{\omega^2_\mathrm{M}}{\omega_\mathrm{H} + \omega_\mathrm{exch}} \left(N^\mathrm{ani}_{xx} N^\mathrm{ani}_{yy} + N^\mathrm{ani}_{yy} - \left(N^\mathrm{ani}_{xy}\right)^2 \right) \right) \tag{D.15}$$

$$= (\omega_\mathrm{H} + \omega_\mathrm{exch})^2 + (\omega_\mathrm{H} + \omega_\mathrm{exch}) \cdot \omega_\mathrm{M} \left(1 + N^\mathrm{ani}_{xx} + N^\mathrm{ani}_{yy}\right) + \omega^2_\mathrm{M} \left(N^\mathrm{ani}_{xx} N^\mathrm{ani}_{yy} + N^\mathrm{ani}_{yy} - \left(N^\mathrm{ani}_{xy}\right)^2 \right) \tag{D.16}$$

$$=: \circ^2 + \circ \cdot p + q \tag{D.17}$$

$$= (\circ - \circ_1) \cdot (\circ - \circ_2) \tag{D.18}$$

with $\circ = (\omega_\mathrm{H} + \omega_\mathrm{exch})$ and $p = \omega_\mathrm{M} \left(1 + N^\mathrm{ani}_{xx} + N^\mathrm{ani}_{yy}\right)$ and $q = \omega^2_\mathrm{M} \left(N^\mathrm{ani}_{xx} N^\mathrm{ani}_{yy} + N^\mathrm{ani}_{yy} - \left(N^\mathrm{ani}_{xy}\right)^2 \right)$ with the roots

$$\circ_{1/2} = -\frac{p}{2} \pm \sqrt{\frac{p^2}{4} - q} \tag{D.19}$$

$$= -\frac{\omega_\mathrm{M} \left(1 + N^\mathrm{ani}_{xx} + N^\mathrm{ani}_{yy}\right)}{2} \pm \sqrt{\frac{\omega^2_\mathrm{M} \left(1 + N^\mathrm{ani}_{xx} + N^\mathrm{ani}_{yy}\right)^2}{4} - \omega^2_\mathrm{M} \left(N^\mathrm{ani}_{xx} N^\mathrm{ani}_{yy} + N^\mathrm{ani}_{yy} - \left(N^\mathrm{ani}_{xy}\right)^2 \right)} \tag{D.20}$$

$$= -\frac{\omega_\mathrm{M}}{2} \left(1 + N^\mathrm{ani}_{xx} + N^\mathrm{ani}_{yy}\right) \pm \frac{\omega_\mathrm{M}}{2} \sqrt{\left(1 + N^\mathrm{ani}_{xx} - N^\mathrm{ani}_{yy}\right)^2 + 4 \left(N^\mathrm{ani}_{xy}\right)^2} \quad . \tag{D.21}$$

For $N^\mathrm{ani}_{xy} = 0$ the problem simplifies to

$$\circ_1 = -\omega_\mathrm{M} N^\mathrm{ani}_{yy} \quad \text{and} \quad \circ_2 = -\omega_\mathrm{M} - \omega_\mathrm{M} N^\mathrm{ani}_{xx} \quad . \tag{D.22}$$

which hence result in

$$\omega^2_{\mathrm{IP-FMR}} = (\omega_\mathrm{H} + \omega_\mathrm{exch} - \circ_1) \cdot (\omega_\mathrm{H} + \omega_\mathrm{exch} - \circ_2) \tag{D.23}$$

$$= \left(\omega_\mathrm{H} + \omega_\mathrm{exch} + \omega_\mathrm{M} N^\mathrm{ani}_{yy}\right) \cdot \left(\omega_\mathrm{H} + \omega_\mathrm{exch} + \omega_\mathrm{M} + \omega_\mathrm{M} N^\mathrm{ani}_{xx}\right) \tag{D.24}$$

for the FMR formula in this case and the anisotropy field components in $\omega_{\mathrm{ani},x} = -\gamma \mu_0 H_{\mathrm{ani},x}$ and $\omega_{\mathrm{ani},y} = \gamma \mu_0 H_{\mathrm{ani},y}$ can be easily identified as unmixed functions of the respective anisotropy tensor element N^ani_{xx} or N^ani_{yy} respectively.

For $N^\mathrm{ani}_{xy} \neq 0$, a mixing occurs and the factorisation into two anisotropy fields does not lead to simple functions of only one respective tensor element for each.

From the derivations in section C.3.2 and section C.3.3, it is clear that $N^\mathrm{ani}_{xy} = 0$ is always true for an orientation perpendicular to at least one of the principal crystal axes, i.e. if the magnetisation projection on any principal crystal axis becomes zero - and hence (since this is for the assumption of an in-plane magnetised thin film) the film normal corresponds to an axis with equally at least one of the projections on the principal crystal axes being zero.

This is the case for a film with the film normal $[001]_{123}$, for which in the derivation in section C.3.2 and section C.3.3 the angle θ_{001} is set to $\theta_{001} = \frac{\pi}{2}$ and the anisotropy tensor elements N^ani_{xx}, N^ani_{xy} and N^ani_{yy} simplify to

$$N^\mathrm{ani}_{xx} = \frac{2K_{c1}}{\mu_0 M_\mathrm{S}^2} \cdot \left(1 - \frac{3}{4} \sin^2(\theta_{001}) \cos^2(\theta_{001}) \cdot \left(7 + \cos(4\varphi_{100})\right)\right) + \frac{2K_{c2}}{\mu_0 M_\mathrm{S}^2} \cdot \sin^2(\varphi_{100}) \cos^2(\varphi_{100}) \cdot \left(6 \sin^2(\theta_{001}) - 20 \sin^4(\theta_{001}) + 15 \sin^6(\theta_{001})\right) \tag{D.25}$$

$$\Rightarrow N^\mathrm{ani}_{xx} = \frac{2K_{c1}}{\mu_0 M_\mathrm{S}^2} + \frac{2K_{c2}}{\mu_0 M_\mathrm{S}^2} \cdot \sin^2(\varphi_{100}) \cos^2(\varphi_{100}) \tag{D.26}$$

and

$$N_{xy}^{\text{ani}} = \frac{2K_{\text{c1}}}{\mu_0 M_{\text{S}}^2} \cdot 3 \cdot \sin\left(\varphi_{100}\right) \cos\left(\varphi_{100}\right) \sin^2\left(\theta_{001}\right) \cos\left(\theta_{001}\right) \cdot \left(\cos^2\left(\varphi_{100}\right) - \sin^2\left(\varphi_{100}\right) \right) + \frac{2K_{\text{c2}}}{\mu_0 M_{\text{S}}^2} \cdot \sin\left(\varphi_{100}\right) \cos\left(\varphi_{100}\right) \sin\left(\theta_{001}\right) \cos\left(\theta_{001}\right) \cdot \left(\cos^2\left(\varphi_{100}\right) - \sin^2\left(\varphi_{100}\right) \right) \cdot \left(3 \cdot \sin\left(\theta_{001}\right) \cos^2\left(\theta_{001}\right) - 2 \cdot \sin^3\left(\theta_{001}\right) \right) \tag{D.27}$$

$$\Rightarrow N_{xy}^{\text{ani}} = 0 \tag{D.28}$$

and

$$N_{yy}^{\text{ani}} = \frac{2K_{\text{c1}}}{\mu_0 M_{\text{S}}^2} \cdot \left(1 - 6 \cdot \sin^2\left(\varphi_{100}\right) \cos^2\left(\varphi_{100}\right) \sin^2\left(\theta_{001}\right) \right) + \frac{2K_{\text{c2}}}{\mu_0 M_{\text{S}}^2} \cdot \sin^2\left(\theta_{001}\right) \cos^2\left(\theta_{001}\right) \cdot \left(\frac{3}{4} \cos\left(4\varphi_{100}\right) + \frac{1}{4} \right) \tag{D.29}$$

$$\Rightarrow N_{yy}^{\text{ani}} = \frac{2K_{\text{c1}}}{\mu_0 M_{\text{S}}^2} \cdot \left(1 - 6 \cdot \sin^2\left(\varphi_{100}\right) \cos^2\left(\varphi_{100}\right) \right) \tag{D.30}$$

as summarised in table D.1.

Table D.1: Cubic anisotropy tensor elements N_{xx}, N_{xy} and N_{yy} for the Kalinikos-Slavin dispersion for an in-plane magnetised thin film with the film normal along $[001]_{123}$: (a) for an arbitrary orientation in the film plane defined by the angle φ_{100} to the crystal axis $[100]_{123}$, as well as for two selected equilibrium positions of the magnetisation M_0 in (b) and (c).

	(a) $\mathbf{M}_0$ with φ_{100} to $[100]_{123}$	(b) $\mathbf{M}_0 \parallel [100]$	(c) $\mathbf{M}_0 \parallel [110]$
N_{xx}^{ani}	$\frac{2K_{\text{c1}}}{\mu_0 M_{\text{S}}^2} + \frac{2K_{\text{c2}}}{\mu_0 M_{\text{S}}^2} \cdot \sin^2\left(\varphi_{100}\right) \cos^2\left(\varphi_{100}\right)$	$\frac{2}{\mu_0 M_{\text{S}}^2} \cdot K_{\text{c1}}$	$\frac{2}{\mu_0 M_{\text{S}}^2} \cdot \left(K_{\text{c1}} + \frac{1}{4} K_{\text{c2}} \right)$
N_{xy}^{ani}	0	0	0
N_{yy}^{ani}	$\frac{2K_{\text{c1}}}{\mu_0 M_{\text{S}}^2} \cdot \left(1 - 6 \cdot \sin^2\left(\varphi_{100}\right) \cos^2\left(\varphi_{100}\right) \right)$	$\frac{2}{\mu_0 M_{\text{S}}^2} \cdot K_{\text{c1}}$	$-\frac{2}{\mu_0 M_{\text{S}}^2} \cdot \frac{1}{2} K_{\text{c1}}$

E

FMR data evaluation comparison

E.1 Test data sets

To compare the different post-processing methods, two sets of data were used both of which correspond to typical S_{21} parameter data from BB-FMR measurements in a non-calibrated VNA setup.

- The first data set will be indicated as *measured data* in the following, as this data set was obtained from BB-FMR measurements using the above detailed setup and measurement technique on a Co_2MnSi thin film sample. The full stack of the sample is shown in figure E.1. A 200 µm thick glass spacer was placed between the sample and the CPW[1].

- The second data set will be labelled *artificial (test) data* as it consists of an artificially constructed data set for test purposes. This data set represents the case of a fictive thin film with similar parameters as the one in the measured data set. To construct this artificial test data set, the (fictive) susceptibility

$$\chi(\omega, H_{\text{ext}}) = \frac{\gamma\mu_0 M_S \left(\gamma\mu_0 H_{\text{ext}} + i\alpha\omega\right)}{(1+\alpha^2)\cdot\left[\omega_{\text{res}}^2 - \omega^2 + i\omega\cdot\Delta\omega_{\text{res}}\right]} \tag{E.1}$$

was calculated for a range of applied field values $H_{\text{ext}} = 1.038\,\text{T}$ to $0\,\text{T}$ in steps of $1\,\text{mT}$ as corresponding to the measurement conditions of the measured data set. The resonance frequency was calculated with the Kittel formula $\omega_{\text{res}} = \gamma\mu_0 \cdot \sqrt{(H_{\text{ext}} + H_{\text{ani}})\cdot(H_{\text{ext}} + H_{\text{ani}} + M_S)}$, introduced in chapter 4, using $M_S = 1.25\,\text{T} \approx 995\,\text{kA/m}$, $H_{\text{ani}} = 0$, $\gamma = 28.75\,\text{GHz/T}$ as obtained from the measured data set. The HWHM[2] of the resonance linewidth is given by $\Delta\omega_{\text{res}} = \alpha\gamma\cdot((H_{\text{ext}} + H_{\text{ani}}) + M_S/2) + \Delta\omega_0$, where $\alpha = 7.5\cdot10^{-4}$ and $\Delta\omega_0 = 45\,\text{MHz}$ were set fixed[3]. This susceptibility was then used for the calculation of the artificial S_{21} spectra

$$S_{21}(\omega, H) = [1 - i\omega\cdot A\cdot\chi(\omega, H)]\cdot S_{21}^{\text{measured data}}(\omega, H_{\text{ext}} = 1.038\,\text{T}) \tag{E.2}$$

where $S_{21}^{\text{measured data}}(\omega, H_{\text{ext}} = 1.038\,\text{T})$ is the measured data spectrum at maximum field[4] providing the frequency dependent background for the whole artificial data set. The coupling factor A was manually adjusted such that similar amplitudes in the resulting data were ensured, yielding $A = 5\times10^{-16}$ as the final value to be used.

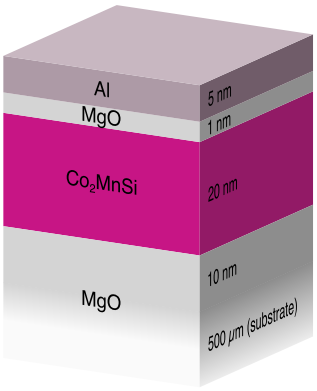

Figure E.1: Schematic of the sample used for measuring the *measured data* set (not to scale).

1: Only because this measurement also served for the test on radiative damping contributions (no indication for radiative damping detected when comparing to the data obtained without glass spacer presented in chapter 6).

2: HWHM = half width half maximum.

3: These parameters were selected since they roughly match the high-frequency behaviour of the measured data set. (Not corresponding to fit results, but only arbitrary set parameters yielding an approximate match.) A different run was performed on another artificial test data set with $\alpha = 5\cdot10^{-4}$ and $\Delta\omega_0 = 50\,\text{MHz}$ yielding analogous results.

4: The detected resonance frequency of the sample in the measured data set is above 44 GHz for fields above 1.035 T. Under the assumption of no other perturbation of magnetic origin at lower frequencies, using the spectrum for the maximum field $\mu_0 H_{\text{ext}} = 1.038\,\text{T}$ as a background reference therefore allows to perform the subsequent analysis on the artificial data set up to frequencies of 44 GHz.

E.2 Background removal approaches

Various data processing approaches were applied to both data sets in order to isolate the signal originating from the magnetic susceptibility of the thin film under investigation from the background signal of non-magnetic origin. As detailed in section 5.2.1, the recorded signal is described by

$$S_{21}(\omega, H_{\text{ext}}) = \frac{V_{\text{meas}}}{V_{\text{in}}} \cdot e^{i\phi} = \frac{V^0_{\text{meas}}(\omega) \cdot [1 - i\omega A \cdot \chi(\omega, H_{\text{ext}})]}{V_{\text{in}}} \cdot e^{i\phi(\omega)} \tag{E.3}$$

for a fixed field H_{ext}. Consequently, all approaches share the common feature of requiring the division by a second S_{21} spectrum[5] in order to remove the frequency dependent phase factor $e^{i\phi(\omega)}$ as well as the background signal $V^0_{\text{meas}}(\omega)/V_{\text{in}}$. The difference mainly lies in the choice of the reference spectrum, i.e. choosing a fixed reference or an equidistant moving reference method.

5: Precisely, the background removal approaches follow the form $(S^A_{xy} - S^B_{xy})/S^C_{xy}$, where often $S^B_{xy} = S^C_{xy}$ is the reference and S^A_{xy} is the spectrum taken at the field of interest (but not always, see the derivative divide procedure on page 101).

E.2.1 Derivative divide

[350]: Maier-Flaig et al. (2018), 'Note: Derivative divide'

Maier-Flaig *et al.* [350] introduced the *derivative divide* background removal method, where the corrected signal is described by

$$\mathrm{d_D}S_{21}(\omega, H) \coloneqq \frac{S_{21}(\omega, H + \Delta H^{\pm}) - S_{21}(\omega, H - \Delta H^{\pm})}{S_{21}(\omega, H) \cdot \Delta H^{\pm}} \tag{E.4}$$

$$\approx -i\omega\tilde{A} \cdot \frac{\mathrm{d}\chi}{\mathrm{d}\omega} \tag{E.5}$$

where $\mathrm{d_D}$ stands for derivative divide and $\Delta H^{\pm}$ is the finite modulation field step width. This method does not require a calibration prior to the measurement, and due to the moving reference procedure[6] is not sensitive to background drifts due to temperature fluctuations.

6: The term *moving reference* refers to the fact that the field difference between all considered spectra is kept constant. Contrary to this, *fixed reference* shall denote the use of a reference taken at a fixed field.
[359]: Weiler et al. (2017), '*Supplemental information:* Helimagnon Resonances in an Intrinsic Chiral Magnonic Crystal'

However, the approximation of $\mathrm{d_D}S_{21}$ as a function of the frequency derivative of the susceptibility function as given in equation E.5 is only true for small field steps, i.e. for $\Delta\omega^{\pm} = \Delta H^{\pm} \cdot \frac{\partial\omega_{\text{res}}}{\partial H_{\text{ext}}} \ll \Delta\omega_{\text{res}}$, otherwise the procedure will induce an over-modulation leading to a distortion of the resonance curves [350] and consequently resulting in an artificial enhancement of the extracted resonance linewidths [359].

To account for this resonance curve distortion in the case of $\Delta\omega^{\pm} \approx \Delta\omega_{\text{res}}$, Maier-Flaig *et al.* [350] suggest fitting a formula

$$\mathrm{d_D}S_{21}(\omega, H) = -i\omega\tilde{A} \cdot \mathrm{CDQ}(\omega, H_{\text{ext}}) \tag{E.6}$$

for a quantitative analysis of the $\mathrm{d_D}S_{21}$ spectra. $\mathrm{CDQ}(\omega, H_{\text{ext}})$ stands for the central difference quotient

$$\mathrm{CDQ}(\omega, H_{\text{ext}}) = \frac{\chi(\omega + \Delta\omega^{\pm}, H_{\text{ext}}) - \chi(\omega - \Delta\omega^{\pm}, H_{\text{ext}})}{2 \cdot \Delta\omega^{\pm}} \tag{E.7}$$

which is used instead of the frequency derivative of the susceptibility

$$\frac{\mathrm{d}\chi}{\mathrm{d}\omega}(\omega, H_{\text{ext}}) = \frac{\gamma\mu_0 M_{\text{S}}\left(2\gamma\mu_0 H_{\text{ext}} \cdot \omega + i\alpha\left(\omega^2_{\text{res}} + \omega^2\right) - i\gamma\mu_0 H_{\text{ext}} \cdot \Delta\omega_{\text{res}}\right)}{(1+\alpha^2) \cdot \left[\omega^2_{\text{res}} - \omega^2 + i\omega \cdot \Delta\omega_{\text{res}}\right]} \tag{E.8}$$

in equation E.5. The qualitative difference between the resulting lineshapes is shown in figure E.2, where the calculated real and imaginary part of the susceptibility $\chi(\omega, H_{\text{ext}})$ from equation E.1, its derivative $\frac{\mathrm{d}\chi}{\mathrm{d}\omega}(\omega, H_{\text{ext}})$, as well

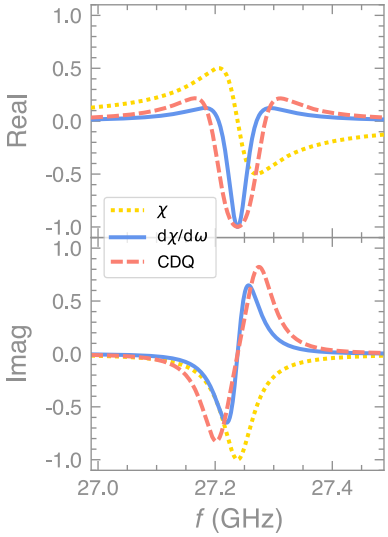

Figure E.2: Calculated real and imaginary part of the normalised susceptibility function χ, its derivative $d\chi/d\omega$ and the central difference quotient CDQ. All curves calculated for the exemplary condition $\mu_0 M_{\text{S}} = 1.25\,\text{T}$, $\gamma = 28.75\,\text{GHz/T}$, $\mu_0 H_{\text{ani}} = 10\,\text{mT}$, $\alpha = 0.001$ and $\Delta\omega_0 = 0$, for an external field $\mu_0 H_{\text{ext}} = 500\,\text{mT}$.

as the central difference quotient CDQ (ω, H_{ext}) are compared. The CDQ line shape resembles the derivative of the susceptibility $\frac{\mathrm{d}\chi}{\mathrm{d}\omega}$, but yields a broader resonance width for the same parameters.

Indeed, the consideration of the resonance curve distortion is of particular importance for samples with large saturation magnetisation and low magnetic damping (and low inhomogeneous linewidth), as is the case of the Co_2Mn-based Heusler compounds used in this work: For Co_2MnSi for instance, the modulation step size $\Delta H^{\pm} = 1\,\text{mT}$ corresponds to a frequency modulation amplitude between approx. 25 MHz and 175 MHz for fields up to 1.04 T applied in the film plane, see figure E.3. Hence, for comparison, both fit functions were applied on the measured data as well as the artificial data in this study.

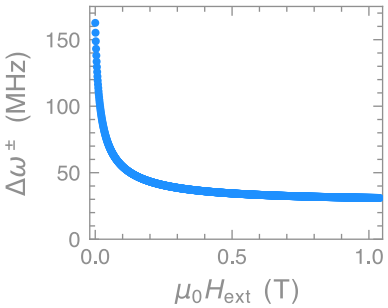

Figure E.3: Frequency modulation amplitude $\Delta\omega^{\pm} = \Delta H^{\pm} \cdot \frac{\partial\omega_{\text{res}}}{\partial H_{\text{ext}}}$ corresponding to the fixed field modulation step size $\Delta H^{\pm} = 1\,\text{mT}$ used in measured data as well as artificial test data. $\Delta\omega^{\pm}$ calculated for a Co_2MnSi sample with $\mu_0 M_S = 1.25\,\text{T}$, $\gamma = 28.75\,\text{GHz/T}$ and $\mu_0 H_{\text{ani}} = 10\,\text{mT}$.

Note: For improved signal-to-noise ratios, the procedure can be modified to

$$\mathrm{d_D}S_{21}(\omega, H_{\text{ext}}) = \frac{\sum_{n=1}^{N} S_{21}(\omega, H_{\text{ext}} + n\cdot\Delta H^{\pm}) - \sum_{n=1}^{N} S_{21}(\omega, H_{\text{ext}} - n\cdot\Delta H^{\pm})}{S_{21}(\omega, H_{\text{ext}}) \cdot \sum_{n=1}^{N} n\cdot\Delta H^{\pm}} \tag{E.9}$$

extending equation E.4 by the sums over N neighbouring spectra. This increases signal modulation and must not be used for extracting the linewidths[7].

E.2.2 Simple off-resonant reference method

Kalarickal *et al.* [351] proposed an analysis method using single S_{21} parameter data based on a transmission line model developed by Barry [353] neglecting microwave reflections and assuming the dominant CPW mode is a transverse electromagnetic (TEM) mode[8]. Bilzer *et al.* [356] apply a similar approach to S_{11} parameter data[9], and both consist of the analysis of an approximate susceptibility function

$$\widetilde{\chi}_{\text{simple}}(\omega, H_{\text{ext}}) = \frac{S_{xy}(\omega, H_{\text{ext}}) - S_{xy}(\omega, H_{\text{ref}})}{S_{xy}(\omega, H_{\text{ref}})} \tag{E.10}$$

where $S_{xy}(\omega, H)$ is the recorded S_{xy} parameter at the field of interest and $S_{xy}(\omega, H_{\text{ref}})$ at the reference field. The difference between both approaches lies in the selection of the reference: While Kalarickal *et al.* [351] use a fixed reference recorded in the same geometry but at off-resonant fields, Bilzer *et al.* [356] propose to use a reference recorded in the perpendicular geometry but at the same field value.

In fact, [351, 355, 356] propose the formula for the logarithm of the S_{xy} parameters, i.e.

$$\widetilde{\chi}^{\text{calib.}}_{\text{simple}}(\omega, H_{\text{ext}}) = \frac{\ln\left[S_{xy}(\omega, H_{\text{ext}})\right] - \ln\left[S_{xy}(\omega, H_{\text{ref}})\right]}{\ln\left[S_{xy}(\omega, H_{\text{ref}})\right]} \tag{E.11}$$

but this form is suitable for data from calibrated FMR measurements only: In that case, the recorded background is little compared to the FMR resonance and the measured signal can be described by an exponential absorption function [355], where the susceptibility is proportional to the absorption coefficient in the exponent and therefore the logarithm is applied. For non-calibrated data where the phase oscillation of the background signal is significant compared to the FMR signal, the description given in equation 5.13[10] is more suitable and hence no logarithm is applied in this case.

The subsequent step typically consists of the fitting of a complex susceptibility function as given in equation 5.10 to the extracted susceptibility data

7: In this work, N was set to $N = 4$ only for the automated peak detection. $N = 1$ was set for the analysis (spectral $\mathrm{d_D}S_{21}$ curve fits) of the fundamental mode, corresponding exactly to equation E.4. $N = 2$ was set for the spectral $\mathrm{d_D}S_{21}$ curve fits of higher order PSSW modes for an increased precision in the resonance position ω_{res} (no linewidth analysis for PSSWs).

[351]: Kalarickal et al. (2006), 'Ferromagnetic resonance linewidth in metallic thin films'

[353]: Barry (1986), 'A Broad-Band, Automated, Stripline Technique for the Simultaneous Measurement of Complex Permittivity and Permeability'

8: Transverse electromagnetic (TEM) modes present neither electric nor magnetic field components in the direction of signal propagation. The fundamental TEM mode is typical for the propagation of electromagnetic waves in coaxial cables and coplanar waveguides [356].

[356]: Bilzer et al. (2008), 'Open-Circuit One-Port Network Analyzer Ferromagnetic Resonance'

9: For full S-matrix data, Bilzer *et al.* [355] propose a sophisticated protocol involving a calibration of the microwave system, reference measurements of the unloaded microwave circuit as well as a reference measurement taken of the loaded circuit at a field perpendicular to the CPW line (i.e. parallel to the x-direction in figure 5.4): By including the recordings of the unloaded microwave circuit, their procedure can account for microwave reflections as well as off-centered sample positioning on the CPW. The reference taken at a perpendicular magnetic field serves to extract the permittivity of the magnetic material.

10: Racalling equation 5.13 here:
$S_{21} = \frac{V^0_{\text{meas}}(\omega)\cdot[1 - i\omega A\cdot\chi(\omega, H_{\text{ext}})]}{V_{\text{in}}} \cdot e^{i\phi(\omega)}$

$\widetilde{\chi}_{\text{simple}}(\omega, H)$ [351]. However, some studies also focus on fitting the real part only [357] or even perform a direct fitting of the S_{21} amplitude [264].

[357]: Kennewell et al. (2010), 'Magnetization pinning at a Py/Co interface measured using broadband inductive magnetometry'

[264]: Kuanr et al. (2005), 'Narrowing of the frequency-linewidth in structured magnetic strips'

In the present study, this simple off-resonant reference division method was used for the comparison with the above detailed derivative divide procedure. To this aim, the background was removed following equation E.10 with an off-resonant moving reference. Subsequently, the susceptibility function given in equation E.1 was fitted to the resulting $\widetilde{\chi}_{\text{simple}}(\omega, H)$ data by fitting real and imaginary curves with shared parameters.

Clearly, the choice of the distance between the moving reference and the spectrum under investigation is crucical: An overlap between the corresponding resonance curves needs to be avoided to ensure a correct description by the fitting function which is of particular relevance for the precise extraction of the resonance linewidth and the linked damping parameter. While this point prinicpally favours a large field distance between the reference and the investigated spectrum, the aforementioned temporal instability of the system favours a reduction of the elapsed time (here translating to the fixed field setting) to minimise parameter changes between the reference spectrum and the spectrum to evaluate.

Therefore, the data analysis following this reference removal procedure was performed with various settings for the constant reference field distance $\Delta H^+ = H_{\text{ref}} - H_{\text{ext}}$, precisely ΔH^+ was varied between 20 mT and 60 mT. This choice was made for the following reason: First, $\Delta H^+ = 20\,\text{mT}$ was set since this reference difference allowed for a sufficient background removal and judged by the resulting spectral curves resulted in a sufficient distance between the corresponding resonance features to allow for a data selection of only the resonance curve in question and hence an automised fitting procedure, as will be presented below. However, the results of this analysis with $\Delta H^+ = 20\,\text{mT}$ could not reproduce the known resonance linewidth set for the artificial data corresponding to the parameters $\alpha = 7.5 \cdot 10^{-4}$ and $\Delta\omega_0 = 45\,\text{MHz}$, and thus the reference field distance was increased[11] in steps of 10 mT until the known fixed parameters could be reproduced by the analysis of the artificial data set. This was achieved for $\Delta H^+ \gtrsim 50\,\text{mT}$, for which the analysis of the artificial data set could reproduce the set parameters. However, as discussed above, the increased reference distance is counterproductive for the background removal, which in this study cannot affect the artificial data set[12] but has significant impact on the measured data set.

11: As will be discussed below, it was concluded that the reference field distance was insufficient and the reference resonance still had an influence on the analysed resonance curve in the fit procedure, albeit yielding a large enough spectral distance of the corresponding resonance curves allowing for a data cut-off of the resonance to be analysed.

12: Because the same frequency dependent background spectrum was set for each spectrum in the artificial data set.

E.2.3 Double off-resonant moving reference method

In order to improve the treatment of data with low signal-to-noise ratios, a modified background removal approach is used in this comparative study in addition to the established data treatment procedures in A and B. This double off-resonant moving reference method is described by

$$\widetilde{\chi}_{\text{double}}(\omega, H_{\text{ext}}) = \frac{S_{xy}(\omega, H_{\text{ext}}) - S_{xy}^{\text{movref}}(\omega, H_{\text{ext}})}{S_{xy}^{\text{fixref}}(\omega, H_{\text{max}})} \tag{E.12}$$

where $S_{xy}^{\text{movref}}(\omega, H_{\text{ext}}) = \frac{1}{2}\left(S_{xy}(\omega, H_{\text{ext}} + \Delta H^{\pm}) + S_{xy}(\omega, H_{\text{ext}} - \Delta H^{\pm})\right)$ is the moving reference constructed from two off-resonant spectra recorded at fields above and below the applied field H_{ext}, and the fixed reference $S_{xy}^{\text{fixref}}(\omega, H_{\text{max}})$ is used for the division to remove the phase oscillation.

Here, the spectrum at $H_{max} = 1.038\,\mathrm{T}$ was taken as the fixed reference for both, the measured data set as well as the artificial test data set. For the moving references with the field distance $\Delta H^{\pm}$ to the spectrum under investigation, the same reflection as detailed above for the case of the simple off-resonant background removal applies: A compromise between a sufficient background suppression favouring a close reference and a sufficient reference distance to avoid an overlap resulting in a distortion of the resonance line shape and hence a falsified extraction of the parameters is desired. Therefore, the same field distances as mentioned above were investigated here, i.e. from $\Delta H^{\pm} = \pm 20\,\mathrm{mT}$ to $\Delta H^{\pm} = \pm 60\,\mathrm{mT}$.

As in the case of the simple off-resonant background removal in B, the susceptibility function given in equation E.1 was fitted to the resulting $\widetilde{\chi}_{\mathrm{double}}(\omega, H_{\mathrm{ext}})$ by fitting the real and imaginary part with shared fit parameters.

E.3 Comparison of results

Figure E.4 presents an overview of the raw S_{21} spectra in the measured data set, of which exemplary spectral curves were shown in figures 5.5 and 5.6. As described above, the significant frequency dependent background does not allow to discern the FMR signal in the raw data.

This subsection will present a detailed discussion of the results obtained from the three data analysis techniques performed on both data sets, for each of which the background removal, the resonance curve fitting and the extracted results will be evaluated.

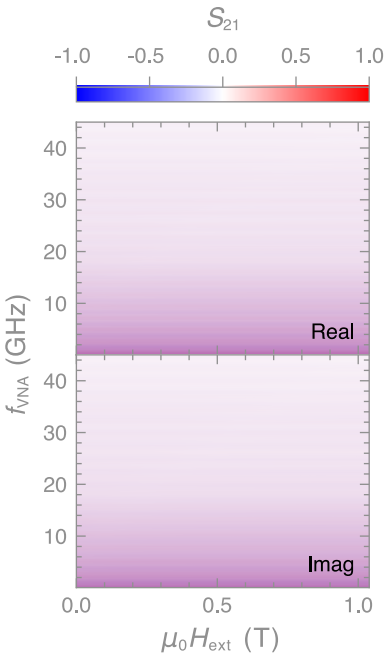

Figure E.4: Raw measured data set for the full field range. An exemplary spectrum of this data was shown in figures 5.5 and 5.6 for a selected field $\mu_0 H_{ext} = 500\,\mathrm{mT}$.

E.3.1 Derivative divide

The results of the derivative divide background removal procedure are presented and discussed in detail in chapter 5, subsection 5.2.2 on page 100 and following.

E.3.2 Simple off-resonant background removal

The simple off-resonant background removal was evaluated for multiple reference distances between $\Delta H^{\mathrm{ref}} = 20\,\mathrm{mT}$ and 60 mT aiming for the best background removal while maintaining a sufficient separation between the respective resonance curves. An overview of the spectra obtained for the minimal distance of $\Delta H^{\mathrm{ref}} = 20\,\mathrm{mT}$ is shown in figure E.5. Typical for the moving reference approach, the corresponding resonance appears in the corrected data as a shadow of the FMR, as indicated in the corresponding exemplary spectral cuts shown in figure E.6 for an external field of $\mu_0 H_{\mathrm{ext}} = 500\,\mathrm{mT}$.

Moreover, the measured data set again shows the broader resonance in the background, overlapping with the narrow FMR resonance curve. Contrary to the background removal by the derivative divide procedure, this background removal approach yields larger emphasis on the broad resonance than on the narrow FMR peaks, as can be seen by comparing the respective spectra in figure E.6 to the ones from the derivative divide procedure in figure 5.9.

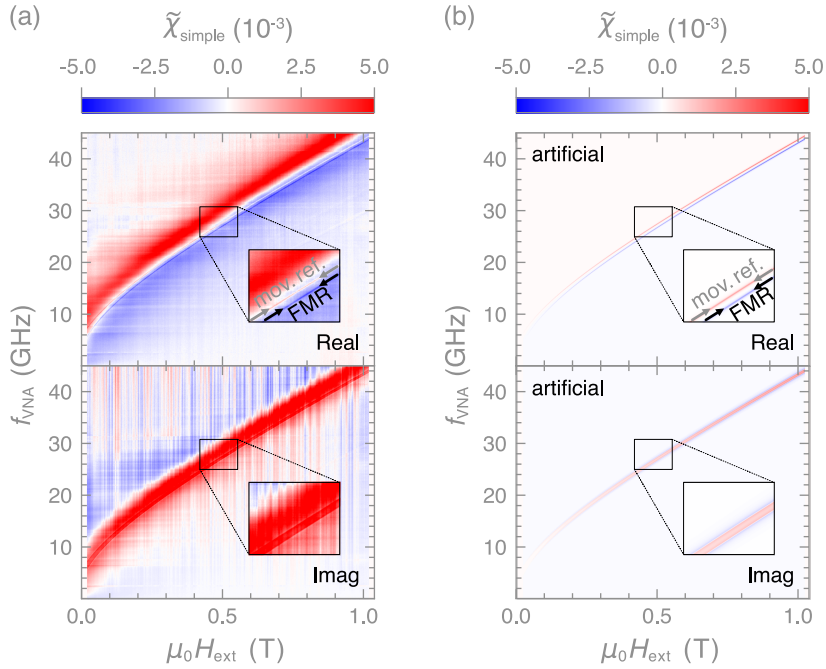

Figure E.5: Full data sets of (a) the measured data and (b) the artificial test data after processing the simple background removal $\widetilde{\chi}_{\mathrm{simple}}$ on the S_{21} parameter with a moving reference at a fixed distance $\Delta H^{\mathrm{ref}} = 20\,\mathrm{mT}$.

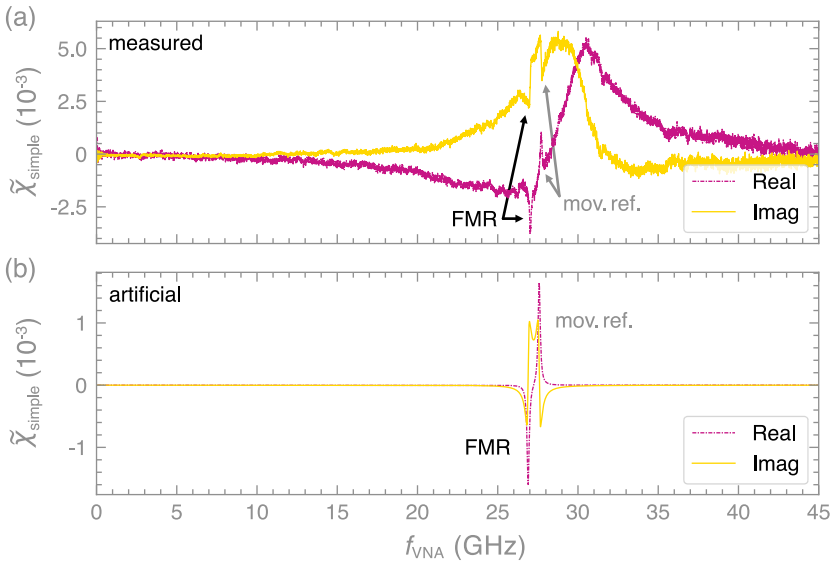

Figure E.6: Exemplary spectra for $\Delta H^{\mathrm{ref}} = 20\,\mathrm{mT}$ of (a) the measured data and (b) the artificial test data at $\mu_0 H_{\mathrm{ext}} = 500\,\mathrm{mT}$. The phase oscillation and a significant part of the frequency dependent background present in the corresponding spectra of the raw data, see figures 5.5 and 5.6 on page 99, is removed. As in the derivative divide spectra, a background signal of a broad resonance remains in the measured data set, while the background in the artificial test data set is fully removed. Compared to the derivative divide procedure, this background removal approach yields lower signal to noise ratios on the measured data.

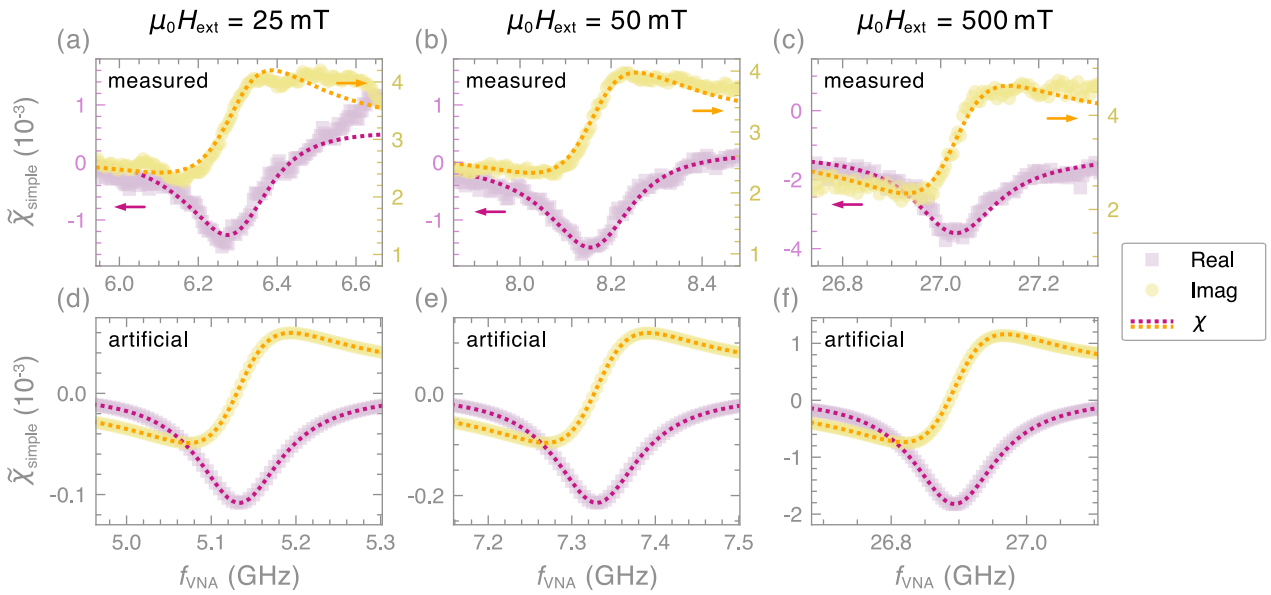

Figure E.7: Zoom-in on data cut-outs around the FMR and exemplary fits of selected resonance curves in the measured as well as the artificial data set for selected fields of $\mu_0 H_{ext}$ = 25 mT, 50 mT and 500 mT and for the minimal reference distance of ΔH^{ref} = 20 mT. Note that the y-axes for the measured data in (a)-(c) are split for real and imaginary part.

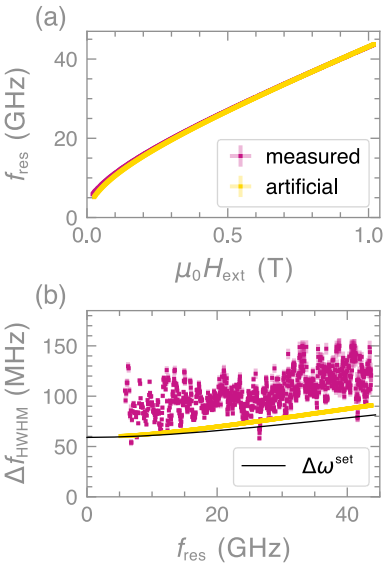

Figure E.8: Results obtained from the simple background removal procedure with $\Delta H^{ref} = 20\,\mathrm{mT}$ for the measured data as well as the artificial data. In (b) the artificially set linewidth is shown in grey in addition to the extracted linewidths from the measured and artificial test data sets.

Indeed, comparably poor signal-to-noise ratios are obtained for the measured data set. As the overlapping broad background resonance is of large amplitude compared to the FMR signal, a nonlinear background is obtained around the FMR resonance. This not only yields varying offsets between real and imaginary data, as can be seen in the zoom-ins in figure E.7 (a)-(c), but also a frequency-dependent background on each part yielding a mismatch between data and fit curves, see for instance in figure E.7 (a). No issues are observed on the artificial data set, as expected from the construction described above.

The extraction of the resonance frequencies shows again to be fairly unaffected by the significant background: Little difference is obtained in figure E.8 (a), comparing the resonance frequency results from the measured data set with significant background and the ideal case of the artificial data set, where the background is fully removed. The slight difference observed towards low magnetic fields is most likely due to a slight mismatch between the real parameters and the parameters assumed for constructing the resonance of the artificial data set, i.e. the saturation magnetisation, the gyromagnetic ratio and the anisotropy field. Indeed, the anisotropy field was set to $H_{ani} = 0$, but the sample presents a non-negligible cubic anisotropy contribution as will be shown in chapter 6.

The extracted resonance linewidths on the other hand are significantly influenced: While no unexpected qualitative behaviour is observed in figure E.8 (b), the noise on the linewidths from the measured data is substantially larger than the noise in the results from the derivative divide procedure shown on the same scale in figure 5.12 (c).

Additionally, when comparing the linewidth extracted from the artificial data set (yellow data points in figure E.8 (b)) to the set linewidth with which the artificial data set was constructed, a clear mismatch is found for increasing resonance frequencies. Consequently, a wrong damping parameter would be extracted from the data treatment as presented in figure E.8 (b). As mentioned above, this discrepancy is linked to the reference field distance and the construction of the artificial data set allowed for an investigation of the effect as a function of the reference field distance ΔH^{ref}.

However, with increasing distance between the reference and the spectrum of interest, the background removal on the real data was found to become

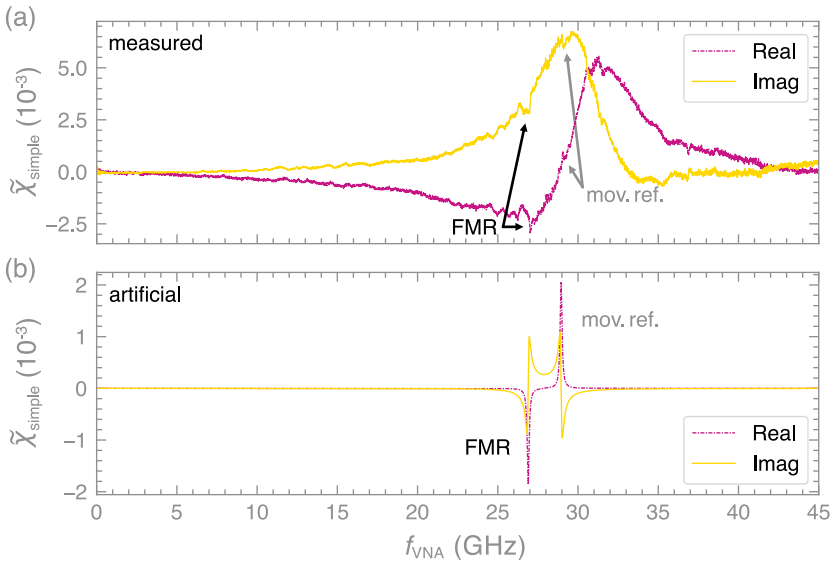

Figure E.9: Exemplary spectra for the maximal reference distance $\Delta H^{ref} = 60\,\mathrm{mT}$ of (a) the measured data and (b) the artificial test data at $\mu_0 H_{ext} = 500\,\mathrm{mT}$. The increased field distance yields a larger separation between the respective resonance curves, as desired. Yet, the increased field distance yields a poor background removal for the measured data set, where the resonance feature is nearly lost in the background/noise.

increasingly poor, as can be seen in the exemplary spectra at $\mu_0 H_{\text{ext}} = 500\,\text{mT}$ shown in figure E.9 for the maximal reference distance of $\Delta H^{\text{ref}} = 60\,\text{mT}$.

In fact, for $\Delta H^{\text{ref}} = 60\,\text{mT}$, the background governs the spectra of the measured data and the FMR resonance features are in the range of the noise, as indicated in figure E.9 (a). The analysis of the artificial data, however, allows to prove the point made above on the importance of the spectral separation of the two resonance curves: Clearly a larger separation is obtained in figure E.9 (b) for the increased reference distance of $\Delta H^{\text{ref}} \geq 60\,\text{mT}$, which indeed allowed to reproduce exactly the artificially set resonance linewidth corresponding to the construction based on the fixed inhomogeneous linewidth and damping parameter, as is shown in figure E.10.

In conclusion, for the simple off-resonant background removal method it was impossible to find a satisfying compromise between a sufficient background removal on the measured data set and the precise reproduction of the constructed linewidth parameters from the artificial data set. While the method might yield improved results for better signal-to-noise ratios, the method is found to be unsuitable for the FMR resonance linewidth analysis of the uncalibrated FMR data in this work.

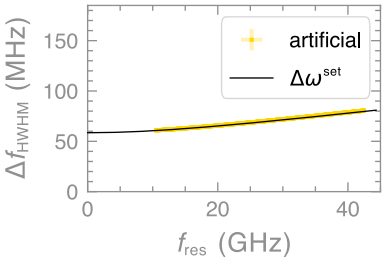

Figure E.10: Results obtained from the simple background removal procedure with $\Delta H^{\text{ref}} = 60\,\text{mT}$ for the artificial data only (since the background removal on the measured data was too poor for a proper fitting). For this reference distance, the artificially set linewidth is exactly reproduced by the fitting of the artificial data set.

E.3.3 Double off-resonant background removal

Consequently, the double off-resonant background removal was introduced aiming at combining the superior signal-to-noise ratio achieved by derivative divide with an off-resonant reference approach in order to avoid the issues on the resonance linewidths in the non-linear frequency range.

Two moving references are used in this procedure, which were chosen with the same field distances as investigated in the simple off-resonant background removal approach in order to ensure comparability with respect to potential time/field-related drifts. The post-processing results for the minimal distance $\Delta H^{\text{ref}} = \pm 20\,\text{mT}$ from the measured as well as the artificial data set are shown in figure E.11. Analogously to the simple reference removal, two shadowing references are now observed on both data sets, as pointed out in the respective insets, which correspond to the FMR of the two moving reference spectra. Moreover, the suppression of the broad background resonance is improved compared to the simple background approach, which is even more apparent in the exemplary spectra shown in figure E.12 for an external field of $\mu_0 H_{\text{ext}} = 500\,\text{mT}$.

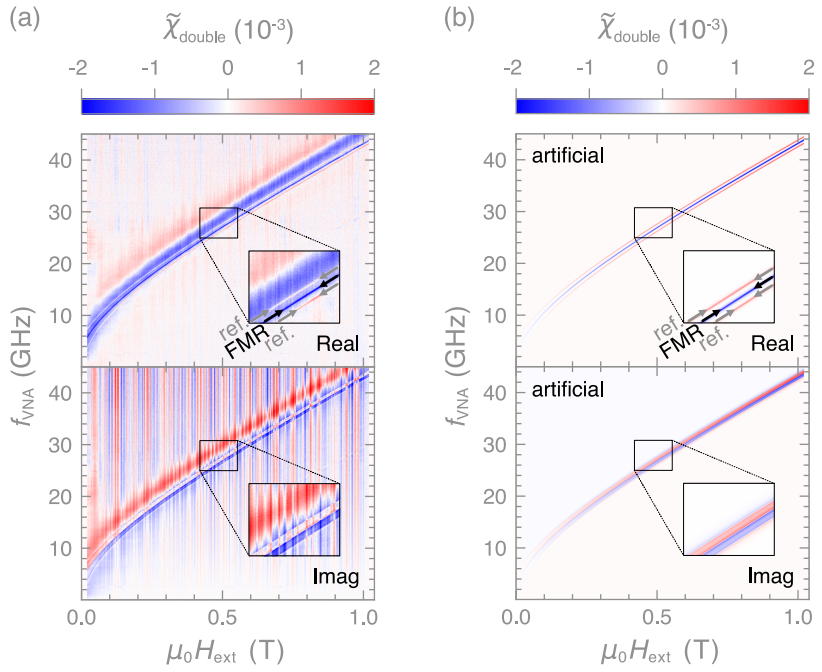

Figure E.11: Full data sets of (a) the measured data and (b) the artificial test data after processing the double moving reference background removal $\widetilde{\chi}_{\mathrm{double}}$ on the S_{21} parameter with two moving references taken at a fixed field distance $\Delta H^{\mathrm{ref}} = \pm 20\,\mathrm{mT}$.

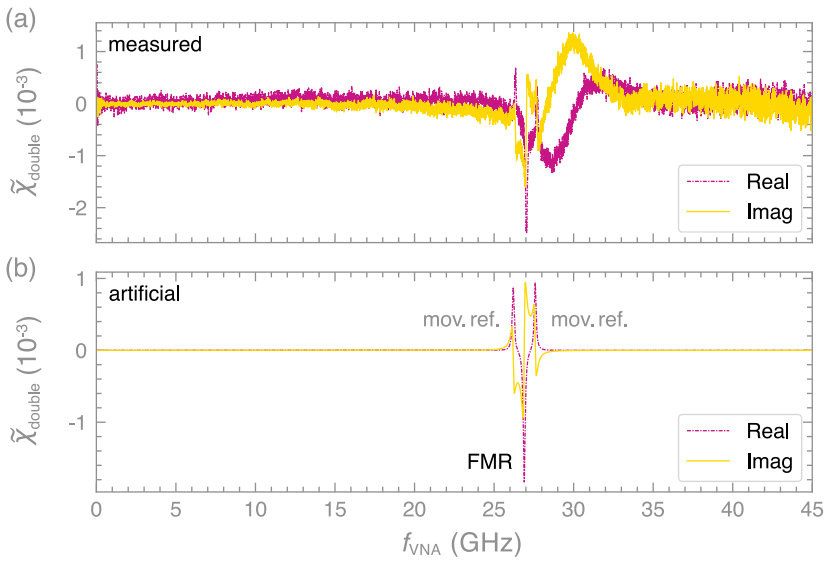

Figure E.12: Exemplary spectra at $\mu_0 H_{\mathrm{ext}} = 500\,\mathrm{mT}$ of (a) the measured data and (b) the artificial test data for the minimal reference distance $\Delta H^{\mathrm{ref}} = \pm 20\,\mathrm{mT}$. As in the derivative divide spectra, a background signal of a broad resonance remains in the measured data set, while the background in the artificial test data set is fully removed. Similar to the results obtained using derivative divide, this background removal approach yields improved signal to noise ratios compared to the simple moving reference approach in B. Yet, countrary to derivative divide, the reference spectra used in this approach are off-resonant, i.e. the resonance does not overlap with the resonance under investigation.

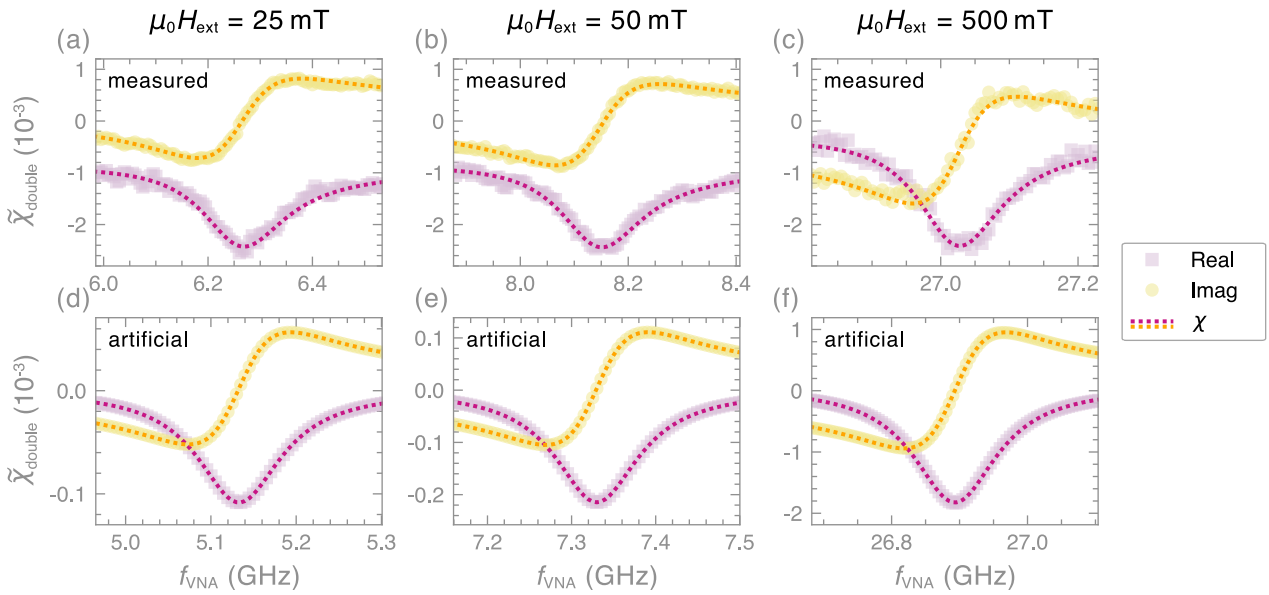

Figure E.13: Zoom-in on data cut-outs around the FMR and exemplary fits of selected resonance curves in the measured as well as the artificial data set for selected fields of $\mu_0 H_{ext}$ = 25 mT, 50 mT and 500 mT and for the minimal reference distance ΔH^{ref} = ±20 mT. Note that the y-axes for the measured data in (a)-(c) are again shared for real and imaginary part as opposed to figure E.7.

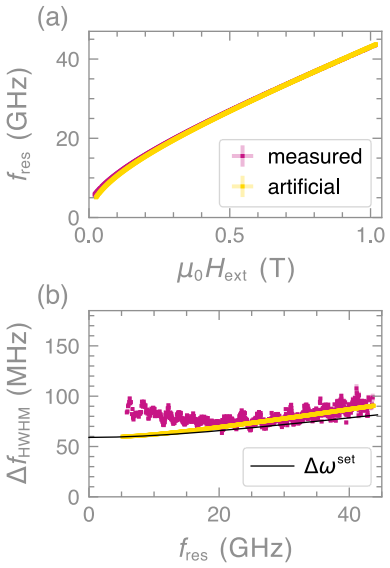

Figure E.14: Results obtained from the double moving reference background removal procedure for the measured data as well as the artificial data for the minimal reference distance $\Delta H^{ref} = \pm 20\,\mathrm{mT}$. In (b) the artificially set linewidth is shown in addition to the extracted linewidths from the measured and artificial test data sets.

Again, the broad resonance in the background is not suppressed as well as by the derivative divide procedure, but much improved signal to noise ratios are achieved compared to the simple off-resonant background removal approach. This is partly due to the double weight of the spectrum of interest in order to account for the double reference removal, see equation E.12, which results in the amplitude of the FMR appearing in general approximately twice as large as the amplitudes of the moving references, as best seen in the post-processing spectra of the artificial data in figure E.12 (b).

Additionally, while the FMR peak (dip) does overlap with the broad resonance in the background, it is generally positioned at slightly lower frequencies and as the ratio of the FMR amplitude vs. the amplitude of the background resonance is much improved, the resulting background in the data cut-outs for the subsequent fitting procedure is much less significant, see the exemplary cut-outs in figure E.13. Given the improved signal-to-noise ratio in the post-processing spectra of the measured data, a better match between the data and the expected line shape is obtained in the fitting procedure, as can be seen in figure E.13 (a)-(c). Notably, this data processing method not only results in a reduced frequency dependent background, but also yields less offset between real and imaginary part, due to the improved suppression of the broad background resonance.

The results obtained from the fitting procedure are shown accordingly in figure E.14. As usual, hardly any influence is observed on the extracted resonance frequencies. The extracted resonance linewidths, however, do present a significant impact: Compared to the simple off-resonant background removal, an increased precision of the fit results is obtained, resulting in a significantly reduced noise on the extracted resonance linewidths extracted from the measured data (compare figures E.8 and E.14). And similar to the derivative divide approach, the resonance linewidth extracted from the measured data and the resonance linewidth extracted from the artificial data overlap for frequencies above 20 GHz, see figure 5.13 in comparison. Moreover, no doubtful steep increase of the resonance linewidth for decreasing frequencies is obtained, as opposed to the derivative divide results.

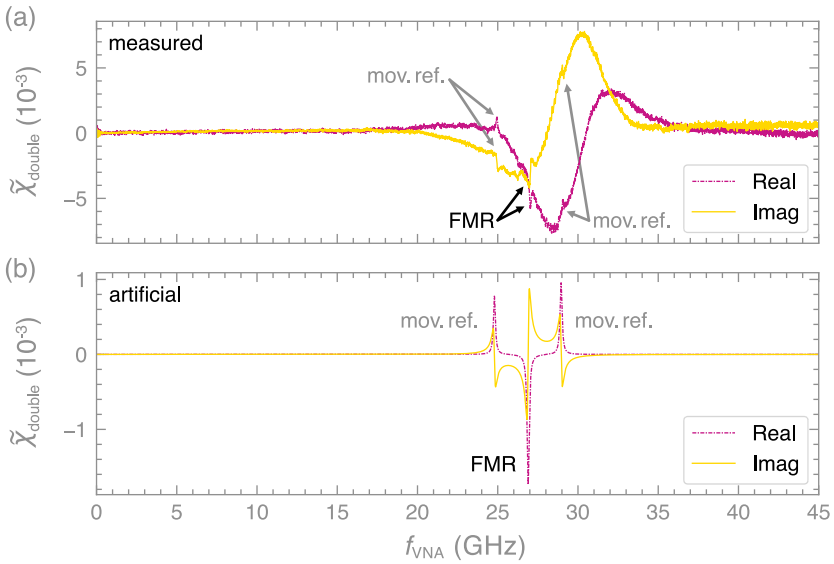

Figure E.15: Exemplary spectra at $\mu_0 H_{ext} = 500\,\mathrm{mT}$ of (a) the measured data and (b) the artificial test data for the maximal reference distance $\Delta H^{ref} = \pm 60\,\mathrm{mT}$.

Still, a mismatch is obtained here as well, again in the falsely increased slope in figure E.14 (b) compared to the known set linewidth on the artificial data set. This discrepancy is due to the too close reference resonance as previously observed for the simple off-resonant background removal above and was again investigated as a function of the reference field distance ΔH^{ref}. As above, the exemplary spectra at $\mu_0 H_{\mathrm{ext}} = 500\,\mathrm{mT}$ for the case of the maximal reference distance $\Delta H^{\mathrm{ref}} = \pm 60\,\mathrm{mT}$ are shown in figure E.15.

Compared to the single off-resonant moving reference approach the exemplary spectra of which are shown in figure E.9, the improved background suppression by the double off-resonant moving reference approach results in significantly improved signal-to-noise ratios on the measured data in figure E.15 (a) (compare to figure E.9 (a)).

The double off-resonant background removal approach allowed for a fitting of the FMR resonance curves even for the measured data with the maximal reference distance of $\Delta H^{\mathrm{ref}} = \pm 60\,\mathrm{mT}$, yet due to the significant background on the spectra of the measured data, the fit quality was drastically reduced, as can be seen in the extracted fit results for the reference distance $\Delta H^{\mathrm{ref}} = \pm 60\,\mathrm{mT}$ shown in figure E.16: The extracted linewidths from the measured data in figure E.16 (b) present much increased noise, are generally larger than what was obtained from $\Delta H^{\mathrm{ref}} = \pm 20\,\mathrm{mT}$ in figure E.14 (b) and the clear behaviour as a function of the resonance could not be reproduced. Of course no such effect is obtained on the artificial data set, where the increased reference distance results in a precise match of the constructed resonance linewidths.

In conclusion, this removal approach was found to not yield any systematic erroneous linewidth behaviour as were obtained in the derivative divide approach. Moreover, it principally results in an improved signal-to-noise ratio compared to the simple off-resonant background approach, and while it can be preferential for the treatment of data with slightly larger signal amplitudes than in this study, it is not practically suitable for the analysis of the uncalibrated data in this work either: Again, no satisfying compromise could be found between the minimal required reference distance of $\Delta H^{\mathrm{ref}} = \pm 60\,\mathrm{mT}$ to ensure the absence of systematical errors in the data analysis on the one hand, and a sufficient background suppression to yield large signal-to-noise ratios and consequently ensure a sufficient fit quality on the other hand.

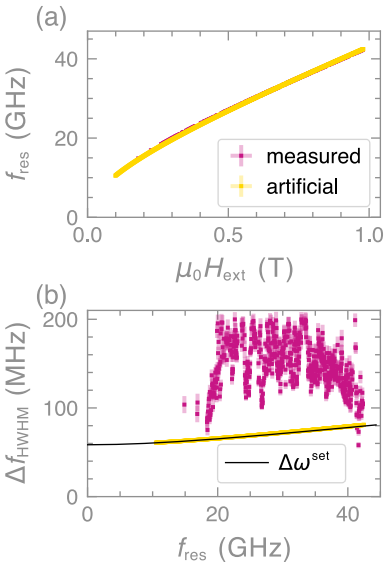

Figure E.16: Results obtained from the double moving reference background removal procedure for the measured data as well as the artificial data for the maximal reference distance $\Delta H^{\mathrm{ref}} = \pm 60\,\mathrm{mT}$. The increase of the reference distance leads to a worse fit quality on the measured data, resulting in the increased average linewidth and increased noise compared to figure E.14.

Conclusions & resulting choice for data treatment

In summary, the influence of three selected data processing approaches was evaluated on non-calibrated in-plane FMR data with respect to the background removal results as well as the quality of the subsequent fitting step for the further resonance parameter analysis. To this aim, two data sets were evaluated: a measured data set as well as an artificially constructed test data set were studied. The artificial data set served as a "control sample" in the study, of which the set resonance frequency, lineshape and linewidths were known from the construction of the data set. Notably, this allowed to determine whether the observed behaviour is atypical but sample-related, or whether it is due to systematic errors induced by the analysis method under investigation.

The extracted resonance frequencies were found to be hardly influenced by the data processing approach, which is in coherence with the results from a comparative data processing study on calibrated data by Bilzer *et al.* [355]. Consequently, the further analysis of the related material parameters, i.e. effective magnetisation, gyromagnetic ratio or Landé factor, and anisotropy field, often extracted in a subsequent step by a fit of the respective parameters in the Kittel function, is rather robust to the choice of data processing approach.

[355]: Bilzer et al. (2007), 'Vector network analyzer ferromagnetic resonance of thin films on coplanar waveguides'

The extraction of the resonance linewidths however, is especially sensitive to the background removal and fitting procedure, as was equally concluded in the comparative study on calibrated FMR data by Bilzer *et al.* [355]. Therefore, the evaluation in this comparative study mainly focused on the resonance linewidth results obtained from the different approaches.

[355]: Bilzer et al. (2007), 'Vector network analyzer ferromagnetic resonance of thin films on coplanar waveguides'

Concerning the data in this work, the results obtained from the investigated data analysis procedures allowed for the following conclusions:

- The best background suppression is obtained with minimal reference distances, corresponding here to the derivative divide approach. The double off-resonant moving reference can yield similar efficiency in the background removal, but only for small distances to the spectrum of interest, for which a resonance lineshape distortion cannot be excluded.
- The resonance lineshape distortion from a modulation with near-resonant references leads to systematic errors in the data evaluation. The strongest effect is observed on the derivative divide procedure, where it leads to a falsified linewidth behaviour for resonance frequencies below $\sim 25\,\mathrm{GHz}$. This erroneous behaviour can only partly be counteracted by the proposed choice of the CDQ as the adequate fitting function.
- Only the off-resonant reference approaches were able to reproduce the resonance linewidth behaviour of the artificial data set for frequencies $f_{\mathrm{res}} \lesssim 25\,\mathrm{GHz}$, for which the derivative divide approach resulted in an unphysical behaviour for either fitting function. However, ensuring the off-resonance is critical for these approaches, since otherwise falsified damping parameters are obtained from the increased slopes for $f_{\mathrm{res}} \gtrsim 25\,\mathrm{GHz}$. Yet, no satisfying compromise could be found which ensures the off-resonance of the reference spectra, while maintaining a decent background suppression on the measured data set.

Due to the superior background suppression and the resulting improved precision on the high-frequency linewidths[13], it is decided to use derivative divide for the analysis of the uncalibrated FMR data in this work. As a result of this comparative analysis study, caution will be employed for the extraction of the resonance linewidth results, and in particular the erroneous behaviour for $f_{\mathrm{res}} \lesssim 25\,\mathrm{GHz}$ can simply be neglected in the corresponding FMR studies.

13: Of highest relevance for the damping parameter extraction.

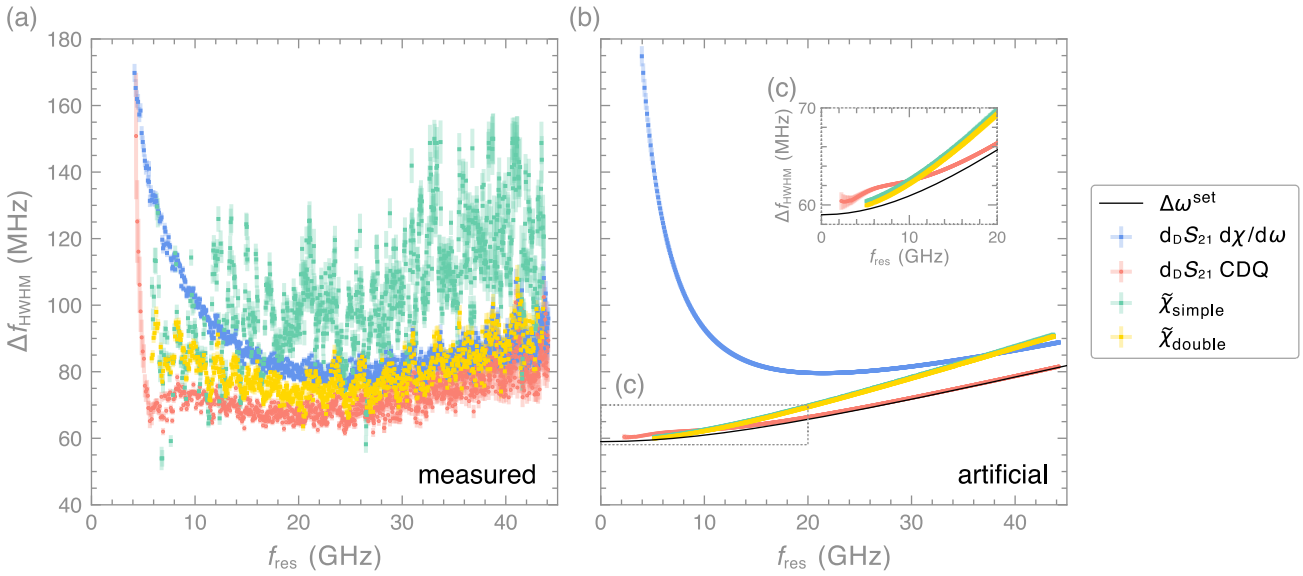

Figure E.17: Comparison of linewidth results obtained through all tested background removal procedures on (a) the measured data set and (b) the artificial test data set. Best results are obtained with the derivative divide approach using the central difference quotient formula, which is mainly related to the superior background suppression. Yet, an unexpected modulation is observed at low frequencies, which coincides with the range where the modulation amplitude drastically increases. It is therefore concluded that for the given measurement conditions and field step size, the approach is well-suitable only for the data with resonance frequencies above $\sim 20 - 25\,\mathrm{GHz}$.

F

Synthèse en français

Remarque : *Le texte dans cette section (résumé en francais, chapitre F dans l'appendice de cette thèse) forme un résumé du contenu de la partie principale de la thèse, qui a été rédigée principalement en anglais. Quelques extraits des introductions et des résumés des différents chapitres sont repris ici, pour lesquels les passages ont été traduits en français. La traduction a été effectué par l'autrice de la thèse. Pour quelques passages, l'outil web deepl.com (traducteur basé sur l'intelligence artificielle (IA)) a été utilisé comme aide à la traduction - ces passages ont ensuite été considérablement remaniés par l'autrice de la thèse.*

Les travaux présentés dans cette thèse intitulée *alliages d'Heusler pour la réalisation de dispositifs magnoniques et spintroniques* ont été menés entre juillet 2021 et juin 2025 dans le cadre d'un programme doctoral binational sous la forme d'une *cotutelle internationale* à l'Institut Jean Lamour, Université de Lorraine (Nancy, France) et le Rheinland-Pfälzische Technische Universität (RPTU) Kaiserslautern-Landau (Kaiserslautern, Allemagne).

Ce travail de doctorat est centré sur les alliages de Heusler à base de Co_2Mn, avec un focus sur l'alliage demi-métallique Co_2MnSi, en étudiant leur applicabilité à des sujets de recherche dans les domaines de la magnonique et de la spintronique.

Ces alliages de Heusler à base de Co_2Mn forment un sous-groupe particulier dans la vaste classe des matériaux de Heusler, connue depuis plus d'un siècle [92]. En effet, la classe des matériaux de Heusler a suscité un intérêt croissant dans la recherche depuis les premiers rapports, dont une partie est résumée en détail dans un livre récent sur le sujet [28]. La classe comprend des composés présentant divers phénomènes magnétiques, notamment le magnétisme itinérant et localisé, le paramagnétisme de Pauli ou l'antiferromagnétisme, entre autres, et s'accompagne en outre de la possibilité de concevoir certains composés pour qu'ils présentent les paramètres souhaités, d'où l'appellation familière de groupe de matériaux « avec des propriétés magnétiques *à la carte* » [93].

En conséquence, les alliages de Heusler présentent un intérêt particulier pour la communauté du magnétisme et, plus spécifiquement, le sous-groupe des alliages de Heusler à base de Co_2Mn a gagné en importance pour les applications dans les domaines de la spintronique et de la magnonique: Les études réalisées au cours des deux dernières décennies uniquement dans ce domaine niche vont de la caractérisation de diverses propriétés magnétiques et magnéto-optiques [94, 95, 98, 99, 101, 102], à des recherches orientées vers l'application telles que l'ingénierie de la polarisation du spin des composés ou de l'anisotropie magnétique [103, 105] ou les effets des processus de microstructuration [99, 106] et les propriétés des ondes de spin dans les microstructures [91, 96, 97, 100], et même quelques applications spécifiques telles que la mise en œuvre d'oscillateurs de vortex [104] ou les cristaux magnoniques [106].

Cette thèse est présentée en trois parties.

F.1 Partie I: Matériaux, croissance de couches minces, et caractérisation structurelle

La première partie est centrée sur les alliages de Heusler à base de Co_2Mn et leurs propriétés particulières qui en font des candidats prometteurs pour les applications spintroniques et magnétiques.

F.1.1 Chapitre 1 : *Bibliographie*. Contexte sur les alliages de Heusler

Le premier chapitre donne un bref aperçu des concepts pertinents des alliages de Heusler afin de fournir une base pour les discussions ultérieures dans cette thèse. Un accent est mis sur les caractéristiques particulières des alliages de Heusler à base de Co_2Mn, en particulier de Co_2MnSi, et sur les implications qui en résultent pour les applications spintroniques/magnétiques, pour lesquelles les propriétés sont placées dans le contexte d'autres matériaux courants dans le domaine, notamment le YIG (isolant typiquement utilisé pour son amortissement ultra-faible), le LSMO (demi-métal avec 100 % polarisation de spin seulement à basses temperatures), et le Permalloy et le CoFeB (métaux normaux, avec une haute aimantation, mais pauvre amortissement).

La principale caractéristique est la demi-métallicité de quelques alliages d'Heusler à base de Co_2Mn, dont notamment le Co_2MnSi : En général, la demi-métallicité est définie comme la propriété des matériaux présentant une structure de bande particulière : Les bandes électroniques d'une seule direction de spin présentent une bande interdite (anglais : band gap) à l'énergie de Fermi dans toute la zone de Brillouin, tandis que pour l'autre direction de spin, une densité d'états non nulle est observée au niveau de Fermi. Par conséquent, seuls les électrons de cette dernière peuvent contribuer à la conduction. Le terme *demi-métal* décrit donc la coexistence de deux comportements de conduction différents (métallique pour un type de spin, semi-conducteur/isolant pour l'autre) dans un seul et même matériau.

Comme le résume le tableau 1.1, tous les composés de Heusler Co_2MnX étudiés présentent une combinaison individuelle des propriétés clés suivantes :

- **Température de Curie élevée** → Assure la stabilité thermique et permet ainsi le fonctionnement du dispositif à température ambiante et au-delà.
- **Polarisation de spin élevée** → Permet l'exploitation des courants de spin (polarisés) et des phénomènes de transport associés par exemple.
- **Faible paramètre d'amortissement de Gilbert** → Promet une augmentation de la durée de vie et de la longueur de propagation des ondes de spin par rapport aux métaux standards (comme le Permalloy ou le CoFeB) entre autres.
- **Magnétisation de saturation élevée** → Conduit à une forte anisotropie de forme, à un seuil réduit pour les phénomènes d'ondes de spin non-linéaires et à un seuil de courant critique accru* qui peut faciliter le fonctionnement des nano-oscillateur à couple de spin (abbréviation anglaise : ST(N)O).
- **Anisotropie cubique** → Il en résulte des trajectoires de précession anisotropes ainsi que des seuils anisotropes pour la dynamique non linéaire, et offre un potentiel pour les dispositifs magnoniques reconfigurables [148].
- **Accordabilité** → Offre la possibilité de concevoir des composés avec des propriétés personnalisées pour répondre aux exigences spécifiques d'une application [116, 153].

Pour les travaux présentés dans cette thèse, l'accent est mis sur le Co_2MnSi, car ce composé présente un paramètre d'amortissement de Gilbert exceptionnellement faible, associé à la plus grande bande interdite de spin minoritaire de la série. De plus, le Co_2MnAl a été choisi comme référence, non seulement en raison de la tunabilité prouvée expérimentalement dans les composés quaternaires $Co_2MnAl_xSi_{1-x}$, mais aussi parce que les deux composés définissent les extrêmes de presque toutes les plages de paramètres répertoriées dans le tableau 1.1.

* Le seuil de courant critique dépend de plusieurs paramètres : Comme détaillé à la page 10, le courant de commutation critique est proportionnel à $\alpha \cdot M_S/P$, c'est-à-dire au paramètre d'amortissement de Gilbert, à l'aimantation de saturation et à la polarisation de spin. Ainsi, l'augmentation/la réduction du courant de commutation résulte d'une compétition entre, d'une part, une forte aimantation à saturation (augmentation) et, d'autre part, une forte polarisation de spin ainsi qu'un faible amortissement (réduction).

F.1.2 Chapitre 2 : *Échantillons.* Croissance de couches minces par épitaxie par jet moléculaire

Ce premier chapitre expérimental est consacré au processus de croissance des couches minces des séries d'échantillons étudiés dans le cadre de ce projet de recherche. Tous les échantillons ont été fabriqués par épitaxie par faisceau moléculaire, la croissance ayant été surveillée in situ par diffraction des électrons à haute énergie et par spectroscopie Auger en complément lors du test de la couverture de nouvelles bicouches de revêtement. Le processus de croissance qu'était suivi dans ce travail a été développé sur le même setup dans des travaux de thèses précedents et est décrit en détail dans la référence [71].

De plus, un aperçu de tous les échantillons apparaissants dans ce manuscrit de thèse est donné dans un tableau pour chaque série, y compris une indication de leur objectif individuel ainsi qu'une liste de leur apparition respective dans ce manuscrit.

F.1.3 Chapitre 3 : *Résultats.* Caractérisation structurelle par microscopie électronique en transmission

Le troisième chapitre présente une étude de caractérisation structurelle basée sur des expériences de microscopie électronique à transmission (MET), qui aboutit à plusieurs conclusions pertinentes pour la poursuite des recherches sur les films minces de Heusler et, en particulier, pour la fabrication de dispositifs magnoniques à partir de microstructures Co_2MnSi.

Résumé des résultats sur l'analyse structurelle des couches minces

Premièrement, un ordre $L2_1$ constamment prédominant est détecté dans tous les échantillons étudiés. Ceci est non seulement souhaitable pour sa relation avec diverses propriétés clés, telles que la bonne stœchiométrie, ou la demi-métallicité / polarisation de spin et le paramètre d'amortissement de Gilbert correspondant. Aussi, la cohérence dans les divers échantillons étudiés par TEM au cours de ce projet est également un signe de la fiabilité du contrôle de la croissance et de la qualité de l'échantillon qui en résulte.

Deuxièmement, l'analyse des interfaces avec le MgO (substrat et couche de recouvrement) permet de conclure à l'existence d'un réseau de dislocations cristallines identifiées comme des dislocations de bord (ajoutement de plans atomiques orientés perpendiculaires aux interfaces). Cette formation est due à l'incompatibilité cristalline entre le réseau cristallin du MgO et celui du Co_2MnSi, et peut être principalement ajustée par une couche tampon adéquate [71], cela a été vérifié sur deux échantillons d'essai de V/Co_2MnGe avec $\sim 5\,\%$ de desaccord cristallin et Cr/Co_2MnGe avec $\sim 0\,\%$ de desaccord cristallin. L'orientation du réseau de dislocations est supposée être parallèle aux directions $[110]_{Co_2MnSi}$, ce qui est conclu à partir de l'imagerie nette réussie de la distorsion au niveau des sites du réseau, malgré une prévision d'environ $10 - 20$ caractéristiques de dislocation dans la direction de sondage. L'impact de l'apparition des dislocations sur l'ordre chimique est exclu sur la base de l'observation de Co_2MnSi ordonné $L2_1$ à proximité immédiate de multiples dislocations. Néanmoins, le réseau de dislocations du réseau cristallin implique une variation directionnelle des hétérogénéités dans l'échantillon, qui peuvent agir comme des centres de pinning pour les domaines et qui peuvent entraîner des contributions d'amortissement anisotropes et hétérogènes [209, 210]. Ce résultat est donc particulièrement pertinent pour l'étude de la dynamique de magnétisation anisotrope dans les films minces, qui est présentée plus tard au chapitre 6.

Troisièmement, la couverture des différentes couches de revêtement a été vérifiée, avec un intérêt particulier pour les empilements de bicouches MgO/Al et MgO/Ti, qui se sont tous deux avérés avoir formé des oxydes au niveau des surfaces exposées. Dans le cas du MgO/Al, la croissance en îlots de la couche d'Al entraîne une rugosité de surface importante, avec des tailles d'îlots et une oxydation variables. Dans le cas du bicouche MgO/Ti, une pile de films homogène est obtenue et l'oxydation du film de Ti déposé entraîne une séparation entre une couche supérieure oxydée et une partie inférieure non oxydée, avec une interface claire entre les deux, indiquant une passivation de ce revêtement.

Résumé des résultats sur l'analyse structurelle des nanostructures

Enfin, une étude de nanofabrication a été menée afin de déterminer les effets de la fabrication et les dommages induits sur les propriétés structurelles du matériau Co_2MnSi.

À ce jour, une étude de Mantion *et al.* [77] est la seule connue[†] qui examine l'impact des défauts structurels d'un processus de fabrication descendant sur les propriétés des ondes de spin d'un dispositif magnonique microstructuré[‡]. Leurs résultats soulignent l'importance des défauts induits par la fabrication sur la dynamique de magnétisation, ce qui est confirmé par des conclusions généralisées similaires issues d'études sur des films minces irradiés par des ions [74–76] ainsi que sur des microfils recouverts de verre [217, 218]. Cependant, les simulations et les hypothèses utilisées dans [77] pour une estimation approximative des dommages induits, ainsi que la négligence des effets d'oxydation sur le Co_2MnSi exposé, malgré une amorphisation prévue de $2-5$ nm d'après des études précédentes [106] soulignent la nécessité d'une quantification structurelle approfondie des effets potentiels de la micro/nanofabrication, en particulier pour un développement réussi de dispositifs magnoniques.

Par conséquent, l'impact d'un processus de micro/nanostructuration typique pour la fabrication de dispositifs spintroniques/magnoniques a été étudié dans le cadre de ce travail. Pour cela, deux échantillons représentatifs de films minces de Co_2MnSi ont été structurés, l'un avec un recouvrement métallique de Pd et l'autre avec un recouvrement bicouche de MgO/Al oxydé. Le même processus de fabrication a été appliqué aux deux échantillons : un masque en résine a été formé sur les films minces par lithographie par faisceau d'électrons et les nanostructures ont été fraisées lors d'une étape de gravure par faisceau d'ions Ar^+. Suite à une préparation de lâmes présentant les coupes transversales des échantillons, les coupes transversales des nanostructures sont étudié par microscopie électronique en transmission à haute resolution (abbréviation anglaise : HRTEM), microscope électronique en transmission à balayage (STEM) et spectroscopie de rayons X à dispersion d'énergie (EDXS).

À l'exception des observations spécifiques aux couches de recouvrement, la fabrication des deux échantillons a donné des résultats similaires. Les principales conclusions de cette étude sur la nanostructuration sont une réduction réussie à des tailles d'environ 50 nm, tant pour les largeurs de guide d'ondes les plus petites que pour les tailles d'espace partiellement gravées.

Une redéposition du recouvrement en Pd est observée, entraînant la formation de structures en « cornes » de Pd courbées vers l'intérieur des guides d'onde. Hormis le redéposition sur les bords du masque de résine photosensible, le revêtement en Pd s'est avéré inchangé.

À l'inverse, le recouvrement bicouche de MgO/Al ne semble pas avoir résisté au processus de fabrication, car aucun signe de magnésium n'a pu être détecté dans le revêtement des structures gravées. Au lieu de cela, du silicium paraît avoir pénétré dans le revêtement. Cette altération chimique est probablement liée à la réaction chimique de la surface de l'échantillon avec le revêtement HMDS utilisé pour l'amélioration de l'adhérence de la resine de lithographie. Néanmoins, les structures sont bien protégées par le revêtement altéré, de manière similaire à la couche d'oxyde sur les bords gravés.

Au niveau des bords gravés (bords des guides d'ondes), pratiquement aucun dommage n'a été observé sur la structure cristalline de Heusler lors des études HRTEM, STEM et EDXS sur les structures, et notamment l'ordre chimique $L2_1$ a été maintenu. Le Co_2MnSi résiduel au fond des espaces partiellement gravés s'est avéré être amorphe et pourrait potentiellement servir au couplage d'échange des structures adjacentes avec une force réduite par rapport à l'interaction d'échange dans le matériau massif. Toutes les interfaces gravées se sont avérées recouvertes d'une couche d'oxyde amorphe, qui se serait formée pendant le processus de gravure par redéposition sur la surface de l'échantillon et qui constitue un revêtement protecteur des nanostructures fabriquées.

Certains mécanismes d'auto-formation potentiels sont discutés, notamment liés au revêtement HMDS, mais une conclusion définitive nécessiterait une analyse plus approfondie et n'est pas nécessaire aux fins de ce travail.

[†] À la connaissance de l'autrice de cette thèse.

[‡] Plusieurs études sur les microfils de Co_2MnSi et l'impact du rapport d'aspect sur l'ordre chimique et les propriétés magnétiques associées sont également disponibles, mais ces fils sont produits par la méthode Taylor-Ulitovsky, un processus en plusieurs étapes impliquant la formation d'un capillaire en verre rempli de Co_2MnSi fondu, qui donne un microfil métallique recouvert de verre après un processus de refroidissement [217]. Ces études concluent à une relation importante entre le rapport d'aspect des microfils et l'ordre chimique qui en résulte ainsi que les propriétés magnétiques associées, mais ce phénomène est principalement lié à la fabrication spécifique des microfils et aux spécifications des dispositifs [218] et ne permet donc pas de tirer des conclusions spécifiques sur les propriétés magnéto-structurelles des microstructures de Co_2MnSi fabriquées à partir de films minces.

F.2 Partie II: Propriétés magnétiques et magnéto-optiques des couches minces d'alliages de Heusler à base de Co_2Mn

La deuxième partie est consacrée aux propriétés magnétiques des couches minces épitaxiées à base de Co_2Mn de type Heusler. Les concepts fondamentaux pertinents du magnétisme (résonance ferromagnétique, amortissement et anisotropies) sont présentés avant une discussion détaillée des propriétés associées étudiées par magnétométrie, par resonance ferromagnétique et par méthodes magnéto-optiques. Cette caractérisation approfondie des couches minces sert de base à la dernière partie de la thèse, qui traite du transport des ondes de spin dans les dispositifs fabriqués à partir de couches similaires.

F.2.1 Chapitre 4 : *Bibliographie*. Concepts fondamentaux du magnétisme, dynamique de spin et interactions magnéto-optiques

Avant d'aborder la caractérisation magnétique des composés de Heusler à base de Co_2Mn, en particulier leur comportement anisotrope, leur dynamique d'aimantation et leur aptitude magnéto-optique, ce chapitre présente brièvement les concepts fondamentaux sous-jacents.

La première section se concentre sur les concepts nécessaires du magnétisme requis pour la discussion de l'aimantation, de l'hystérésis et de l'anisotropie dans le cadre d'une étude magnétométrique au chapitre 6.1. Une attention particulière est accordée au terme d'anisotropie cubique du second ordre et à ses implications sur la symétrie magnétique dans les cristaux.

La deuxième section de ce chapitre présente brièvement le cadre conceptuel des oscillations de magnétisation sur la base duquel les résultats de la spectroscopie de résonance ferromagnétique seront discutés dans le chapitre suivant 6.2. L'équation phénoménologique de Landau-Lifshitz-Gilbert [253, 254] est présentée comme la description sous-jacente de la dynamique de l'aimantation. Suivant, la description de la resonance ferromagnétique (abbréviation anglaise: FMR) est effectuée en analogie avec l'approche bien connue de Smit, Beljers et Suhl [261, 262].

La troisième section présente les phénomènes magnéto-optiques et les concepts de base nécessaires à l'étude des phénomènes magnéto-optiques dans le chapitre 7, notamment les principes fondamentaux de l'effet Kerr magnéto-optique (abbréviation anglaise: MOKE) et de la diffusion Brillouin (abbréviation anglaise: BLS). Dans les expériences MOKE et BLS, la lumière réfléchie/rétrodiffusée est étudiée et les signaux magnéto-optiques résultant des deux effets sont effectivement liés [296], ce qui est motivé dans cette section du chapitre théorique par une brève description de l'origine microscopique sous-jacente et la relation conceptuelle des deux phénomènes avec le tenseur magnéto-optique.

F.2.2 Chapitre 5 : *Méthodes*. Magnétometrie à échantillon vibrant (VSM), résonance ferromagnétique (FMR), magnétometrie Kerr (MOKE) et spectroscopie de diffusion Brillouin (BLS)

Ce chapitre méthodique introduit les conceptes des méthodes experimentales utilisés pour la caractérisation magnétique et magnéto-optique des couches minces d'alliages de Heusler à base de Co_2Mn.

La magnétométrie à échantillon vibrant (VSM) est utilisée pour mesurer les courbes d'hystérésis, c'est-à-dire le moment magnétique absolu des échantillons en fonction du champ externe appliqué. Cette technique a été développée dans les années 1950 [328] et est aujourd'hui une technique standard pour mesurer le moment magnétique absolu d'un échantillon. Les VSM sont insensibles aux hétérogénéités magnétiques statiques [330] et sont donc largement utilisés dans les laboratoires de recherche modernes, avec des applications allant des configurations personnalisées [331–333] aux appareils commerciaux [334, 335].

La spectroscopie à résonance ferromagnétique (FMR) est une technique puissante permettant d'étudier les caractéristiques de la dynamique de l'aimantation dans les matériaux magnétiques. Le principe de base des mesures FMR est l'absorption résonante d'un champ micro-ondes alternatif par le système magnétique de l'échantillon. Cette absorption résonante est généralement décrite par le tenseur de susceptibilité dynamique introduit au chapitre 4.2.2.

Il existe différentes méthodes expérimentales pour étudier la résonance ferromagnétique, qui peuvent généralement être classées en fonction de leur propriété statique : les mesures à champ fixe, souvent appelées « FMR à large bande (BB-FMR) » car la fréquence micro-ondes est balayée dans ce cas [345, 346], et les mesures à fréquence fixe appelées *FMR à balayage de champ* dans ce travail, où le champ magnétique est balayé pour des fréquences fixes [263]. Compte tenu de la dépendance du tenseur de susceptibilité dans l'équation 5.8 par rapport aux dérivées secondes de la densité d'énergie totale, qui est une fonction du champ magnétique appliqué, la différence fondamentale entre les deux approches de mesure est directement apparente : Une expérience spectroscopique au sens strict, c'est-à-dire sans perturbation de l'état magnétique sondé, n'est réalisée que dans l'approche BB-FMR [345] car l'approche FMR à balayage de champ implique une variation de l'énergie du système[§].

Dans cette thèse, la méthode BB-FMR a été choisie pour effectuer les mesures FMR. Contrairement aux études typiques, le circuit micro-ondes n'a pas été calibré, car la suppression du signal de fond non magnétique a été effectuée lors d'une étape de post-traitement des données.

Le post-traitement des données acquises à partir des mesures BB-FMR est couramment effectué dans les études publiées dans la littérature, voir par exemple [264, 348, 350, 351, 353–357], dans le but d'accéder au signal lié à la susceptibilité magnétique et d'éliminer le bruit de fond complexe dépendant de la fréquence introduit ci-dessus. Il est connu que la précision des paramètres extraits dépend fortement du protocole de post-traitement, avec une sensibilité particulière en ce qui concerne les largeurs de raie extraites : les différences peuvent atteindre 10 % [355], ce qui rend le choix de l'évaluation des données crucial pour l'analyse du comportement de la largeur de raie de résonance[¶] en particulier lorsque l'on cherche à extraire l'amortissement magnétique et les inhomogénéités du système, qui définissent par exemple la durée de vie des ondes de spin dans les études utilisant le transport magnonique.

Dans une note récente de Maier-Flaig et al. [350], le *derivative divide*, une méthode d'analyse des mesures BB-FMR non calibrées est présentée, qui ne nécessite ni pré-calibrage du circuit micro-ondes ni mesures de référence séparées. Semblable à une dérivée, cette méthode est module les formes des lignes de résonance [350], un effet notamment critique pour les matériaux présentant des courbes de résonance fines, comme typiquement obtenu par des matériaux à faible amortissement.

Par conséquent, compte tenu de la sensibilité connue (en particulier des largeurs de ligne de résonance extraites) en fonction de l'approche d'analyse des données, une étude approfondie des effets potentiels induits par le post-traitement a été menée afin de minimer le risque d'erreurs systématiques dans les études ultérieures. Les résultats sont discutés dans la sous-section 5.2.2. Il est conclu que l'effet d'une surmodulation est particulièrement important dans le cas des données FMR dans le plan de matériaux présentant une aimantation à saturation élevée et un faible amortissement magnétique, car on peut s'attendre à des largeurs de raies de résonance étroites avec une non-linéarité de Kittel significative persistant sur une large gamme de fréquences[‖]. Néanmoins, les résultats supérieurs en ce qui concerne la suppression du bruit de fond, font de la procédure de *derivative divide* l'approche privilégiée pour l'analyse ultérieure des données, en particulier pour les données à haute fréquence qui sont justement les plus importantes pour l'extraction du paramètre d'amortissement de Gilbert. Il convient toutefois de noter qu'une prudence particulière s'impose dans l'interprétation de la largeur de raie non homogène dans ce cas.

La magnétométrie Kerr est introduite et utilisée dans cette thèse afin d'étudier le signal magnéto-optique et les anisotropies magnéto-optiques des films minces. Cette technique repose sur l'effet magnéto-optique Kerr (MOKE), c'est-à-dire le changement de polarisation de la lumière lors de sa réflexion sur un échantillon magnétique, comme introduit au chapitre 4.3, qui a été exploité pour l'étude de divers phénomènes dans les matériaux magnétiques depuis les rapports éponymes de Kerr dans les années 1870 [293, 294].

La spectroscopie de la diffusion Brillouin est une méthode clé pour l'étude des ondes de spin - le sujet principal de la domaine de recherche en magnonique. La diffusion Brillouin est nommée d'après la prédiction théorique de

[§] Ceci est particulièrement important lors de l'étude de matériaux présentant des textures magnétiques, où une modification du champ externe implique directement un changement dans la configuration magnétique [347].

[¶] Il est également nécessaire de préciser la procédure d'analyse des données choisie, ce qui n'est malheureusement pas toujours indiqué [358].

[‖] En principe, la modulation pourrait être réduite en affinant la taille du pas de modulation du champ, c'est-à-dire $\Delta H^{\pm}$. Comme le plus petit pas de modulation possible pour cette mesure a déjà été choisi ici, c'est-à-dire $\Delta H^{\pm} = 1\,\mathrm{mT}$, la taille du pas du champ devrait être encore réduite. Cependant, lorsque l'on souhaite balayer de grandes plages de champ (en particulier pour les matériaux avec un M_S élevé et un faible amortissement), cela présente l'inconvénient d'augmenter considérablement le temps de mesure et la quantité de données collectées.

Brillouin [295] et décrit le processus de la diffusion inélastique de la lumière par les ondes dans un solide, ici les ondes de spin**.

F.2.3 Chapitre 6 : *Résultats*. Propriétés magnétiques des couches minces épitaxiés des alliages de Heusler Co_2MnSi and Co_2MnAl

Ce chapitre présente une étude approfondie des propriétés statiques et dynamiques des composés de Heusler Co_2MnSi et Co_2MnAl[††] à l'aide de la magnétométrie à échantillon vibrant et de la spectroscopie de résonance ferromagnétique.

L'étude VSM a permis d'extraire les paramètres définissant les boucles d'hystérésis et les résultats ont été résumés dans le tableau 6.1 à la page 117. Pour la suite de cette étude, le résultat le plus important des mesures VSM est certainement l'aimantation à saturation extraite, où, pour les deux composés, les valeurs attendues d'après la littérature ont été reproduites. De plus, les courbes d'hystérésis ont présenté une signature anisotrope dans les deux cas, bien que plus prononcée sur le film Co_2MnSi.

Cette anisotropie a été étudiée plus en détail dans les mesures FMR, où une anisotropie cubique a été observée dans les deux composés avec la signature de rotation dans le plan attendue correspondant à des constantes d'anisotropie cubique de premier ordre négatives. Cependant, pour les deux échantillons, il s'est avéré nécessaire de prendre en compte une contribution d'anisotropie cubique du second ordre ou d'anisotropie uniaxiale hors plan en plus de l'anisotropie cubique du premier ordre afin d'obtenir une description correcte du système[‡‡].

L'analyse des données obtenues à partir du film Co_2MnSi suggère que la meilleure description des données mesurées est obtenue par une combinaison de l'anisotropie cubique du premier et du deuxième ordre avec les constantes d'anisotropie répertoriées dans le tableau 6.3. Dans ce cas, le rapport des constantes d'anisotropie s'élève à $K_{c2}/|K_{c1}| \approx 4.65$, ce qui se traduit par une identification des axes principaux du réseau cubique $\langle 100 \rangle$ comme axes durs, et des diagonales des faces $\langle 110 \rangle$ comme axes faciles de l'énergie d'anisotropie magnétocristalline, comme cela a été présenté à la page 71.

Pour l'échantillon Co_2MnAl, une meilleure correspondance qualitative avec les données de rotation suggère également une contribution probable de l'anisotropie cubique du second ordre, mais les faibles amplitudes de résonance et le rapport signal/bruit relativement médiocre, ainsi que l'absence d'un ensemble de données hors plan, ne permettent pas de tirer d'autres conclusions. De plus, les données FMR dans le plan sur le film (non recuit) Co_2MnAl suggèrent une augmentation notable de l'aimantation effective d'environ 200 mT, ce qui souligne l'importance d'une analyse plus approfondie de l'anisotropie pour l'utilisation comme échantillon de référence prévu.

De plus, la discussion sur les implications de symétrie découlant des différents termes d'anisotropie souligne l'importance d'une géométrie de mesure judicieuse lorsqu'on cherche à distinguer les différents termes. Il s'agit d'une conclusion généralisée applicable à tout système cubique, et particulièrement importante dans le contexte de l'intérêt croissant pour les applications de l'anisotropie magnétique perpendiculaire.

Enfin, les largeurs de raie de résonance ont été brièvement analysées, ce qui a permis d'obtenir une indication d'un amortissement anisotrope avec une variation de 10 % et des valeurs les plus faibles pour une application de champ le long des directions $\langle 100 \rangle$ (axes durs). Cependant, bien que cela corresponde à des observations similaires rapportées dans [392], cela est contredit dans la présente étude par la variation de la largeur de raie de résonance anisotrope non homogène, qui pourrait être attribuée à une contribution de diffusion à deux magnons dépendante de l'angle, liée aux dislocations du réseau aux interfaces. Toutefois, une distorsion des largeurs de raies de résonance due à la modulation résultant du traitement des données (comme determiné par l'étude systematique sur le traitement de données dans le chapitre précedent) ne peut être exclue comme facteur affectant l'analyse.

** Entre outre, la technique peut aussi être utilisée pour l'études des ondes élastiques, par exemple.
†† Co_2MnAl non recuit.
‡‡ Il convient de souligner que, bien qu'une combinaison des deux ne puisse être exclue, elle entraînerait une surparamétrisation du système pour les ensembles de données disponibles et n'a donc pas été prise en compte dans l'analyse.

F.2.4 Chapitre 7 : *Résultats.* Signal magnéto-optique des couches minces des alliages de Heusler à base de Co_2Mn

Ce chapitre présente une brève étude magnéto-optique de divers composés Heusler de Co_2MnX avec X={Al_xSi_{1-x}, Ge_xGa_{1-x}, Sn} par magnétométrie MOKE longitudinale (LMOKE) et par spectroscopie BLS, les deux techniques étant réliées par les amplitudes du signal liées à l'angle de Kerr complexe $\Phi = \theta + i\ell$. Les mesures MOKE et BLS présentées dans ce chapitre ont été réalisées dans le cadre d'un projet de recherche de master (M1) mené par Nicolas Fermon de l'école normale supérieure Paris-Saclay [360] et encadré par l'autrice de cette thèse. L'analyse discutée dans ce chapitre 7 a été effectuée par l'autrice de cette thèse en étendant l'analyse présentée dans [360].

Précisement, une étude rotationnelle du LMOKE en fonction de l'orientation cristallographique et de la longueur d'onde laser appliquée est réalisée dans une gamme de longueurs d'onde de $\lambda \approx 550 - 900$ nm. Pour l'interpretation des effects lineaires et quadratiques, linMOKE et QMOKE [94, 310, 361–365], les contributions symétriques et antisymétriques ont été séparées de manière analogue aux références [94, 364] par une simple considération de symétrie.

L'échantillon de Co_2MnSi était le seul échantillon présentant un effet MOKE quadratique significatif dans la rotation de Kerr étudiée θ, qui s'est avéré maximal pour une projection de lumière incidente le long d'un axe principal du réseau cubique $\langle 100 \rangle$ correspondant à l'axe dur dans les échantillons étudiés. Les amplitudes MOKE quadratiques les plus importantes ont été obtenues entre 550 nm et 650 nm et un changement de signe est apparu entre 700 nm et 850 nm. L'effet MOKE linéaire s'est évanoui à environ 600 nm, la rotation linMOKE présentant également un changement de signe à cette longueur d'onde. La dépendance de la longueur d'onde de la rotation linMOKE et QMOKE correspond aux résultats d'une étude indépendante [82].

Co_2MnAl, Co_2MnGa et Co_2MnSn ont tous montré des effets QMOKE négligeables par rapport au signal linMOKE, qui sont principalement liés à l'apparition naturelle d'une contribution quadratique provenant du tenseur magnéto-optique linéaire. Co_2MnAl a été choisi pour une comparaison approfondie avec Co_2MnSi dans l'étude dépendant de la longueur d'onde et l'évolution obtenue de la rotation de Kerr de Co_2MnAl ne montre pratiquement aucune contribution QMOKE et une rotation linMOKE presque constante pour $\lambda = 550 - 900$ nm.

Sur la base de ces résultats, les intensités de signal BLS obtenues ont été discutées : L'amplitude relativement faible du signal BLS pour Co_2MnSi à $\lambda = 532$ nm s'est avérée être liée à l'angle de Kerr complexe qui s'évanouit, puisque $I_{BLS} \sim |\Phi|^2$. En effet, Co_2MnSi ainsi que le composé ternaire apparenté $Co_2MnSi_{0.25}Al_{0.75}$ ont montré la plus grande différence dans les intensités BLS pour $\lambda = 532$ nm et $\lambda = 457$ nm par rapport aux autres composés de la série.

Cette brève étude de la réponse magnéto-optique obtenue à partir de Co_2MnX avec X={Al_xSi_{1-x}, Ge_xGa_{1-x}, Sn} a confirmé un comportement magnéto-optique complexe, en particulier pour le composé de Heusler Co_2MnSi, où, contrairement aux approches standard, les réponses magnéto-optiques quadratiques ne sont pas négligeables et la dépendance de l'angle de Kerr complexe par rapport à la longueur d'onde suggère clairement de choisir judicieusement les longueurs d'onde de sondage.

Pour les longueurs d'onde des lasers BLS disponibles $\lambda = 457$ nm, $\lambda = 491$ nm et $\lambda = 532$ nm dans les experiences de BLS à Kaiserslautern, la dépendance en longueur d'onde de l'angle Kerr complexe prédit les meilleurs résultats pour $\lambda = 457$ nm et les plus mauvais pour $\lambda = 532$ nm. Cela est confirmé par le fait que le signal relatif de Co_2MnSi est nettement inférieur à celui des autres composés de l'étude BLS à $\lambda = 532$ nm (fait en 2020 [83]) et qu'il est du même ordre de grandeur que tous les autres composés de l'étude BLS à $\lambda = 457$ nm (fait en 2023). Enfin, l'importance de l'optimisation de l'installation, en particulier pour l'exploitation de cette gamme de longueurs d'onde d'angles de Kerr peu attendus, est soulignée par rapport à la comparaison directe des amplitudes de signal normalisées de Co_2MnSi obtenues à $\lambda = 532$ nm et à $\lambda = 457$ nm : Bien que l'intensité attendue de l'angle de Kerr s'évanouisse à $\lambda = 532$ nm, les spectres BLS ont été détectés avec succès à partir de Co_2MnSi à cette longueur d'onde et ont même nécessité moins de moyennage. Il est donc possible d'optimiser les facteurs externes pour obtenir une sensibilité suffisante, comme indiqué en détail dans la partie principale de ce chapitre 7. En outre, il convient de noter que le signal des ondes de spin thermiques étudiées dans cette étude est généralement beaucoup plus faible que celui auquel on peut s'attendre dans les études magnoniques typiques avec une excitation externe, par exemple avec des antennes.

F.3 Partie III: Transport magnonique non linéaire dans les microstructures à base de Co_2MnSi

La troisième partie de cette thèse se concentre sur l'étude des phénomènes de transport de spin magnonique et de leurs caractéristiques dans les microstructures de l'alliage Heusler Co_2MnSi. Dans les applications spintroniques, le transport de spin s'accompagne généralement d'un transport de charge simultané sous la forme d'un courant polarisé en spin. D'autre part, le domaine de la magnonique est centré sur les ondes de spin, qui forment essentiellement un mécanisme de transport de spin indépendant du courant de charge. Le composé Co_2MnSi constitue un cas très particulier pour les deux types de transport : sa polarisation de spin à 100% produit des courants entièrement polarisés pour les applications spintroniques, et l'amortissement Gilbert ultra-faible qui y est associé promet une longue durée de vie des ondes de spin dans les dispositifs magnoniques.

Introduite dans la partie précédente de la thèse, l'équation phénoménologique de Landau-Lifshitz-Gilbert (LLG) est l'équation fondamentale pour la description de la dynamique d'aimantation collective dans ce travail et occupe également une place centrale dans cette troisième partie : les oscillations et les ondes d'aimantation collective en sont les solutions formelles, et le cas particulier de la précession spatialement homogène, c'est-à-dire l'oscillation avec un vecteur d'onde nul, est la résonance ferromagnétique (FMR), qui était un sujet central dans la partie précédente de ce travail. Dans la présente partie, l'ensemble complet des solutions présente un intérêt, y compris les solutions à vecteur d'onde non nul, appelées *ondes de spin*, avec les quasi-particules associées généralement appelées *magnons*.

F.3.1 Chapitre 8 : *Bibliographie et calculations*. Concepts fondamentaux du transport de spin magnonique à base des ondes de spin linéaires et non-linéaires, et évaluation des effets d'anisotropie cubique.

Ce chapitre présente certains concepts fondamentaux de la dynamique d'aimantation linéaire et non-linéaire, en mettant l'accent sur les thèmes pertinents pour les chapitres suivants. L'équation LLG est une équation intrinsèquement non-linéaire [394] et, à ce titre, peut décrire des dynamiques d'aimantation assez complexes, voire chaotiques [288, 396–400], mais ne fournit pas d'accès direct à une solution analytique générale. Une approche couramment adoptée pour la description des modes d'ondes de spin est la linéarisation de l'équation LLG, comme cela a été fait au chapitre 4 pour la dérivation de la FMR. Comme cette approximation n'est valable que pour la dynamique d'aimantation proche de l'équilibre[§§], elle implique une classification en deux régimes distincts d'ondes de spin : Le terme *ondes de spin linéaires* est couramment utilisé pour les ondes de spin proches de l'équilibre, pour lesquelles la linéarisation de l'équation LLG est une approximation valable. Pour les *ondes de spin non-linéaires*, la précession s'écarte considérablement de l'aimantation d'équilibre et l'approximation n'est plus valable. Une approche théorique différente est donc nécessaire pour décrire les phénomènes d'ondes de spin non-linéaires, par exemple par une approche Hamiltonienne [401, 402]. Cette classification est adoptée dans ce chapitre afin d'introduire les concepts sous-jacents de la dynamique des ondes de spin linéaires et non-linéaires, qui sont fondamentaux pour la discussion ultérieure des résultats expérimentaux. Comme dans le chapitre 4 précédent sur les fondements théoriques, seul un bref résumé des concepts essentiels est présenté et il est renvoyé aux livres spécialisées pour une description plus complète, par exemple dans [225, 227, 229, 403].

La première section 8.1 de ce chapitre est consacrée aux concepts des ondes de spin linéaires et l'évaluation des effets d'anisotropie notamment pour la géometrie des études suivantes. La relation de dispersion approximative de Kalinikos-Slavin [378, 379] pour les films minces anisotropes aimantés dans le plan y est brièvement présenté et l'intégration des termes d'anisotropie est discuté en détail.

Cette section et notamment la discussion des calculs des effets de l'anisotropie aboutit à plusieurs conclusions importantes pour l'analyse suivante :

- Pour un film de Co_2MnSi dans une géométrie d'échantillon correspondant au cas étudié au chapitre 10, l'anisotropie cubique avec des constantes tirées de la caractérisation FMR du chapitre 6 produit un décalage de fréquence dans la relation de dispersion, qui diminue généralement lorsque le vecteur d'onde k_{ip} augmente.

[§§] Proche de l'équilibre signifie avec de petits angles de précession, c'est-à-dire des amplitudes dynamiques négligeables par rapport à l'aimantation statique $\mathbf{M}_0$.

- Le décalage de fréquence induit par l'anisotropie s'est avéré important pour la géométrie Damon-Eshbach uniquement pour des vecteurs d'onde très petits $k_{ip} \lesssim 2\,\mathrm{rad}/\mu\mathrm{m}$, au-delà desquels le changement est $\lesssim 5\%$.
- L'impact le plus important de l'anisotropie cubique a été observé sur la géométrie Backward-Volume, et pour $k_{ip} \lesssim 30\,\mathrm{rad}/\mu\mathrm{m}$, l'anisotropie cubique entraîne non seulement des décalages de fréquence de $\gtrsim 5\%$, mais aussi une baisse reliée de la vitesse de groupe de $\gtrsim 10\%$, ainsi qu'un décalage conséquent du minimum de la bande vers des valeurs plus élevées de k_{ip}.

En conséquence, la prise en compte de l'anisotropie cubique pure du premier ordre (et la négligence d'une contribution du second ordre) est supposée être une approximation valable pour la dispersion de Damon-Eshbach, ce qui permet notamment l'utilisation de TetraX comme détaillé au chapitre 9. Cependant, il convient de noter qu'il faut faire preuve de prudence pour les analyses quantitatives, en particulier celles portant sur les effets non-linéaires pouvant impliquer des partenaires de diffusion avec d'autres directions de propagation.

La deuxième section 8.2 de ce chapitre donne un aperçu des concepts pertinents de la dynamique non-linéaire des ondes de spin. Tout d'abord, les processus de diffusion multi-magnons sont introduits comme une forme de conversion d'énergie non-linéaire au sein du système magnétique, dont les instabilités de Suhl de premier et deuxième ordre constituent un cas particulier concernant la conversion d'énergie d'un mode directement pompé en modes d'ondes de spin secondaires. L'intérêt pour ce type de diffusion multi-magnon est né avec l'analyse des « effets anormaux dans l'absorption des micro-ondes par les ferromagnétiques à des puissances de signal élevées » [288] par Suhl en 1957. Depuis lors, les processus de diffusion multi-magnon ont été étudiés dans divers contextes, par exemple pour leurs effets sur la relaxation des modes d'ondes de spin [86, 291, 419–421], les effets qui en découlent sur la commutation de magnétisation [422], ou la formation résultante de condensats de Bose-Einstein de magnons en tant qu'états quantiques macroscopiques [423–426]. Avec l'intérêt croissant pour les approches de calcul neuromorphique et de calcul quantique, ces effets de diffusion non linéaires et leurs implications ont pris une importance croissante pour le développement de dispositifs magnoniques non conventionnels promettant une capacité de réglage, par exemple par la géométrie des dispositifs [427], les ondes acoustiques de surface [428], les courants de spin [60] ou le refroidissement rapide de magnons [429].

Aussi, le phénomène du décalage de fréquence non-linéaire est présenté, qui peut entraîner un décalage de la relation de dispersion en fonction des coefficients d'auto-interaction $\widetilde{W}_{\mathbf{kk},\mathbf{kk}}$ et de l'amplitude des ondes de spin. Le décalage non linéaire a traditionnellement fait l'objet d'études approfondies en ce qui concerne l'effet de repliement (anglais : foldover effect) sur la réponse FMR [402] analogue à un pendule classique, et la bistabilité du système qui en résulte [430–434]. Récemment, les décalages non-linéaires ont été largement étudiés en relation avec la dynamique non linéaire observée dans les oscillateurs spintroniques [130, 435–443] : Concernant ces dispositifs, les décalages non-linéaires de fréquence peuvent entraîner des fréquences d'oscillation inférieures à la FMR [439], sont cruciaux pour la description précise de la largeur de raie d'oscillation dans les STNO [437], peuvent conduire à la formation d'un mode soliton magnon régissant les auto-oscillations non-linéaires dans les nano-oscillateurs à effet Hall de spin [435], peuvent faciliter la synchronisation de plusieurs oscillateurs [441, 442] et peuvent être controlés par des courants de spin [443].

Les deux phénomènes peuvent être décrits dans le formalisme hamiltonien de la dynamique non-linéaire des ondes de spin, dont les concepts sont donc brièvement présentés dans la troisième sous-section.

Cette section sur la dynamique non-linéaire des ondes de spin aboutit également à quelques conclusions importantes pour l'analyse suivante :

- Pour un film de Co_2MnSi dans une géométrie d'échantillon correspondant au cas étudié au chapitre 10, le décalage de la relation de dispersion induit par l'anisotropie implique des seuils de fréquence au niveau de 8.7 GHz et 12.8 GHz qui doivent être dépassées pour que l'instabilité de Suhl du premier ordre soit possible à des champs externes de 10 mT et 30 mT, respectivement.
- Même si l'instabilité de Suhl du premier ordre est non-résonante pour les champs étudiés, la cascade de deux processus non-résonants à trois magnons via un état magnon virtuel aboutit à un processus "effectif" à quatre magnons, et les interactions à trois magnons doivent donc tout de même être prises en compte dans la description des termes de diffusion à quatre magnons. Ceci est pris en compte par un facteur de correction, et en raison de la forte aimantation à saturation du composé de Heusler Co_2MnSi, cette correction à trois magnons devrait être importante dans les dispositifs faits à partir de ce matériau.

- Les instabilités de Suhl sont des processus de seuil qui s'auto-amplifient au-dessus d'une amplitude critique de l'onde de spin primaire, ce qui entraîne une augmentation exponentielle des amplitudes de l'onde de spin secondaire.
- Le décalage non-linéaire de fréquence auto-induit n'est pas un processus seuil et devrait être proportionnel à l'amplitude de l'onde de spin.

Ces implications sont importantes pour l'étude des ondes de spin dans les guides d'ondes micro-dimensionnés à base du demi-métal Co_2MnSi, notamment pour la discussion présentée au chapitre 10.

F.3.2 Chapitre 9 : *Méthodes*. Dispositif magnonique, technique de BLS microfocalisée et résolue en temps.

Dans ce chapitre méthodologique, la géométrie de l'échantillon est présentée ainsi que les méthodes expérimentales utilisées dans la suite : Le guide d'ondes étudié fait partie d'un dispositif à décalage Doppler à ondes de spin [43, 91] fabriqué à partir d'un film mince de Co_2MnSi. Les spécifications du dispositif et de l'échantillon sous-jacent sont introduits dans la première section 9.1. La dynamique des ondes de spin a été étudiée par diffusion microfocalisée de la lumière de Brillouin (μBLS), une technique magnéto-optique puissante qui repose sur le même principe que la technique BLS conventionnelle présentée au chapitre 5. Les bases de cette technique sont brievements introduits dans la section suivante 9.2.

F.3.3 Chapitre 10 : *Résultats*. Ondes de spin non linéaires dans un guide d'ondes micro-dimensionné semi-métallique à base de Co_2MnSi

Ce chapitre 10 présente les premières recherches explorant l'excitation et la propagation des ondes de spin dans des guides d'ondes microstructurés semi-métalliques en Co_2MnSi. Cette étude est le fruit d'une collaboration avec l'Institut de physique et chimie des matériaux de Strasbourg (IPCMS) à Strasbourg, initiée dans le cadre du projet ANR MARIN (ANR-20-CE24-0012).

Les spectres d'excitation des ondes de spin ont été étudiés par spectroscopie de diffusion de lumière Brillouin micro-focalisée dans un guide d'ondes épitaxial Co_2MnSi de taille microscopique d'une largeur de 10 μm, structuré à partir de l'échantillon S1.1 cité dans le tableau 2.1 à la page 29. Les spécifications du dispositif sont détaillées dans la section 9.1 du chapitre précédent. Le même dispositif avait déjà été étudié dans le cadre des travaux de doctorat de José Solano [91], où il a notamment été conclu que la demi-métallicité du Co_2MnSi persistait même dans ce dispositif microstructuré, comme l'ont confirmé les expériences de décalage Doppler des ondes de spin [43].

L'analyse de l'anisotropie magnétocristalline[¶¶] sur des films Co_2MnSi comparables a montré des effets de symétrie intéressants, comme discuté dans les chapitres 6 et 8. Une attention particulière est donc accordée à l'orientation du dispositif utilisé dans cette étude : l'axe de propagation du guide d'ondes sélectionné correspond à la direction $[110]_{Co_2MnSi}$, et l'axe hors plan à $[001]_{Co_2MnSi}$, comme dans tous les échantillons de cette thèse. Toutes les mesures pour l'étude présentée dans ce chapitre 10 ont été réalisées dans la géométrie Damon-Eshbach, c'est-à-dire $\mathbf{M}_0 \parallel \mathbf{H}_{ext} \perp \mathbf{k}_{ip}$. Compte tenu de la symétrie cubique du système avec $K_{c1} < 0$ pour Co_2MnSi, la direction de propagation ainsi que la direction de l'aimantation correspondent à un minimum d'énergie dans le plan de l'anisotropie magnétocristalline[***], ce qui a quelques implications, comme détaillé dans le chapitre 8 : Pour les petites oscillations de l'aimantation autour de cet axe (par opposition à la direction de haute symétrie $[100]_{Co_2MnSi}$), l'énergie d'anisotropie ne présente qu'une symétrie de rotation partielle, ce qui a un effet sur l'ellipticité de la précession, contrebalançant partiellement (mais de façon marginale pour les constantes du matériau étudié dans ce chapitre) l'ellipticité induite par l'énergie de démagnétisation. De plus, la dispersion des ondes de spin et les vitesses de groupe corrélées sont affectées par la contribution de l'anisotropie, ce qui entraîne notamment un

[¶¶] Comme indiqué à la page 175, l'anisotropie magnéto-optique n'est pas prise en compte dans cette étude μBLS, car le cône focal de l'objectif du microscope produit un éclairage (et un sondage) entièrement isotrope.

[***] Qui, en fonction de la contribution de l'anisotropie cubique du second ordre, peut être identifié comme un axe moyen ou facile (de l'énergie d'anisotropie magnétocristalline), comme indiqué dans le tableau 4.1 à la page 71 : Si $K_{c2} = 0$, comme supposé dans la caractérisation dans [91] dont les résultats sont répertoriés dans le tableau 9.1 à la page 174, ce minimum dans le plan est un axe moyen et les minima globaux de l'énergie d'anisotropie cubique sont alignés avec les directions ⟨111⟩. Si $K_{c2} > 9/4 \cdot |K_{c1}|$, comme c'est le cas pour l'autre échantillon de Co_2MnSi étudié au chapitre 6 dont les résultats sont présentés dans le tableau 6.9 à la page 136, le minimum dans le plan est un minimum global et correspond à un axe facile du hypersurface d'énergie potentielle.

déplacement du bas de la bande vers des fréquences plus élevées et des vecteurs d'onde dans le plan plus grands, et par conséquent une augmentation des seuils d'instabilité non linéaire de Suhl.

En synthèse, cette étude exploratoire préliminaire de la dynamique non linéaire des ondes de spin dans le dispositif micro-dimensionné à décalage Doppler des ondes de spin a permis de tirer diverses conclusions qui soulignent le potentiel du composé Heusler semi-métallique Co_2MnSi pour d'autres applications magnoniques.

Tout d'abord, en ce qui concerne l'étude magnéto-optique du chapitre 7, un bruit important est observé tout au long de l'étude de ce chapitre 10, provenant du signal magnéto-optique généralement faible de ce composé dans le domaine visible. Un rapport signal/bruit magnéto-optique similairement médiocre provenant de ce matériau a également été observé dans les spectres BLS lors d'études précédentes menées par le groupe de magnétisme de Kaiserslautern [72, 382], ce qui a certainement motivé en partie le passage ultérieur au composé $Co_2Mn_{0.6}Fe_{0.4}Si$ dans des études plus récentes [84, 86, 87]. Par conséquent, malgré le signal magnéto-optique relativement faible et les longs délais d'acquisition des données qui en découlent, la réussite de l'étude réalisée par µBLS avec $\lambda = 491$ nm présentée dans ce chapitre 10 peut être considérée comme un signe encourageant pour l'exploitation future de dispositifs magnoniques semi-métalliques à base de Co_2MnSi notamment pour le sondage par µBLS.

Deuxièmement, dans cette étude préliminaire, aucun signe de processus de diffusion à trois magnons (instabilité de Suhl de premier ordre) n'a pu être observé. En particulier, pour le champ appliqué le plus faible à $\mu_0 H_{ext} \approx 8.9$ mT, cela indique l'impact significatif de l'anisotropie cubique qui augmente la fréquence de coupure pour la diffusion à trois magnons discutée autour de la figure 8.12 du chapitre 8. À cet égard, le Co_2MnAl non recuit, qui produit une contribution d'anisotropie cubique du second ordre déterminante dans le chapitre 6, pourrait constituer un cas intéressant à étudier dans des conditions similaires afin d'explorer plus en détail les effets du terme K_{c2}: Des calculs similaires à ceux du chapitre 8 pour un champ appliqué de 30 mT selong de la direction [110], ont un impact sur l'ellipticité de précession équivalant à ~ 23% de la force de démagnétisation, et une augmentation pouvant atteindre 20% des fréquences des ondes de spin, notamment pour les grands vecteurs d'onde. Naturellement, cela doit avoir un impact significatif sur la dynamique non linéaire dans cette direction. Et comme le terme K_{c2} ne peut pas affecter l'aimantation selon de la direction [100], on peut s'attendre à une différence qualitative assez importante si l'anisotropie est vraiment aussi élevée que déterminée dans le chapitre 8[†††].

Troisièmement, l'étude en fonction de la puissance appliqué, notamment focalisé au seuil critique de l'instabilité de Suhl du second ordre aboutit à plusieurs conclusions :

- Les seuils d'excitation non linéaires dans ce dispositif sont principalement définis par les caractéristiques de l'antenne. Plus précisément, les puissances seuils critiques imitent le spectre d'efficacité d'excitation sélective de l'antenne et des seuils de puissance critiques remarquablement bas, pouvant atteindre $P_{rf} = -11$ dBm $\approx$ 80 µW, sont obtenus à l'efficacité d'excitation maximale. Bien qu'il soit souligné qu'une comparaison directe entre des études sur différents échantillons et configurations est plutôt insignifiante, ces seuils de puissance historiquement bas mettent en évidence le potentiel d'applications supplémentaires pour exploiter la dynamique d'aimantation non linéaire dans le Co_2MnSi.
- En raison de l'efficacité d'excitation sélective du vecteur d'onde défini, le décalage non linéaire s'avère produire un gain remarquable lorsqu'il se rapproche du maximum, et de manière analogue, une baisse remarquable lorsqu'il s'en éloigne. Ce dernier cas produit une sorte de comportement d'auto-limitation.
- Une baisse de l'intensité avant l'apparition des modes secondaires détectés est observée, ce qui est probablement lié à l'apparition d'un pré-plateau dans les mesures résolues en temps. Ces deux phénomènes indiquent des processus de diffusion invisibles qui redistribuent l'énergie du mode primaire directement excité vers des modes secondaires non détectables, potentiellement en raison d'un processus sous-jacent de conservation de fréquence impliquant les modes de largeur d'ordre supérieur. Cependant, divers autres facteurs entrent en jeu et il n'est pas possible de tirer une conclusion définitive sans mener des recherches plus approfondies.

Ces résultats sont particulièrement prometteurs pour une exploitation plus poussée du Co_2MnSi semi-métallique pour la dynamique de l'aimantation non linéaire : En particulier, la combinaison des seuils de puissance critiques remarquablement bas obtenus dans cette étude et de la polarisation de spin prouvée dans le même dispositif dans l'étude [91] constitue une excellente motivation pour poursuivre les recherches. Deux exemples ont été discutés en détail : l'exploitation de la polarisation de spin des courants injectés pour renforcer le comportement non linéaire en analogie avec [60], ou la recherche d'une auto-amplification non linéaire sélective en fréquence par

[†††] Il faut tenir en compte du fait que les données de l'étude FMR rotationelle sur ce composée discutés dans le chapitre 8 étaient assez bruitées.

couplage à des résonateurs magnoniques en anneau [54], et éventuellement vers une application du comportement d'auto-amplification/auto-limitation sélective induit par un décalage non linéaire pour les circuits magnoniques neuronaux.

Enfin, en particulier en combinaison avec les résultats impeccables de nanofabrication du chapitre 3 et en combinaison avec la polarisation de spin exploitable [91], cette étude met en évidence le grand potentiel du composé demi-métallique Co_2MnSi, en particulier pour les applications à l'intersection entre la magnonique et la spintronique, et suscite donc un vif intérêt pour la poursuite des recherches expérimentales, en particulier dans le domaine des dispositifs hybrides magnoniques-spintroniques.

Bibliography

Here are the references in citation order.

[1] A. Fert. *'Nobel Lecture: Origin, development, and future of spintronics'*. In: *Reviews of Modern Physics* **80**, 4 (2008), pp. 1517–1530. DOI: 10.1103/RevModPhys.80.1517 (cited on page 1).

[2] P. A. Grünberg. *'Nobel Lecture: From spin waves to giant magnetoresistance and beyond'*. In: *Reviews of Modern Physics* **80**, 4 (2008), pp. 1531–1540. DOI: 10.1103/RevModPhys.80.1531 (cited on page 1).

[3] M. N. Baibich, J. M. Broto, A. Fert, F. N. Van Dau, F. Petroff, P. Etienne, G. Creuzet, A. Friederich, and J. Chazelas. *'Giant Magnetoresistance of (001)Fe/(001)Cr Magnetic Superlattices'*. In: *Physical Review Letters* **61**, 21 (1988), pp. 2472–2475. DOI: 10.1103/PhysRevLett.61.2472 (cited on pages 1, 10).

[4] G. Binasch, P. Grünberg, F. Saurenbach, and W. Zinn. *'Enhanced magnetoresistance in layered magnetic structures with antiferromagnetic interlayer exchange'*. In: *Physical Review B* **39**, 7 (1989), pp. 4828–4830. DOI: 10.1103/PhysRevB.39.4828 (cited on pages 1, 10).

[5] J. Daughton. *'GMR applications'*. In: *Journal of Magnetism and Magnetic Materials* **192**, 2 (1999), pp. 334–342. DOI: 10.1016/S0304-8853(98)00376-X (cited on page 1).

[6] H. Ohno. *'Toward Functional Spintronics'*. In: *Science* **291**, 5505 (2001), pp. 840–841. DOI: 10.1126/science.1058371 (cited on page 1).

[7] S. A. Wolf, D. D. Awschalom, R. A. Buhrman, J. M. Daughton, S. Von Molnár, M. L. Roukes, A. Y. Chtchelkanova, and D. M. Treger. *'Spintronics: A Spin-Based Electronics Vision for the Future'*. In: *Science* **294**, 5546 (2001), pp. 1488–1495. DOI: 10.1126/science.1065389 (cited on page 1).

[8] D. Grundler. *'Spintronics'*. In: *Physics World* **15**, 4 (2002), pp. 39–43. DOI: 10.1088/2058-7058/15/4/38 (cited on page 1).

[9] I. Žutić, J. Fabian, and S. Das Sarma. *'Spintronics: Fundamentals and applications'*. In: *Reviews of Modern Physics* **76**, 2 (2004), pp. 323–410. DOI: 10.1103/RevModPhys.76.323 (cited on page 1).

[10] C. Chappert, A. Fert, and F. N. Van Dau. *'The emergence of spin electronics in data storage'*. In: *Nature Materials* **6**, 11 (2007), pp. 813–823. DOI: 10.1038/nmat2024 (cited on page 1).

[11] S. Bader and S. Parkin. *'Spintronics'*. In: *Annual Review of Condensed Matter Physics* **1**, 1 (2010), pp. 71–88. DOI: 10.1146/annurev-conmatphys-070909-104123 (cited on page 1).

[12] E. Y. Tsymbal and Ž. Igor. Spintronics Handbook: Spin Transport and Magnetism, Second Edition: Metallic Spintronics-Volume One. Ed. by E. Y. Tsymbal and I. Žutić. 2nd ed. CRC Press, 2019. DOI: 10.1201/9780429423079 (cited on page 1).

[13] M. Dyakonov and V. Perel. *'Current-induced spin orientation of electrons in semiconductors'*. In: *Physics Letters A* **35**, 6 (1971), pp. 459–460. DOI: 10.1016/0375-9601(71)90196-4 (cited on page 1).

[14] J. E. Hirsch. *'Spin Hall Effect'*. In: *Physical Review Letters* **83**, 9 (1999), pp. 1834–1837. DOI: 10.1103/PhysRevLett.83.1834 (cited on page 1).

[15] Y. K. Kato, R. C. Myers, A. C. Gossard, and D. D. Awschalom. *'Observation of the Spin Hall Effect in Semiconductors'*. In: *Science* **306**, 5703 (2004), pp. 1910–1913. DOI: 10.1126/science.1105514 (cited on page 1).

[16] E. Saitoh, M. Ueda, H. Miyajima, and G. Tatara. *'Conversion of spin current into charge current at room temperature: Inverse spin-Hall effect'*. In: *Applied Physics Letters* **88**, 18 (2006), p. 182509. DOI: 10.1063/1.2199473 (cited on page 1).

[17] J. Slonczewski. *'Current-driven excitation of magnetic multilayers'*. In: *Journal of Magnetism and Magnetic Materials* **159**, 1-2 (1996), pp. L1–L7. DOI: 10.1016/0304-8853(96)00062-5 (cited on pages 1, 10).

[18] L. Berger. *'Emission of spin waves by a magnetic multilayer traversed by a current'*. In: *Physical Review B* **54**, 13 (1996), pp. 9353–9358. DOI: 10.1103/PhysRevB.54.9353 (cited on pages 1, 10).

[19] J. A. Katine, F. J. Albert, R. A. Buhrman, E. B. Myers, and D. C. Ralph. *'Current-Driven Magnetization Reversal and Spin-Wave Excitations in Co / Cu / Co Pillars'*. In: *Physical Review Letters* **84**, 14 (2000), pp. 3149–3152. DOI: 10.1103/PhysRevLett.84.3149 (cited on page 1).

[20] S. Zhang and Z. Li. *'Roles of Nonequilibrium Conduction Electrons on the Magnetization Dynamics of Ferromagnets'*. In: *Physical Review Letters* **93**, 12 (2004), p. 127204. DOI: 10.1103/PhysRevLett.93.127204 (cited on page 1).

[21] T. Yang, T. Kimura, and Y. Otani. *'Giant spin-accumulation signal and pure spin-current-induced reversible magnetization switching'*. In: *Nature Physics* **4**, 11 (2008), pp. 851–854. DOI: 10.1038/nphys1095 (cited on page 1).

[22] A. Brataas, A. D. Kent, and H. Ohno. *'Current-induced torques in magnetic materials'*. In: *Nature Materials* **11**, 5 (2012), pp. 372–381. DOI: 10.1038/nmat3311 (cited on page 1).

[23] R. A. De Groot, F. M. Mueller, P. G. V. Engen, and K. H. J. Buschow. *'New Class of Materials: Half-Metallic Ferromagnets'*. In: *Physical Review Letters* **50**, 25 (1983), pp. 2024–2027. DOI: 10.1103/PhysRevLett.50.2024 (cited on pages 1, 8, 9).

[24] B. Hillebrands and C. Felser. *'High-spin polarization of Heusler alloys'*. In: *Journal of Physics D: Applied Physics* **39**, 5 (2006). DOI: 10.1088/0022-3727/39/5/E01 (cited on pages 1, 2).

[25] T. Graf, C. Felser, and S. S. Parkin. *'Simple rules for the understanding of Heusler compounds'*. In: *Progress in Solid State Chemistry* **39**, 1 (2011), pp. 1–50. DOI: 10.1016/j.progsolidstchem.2011.02.001 (cited on pages 1, 8, 130).

[26] S. Mizukami and A. A. Serga. *'Advancement in Heusler compounds and other spintronics material designs and applications'*. In: *Journal of Physics D: Applied Physics* **48**, 16 (2015), p. 160301. DOI: 10.1088/0022-3727/48/16/160301 (cited on page 1).

[27] A. Hirohata, H. Sukegawa, H. Yanagihara, I. Zutic, T. Seki, S. Mizukami, and R. Swaminathan. *'Roadmap for Emerging Materials for Spintronic Device Applications'*. In: *IEEE Transactions on Magnetics* **51**, 10 (2015), pp. 1–11. DOI: 10.1109/TMAG.2015.2457393 (cited on page 1).

[28] C. Felser and A. Hirohata, eds. Heusler Alloys: Properties, Growth, Applications. Springer Series in Materials Science. ISSN: 0933-033X, 2196-2812. Cham: Springer International Publishing, 2016. DOI: 10.1007/978-3-319-21449-8 (cited on pages 1, 2, 7, 269).

[29] Y. Xie, S.-Y. Zhang, Y. Yin, N. Zheng, A. Ali, M. Younis, S. Ruan, and Y.-J. Zeng. *'Emerging ferromagnetic materials for electrical spin injection: towards semiconductor spintronics'*. In: *npj Spintronics* **3**, 1 (2025), p. 10. DOI: 10.1038/s44306-024-00070-z (cited on page 1).

[30] L. Šmejkal, J. Sinova, and T. Jungwirth. *'Beyond Conventional Ferromagnetism and Antiferromagnetism: A Phase with Nonrelativistic Spin and Crystal Rotation Symmetry'*. In: *Physical Review X* **12**, 3 (2022), p. 031042. DOI: 10.1103/PhysRevX.12.031042 (cited on page 1).

[31] L. Šmejkal, J. Sinova, and T. Jungwirth. *'Emerging Research Landscape of Altermagnetism'*. In: *Physical Review X* **12**, 4 (2022), p. 040501. DOI: 10.1103/PhysRevX.12.040501 (cited on page 1).

[32] O. Fedchenko, J. Minár, A. Akashdeep, S. W. D'Souza, D. Vasilyev, O. Tkach, L. Odenbreit, Q. Nguyen, D. Kutnyakhov, N. Wind, L. Wenthaus, M. Scholz, K. Rossnagel, M. Hoesch, M. Aeschlimann, B. Stadtmüller, M. Kläui, G. Schönhense, T. Jungwirth, A. B. Hellenes, G. Jakob, L. Šmejkal, J. Sinova, and H.-J. Elmers. *'Observation of time-reversal symmetry breaking in the band structure of altermagnetic RuO_2'*. In: *Science Advances* **10**, 5 (2024), eadj4883. DOI: 10.1126/sciadv.adj4883 (cited on page 1).

[33] Y. Kajiwara, K. Harii, S. Takahashi, J. Ohe, K. Uchida, M. Mizuguchi, H. Umezawa, H. Kawai, K. Ando, K. Takanashi, S. Maekawa, and E. Saitoh. *'Transmission of electrical signals by spin-wave interconversion in a magnetic insulator'*. In: *Nature* **464**, 7286 (2010), pp. 262–266. DOI: 10.1038/nature08876 (cited on page 1).

[34] V. Kruglyak and R. Hicken. *'Magnonics: Experiment to prove the concept'*. In: *Journal of Magnetism and Magnetic Materials* **306**, 2 (2006), pp. 191–194. DOI: 10.1016/j.jmmm.2006.02.242 (cited on page 1).

[35] A. A. Serga, A. V. Chumak, and B. Hillebrands. *'YIG magnonics'*. In: *Journal of Physics D: Applied Physics* **43**, 26 (2010), p. 264002. DOI: 10.1088/0022-3727/43/26/264002 (cited on page 1).

[36] A. Khitun, M. Bao, and K. L. Wang. *'Magnonic logic circuits'*. In: *Journal of Physics D: Applied Physics* **43**, 26 (2010), p. 264005. DOI: 10.1088/0022-3727/43/26/264005 (cited on page 1).

[37] B. Lenk, H. Ulrichs, F. Garbs, and M. Münzenberg. *'The building blocks of magnonics'*. In: *Physics Reports* **507**, 4-5 (2011), pp. 107–136. DOI: 10.1016/j.physrep.2011.06.003 (cited on page 1).

[38] A. V. Chumak, V. I. Vasyuchka, A. A. Serga, and B. Hillebrands. *'Magnon spintronics'*. In: *Nature Physics* **11**, 6 (2015), pp. 453–461. DOI: 10.1038/nphys3347 (cited on page 1).

[39] P. Pirro, V. I. Vasyuchka, A. A. Serga, and B. Hillebrands. *'Advances in coherent magnonics'*. In: *Nature Reviews Materials* **6**, 12 (2021), pp. 1114–1135. DOI: 10.1038/s41578-021-00332-w (cited on page 1).

[40] A. Barman, G. Gubbiotti, S. Ladak, A. O. Adeyeye, M. Krawczyk, J. Gräfe, C. Adelmann, S. Cotofana, A. Naeemi, V. I. Vasyuchka, B. Hillebrands, S. A. Nikitov, H. Yu, D. Grundler, A. V. Sadovnikov, A. A. Grachev, S. E. Sheshukova, J.-Y. Duquesne, M. Marangolo, G. Csaba, W. Porod, V. E. Demidov, S. Urazhdin, S. O. Demokritov, E. Albisetti, D. Petti, R. Bertacco, H. Schultheiss, V. V. Kruglyak, V. D. Poimanov, S. Sahoo, J. Sinha, H. Yang, M. Münzenberg, T. Moriyama, S. Mizukami, P. Landeros, R. A. Gallardo, G. Carlotti, J.-V. Kim, R. L. Stamps, R. E. Camley, B. Rana, Y. Otani, W. Yu, T. Yu, G. E. W. Bauer, C. Back, G. S. Uhrig, O. V. Dobrovolskiy, B. Budinska, H. Qin, S. Van Dijken, A. V. Chumak, A. Khitun, D. E. Nikonov, I. A. Young, B. W. Zingsem, and M. Winklhofer. *'The 2021 Magnonics Roadmap'*. In: *Journal of Physics: Condensed Matter* **33**, 41 (2021), p. 413001. DOI: 10.1088/1361-648X/abec1a (cited on pages 1, 46).

[41] A. V. Chumak et al. *'Advances in Magnetics Roadmap on Spin-Wave Computing'*. In: *IEEE Transactions on Magnetics* **58**, 6 (2022), pp. 1–72. DOI: 10.1109/TMAG.2022.3149664 (cited on page 1).

[42] B. Flebus, D. Grundler, B. Rana, Y. Otani, I. Barsukov, A. Barman, G. Gubbiotti, P. Landeros, J. Akerman, U. Ebels, P. Pirro, V. E. Demidov, K. Schultheiss, G. Csaba, Q. Wang, F. Ciubotaru, D. E. Nikonov, P. Che, R. Hertel, T. Ono, D. Afanasiev, J. Mentink, T. Rasing, B. Hillebrands, S. V. Kusminskiy, W. Zhang, C. R. Du, A. Finco, T. Van Der Sar, Y. K. Luo, Y. Shiota, J. Sklenar, T. Yu, and J. Rao. *'The 2024 magnonics roadmap'*. In: *Journal of Physics: Condensed Matter* **36**, 36 (2024), p. 363501. DOI: 10.1088/1361-648X/ad399c (cited on pages 1, 205).

[43] V. Vlaminck and M. Bailleul. *'Current-Induced Spin-Wave Doppler Shift'*. In: *Science* **322**, 5900 (2008), pp. 410–413. DOI: 10.1126/science.1162843 (cited on pages 1, 10, 171, 198, 279).

[44] M. Madami, S. Bonetti, G. Consolo, S. Tacchi, G. Carlotti, G. Gubbiotti, F. B. Mancoff, M. A. Yar, and J. Åkerman. *'Direct observation of a propagating spin wave induced by spin-transfer torque'*. In: *Nature Nanotechnology* **6**, 10 (2011), pp. 635–638. DOI: 10.1038/nnano.2011.140 (cited on page 1).

[45] M. Evelt, V. E. Demidov, V. Bessonov, S. O. Demokritov, J. L. Prieto, M. Muñoz, J. Ben Youssef, V. V. Naletov, G. De Loubens, O. Klein, M. Collet, K. Garcia-Hernandez, P. Bortolotti, V. Cros, and A. Anane. *'High-efficiency control of spin-wave propagation in ultra-thin yttrium iron garnet by the spin-orbit torque'*. In: *Applied Physics Letters* **108**, 17 (2016), p. 172406. DOI: 10.1063/1.4948252 (cited on page 1).

[46] O. Gladii, M. Collet, K. Garcia-Hernandez, C. Cheng, S. Xavier, P. Bortolotti, V. Cros, Y. Henry, J.-V. Kim, A. Anane, and M. Bailleul. *'Spin wave amplification using the spin Hall effect in permalloy/platinum bilayers'*. In: *Applied Physics Letters* **108**, 20 (2016), p. 202407. DOI: 10.1063/1.4952447 (cited on page 1).

[47] T. Meyer, T. Bracher, F. Heussner, A. A. Serga, H. Naganuma, K. Mukaiyama, M. Oogane, Y. Ando, B. Hillebrands, and P. Pirro. *'Realization of a Spin-Wave Switch Based on the Spin-Transfer-Torque Effect'*. In: *IEEE Magnetics Letters* **9** (2018), pp. 1–5. DOI: 10.1109/LMAG.2018.2803737 (cited on page 1).

[48] V. E. Demidov, S. Urazhdin, A. Anane, V. Cros, and S. O. Demokritov. *'Spin-orbit-torque magnonics'*. In: *Journal of Applied Physics* **127**, 17 (2020), p. 170901. DOI: 10.1063/5.0007095 (cited on page 1).

[49] R. Salikhov, I. Ilyakov, L. Körber, A. Kákay, R. A. Gallardo, A. Ponomaryov, J.-C. Deinert, T. V. A. G. De Oliveira, K. Lenz, J. Fassbender, S. Bonetti, O. Hellwig, J. Lindner, and S. Kovalev. *'Coupling of terahertz light with nanometre-wavelength magnon modes via spin–orbit torque'*. In: *Nature Physics* **19**, 4 (2023), pp. 529–535. DOI: 10.1038/s41567-022-01908-1 (cited on page 1).

[50] J. Torrejon, M. Riou, F. A. Araujo, S. Tsunegi, G. Khalsa, D. Querlioz, P. Bortolotti, V. Cros, K. Yakushiji, A. Fukushima, H. Kubota, S. Yuasa, M. D. Stiles, and J. Grollier. *'Neuromorphic computing with nanoscale spintronic oscillators'*. In: *Nature* **547**, 7664 (2017), pp. 428–431. DOI: 10.1038/nature23011 (cited on pages 2, 10).

[51] J. Grollier, D. Querlioz, K. Y. Camsari, K. Everschor-Sitte, S. Fukami, and M. D. Stiles. *'Neuromorphic spintronics'*. In: *Nature Electronics* **3**, 7 (2020), pp. 360–370. DOI: 10.1038/s41928-019-0360-9 (cited on pages 2, 10, 205).

[52] C. H. Marrows, J. Barker, T. A. Moore, and T. Moorsom. *'Neuromorphic computing with spintronics'*. In: *npj Spintronics* **2**, 1 (2024), p. 12. DOI: 10.1038/s44306-024-00019-2 (cited on pages 2, 10, 205).

[53] T. Brächer and P. Pirro. *'An analog magnon adder for all-magnonic neurons'*. In: *Journal of Applied Physics* **124**, 15 (2018), p. 152119. DOI: 10.1063/1.5042417 (cited on pages 2, 197, 208).

[54] Q. Wang, A. Hamadeh, R. Verba, V. Lomakin, M. Mohseni, B. Hillebrands, A. V. Chumak, and P. Pirro. *'A nonlinear magnonic nano-ring resonator'*. In: *npj Computational Materials* **6**, 1 (2020), p. 192. DOI: 10.1038/s41524-020-00465-6 (cited on pages 2, 4, 197, 203, 208, 281).

[55] Á. Papp, W. Porod, and G. Csaba. *'Nanoscale neural network using non-linear spin-wave interference'*. In: *Nature Communications* **12**, 1 (2021), p. 6422. DOI: 10.1038/s41467-021-26711-z (cited on page 2).

[56] K. G. Fripp, Y. Au, A. V. Shytov, and V. V. Kruglyak. *'Nonlinear chiral magnonic resonators: Toward magnonic neurons'*. In: *Applied Physics Letters* **122**, 17 (2023), p. 172403. DOI: 10.1063/5.0149466 (cited on pages 2, 197, 208).

[57] Q. Wang, G. Csaba, R. Verba, A. V. Chumak, and P. Pirro. *'Nanoscale magnonic networks'*. In: *Physical Review Applied* **21**, 4 (2024), p. 040503. DOI: 10.1103/PhysRevApplied.21.040503 (cited on page 2).

[58] D. Breitbach, M. Bechberger, B. Heinz, A. Hamadeh, J. Maskill, K. O. Levchenko, B. Lägel, C. Dubs, Q. Wang, R. Verba, and P. Pirro. *'Nonlinear erasing of propagating spin-wave pulses in thin-film Ga:YIG'*. In: *Applied Physics Letters* **124**, 9 (2024), p. 092405. DOI: 10.1063/5.0189648 (cited on pages 2, 197).

[59] A. Hamadeh, D. Breitbach, M. Ender, A. Koujok, M. Mohseni, F. Kohl, J. Maskill, M. Bechberger, and P. Pirro. *'Hybrid magnonic-oscillator system'*. In: *Journal of Applied Physics* **132**, 18 (2022), p. 183904. DOI: 10.1063/5.0123471 (cited on page 2).

[60] T. Hache, L. Körber, T. Hula, K. Lenz, A. Kákay, O. Hellwig, J. Lindner, J. Fassbender, and H. Schultheiss. *'Control of Four-Magnon Scattering by Pure Spin Current in a Magnonic Waveguide'*. In: *Physical Review Applied* **20**, 1 (2023), p. 014062. DOI: 10.1103/PhysRevApplied.20.014062 (cited on pages 2, 163, 197, 198, 203, 208, 278, 280).

[61] H. Merbouche, B. Divinskiy, D. Gouéré, R. Lebrun, A. El Kanj, V. Cros, P. Bortolotti, A. Anane, S. O. Demokritov, and V. E. Demidov. *'True amplification of spin waves in magnonic nano-waveguides'*. In: *Nature Communications* **15**, 1 (2024), p. 1560. DOI: 10.1038/s41467-024-45783-1 (cited on pages 2, 10).

[62] R. M. Menezes, J. Mulkers, C. C. De Souza Silva, B. Van Waeyenberge, and M. V. Milošević. *'Toward magnonic logic and neuromorphic computing: controlling spin waves by spin-polarized current'*. In: *Physical Review Applied* **22**, 5 (2024), p. 054056. DOI: 10.1103/PhysRevApplied.22.054056 (cited on page 2).

[63] P. Webster. *'Magnetic and chemical order in Heusler alloys containing cobalt and manganese'*. In: *Journal of Physics and Chemistry of Solids* **32**, 6 (1971), pp. 1221–1231. DOI: 10.1016/S0022-3697(71)80180-4 (cited on pages 2, 14, 16, 112).

[64] C. Guillemard, S. Petit-Watelot, L. Pasquier, D. Pierre, J. Ghanbaja, J.-C. Rojas-Sánchez, A. Bataille, J. Rault, P. Le Fèvre, F. Bertran, and S. Andrieu. *'Ultralow Magnetic Damping in Co_2Mn-Based Heusler Compounds: Promising Materials for Spintronics'*. In: *Physical Review Applied* **11**, 6 (2019), p. 064009. DOI: 10.1103/PhysRevApplied.11.064009 (cited on pages 2, 11, 13, 14, 23, 82, 134, 205).

[65] J. Schmalhorst, S. Kämmerer, M. Sacher, G. Reiss, A. Hütten, and A. Scholl. *'Interface structure and magnetism of magnetic tunnel junctions with a Co 2 Mn Si electrode'*. In: *Physical Review B* **70**, 2 (2004), p. 024426. DOI: 10.1103/PhysRevB.70.024426 (cited on page 2).

[66] Y. Sakuraba, J. Nakata, M. Oogane, H. Kubota, Y. Ando, A. Sakuma, and T. Miyazaki. *'Huge Spin-Polarization of $L2_1$ -Ordered Co_2 MnSi Epitaxial Heusler Alloy Film'*. In: *Japanese Journal of Applied Physics* **44**, 8L (2005), p. L1100. DOI: 10.1143/JJAP.44.L1100 (cited on page 2).

[67] Y. Sakuraba, M. Hattori, M. Oogane, Y. Ando, H. Kato, A. Sakuma, T. Miyazaki, and H. Kubota. *'Giant tunneling magnetoresistance in Co_2MnSi/Al–O/Co_2MnSi magnetic tunnel junctions'*. In: *Applied Physics Letters* **88**, 19 (2006), p. 192508. DOI: 10.1063/1.2202724 (cited on page 2).

[68] S. Ishida, S. Fujii, S. Kashiwagi, and S. Asano. *'Search for Half-Metallic Compounds in Co_2MnZ (Z=IIIb, IVb, Vb Element)'*. In: *Journal of the Physical Society of Japan* **64**, 6 (1995), pp. 2152–2157. DOI: 10.1143/JPSJ.64.2152 (cited on pages 2, 8, 13).

[69] M. Jourdan, J. Minár, J. Braun, A. Kronenberg, S. Chadov, B. Balke, A. Gloskovskii, M. Kolbe, H. Elmers, G. Schönhense, H. Ebert, C. Felser, and M. Kläui. *'Direct observation of half-metallicity in the Heusler compound Co_2MnSi'*. In: *Nature Communications* **5**, 1 (2014), p. 3974. DOI: 10.1038/ncomms4974 (cited on pages 2, 11, 13, 205).

[70] S. Andrieu, A. Neggache, T. Hauet, T. Devolder, A. Hallal, M. Chshiev, A. M. Bataille, P. Le Fèvre, and F. Bertran. *'Direct evidence for minority spin gap in the Co_2MnSi Heusler compound'*. In: *Physical Review B* **93**, 9 (2016), p. 094417. DOI: 10.1103/PhysRevB.93.094417 (cited on pages 2, 13, 205).

[71] C. Guillemard, S. Petit-Watelot, T. Devolder, L. Pasquier, P. Boulet, S. Migot, J. Ghanbaja, F. Bertran, and S. Andrieu. *'Issues in growing Heusler compounds in thin films for spintronic applications'*. In: *Journal of Applied Physics* **128**, 24 (2020), p. 241102. DOI: 10.1063/5.0014241 (cited on pages 2, 9, 11–18, 23–26, 32, 33, 35, 37–39, 43, 46, 112, 114, 116, 117, 121, 129, 142, 271).

[72] O. Gaier, J. Hamrle, S. J. Hermsdoerfer, H. Schultheiß, B. Hillebrands, Y. Sakuraba, M. Oogane, and Y. Ando. *'Influence of the $L2_1$ ordering degree on the magnetic properties of Co_2MnSi Heusler films'*. In: *Journal of Applied Physics* **103**, 10 (2008), p. 103910. DOI: 10.1063/1.2931023 (cited on pages 2, 12, 13, 15, 16, 18, 25, 26, 42, 46, 89, 129, 138, 202, 207, 208, 280).

[73] J. M. Shaw, E. K. Delczeg-Czirjak, E. R. J. Edwards, Y. Kvashnin, D. Thonig, M. A. W. Schoen, M. Pufall, M. L. Schneider, T. J. Silva, O. Karis, K. P. Rice, O. Eriksson, and H. T. Nembach. *'Magnetic damping in sputter-deposited Co_2MnGe Heusler compounds with A2, B2, and $L2_1$ orders: Experiment and theory'*. In: *Physical Review B* **97**, 9 (2018), p. 094420. DOI: 10.1103/PhysRevB.97.094420 (cited on pages 2, 12, 13).

[74] J. Hamrle, S. Blomeier, O. Gaier, B. Hillebrands, H. Schneider, G. Jakob, B. Reuscher, A. Brodyanski, M. Kopnarski, K. Postava, and C. Felser. *'Ion beam induced modification of exchange interaction and spin–orbit coupling in the Co_2FeSi Heusler compound'*. In: *Journal of Physics D: Applied Physics* **40**, 6 (2007), pp. 1558–1562. DOI: 10.1088/0022-3727/40/6/S08 (cited on pages 2, 46, 53, 89, 272).

[75] I. Abdallah, N. Ratel-Ramond, C. Magen, B. Pecassou, R. Cours, A. Arnoult, M. Respaud, J. F. Bobo, G. BenAssayag, E. Snoeck, and N. Biziere. *'Structural and magnetic properties of He^+ irradiated Co_2MnSi Heusler alloys'*. In: *Materials Research Express* **3**, 4 (2016), p. 046101. DOI: 10.1088/2053-1591/3/4/046101 (cited on pages 2, 46, 272).

[76] I. Abdallah, B. Pradines, N. Ratel-Ramond, G. BenAssayag, R. Arras, L. Calmels, J. F. Bobo, E. Snoeck, and N. Biziere. *'Evolution of magnetic properties and damping coefficient of Co_2MnSi Heusler alloy with Mn/Si and Co/Mn atomic disorder'*. In: *Journal of Physics D: Applied Physics* **50**, 3 (2017), p. 035003. DOI: 10.1088/1361-6463/50/3/035003 (cited on pages 2, 12, 13, 46, 53, 121, 272).

[77] S. Mantion and N. Biziere. *'Influence of Ga+ milling on the spin waves modes in a Co_2MnSi Heusler magnonic crystal'*. In: *Journal of Applied Physics* **131**, 11 (2022), p. 113905. DOI: 10.1063/5.0085623 (cited on pages 2, 3, 46, 205, 272).

[78] H. Chudo, K. Ando, K. Saito, S. Okayasu, R. Haruki, Y. Sakuraba, H. Yasuoka, K. Takanashi, and E. Saitoh. *'Spin pumping efficiency from half metallic Co_2MnSi'*. In: *Journal of Applied Physics* **109**, 7 (2011), p. 073915. DOI: 10.1063/1.3556433 (cited on page 2).

[79] Y. Sasaki, S. Sugimoto, Y. K. Takahashi, and S. Kasai. *'Spin injection efficiency through the pumping in epitaxial Co2MnSi/Pt thin film'*. In: *AIP Advances* **10**, 8 (2020), p. 085311. DOI: 10.1063/5.0008393 (cited on page 2).

[80] J. Létang, C. De Melo, C. Guillemard, A. Vecchiola, D. Rontani, S. Petit-Watelot, M.-W. Yoo, T. Devolder, K. Bouzehouane, V. Cros, S. Andrieu, and J.-V. Kim. *'Nanocontact vortex oscillators based on Co_2MnGe pseudo spin valves'*. In: *Physical Review B* **103**, 22 (2021), p. 224424. DOI: 10.1103/PhysRevB.103.224424 (cited on pages 2, 23, 117).

[81] C. De Melo, C. Guillemard, A. Friedel, V. Palin, J. Rojas-Sánchez, S. Petit-Watelot, and S. Andrieu. *'Unveiling transport properties of Co_2MnSi Heusler epitaxial thin films with ultra-low magnetic damping'*. In: *Applied Materials Today* **25** (2021), p. 101174. DOI: 10.1016/j.apmt.2021.101174 (cited on pages 2, 11, 13, 14, 23, 39, 42, 129, 134, 135, 206).

[82] R. Silber, D. Král, O. Stejskal, T. Kubota, Y. Ando, J. Pištora, M. Veis, J. Hamrle, and T. Kuschel. *'Scaling of quadratic and linear magneto-optic Kerr effect spectra with $L2_1$ ordering of Co_2MnSi Heusler compound'*. In: *Applied Physics Letters* **116**, 26 (2020), p. 262401. DOI: 10.1063/5.0008427 (cited on pages 2, 3, 89, 137, 143, 145–147, 207, 276).

[83] A. M. Friedel. Thin film materials with ultralow damping for novel magnonic phenomena. Diplomarbeit. Kaiserslautern, Germany: Technische Universität Kaiserslautern, 2021. DOI: 10.26204/KLUEDO/9524 (cited on pages 2, 18, 23, 28, 30, 35, 39, 42, 95, 114, 121, 129, 135, 137, 145, 146, 148, 206, 208, 276).

[84] T. Sebastian, Y. Ohdaira, T. Kubota, P. Pirro, T. Brächer, K. Vogt, A. A. Serga, H. Naganuma, M. Oogane, Y. Ando, and B. Hillebrands. *'Low-damping spin-wave propagation in a micro-structured $Co_2Mn_{0.6}Fe_{0.4}Si$ Heusler waveguide'*. In: *Applied Physics Letters* **100**, 11 (2012), p. 112402. DOI: 10.1063/1.3693391 (cited on pages 2, 202, 208, 280).

[85] T. Sebastian, T. Brächer, P. Pirro, A. A. Serga, B. Hillebrands, T. Kubota, H. Naganuma, M. Oogane, and Y. Ando. *'Nonlinear Emission of Spin-Wave Caustics from an Edge Mode of a Microstructured $Co_2Mn_{0.6}Fe_{0.4}Si$ Waveguide'*. In: *Physical Review Letters* **110**, 6 (2013), p. 067201. DOI: 10.1103/PhysRevLett.110.067201 (cited on pages 2, 208).

[86] P. Pirro, T. Sebastian, T. Brächer, A. A. Serga, T. Kubota, H. Naganuma, M. Oogane, Y. Ando, and B. Hillebrands. *'Non-Gilbert-damping Mechanism in a Ferromagnetic Heusler Compound Probed by Nonlinear Spin Dynamics'*. In: *Physical Review Letters* **113**, 22 (2014), p. 227601. DOI: 10.1103/PhysRevLett.113.227601 (cited on pages 2, 4, 162, 167, 177, 193, 202, 208, 278, 280).

[87] T. Sebastian, Y. Kawada, B. Obry, T. Brächer, P. Pirro, D. A. Bozhko, A. A. Serga, H. Naganuma, M. Oogane, Y. Ando, and B. Hillebrands. *'All-optical characterisation of the spintronic Heusler compound $Co_2Mn_{0.6}Fe_{0.4}Si$'*. In: *Journal of Physics D: Applied Physics* **48**, 16 (2015), p. 164015. DOI: 10.1088/0022-3727/48/16/164015 (cited on pages 2, 202, 208, 280).

[88] T. Sebastian and B. Hillebrands. *'Chapter 13: $Co_2Mn_{0.6}Fe_{0.4}Si$: A Heusler Compound Opening New Perspectives in Magnon Spintronics'*. In: *Heusler Alloys*. Ed. by C. Felser and A. Hirohata. Vol. 222. Series Title: Springer Series in Materials Science. Cham: Springer International Publishing, 2016, pp. 321–340. DOI: 10.1007/978-3-319-21449-8_13 (cited on pages 2, 208).

[89] T. Stückler, C. Liu, H. Yu, F. Heimbach, J. Chen, J. Hu, S. Tu, M. Alam, J. Zhang, Y. Zhang, I. L. Farrell, C. Emeny, S. Granville, Z.-M. Liao, D. Yu, and W. Zhao. *'Spin wave propagation detected over 100um in half-metallic Heusler alloy Co_2MnSi'*. In: *Journal of Magnetism and Magnetic Materials* **450** (2018), pp. 13–17. DOI: 10.1016/j.jmmm.2017.09.074 (cited on pages 2, 11).

[90] S. Mantion, A. Torres Dias, M. Madami, S. Tacchi, and N. Biziere. *'Reconfigurable spin wave modes in a Heusler magnonic crystal'*. In: *Journal of Applied Physics* **135**, 5 (2024), p. 053902. DOI: 10.1063/5.0189486 (cited on pages 2, 14, 208).

[91] J. N. Solano Córdova. *'Temperature dependent spin wave study of magnetic properties and spin-polarized electron transport in $Fe_{1-X}V_X$ and Co_2MnSi epitaxial films'*. PhD thesis. Strasbourg, France: Université de Strasbourg, 2024 (cited on pages 2, 4, 7, 43, 122, 124, 134, 171, 173, 174, 177, 178, 183, 188, 197, 198, 203, 208, 209, 269, 279–281).

[92] A. A. Knowlton and O. C. Clifford. *'The Heusler alloys'*. In: *Transactions of the Faraday Society* **8**, October (1912), p. 195. DOI: 10.1039/tf9120800195 (cited on pages 7, 269).

[93] I. Galanakis. *'Chapter 1: Theory of Heusler and Full-Heusler Compounds'*. In: *Heusler Alloys*. Ed. by C. Felser and A. Hirohata. Vol. 222. Series Title: Springer Series in Materials Science. Cham: Springer International Publishing, 2016, pp. 3–36. DOI: 10.1007/978-3-319-21449-8_1 (cited on pages 7, 8, 11, 269).

[94] O. Gaier. *'A study of exchange interaction, magnetic anisotropies, and ion beam induced effects in thin films of Co_2-based Heusler compounds'*. PhD thesis. Kaiserslautern, Germany: Technische Universität Kaiserslautern, 2009 (cited on pages 7, 107, 108, 269, 276).

[95] G. Ortiz Hernandez. *'Élaboration et étude des propriétés physiques de couches minces monocristallines d'alliage de Heusler à faible amortissement magnétique pour composants hyperfréquences'*. PhD thesis. Toulouse, France: Université Toulouse 3, 2013 (cited on pages 7, 269).

[96] T. Sebastian. *'Linear and nonlinear spin dynamics in $Co_2Mn_{0.6}Fe_{0.4}Si$ Heusler microstructures'*. PhD thesis. Kaiserslautern, Germany: Technische Universität Kaiserslautern, 2013 (cited on pages 7, 269).

[97] P. Pirro. *'Lineare und nichtlineare Spinwelleninteraktionen in magnetischen Mikrostrukturen'*. PhD thesis. Kaiserslautern, Germany: Technische Universität Kaiserslautern, 2014 (cited on pages 7, 161–163, 165, 166, 168, 177, 187–191, 196, 198, 202, 208, 269).

[98] A. Neggache. *'Propriétés électroniques des alliages d'Heusler $Co_{1.5}Fe_{1.5}Ge$ et Co_2MnSi'*. PhD thesis. Nancy, France: Université de Lorraine, 2014 (cited on pages 7, 269).

[99] I. Abdallah. *'Spin dynamics and structural modifications of Co_2MnSi Heusler alloys by helium ions irradiation'*. PhD thesis. Toulouse, France: Université Toulouse 3, 2016 (cited on pages 7, 269).

[100] T. Meyer. *'Spin Orbit Torque Driven Spin Wave Dynamics in Microstructured Heusler Magnon Conduits'*. PhD thesis. Kaiserslautern, Germany: Technische Universität Kaiserslautern, 2017 (cited on pages 7, 176, 269).

[101] B. Pradines. *'Structure électronique et propriétés magnétiques statiques et dynamiques d'alliages d'Heusler partiellement désordonnés et d'hétérostructures tout-Heusler'*. PhD thesis. Toulouse, France: Université Toulouse 3, 2017 (cited on pages 7, 269).

[102] R. Silber. *'Quadratic magnetooptic Kerr effect spectroscopy of magnetic thin films with cubic crystal structure'*. PhD thesis. Ostrava, Czech Republic and Bielefeld, Germany: Technical University of Ostrava and Bielefeld University, 2019 (cited on pages 7, 107, 108, 141, 144, 269).

[103] C. Guillemard. *'Half-metal magnets Heusler compounds for spintronics'*. PhD thesis. Nancy, France: Université de Lorraine, 2019 (cited on pages 7, 16, 21–24, 26, 28, 30, 33, 37, 43, 44, 116, 117, 129, 130, 140, 269).

[104] J. Létang. *'États chaotiques et effets de modulation dans des oscillateurs à vortex'*. PhD thesis. Orsay, France: Université Paris-Saclay, 2020 (cited on pages 7, 269).

[105] V. Palin. *'Heusler compounds for spin-orbitronics: exploration of topological effects and magnetic anisotropy engineering'*. PhD thesis. Université de Lorraine, 2023 (cited on pages 7, 18, 23, 27, 269).

[106] S. Mantion. *'Study of Co_2MnSi Heusler alloy magnonic crystals'*. PhD thesis. Toulouse, France: Université Toulouse 3, 2023 (cited on pages 7, 46, 269, 272).

[107] A. Islam. *'Voltage Control of Perpendicular Magnetic Anisotropy of CoFeB and Co_2MnGa-based Stacks for Sensing Applications'*. PhD thesis. Te Herenga Waka-Victoria University of Wellington, 2025. DOI: 10.26686/wgtn.28621430 (cited on page 7).

[108] H. C. Kandpal, G. H. Fecher, and C. Felser. *'Calculated electronic and magnetic properties of the half-metallic, transition metal based Heusler compounds'*. In: *Journal of Physics D: Applied Physics* **40**, 6 (2007), pp. 1507–1523. DOI: 10.1088/0022-3727/40/6/S01 (cited on pages 8, 9, 13).

[109] C. M. Fang, G. A. De Wijs, and R. A. De Groot. *'Spin-polarization in half-metals (invited)'*. In: *Journal of Applied Physics* **91**, 10 (2002), pp. 8340–8344. DOI: 10.1063/1.1452238 (cited on pages 8, 12).

[110] J.-H. Park, E. Vescovo, H.-J. Kim, C. Kwon, R. Ramesh, and T. Venkatesan. *'Direct evidence for a half-metallic ferromagnet'*. In: *Nature* **392**, 6678 (1998), pp. 794–796. DOI: 10.1038/33883 (cited on pages 8, 11, 14).

[111] J. Friedel. *'Metallic alloys'*. In: *Il Nuovo Cimento* **7**, S2 (1958), pp. 287–311. DOI: 10.1007/BF02751483 (cited on page 9).

[112] A. Williams, V. Moruzzi, A. Malozemoff, and K. Terakura. *'Generalized Slater-Pauling curve for transition-metal magnets'*. In: *IEEE Transactions on Magnetics* **19**, 5 (1983), pp. 1983–1988. DOI: 10.1109/TMAG.1983.1062706 (cited on page 9).

[113] J. Kübler. *'First principle theory of metallic magnetism'*. In: *Physica B+C* **127**, 1-3 (1984), pp. 257–263. DOI: 10.1016/S0378-4363(84)80039-X (cited on page 9).

[114] I. Galanakis, P. H. Dederichs, and N. Papanikolaou. *'Slater-Pauling behavior and origin of the half-metallicity of the full-Heusler alloys'*. In: *Physical Review B* **66**, 17 (2002), p. 174429. DOI: 10.1103/PhysRevB.66.174429 (cited on pages 9, 13, 112, 114, 116).

[115] P. J. Brown, K. U. Neumann, P. J. Webster, and K. R. A. Ziebeck. *'The magnetization distributions in some Heusler alloys proposed as half-metallic ferromagnets'*. In: *Journal of Physics: Condensed Matter* **12**, 8 (2000), pp. 1827–1835. DOI: 10.1088/0953-8984/12/8/325 (cited on page 9).

[116] C. Guillemard, W. Zhang, G. Malinowski, C. De Melo, J. Gorchon, S. Petit-Watelot, J. Ghanbaja, S. Mangin, P. Le Fèvre, F. Bertran, and S. Andrieu. *'Engineering $Co_2MnAl_xSi_{1-x}$ Heusler Compounds as a Model System to Correlate Spin Polarization, Intrinsic Gilbert Damping, and Ultrafast Demagnetization'*. In: *Advanced Materials* **32**, 26 (2020), p. 1908357. DOI: 10.1002/adma.201908357 (cited on pages 9, 15, 16, 23, 270).

[117] A. Kumar, N. Srivastava, V. Chaudhary, A. K. Atul, S. Jharwal, A. S. Negi, B. Prajapati, R. P. Singh, M. Kumar, and J. Kumar. *'Exploring the physical properties of Co_2MnSi full Heusler alloy: a first principles study'*. In: *Optical and Quantum Electronics* **56**, 3 (2024), p. 358. DOI: 10.1007/s11082-023-05970-8 (cited on pages 10, 13, 14, 16, 129, 130).

[118] M. Julliere. *'Tunneling between ferromagnetic films'*. In: *Physics Letters A* **54**, 3 (1975), pp. 225–226. DOI: 10.1016/0375-9601(75)90174-7 (cited on page 10).

[119] S. Ikegawa, F. B. Mancoff, and S. Aggarwal. *'Commercialization of MRAM – Historical and Future Perspective'*. In: *2021 IEEE International Interconnect Technology Conference (IITC)*. Kyoto, Japan: IEEE, 2021, pp. 1–3. DOI: 10.1109/IITC51362.2021.9537434 (cited on page 10).

[120] D. C. Worledge and G. Hu. *'Spin-transfer torque magnetoresistive random access memory technology status and future directions'*. In: *Nature Reviews Electrical Engineering* **1**, 11 (2024), pp. 730–747. DOI: 10.1038/s44287-024-00111-z (cited on page 10).

[121] L. Liu, O. J. Lee, T. J. Gudmundsen, D. C. Ralph, and R. A. Buhrman. *'Current-Induced Switching of Perpendicularly Magnetized Magnetic Layers Using Spin Torque from the Spin Hall Effect'*. In: *Physical Review Letters* **109**, 9 (2012), p. 096602. DOI: 10.1103/PhysRevLett.109.096602 (cited on page 10).

[122] J. Z. Sun. *'Spin-current interaction with a monodomain magnetic body: A model study'*. In: *Physical Review B* **62**, 1 (2000), pp. 570–578. DOI: 10.1103/PhysRevB.62.570 (cited on page 10).

[123] S. I. Kiselev, J. C. Sankey, I. N. Krivorotov, N. C. Emley, R. J. Schoelkopf, R. A. Buhrman, and D. C. Ralph. *'Microwave oscillations of a nanomagnet driven by a spin-polarized current'*. In: *Nature* **425**, 6956 (2003), pp. 380–383. DOI: 10.1038/nature01967 (cited on page 10).

[124] S. Yang, J. Shin, T. Kim, K.-W. Moon, J. Kim, G. Jang, D. S. Hyeon, J. Yang, C. Hwang, Y. Jeong, and J. P. Hong. *'Integrated neuromorphic computing networks by artificial spin synapses and spin neurons'*. In: *NPG Asia Materials* **13**, 1 (2021), p. 11. DOI: 10.1038/s41427-021-00282-3 (cited on page 10).

[125] T. Böhnert, Y. Rezaeiyan, M. S. Claro, L. Benetti, A. S. Jenkins, H. Farkhani, F. Moradi, and R. Ferreira. *'Weighted spin torque nano-oscillator system for neuromorphic computing'*. In: *Communications Engineering* **2**, 1 (2023), p. 65. DOI: 10.1038/s44172-023-00117-9 (cited on page 10).

[126] K. Roy, C. Wang, S. Roy, A. Raghunathan, K. Yang, and A. Sengupta. *'Spintronic neural systems'*. In: *Nature Reviews Electrical Engineering* **1**, 11 (2024), pp. 714–729. DOI: 10.1038/s44287-024-00107-9 (cited on page 10).

[127] S. O. Demokritov and A. N. Slavin, eds. Magnonics: from fundamentals to applications. Topics in applied physics 125. Berlin Heidelberg: Springer, 2013. DOI: 10.1007/978-3-642-30247-3 (cited on page 10).

[128] N. Locatelli, V. Cros, and J. Grollier. *'Spin-torque building blocks'*. In: *Nature Materials* **13**, 1 (2014), pp. 11–20. DOI: 10.1038/nmat3823 (cited on page 10).

[129] S. Urazhdin, V. E. Demidov, H. Ulrichs, T. Kendziorczyk, T. Kuhn, J. Leuthold, G. Wilde, and S. O. Demokritov. *'Nanomagnonic devices based on the spin-transfer torque'*. In: *Nature Nanotechnology* **9**, 7 (2014), pp. 509–513. DOI: 10.1038/nnano.2014.88 (cited on page 10).

[130] A. Slavin and V. Tiberkevich. *'Nonlinear Auto-Oscillator Theory of Microwave Generation by Spin-Polarized Current'*. In: *IEEE Transactions on Magnetics* **45**, 4 (2009), pp. 1875–1918. DOI: 10.1109/TMAG.2008.2009935 (cited on pages 11, 164, 278).

[131] G. Gurjar, V. Sharma, S. Patnaik, and B. K. Kuanr. *'Structural and magnetic properties of high quality single crystalline YIG thin film: A comparison with the bulk YIG'*. In: Hisar, Haryana, India, 2019, p. 030323. DOI: 10.1063/1.5113162 (cited on pages 11, 14).

[132] C. Dubs, O. Surzhenko, R. Thomas, J. Osten, T. Schneider, K. Lenz, J. Grenzer, R. Hübner, and E. Wendler. *'Low damping and microstructural perfection of sub-40nm-thin yttrium iron garnet films grown by liquid phase epitaxy'*. In: *Physical Review Materials* **4**, 2 (2020), p. 024416. DOI: 10.1103/PhysRevMaterials.4.024416 (cited on pages 11, 14, 124).

[133] B. Rana, Y. Fukuma, K. Miura, H. Takahashi, and Y. Otani. *'Supplementary Material: Excitation of coherent propagating spin waves in ultrathin CoFeB film by voltage-controlled magnetic anisotropy'*. In: *Applied Physics Letters* **111**, 5 (2017), p. 052404. DOI: 10.1063/1.4990724 (cited on pages 11, 14).

[134] T. Manago, K. Yamanoi, S. Kasai, and S. Mitani. *'Damping factor estimation using spin wave attenuation in permalloy film'*. In: *Journal of Applied Physics* **117**, 17 (2015), p. 17D121. DOI: 10.1063/1.4914538 (cited on pages 11, 14).

[135] S. Picozzi, A. Continenza, and A. Freeman. *'First principles study of electronic and magnetic properties of Co_2MnGe/GaAs interfaces'*. In: *Journal of Physics and Chemistry of Solids* **64**, 9-10 (2003), pp. 1697–1701. DOI: 10.1016/S0022-3697(03)00121-5 (cited on page 11).

[136] S. Picozzi, A. Continenza, and A. J. Freeman. *'Spin injection at Heusler/semiconductor interfaces: First-principles determination of potential discontinuity and half-metallicity'*. In: *Journal of Applied Physics* **94**, 7 (2003), pp. 4723–4725. DOI: 10.1063/1.1608469 (cited on page 11).

[137] A. Kumar, S. Chaudhary, and S. Chandra. *'Effect of point defects and lattice distortions on the structural, electronic, and magnetic properties of Co_2MnAl Heusler alloy'*. In: *Physical Review Materials* **8**, 3 (2024), p. 034405. DOI: 10.1103/PhysRevMaterials.8.034405 (cited on page 11).

[138] T. Saito and D. Nishio-Hamane. *'Magnetic and thermoelectric properties of Co_2MnT (T = Ga, Si) Heusler compounds'*. In: *Physica B: Condensed Matter* **603** (2021), p. 412761. DOI: 10.1016/j.physb.2020.412761 (cited on page 12).

[139] A. Sakuma. *'First-principles study of the Gilbert damping constants of Heusler alloys based on the torque correlation model'*. In: *Journal of Physics D: Applied Physics* **48**, 16 (2015), p. 164011. DOI: 10.1088/0022-3727/48/16/164011 (cited on page 12).

[140] B. Pradines, R. Arras, I. Abdallah, N. Biziere, and L. Calmels. *'First-principles calculation of the effects of partial alloy disorder on the static and dynamic magnetic properties of Co_2MnSi'*. In: *Physical Review B* **95**, 9 (2017), p. 094425. DOI: 10.1103/PhysRevB.95.094425 (cited on pages 12, 13, 42).

[141] A. Kumar, V. Barwal, R. K. Meena, S. Chaudhary, and S. Chandra. *'B2-disorder effects on the structural, electronic and magnetic properties of Co_2MnAl Heusler alloy'*. In: *Journal of Magnetism and Magnetic Materials* **563** (2022), p. 169871. DOI: 10.1016/j.jmmm.2022.169871 (cited on page 12).

[142] C. Guillemard, S. Petit-Watelot, J.-C. Rojas-Sánchez, J. Hohlfeld, J. Ghanbaja, A. Bataille, P. Le Fèvre, F. Bertran, and S. Andrieu. *'Polycrystalline Co_2Mn-based Heusler thin films with high spin polarization and low magnetic damping'*. In: *Applied Physics Letters* **115**, 17 (2019), p. 172401. DOI: 10.1063/1.5121614 (cited on pages 13, 15–17).

[143] S. Fujii, S. Sugimura, Ishida, and S. Asano. *'Hyperfine fields and electronic structures of the Heusler alloys Co_2MnX (X=Al, Ga, Si, Ge, Sn)'*. In: *Journal of Physics: Condensed Matter* **2**, 43 (1990), pp. 8583–8589. DOI: 10.1088/0953-8984/2/43/004 (cited on page 13).

[144] S. Picozzi, A. Continenza, and A. J. Freeman. *'Co_2MnX (X = Si , Ge, Sn) Heusler compounds: An ab initio study of their structural, electronic, and magnetic properties at zero and elevated pressure'*. In: *Physical Review B* **66**, 9 (2002), p. 094421. DOI: 10.1103/PhysRevB.66.094421 (cited on page 13).

[145] J. Kübler, G. H. Fecher, and C. Felser. *'Understanding the trend in the Curie temperatures of Co_2-based Heusler compounds: Ab initio calculations'*. In: *Physical Review B* **76**, 2 (2007), p. 024414. DOI: 10.1103/PhysRevB.76.024414 (cited on pages 13, 14).

[146] C. Liu, C. K. A. Mewes, M. Chshiev, T. Mewes, and W. H. Butler. *'Origin of low Gilbert damping in half metals'*. In: *Applied Physics Letters* **95**, 2 (2009), p. 022509. DOI: 10.1063/1.3157267 (cited on pages 13, 14, 81, 82).

[147] A. Conca, E. T. Papaioannou, S. Klingler, J. Greser, T. Sebastian, B. Leven, J. Lösch, and B. Hillebrands. *'Annealing influence on the Gilbert damping parameter and the exchange constant of CoFeB thin films'*. In: *Applied Physics Letters* **104**, 18 (2014), p. 182407. DOI: 10.1063/1.4875927 (cited on page 14).

[148] S. Mantion and N. Biziere. *'Cubic Anisotropy for a Reconfigurable Magnonic Crystal Based on Co_2MnSi Heusler Alloy'*. In: *Physical Review Applied* **17**, 4 (2022), p. 044054. DOI: 10.1103/PhysRevApplied.17.044054 (cited on pages 14–16, 270).

[149] A. Kharmouche. *'An experimental study of the static magnetic properties of Co thin films'*. In: *The European Physical Journal B* **97**, 6 (2024), p. 87. DOI: 10.1140/epjb/s10051-024-00729-w (cited on page 14).

[150] V. Cherepanov, I. Kolokolov, and V. L'vov. *'The saga of YIG: Spectra, thermodynamics, interaction and relaxation of magnons in a complex magnet'*. In: *Physics Reports* **229**, 3 (1993), pp. 81–144. DOI: 10.1016/0370-1573(93)90107-O (cited on page 14).

[151] I. Abdallah, B. Pradines, N. Ratel-Ramond, G. BenAssayag, R. Arras, L. Calmels, J. F. Bobo, E. Snoeck, and N. Biziere. *'Corrigendum: Evolution of magnetic properties and damping coefficient of Co_2MnSi Heusler alloy with Mn/Si and Co/Mn atomic disorder (2017 J. Phys. D: Appl. Phys . **50** 035003)'*. In: *Journal of Physics D: Applied Physics* **50**, 35 (2017), p. 359501. DOI: 10.1088/1361-6463/aa7e24 (cited on pages 15, 16).

[152] S.-Z. Qiao, J. Zhang, Y.-F. Qin, R.-R. Hao, H. Zhong, D.-P. Zhu, Y. Kang, S.-S. Kang, S.-Y. Yu, G.-B. Han, S.-S. Yan, and L.-M. Mei. *'Structural and Magnetic Properties of Co_2MnSi Thin Film with a Low Damping Constant'*. In: *Chinese Physics Letters* **32**, 5 (2015), p. 057601. DOI: 10.1088/0256-307X/32/5/057601 (cited on page 15).

[153] T. Kubota, J. Hamrle, Y. Sakuraba, O. Gaier, M. Oogane, A. Sakuma, B. Hillebrands, K. Takanashi, and Y. Ando. *'Structure, exchange stiffness, and magnetic anisotropy of $Co_2MnAl_xSi_{1-x}$Heusler compounds'*. In: *Journal of Applied Physics* **106**, 11 (2009), p. 113907. DOI: 10.1063/1.3265428 (cited on pages 15, 16, 127–129, 208, 270).

[154] M. Özduran, A. Candan, S. Akbudak, A. Kushwaha, and A. İyigör. *'Structural, elastic, electronic, and magnetic properties of Si-doped Co_2MnGe full-Heusler type compounds'*. In: *Journal of Alloys and Compounds* **845** (2020), p. 155499. DOI: 10.1016/j.jallcom.2020.155499 (cited on page 15).

[155] S. Chernov, C. Lidig, O. Fedchenko, K. Medjanik, S. Babenkov, D. Vasilyev, M. Jourdan, G. Schönhense, and H. J. Elmers. *'Band structure tuning of Heusler compounds: Spin- and momentum-resolved electronic structure analysis of compounds with different band filling'*. In: *Physical Review B* **103**, 5 (2021), p. 054407. DOI: 10.1103/PhysRevB.103.054407 (cited on page 15).

[156] T. Ambrose, J. J. Krebs, and G. A. Prinz. *'Magnetic properties of single crystal Co_2MnGe Heusler alloy films'*. In: *Journal of Applied Physics* **87**, 9 (2000), pp. 5463–5465. DOI: 10.1063/1.373373 (cited on page 16).

[157] F. Y. Yang, C. H. Shang, C. L. Chien, T. Ambrose, J. J. Krebs, G. A. Prinz, V. I. Nikitenko, V. S. Gornakov, A. J. Shapiro, and R. D. Shull. *'Multistep magnetic switching in single-crystal (001) Co_2MnGe films'*. In: *Physical Review B* **65**, 17 (2002), p. 174410. DOI: 10.1103/PhysRevB.65.174410 (cited on pages 16, 114).

[158] L. Ritchie, G. Xiao, Y. Ji, T. Y. Chen, C. L. Chien, M. Zhang, J. Chen, Z. Liu, G. Wu, and X. X. Zhang. *'Magnetic, structural, and transport properties of the Heusler alloys Co_2MnSi and NiMnSb'*. In: *Physical Review B* **68**, 10 (2003), p. 104430. DOI: 10.1103/PhysRevB.68.104430 (cited on pages 16, 112).

[159] M. Belmeguenai, F. Zighem, Y. Roussigné, S.-M. Chérif, P. Moch, K. Westerholt, G. Woltersdorf, and G. Bayreuther. *'Microstrip line ferromagnetic resonance and Brillouin light scattering investigations of magnetic properties of Co_2MnGe Heusler thin films'*. In: *Physical Review B* **79**, 2 (2009), p. 024419. DOI: 10.1103/PhysRevB.79.024419 (cited on page 16).

[160] K. Meng, J. Miao, X. Xu, J. Zhao, and Y. Jiang. *'Thickness dependence of magnetic anisotropy and intrinsic anomalous Hall effect in epitaxial Co_2MnAl film'*. In: *Physics Letters A* **381**, 13 (2017), pp. 1202–1206. DOI: 10.1016/j.physleta.2017.02.004 (cited on pages 16, 129).

[161] P. Swekis, A. S. Sukhanov, Y.-C. Chen, A. Gloskovskii, G. H. Fecher, I. Panagiotopoulos, J. Sichelschmidt, V. Ukleev, A. Devishvili, A. Vorobiev, D. S. Inosov, S. T. B. Goennenwein, C. Felser, and A. Markou. *'Magnetic and Electronic Properties of Weyl Semimetal Co_2MnGa Thin Films'*. In: *Nanomaterials* **11**, 1 (2021), p. 251. DOI: 10.3390/nano11010251 (cited on page 16).

[162] L. Royer. *'Recherches expérimentales sur l'épitaxie ou orientation mutuelle de cristaux d'espèces différentes'*. In: *Bulletin de la Société française de Minéralogie* **51**, 1 (1928), pp. 7–159. DOI: 10.3406/bulmi.1928.4034 (cited on page 17).

[163] S. Andrieu and P. Müller. Les surfaces solides: concepts et méthodes. Savoirs actuels. Les Ulis Paris: EDP sciences CNRS éd, 2005 (cited on pages 17, 19–22, 24).

[164] INFICON. Brochure: IC6 Thin Film Deposition Controller for Optical Applications. 2015 (cited on page 18).

[165] M. Knudsen. *'Die Gesetze der Molekularströmung und der inneren Reibungsströmung der Gase durch Röhren'*. In: *Annalen der Physik* **333**, 1 (1909), pp. 75–130. DOI: 10.1002/andp.19093330106 (cited on page 18).

[166] M. Knudsen. *'Die Molekularströmung der Gase durch Öffnungen und die Effusion'*. In: *Annalen der Physik* **333**, 5 (1909), pp. 999–1016. DOI: 10.1002/andp.19093330505 (cited on page 18).

[167] W. Braun. Applied RHEED. Vol. 154. Springer Tracts in Modern Physics. Berlin, Heidelberg: Springer Berlin Heidelberg, 1999. DOI: 10.1007/BFb0109548 (cited on page 19).

[168] J. Chevrier, V. L. Thanh, R. Buys, and J. Derrien. *'A RHEED Study of Epitaxial Growth of Iron on a Silicon Surface: Experimental Evidence for Kinetic Roughening'*. In: *Europhysics Letters (EPL)* **16**, 8 (1991), pp. 737–742. DOI: 10.1209/0295-5075/16/8/006 (cited on page 19).

[169] J. Harris, B. Joyce, and P. Dobson. *'Oscillations in the surface structure of Sn-doped GaAs during growth by MBE'*. In: *Surface Science Letters* **103**, 1 (1981), pp. L90–L96. DOI: 10.1016/0167-2584(81)90682-4 (cited on page 19).

[170] J. M. Van Hove, P. R. Pukite, and P. I. Cohen. *'The dependence of RHEED oscillations on MBE growth parameters'*. In: *Journal of Vacuum Science & Technology B: Microelectronics Processing and Phenomena* **3**, 2 (1985), pp. 563–567. DOI: 10.1116/1.583180 (cited on page 19).

[171] P. Dobson, B. Joyce, J. Neave, and J. Zhang. *'Current understanding and applications of the RHEED intensity oscillation technique'*. In: *Journal of Crystal Growth* **81**, 1-4 (1987), pp. 1–8. DOI: 10.1016/0022-0248(87)90355-1 (cited on page 19).

[172] G. Petrich, P. Pukite, A. Wowchak, G. Whaley, P. Cohen, and A. Arrott. *'On the origin of RHEED intensity oscillations'*. In: *Journal of Crystal Growth* **95**, 1-4 (1989), pp. 23–27. DOI: 10.1016/0022-0248(89)90342-4 (cited on page 19).

[173] W. Braun, L. Däweritz, and K. H. Ploog. *'New model for reflection high-energy electron diffraction intensity oscillations'*. In: *Journal of Vacuum Science & Technology B: Microelectronics and Nanometer Structures Processing, Measurement, and Phenomena* **16**, 4 (1998), pp. 2404–2412. DOI: 10.1116/1.590182 (cited on page 19).

[174] J. Haeni, C. Theis, and D. Schlom. *'RHEED Intensity Oscillations for the Stoichiometric Growth of SrTiO3 Thin Films by Reactive Molecular Beam Epitaxy'*. In: *Journal of Electroceramics* **4**, 2/3 (2000), pp. 385–391. DOI: 10.1023/A:1009947517710 (cited on page 19).

[175] L. A. Fejgin. Structure Analysis by Small-Angle X-Ray and Neutron Scattering. New York, NY: Springer, 1987 (cited on page 19).

[176] H. Ibach and H. Lüth. Solid-State Physics: An Introduction to Principles of Materials Science. Berlin, Heidelberg: Springer Berlin Heidelberg, 2009. DOI: 10.1007/978-3-540-93804-0 (cited on pages 19, 20, 41, 46).

[177] H. Ibach and H. Lüth. Festkörperphysik: Einführung in die Grundlagen. 7. Aufl. 2009. Springer-Lehrbuch. Berlin, Heidelberg: Springer Berlin Heidelberg, 2009. DOI: 10.1007/978-3-540-85795-2 (cited on pages 20, 41).

[178] M. Volmer and A. Weber. *'Keimbildung in übersättigten Gebilden'*. In: *Zeitschrift für Physikalische Chemie* **119U**, 1 (1926), pp. 277–301. DOI: 10.1515/zpch-1926-11927 (cited on page 21).

[179] I. N. Stranski and L. Krastanow. *'Zur Theorie der orientierten Ausscheidung von Ionenkristallen aufeinander'*. In: *Monatshefte für Chemie* **71**, 1 (1937), pp. 351–364. DOI: 10.1007/BF01798103 (cited on page 21).

[180] F. Frank and J. van der Merwe. *'One-dimensional dislocations. I. Static theory'*. In: *Proceedings of the Royal Society of London. Series A. Mathematical and Physical Sciences* **198**, 1053 (1949), pp. 205–216. DOI: 10.1098/rspa.1949.0095 (cited on page 21).

[181] F. Frank and J. van der Merwe. *'One-dimensional dislocations. II. Misfitting monolayers and oriented overgrowth'*. In: *Proceedings of the Royal Society of London. Series A. Mathematical and Physical Sciences* **198**, 1053 (1949), pp. 216–225. DOI: 10.1098/rspa.1949.0096 (cited on page 21).

[182] F. Frank and J. van der Merwe. *'One-dimensional dislocations. III. Influence of the second harmonic term in the potential representation, on the properties of the model'*. In: *Proceedings of the Royal Society of London. Series A. Mathematical and Physical Sciences* **200**, 1060 (1949), pp. 125–134. DOI: 10.1098/rspa.1949.0163 (cited on page 21).

[183] A. Neggache, T. Hauet, F. Bertran, P. Le Fèvre, S. Petit-Watelot, T. Devolder, P. Ohresser, P. Boulet, C. Mewes, S. Maat, J. R. Childress, and S. Andrieu. *'Testing epitaxial $Co_{1.5}Fe_{1.5}Ge(001)$ electrodes in MgO-based magnetic tunnel junctions'*. In: *Applied Physics Letters* **104**, 25 (2014), p. 252412. DOI: 10.1063/1.4885354 (cited on page 22).

[184] P. Auger. *'Sur l'effet photoélectrique composé'*. In: *Journal de Physique et le Radium* **6**, 6 (1925), pp. 205–208. DOI: 10.1051/jphysrad:0192500606020500 (cited on page 22).

[185] L. Meitner. *'Über die Entstehung der beta-Strahl-Spektren radioaktiver Substanzen'*. In: *Zeitschrift für Physik* **9**, 1 (1922), pp. 131–144. DOI: 10.1007/BF01326962 (cited on page 22).

[186] S. Hofmann. Auger- and X-ray photoelectron spectroscopy in materials science: a user-oriented guide. Springer series in surface sciences 49. Heidelberg: Springer Verlag, 2013 (cited on page 22).

[187] E. H. S. Burhop. *'The Auger effect'*. In: *Proceedings of the Royal Society of London. Series A - Mathematical and Physical Sciences* **148**, 864 (1935), pp. 272–284. DOI: 10.1098/rspa.1935.0018 (cited on page 22).

[188] V. Palin, C. Guillemard, C. De Melo, S. Migot, P. Gargiani, M. Valvidares, F. Bertran, and S. Andrieu. *'Engineering of perpendicular magnetic anisotropy in half-metallic magnetic Heusler epitaxial thin films'*. In: *Physical Review Applied* **20**, 5 (2023), p. 054017. DOI: 10.1103/PhysRevApplied.20.054017 (cited on pages 23, 129).

[189] M. Sicot, S. Andrieu, C. Tiusan, F. Montaigne, and F. Bertran. *'On the quality of molecular-beam epitaxy grown Fe/MgO and Co/MgO(001) interfaces'*. In: *Journal of Applied Physics* **99**, 8 (2006), p. 08D301. DOI: 10.1063/1.2165914 (cited on page 23).

[190] K. Omoto, K. Tsuda, and M. Tanaka. *'Simulations of Kikuchi patterns due to thermal diffuse scattering on MgO crystals'*. In: *Journal of Electron Microscopy* **51**, 1 (2002), pp. 67–78. DOI: 10.1093/jmicro/51.1.67 (cited on page 24).

[191] J. Pawlak, M. Przybylski, and Z. Mitura. *'An Analysis of Kikuchi Lines Observed with a RHEED Apparatus for a TiO2-Terminated SrTiO3 (001) Crystal'*. In: *Materials* **14**, 22 (2021), p. 7077. DOI: 10.3390/ma14227077 (cited on page 24).

[192] T. Gotoh, S. Murakami, K. Kinosita, and Y. Murata. *'Surface Rumpling of MgO(001) Deduced from Changes in RHEED Kikuchi Pattern. I. Experimental'*. In: *Journal of the Physical Society of Japan* **50**, 6 (1981), pp. 2063–2068. DOI: 10.1143/JPSJ.50.2063 (cited on page 24).

[193] S. Kämmerer, A. Thomas, A. Hütten, and G. Reiss. *'Co_2MnSi Heusler alloy as magnetic electrodes in magnetic tunnel junctions'*. In: *Applied Physics Letters* **85**, 1 (2004), pp. 79–81. DOI: 10.1063/1.1769082 (cited on pages 25, 117).

[194] Y. V. Kudryavtsev, V. A. Oksenenko, Y. P. Lee, Y. H. Hyun, J. B. Kim, J. S. Park, S. Y. Park, and J. Dubowik. *'Evolution of the magnetic properties of Co_2MnGa Heusler alloy films: From amorphous to ordered films'*. In: *Physical Review B* **76**, 2 (2007), p. 024430. DOI: 10.1103/PhysRevB.76.024430 (cited on page 25).

[195] S. Trudel, G. Wolf, J. Hamrle, B. Hillebrands, P. Klaer, M. Kallmayer, H.-J. Elmers, H. Sukegawa, W. Wang, and K. Inomata. *'Effect of annealing on $Co_2FeAl_{0.5}Si_{0.5}$thin films: A magneto-optical and x-ray absorption study'*. In: *Physical Review B* **83**, 10 (2011), p. 104412. DOI: 10.1103/PhysRevB.83.104412 (cited on pages 25, 89).

[196] Y. Takamura, R. Nakane, and S. Sugahara. *'Analysis of $L2_1$-ordering in full-Heusler Co_2FeSi alloy thin films formed by rapid thermal annealing'*. In: *Journal of Applied Physics* **105**, 7 (2009), 07B109. DOI: 10.1063/1.3075989 (cited on page 25).

[197] L. Szymoniak, D. Claveau-Mallet, M. Haddad, and B. Barbeau. *'Application of Magnesium Oxide Media for Remineralization and Removal of Divalent Metals in Drinking Water Treatment: A Review'*. In: *Water* **14**, 4 (2022), p. 633. DOI: 10.3390/w14040633 (cited on page 26).

[198] H. Perera, V. Gurunanthanan, A. Singh, M. Mantilaka, G. Das, and S. Arya. *'Magnesium oxide (MgO) nanoadsorbents in wastewater treatment: A comprehensive review'*. In: *Journal of Magnesium and Alloys* **12**, 5 (2024), pp. 1709–1773. DOI: 10.1016/j.jma.2024.05.003 (cited on page 26).

[199] T. Kado. *'Structure of Ti films deposited on MgO(001) substrates'*. In: *Surface Science* **454-456** (2000), pp. 783–789. DOI: 10.1016/S0039-6028(00)00139-4 (cited on page 26).

[200] J. Sun, D. Wang, Y. Zhang, C. Sheng, M. Dargusch, G. Wang, D. St John, and Q. Zhai. *'Heterogeneous nucleation of pure Al on MgO single crystal substrate accompanied by a $MgAl_2O_4$ buffer layer'*. In: *Journal of Alloys and Compounds* **753** (2018), pp. 543–550. DOI: 10.1016/j.jallcom.2018.04.263 (cited on page 26).

[201] G. E. McGuire. Auger Electron Spectroscopy Reference Manual. Boston, MA: Springer US, 1979. DOI: 10.1007/978-1-4757-1702-0 (cited on page 27).

[202] M. P. Oxley, A. R. Lupini, and S. J. Pennycook. *'Ultra-high resolution electron microscopy'*. In: *Reports on Progress in Physics* **80**, 2 (2017), p. 026101. DOI: 10.1088/1361-6633/80/2/026101 (cited on page 33).

[203] J. Orloff, M. Utlaut, and L. Swanson. High Resolution Focused Ion Beams: FIB and its Applications. Boston, MA: Springer US, 2003. DOI: 10.1007/978-1-4615-0765-9 (cited on page 33).

[204] L. Giannuzzi and F. Stevie. *'A review of focused ion beam milling techniques for TEM specimen preparation'*. In: *Micron* **30**, 3 (1999), pp. 197–204. DOI: 10.1016/S0968-4328(99)00005-0 (cited on page 34).

[205] L. A. Giannuzzi and F. A. Stevie, eds. Introduction to Focused Ion Beams: Instrumentation, Theory, Techniques and Practice. Boston, MA: Springer US, 2005. DOI: 10.1007/b101190 (cited on page 34).

[206] W. Kwong and W. Zhang. *'Electron-beam assisted platinum deposition as a protective layer for FIB and TEM applications'*. In: *ISSM 2005, IEEE International Symposium on Semiconductor Manufacturing, 2005.* San Jose, CA, USA: IEEE, 2005, pp. 469–471. DOI: 10.1109/ISSM.2005.1513408 (cited on page 34).

[207] M. M. J. Treacy, A. Howie, and C. J. Wilson. *'Z contrast of platinum and palladium catalysts'*. In: *Philosophical Magazine A* **38**, 5 (1978), pp. 569–585. DOI: 10.1080/01418617808239255 (cited on page 35).

[208] T. Nakatani, Y. Takahashi, T. Ishikawa, M. Yamamoto, and K. Hono. *'Structural characterizations of Co_2MnSi/MgO/Co_2MnSi magnetic tunnel junctions by transmission electron microscopy'*. In: *Journal of Magnetism and Magnetic Materials* **322**, 3 (2010), pp. 357–361. DOI: 10.1016/j.jmmm.2009.09.059 (cited on page 35).

[209] B. Heinrich, G. Woltersdorf, R. Urban, O. Mosendz, G. Schmidt, P. Bach, L. Molenkamp, and E. Rozenberg. *'Magnetic properties of NiMnSb(001) films grown on InGaAs/InP(001)'*. In: *Journal of Applied Physics* **95**, 11 (2004), pp. 7462–7464. DOI: 10.1063/1.1687274 (cited on pages 43, 60, 83, 84, 134, 206, 271).

[210] G. Woltersdorf, B. Heinrich, J. Woltersdorf, and R. Scholz. *'Spin dynamics in ultrathin film structures with a network of misfit dislocations'*. In: *Journal of Applied Physics* **95**, 11 (2004), pp. 7007–7009. DOI: 10.1063/1.1669219 (cited on pages 43, 60, 135, 206, 271).

[211] A. V. Chumak, A. A. Serga, and B. Hillebrands. *'Magnon transistor for all-magnon data processing'*. In: *Nature Communications* **5**, 1 (2014), p. 4700. DOI: 10.1038/ncomms5700 (cited on page 46).

[212] B. Heinz, T. Brächer, M. Schneider, Q. Wang, B. Lägel, A. M. Friedel, D. Breitbach, S. Steinert, T. Meyer, M. Kewenig, C. Dubs, P. Pirro, and A. V. Chumak. *'Propagation of Spin-Wave Packets in Individual Nanosized Yttrium Iron Garnet Magnonic Conduits'*. In: *Nano Letters* **20**, 6 (2020), pp. 4220–4227. DOI: 10.1021/acs.nanolett.0c00657 (cited on page 46).

[213] N. Abid, A. M. Khan, S. Shujait, K. Chaudhary, M. Ikram, M. Imran, J. Haider, M. Khan, Q. Khan, and M. Maqbool. *'Synthesis of nanomaterials using various top-down and bottom-up approaches, influencing factors, advantages, and disadvantages: A review'*. In: *Advances in Colloid and Interface Science* **300** (2022), p. 102597. DOI: 10.1016/j.cis.2021.102597 (cited on page 46).

[214] M. B. Jungfleisch, W. Zhang, W. Jiang, H. Chang, J. Sklenar, S. M. Wu, J. E. Pearson, A. Bhattacharya, J. B. Ketterson, M. Wu, and A. Hoffmann. *'Spin waves in micro-structured yttrium iron garnet nanometer-thick films'*. In: *Journal of Applied Physics* **117**, 17 (2015), p. 17D128. DOI: 10.1063/1.4916027 (cited on page 46).

[215] M. Kiechle, A. Papp, S. Mendisch, V. Ahrens, M. Golibrzuch, G. H. Bernstein, W. Porod, G. Csaba, and M. Becherer. *'Spin-Wave Optics in YIG Realized by Ion-Beam Irradiation'*. In: *Small* **19**, 21 (2023), p. 2207293. DOI: 10.1002/smll.202207293 (cited on page 46).

[216] J. Greil, M. Kiechle, A. Papp, P. Neumann, Z. Kovács, J. Volk, F. Schulz, S. Wintz, M. Weigand, G. Csaba, and M. Becherer. *'The effect of Ga-ion irradiation on sub-micron-wavelength spin waves in yttrium-iron-garnet films'*. In: *Nanotechnology* **36**, 13 (2025), p. 135301. DOI: 10.1088/1361-6528/adad7d (cited on page 46).

[217] M. Salaheldeen, A. Talaat, M. Ipatov, V. Zhukova, and A. Zhukov. *'Preparation and Magneto-Structural Investigation of Nanocrystalline CoMn-Based Heusler Alloy Glass-Coated Microwires'*. In: *Processes* **10**, 11 (2022), p. 2248. DOI: 10.3390/pr10112248 (cited on pages 46, 272).

[218] A. Wederni, M. Salaheldeen, M. Ipatov, V. Zhukova, and A. Zhukov. *'Influence of the Geometrical Aspect Ratio on the Magneto-Structural Properties of Co_2MnSi Microwires'*. In: *Metals* **13**, 10 (2023), p. 1692. DOI: 10.3390/met13101692 (cited on pages 46, 272).

[219] B. Heinz, T. Brächer, M. Schneider, Q. Wang, B. Lägel, A. M. Friedel, D. Breitbach, S. Steinert, T. Meyer, M. Kewenig, C. Dubs, P. Pirro, and A. V. Chumak. *'Supplementary Material: Propagation of Spin-Wave Packets in Individual Nanosized Yttrium Iron Garnet Magnonic Conduits'*. In: *Nano Letters* **20**, 6 (2020), pp. 4220–4227. DOI: 10.1021/acs.nanolett.0c00657 (cited on page 47).

[220] MicroChemicals. *Application Note* Substrate Pretreatment: Cleaning and Adhesion Promotion. 2025. URL: https://www.microchemicals.com/dokumente/application_notes/substrate_cleaning_adhesion_photoresist.pdf (cited on pages 58, 59).

[221] V. N. Demin, T. P. Smirnova, V. O. Borisov, G. N. Grachev, A. L. Smirnov, and M. N. Khomyakov. *'Laser plasmochemical synthesis of hard protective SiCN films'*. In: *Surface Engineering* **31**, 8 (2015), pp. 628–633. DOI: 10.1179/1743294414Y.0000000443 (cited on page 58).

[222] A. I. Menshakov, D. R. Emlin, Y. S. Surkov, and S. O. Cholakh. *'Investigation of the conditions for the formation of SiCN-based coatings in arc discharge with self-heated hollow cathode'*. In: *Journal of Physics: Conference Series* **1134** (2018), p. 012039. DOI: 10.1088/1742-6596/1134/1/012039 (cited on page 58).

[223] S. Yoshimura, S. Sugimoto, T. Takeuchi, K. Murai, and M. Kiuchi. *'Low-energy Ar+ and N+ ion beam induced chemical vapor deposition using hexamethyldisilazane for the formation of nitrogen containing SiC and carbon containing SiN films'*. In: *PLOS ONE* **16**, 10 (2021). Ed. by M. P. Balanay, e0259216. DOI: 10.1371/journal.pone.0259216 (cited on pages 58, 206).

[224] A. H. Morrish. The physical principles of magnetism. New York: IEEE Press, 2001 (cited on pages 65, 66, 69, 70, 72, 76, 221).

[225] A. G. Gurevich and G. A. Melkov. Magnetization oscillations and waves. Boca Raton: CRC Press, 1996 (cited on pages 65, 69, 75, 76, 97, 151, 162, 168, 277).

[226] B. Hillebrands and S. Blügel. *'5. Magnetismus'*. In: *Bergmann, Schaefer: Lehrbuch der Experimentalphysik, Band 6: Festkörper*. de Gruyter, 2005 (cited on pages 65, 68, 69).

[227] D. D. Stancil and A. Prabhakar. Spin waves: theory and applications. OCLC: ocn209335955. New York: Springer, 2009 (cited on pages 65, 69–73, 76, 151, 153, 155, 162, 165, 221, 223, 228, 277).

[228] S. Chikazumi and C. D. Graham. Physics of ferromagnetism. 2. ed., 1. publ. in paperback. International series of monographs on physics 94. Oxford: Oxford Univ. Press, 2009 (cited on page 65).

[229] S. M. Rezende. Fundamentals of Magnonics. Vol. 969. Lecture Notes in Physics. Cham: Springer International Publishing, 2020. DOI: 10.1007/978-3-030-41317-0 (cited on pages 65, 72, 83, 109, 151, 162, 277).

[230] C. Abert. *'Micromagnetics and spintronics: models and numerical methods'*. In: *The European Physical Journal B* **92**, 6 (2019), p. 120. DOI: 10.1140/epjb/e2019-90599-6 (cited on page 66).

[231] W. Heisenberg. *'Zur Theorie des Ferromagnetismus'*. In: *Zeitschrift für Physik* **49**, 9-10 (1928), pp. 619–636. DOI: 10.1007/BF01328601 (cited on page 66).

[232] L. Bergmann and C. Schaefer. Aufbau der Materie. Lehrbuch der Experimentalphysik, Band IV, Teil 1. Berlin: Walter de Gruyter & Co., 1975 (cited on page 67).

[233] Y. Henry, O. Gladii, and M. Bailleul. Propagating spin-wave normal modes: A dynamic matrix approach using plane-wave demagnetizating tensors. Version Number: 1. 2016. DOI: 10.48550/ARXIV.1611.06153. URL: https://arxiv.org/abs/1611.06153 (cited on pages 67, 153, 155, 162, 230).

[234] O. Gaier, J. Hamrle, S. Trudel, B. Hillebrands, H. Schneider, and G. Jakob. *'Exchange stiffness in the Co_2FeSi Heusler compound'*. In: *Journal of Physics D: Applied Physics* **42**, 23 (2009), p. 232001. DOI: 10.1088/0022-3727/42/23/232001 (cited on page 67).

[235] T. Iwashita and N. Uryû. *'Effects of biquadratic exchange in ferromagnets'*. In: *Physical Review B* **14**, 7 (1976), pp. 3090–3096. DOI: 10.1103/PhysRevB.14.3090 (cited on page 67).

[236] E. A. Harris and J. Owen. *'Biquadratic Exchange Between Mn^{2+} Ions in MgO'*. In: *Physical Review Letters* **11**, 1 (1963), pp. 9–10. DOI: 10.1103/PhysRevLett.11.9 (cited on page 67).

[237] M. Hoffmann and S. Blügel. *'Systematic derivation of realistic spin models for beyond-Heisenberg solids'*. In: *Physical Review B* **101**, 2 (2020), p. 024418. DOI: 10.1103/PhysRevB.101.024418 (cited on page 67).

[238] P. Bruno. *'Interlayer exchange coupling: a unified physical picture'*. In: *Journal of Magnetism and Magnetic Materials* **121**, 1-3 (1993), pp. 248–252. DOI: 10.1016/0304-8853(93)91197-F (cited on page 67).

[239] A. Kartsev, M. Augustin, R. F. L. Evans, K. S. Novoselov, and E. J. G. Santos. *'Biquadratic exchange interactions in two-dimensional magnets'*. In: *npj Computational Materials* **6**, 1 (2020), p. 150. DOI: 10.1038/s41524-020-00416-1 (cited on page 67).

[240] A. Fuß, S. Demokritov, P. Grünberg, and W. Zinn. *'Short- and long period oscillations in the exchange coupling of Fe across epitaxially grown Al- and Au-interlayers'*. In: *Journal of Magnetism and Magnetic Materials* **103**, 3 (1992), pp. L221–L227. DOI: 10.1016/0304-8853(92)90192-Q (cited on page 67).

[241] C. Gutierrez, J. Krebs, M. Filipkowski, and G. Prinz. *'Strong temperature dependence of the 90° coupling in Fe/Al/Fe(001) magnetic trilayers'*. In: *Journal of Magnetism and Magnetic Materials* **116**, 3 (1992), pp. L305–L310. DOI: 10.1016/0304-8853(92)90106-X (cited on page 67).

[242] J. C. Slonczewski. *'Origin of biquadratic exchange in magnetic multilayers (invited)'*. In: *Journal of Applied Physics* **73**, 10 (1993), pp. 5957–5962. DOI: 10.1063/1.353483 (cited on page 67).

[243] S. Bosu, Y. Sakuraba, K. Saito, H. Wang, S. Mitani, and K. Takanashi. *'Interlayer coupling in epitaxial Co_2MnSi/X/Co_2MnSi (X=Cr and V) trilayer structures'*. In: *Journal of Physics: Conference Series* **83** (2007), p. 012013. DOI: 10.1088/1742-6596/83/1/012013 (cited on page 67).

[244] S. Bosu, Y. Sakuraba, K. Saito, Hai Wang, S. Mitani, and K. Takanashi. *'Biquadratic Exchange Coupling in Epitaxial Co_2MnSi/Cr/Fe Trilayers'*. In: *IEEE Transactions on Magnetics* **44**, 11 (2008), pp. 2620–2623. DOI: 10.1109/TMAG.2008.2002504 (cited on page 67).

[245] S. Bosu, Y. Sakuraba, K. Saito, H. Wang, S. Mitani, and K. Takanashi. *'Chemical ordering dependence of interlayer exchange coupling in Co-Mn-Si/Cr/Co-Mn-Si trilayer structures'*. In: *Physical Review B* **81**, 5 (2010), p. 054426. DOI: 10.1103/PhysRevB.81.054426 (cited on page 67).

[246] W. Kakeno, S. Honda, H. Itoh, and J. Inoue. *'Ab initio study of magnetic structure and exchange coupling in Co_2MnSi / Cr / Co_2MnSi trilayers'*. In: *Physical Review B* **82**, 1 (2010), p. 014413. DOI: 10.1103/PhysRevB.82.014413 (cited on page 67).

[247] H. S. Goripati, M. Hayashi, T. Furubayashi, T. Taniguchi, H. Sukegawa, Y. K. Takahashi, and K. Hono. *'Bi-quadratic interlayer exchange coupling in Co_2MnSi/Ag/Co_2MnSi pseudo spin-valve'*. In: *Journal of Applied Physics* **110**, 12 (2011), p. 123914. DOI: 10.1063/1.3671634 (cited on pages 67, 117).

[248] M. Inoue, K. Inubushi, D. Mouri, T. Tanimoto, K. Nakada, K. Kondo, M. Yamamoto, and T. Uemura. *'Origin of biquadratic interlayer exchange coupling in Co_2MnSi-based current-perpendicular-to-plane pseudo spin valves'*. In: *Applied Physics Letters* **114**, 6 (2019), p. 062401. DOI: 10.1063/1.5082605 (cited on page 67).

[249] J. D. Jackson. Klassische Elektrodynamik: DE GRUYTER, 2013. DOI: 10.1515/9783110334470 (cited on page 68).

[250] B. D. Cullity and C. D. Graham. Introduction to magnetic materials. Second edition. Piscataway: IEEE Press, 2009. DOI: 10.1002/9780470386323 (cited on pages 70, 71).

[251] E. C. Stoner and E. P. Wohlfarth. *'A mechanism of magnetic hysteresis in heterogeneous alloys'*. In: *Philosophical Transactions of the Royal Society of London. Series A, Mathematical and Physical Sciences* **240**, 826 (1948), pp. 599–642. DOI: 10.1098/rsta.1948.0007 (cited on page 74).

[252] W. Döring. *'Über die Trägheit der Wände zwischen Weißschen Bezirken'*. In: *Zeitschrift für Naturforschung A* **3**, 7 (1948), pp. 373–379. DOI: 10.1515/zna-1948-0701 (cited on page 74).

[253] L. D. Landau and E. M. Lifshitz. *'On the theory of the dispersion of magnetic permeability in ferromagnetic bodies'*. In: *Physikalische Zeitschrift der Sowjetunion* **8** (1935), pp. 153–169 (cited on pages 75, 273).

[254] T. Gilbert. *'A Phenomenological Theory of Damping in Ferromagnetic Materials'*. In: *IEEE Transactions on Magnetics* **40**, 6 (2004), pp. 3443–3449. DOI: 10.1109/TMAG.2004.836740 (cited on pages 75, 81, 273).

[255] T. L. Gilbert. *'Formulation, foundations and applications of the phenomenological theory of ferromagnetism'*. PhD thesis. Chicago, Illinois: Illinois Institute of Technology, 1956 (cited on pages 75, 76).

[256] D. A. Garanin. *'Fokker-Planck and Landau-Lifshitz-Bloch equations for classical ferromagnets'*. In: *Physical Review B* **55**, 5 (1997), pp. 3050–3057. DOI: 10.1103/PhysRevB.55.3050 (cited on page 75).

[257] U. Atxitia, D. Hinzke, and U. Nowak. *'Fundamentals and applications of the Landau–Lifshitz–Bloch equation'*. In: *Journal of Physics D: Applied Physics* **50**, 3 (2017), p. 033003. DOI: 10.1088/1361-6463/50/3/033003 (cited on page 75).

[258] J. Mallinson. *'On damped gyromagnetic precession'*. In: *IEEE Transactions on Magnetics* **23**, 4 (1987), pp. 2003–2004. DOI: 10.1109/TMAG.1987.1065181 (cited on page 76).

[259] R. Kikuchi. *'On the Minimum of Magnetization Reversal Time'*. In: *Journal of Applied Physics* **27**, 11 (1956), pp. 1352–1357. DOI: 10.1063/1.1722262 (cited on page 76).

[260] C. Kittel. *'On the Theory of Ferromagnetic Resonance Absorption'*. In: *Physical Review* **73**, 2 (1948), pp. 155–161. DOI: 10.1103/PhysRev.73.155 (cited on pages 76, 78).

[261] J. Smit and H. G. Beljers. *'Ferromagnetic resonance absorption in $BaFe_{12}O_{19}$, a highly anisotropic crystal'*. In: *Philips Research Reports* **10** (1955), pp. 113–130 (cited on pages 76, 273).

[262] H. Suhl. *'Ferromagnetic Resonance in Nickel Ferrite Between One and Two Kilomegacycles'*. In: *Physical Review* **97**, 2 (1955), pp. 555–557. DOI: 10.1103/PhysRev.97.555.2 (cited on pages 76, 273).

[263] I. S. Maksymov and M. Kostylev. *'Broadband stripline ferromagnetic resonance spectroscopy of ferromagnetic films, multilayers and nanostructures'*. In: *Physica E: Low-dimensional Systems and Nanostructures* **69** (2015), pp. 253–293. DOI: 10.1016/j.physe.2014.12.027 (cited on pages 79, 97, 99, 274).

[264] B. Kuanr, R. E. Camley, and Z. Celinski. *'Narrowing of the frequency-linewidth in structured magnetic strips: Experiment and theory'*. In: *Applied Physics Letters* **87**, 1 (2005), p. 012502. DOI: 10.1063/1.1968433 (cited on pages 80, 100, 133, 256, 274).

[265] B. Heinrich. *'5. Spin Relaxation in Magnetic Metallic Layers and Multilayers'*. In: *Ultrathin Magnetic Structures III*. Ed. by J. A. C. Bland and B. Heinrich. Berlin, Heidelberg: Springer Berlin Heidelberg, 2005, pp. 143–210. DOI: 10.1007/3-540-27163-5_5 (cited on pages 81–84).

[266] V. Kamberský. *'On the Landau–Lifshitz relaxation in ferromagnetic metals'*. In: *Canadian Journal of Physics* **48**, 24 (1970), pp. 2906–2911. DOI: 10.1139/p70-361 (cited on page 82).

[267] J. Cochran and B. Heinrich. *'Microwave transmission through ferromagnetic metals'*. In: *IEEE Transactions on Magnetics* **16**, 5 (1980), pp. 660–665. DOI: 10.1109/TMAG.1980.1060688 (cited on page 82).

[268] B. Khodadadi, A. Rai, A. Sapkota, A. Srivastava, B. Nepal, Y. Lim, D. A. Smith, C. Mewes, S. Budhathoki, A. J. Hauser, M. Gao, J.-F. Li, D. D. Viehland, Z. Jiang, J. J. Heremans, P. V. Balachandran, T. Mewes, and S. Emori. *'Conductivitylike Gilbert Damping due to Intraband Scattering in Epitaxial Iron'*. In: *Physical Review Letters* **124**, 15 (2020), p. 157201. DOI: 10.1103/PhysRevLett.124.157201 (cited on page 82).

[269] B. Heinrich, R. Urban, and G. Woltersdorf. *'Magnetic relaxation in metallic films: Single and multilayer structures'*. In: *Journal of Applied Physics* **91**, 10 (2002), pp. 7523–7525. DOI: 10.1063/1.1447215 (cited on page 82).

[270] J. M. Lock. *'Eddy current damping in thin metallic ferromagnetic films'*. In: *British Journal of Applied Physics* **17**, 12 (1966), pp. 1645–1647. DOI: 10.1088/0508-3443/17/12/415 (cited on page 82).

[271] R. W. Sanders, D. Paquette, V. Jaccarino, and S. M. Rezende. *'Radiation damping in magnetic resonance. II. Continuous-wave antiferromagnetic-resonance experiments'*. In: *Physical Review B* **10**, 1 (1974), pp. 132–138. DOI: 10.1103/PhysRevB.10.132 (cited on page 82).

[272] G. Wende. *'Radiation damping in FMR measurements in a nonresonant rectangular waveguide'*. In: *Physica Status Solidi (a)* **36**, 2 (1976), pp. 557–567. DOI: 10.1002/pssa.2210360216 (cited on page 82).

[273] M. A. W. Schoen, J. M. Shaw, H. T. Nembach, M. Weiler, and T. J. Silva. *'Radiative damping in waveguide-based ferromagnetic resonance measured via analysis of perpendicular standing spin waves in sputtered permalloy films'*. In: *Physical Review B* **92**, 18 (2015), p. 184417. DOI: 10.1103/PhysRevB.92.184417 (cited on pages 82, 83).

[274] T. Kobayashi, R. C. Barker, J. L. Bleustein, and A. Yelon. *'Ferromagnetoelastic Resonance in Thin Films. I. Formal Treatment'*. In: *Physical Review B* **7**, 7 (1973), pp. 3273–3285. DOI: 10.1103/PhysRevB.7.3273 (cited on page 83).

[275] H. Suhl. *'Theory of the magnetic damping constant'*. In: *IEEE Transactions on Magnetics* **34**, 4 (1998), pp. 1834–1838. DOI: 10.1109/20.706720 (cited on page 83).

[276] H. Man, Z. Shi, G. Xu, Y. Xu, X. Chen, S. Sullivan, J. Zhou, K. Xia, J. Shi, and P. Dai. *'Direct observation of magnon-phonon coupling in yttrium iron garnet'*. In: *Physical Review B* **96**, 10 (2017), p. 100406. DOI: 10.1103/PhysRevB.96.100406 (cited on page 83).

[277] S. Streib, N. Vidal-Silva, K. Shen, and G. E. W. Bauer. *'Magnon-phonon interactions in magnetic insulators'*. In: *Physical Review B* **99**, 18 (2019), p. 184442. DOI: 10.1103/PhysRevB.99.184442 (cited on page 83).

[278] D. A. Bozhko, V. I. Vasyuchka, A. V. Chumak, and A. A. Serga. *'Magnon-phonon interactions in magnon spintronics (Review article)'*. In: *Low Temperature Physics* **46**, 4 (2020), pp. 383–399. DOI: 10.1063/10.0000872 (cited on page 83).

[279] M. Weiler, G. Woltersdorf, M. Althammer, H. Huebl, and S. T. Goennenwein. *'Spin Pumping and Spin Currents in Magnetic Insulators'*. In: *Solid State Physics*. Vol. 64. Elsevier, 2013, pp. 123–156. DOI: 10.1016/B978-0-12-408130-7.00005-8 (cited on page 83).

[280] Y. Tserkovnyak, A. Brataas, and G. E. W. Bauer. *'Enhanced Gilbert Damping in Thin Ferromagnetic Films'*. In: *Physical Review Letters* **88**, 11 (2002), p. 117601. DOI: 10.1103/PhysRevLett.88.117601 (cited on page 83).

[281] Y. Tserkovnyak, A. Brataas, and G. E. W. Bauer. *'Spin pumping and magnetization dynamics in metallic multilayers'*. In: *Physical Review B* **66**, 22 (2002), p. 224403. DOI: 10.1103/PhysRevB.66.224403 (cited on page 83).

[282] Y. Tserkovnyak, A. Brataas, G. E. W. Bauer, and B. I. Halperin. *'Nonlocal magnetization dynamics in ferromagnetic heterostructures'*. In: *Reviews of Modern Physics* **77**, 4 (2005), pp. 1375–1421. DOI: 10.1103/RevModPhys.77.1375 (cited on page 84).

[283] R. Arias and D. L. Mills. *'Extrinsic contributions to the ferromagnetic resonance response of ultrathin films'*. In: *Physical Review B* **60**, 10 (1999), pp. 7395–7409. DOI: 10.1103/PhysRevB.60.7395 (cited on page 84).

[284] G. Woltersdorf and B. Heinrich. *'Two-magnon scattering in a self-assembled nanoscale network of misfit dislocations'*. In: *Physical Review B* **69**, 18 (2004), p. 184417. DOI: 10.1103/PhysRevB.69.184417 (cited on page 84).

[285] R. D. McMichael, M. D. Stiles, P. J. Chen, and W. F. Egelhoff. *'Ferromagnetic resonance linewidth in thin films coupled to NiO'*. In: *Journal of Applied Physics* **83**, 11 (1998), pp. 7037–7039. DOI: 10.1063/1.367725 (cited on page 84).

[286] K. Lenz, H. Wende, W. Kuch, K. Baberschke, K. Nagy, and A. Jánossy. *'Two-magnon scattering and viscous Gilbert damping in ultrathin ferromagnets'*. In: *Physical Review B* **73**, 14 (2006), p. 144424. DOI: 10.1103/PhysRevB.73.144424 (cited on page 84).

[287] J. Lindner, K. Lenz, E. Kosubek, K. Baberschke, D. Spoddig, R. Meckenstock, J. Pelzl, Z. Frait, and D. Mills. *''Non-Gilbert-type' damping of magnetic excitations in ultrathin ferromagnets: importance of magnon–magnon scattering'*. In: *Journal of Magnetism and Magnetic Materials* **272-276** (2004), E1653–E1654. DOI: 10.1016/j.jmmm.2003.12.594 (cited on page 84).

[288] H. Suhl. *'The theory of ferromagnetic resonance at high signal powers'*. In: *Journal of Physics and Chemistry of Solids* **1**, 4 (1957), pp. 209–227. DOI: 10.1016/0022-3697(57)90010-0 (cited on pages 84, 151, 162, 164, 168, 277, 278).

[289] E. Schlömann. *'Fine Structure in the Decline of the Ferromagnetic Resonance Absorption with Increasing Power Level'*. In: *Physical Review* **116**, 4 (1959), pp. 828–837. DOI: 10.1103/PhysRev.116.828 (cited on pages 84, 165).

[290] E. Schlömann, J. J. Green, and U. Milano. *'Recent Developments in Ferromagnetic Resonance at High Power Levels'*. In: *Journal of Applied Physics* **31**, 5 (1960), S386–S395. DOI: 10.1063/1.1984759 (cited on pages 84, 164).

[291] A. Y. Dobin and R. H. Victora. *'Intrinsic nonlinear ferromagnetic relaxation (invited)'*. In: *Journal of Applied Physics* **95**, 11 (2004), pp. 7139–7144. DOI: 10.1063/1.1651812 (cited on pages 84, 162, 165, 278).

[292] M. Faraday. *'I. Experimental researches in electricity.—Nineteenth series'*. In: *Philosophical Transactions of the Royal Society of London* **136** (1846), pp. 1–20. DOI: 10.1098/rstl.1846.0001 (cited on page 85).

[293] J. Kerr. *'XLIII. On rotation of the plane of polarization by reflection from the pole of a magnet'*. In: *The London, Edinburgh, and Dublin Philosophical Magazine and Journal of Science* **3**, 19 (1877), pp. 321–343. DOI: 10.1080/14786447708639245 (cited on pages 85, 106, 274).

[294] J. Kerr. *'XXIV. On reflection of polarized light from the equatorial surface of a magnet'*. In: *The London, Edinburgh, and Dublin Philosophical Magazine and Journal of Science* **5**, 30 (1878), pp. 161–177. DOI: 10.1080/14786447808639407 (cited on pages 85, 106, 274).

[295] L. Brillouin. *'Diffusion de la lumière et des rayons X par un corps transparent homogène: Influence de l'agitation thermique'*. In: *Annales de Physique* **9**, 17 (1922), pp. 88–122. DOI: 10.1051/anphys/192209170088 (cited on pages 85, 275).

[296] J. Hamrle, J. Pištora, B. Hillebrands, B. Lenk, and M. Münzenberg. *'Analytical expression of the magneto-optical Kerr effect and Brillouin light scattering intensity arising from dynamic magnetization'*. In: *Journal of Physics D: Applied Physics* **43**, 32 (2010), p. 325004. DOI: 10.1088/0022-3727/43/32/325004 (cited on pages 85, 91, 182, 273).

[297] E. Beaurepaire, J.-C. Merle, A. Daunois, and J.-Y. Bigot. *'Ultrafast Spin Dynamics in Ferromagnetic Nickel'*. In: *Physical Review Letters* **76**, 22 (1996), pp. 4250–4253. DOI: 10.1103/PhysRevLett.76.4250 (cited on page 85).

[298] J. Hohlfeld, E. Matthias, R. Knorren, and K. H. Bennemann. *'Nonequilibrium Magnetization Dynamics of Nickel'*. In: *Physical Review Letters* **78**, 25 (1997), pp. 4861–4864. DOI: 10.1103/PhysRevLett.78.4861 (cited on page 85).

[299] M. Montazeri, P. Upadhyaya, M. C. Onbasli, G. Yu, K. L. Wong, M. Lang, Y. Fan, X. Li, P. Khalili Amiri, R. N. Schwartz, C. A. Ross, and K. L. Wang. *'Magneto-optical investigation of spin–orbit torques in metallic and insulating magnetic heterostructures'*. In: *Nature Communications* **6**, 1 (2015), p. 8958. DOI: 10.1038/ncomms9958 (cited on page 85).

[300] C. Stamm, C. Murer, M. Berritta, J. Feng, M. Gabureac, P. M. Oppeneer, and P. Gambardella. *'Magneto-Optical Detection of the Spin Hall Effect in Pt and W Thin Films'*. In: *Physical Review Letters* **119**, 8 (2017), p. 087203. DOI: 10.1103/PhysRevLett.119.087203 (cited on page 85).

[301] A. Hirohata, Y. Baba, B. A. Murphy, B. Ng, Y. Yao, K. Nagao, and J.-y. Kim. *'Magneto-optical detection of spin accumulation under the influence of mechanical rotation'*. In: *Scientific Reports* **8**, 1 (2018), p. 1974. DOI: 10.1038/s41598-018-20269-5 (cited on page 85).

[302] J. Hamrle. *'Magneto-optical determination of the in-depth magnetization profile in magnetic multilayers'*. PhD thesis. Université Paris Sud - Paris XI, and Charles University Prague, 2003 (cited on page 86).

[303] P. Bruno, Y. Suzuki, and C. Chappert. *'Magneto-optical Kerr effect in a paramagnetic overlayer on a ferromagnetic substrate: A spin-polarized quantum size effect'*. In: *Physical Review B* **53**, 14 (1996), pp. 9214–9220. DOI: 10.1103/PhysRevB.53.9214 (cited on page 86).

[304] H. S. Bennett and E. A. Stern. *'Faraday Effect in Solids'*. In: *Physical Review* **137**, 2A (1965), A448–A461. DOI: 10.1103/PhysRev.137.A448 (cited on page 86).

[305] P. S. Pershan. *'Magneto-Optical Effects'*. In: *Journal of Applied Physics* **38**, 3 (1967), pp. 1482–1490. DOI: 10.1063/1.1709678 (cited on page 86).

[306] P. M. Oppeneer, T. Maurer, J. Sticht, and J. Kübler. *'Ab initio calculated magneto-optical Kerr effect of ferromagnetic metals: Fe and Ni'*. In: *Physical Review B* **45**, 19 (1992), pp. 10924–10933. DOI: 10.1103/PhysRevB.45.10924 (cited on page 86).

[307] W. Wettling. *'Magneto-optics of ferrites'*. In: *Journal of Magnetism and Magnetic Materials* **3**, 1-2 (1976), pp. 147–160. DOI: 10.1016/0304-8853(76)90026-3 (cited on page 87).

[308] S. Višnovský. *'Magneto-optical permittivity tensor in crystals'*. In: *Czechoslovak Journal of Physics* **36**, 12 (1986), pp. 1424–1433. DOI: 10.1007/BF01959567 (cited on pages 87, 88).

[309] J. Hamrlová, J. Hamrle, K. Postava, and J. Pištora. *'Quadratic-in-magnetization permittivity and conductivity tensor in cubic crystals'*. In: *physica status solidi (b)* **250**, 10 (2013), pp. 2194–2205. DOI: 10.1002/pssb.201349031 (cited on pages 88, 90).

[310] J. Hamrle, S. Blomeier, O. Gaier, B. Hillebrands, H. Schneider, G. Jakob, K. Postava, and C. Felser. *'Huge quadratic magneto-optical Kerr effect and magnetization reversal in the Co_2FeSi Heusler compound'*. In: *Journal of Physics D: Applied Physics* **40**, 6 (2007), pp. 1563–1569. DOI: 10.1088/0022-3727/40/6/S09 (cited on pages 88–90, 108, 276).

[311] R. Osgood, R. White, and B. Clemens. *'Asymmetric magneto-optic response in epitaxial Fe(110)/Mo(110) thin films'*. In: *IEEE Transactions on Magnetics* **31**, 6 (1995), pp. 3331–3333. DOI: 10.1109/20.490373 (cited on page 89).

[312] R. M. Osgood, B. M. Clemens, and R. L. White. *'Asymmetric magneto-optic response in anisotropic thin films'*. In: *Physical Review B* **55**, 14 (1997), pp. 8990–8996. DOI: 10.1103/PhysRevB.55.8990 (cited on page 89).

[313] K. Postava, H. Jaffres, A. Schuhl, F. Nguyen Van Dau, M. Goiran, and A. Fert. *'Linear and quadratic magneto-optical measurements of the spin reorientation in epitaxial Fe films on MgO'*. In: *Journal of Magnetism and Magnetic Materials* **172**, 3 (1997), pp. 199–208. DOI: 10.1016/S0304-8853(97)00098-X (cited on page 89).

[314] R. Carey, D. M. Newman, and M. L. Wears. *'Asymmetric nonlinear magneto-optic effects in PtMnSb thin films'*. In: *Journal of Applied Physics* **83**, 11 (1998), pp. 6739–6741. DOI: 10.1063/1.367786 (cited on page 89).

[315] Y. I. Kuz'min, M. M. Kirillova, and I. D. Lobov. *'Optical absorption and magnetooptical effects in the Heusler alloy NiMnSb'*. In: *The Physics of Metals and Metallography* **106**, 6 (2008), pp. 557–565. DOI: 10.1134/S0031918X08120041 (cited on page 89).

[316] I. D. Lobov, A. A. Makhnev, and M. M. Kirillova. *'Optical and magnetooptical properties of Heusler alloys XMnSb (X = Co, Pt)'*. In: *The Physics of Metals and Metallography* **113**, 2 (2012), pp. 135–145. DOI: 10.1134/S0031918X12020081 (cited on page 89).

[317] P. Muduli, W. Rice, L. He, and F. Tsui. *'Composition dependence of magnetic anisotropy and quadratic magnetooptical effect in epitaxial films of the Heusler alloy Co_2MnGe'*. In: *Journal of Magnetism and Magnetic Materials* **320**, 23 (2008), pp. L141–L143. DOI: 10.1016/j.jmmm.2008.06.027 (cited on page 89).

[318] P. K. Muduli, W. C. Rice, L. He, B. A. Collins, Y. S. Chu, and F. Tsui. *'Study of magnetic anisotropy and magnetization reversal using the quadratic magnetooptical effect in epitaxial $Co_xMn_yGe_z$ (111) films'*. In: *Journal of Physics: Condensed Matter* **21**, 29 (2009), p. 296005. DOI: 10.1088/0953-8984/21/29/296005 (cited on page 89).

[319] S. Trudel, G. Wolf, H. Schultheiß, J. Hamrle, and B. Hillebrands. *'Tandem magneto-optical Kerr effect magnetometer for the study of quadratic effects'*. In: *Journal of Physics: Conference Series* **200**, 11 (2010), p. 112010. DOI: 10.1088/1742-6596/200/11/112010 (cited on page 89).

[320] S. Trudel, G. Wolf, H. Schultheiß, J. Hamrle, B. Hillebrands, T. Kubota, and Y. Ando. *'Note: Probing quadratic magneto-optical Kerr effects with a dual-beam system'*. In: *Review of Scientific Instruments* **81**, 2 (2010), p. 026105. DOI: 10.1063/1.3276715 (cited on page 89).

[321] S. Trudel, J. Hamrle, B. Hillebrands, T. Taira, and M. Yamamoto. *'Magneto-optical investigation of epitaxial nonstoichiometric Co_2MnGe thin films'*. In: *Journal of Applied Physics* **107**, 4 (2010), p. 043912. DOI: 10.1063/1.3296350 (cited on page 89).

[322] G. Wolf, J. Hamrle, S. Trudel, T. Kubota, Y. Ando, and B. Hillebrands. *'Quadratic magneto-optical Kerr effect in Co_2MnSi'*. In: *Journal of Applied Physics* **110**, 4 (2011), p. 043904. DOI: 10.1063/1.3622512 (cited on page 89).

[323] J. Liu, S. Qiao, S. Wang, and G. Fu. *'Linear and quadratic magneto-optical Kerr effect investigation of $Co_2Mn_{1.30}Si_{0.84}$ epitaxially grown on MgO'*. In: *Solid State Communications* **250** (2017), pp. 31–34. DOI: 10.1016/j.ssc.2016.10.016 (cited on page 89).

[324] A. Hubert and G. Traeger. *'Magneto-optical sensitivity functions of thin-film systems'*. In: *Journal of Magnetism and Magnetic Materials* **124**, 1-2 (1993), pp. 185–202. DOI: 10.1016/0304-8853(93)90087-I (cited on page 89).

[325] G. Srinivasan, C. E. Patton, and J. G. Booth. *'Brillouin light scattering detection of ferromagnetic resonance in thin films'*. In: *Journal of Applied Physics* **63**, 8 (1988), pp. 3344–3346. DOI: 10.1063/1.340802 (cited on pages 90, 110).

[326] M. Buchmeier, H. Dassow, D. E. Bürgler, and C. M. Schneider. *'Intensity of Brillouin light scattering from spin waves in magnetic multilayers with noncollinear spin configurations: Theory and experiment'*. In: *Physical Review B* **75**, 18 (2007), p. 184436. DOI: 10.1103/PhysRevB.75.184436 (cited on pages 90, 91, 182).

[327] J. Cochran and J. Dutcher. *'Calculation of the intensity of light scattered from magnons in thin films'*. In: *Journal of Magnetism and Magnetic Materials* **73**, 3 (1988), pp. 299–310. DOI: 10.1016/0304-8853(88)90095-9 (cited on pages 91, 110, 182).

[328] G. W. Van Oosterhout. *'A rapid method for measuring coercive force and other ferromagnetic properties of very small samples'*. In: *Applied Scientific Research, Section B* **6**, 1 (1957), pp. 101–104. DOI: 10.1007/BF02920365 (cited on pages 93, 273).

[329] D. O. Smith. *'Development of a Vibrating-Coil Magnetometer'*. In: *Review of Scientific Instruments* **27**, 5 (1956), pp. 261–268. DOI: 10.1063/1.1715538 (cited on page 93).

[330] S. Foner. *'Versatile and Sensitive Vibrating-Sample Magnetometer'*. In: *Review of Scientific Instruments* **30**, 7 (1959), pp. 548–557. DOI: 10.1063/1.1716679 (cited on pages 93, 94, 273).

[331] T. El-Alaily, M. El-Nimr, S. Saafan, M. Kamel, T. Meaz, and S. Assar. *'Construction and calibration of a low cost and fully automated vibrating sample magnetometer'*. In: *Journal of Magnetism and Magnetic Materials* **385** (2015), pp. 25–30. DOI: https://doi.org/10.1016/j.jmmm.2015.03.051 (cited on pages 93, 273).

[332] V. Lopez-Dominguez, A. Quesada, J. C. Guzmán-Mínguez, L. Moreno, M. Lere, J. Spottorno, F. Giacomone, J. F. Fernández, A. Hernando, and M. A. García. *'A simple vibrating sample magnetometer for macroscopic samples'*. In: *Review of Scientific Instruments* **89**, 3 (2018), p. 034707. DOI: 10.1063/1.5017708 (cited on pages 93, 273).

[333] D. Jordán, D. González-Chávez, D. Laura, L. León Hilario, E. Monteblanco, A. Gutarra, and L. Avilés-Félix. *'Detection of magnetic moment in thin films with a home-made vibrating sample magnetometer'*. In: *Journal of Magnetism and Magnetic Materials* **456** (2018), pp. 56–61. DOI: 10.1016/j.jmmm.2018.01.088 (cited on pages 93, 273).

[334] MicroSense. EasyVSM Brochure. 2023. URL: https://www.kla.com/wp-content/uploads/MicroSense_EasyVSM_Brochure.pdf (cited on pages 93, 273).

[335] QuantumDesign. Vibrating Sample Magnetometer (VSM) Brochure. 2024. URL: https://www.qdusa.com/siteDocs/productBrochures/1084-500_PPMS_VSM.pdf (cited on pages 93, 273).

[336] J. Bernards, G. Van Engelen, and H. Cramer. *'An improved detection coil system for a biaxial vibrating sample magnetometer'*. In: *Journal of Magnetism and Magnetic Materials* **123**, 1-2 (1993), pp. 141–146. DOI: 10.1016/0304-8853(93)90023-U (cited on page 94).

[337] QuantumDesign. Correcting for the Absolute Field Error using the Pd Standard. 2020. URL: https://www.qdusa.com/siteDocs/appNotes/1500-021.pdf (cited on page 94).

[338] QuantumDesign. Palladium Reference Samples. URL: https://www.qdusa.com/siteDocs/appNotes/1041-001.pdf (cited on page 94).

[339] J. Lindemuth, J. Krause, and B. Dodrill. *'Finite sample size effects on the calibration of vibrating sample magnetometer'*. In: *IEEE Transactions on Magnetics* **37**, 4 (2001), pp. 2752–2754. DOI: 10.1109/20.951296 (cited on page 94).

[340] QuantumDesign. Accuracy of Reported Sample Moment: Using the Sample Geometry Simulator. 2021. URL: https://www.qdusa.com/siteDocs/appNotes/1500-020.pdf (cited on page 94).

[341] QuantumDesign. Mounting Samples Loosely Causes Moment Noise in VSM Measurements. 2010. URL: https://www.qdusa.com/siteDocs/appNotes/1500-009.pdf (cited on page 95).

[342] M. Khalid, A. Setzer, M. Ziese, P. Esquinazi, D. Spemann, A. Pöppl, and E. Goering. *'Ubiquity of ferromagnetic signals in common diamagnetic oxide crystals'*. In: *Physical Review B* **81**, 21 (2010), p. 214414. DOI: 10.1103/PhysRevB.81.214414 (cited on page 95).

[343] J. Li, Y. Jiang, Y. Li, D. Yang, Y. Xu, and M. Yan. *'Origin of room temperature ferromagnetism in MgO films'*. In: *Applied Physics Letters* **102**, 7 (2013), p. 072406. DOI: 10.1063/1.4793308 (cited on page 95).

[344] Quantum Design. Vibrating Sample Magnetometer (VSM) Option User's Manual, 5th edition, Part Number 1096-100, B0. 2011 (cited on page 95).

[345] S. Hoon, G. Lawson, F. Thompson, B. Dean, and R. Chantrell. *'Field dependent rf absorption spectra of particulate magnetic recording materials'*. In: *Journal of Magnetism and Magnetic Materials* **104-107** (1992), pp. 967–968. DOI: 10.1016/0304-8853(92)90445-T (cited on pages 97, 98, 274).

[346] V. P. Denysenkov and A. M. Grishin. *'Broadband ferromagnetic resonance spectrometer'*. In: *Review of Scientific Instruments* **74**, 7 (2003), pp. 3400–3405. DOI: 10.1063/1.1581395 (cited on pages 97, 274).

[347] T. Schwarze, J. Waizner, M. Garst, A. Bauer, I. Stasinopoulos, H. Berger, C. Pfleiderer, and D. Grundler. *'Universal helimagnon and skyrmion excitations in metallic, semiconducting and insulating chiral magnets'*. In: *Nature Materials* **14**, 5 (2015), pp. 478–483. DOI: 10.1038/nmat4223 (cited on pages 97, 274).

[348] G. Counil, J.-V. Kim, T. Devolder, C. Chappert, K. Shigeto, and Y. Otani. *'Spin wave contributions to the high-frequency magnetic response of thin films obtained with inductive methods'*. In: *Journal of Applied Physics* **95**, 10 (2004), pp. 5646–5652. DOI: 10.1063/1.1697641 (cited on pages 98, 100, 274).

[349] I. Harward, T. O'Keevan, A. Hutchison, V. Zagorodnii, and Z. Celinski. *'A broadband ferromagnetic resonance spectrometer to measure thin films up to 70 GHz'*. In: *Review of Scientific Instruments* **82**, 9 (2011), p. 095115. DOI: 10.1063/1.3641319 (cited on page 98).

[350] H. Maier-Flaig, S. T. B. Goennenwein, R. Ohshima, M. Shiraishi, R. Gross, H. Huebl, and M. Weiler. *'Note: Derivative divide, a method for the analysis of broadband ferromagnetic resonance in the frequency domain'*. In: *Review of Scientific Instruments* **89**, 7 (2018), p. 076101. DOI: 10.1063/1.5045135 (cited on pages 98, 100–104, 118, 120, 254, 274).

[351] S. S. Kalarickal, P. Krivosik, M. Wu, C. E. Patton, M. L. Schneider, P. Kabos, T. J. Silva, and J. P. Nibarger. *'Ferromagnetic resonance linewidth in metallic thin films: Comparison of measurement methods'*. In: *Journal of Applied Physics* **99**, 9 (2006), p. 093909. DOI: 10.1063/1.2197087 (cited on pages 99, 100, 133, 255, 256, 274).

[352] A. Bystrov, Y. Wang, and P. Gardner. *'Analysis of Vector Network Analyzer Thermal Drift Error'*. In: *Metrology* **2**, 2 (2022), pp. 150–160. DOI: 10.3390/metrology2020010 (cited on page 99).

[353] W. Barry. *'A Broad-Band, Automated, Stripline Technique for the Simultaneous Measurement of Complex Permittivity and Permeability'*. In: *IEEE Transactions on Microwave Theory and Techniques* **34**, 1 (1986), pp. 80–84. DOI: 10.1109/TMTT.1986.1133283 (cited on pages 100, 255, 274).

[354] D. Pain, M. Ledieu, O. Acher, A. L. Adenot, and F. Duverger. *'An improved permeameter for thin film measurements up to 6 GHz'*. In: *Journal of Applied Physics* **85**, 8 (1999), pp. 5151–5153. DOI: 10.1063/1.369107 (cited on pages 100, 274).

[355] C. Bilzer, T. Devolder, P. Crozat, C. Chappert, S. Cardoso, and P. P. Freitas. *'Vector network analyzer ferromagnetic resonance of thin films on coplanar waveguides: Comparison of different evaluation methods'*. In: *Journal of Applied Physics* **101**, 7 (2007), p. 074505. DOI: 10.1063/1.2716995 (cited on pages 100, 104, 255, 266, 274).

[356] C. Bilzer, T. Devolder, P. Crozat, and C. Chappert. *'Open-Circuit One-Port Network Analyzer Ferromagnetic Resonance'*. In: *IEEE Transactions on Magnetics* **44**, 11 (2008), pp. 3265–3268. DOI: 10.1109/TMAG.2008.2004379 (cited on pages 100, 255, 274).

[357] K. J. Kennewell, M. Kostylev, N. Ross, R. Magaraggia, R. L. Stamps, M. Ali, A. A. Stashkevich, D. Greig, and B. J. Hickey. *'Magnetization pinning at a Py/Co interface measured using broadband inductive magnetometry'*. In: *Journal of Applied Physics* **108**, 7 (2010), p. 073917. DOI: 10.1063/1.3488618 (cited on pages 100, 256, 274).

[358] O. Mosendz, B. Kardasz, D. Schmool, and B. Heinrich. *'Spin dynamics at low microwave frequencies in crystalline Fe ultrathin film double layers using co-planar transmission lines'*. In: *Journal of Magnetism and Magnetic Materials* **300**, 1 (2006), pp. 174–178. DOI: 10.1016/j.jmmm.2005.10.058 (cited on pages 100, 274).

[359] M. Weiler, A. Aqeel, M. Mostovoy, A. Leonov, S. Geprägs, R. Gross, H. Huebl, T. T. M. Palstra, and S. T. B. Goennenwein. *'Supplemental information: Helimagnon Resonances in an Intrinsic Chiral Magnonic Crystal'*. In: *Physical Review Letters* **119**, 23 (2017), p. 237204. DOI: 10.1103/PhysRevLett.119.237204 (cited on pages 102, 254).

[360] N. Fermon. Etude des alliages de Heusler de type Co_2MnZ par diffusion Brillouin et effet Kerr magnéto-optique. Rapport de stage M1 physique fondamentale. Gif-sur-Yvette, France: Ecole normale supérieure Paris-Saclay, 2023 (cited on pages 107, 110, 137, 207, 208, 276).

[361] R. Mattheis and G. Quednau. *'Separation of the Voigt Effect in Longitudinal Kerr Magnetometry'*. In: *physica status solidi (a)* **172**, 2 (1999), r7–r8. DOI: 10.1002/(SICI)1521-396X(199904)172:2<R7::AID-PSSA99997>3.0.CO;2-0 (cited on pages 108, 276).

[362] R. Mattheis and G. Quednau. *'Determination of the anisotropy field strength in ultra-thin magnetic films using longitudinal MOKE and a rotating field: the ROTMOKE method'*. In: *Journal of Magnetism and Magnetic Materials* **205**, 2-3 (1999), pp. 143–150. DOI: 10.1016/S0304-8853(99)00526-0 (cited on pages 108, 276).

[363] K. Postava, D. Hrabovský, J. Pištora, A. R. Fert, S. Višňovský, and T. Yamaguchi. *'Anisotropy of quadratic magneto-optic effects in reflection'*. In: *Journal of Applied Physics* **91**, 10 (2002), pp. 7293–7295. DOI: 10.1063/1.1449436 (cited on pages 108, 276).

[364] T. Mewes, H. Nembach, M. Rickart, and B. Hillebrands. *'Separation of the first- and second-order contributions in magneto-optic Kerr effect magnetometry of epitaxial FeMn/NiFe bilayers'*. In: *Journal of Applied Physics* **95**, 10 (2004), pp. 5324–5329. DOI: 10.1063/1.1697640 (cited on pages 108, 276).

[365] J. H. Liang, J. Z. Cao, J. X. Li, and Y. Z. Wu. *'Separation of linear and quadratic magneto-optic Kerr effects in ultra-thin Fe films using a rotating field method'*. In: *Journal of Applied Physics* **117**, 17 (2015), 17E129. DOI: 10.1063/1.4918776 (cited on pages 108, 276).

[366] T. Sebastian, K. Schultheiss, B. Obry, B. Hillebrands, and H. Schultheiss. *'Micro-focused Brillouin light scattering: imaging spin waves at the nanoscale'*. In: *Frontiers in Physics* **3** (2015). DOI: 10.3389/fphy.2015.00035 (cited on pages 109, 110, 145, 175, 176).

[367] J. Cochran. *'3.2 Light Scattering from Ultrathin Magnetic Layers and Bilayers'*. In: *Ultrathin Magnetic Structures II*. Ed. by B. Heinrich and J. A. C. Bland. Berlin, Heidelberg: Springer Berlin Heidelberg, 1994, pp. 195–296 (cited on pages 109, 110).

[368] M. S. Geilen. *'Excitation of spin waves by magneto-elastic effects'*. PhD thesis. Kaiserslautern, Germany: Technische Universität Kaiserslautern, 2022 (cited on pages 109, 176).

[369] B. Heinz. *'Nano-scaled yttrium iron garnet conduits for magnonic networks'*. PhD thesis. Kaiserslautern, Germany: Technische Universität Kaiserslautern, 2021 (cited on pages 109, 175, 176).

[370] T. Brächer. *'Parallel parametric amplification of spin waves in micro-structures'*. PhD thesis. Kaiserslautern, Germany: Technische Universität Kaiserslautern, 2015 (cited on pages 110, 162, 176).

[371] T. Uemura, Y. Imai, S. Kawagishi, K.-i. Matsuda, and M. Yamamoto. *'Epitaxial growth and characterization of Co_2MnSi thin films on GaAs with MgO interlayer'*. In: *Physica E: Low-dimensional Systems and Nanostructures* **40**, 6 (2008), pp. 2025–2027. DOI: 10.1016/j.physe.2007.09.073 (cited on page 114).

[372] J. Liu and S. Qiao. *'Static and dynamic magnetic properties of B2 ordered Co_2MnAl film epitaxially grown on GaAs'*. In: *Journal of Alloys and Compounds* **648** (2015), pp. 706–710. DOI: 10.1016/j.jallcom.2015.07.081 (cited on page 115).

[373] V. Barwal, S. Husain, N. Behera, E. Goyat, and S. Chaudhary. *'Growth dependent magnetization reversal in Co_2MnAl full Heusler alloy thin films'*. In: *Journal of Applied Physics* **123**, 5 (2018), p. 053901. DOI: 10.1063/1.5004425 (cited on pages 115, 116).

[374] M. J. Pechan, C. Yu, D. Carr, and C. J. Palmstrøm. *'Remarkable strain-induced magnetic anisotropy in epitaxial Co2MnGa (001) films'*. In: *Journal of Magnetism and Magnetic Materials* **286** (2005), pp. 340–345. DOI: 10.1016/j.jmmm.2004.09.090 (cited on page 117).

[375] Y. Li, J. Xia, G. Wang, H. Yuan, and H. Chen. *'High-performance giant-magnetoresistance junction with B 2-disordered Heusler alloy based Co2MnAl/Ag/Co2MnAl trilayer'*. In: *Journal of Applied Physics* **118**, 5 (2015), p. 053902. DOI: 10.1063/1.4927834 (cited on page 117).

[376] H. L. Yu, H. B. Zhang, X. F. Jiang, Y. Zheng, and G. W. Yang. *'Transport and magnetic properties of the Co2MnSi/Al/Co2MnSi trilayer'*. In: *Applied Physics Letters* **100**, 22 (2012), p. 222407. DOI: 10.1063/1.4725513 (cited on page 117).

[377] L. Baselgia, M. Warden, F. Waldner, S. L. Hutton, J. E. Drumheller, Y. Q. He, P. E. Wigen, and M. Maryško. *'Derivation of the resonance frequency from the free energy of ferromagnets'*. In: *Physical Review B* **38**, 4 (1988), pp. 2237–2242. DOI: 10.1103/PhysRevB.38.2237 (cited on page 121).

[378] B. A. Kalinikos and A. N. Slavin. *'Theory of dipole-exchange spin wave spectrum for ferromagnetic films with mixed exchange boundary conditions'*. In: *Journal of Physics C: Solid State Physics* **19**, 35 (1986), pp. 7013–7033. DOI: 10.1088/0022-3719/19/35/014 (cited on pages 121, 152, 153, 155, 223, 230, 249, 277).

[379] B. A. Kalinikos, M. P. Kostylev, N. V. Kozhus, and A. N. Slavin. *'The dipole-exchange spin wave spectrum for anisotropic ferromagnetic films with mixed exchange boundary conditions'*. In: *Journal of Physics: Condensed Matter* **2**, 49 (1990), pp. 9861–9877. DOI: 10.1088/0953-8984/2/49/012 (cited on pages 121, 152, 153, 155, 223, 230, 249, 277).

[380] S. Lee, S. Grudichak, J. Sklenar, C. C. Tsai, M. Jang, Q. Yang, H. Zhang, and J. B. Ketterson. *'Ferromagnetic resonance of a YIG film in the low frequency regime'*. In: *Journal of Applied Physics* **120**, 3 (2016), p. 033905. DOI: 10.1063/1.4956435 (cited on page 124).

[381] M. Belmeguenai, F. Zighem, D. Faurie, H. Tuzcuoglu, S.-M. Chérif, P. Moch, K. Westerholt, and W. Seiler. *'Structural and magnetic properties of Co_2MnSi thin films'*. In: *physica status solidi (a)* **209**, 7 (2012), pp. 1328–1333. DOI: 10.1002/pssa.201228039 (cited on page 127).

[382] J. Hamrle, O. Gaier, S.-G. Min, B. Hillebrands, Y. Sakuraba, and Y. Ando. *'Determination of exchange constants of Heusler compounds by Brillouin light scattering spectroscopy: application to Co_2MnSi'*. In: *Journal of Physics D: Applied Physics* **42**, 8 (2009), p. 084005. DOI: 10.1088/0022-3727/42/8/084005 (cited on pages 127, 202, 208, 280).

[383] R. Y. Umetsu, A. Okubo, A. Fujita, T. Kanomata, K. Ishida, and R. Kainuma. *'Spin Wave-Stiffness Constants of Half-Metallic Ferromagnets Co_2YZ (Y=Cr, Mn, and Fe, Z=Ga, Al, and Si) Heusler Alloys'*. In: *IEEE Transactions on Magnetics* **47**, 10 (2011), pp. 2451–2454. DOI: 10.1109/TMAG.2011.2158521 (cited on page 128).

[384] M. Maryško. *'Ferromagnetic resonance relations in {110} garnet films with induced orthorhombic anisotropy'*. In: *Czechoslovak Journal of Physics B* **31** (1981), pp. 1187–1190. DOI: 10.1007/BF01604784 (cited on page 129).

[385] C. Mellinger, J. Waybright, X. Zhang, C. Schmidt, and X. Xu. *'Perpendicular magnetic anisotropy in conducting $NiCo_2O_4$ films from spin-lattice coupling'*. In: *Physical Review B* **101**, 1 (2020), p. 014413. DOI: 10.1103/PhysRevB.101.014413 (cited on page 129).

[386] G. H. O. Daalderop, P. J. Kelly, and F. J. A. Den Broeder. *'Prediction and confirmation of perpendicular magnetic anisotropy in Co/Ni multilayers'*. In: *Physical Review Letters* **68**, 5 (1992), pp. 682–685. DOI: 10.1103/PhysRevLett.68.682 (cited on page 129).

[387] J.-M. Beaujour, D. Ravelosona, I. Tudosa, E. E. Fullerton, and A. D. Kent. *'Ferromagnetic resonance linewidth in ultrathin films with perpendicular magnetic anisotropy'*. In: *Physical Review B* **80**, 18 (2009), p. 180415. DOI: 10.1103/PhysRevB.80.180415 (cited on page 129).

[388] K. Munira, J. Romero, and W. H. Butler. *'Achieving perpendicular anisotropy in half-metallic Heusler alloys for spin device applications'*. In: *Journal of Applied Physics* **115**, 17 (2014), 17B731. DOI: 10.1063/1.4866703 (cited on page 129).

[389] J. H. Van Vleck. *'On the Anisotropy of Cubic Ferromagnetic Crystals'*. In: *Physical Review* **52**, 11 (1937), pp. 1178–1198. DOI: 10.1103/PhysRev.52.1178 (cited on page 129).

[390] M. Maryško. *'Ferromagnetic resonance relations in {111}-oriented garnet films'*. In: *Czechoslovak Journal of Physics B* **30** (1980), pp. 1269–1278. DOI: 10.1007/BF01605626 (cited on pages 129, 130).

[391] T. J. Silva, C. S. Lee, T. M. Crawford, and C. T. Rogers. *'Inductive measurement of ultrafast magnetization dynamics in thin-film Permalloy'*. In: *Journal of Applied Physics* **85**, 11 (1999), pp. 7849–7862. DOI: 10.1063/1.370596 (cited on page 133).

[392] R. Yilgin, Y. Sakuraba, M. Oogane, S. Mizukami, Y. Ando, and T. Miyazaki. *'Anisotropic Intrinsic Damping Constant of Epitaxial Co_2MnSi Heusler Alloy Films'*. In: *Japanese Journal of Applied Physics* **46**, 3L (2007), p. L205. DOI: 10.1143/JJAP.46.L205 (cited on pages 134, 136, 207, 275).

[393] R. Silber, D. Král, O. Stejskal, T. Kubota, Y. Ando, J. Pištora, M. Veis, J. Hamrle, and T. Kuschel. Longitudinal and quadratic magnetooptic Kerr effect spectra of Co_2MnSi Heusler compound. 2020. DOI: 10.5281/ZENODO.3725536. URL: https://zenodo.org/record/3725536 (cited on pages 143, 146, 147).

[394] A. De Laire. *'Recent results for the Landau–Lifshitz equation'*. In: *SeMA Journal* **79**, 2 (2022), pp. 253–295. DOI: 10.1007/s40324-021-00254-1 (cited on pages 151, 277).

[395] S. Rezende and F. De Aguiar. *'Spin-wave instabilities, auto-oscillations, and chaos in yttrium-iron-garnet'*. In: *Proceedings of the IEEE* **78**, 6 (1990), pp. 893–908. DOI: 10.1109/5.56906 (cited on page 151).

[396] L. F. Álvarez, O. Pla, and O. Chubykalo. *'Quasiperiodicity, bistability, and chaos in the Landau-Lifshitz equation'*. In: *Physical Review B* **61**, 17 (2000), pp. 11613–11617. DOI: 10.1103/PhysRevB.61.11613 (cited on pages 151, 277).

[397] G. Bertotti, C. Serpico, and I. D. Mayergoyz. *'Nonlinear Magnetization Dynamics under Circularly Polarized Field'*. In: *Physical Review Letters* **86**, 4 (2001), pp. 724–727. DOI: 10.1103/PhysRevLett.86.724 (cited on pages 151, 277).

[398] J. He and S. Zhang. *'Localized steady-state domain wall oscillators'*. In: *Applied Physics Letters* **90**, 14 (2007), p. 142508. DOI: 10.1063/1.2719646 (cited on pages 151, 277).

[399] S. Petit-Watelot, J.-V. Kim, A. Ruotolo, R. M. Otxoa, K. Bouzehouane, J. Grollier, A. Vansteenkiste, B. Van De Wiele, V. Cros, and T. Devolder. *'Commensurability and chaos in magnetic vortex oscillations'*. In: *Nature Physics* **8**, 9 (2012), pp. 682–687. DOI: 10.1038/nphys2362 (cited on pages 151, 277).

[400] M. Manfrini, J.-V. Kim, S. Petit-Watelot, W. Van Roy, L. Lagae, C. Chappert, and T. Devolder. *'Propagation of magnetic vortices using nanocontacts as tunable attractors'*. In: *Nature Nanotechnology* **9**, 2 (2014), pp. 121–125. DOI: 10.1038/nnano.2013.265 (cited on pages 151, 277).

[401] P. Krivosik and C. E. Patton. *'Hamiltonian formulation of nonlinear spin-wave dynamics: Theory and applications'*. In: *Physical Review B* **82**, 18 (2010), p. 184428. DOI: 10.1103/PhysRevB.82.184428 (cited on pages 151, 162, 164–168, 277).

[402] V. Tyberkevych, A. Slavin, P. Artemchuk, and G. Rowlands. Vector Hamiltonian Formalism for Nonlinear Magnetization Dynamics. Version Number: 1. 2020. DOI: 10.48550/ARXIV.2011.13562. URL: https://arxiv.org/abs/2011.13562 (cited on pages 151, 162, 164, 165, 277, 278).

[403] V. S. L'vov. Wave Turbulence under Parametric Excitation: Applications to Magnets. Springer Series in Nonlinear Dynamics Ser. Berlin, Heidelberg: Springer Berlin / Heidelberg, 1994 (cited on pages 151, 162, 165, 189, 277).

[404] C. Herring and C. Kittel. *'On the Theory of Spin Waves in Ferromagnetic Media'*. In: *Physical Review* **81**, 5 (1951), pp. 869–880. DOI: 10.1103/PhysRev.81.869 (cited on page 152).

[405] C. Herring and C. Kittel. *'The Theory of Spin Waves in Ferromagnetic Media'*. In: *Physical Review* **88**, 6 (1952), pp. 1435–1435. DOI: 10.1103/PhysRev.88.1435.3 (cited on page 152).

[406] R. Damon and J. Eshbach. *'Magnetostatic modes of a ferromagnet slab'*. In: *Journal of Physics and Chemistry of Solids* **19**, 3-4 (1961), pp. 308–320. DOI: 10.1016/0022-3697(61)90041-5 (cited on pages 152, 154).

[407] M. Hurben and C. Patton. *'Theory of magnetostatic waves for in-plane magnetized isotropic films'*. In: *Journal of Magnetism and Magnetic Materials* **139**, 3 (1995), pp. 263–291. DOI: 10.1016/0304-8853(95)90006-3 (cited on pages 152, 154).

[408] A. Mahmoud, F. Ciubotaru, F. Vanderveken, A. V. Chumak, S. Hamdioui, C. Adelmann, and S. Cotofana. *'Introduction to spin wave computing'*. In: *Journal of Applied Physics* **128**, 16 (2020), p. 161101. DOI: 10.1063/5.0019328 (cited on page 154).

[409] M. P. Kostylev, G. Gubbiotti, J.-G. Hu, G. Carlotti, T. Ono, and R. L. Stamps. *'Dipole-exchange propagating spin-wave modes in metallic ferromagnetic stripes'*. In: *Physical Review B* **76**, 5 (2007), p. 054422. DOI: 10.1103/PhysRevB.76.054422 (cited on page 161).

[410] S. O. Demokritov, ed. Spin Wave Confinement. 1st ed. Jenny Stanford Publishing, 2019. DOI: 10.1201/9780429066535 (cited on page 161).

[411] R. I. Joseph and E. Schlömann. *'Demagnetizing Field in Nonellipsoidal Bodies'*. In: *Journal of Applied Physics* **36**, 5 (1965), pp. 1579–1593. DOI: 10.1063/1.1703091 (cited on page 161).

[412] C. Bayer, J. Jorzick, S. O. Demokritov, A. N. Slavin, K. Y. Guslienko, D. V. Berkov, N. L. Gorn, M. P. Kostylev, and B. Hillebrands. *'Chapter 2: Spin-Wave Excitations in Finite Rectangular Elements'*. In: *Spin Dynamics in Confined Magnetic Structures III*. Ed. by B. Hillebrands and A. Thiaville. Vol. 101. Series Title: Topics in Applied Physics. Springer Berlin Heidelberg, 2006, pp. 57–103. DOI: 10.1007/10938171_2 (cited on page 161).

[413] A. Vansteenkiste, J. Leliaert, M. Dvornik, M. Helsen, F. Garcia-Sanchez, and B. Van Waeyenberge. *'The design and verification of MuMax3'*. In: *AIP Advances* **4**, 10 (2014), p. 107133. DOI: 10.1063/1.4899186 (cited on page 162).

[414] L. Körber, G. Quasebarth, A. Hempel, F. Zahn, A. Otto, E. Westphal, R. Hertel, and A. Kakay. TetraX: Finite-Element Micromagnetic-Modeling Package. 2022. DOI: 10.14278/RODARE.1418. URL: https://rodare.hzdr.de/record/1418 (cited on page 162).

[415] L. Körber, G. Quasebarth, A. Otto, and A. Kákay. *'Finite-element dynamic-matrix approach for spin-wave dispersions in magnonic waveguides with arbitrary cross section'*. In: *AIP Advances* **11**, 9 (2021), p. 095006. DOI: 10.1063/5.0054169 (cited on page 162).

[416] L. Körber, A. Hempel, A. Otto, R. A. Gallardo, Y. Henry, J. Lindner, and A. Kákay. *'Finite-element dynamic-matrix approach for propagating spin waves: Extension to mono- and multi-layers of arbitrary spacing and thickness'*. In: *AIP Advances* **12**, 11 (2022), p. 115206. DOI: 10.1063/5.0107457 (cited on page 162).

[417] M. T. Weiss. *'Microwave and Low-Frequency Oscillation Due to Resonance Instabilities in Ferrites'*. In: *Physical Review Letters* **1**, 7 (1958), pp. 239–241. DOI: 10.1103/PhysRevLett.1.239 (cited on pages 162, 164).

[418] R. Verba, V. Tiberkevich, and A. Slavin. *'Hamiltonian formalism for nonlinear spin wave dynamics under antisymmetric interactions: Application to Dzyaloshinskii-Moriya interaction'*. In: *Physical Review B* **99**, 17 (2019), p. 174431. DOI: 10.1103/PhysRevB.99.174431 (cited on pages 162, 165, 167).

[419] H. M. Olson, P. Krivosik, K. Srinivasan, and C. E. Patton. *'Ferromagnetic resonance saturation and second order Suhl spin wave instability processes in thin Permalloy films'*. In: *Journal of Applied Physics* **102**, 2 (2007), p. 023904. DOI: 10.1063/1.2756481 (cited on pages 162, 278).

[420] H. T. Nembach, K. L. Livesey, M. P. Kostylev, P. Martin-Pimentel, S. J. Hermsdoerfer, B. Leven, J. Fassbender, and B. Hillebrands. *'Magneto-optical observation of four-wave scattering in a 15-nm $Ni_{81}Fe_{19}$ film during large-angle magnetization precession'*. In: *Physical Review B* **84**, 18 (2011), p. 184413. DOI: 10.1103/PhysRevB.84.184413 (cited on pages 162, 278).

[421] H. Schultheiss, K. Vogt, and B. Hillebrands. *'Direct observation of nonlinear four-magnon scattering in spin-wave microconduits'*. In: *Physical Review B* **86**, 5 (2012), p. 054414. DOI: 10.1103/PhysRevB.86.054414 (cited on pages 162, 197, 278).

[422] K. L. Livesey, M. P. Kostylev, and R. L. Stamps. *'Parametric spin wave excitation and cascaded processes during switching in thin films'*. In: *Physical Review B* **75**, 17 (2007), p. 174427. DOI: 10.1103/PhysRevB.75.174427 (cited on pages 162, 167, 187, 193, 278).

[423] T. Nikuni, M. Oshikawa, A. Oosawa, and H. Tanaka. *'Bose-Einstein Condensation of Dilute Magnons in $TlCuCl_3$'*. In: *Physical Review Letters* **84**, 25 (2000), pp. 5868–5871. DOI: 10.1103/PhysRevLett.84.5868 (cited on pages 162, 278).

[424] T. Giamarchi, C. Rüegg, and O. Tchernyshyov. *'Bose-Einstein condensation in magnetic insulators'*. In: *Nature Physics* **4**, 3 (2008), pp. 198–204. DOI: 10.1038/nphys893 (cited on pages 162, 278).

[425] M. Schneider, T. Brächer, D. Breitbach, V. Lauer, P. Pirro, D. A. Bozhko, H. Y. Musiienko-Shmarova, B. Heinz, Q. Wang, T. Meyer, F. Heussner, S. Keller, E. T. Papaioannou, B. Lägel, T. Löber, C. Dubs, A. N. Slavin, V. S. Tiberkevich, A. A. Serga, B. Hillebrands, and A. V. Chumak. *'Bose-Einstein condensation of quasiparticles by rapid cooling'*. In: *Nature Nanotechnology* **15**, 6 (2020), pp. 457–461. DOI: 10.1038/s41565-020-0671-z (cited on pages 162, 278).

[426] M. Schneider, D. Breitbach, R. O. Serha, Q. Wang, A. A. Serga, A. N. Slavin, V. S. Tiberkevich, B. Heinz, B. Lägel, T. Brächer, C. Dubs, S. Knauer, O. V. Dobrovolskiy, P. Pirro, B. Hillebrands, and A. V. Chumak. *'Control of the Bose-Einstein Condensation of Magnons by the Spin Hall Effect'*. In: *Physical Review Letters* **127**, 23 (2021), p. 237203. DOI: 10.1103/PhysRevLett.127.237203 (cited on pages 162, 278).

[427] M. Mohseni, Q. Wang, B. Heinz, M. Kewenig, M. Schneider, F. Kohl, B. Lägel, C. Dubs, A. V. Chumak, and P. Pirro. *'Controlling the Nonlinear Relaxation of Quantized Propagating Magnons in Nanodevices'*. In: *Physical Review Letters* **126**, 9 (2021), p. 097202. DOI: 10.1103/PhysRevLett.126.097202 (cited on pages 163, 187, 189–191, 193, 201, 208, 278).

[428] M. Geilen, R. Verba, A. Hamadeh, A. Nicoloiu, D. Narducci, A. Dinescu, M. Ender, M. Mohseni, F. Ciubotaru, M. Weiler, A. Müller, B. Hillebrands, C. Adelmann, and P. Pirro. *'Parametric Excitation and Instabilities of Spin Waves Driven by Surface Acoustic Waves'*. In: *Advanced Physics Research* **4**, 1 (2025), p. 2400086. DOI: 10.1002/apxr.202400086 (cited on pages 163, 278).

[429] D. Breitbach, M. Schneider, B. Heinz, F. Kohl, J. Maskill, L. Scheuer, R. O. Serha, T. Brächer, B. Lägel, C. Dubs, V. S. Tiberkevich, A. N. Slavin, A. A. Serga, B. Hillebrands, A. V. Chumak, and P. Pirro. *'Stimulated Amplification of Propagating Spin Waves'*. In: *Physical Review Letters* **131**, 15 (2023), p. 156701. DOI: 10.1103/PhysRevLett.131.156701 (cited on pages 163, 278).

[430] Y. Zhang, C. Patton, and M. Kogekar. *'Ferromagentic resonance foldover in single crystal YIG films–Sample heating or suhl instability'*. In: *IEEE Transactions on Magnetics* **22**, 5 (1986), pp. 993–995. DOI: 10.1109/TMAG.1986.1064446 (cited on pages 164, 278).

[431] M. Chen, C. Patton, G. Srinivasan, and Y. Zhang. *'Ferromagnetic resonance foldover and spin-wave instability in single-crystal YIG films'*. In: *IEEE Transactions on Magnetics* **25**, 5 (1989), pp. 3485–3487. DOI: 10.1109/20.42343 (cited on pages 164, 278).

[432] Y. Fetisov, C. Patton, and V. Synogach. *'Nonlinear ferromagnetic resonance and foldover in yttrium iron garnet thin films-inadequacy of the classical model'*. In: *IEEE Transactions on Magnetics* **35**, 6 (1999), pp. 4511–4521. DOI: 10.1109/20.809144 (cited on pages 164, 278).

[433] Y. Fetisov and C. Patton. *'Thermal Microwave Foldover and Bistability in Ferromagnetic Resonance'*. In: *IEEE Transactions on Magnetics* **40**, 2 (2004), pp. 473–482. DOI: 10.1109/TMAG.2004.824132 (cited on pages 164, 278).

[434] D. V. Slobodianiuk, G. A. Melkov, K. Schultheiss, H. Schultheiss, and R. V. Verba. *'Nonlinear Ferromagnetic Resonance in the Presence of Three-Magnon Scattering in Magnetic Nanostructures'*. In: *IEEE Magnetics Letters* **10** (2019), pp. 1–5. DOI: 10.1109/LMAG.2019.2913132 (cited on pages 164, 278).

[435] A. Slavin and V. Tiberkevich. *'Spin Wave Mode Excited by Spin-Polarized Current in a Magnetic Nanocontact is a Standing Self-Localized Wave Bullet'*. In: *Physical Review Letters* **95**, 23 (2005), p. 237201. DOI: 10.1103/PhysRevLett.95.237201 (cited on pages 164, 278).

[436] S. M. Rezende, F. M. De Aguiar, and A. Azevedo. *'Magnon excitation by spin-polarized direct currents in magnetic nanostructures'*. In: *Physical Review B* **73**, 9 (2006), p. 094402. DOI: 10.1103/PhysRevB.73.094402 (cited on pages 164, 278).

[437] J.-V. Kim, V. Tiberkevich, and A. N. Slavin. *'Generation Linewidth of an Auto-Oscillator with a Nonlinear Frequency Shift: Spin-Torque Nano-Oscillator'*. In: *Physical Review Letters* **100**, 1 (2008), p. 017207. DOI: 10.1103/PhysRevLett.100.017207 (cited on pages 164, 165, 278).

[438] A. Dussaux, A. V. Khvalkovskiy, P. Bortolotti, J. Grollier, V. Cros, and A. Fert. *'Field dependence of spin-transfer-induced vortex dynamics in the nonlinear regime'*. In: *Physical Review B* **86**, 1 (2012), p. 014402. DOI: 10.1103/PhysRevB.86.014402 (cited on pages 164, 278).

[439] M. Ranjbar, P. Durrenfeld, M. Haidar, E. Iacocca, M. Balinskiy, T. Q. Le, M. Fazlali, A. Houshang, A. A. Awad, R. K. Dumas, and J. Akerman. *'CoFeB-Based Spin Hall Nano-Oscillators'*. In: *IEEE Magnetics Letters* **5** (2014), pp. 1–4. DOI: 10.1109/LMAG.2014.2375155 (cited on pages 164, 278).

[440] V. E. Demidov, H. Ulrichs, S. V. Gurevich, S. O. Demokritov, V. S. Tiberkevich, A. N. Slavin, A. Zholud, and S. Urazhdin. *'Synchronization of spin Hall nano-oscillators to external microwave signals'*. In: *Nature Communications* **5**, 1 (2014), p. 3179. DOI: 10.1038/ncomms4179 (cited on pages 164, 278).

[441] N. Locatelli, A. Hamadeh, F. Abreu Araujo, A. D. Belanovsky, P. N. Skirdkov, R. Lebrun, V. V. Naletov, K. A. Zvezdin, M. Muñoz, J. Grollier, O. Klein, V. Cros, and G. De Loubens. *'Efficient Synchronization of Dipolarly Coupled Vortex-Based Spin Transfer Nano-Oscillators'*. In: *Scientific Reports* **5**, 1 (2015), p. 17039. DOI: 10.1038/srep17039 (cited on pages 164, 278).

[442] Y. Li, X. De Milly, O. Klein, V. Cros, J. Grollier, and G. De Loubens. *'Selective control of vortex polarities by microwave field in two robustly synchronized spin-torque nano-oscillators'*. In: *Applied Physics Letters* **112**, 2 (2018), p. 022405. DOI: 10.1063/1.5012768 (cited on pages 164, 278).

[443] B. Divinskiy, V. E. Demidov, S. Urazhdin, R. Freeman, A. B. Rinkevich, and S. O. Demokritov. *'Controllable excitation of quasi-linear and bullet modes in a spin-Hall nano-oscillator'*. In: *Applied Physics Letters* **114**, 4 (2019), p. 042403. DOI: 10.1063/1.5064841 (cited on pages 164, 278).

[444] V. E. Zakharov, V. S. L'vov, and S. S. Starobinets. *'Spin-wave turbulence beyond the parametric excitation threshold'*. In: *Soviet Physics Uspekhi* **17**, 6 (1975), pp. 896–919. DOI: 10.1070/PU1975v017n06ABEH004404 (cited on page 165).

[445] T. Holstein and H. Primakoff. *'Field Dependence of the Intrinsic Domain Magnetization of a Ferromagnet'*. In: *Physical Review* **58**, 12 (1940), pp. 1098–1113. DOI: 10.1103/PhysRev.58.1098 (cited on page 165).

[446] L. Giovannini, R. Zivieri, G. Gubbiotti, G. Carlotti, L. Pareti, and G. Turilli. *'Theory of Brillouin cross section for scattering from magnetic multilayers: Second-order magneto-optic effect in Ni/Cu bilayers and trilayers'*. In: *Physical Review B* **63**, 10 (2001), p. 104405. DOI: 10.1103/PhysRevB.63.104405 (cited on page 182).

[447] O. Wojewoda. *'Brillouin light scattering characterization of nanoscale spin waves'*. PhD thesis. Brno, Czech Republic: Brno University of Technology, 2024 (cited on page 182).

[448] V. E. Demidov, S. O. Demokritov, K. Rott, P. Krzysteczko, and G. Reiss. *'Self-focusing of spin waves in Permalloy microstripes'*. In: *Applied Physics Letters* **91**, 25 (2007), p. 252504. DOI: 10.1063/1.2825421 (cited on page 188).

[449] V. E. Demidov, S. O. Demokritov, K. Rott, P. Krzysteczko, and G. Reiss. *'Mode interference and periodic self-focusing of spin waves in permalloy microstripes'*. In: *Physical Review B* **77**, 6 (2008), p. 064406. DOI: 10.1103/PhysRevB.77.064406 (cited on page 188).

[450] A. Savitzky and M. J. E. Golay. *'Smoothing and Differentiation of Data by Simplified Least Squares Procedures.'* In: *Analytical Chemistry* **36**, 8 (1964), pp. 1627–1639. DOI: 10.1021/ac60214a047 (cited on page 190).

[451] A. J. E. Kreil, D. A. Bozhko, H. Y. Musiienko-Shmarova, V. I. Vasyuchka, V. S. L'vov, A. Pomyalov, B. Hillebrands, and A. A. Serga. *'From Kinetic Instability to Bose-Einstein Condensation and Magnon Supercurrents'*. In: *Physical Review Letters* **121**, 7 (2018), p. 077203. DOI: 10.1103/PhysRevLett.121.077203 (cited on page 193).

[452] K. Sobucki, I. Lyubchanskii, M. Krawczyk, and P. Gruszecki. *'Goos–Hänchen shift of inelastically scattered spin-wave beams and cascade nonlinear magnon processes'*. In: *Scientific Reports* **15**, 1 (2025), p. 5538. DOI: 10.1038/s41598-025-86879-y (cited on page 193).

[453] H. Schultheiß. *'Kohärenz und Dämpfungsverhalten von Spinwellen in magnetischen Mikrostrukturen'*. PhD thesis. Kaiserslautern, Germany: Technische Universität Kaiserslautern, 2010 (cited on pages 197, 198).

[454] Q. Wang, R. Verba, B. Heinz, M. Schneider, O. Wojewoda, K. Davídková, K. Levchenko, C. Dubs, N. J. Mauser, M. Urbánek, P. Pirro, and A. V. Chumak. *'Deeply nonlinear excitation of self-normalized short spin waves'*. In: *Science Advances* **9**, 32 (2023), eadg4609. DOI: 10.1126/sciadv.adg4609 (cited on page 197).

[455] S. Odintsov, S. Sheshukova, S. Nikitov, and A. Sadovnikov. *'Lateral and vertical spin-wave transport in a multimode magnonic ring coupler'*. In: *Physical Review Applied* **22**, 1 (2024), p. 014042. DOI: 10.1103/PhysRevApplied.22.014042 (cited on pages 197, 208).

[456] F. Vilsmeier, T. Taniguchi, M. Lindner, C. Riedel, and C. Back. Spin wave propagation in a ring-shaped magnonic waveguide. arXiv:2504.17920 [cond-mat]. 2025. DOI: 10.48550/arXiv.2504.17920. URL: http://arxiv.org/abs/2504.17920 (cited on pages 197, 208).

[457] A. V. Chumak, P. Dhagat, A. Jander, A. A. Serga, and B. Hillebrands. *'Reverse Doppler effect of magnons with negative group velocity scattered from a moving Bragg grating'*. In: *Physical Review B* **81**, 14 (2010), p. 140404. DOI: 10.1103/PhysRevB.81.140404 (cited on page 198).

[458] T. Brächer, P. Pirro, and B. Hillebrands. *'Parallel pumping for magnon spintronics: Amplification and manipulation of magnon spin currents on the micron-scale'*. In: *Physics Reports* **699** (2017), pp. 1–34. DOI: 10.1016/j.physrep.2017.07.003 (cited on page 206).

[459] B. Heinz, M. Mohseni, A. Lentfert, R. Verba, M. Schneider, B. Lägel, K. Levchenko, T. Brächer, C. Dubs, A. V. Chumak, and P. Pirro. *'Parametric generation of spin waves in nanoscaled magnonic conduits'*. In: *Physical Review B* **105**, 14 (2022), p. 144424. DOI: 10.1103/PhysRevB.105.144424 (cited on page 206).

[460] O. Wojewoda, F. Ligmajer, M. Hrtoň, J. Klíma, M. Dhankhar, K. Davídková, M. Staňo, J. Holobrádek, J. Krčma, J. Zlámal, T. Šikola, and M. Urbánek. *'Observing high-k magnons with Mie-resonance-enhanced Brillouin light scattering'*. In: *Communications Physics* **6**, 1 (2023), p. 94. DOI: 10.1038/s42005-023-01214-z (cited on page 207).

List of Figures

1.1 Heusler materials - schematic of lattice structure and periodic table of possible combinations 8
1.2 Heusler materials - Slater-Pauling behaviour of half-metallic X_2YZ Heusler compounds 9
1.3 Heusler materials - exemplary half-metallic DOS calculated for Co_2MnSi 10
1.4 Heusler materials - chemical disorder types in Heusler compounds 12

2.1 Samples - schematic of the MBE system used for the thin film growth 18
2.2 Samples - definition of the vectors for the atomic form factor and the structure factor 20
2.3 Samples - reciprocal lattice from a 2D atomic plane 21
2.4 Samples - RHEED pattern presenting signs of 3D growth 21
2.5 Samples - RHEED pattern presenting signs of chemical ordering 22
2.6 Samples - schematic of the epitaxial relationship of Co2MnSi on MgO 23
2.7 Samples - RHEED images of the MgO buffer layer and the Co_2MnSi layer grown on top 24
2.8 Samples - exemplary growth rate regulations for the Co_2MnSi growth 25
2.9 Samples - RHEED images before and after the annealing of the Co_2MnSi layer 26
2.10 Samples - Auger spectrum after deposition of the MgO/Ti capping bilayer 27

3.1 Structural characterisation - example of a FIB cross section at various stages in the process. 34
3.2 Structural characterisation - illustration of the (110) atomic planes of the Heusler lattice for the different disorders. 35
3.3 Structural characterisation - Fourier filtering of TEM/STEM micrographs. 36
3.4 Structural characterisation - chemical ordering analysis of Co_2MnSi in HAADF-STEM. 38
3.5 Structural characterisation - MgO / Co_2MnSi / MgO epitaxy in HRTEM. 39
3.6 Structural characterisation - schematic of the epitaxial relationship of Co2MnSi on MgO 39
3.7 Structural characterisation - dislocation analysis at the Co_2MnSi interfaces in HAADF-STEM. 40
3.8 Structural characterisation - directly imaged dislocations at the Co_2MnSi interfaces. 40
3.9 Structural characterisation - schematic of an edge dislocation. 41
3.10 Structural characterisation - tuning of dislocations by a seed layer. 41
3.11 Structural characterisation - directly imaged dislocations at the Co_2MnSi interfaces. 42
3.12 Structural characterisation - tuning of dislocations by a seed layer. 42
3.13 Structural characterisation - continuous Pt, Pd, MgO/Ti capping films. 43
3.14 Structural characterisation - example of an Au capping film with gaps. 44
3.15 Structural characterisation - islands in the MgO/Ti bilayer capping. 44
3.17 Structural characterisation - uneven MgO buffer layer site in HAADF-STEM. 45
3.16 Structural characterisation - EDXS mapping of the incomplete MgO/Al capping. 45
3.18 Structural characterisation - the lithography process. 47
3.19 Structural characterisation - overview of the nanostructures on two TEM lamellas. 49
3.20 Structural characterisation - exemplary cross sections of two etched waveguides 50
3.21 Structural characterisation - minimal etched waveguide widths. 51
3.22 Structural characterisation - minimal etched gap sizes. 52
3.23 Structural characterisation - exemplary cross sections of two etched waveguides 53
3.24 Structural characterisation - EDXS elemental mapping after the micro/nano-structuring process. . . 54
3.25 Structural characterisation - EDXS elemental mapping after the micro/nano-structuring process. . . 55
3.26 Structural characterisation - $L2_1$ order in the etched Co_2MnSi waveguides. 57

4.1 Magnetism concepts - schematic of the 1D ferromagnetic and anti-ferromagnetic ordering 66
4.2 Magnetism concepts - first order cubic magnetocrystalline anisotropy energy 70
4.3 Magnetism concepts - second order cubic anisotropy energy 70

4.4 Magnetism concepts - first and second order cubic anisotropy energy for constants of opposite sign 71
4.5 Magnetism concepts - first order uniaxial anisotropy energy . . . 72
4.6 Magnetism concepts - schematic of a typical hysteresis loop and its key properties. . . . 74
4.7 Magnetisation dynamics - schematic of the undamped precession of the magnetisation . . . 75
4.8 Magnetisation dynamics - schematic of the damped magnetisation oscillation . . . 76
4.9 Magnetisation dynamics - angles and coordinate definitions for the linearisation of the LLG . . . 77
4.10 Magneto-optical interactions - simplified sketch of MOKE transitions . . . 86

5.1 VSM - schematic of the VSM setup . . . 94
5.2 FMR - calculated real and imaginary curves of the susceptibility tensor component $\chi_{\varphi\varphi}$ . . . 97
5.3 FMR - schematic of the BB-FMR setup with rotating field option . . . 98
5.4 FMR - schematic of a sample on a coplanar waveguide . . . 98
5.5 FMR - BB-FMR data analysis study - raw S_{21} data - zoom on FMR . . . 99
5.6 FMR - BB-FMR data analysis study - raw S_{21} data - full spectrum . . . 99
5.7 FMR - BB-FMR data analysis study - derivative divide - 2D maps . . . 102
5.8 FMR - BB-FMR data analysis study - frequency modulation amplitude in derivative divide procedure 102
5.9 FMR - BB-FMR data analysis study - derivative divide - spectra . . . 103
5.10 FMR - BB-FMR data analysis study - functions used in the derivative divide procedure . . . 103
5.11 FMR - BB-FMR data analysis study - derivative divide - fit curves . . . 104
5.12 FMR - BB-FMR data analysis study - derivative divide - results . . . 105
5.13 FMR - BB-FMR data analysis study - derivative divide - zoom-in on linewidth results . . . 105
5.14 MOKE - schematic of LMOKE, TMOKE and PMOKE setup geometries . . . 107
5.15 MOKE - schematic of the LMOKE setup in this work . . . 107
5.16 BLS - schematic of Stokes and Anti-Stokes process . . . 109
5.17 BLS - schematic of tandem Fabry-Pérot interferometer . . . 109
5.18 BLS - schematic of backscattering geometry . . . 110

6.2 VSM study - in-plane hysteresis loops from the 20 nm thick Co_2MnSi film. . . . 112
6.1 Sample for FMR/VSM study - Co_2MnSi thin film stack . . . 112
6.3 VSM study - results from the 20 nm thick Co_2MnSi film. . . . 113
6.4 Sample for FMR/VSM study - Co_2MnAl thin film stack . . . 114
6.5 VSM study - in-plane hysteresis loops from the 20 nm thick Co_2MnAl film. . . . 115
6.6 VSM study - results from the 20 nm thick Co_2MnAl film. . . . 115
6.7 VSM study - direct comparison of the in-plane hysteresis loops from Co_2MnSi and Co_2MnAl. . . . 116
6.8 VSM study - direct comparison of the remanence and coercive field from Co_2MnSi and Co_2MnAl. . . 116
6.9 FMR study - overview of the spectra along the high symmetry directions . . . 119
6.10 FMR study - overview of the rotational data at fixed fields . . . 120
6.11 FMR study - exemplary resonance curves from both samples . . . 121
6.12 FMR study - rotational FMR analysis of the Co_2MnSi film . . . 125
6.13 FMR study - out-of-plane data and anisotropy fits for Co_2MnSi . . . 126
6.14 FMR study - fit result for Co_2MnSi . . . 127
6.15 FMR study - rotational FMR analysis of the Co_2MnAl film . . . 128
6.16 FMR anisotropy energies - second order cubic vs. PMA contribution . . . 130
6.17 FMR study - energy surface plots corresponding to anisotropy results in this study . . . 131
6.18 FMR study - Co_2MnSi linewidth from FMR . . . 133

7.1 Magneto-optical study - separation of anti-symmetric linMOKE and symmetric QMOKE contributions on exemplary measurements of Co_2MnSi . . . 138
7.2 Magneto-optical study - magnetic anisotropy in the remanent linMOKE Kerr rotation for Co_2MnAl, Co_2MnSi, Co_2MnGa, Co_2MnSn . . . 139

7.3 Magneto-optical study - magneto-optical anisotropy in the remanent QMOKE Kerr rotation for Co_2MnAl, Co_2MnSi, Co_2MnGa, Co_2MnSn . . . 140
7.4 Magneto-optical study - magneto-optical anisotropy in the area of the QMOKE Kerr rotation for Co_2MnAl, Co_2MnSi, Co_2MnGa, Co_2MnSn . . . 141
7.5 Magneto-optical study - angle-resolved wavelength dependence of the linMOKE and QMOKE Kerr rotation for Co_2MnSi . . . 143
7.6 Magneto-optical study - angle-resolved wavelength dependence of the linMOKE and QMOKE Kerr rotation from Co_2MnAl . . . 144
7.7 Magneto-optical study - thermal BLS signal intensities for various Co_2MnX compounds at $\lambda = 457\,\mathrm{nm}$ and $\lambda = 532\,\mathrm{nm}$ and the relation to the complex Kerr angle for Co_2MnSi . . . 146

8.1 Linear spin waves - coordinate definitions for the Kalinikos-Slavin disperison relation . . . 153
8.2 Linear spin waves - calculated spin wave dispersion for a Co_2MnSi thin film neglecting anisotropy . 154
8.3 Linear spin waves - recalling the coordinate definitions for the definition of anisotropy tensors . . . 155
8.4 Linear spin waves - illustration of the anisotropy effect on the magnetisation trajectory . . . 156
8.5 Linear spin waves - calculated spin wave dispersion relations in an anisotropic Co_2MnSi film . . . 158
8.6 Linear spin waves - cubic anisotropy induced frequency shift on the DE and BV dispersion . . . 158
8.7 Linear spin waves - group velocity of spin waves in an anisotropic Co_2MnSi thin film . . . 159
8.8 Linear spin waves - cubic anisotropy induced reduction of the group velocity on the DE and BV dispersion . . . 159
8.9 Linear spin waves - cubic anisotropy induced frequency shift on the DE and BV dispersion . . . 160
8.10 Linear spin waves - cubic anisotropy induced frequency shift on the DE and BV dispersion . . . 160
8.11 Nonlinear spin waves - illustration of the three-magnon and four-magnon scattering process . . . 163
8.12 Nonlinear spin waves - estimation of the first and second order Suhl instability ranges for this work 163
9.1 Sample for the spin wave study - thin film stack . . . 171

9.2 Sample for the spin wave study - HRTEM micrograph of a cross section of the thin film sample . . . 172
9.3 Sample for the spin wave study - antenna excitation spectrum . . . 173
9.4 Sample for the spin wave study - schematic of device geometry . . . 174
9.5 µBLS - illustration of the µBLS setup . . . 176

10.1 Spin wave study - Overview excitation spectra at $|\mu_0 H_{\mathrm{set}}| \approx 8.9\,\mathrm{mT}$ and $P_{\mathrm{rf}} = 0\,\mathrm{dBm} = 1\,\mathrm{mW}$ . . . 179
10.2 Spin wave study - Overview excitation spectra at $|\mu_0 H_{\mathrm{set}}| \approx 30.8\,\mathrm{mT}$ and $P_{\mathrm{rf}} = 0\,\mathrm{dBm} = 1\,\mathrm{mW}$ . . . 180
10.3 Spin wave study - direct excitation and dispersion relation . . . 181
10.4 Spin wave study - direct excitation for $|\mu_0 H_{\mathrm{ext}}| = 30.8\,\mathrm{mT}$ . . . 183
10.5 Spin wave study - excitation power sweep for $|\mu_0 H_{\mathrm{ext}}| = 30.8\,\mathrm{mT}$ . . . 184
10.6 Spin wave study - characteristic spectra at $|\mu_0 H_{\mathrm{ext}}| = 30.8\,\mathrm{mT}$ . . . 186
10.7 Spin wave study - onset frequencies at $|\mu_0 H_{\mathrm{ext}}| = 30.8\,\mathrm{mT}$ . . . 187
10.8 Spin wave study - onset frequencies at $|\mu_0 H_{\mathrm{ext}}| = 30.8\,\mathrm{mT}$ . . . 187
10.9 Spin wave study - characteristic power traces at $|\mu_0 H_{\mathrm{ext}}| = 30.8\,\mathrm{mT}$ . . . 190
10.10 Spin wave study - power scaling factor at $|\mu_0 H_{\mathrm{ext}}| = 30.8\,\mathrm{mT}$ . . . 191
10.11 Spin wave study - signature of nonlinear shift in power traces above and below the first excitation maximum at $|\mu_0 H_{\mathrm{ext}}| = 30.8\,\mathrm{mT}$ . . . 193
10.12 Spin wave study - signature of nonlinear shift in power traces at $|\mu_0 H_{\mathrm{ext}}| = 30.8\,\mathrm{mT}$ . . . 194
10.13 Spin wave study - critical power threshold extraction at $|\mu_0 H_{\mathrm{ext}}| = 30.8\,\mathrm{mT}$ . . . 195
10.14 Spin wave study - critical power threshold and onset of (detected) nonlinear modes at $|\mu_0 H_{\mathrm{ext}}| = 30.8\,\mathrm{mT}$ 196
10.15 Spin wave study - frequency shift of the secondary modes in the supercritical regime $|\mu_0 H_{\mathrm{ext}}| = 30.8\,\mathrm{mT}$ 198
10.16 Spin wave study - time resolved measurement overview at $|\mu_0 H_{\mathrm{ext}}| = 8.9\,\mathrm{mT}$ . . . 199
10.17 Spin wave study - time resolved instability onset at $|\mu_0 H_{\mathrm{ext}}| = 8.9\,\mathrm{mT}$ . . . 200

A.1 Appendix - RHEED image sequence of the entire process from sample Q240212 . . . 213
A.2 Appendix - RHEED image sequence of the entire process from sample Q220102 . . . 214

B.1 Appendix - EDXS mapping from the test sample Q240208 216
B.2 Appendix - EDXS mapping from the test sample Q240208 216
B.3 Appendix - EDXS mapping from the non-structured sample Q240212 217
B.4 Appendix - EDXS mapping from the non-structured sample Q240212 218
B.5 Appendix - EDXS mapping from the structured sample Q240212 219
B.6 Appendix - EDXS mapping from the structured sample Q240212 220

E.1 FMR - BB-FMR data analysis study - sample stack used for acquiring the measured data set 253
E.2 FMR - BB-FMR data analysis study - functions used in the derivative divide procedure 254
E.3 FMR - BB-FMR data analysis study - frequency modulation amplitude in derivative divide procedure 255
E.4 FMR - BB-FMR data analysis study - 2D map of raw measured data 257
E.5 FMR - BB-FMR data analysis study - simple background removal - 2D maps 258
E.6 FMR - BB-FMR data analysis study - simple background removal - spectra for $\Delta H^{\mathrm{ref}} = 20\,\mathrm{mT}$ 258
E.7 FMR - BB-FMR data analysis study - simple background removal - fit curves 259
E.8 FMR - BB-FMR data analysis study - simple background removal - results 260
E.9 FMR - BB-FMR data analysis study - simple background removal - spectra for $\Delta H^{\mathrm{ref}} = 60\,\mathrm{mT}$ 260
E.10 FMR - BB-FMR data analysis study - simple background removal - results 261
E.11 FMR - BB-FMR data analysis study - double moving reference background removal - 2D maps . . . 262
E.12 FMR - BB-FMR data analysis study - double moving reference background removal - spectra 262
E.13 FMR - BB-FMR data analysis study - double moving reference background removal - fit curves . . . 263
E.14 FMR - BB-FMR data analysis study - double moving reference background removal - results 264
E.15 FMR - BB-FMR data analysis study - double moving reference background removal - spectra 264
E.16 FMR - BB-FMR data analysis study - double moving reference background removal - results 265
E.17 FMR - BB-FMR data analysis study - final comparison of linewidth results 267

List of Tables

1.1 Heusler materials - summarised reference values of the Co_2Mn-based Heusler compounds in this thesis. 16

2.1 Samples - Co_2MnSi sample series for nanostructuring. 29
2.2 Samples - Co_2MnX sample series for the magneto-optical study. 30
2.3 Samples - bilayer sample series for test purposes and a coupling study. 31
2.4 Samples - seed layer sample series for a side study on the formation of edge dislocations along the interface. 32

4.1 Magnetism concepts - effect of the second order cubic anisotropy contribution. 71
4.2 Magneto-optical interactions - categorisation of magneto-optical and related magnetotransport effects. 90

6.1 VSM study - results from the annealed $MgO/Co_2MnSi/MgO/Al$ thin film sample and the non-annealed $MgO/Co_2MnAl/MgO/Ti$ thin film sample. 117
6.2 FMR study - field direction definitions. 118
6.3 FMR study - Fit results from the rotational FMR analysis of the Co_2MnSi film 124
6.4 FMR study - comparison of the R^2 values from the different analysis approaches on the Co_2MnSi film 125
6.5 FMR study - Fit results from the rotational FMR analysis of the Co_2MnSi film 128
6.6 FMR study - comparison of the R^2 values from the different analysis approaches on the Co_2MnAl film 128
6.7 FMR study - inhomogeneous linewidth and Gilbert damping for the Co_2MnSi film 134
6.8 FMR study - summary of the results for the Co_2MnAl film. 136
6.9 FMR study - summary of the results for the Co_2MnSi film. 136

9.1 Sample for the spin wave study - parameters. 174

D.1 Cubic anisotropy tensor elements N_{xx}, N_{xy} and N_{yy} for the Kalinikos-Slavin dispersion for an in-plane magnetised thin film with the film normal along $[001]_{123}$: (a) for an arbitrary orientation in the film plane defined by the angle φ_{100} to the crystal axis $[100]_{123}$, as well as for two selected equilibrium positions of the magnetisation M_0 in (b) and (c). 252

List of symbols and abbreviations

Character	Name	Specification
E_F	Fermi energy	
$P\,(E_F)$	Spin polarisation at the Fermi energy	
M_S	Saturation magnetisation	in kA/m
M_{eff}	Effective magnetisation	in kA/m
$\mathbf{H}_{ext}$, H_{ext}	External (applied) field	in kA/m
$\mathbf{H}_{eff}$, H_{eff}	Total effective field	in kA/m
F_{ani}, ρ_{ani}, H_{ani}	Anisotropy energy, density and associated effective field contribution	
F_{exch}, ρ_{exch}, H_{exch}	Exchange energy, density and associated effective field contribution	
γ, γ_{LL}, γ_{LLG}	Gyromagnetic ratio	mostly in GHz/T
ω_0	Larmor frequency for effective field	$\omega_0 = \gamma\mu_0 H_{eff}$
ω_H	Larmor frequency for external field	$\omega_H = \gamma\mu_0 H_{ext}$
ω_M	Larmor frequency corresponding to M_S	$\omega_M = \gamma\mu_0 M_S$
A_{exch}	Exchange constant	in J/m, see eq.4.10
D	Exchange stiffness, Spin wave stiffness	in $J \cdot m^2$, see eq.4.10
D_B	Exchange field	in $T \cdot m^2$, see eq.4.10
d	(Film) thickness	
w	(Waveguide) width	
g	(Gap) width	
$\mathbf{k}_{ip}$ (k_{ip})	In-plane wave vector (number)	

Alphabetical Index

anisotropy, 7, 68
  cubic, 69
  easy axis, 70, 72
  hard axis, 70, 72
  magnetocrystalline, 69, 72
  shape, 69
  uniaxial, 72
applications
  magnetic tunnel junctions, 10
  spin valves, 10

crystal structure
  $L2_1$, 8
  $L2_1$, 7

damping, 81
  Eddy currents, 82
  electron scattering, 81
  Foucault's currents, 82
  Gilbert, 75
  interband, 81
  intraband, 81
  Landau-Lifshitz, 75
  magnon-phonon, 83
  radiation, 82
  radiative, 82
  viscous, 76, 81
defects
  chemical, 74
  lattice dislocations, 74
demagnetisation
  energy, 68, 69
  field, 69
  tensor, 69
dipolar
  fields, 68
  interaction, 68
dissipation, 81
domain
  magnetic, 69, 74
  multi-, 74
  nucleation, 74
  pinning, 74

effective
  field, 73
energy
  anisotropy, 70, 72, 74
  demagnetisation, 68, 69, 74
  dipolar, 68
  exchange, 66
  total, 73
  Zeeman, 73
exchange
  biquadratic, 67
  constant, 67, 79
  energy, 66
  Heisenberg, 66
  interaction, 66, 68
  length, 69
  non-Heisenberg, 67
  stiffness, 67

field
  coercive, 74
  effective, 73
  saturation, 74

gyromagnetic ratio, 75

half-metals, 8
  Co_2MnSi, 10
  Co_2MnSi, 7
  implications, 10
  spin polarisation, 10
Heusler compounds, 7
  crystal structure, 7, 8
  full Heusler, 7
  half-Heusler, 7
  $L2_1$ order, 8
  $L2_1$ order, 7
  semi-Heusler, 7
hysteresis, 73, 74

Landau-Lifshitz equation, 75
Landau-Lifshitz-Gilbert, 81
Landau-Lifshitz-Gilbert equation, 75
linewidth
  broadening, 81
  inhomogeneous, 81

macrospin approximation, 73
magnetisation
  dynamics, 75
  oscillations, 75
magnonic crystal, 7
microstructure, 7

oscillators
  vortex oscillators, 7

preface, xii

remanence
  magnetisation, 74

saturation
  field, 74
  magnetisation, 74
scattering
  electron scattering, 81
  interband, 81
  intraband, 81
  magnon-phonon, 83
spin polarisation, 7, 10
spin transfer torque (STT), 10
spin wave
  instability, 162
  perpendicular standing, 79
  scattering, 162
spin waves
  Hamilton formalism, 165
  nonlinear, 165
spin-orbit
  coupling, 69
Stoner-Wohlfarth, 74

Publications

Planned / in preparation — corresponding to the content of the dissertation

2025 **Non-destructive nanostructuring of epitaxial, half-metallic $L2_1$-ordered Co_2MnSi Heusler thin films preserving crystal and chemical ordering**
Corresponding to chapter 3.3 of the dissertation; publication as first author

2025 **Epitaxial Co_2MnSi and Co_2MnAl Heusler thin films with significant first and second order cubic anisotropy**
Corresponding to chapter 6 of the dissertation; publication as first author

2025 **Magneto-optical properties of Co_2Mn-based Heusler compounds: Quadratic magneto-optical Kerr effect and thermal BLS intensity**
Corresponding to chapter 7 of the dissertation; publication as first author

2025 **Low nonlinear threshold and significant nonlinear shift in a microsized, half-metallic Co_2MnSi Heusler waveguide: Towards half-metal magnonics**
Corresponding to chapter 10 of the dissertation; publication as first author in collaboration with IPCMS

Publication as a co-author — in relation with the content of this dissertation

2021/04 **Unveiling transport properties of Co_2MnSi Heusler epitaxial thin films with ultra-low magnetic damping**
C. de Melo, C. Guillemard, A.M. Friedel, V. Palin, J.C. Rojas-Sanchez, S. Petit-Watelot, S. Andrieu
Applied Materials Today **25**, 101174 (2021)

Contributions to published works — outside the frame of this dissertation

2023/04 **Interfacial engineering of ferromagnetism in wafer-scale van der Waals Fe_4GeTe_2 far above room temperature**
H. Wang, H. Lu, Z. Guo, A. Li, P. Wu, J. Li, Z. Sun, P. Li, H. Damas, A.M. Friedel, S. Migot, J. Ghanbaja, S. Petit-Watelot, T. Hauet, J. Robertson, S. Mangin, W. Zhao, T. Nie
Nature Communications **14**, 2483 (2023)

2023/02 **Quantifying Li-content for Compositional Tailoring of Lithium Ferrite Ceramics**
C. Granados-Miralles, A. Serrano, P. Prieto, J.Guzman-Minguez, J.E. Prieto, A.M. Friedel, E. Garcia-Martin, J.F. Fernandez, A. Quesada
Journal of the European Ceramic Society **43**, 8, 3351 (2023)

2022/08 **A Highly Sensitive Magnetic Field SAW Sensor on Metglas**
P. Mengue, O. Elmazria, B. Paulmier, A.M. Friedel, S. Petit-Watelot, T. Hauet, S. Zhgoon, D. Lacour, M. Hehn, S. Hage-Ali
Conference paper: 2022 Joint Conference of the European Frequency and Time Forum and IEEE International Frequency Control Symposium (EFTF/IFCS)

2020/04 **Propagation of Spin-Wave Packets in Individual Nanosized Yttrium Iron Garnet Magnonic Conduits**
B. Heinz, T. Brächer, M. Schneider, Q. Wang, B. Lägel, A.M. Friedel, D. Breitbach, S. Steinert, T. Meyer, M. Kewenig, C. Dubs, P. Pirro, A.V. Chumak
Nano Letters **20**, 6, 4220-4227 (2020)

Anna Maria FRIEDEL, Dipl.-Phys.

annamariafriedel 0000-0002-7523-0375

Professional career

Since 10/2025 — **Post-doctoral researcher.**
RPTU Kaiserslautern-Landau, Kaiserslautern, Germany
Labs: - Prof. Dr. Burkard Hillebrands' group on magnetism,
- Jun.-Prof. Dr. Philipp Pirro's junior group on nanoscaled magnonic hybrids

07/2021 – 09/2025 — **PhD researcher in an international doctorate *(cotutelle internationale)*.**
Institut Jean Lamour, UMR CNRS / Université de Lorraine, Nancy, France
& RPTU Kaiserslautern-Landau, Kaiserslautern, Germany
Labs: - Spintronics and Nanomagnetism team, lead by Prof. Dr. Stéphane Mangin and Assoc.-Prof. Dr. Thomas Hauet,
- Prof. Dr. Burkard Hillebrands' group on magnetism,
- Jun.-Prof. Dr. Philipp Pirro's junior group on nanoscaled magnonic hybrids

09/2022 – 12/2023 — **Teaching assistant.**
Ecole nationale supérieure des Mines de Nancy, Nancy, France

05/2022 – 07/2022 — **Visiting PhD researcher.**
Imdea Nanociencia & CSIC Instituto de Cerámica y Vidrio (ICV), Madrid, Spain
Labs: - Spin Orbitronics group, Imdea Nanociencia, lead by Dr. Paolo Perna,
- Ceramics for Smart Systems team, CSIC ICV, lead by Prof. Dr. José F. Fernandez

05/2021 – 06/2021 — **Junior researcher.**
Institut Jean Lamour, UMR CNRS / Université de Lorraine, Nancy, France
Lab: Spintronics and Nanomagnetism team, lead by Prof. Dr. Stéphane Mangin

11/2016 – 01/2021 — **Student research assistant.**
TU Kaiserslautern, Kaiserslautern, Germany
Lab: Prof. Dr. Burkard Hillebrands' group on magnetism

11/2015 – 12/2016 — **Student research assistant.**
TU Kaiserslautern, Kaiserslautern, Germany
Lab: Prof. Dr. Christiane Ziegler's group on physics and biophysics of complex interfaces

05/2015 – 05/2017 — **Student research assistant.**
Universität des Saarlandes, Homburg, Germany
Lab: Prof. Dr. Norbert Graf's research group on paediatric oncology

Education & Qualifications

07/2021 – 09/2025 — **Doctoral studies** - joint, international doctorate.
Université de Lorraine, France & RPTU Kaiserslautern-Landau, Germany
Degree: Dr. er. nat. (*PhD in physics*), grade: 0.7
Defence: 03 September 2025
Thesis title: *Heusler compounds for magnonic and spintronic applications*
Thesis supervisors: Prof. Dr. Stéphane Andrieu,
Assoc.-Prof. Dr. Sébastien Petit-Watelot,
Jun.-Prof. Dr. Philipp Pirro.

04/2015 – 01/2021 — **Physics degree**, TU Kaiserslautern, Germany.
Degree: Diplom-Physikerin (*equiv. M.Sc. in physics*, 12 January 2021, grade: 1.4)
Thesis title: *Thin film materials with ultralow damping for novel magnonic phenomena (Thesis grade: 1.0)*
Thesis supervisor: Jun.-Prof. Dr. Philipp Pirro.

Education & Qualifications (continued)

01/2020 – 08/2020 — **Research internship for master thesis work.** - *(funded by excellence scholarship)*
Institut Jean Lamour, UMR CNRS / Université de Lorraine, Nancy, France
Lab: Spintronics and Nanomagnetism team, lead by Prof. Dr Stéphane Mangin
Project: Thin film materials with ultralow damping for novel magnonic phenomena
Supervisors: Prof. Dr. Stéphane Andrieu, Assoc.-Prof. Dr. Sébastien Petit-Watelot

04/2018 – 08/2018 — **Extracurricular research internship.**
Ångström laboratoriet, Uppsala University, Uppsala, Sweden
Lab: Division of Materials Physics, lead by Prof. Dr. Björgvin Hjörvarsson
Project: Investigating magneto-optical effects in 3D-magnetoplasmonic structures using Faraday rotation and magneto-optical Kerr effect (MOKE)
Supervisors: Prof. Dr. Vassilios Kapaklis, Dr. Richard Rowan-Robinson

06/2017 – 07/2017 — **Extracurricular research internship.**
University of Alabama, Tuscaloosa, Alabama, USA
Lab: Mewes' Magnetics Laboratory, Center for Materials for Information Technology
Project: Thin film characterization using ferromagnetic resonance (FMR) and magneto-optical Kerr effect (MOKE) techniques
Supervisors: Prof. Dr. Tim Mewes, Prof. Dr. Claudia Mewes, Dr. Jamileh Beik Mohammadi

10/2014 – 03/2015 — **Studies in biophysics**, TU Kaiserslautern, Germany.

09/2012 – 02/2014 — **Studies in computer science**, University of applied sciences Kaiserslautern, Germany.
Extracurricular early university studies during secondary school.

08/2006 – 06/2014 — **Secondary school**, Saarpfalz-Gymnasium Homburg, Germany.
Diploma: Allgemeine Hochschulreife (13. June 2014, grade: 1.5)

03/2012 – 06/2012 — **3-month language study stay**, EF Language School Bournemouth, United Kingdom.

Awards & scholarships

08/2025 — ***Cotutelle de thèse* stipend for bi-national thesis**, Franco-German University, Germany.
Stipend by the Franco-German University (Deutsch-Französische Hochschule / Université Franco-Allemande) covering language courses and mobility expenses.

08/2023 — **Best poster award at the Magnonics 2023 conference.**
One of six awards for the best scientific poster presentations at the conference.

01/2022 — **Prix Universitaire Franco-Allemand Grand'Est 2022.**
French-German award for the best thesis (master's/diploma) in the category of natural sciences / engineering / mathematics / computer science / medicine.

01/2020 - 08/2020 — **Excellence scholarship**, Lorraine Université d'Excellence.
Scholarship for a stay in France to conduct end-of-studies research for the diploma thesis.

06/2017 - 07/2017 — **Scholarship for research internship**, University of Alabama, USA.
Scholarship for a stay in the United States for extracurricular research.

10/2014 - 09/2015 — **Anfängerinnenstipendium**, TU Kaiserslautern.
Scholarship for outstanding first-year female students - one of five students selected from all disciplines in the University.

08/2014 - 07/2024 — **Online-Stipendium**, e-fellows.net.
Online scholarship for material support and networking among outstanding students at all levels. To be renewed with application and evaluation each year.

Third-party funding

Total amount of third-party funding: $4,200

01/2022 – 12/2022 **IEEE Seed Funding - Grant for joint projects by young researchers**
Project title: "Low-Damping Spinel Ferrites for High-Efficiency Spin-Orbitronic Devices (HESIOD)"
Funding provider: IEEE Magnetics Society
Total amount: $10,000, own share: $4,200
Function: Co-applicant; other applicants: C. Granados-Miralles (Instituto de Cerámica y Vidrio, CSIC, Madrid, Spain), I. Arnay (IMDEA Nanociencia, Madrid, Spain)

Academic services, self-administration & community involvement

Conference organisation

2023 Organising committee, IEEE Around-the-Clock Around-the-Globe Magnetics Conference 2023 (online), hosted by the IEEE Magnetism Society.

2022 Organising committee, Ultrafast Magnetism Conference 2022, Nancy, France.

Committee work & further involvement

2023 - 2025 **Student representative**, AG Magnetismus, RPTU Kaiserslautern-Landau.

2020 - 2024 **Mentor for first year students**. RPTU Kaiserslautern-Landau, Germany.

Memberships

German physical society, division of magnetism; IEEE magnetics society

Scientific presentations

Invited talks (2)

06/2023 Workshop on Interdisciplinary Spin Physics, Tohoko University, Sendai, Japan

09/2022 DPG meeting of the condensed matter section, Regensburg, Germany
– Finalist in INNOMAG prize session

Contributed talks (1)

01/2022 MMM/Intermag 2022, New Orleans, Lousiana, USA

Poster presentations (7)

09/2023 Spin Electronic and Nanomagnetism Colloquium 2023, Nancy, France

08/2023 Magnonics 2023, Le-Touquet-Paris-Plage, France
– Best Poster Award

09/2022 Ultrafast Magnetism Conference 2022, Nancy, France

09/2021 DPG meeting of the condensed matter section, online

09/2021 European School on Magnetism, Cluj-Napoca, Romania

08/2019 Joint European Magnetic Symposia, Uppsala, Sweden

06/2019 York-Tohoku-Kaiserslautern Research Symposium, York, United-Kingdom

Scientific publications

Journal Articles

1. C. Granados-Miralles, A. Serrano, P. Prieto, J. Guzmán-Mínguez, J. Prieto, **A. M. Friedel**, E. García-Martín, J. Fernández, and A. Quesada, "Quantifying Li-content for compositional tailoring of lithium ferrite ceramics," *Journal of the European Ceramic Society*, vol. 43, no. 8, pp. 3351–3359, 2023, ISSN: 0955-2219. DOI: 10.1016/j.jeurceramsoc.2023.02.011.

2. H. Wang, H. Lu, Z. Guo, A. Li, P. Wu, J. Li, W. Xie, Z. Sun, P. Li, H. Damas, **A. M. Friedel**, S. Migot, J. Ghanbaja, L. Moreau, Y. Fagot-Revurat, S. Petit-Watelot, T. Hauet, J. Robertson, S. Mangin, W. Zhao, and T. Nie, "Interfacial engineering of ferromagnetism in wafer-scale van der waals Fe_4GeTe_2 far above room temperature," *Nature Communications*, vol. 14, no. 1, p. 2483, Apr. 2023, ISSN: 2041-1723. DOI: 10.1038/s41467-023-37917-8.

3. C. de Melo, C. Guillemard, **A. M. Friedel**, V. Palin, J. C. Rojas-Sánchez, S. Petit-Watelot, and S. Andrieu, "Unveiling transport properties of Co_2MnSi heusler epitaxial thin films with ultra-low magnetic damping," *Applied Materials Today*, vol. 25, p. 101 174, 2021, ISSN: 2352-9407. DOI: 10.1016/j.apmt.2021.101174.

4. B. Heinz, T. Brächer, M. Schneider, Q. Wang, B. Lägel, **A. M. Friedel**, D. Breitbach, S. Steinert, T. Meyer, M. Kewenig, C. Dubs, P. Pirro, and A. V. Chumak, "Propagation of spin-wave packets in individual nanosized yttrium iron garnet magnonic conduits," *Nano Letters*, vol. 20, no. 6, pp. 4220–4227, 2020. DOI: 10.1021/acs.nanolett.0c00657.

Conference Proceedings

1. P. Mengue, O. Elmazria, B. Paulmier, **A. M. Friedel**, S. Petit-Watelot, T. Hauet, S. Zhgoon, D. Lacour, M. Hehn, and S. Hage-Ali, "A highly sensitive magnetic field saw sensor on metglas," in *2022 Joint Conference of the European Frequency and Time Forum and IEEE International Frequency Control Symposium (EFTF/IFCS)*, 2022, pp. 1–2. DOI: 10.1109/EFTF/IFCS54560.2022.9850624.

Teaching experience

Supervision of master's theses

2023 Nicolas Fermon, M1 master thesis, École normale supérieure Paris-Saclay, France.
(*Carried out at RPTU Kaiserslautern-Landau, Kaiserslautern, Germany*)

Supervision of bachelor's theses / research projects

2023 Benjamin Brachmann, 3-months undergraduate project work, RPTU Kaiserslautern-Landau, Germany.

Courses

Acad. Year	University	Course title	Type	Hours
2022/23, 2023/24	École nationale supérieure des Mines de Nancy	Quantum physics	Tutorial course (*Travaux dirigés*)	2h/week, 1 semester/year

Further training in university didactics

01/2023 One-week seminar "Introduction to university teaching", Université de Lorraine, Nancy, France
(*PA1.1 MDD 11 - Initiation à la pédagogie universitaire*)